

Shrestha, Suman Kumar (2000) *Corrosion and erosion-corrosion of High Velocity Oxy-Fuel (HVOF) sprayed NiCrSiB coatings.* PhD thesis.

http://theses.gla.ac.uk/2866/

Copyright and moral rights for this thesis are retained by the author

A copy can be downloaded for personal non-commercial research or study, without prior permission or charge

This thesis cannot be reproduced or quoted extensively from without first obtaining permission in writing from the Author

The content must not be changed in any way or sold commercially in any format or medium without the formal permission of the Author

When referring to this work, full bibliographic details including the author, title, awarding institution and date of the thesis must be given

Glasgow Theses Service
http://theses.gla.ac.uk/
theses@gla.ac.uk

Dedicated to my parents and my wife



UNIVERSITY
of
GLASGOW

Corrosion and Erosion-Corrosion of High Velocity Oxy-Fuel (HVOF) Sprayed NiCrSiB Coatings

A Thesis

Submitted in fulfilment for the degree of Doctor of Philosophy (Ph.D.)

by

Suman Kumar Shrestha, M.Sc. (Hons.), Russia.

Department of Mechanical Engineering,
University of Glasgow,
February, 2000

© Suman Kumar Shrestha, 2000

List of Publications

Electrochemical and Mechanical Interactions during Erosion-Corrosion of a High-Velocity Oxy-Fuel Coating and a Stainless Steel

T. Hodgkiess*, A. Neville and S. Shrestha*

(*Wear*, 233-235, 1999, p.623-634)

*Department of Mechanical Engineering, University of Glasgow, Glasgow G12 8QQ, Scotland.
Department of Mechanical and Chemical Engineering, Heriot-Watt University, Edinburgh, Scotland.

Summary

This research focuses on an investigation of surface coatings of the type NiCrSiB self-fluxing cermet produced by the state-of-the-art High Velocity Oxy-Fuel (HVOF) thermal spraying technique. Two coatings were investigated of the same generic type, supplied by two different commercial coating manufacturers. Detailed coating characterizations were supported by extensive use of light optical and scanning electron microscopes and also an atomic force microscope, X-ray diffraction, Talysurf, Microhardness indenter and also image analysis software.

Pure electrochemical corrosion and the erosion-corrosion behaviour of the coatings in saline aqueous environments have been studied using electrochemical-monitoring techniques. The research also targeted assessing the influence of various parameters such as temperature, time, velocity and solid particle content, coating hardness, porosity and substrate material. The extent and morphology of material deterioration under various environmental conditions have been assessed utilizing the various techniques described in the first paragraph. Correlation between accelerated laboratory tests and the real time behaviour of materials has been successfully made.

Moreover, one of the coatings was subjected to post-spray surface treatments by vacuum sealing with polymer impregnation and high temperature vacuum-furnace fusion and the effect of such post-spray surface modifications on the coating integrity and durability was studied in detail. Evidence was secured of significant potential benefits in terms of erosion-corrosion resistance obtained by the post-spray fusion operation. A standard austenitic stainless steel alloy (UNS S31603) was also investigated in parallel for comparison purposes.

The study provided clear evidence of complex corrosion behaviour of such multiphase coatings and also the crucial role of the corrosion processes in governing the extent and mechanism of erosion-corrosion of the materials. This also enabled the proportions of material losses on a given material attributed to pure corrosion, pure erosion and a synergistic factor to be elucidated. In addition, initial attempts have been made to relate the extent of damage to a hydrodynamic flow pattern of the liquid jet.

Acknowledgements

I am indebted to the following:

- Dr. Trevor Hodgkiess (University of Glasgow) and Dr. Anne Neville (Heriot-Watt University) for their knowledge, guidance and criticisms, without which the collaborative work reported in this thesis, would not have been possible. I also wish to acknowledge their contribution to the three papers, which cover the significant proportion of the thesis.

- The *Committee of the Vice Chancellors and Principles* (CVCP) for *the Overseas Research Student* (ORS) award and the *Faculty of Engineering Research Scholarship* of the University of Glasgow, which have funded this research work.

- The administrative and technical staffs at the department of mechanical engineering for their support during the research period.

- Professor Vladimir Konstantinovich Polykov from the *St. Petersburg State University of Technology and Design*, St. Petersburg, Russia for his advice and switching my mind to become a researcher.

- Aftab for his friendship and help to keep my computer running. Shahid for all the friendship in the office.

- My wife for the support and uncomplaining sacrifice and most of the photographic prints she has done for the thesis.

- My parents for their guidance, support, encouragement, praying and my God who has enabled and sustained me.

Contents

Title page i

List of Publications ii

Summary iii

Acknowledgements iv

Contents v

List of Figures xii

List of Tables xxviii

Definitions xxxii

Symbols and Abbreviations xxxii

List of References

CHAPTER 1. INTRODUCTION

1.1 General Introduction 1-1

1.2 Outline of the thesis 1-6

CHAPTER 2. CORROSION

2.1 Background 2-1

The marine and offshore industry 2-2

2.2 Theoretical considerations of Corrosion Behaviour 2-3

Aqueous corrosion monitoring 2-7

Potentiodynamic Polarisation measurements 2-8

Polarisation resistance 2-9

Electrochemical Impedance Spectroscopy (EIS) 2-11

Passivity 2-13

Types of corrosion

Uniform corrosion 2-15

Localised corrosion 2-15

Intergranular corrosion 2-15

Crevice corrosion 2-16

Pitting 2-18

Bimetallic or Galvanic Corrosion 2-19

Hydrogen Damage 2-20

Flow induced corrosion 2-20

2.3 Corrosion control and prevention 2-22
Design 2-23
Material selection 2-23
Inhibitors 2-24
Coatings 2-25
Thermal Spraying 2-25
Electrochemical protection 2-26
Anodic protection 2-27
2.4 Corrosion of stainless steel 2-28

CHAPTER 3. EROSION-CORROSION

3.1 Introduction 3-1
3.2 Basic hydrodynamics of liquid erosion, mass transfer, cavitation and impingement attack 3-3
Turbulent jet geometry 3-5
Mass transfer 3-6
Cavitation 3-8
Impingement attack 3-9
3.3 Basics of solid erosion 3-10
3.3.1 Influencing factors
Particle movement 3-12
Erosive particles 3-14
Wall material 3-17
3.4 Basics of solid-liquid erosion 3-18
3.5 Aqueous erosion-corrosion interactions 3-25
3.6 Methods for evaluating wear rates 3-27
3.7 General material characteristics 3-31
Liquid flow systems 3-31
Solid and Solid-liquid flow systems 3-35
Dry erosion 3-35
Solid aqueous erosion 3-36

CHAPTER 4. SURFACE ENGINEERING

Introduction 4-1

4.1 A brief review of general thermal spray processes 4-2

Flame Spraying (FS) 4-3

Arc Spraying (AS) 4-4

Atmospheric Plasma Spraying (APS) 4-5

Vacuum Plasma Spraying (VPS) 4-5

Detonation Gun Spraying (DGS) 4-6

High Velocity Oxy-Fuel (HVOF) Spraying 4-7

New Spraying Techniques 4-8

Laser Spraying (LS) 4-8

Underwater Thermal Spraying 4-9

4.2 Application and Industrial Relevance 4-10

High Velocity Oxy-Fuel (HVOF) coatings 4-13

4.3 HVOF technology, process 4-16

HVOF Spray Processing

1. Powder preparation 4-20

2. Surface preparation 4-20

3. Spray process 4-21

HVOF parameters 4-24

Finishing Treatment

Polymer sealing process: 4-25

Heat treatment: 4-26

4.4 Coatings property, morphology 4-27

Density and porosity 4-29

CHAPTER 5. CORROSION AND EROSION-CORROSION OF HVOF SPRAYED CERMET COATINGS

Introduction 5-1

5.1 Corrosion 5-1

5.2 Erosion-corrosion 5-7

5.3 Summary and rationalisation for the experimental program 5-13

CHAPTER 6. MATERIALS, EXPERIMENTAL AND EXAMINATION TECHNIQUES

6.1 Specimen preparation 6-1

6.1.1 Coating manufacture, spray process and parameters 6-2

6.1.2 Mounting and polishing techniques 6-4

6.1.3 Metallographic investigation 6-5

6.2 Corrosion measurement 6-5

6.3 Erosion-corrosion measurement 6-6

6.3.1 Liquid erosion-corrosion measurement 6-6

6.3.2 Solid-liquid erosion-corrosion measurement 6-8

6.4 Examination techniques 6-9

6.4.1 Scanning electron microscopy (SEM) 6-10

6.4.2 Atomic Force Microscopy (AFM) 6-12

6.4.3 Talysurf 6-13

6.4.4 X-ray diffraction (XRD) 6-13

CHAPTER 7. *Coating A* Results

7.1 Powder characterisation 7-1

7.2 Pre-microscopy of coating 7-4

7.3 Corrosion of coating AI and stainless steel

Anodic Polarisation 7-14

As received coating 7-14

Effect of polishing 7-16

Effect of substrate material 7-17

Cathodic Polarisation Test 7-18

Post experimental examination

Examination after anodic polarisation 7-19

Extended exposure test 7-25

7.4 Corrosion of coating AII

Anodic polarisation under static condition 7-30

As received coating 7-30

Effect of polishing 7-30

Examination after anodic polarisation 7-32

Extended exposure test 7-34
Anodic polarisation under liquid impingement 7-41
Galvanic Interaction between Coating and Substrate 7-42
Corrosion of splat particles 7-43
Corrosion of powder particles 7-46
7.5 Liquid and solid-liquid erosion-corrosion of Coating AI
Weight loss measurement 7-47
Anodic polarisation 7-50
Microscopic observations after solid-free liquid impingement. 7-51
Microscopic observations after solid-liquid impingement 7-55
As received coatings 7-62
Cathodic polarisation 7-65
Potentiostatic tests 7-65
Microscopic observations after potentiostatic tests. 7-67
Calculation of pure corrosion 'C' and synergy 'S' values 7-72
7.6 Effect of pre-erosion and effect of pre-corrosion
Experimental procedure 7-75
Effect of pre-corrosion on erosion-corrosion 7-77
Microscopic observations of pre-erosion test 7-78
Microscopic observations of pre-corrosion test 7-80

CHAPTER 8. *Coating B* Results
8.1 Powder characterisation 8-1
8.2 Characterisation of Coating B
Visual examination of as-received coatings 8-4
As-sprayed/vacuum-sealed coating 8-4
Vacuum fused coating 8-6
Hardness measurement 8-11
X-ray diffraction 8-12
8.3 Corrosion of coating BI
Electrochemical corrosion tests at ambient temperature 8-17
Effect of temperature 8-19
Effect of pre-corrosion 8-21
Cathodic polarisation 8-22

Attack Mechanisms 8-23
Microscopy after pre-corrosion tests 8-29
Extended Exposure Tests 8-32
Assessment of Galvanic Interactions between Coating and Substrate 8-37
8.4 High velocity liquid impingement of Coating BI
Electrochemical corrosion behaviour at 18° C 8-40
Effect of continuation 8-44
Effect of high-velocity jet impingement 8-46
Effect of temperature under high-velocity jet impingement 8-48
Microscopic observations after high-velocity impingement 8-52
Observations after 1-hour free impingement at 18°C 8-52
Observation after anodic polarisation 8-56
8.5 High velocity liquid erosion-corrosion of Coating BII
Weight loss measurement 8-67
Anodic polarisation 8-68
Attack mechanisms after erosion-corrosion under high-velocity jet 8-70
Central wear region 8-72
Outer wear region 8-74
8.6 Liquid and solid-liquid erosion-corrosion of Coating BII
Weight loss measurement 8-78
Surface Topography 8-82
Anodic polarisation 8-83
Cathodic protection 8-84
Microscopic observations after solid-free liquid impingement 8-85
Microscopic observations after solid-liquid impingement 8-90

CHAPTER 9.

9.1 Liquid erosion-corrosion of stainless steel with different radii
Objective 9-1
Experimental technique 9-2
Results 9-3
Cathodic polarisation 9-5
Galvanic current measurement 9-5
Microscopic observations after impingement tests 9-6

CHAPTER 10. DISCUSSION

10.1 General 10-1

10.2 Powder characterisation 10-2

10.3 Coating characterisation 10-3

10.4 Post surface modification 10-5

10.5 Specimen preparation 10-6

10.6 Electrochemical behaviour and corrosion mechanism

Electrochemical behaviour of coating A and the stainless steel 10-9

Attack mechanisms of Coating A and stainless steel 10-10

Galvanic Interactions between a coating and the substrate 10-13

Electrochemical corrosion of Coating BI and attack mechanism 10-15

Effect of surface modification in the corrosion behaviour of Coating BI 10-16

Effect of increased temperature in corrosion behaviour of Coating BI 10-17

Effect of pre-corrosion on the electrochemical behaviour of Coating BI 10-18

10.7 Erosion-corrosion behaviour in solid-liquid and liquid impingement

Erosion-corrosion mechanism of Coating AI and UNS S31603 10-18

Erosion-corrosion mechanism of Coating BII 10-22

10.8 Electrochemical and mechanical interactions under 72ms^{-1} high-velocity impingement of Coating BI 10-24

10.9 Effect of pre-erosion and pre-corrosion 10-29

10.10 Different regions under high-velocity liquid jet. 10-30

CHAPTER 11. Concluding Remarks and Recommendations for Future Work 11-1

List of Figures

CHAPTER 1

Figure 1.1 Examples of component failures due to liquid erosion: a) Cylinder from downhole drilling tool (Low alloy high strength steel); b) Throttle-valve of a steam turbine (UNS S31603) (photos printed with permission of Weir Pumps Ltd.)

Figure 1.2 Severe solid-liquid erosion experienced by pump components: a) Grey cast iron pump impeller; b) Impeller vane of stainless steel type UNS S31603; c) Cyclone separator of an austenitic stainless steel type UNS S31603; d) Duplex stainless steel impeller (photos with permission of Weir Pumps Ltd.)

CHAPTER 2

Figure 2.1.1 a) collapse of a nose wheel of a Royal Navy Sea harrier due to bi-metallic corrosion between the stainless steel bearing and the magnesium alloy wheel b) Pitting corrosion in a pipe component.

Figure 2.2.1 Metal corrosion at the surface in aqueous environment.

Figure 2.2.2 Schematic diagram of a three-electrode electrochemical cell: R-reference electrode, W-working electrode, A-auxiliary electrode

Figure 2.2.3 A schematic diagram of determining i_{corr} by Tafel extrapolation method.

Figure 2.2.4 Concentration polarisation effect slows down the cathodic reaction

Figure 2.2.5 A schematic model of a corroding electrode. (a) Simple equivalent circuit. (b) A Nyquist plot of impedance data in which real (x-axis) and imaginary (y-axis) components of impedance

Figure 2.2.6 Ashworth's schematic representation of a corrosion system

Figure 2.2.7 Electrochemical representation of active passive behaviour and loop formation; E_b - Breakdown potential; E_r - repassivation potential; A- area of hysterisis loop; i_{max} – maximum current density.

Figure 2.2.8 Localised attack at grain boundaries of metal

Figure 2.2.9 The Fontana-Greene mechanism of crevice corrosion (a) Initial conditions: corrosion occurs over whole of the metal surface. (b) Final conditions: metal dissolution occurs only inside the crevice where acidity increases, concentration of chloride ion increases, and the reaction becomes self-sustaining (Trethewey and Chamberlain, 1995).

Figure 2.2.10 The pitting mechanism under a water droplet due to differential aeration (a) General corrosion over the whole of the wetted metal surface depletes the oxygen levels in the adjacent electrolyte, (b) Longer diffusion path for oxygen to reach the central area makes this the anode. Metal dissolution occurs in the centre of the droplet and reaction of metal ions with hydroxyl ions formed at the edge generates a ring of rust around the corrosion pit.

Figure 2.2.11 A possible site for galvanic corrosion within coupling of two metals

Figure 2.2.12 Schematic polarisation curves showing depolarised oxygen-reduction in flowing systems

Figure 2.3.1 Ashworth's schematic diagram of a corrosion control system

Figure 2.3.2 Relative corrosion rates in moving, aerated seawater at ambient temperature.

Figure. 2.4.1 The effect of composition and microstructure on some forms of localised corrosion of stainless steels (Ylasaari et al., 1997)

CHAPTER 3

Figure 3.1.1 Classification of flow-induced corrosion.

Figure 3.2.1 A fine liquid jet impinging on a metallic surface (in laboratory test).

Figure 3.2.2 a) Comet pit attack on UNS S31603 stainless steel in rapid laboratory test (after anodic polarisation at 50°C, pH = 8.2, 72ms^{-1}) under solid-free liquid (artificial seawater) impingement test; and b) streams of comet pits on UNS S31603 stainless steel pipe after 4 weeks' service in a paper mill starch line at 80°C, pH = 9.1, 0.6-1ms^{-1} flow velocity, arrows showing liquid flow directionality

Figure 3.2.3 Submerged jet also called as free turbulent jet impinging onto a horizontal solid plate, showing typical velocity profiles in the main stream and the radial wall jet region (Davies, 1972; Rajaratnam, 1976)

Figure 3.2.4 Erosion-corrosion in a) pump casing, b) pipe elbow.

Figure 3.3.1.1 (a) Schematic diagram showing the influence of impact angle on erosion rate in the case of ductile and brittle material; (b) variation of erosion rate with particle size at different impact velocities; (c) influence of impact angle on erosion rate in the case of spherical and angular particles; (d) influence of flux rate on the erosion rate (Sundarrajan and Roy, 1997).

Figure 3.3.1.2 Erosion rates of 1020 steel by calcite, apatite, SiO_2, Al_2O_3 and SiC (Levy, 1995).

Figure 3.4.1. Solid-liquid erosion in a pipe bend

Figure 3.4.2 Effect of approach angle in wear rate of a ductile metal α_1, α_2 being the approach angles (Wilson, 1995).

Figure 3.4.3 Diagram showing the forces, which can act on a particle in contact with a solid surface (Hutchings, 1992)

Figure 3.4.4 Solid particle trajectories of two-phase flow a) in gas stream (Humphrey, 1990); (b) in liquid (water) stream (Benchaita et al., 1983).

Figure 3.4.5 a) The variation of collision efficiency with viscosity and; b) The variation of impact velocity with viscosity (Clark, 1991).

Figure 3.4.6 Erosion rate of aluminium at an impact velocity of $4.5ms^{-1}$ as a function of impact angle α: (a) aqueous sand slurry erosion; (b) air-borne sand erosion.

Figure. 3.6.1 A schematic diagram of a sand and erosion probe.

Figure 3.7.1 Mass loss vs. exposure duration in a water tunnel (SUS-stainless steel; S-carbon steel; C-brass; F-armco iron; A-aluminium) (Sakamoto et al., 1995b)

Figure 3.7.2 Effect of cavitation on free corrosion potential of duplex stainless steel in seawater (Al-Hashem, 1997).

Figure 3.7.3 Variation of protection efficiency of AISI321 as a function of applied potential in $10\%H_2SO_4$ + 15% corrundum sand at $5ms^{-1}$ (Yao et al., 1995).

CHAPTER 4

Figure 4.1 Methods of surface engineering (Hutchings, 1992)

Figure 4.1.1. Schematic diagrams of flame spraying (a) wire form (b) powder form.

Figure 4.1.2. A schematic diagram of arc spraying; 1, carrier gas; 2, torch outer shield; 3, stream of molten particles; 4, electric arc; 5, electrode wires; 6, substrate

Figure 4.1.3. A schematic diagram of a plasma spraying gun.

Figure 4.1.4. A schematic diagram of a vacuum plasma spraying. 1, working gases inlet; 2, anode; 3, vacuum environment; 4, transferred arc generator; 5, powder injection port; 6, plasma arc generator.

Figure 4.1.5. A schematic diagram of oxygen-fuel detonation gun, D-Gun™ (Tucker and Ashary, 1995).

Figure 4.1.6 A schematic diagram of a High Velocity Oxy-Fuel (HVOF) gun (Irving et al., 1993)

Figure 4.1.7 A schematic diagram of underwater spraying with the HVOF Gun

Figure 4.2.1 Application of thermal spray coating on automotive component (left) (Huchin, 1998) and a plasma gun spraying a cylinder (right).

Figure 4.2.2 Part of a flexographic machine. 1, anilox roll; 2, doctor blade; 3, ink container; 4, printing roll

Figure 4.2.3 Valve balls, flow bore up to 300-400mm a) uncoated and b) coated in Co-based alloy, HRC 45; c) valve gates with flow bore up to 165mm coated in Ni-based alloy, HRC 50; d) valve needle for use in steam generation coated with Ni-based alloy containing WC, using a dual process of high pressure HVOF and subsequent vacuum furnace fusion (Photographs kindly supplied by Pro-Vacuum Ltd.).

Figure 4.3.1 The closed loop of integrated research in Coating Technology (Jacobson and McGuire, 1983)

Figure 4.*3.2* The evolution of HVOF spray guns (Thorpe and Richter, 1992)

Figure 4.3.3 JP-5000 high pressure HVOF system

Figure 4.3.4 Principal stages in HVOF spray processing

Figure 4.3.5 A schematic diagram of the atomisation process.

Figure 4.3.6 Schematic diagrams of automated HVOF spray a) on static component, b) on cylindrical component and c) formation of lamellar splats.

Figure 4.3.7 LaserStrobe ™ for flow visualisation in HVOF spraying process.

Figure 4.3.8 Bond strengths of various thermal spray techniques (Pro-Vacuum Ltd.), figures in thousand psi (1MPa ~ 145 psi)

Figure 4.4.1. A schematic diagram illustrating material characteristics of a thermal spray coating.

Figure 4.4.2 Microhardness of various thermal spray systems

Figure 4.4.3 A schematic of various types of pores in a thermal sprayed coating.

CHAPTER 5

Figure5.2.1 a) Effect of sand concentration on material loss rate at flow velocity 14.3ms^{-1} (Bjordal et al., 1995a); b) Effect of circumferential velocity on material loss (Bjordal et al., 1995b).

CHAPTER 6

Figure 6.1.1 Samples assembled for HVOF spraying.

Figure 6.1.2.1 Schematic diagrams of a working electrode a) for static corrosion test painted with lacomit varnish; and b) for impingement test with an araldite strip to seal the coating/substrate interface.

Figure 6.3.1.1 a) a schematic diagram of a liquid jet impingement rig comprising a three-electrode cell: where, R-reference electrode, A-auxiliary electrode, W-working electrode,VM-voltmeter, AM-ammeter, and b) same liquid jet impingement rig.

Figure 6.3.2.1 a), b) Solid-liquid impingement rig, where A-auxiliary; W-working; and R-reference electrodes; c) schematic view of a nozzle made of high wear resistant Nylon.

Figure 6.4.1 Point analysis of the sample (Engel and Klingele, 1981)

Figure 6.4.2 A schematic diagram of atomic force microscope (AFM

Figure 6.4.3 a) Principles of a Talysurf; b) profilometric trace of a surface, where the peaks and spacing between them are distorted due to difference in horizontal and vertical magnifications (Sarkar, 1977)

CHAPTER 7

Figure 7.1.1 SEM micrograph showing gas atomised powder particles possessing rough and smooth textures

Figure 7.1.2 Split SEM micrograph of a polished single powder particle (left) secondary electron and (right) back scattered electron images.

Figure 7.1.3 XRD pattern of *Coating* A powder

Figure 7.2.1 Back-scattered SEM cross sectional image of a polished as-received *coating A*, showing splat lamellae, micro roughness of the as-sprayed layer and a very little coating porosity.

Figure 7.2.2 Optical micrographs: a) abundance of several splats with metal matrix; b) showing: (top left) intersplat void; (bottom left) possible pull out during polishing; and (right) boundary void of fully unmelted powder particle.

Figure 7.2.3 A highly porous WC/CoCr coating with a slight interfacial separation.

Figure 7.2.4 Back scattered SEM image of polished surface of as-received coating AI.

Figure 7.2.5 a) Split SEM image of *Coating* AII showing black globular and tiny grey hardphase particles embedded in the NiCrFe matrix; b) split SEM image of above tiny grey hard particles; c) back-scattered image showing several clear splats (1) containing many black hard phase particles (2, 3) containing mainly tiny grey hard phase particles.
Figure 7.2.6 XRD patterns of *Coating* AI
Figure 7.2.7 XRD patterns of *Coating* AII
Figure 7.2.8 AFM image of Coating AI showing hardphase particle protruding out from the surface.

Figure 7.3.1 Anodic polarisation of a stainless steel UNS S31603 (ground to 1200 grit) and as-received coating compared to 'active' corrosion behaviour of carbon steel in 3.5% NaCl at 18±2°C (arrows showing forward and reversed scan of the polarisation curve).
Figure 7.3.2 Stainless steel showing higher initial current density in a passive region E_b-E_{corr} and a scatter in breakdown potential.
Figure 7.3.3 Replicate experiments on polished surfaces of Coating AI with stainless substrate showing no repassivation behaviour manifested by no intersection between the forward and reversed scans shown by arrows.
Figure 7.3.4 Effect of polishing on coating AI/ss, resulting reduction in E_b and E_{corr}.
Figure 7.3.5 Expanded forward scans of as-received coating AI with carbon steel and stainless steel substrates.
Figure 7.3.6 Cathodic polarisation of as-received *Coating* AI and UNS S31603 (1200 grit) at 18°C.
Figure 7.3.7 Corrosion mechanism of the *Coating* AI: a) polished surface of the surface prior to polarisation test; b) crevice corrosion after anodic polarisation in 3.5%NaCl at 18°C; c) macro-pit due to splat dislodgement; and d) micro-pits due to removal of hard particles after polarisation
Figure 7.3.8 Crevice corrosion mechanism in the stainless steel: a) severe crevice under the lacomit strip; b) higher magnification of the crevice showing intergranular attack; c) pitting inside the crevice.
Figure 7.3.9 Pitting in a stainless steel: a) low magnification SEM image showing several pits on the surface after anodic polarisation at ambient temperature; b) higher magnification of the above pits; c) intergranular attack within the pit.

Figure 7.3.10 a) Corrosion of the coating AI after 2 weeks exposure to 3.5% NaCl solution; b) several splats corroded in the exposed area; c) spall of splats after corrosion attack around the splat boundary; d) severe crevice corrosion of the coating under the lacomit strip.

Figure 7.3.11 a) Crevice corrosion; and b) pitting at exposed area of stainless steel UNS S31603 after 1 month natural exposure to 3.5% NaCl solution at ambient temperature.

Figure 7.4.1 Anodic polarisation of as-received Coating AII in static 3.5% NaCl, 18°C.

Figure 7.4.2 Anodic polarisation of coatings AII/ss ans AII/cs after polishing.

Figure 7.4.3 Comparison of breakdown potentials of as-received and polished surfaces after anodic polarisation in 3.5% NaCl solution at 18°C.

Figure 7.4.4 a) Crevice attack at the lacomit/coating interface; b) corrosion of matrix more pronounced near hard [articles; c) macro-pitting after splat loss; and d) micro-pitting due to hard particles dislodgement of coating AII after anodic polarisation in 3.5% NaCl solution at 18 °C.

Figure 7.4.5 a) Polished surface of coating AII before experiment; b) corrosion attack after 1 week; c) 2 weeks; d) 3 weeks; and e) 1-month of free immersion in 3.5% NaCl solution at 18°C.

Figure 7.4.6 General corrosion of exposed surface after 1 month exposure in 3.5% NaCl solution at ambient temperature (specimen was cleaned with Clarke's solution and washed ultrasonically).

Figure 7.4.7 Crevice region under the lacomit strip showing: a) Splat boundary attack around individual splat particle; b) macropits left after dislodging of above splats; c) undermining splat boundary attack of next layer particle.

Figure 7.4.8 Micro pitting due to loss of hard particles and dislocation around splat boundary at exposed area of the sample after 1-month free corrosion.

Figure 7.4.9 a) Corrosion attack initiated in a particle with abundant tiny grey hardphase particle; and b) higher magnification of above splat showing preferential dissolution of matrix '2' around grey Mo rich hardphase particle '1'.

Figure 7.4.10 Anodic polarisation of as-received and polished surfaces of the coating AII under liquid impingement (3.5% NaCl, 17ms^{-1}, 18°C).

Figure 7.4.11 Severe corrosion attack at coating/substrate interface after 1-week immersion in 3.5% NaCl solution at 18°C.

Figure 7.4.12 a) Particle splats of a polished specimen prior to corrosion test marked with diamond indentation 'd_6'; and b) same particle splats after 2-weeks free corrosion in 3.5% NaCl solution at ambient temperature.

Figure 7.4.13 Individual powder particles embedded in a cold mounting resin.

Figure 7.5.1. Average weight loss trend during a) solid-free liquid; b) solid/liquid impingement at 17ms^{-1}, 18°C and 3.5% NaCl solution; and column charts showing total weight loss 'TWL' and weight loss due to pure erosion 'E' under CP: c) after 6 days of liquid impingement; d) after 1 hour solid/liquid impingement.

Figure 7.5.2. Anodic polarisation in liquid and solid/liquid impingement tests (Replicate tests conducted are shown in

Figure 7.5.3 Comet pits on coating (a) after 6 days solid-free liquid impingement; (b) after anodic polarisation and stainless steel (c) after 6-days solid-free liquid impingement; (d) after anodic polarisation.

Figure 7.5.4 a) Coating showing comet pits, splat boundary attack and preferential attack around hard phase particles after 6 days liquid impingement; b) comet stream emanating from hard particle/matrix interface; and c) deep pit at head of one of above comets after removing corrosion product with Clarke's solution.

Figure 7.5.5 Sulphide inclusion emanating from the comet head directing towards the liquid flow and several tiny pits surrounding it on the free surface of the stainless steel specimen.

Figure 7.5.6 a) Wear scars after 2 hours solid/liquid impingement on coating AI (left) and stainless steel (right); b), c) Higher magnifications of above wear scars of stainless steel and coating respectively showing smooth and rough surfaces.

Figure 7.5.7 Talysurf traces of *Coating* AI and stainless steel after 2-hours of free solid/liquid impingement (800ppm silica sand).

Figure 7.5.8 In central wear scars of (a) stainless steel; and (b) coating AI after 1 hour solid/liquid impingement.

Figure 7.5.9 SEM micrographs of outer region; a) coating and b) stainless steel.

Figure 7.5.10 Optical micrograph showing cross-sectional view of outer region of a stainless steel specimen after 1-hour solid/liquid impingement showing plastically deformed craters.

Figure 7.5.11 Micrographs of a) coating AI; and b) stainless steel at a distance of 5mm away from the centre after anodic polarisation under solid/liquid impingement

Figure 7.5.12 a) Optical micrograph showing macro pitting due to chunk removal; and b) SEM micro graph showing micro pitting due to micro-galvanic attack at the hard particle/matrix interface.

Figure 7.5.13 SEM micrographs a) craters with raised lips; b) deep groove at central wear region; and c) severe skidding tracks at higher shear zone of stainless steel after anodic polarisation under solid/liquid impingement.

Figure 7.5.14 a) Anodic polarisation curves of as-received and polished surfaces under liquid impingement; b) Average weight losses from replicate experiments of as-received and polished surfaces after 1-hour solid/liquid impingement in 3.5% NaCl,18°C, 17ms^{-1}

Figure 7.5.15 Cross section showing fragments of material detaching from the surface of as-received coating after 1-hour solid/liquid impingement.

Figure 7.5.16 Polishing of as-sprayed surface by sand particles and smoothening of central wear region of as-sprayed surface after 1-hour solid/liquid impingement.

Figure 7.5.17 Cathodic polarisation of coating AI under static and under solid/liquid impingement conditions: a) linear; and b) logarithmic (E_h - hydrogen evolution potential; E_p - cathodic protection potential).

Figure 7.5.18 Cathodic currents of *Coating* AI and stainless steel under liquid impingement with 2-days CP.

Figure 7.5.19 Cathodic currents of coating AI and stainless steel under solid/liquid impingement.

Figure 7.5.20 Colour film formed on a) *Coating* AI; and b) stainless steel after 2-days CP under liquid impingement.

Figure 7.5.21 a) Calcium rich deposit formed during liquid impingement under CP of 2 days; b) comets emanating from the surface beneath the deposit at the outer region and; c) thickening of deposit after 6 days of CP.

Figure 7.5.22 Breaking of coloured films a) coating; and b) stainless steel under 1-hour CP at a distance of 5mm from centre during solid/liquid impingement.

Figure 7.5.23 Silica sand type A: a) before test; and b) after 3 hours of solid/liquid impingement in 3.5% NaCl solution.

Figure 7.5.24 Distribution of sand particle type A before and after 3 hours test

Considering bulk composition of the coating from Table 7.2.1 we can find average atomic weight and average charge of the coating.

Figure 7.5.25 Cathodic and anodic polarisation curves of *Coating* AI under solid/liquid impingement.

Figure 7.6.1 A schematic diagram of solid/liquid impingement rig.

Figure 7.6.2 a) Static anodic polarisation curves of polished and pre-eroded surfaces of *Coating* AII; and b) the same expanded to a current density of $100\mu A/cm^2$.

Figure 7.6.3 Anodic polarisation curves under solid/liquid condition of as-polished and 5-week pre-corroded surfaces of Coating AII.

Figure 7.6.4 a) Central wear scar after 1-hour solid/liquid impingement; and b) same at higher magnification showing macro pitting.

Figure 7.6.5 Region 2mm away from the centre: a) after 1-hour solid/liquid impingement without polarisation; and b) same region after anodic polarisation in static condition.

Figure 7.6.6 Wear scars of the coating after anodic polarisation under solid/liquid impingement of a) as-polished; and b) 5-week pre-corroded surfaces.

Figure 7.6.7 a) Central wear region of the coating after anodic polarisation under solid/liquid impingement; b) Central region under the impinging jet of 5-week pre-corroded surface after 1-hour free solid/liquid impingement; and c) the central region of the 5-week pre-corroded surface after anodic polarisation under solid/liquid impingement.

CHAPTER 8

Figure 8.1.1 a) SEM micrograph showing water atomised powder particles possessing rough and smooth textures; b) back-scattered SEM image of a polished powder particle.

Figure 8.1.2 XRD pattern of *Coating* B powder.

Figure 8.2.1 a) Back scattered cross sectional SEM image of sprayed/sealed coating; b) coating defects due to inter lamellae void, splat boundary separation, micro-void in the particle splat; and c) back scattered image of polished surface showing black globular hard phase particles.

Figure 8.2.2 a) Back scattered cross sectional SEM image of fused coating BII; b) distribution of dark acicular hard particles; and c) distribution of Mo rich blocky white '3' particles .

Figure 8.3.7 Crevice corrosion of the vacuum-fused coating under the central lacomit strip after anodic polarisation in static seawater at: a) 18°C; and b) 50°C.

Figure 8.3.8 Back-scattered SEM micrographs of vacuum-fused coating after anodic polarisation at 50°C: a) preferential matrix dissolution under crevice; and b) micropitting at exposed region.

Figure. 8.3.9 Light optical micrographs of the sprayed coating after 5-days pre-corrosion: a) without anodic polarisation; and b) after anodic polarisation.

Figure. 8.3.10 Light optical micrographs of the vacuum-fused coating after 5 days pre-corrosion: a) without anodic polarisation; and b) after anodic polarisation.

Figure 8.3.11 a) Corrosion product on sprayed coating after 2 weeks of immersion in static seawater at 18°C; and micropitting on vacuum fused coating after the same period of exposure.

Figure 8.3.12 Light optical micrographs of a) sprayed; b) fused; and c) UNS S31603 after 1-month free immersion in static seawater at 18°C (U- under lacomit strip; C-crevice; E-exposed area).

Figure 8.3.13 Secondary SEM micrographs of the as-sprayed coating showing a) severe crevice attack under the lacomit strip; b) corrosion attack at exposed surface; and c) micropitting due to fall of Cr rich hardphase particles on the exposed surface.

Figure 8.3.14 a) Severe crevice under the lacomit strip; and b) preferential dissolution of the matrix surrounding the hard particles of vacuum-fused coating after 1-month immersion in static seawater at 18°C.

Figure 8.3.15 SEM micrographs showing severe corrosion attack at coating/substrate interface: a) as-sprayed; and b) vacuum-fused coatings after 1-month immersion in artificial seawater at 18°C.

Figure 8.3.16 Light optical micrographs of a) sprayed; and b) fused coating after polishing 1-month corroded cross sections in diamond suspension.

Figure 8.4.1 Anodic polarisation results of the polished surfaces under high-velocity seawater jet impingement (18/72 refers to 18° and 72ms^{-1}): a) full scan; and b) forward scan with maximum current density of 100μA/cm^2.

Figure 8.4.2 Scattering of a) E_{corr}; and b) E_b during anodic polarisation under high velocity impingement of seawater at 18°C.

Figure 8.4.3 Anodic polarisation showing the effect of continuation: a) as-sprayed; b) vacuum-sealed; c) vacuum-fused coatings; and d) stainless steel UNS S31603.

Figure 8.4.4 Reduction of breakdown potential 'E_b' of polished surfaces of the materials after being imposed a high-velocity impingement of seawater jet at18°C.

Figure 8.4.5 Anodic polarisation of polished surfaces under static and high velocity liquid impingement in seawater at 18°C: a) sprayed; b) sealed; c) fused coatings; and d) UNS S31603.

Figure 8.4.6 Anodic polarisation results showing the difference erosion-corrosion behaviour at 18 and 50°C, 72ms^{-1}: a) sprayed; b) sealed; c) fused coatings; and d) UNS S31603 all in polished condition.

Figure 8.4.7 Forward scans from anodic polarisation results under high-velocity 72ms^{-1} impingement at 50°C a) polished; and b) as-received surfaces of the coatings.

Figure 8.4.8 Comparison of breakdown potentials 'E_b' of the polished surfaces.

Figure 8.4.9 Light optical micrographs of central wear regions under the jet on polished surfaces of: a) UNS S31603 (unsubmerged); b) UNS S31603 (submerged); c) sprayed; and d) sealed coatings (unsubmerged) after 1-hour high-velocity 72ms^{-1} seawater jet impingement at 18°C.

Figure 8.4.10 SEM micrographs of the central wear region after 1-hour impingement in unsubmerged condition: a) back scattered image showing splat boundary attack, flaking of chunks and crack propagation; and b) secondary image showing material removal on the sprayed coating; c) ductile ploughing of the matrix on the fused coating with raised lips from the crater at 72ms^{-1}.

Figure 8.4.11 Corrosion attack at outer region of the specimen a) sprayed; b) sealed; c) fused coatings; and d) UNS S31603 after 1-hour high-velocity seawater jet impingement and anodic polarisation at 18°C.

Figure 8.4.12 Corrosion attack on sprayed/sealed coating after anodic polarisation under 72ms^{-1} impingement at 18°C: a) Cracking and macropits due to dislodgement of chunk materials (central region); b) crack propagation from the existing pit (central region); c) attack at the hardphase/matrix interface; and d) crevice corrosion.

Figure 8.4.13 a) Optical micrograph showing severe crevice corrosion under the araldite strip; and b) SEM micrograph of the same region showing corrosion mechanism associated with preferential dissolution of the matrix leaving the unsupported hardphase particles resulting in their dislodgement at 18°C.

Figure 8.4.14 Corrosion attack at the outer region after anodic polarisation at 72ms^{-1} at 50°C: a) sprayed; b) sealed; c) fused coatings; and d) UNS S31603.

Figure 8.4.15 a) Severe matrix corrosion; and b) comet pit; c) severe crevice corrosion on the surface of a fused coating; and d) comet attack on the stainless surface after anodic polarisation at $72ms^{-1}$ and 50°C.

Figure 8.5.1 Average weight loss after 6 days solid-free liquid impingement under $72ms^{-1}$ jet velocity and 18°C.

Figure 8.5.2 a) Anodic polarisation of *Coating* BII (on stainless steel substrate) after 2-days high-velocity impingement at $72ms^{-1}$ and 18°C; b) expanded anodic polarisation of the same; and c) Tafel extrapolation of the same; and d) reference Tafel extrapolation plots for *Coating* BI (on carbon steel substrate) from anodic polarisation results performed after 1-hour high-velocity impingement.

Figure 8.5.3 SEM micrographs showing damage under central jet after 6-days of solid-free $72ms^{-1}$ impingement without polarisation: a) sprayed coating; b) fused coating; and c) UNS S31603 in submerged condition.

Figure 8.5.4 Higher magnification SEM images of central region of the sprayed coating after 6-days free impingement showing a) corrosion product emanating from a macropit and crack propagation; b) corrosion attack around several splat particles.

Figure 8.5.5 SEM images showing central wear region of a) vacuum fused coating after 6-days free-impingement; b) pitting corrosion within the local pit (anode) after 2-days free-impingement and anodic polarisation; and c) UNS S31603 after 6-days of solid-free liquid impingement at $72ms^{-1}$ jet velocity and normal impact.

Figure 8.5.6 Corrosion attack at outer region 5mm away from the centre; a) macro loss due to comets on as-sprayed coating; and b) micro loss due to micropitting on vacuum-fused coating after 2-days of high velocity liquid impingement plus anodic polarisation.

Figure 8.5.7 a) Stream of comets at region 5mm away from the centre showing middle region 'M' and outer region 'O'; b) higher magnification of one of the comet heads from region 'O' showing deep pit; and c) higher magnification of the depressed region 'M' showing intergranular attack on UNS S31603 after 2-days of impingement plus anodic polarisation.

Figure 8.5.8 SEM secondary image of a skidding track (low angle attack) on UNS S31603 at outer region after 2-days of solid-free high velocity liquid impingement.

Figure 8.6.1 Total weight loss (TWL) of polished surfaces under solid-free liquid impingement ($17ms^{-1}$, 18°C, 90° impingement).

Figure 8.6.2 Weight loss trend of HVOF polished coatings under 800 ppm solid-liquid impingement in 3.5%NaCl at 18°C.

Figure 8.6.3 Weight loss of coatings in as-received and polished conditions after 3-hours solid-liquid impingement.

Figure 8.6.4 Talysurf traces under central wear scars after 4-hours solid-liquid impingement with CP.

Figure 8.6.5 Anodic polarization in impingement tests ($17ms^{-1}$, 18°C, 3.5% NaCl salt-water, pH 8).

Figure 8.6.6 Corrosion current densities of the coatings under solid-free liquid and solid-liquid impingement conditions.

Figure 8.6.7 Cathodic currents of the as-sprayed and vacuum-fused coatings under solid-liquid impingement.

Figure 8.6.8 Light optical micrograph of a) as-sprayed; and (b) vacuum fused coatings after 6-days solid-free liquid impingement under jet velocity of $17ms^{-1}$.

Figure 8.6.9 Comet shaped attacks on coatings after solid-free liquid impingement under jet velocity of $17ms^{-1}$.

Figure 8.6.10 Corrosion attack on sprayed coating after 6-days of solid-free liquid impingement under $17ms^{-1}$ jet velocity at 18°C: a) attack at particle splat boundaries; b) comet-shaped corrosion product emanating from underneath the particle; c) macropit at comet head due to splat dislodgement; d) deep pit at the comet head; and e) micropitting

Figure 8.6.11 Back-scattered SEM micrographs of the vacuum-fused coating showing: a) micropitting on the exposed surface; and b) micropitting mechanism due to loss of hard particles after 6-days of solid-free liquid impingement ($17ms^{-1}$, 18°C).

Figure 8.6.12 Back-scattered SEM micrographs of a) as-sprayed; and b) vacuum-fused coatings after 6-days of solid-free liquid impingement ($17ms^{-1}$, 18°C) under cathodic protection (CP) at -800mV SCE.

Figure 8.6.13 Central wear scars after 1-hour sand-liquid impingement: a) on the as-sprayed coating; b) vacuum-fused coating; c) higher magnification of 'a' showing large holes; and d) higher magnification of 'b' showing smoother surface.

Figure 8.6.14 Secondary SEM micrographs of central wear region: a), b) as-sprayed; and c) vacuum-fused coating after 1-hour sand-liquid impingement.

Figure 8.6.15 Secondary SEM micrographs showing material removal mechanism at low angle impingement: a), b) sprayed/sealed; and c) vacuum-fused coatings under sand-liquid impingement ($17ms^{-1}$, 18°C).

Figure 8.6.16 Material loss on the sprayed/sealed coating associated with particle splat boundary attack at outer region.

CHAPTER 9

Figure 9.1 a) assembly of concentric specimens: central 'C', outer 'O' mounted in a non-conductive epoxy resin; b) schematic diagram of the liquid impingement rig, P_1 - low pressure pump, P_2 - high pressure pump.

Figure 9.2 Anodic polarisation results under solid-free impingement: a) $17ms^{-1}$; b) $72ms^{-1}$; and c) static condition in 3.5% NaCl solution at 18°C.

Figure 9.3 Cathodic polarisation under solid-free liquid impingement at $17ms^{-1}$.

Figure 9.4 Galvanic current between inner and outer specimens recorded during 3 hours of solid-free liquid impingement ($72ms^{-1}$) at E_{corr}.

Figure 9.5 Corrosion attack on central specimen after anodic polarisation under impingement of $17ms^{-1}$.

Figure 9.6 Anodic polarisation under 72ms-1 impinging velocity: a) optical micrograph of central wear region; b) higher magnification of the central region showing tiny pits and ductile ploughing; c) pitting of outer specimen.

Figure 9.7 Optical micrograph showing pitting attack on central specimen after anodic polarisation in static condition.

CHAPTER 10

Figure 10.3.1 Overlapping of two powder particles different in hardphase content.

Figure 10.3.2 Cross-sectional schematic representation of splat boundary and inter-lamellae void formed during coating formation.

Figure 10.4.1 Schematic diagram of the HVOF sprayed coating with polymer sealant. The sealant is shown in light grey colour for highly exaggerated schematic representation.

Figure.10.5.1 Vacuum fused coating showing anodic polarisation results with sealed and unsealed edges in high-velocity seawater jet impingement test at 72ms^{-1}, 18°C (coating was applied onto a carbon steel substrate).

Figure.10.5.2 Cross section view of an as-sprayed coating showing severe corrosion attack at the coating/substrate interface after anodic polarisation in static seawater at 18°C due to leakage of corrosive fluid through a pinhole on lacomit strip.

Figure 10.6.1 Stage I- Plan surface as-polished, Stage II - Attack around splat boundary 'B' of a splattered particle, corrosion attack initiation around hardphase particles 'hp' and matrix 'M' starts changing colour into light brown, Stage III - Continuation of corrosion of 'M' with conversion into dark brown and around 'hp', Stage IV – Hardphase particles 'hp' and splat particles loss resulting in both micropitting and macropitting.

Figure 10.7.1 Breakdown of total weight loss into pure erosion (E), pure corrosion (C) and interactive synergy (S) components under solid-liquid impingement.

Figure 10.8.1 Ranking of materials in terms of 'E_b' under solid-free high-velocity liquid impingement.

List of Tables

CHAPTER 2

Table 2.3.1 Types of protective coatings and coating methods.

CHAPTER 3

Table 3.3.1 Examples of components subjected to solid particle erosion (Sundarrajan and Roy, 1997).

Table 3.3.1.1 Hardness values of some of the bulk materials, hard coatings and alloy phases (Hutchings, 1992).

Table 3.4.1 Factors that affect erosion of surface by solid particle impact (Humphrey, 1990).

Table. 3.5.1 Two approaches defining the synergistic factor.

Table 3.7.1 Wear rates and synergism of three different steels as a function of impeller speed and temperature with 2% silica sand in a Na_2SO_4 solution (Madsen, 1988) ND - not determined.

Table 3.7.2 Total weight loss distribution under solid-liquid impingement at 50 °C after 1 hour (Neville and Hodgkiess, 1997).

CHAPTER 4

Table 4.3.1 Comparison of HVOF with other thermal spray processes (Kumar and Modi, 1995).

Table 4.3.2 Benefits of HVOF process (Thorpe and Richter, 1992).

CHAPTER 5

Table 5.2.1 Cavitation erosion rates of the coatings (Kreye et al., 1998).

Table 5.2.2 Erosion-corrosion resistance of HVOF sprayed cermet coatings with different binder metals.

CHAPTER 6

Table 6.1.1.1 Powder characteristics of *Coating B* (manufacturer's data).

Table 6.1.1.2 Compositions of substrate materials.

Table 6.3.2.1 Particle size distribution of sand type A.

Table 6.3.2.2 Particle size distribution of sand type B (Congleton HST60).

CHAPTER 7

Table 7.1.1 SEM microanalysis of 20x20μm powder particles (average wt. % of 4 analyses).

Table 7.2.1 Microanalysis on polished surface of as-received *Coating* AI (values shown in wt. %).

Table 7.2.2 Microanalysis on polished surface of as-received *Coating* AII (values shown in wt. % taken from 5 analyses).

Table 7.2.3 Average area (10x10μm) analyses of different splats (Fig. 7.1.2.5b) on polished surface of as-received *Coating* AII (values shown in wt. % taken from 3 analyses).

Table 7.2.4 Properties of the coatings and a stainless steel.

Table 7.2.5 Force spectroscopy measurements of matrix and hardphase particle.

Table 7.3.1 Average values of 'E_b', 'E_{corr}', extent of passive range 'E_b-E_{corr}' and maximum current density 'i_{max}' of *Coating* AI (Values are average of 3 measurements with scattering of ±7%).

Table 7.3.2 50x50μm area analysis inside and outside the pit of Fig. 7.3.9b.

Table 7.4.1 Breakdown potential 'E_b', extent of passive range 'E_b-E_{corr}' and maximum current density 'i_{max}' of coating AII (Values are average of 3 measurements with scattering of ±5%).

Table 7.4.2 Area analyses of particle splats around indentation 'd_6' (Fig. 7.4.12) before and after the 2-weeks free corrosion test (values in brackets) in 3.5% NaCl solution at 18°C.

Table 7.5.1 Weight loss results under solid-free liquid impingement of 17ms^{-1}.

Table 7.5.2 Weight loss under solid-liquid impingement at 17ms^{-1}.

Table 7.5.3 Physical properties of the alloying elements of *Coating* AI and stainless steel.

Table 7.5.4 Breakdown of 'E', 'C' and 'S' under solid-free liquid impingement.

Table 7.5.5 Breakdown of 'E', 'C' and 'S' under solid/liquid impingement.

Table 7.6.1 Corrosion current densities and corrosion rates of coatings.

CHAPTER 8

Table 8.1.1 Average SEM microanalysis of as-received powder particles.

Table 8.2.1 Microanalysis on polished surface of as-received sprayed/sealed coating (values shown in wt. %).

Table 8.2.2 Microanalysis of as-received *Vacuum fused* BII coating representing Fig. 8.2.2, Fig. 8.2.3 and Fig. 8.2.4 (values shown in wt. %). Values in bold italic numbers

represent for coating BI with carbon steel substrate; analyses in all other zones for BI are similar to BII (HP - hardphase particle).

Table 8.2.3 Characterisation of coatings properties.

Table 8.2.4 Vickers microhardness at different regions of the fused coating BI (Average of 3 readings).

Table 8.3.1 Parameters of as received and polished coatings from anodic polarisation in static saline solution at 18°C.

Table 8.3.2. Parameters of polished coatings from anodic polarisation in static saline solution at 50°C.

Table 8.3.3. Corrosion mechanisms of the coatings after anodic polarisation at two temperatures.

Table 8.4.1 Electrochemical parameters under $72ms^{-1}$ impingement.

Table 8.4.2. Corrosion mechanisms on coatings after anodic polarisation at two temperatures under $72ms^{-1}$ impingement.

Table 8.5.1 Weight loss results (mg.) of polished specimens under solid-free liquid impingement at 18°C and $72ms^{-1}$.

Table 8.5.2 Breakdown of 'E', 'C' and 'S' under 2-days of solid-free liquid impingement at $72ms^{-1}$ and 18°C.

Table 8.6.1 Weight loss results of polished surfaces under solid-free liquid impingement at $17ms^{-1}$.

Table 8.6.2 Weight loss results of polished surfaces under solid-liquid impingement at $17ms^{-1}$.

Table 8.6.3 Breakdown of 'E', 'C' and 'S' under solid-free liquid impingement.

Table 8.6.4 Breakdown of 'E', 'C' and 'S' under solid/liquid impingement.

Table 8.6.5 Weight loss of as-received surfaces under solid-liquid impingement at $17ms^{-1}$.

Definitions

free impingement -

liquid or solid/liquid impingement at E_{corr} without any electrochemical polarisation test.

normal impact -

90° impact angle at which the liquid or solid-liquid jet hits the target surface.

submerged condition -

both working electrode (specimen) and impinging electrolyte jet being kept immersed in a stationary miscible fluid of the same electrolyte.

unsubmerged condition -

the impinging jet hits the working electrode surface in air medium (i.e. the specimen is not immersed in the working fluid).

Symbols and Abbreviations

Symbols

i	current density, $\mu A/cm^2$
i_L	limiting current density, $\mu A/cm^2$
i_{max}	maximum current density of a full reversed scan during anodic polarisation, $\mu A/cm^2$
i_{corr}	corrosion current density, $\mu A/cm^2$
E	electrode potential, mV (SCE)
E_b	breakdown potential
E_h	hydrogen evolution potential, mV (SCE)
E_{corr}	free corrosion potential, mV (SCE)

Abbreviations

Avg.	average
AFM	atomic force microscope
CP	cathodic protection
stainless steel	uncoated stainless steel (UNS S31603) specimen
carbon steel	uncoated carbon steel (BS En8) specimen
ss	stainless steel substrate of the coating
cs	carbon steel substrate of the coating
TSC	thermal spray coating
TWL	total weight loss
SEM	scanning electron microscope
OM	optical microscope
XRD	X-ray diffraction
EDS	energy dispersive spectrum
EPMA	electron probe micro-analysis
EC	erosion-corrosion
SCE	saturated calomel electrode
particle splat	flattened 'splat particle', which is formed on the coating after the powder particle strikes the surface (usually seen under the microscope on a polished plan view.
lamella	'splat lamella' which is same as particle splat but seen under the microscope in cross-section
hardphase	'hardphase particle' which is a discrete particle that forms a skeletal network in a ductile metal matrix in a multiphase coating
matrix	a binder phase mainly of metal that constitutes a major proportion of a multiphase coating.

CHAPTER 1. INTRODUCTION

1.1 General Introduction

The protection of metal components from corrosion and erosion-corrosion is a matter of concern to many engineers, designers and material scientists. It covers most engineering fields and, requires a considerable degree of understanding of the processes involved to achieve economic solutions to the problems that arise. Metal components nowadays are required to withstand various aggressive conditions and their application must be selected from the viewpoint of their degradation due to interaction with the environment. Often, material selection represents a formidable task since it concerns performance, maintenance and economic factors such as the initial capital expenditure.

The adverse effects of corrosion and erosion-corrosion are prominent in a range of industrial sectors. Corrosion or erosion-corrosion affects almost every industry. Some examples are corrosion of reinforced concrete in bridges, corrosion of steel structures in building and construction industry (Covino et al. 1999), corrosion of offshore platforms, pipes, risers, valves, tanks in oil industry, corrosion of ship hulls in marine sector, corrosion of gas turbines, heat exchanger tubes, engines and many others e.g. chemical processing, refining (Abd-El-Kader and El-Raghy, 1986; Kane and Cayard, 1999), energy production systems such as fluidised bed combustor (FBC) boilers and coal gasifiers (Stringer et al., 1989; Wang et al., 1992; Levy, 1995), electrical, nuclear and biomedical industries.

The marine environment is probably one of the most aggressive and often the most severe and costly failures due to corrosion which occur in seawater handling systems. The failure is much accentuated when corrosion occurs in combination with erosion. This type of attack mechanism is mostly observed on fast moving parts or elements subject to high-velocity flows such as pump casings, pump shafts and impellers, nozzle and valve seats, tubes, tees, flanges and elbows etc. The increased corrosion rate by high velocity can be associated with the mechanical wear by the moving fluid, 'liquid erosion' and is much enhanced when solid particles are present, 'solid-liquid erosion'.

Solid particles in a liquid stream are quite common in the process industry, oil and gas refinery industry, and pipelines carrying sand/water slurries in mining operations. Particle generation might also be due to wear of components of the tribological systems. Material degradation due to corrosion or erosion-corrosion will generally depend on the production characteristics for the systems; i.e. production rates, pressure and temperature, the presence of corrosive components and erosive solid particles and the material property itself.

Substantial direct and indirect costs are typically associated with failure of components such as impellers, shafts and pipings. Inaccessibility, particularly in oil and gas industry makes the maintenance and quick replacement troublesome. Examples of some severe material degradation due to liquid erosion are shown in Fig. 1.1.

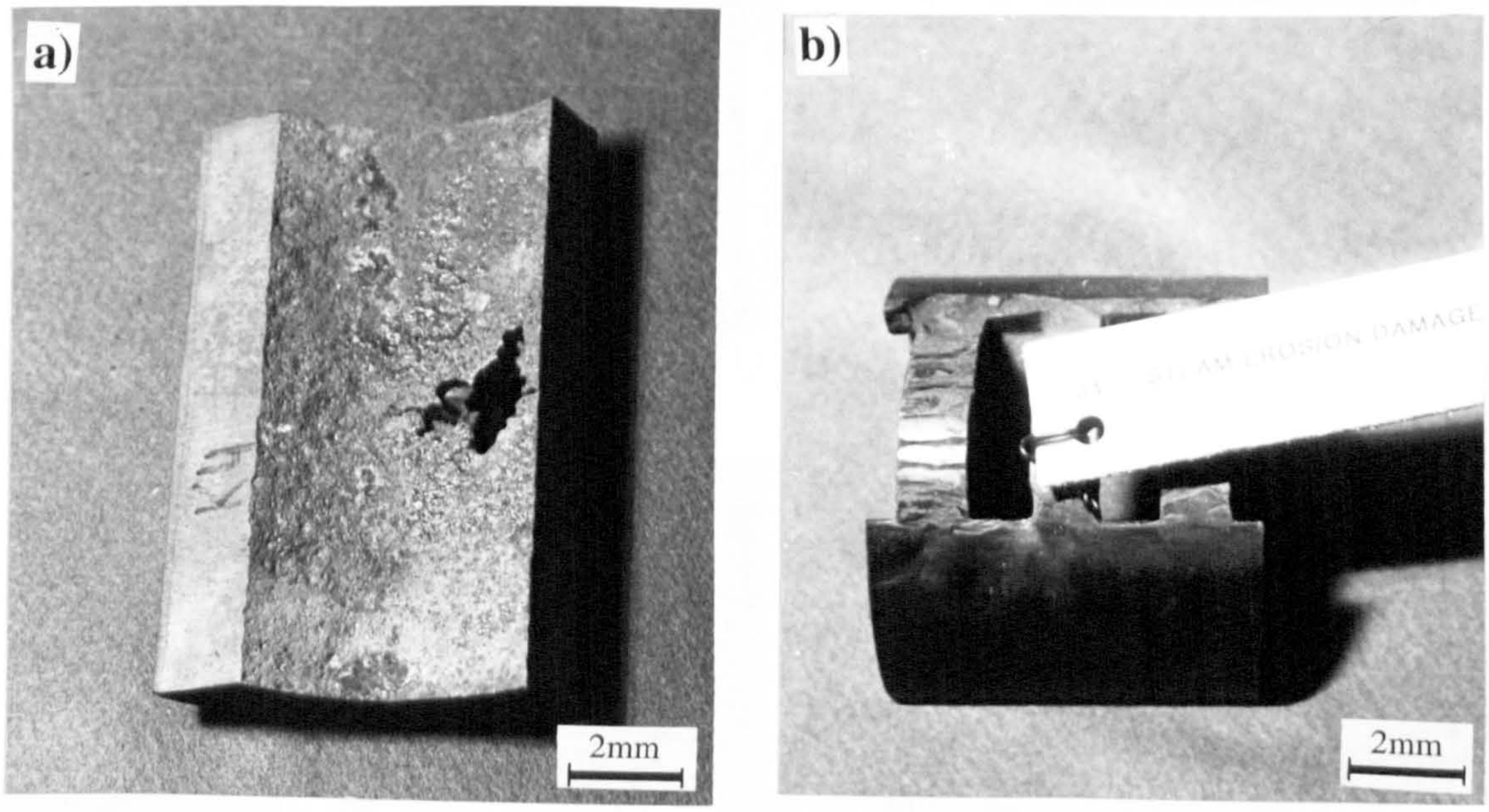
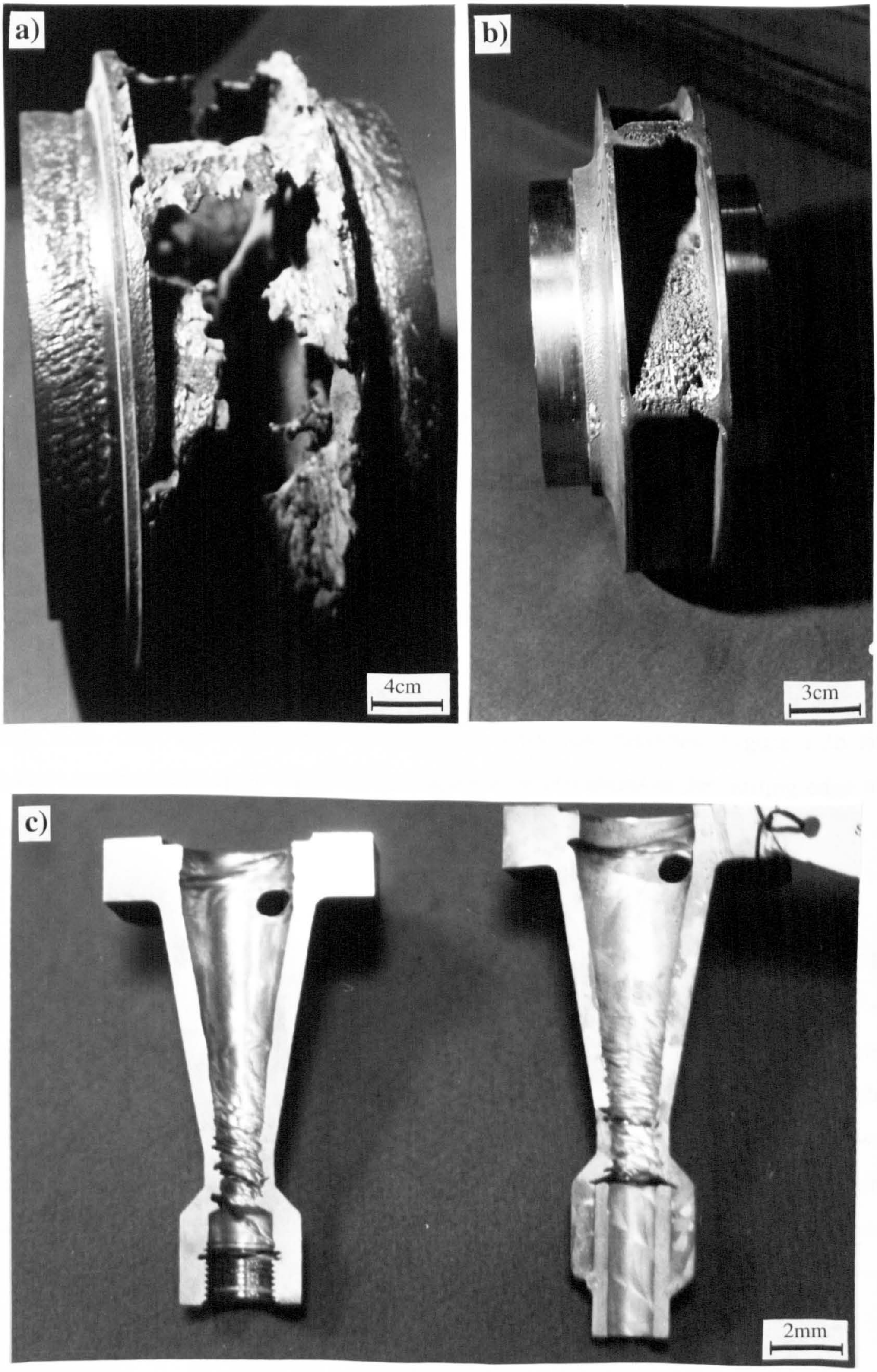


Figure 1.1 Examples of component failures due to liquid erosion: a) Cylinder from downhole drilling tool (Low alloy high strength steel); b) Throttle-valve of a steam turbine (UNS S31603) (photos printed with permission of Weir Pumps Ltd.).

Figure 1.1a shows a section of a cylinder from downhole drilling tool used for drilling in mud. Originally a fatigue crack initiated but before fatigue failure, escaping liquid through crack resulted in a severe erosion-corrosion at existing defects with through

perforation. In Fig. 1.1b a throttle valve of a steam turbine deteriorated due to erosion-corrosion by escaping steam.



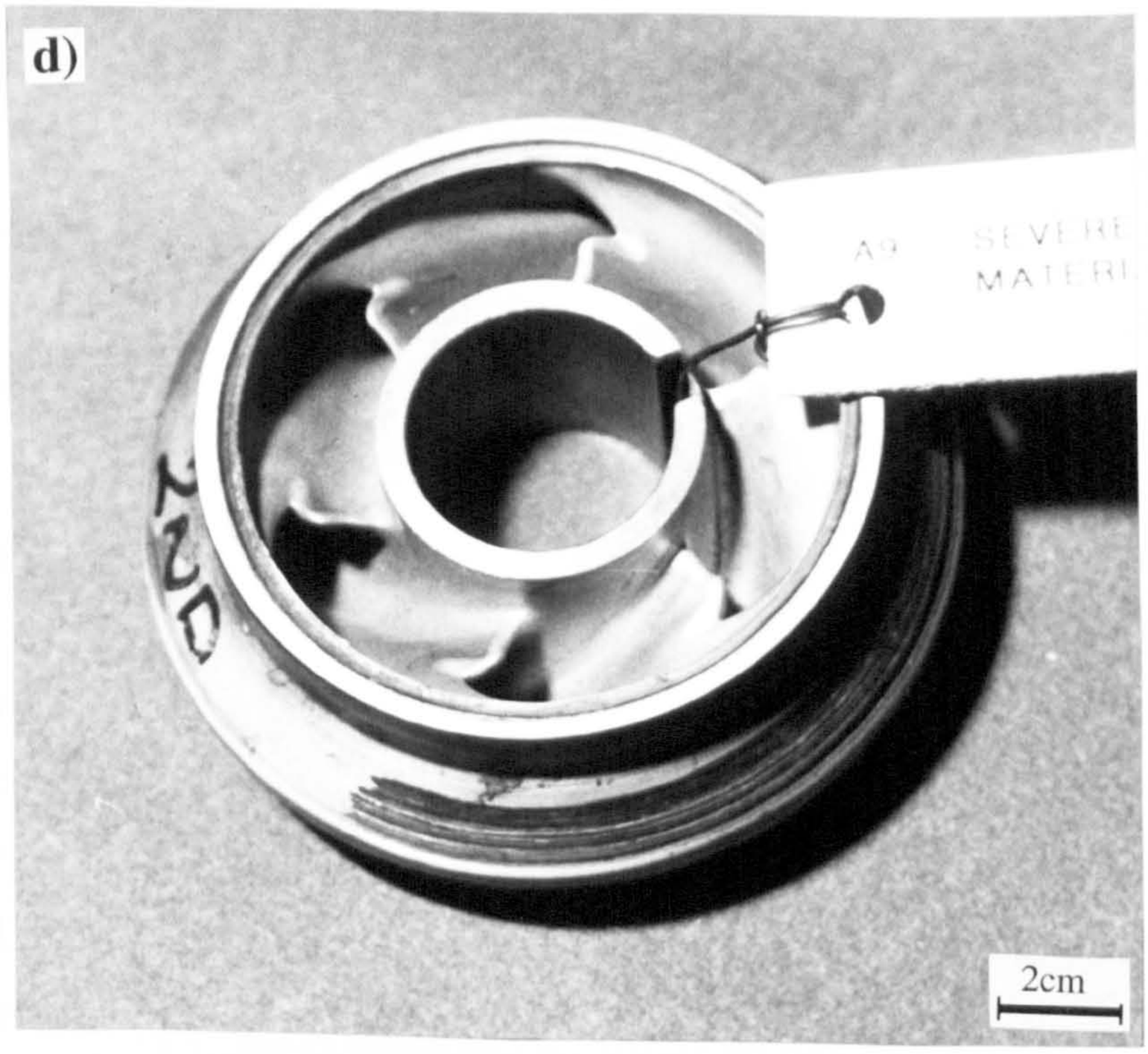


Figure 1.2 Severe solid-liquid erosion experienced by pump components: a) Gray cast iron pump impeller; b) Impeller vane of stainless steel type UNS S31603; c) Cyclone separator of an austenitic stainless steel type UNS S31603; d) Duplex stainless steel impeller (photos printed with permission of Weir Pumps Ltd.).

A spectacular severe erosion-corrosion of a gray cast iron pump impeller is shown in Fig. 1.2a. used for river water contaminated with coal particles. Figure 1.2b shows severe cavitation damage with a large amount of perforations at the trailing edge of the vanes of a stainless steel impeller (type UNS S31603) due to collapse of bubbles, used for pumping seawater.

Wastewater is pumped to the inlet at high pressure in a cyclone separator (made of UNS S31603 stainless steel) in Fig. 1.2c, where the dirty water, contaminated with solid particles, due to gravity move downwards in a spiral movement and discharge through a low pressure pump. Clean water is separated from the upper level. The picture shows severe channelling tracks due to erosion-corrosion at the bottom of the separator within a very short time scale (approximately a month). Figure 1.2d shows a duplex stainless steel impeller from downhole pump that suffered an extensive low angle impingement attack on impeller vanes used for oil/sand pumping.

Often the bulk properties of a material are different from required surface properties to function in a particular solid-liquid medium and it is often technically and economically difficult to achieve all the required properties in a single material. Even very good corrosion resistant alloys such as austenitic and duplex stainless steels, which perform very well in moving fluids (due to their passive film), are sometimes ineffective and prone to severe material degradation when solids are present.

Surface engineering is increasingly being used as a potential remedy for such degradation and encompasses techniques and processes capable of creating and/or modifying surfaces to provide enhanced performance such as corrosion and wear resistance of the surface material by optimizing surface/substrate properties and performance; coatings technology; characterization, evaluation of surfaces and interfaces (Datta and Gray, 1993). In this way the base metal can be chosen from its structural properties such as strength or weight and a coating can be applied on to a substrate material to provide the required surface properties against wear and corrosion and this can be achieved economically.

It is well known that thermal sprayed cermet coatings have been primarily developed for wear resistance but they are increasingly in demand to function in various corrosive and erosive hostile environments and to date very little is understood about the mechanisms involved in their degradation. Also, guidelines for industry that exist are very limited and so the challenge is to improve the understanding of material degradation in aggressive environments. Ample literatures can be found for newly developed thermal sprayed coatings (TCSs), in particular (WC/Co, WC/CoCr, Zirconium Nitride, TiN etc.) in abrasive, adhesive and erosive wear (Tucker, 1998) and in erosive-corrosive wear (Bardal et al., 1995). Corrosion rates of different sprayed and fused coatings in a number of acidic environments have been reported by Dvorak (1998). It has been demonstrated that the durability of HVOF coatings is dependent on temperature but salinity has a lesser effect on the coatings performance (Hodgkiess and Neville, 1998a). Some authors have deduced that the three major drawbacks of the TSCs are i) oxide content, ii) open porosity, iii) material degradation during spraying despite the development of advanced HP/HVOF processes capable of producing coatings with porosity less than 1% and oxide 2% (Tobe, 1998). However, recent studies (Neville and Hodgkiess, 1996; 1997a; Hodgkiess and Neville, 1998a) have

shown that HVOF sprayed coatings, similar to stainless steels are susceptible to localized corrosion mechanisms even if the oxide content is low and there is no interconnected porosity; corrosion of the coating itself (which include matrix corrosion, corrosion at hardphase particle/matrix interface, coating/substrate interface) is an integral part of the durability and this should be addressed.

Although there has been substantial effort within industry and academia to assess the mechanical wear behaviour of TSCs, very much less attention has been paid to durability in conditions where mechanical wear exists in combination with electrochemical corrosion. The total material loss 'TWL' in a flowing aqueous environment (where erosion-corrosion occurs together) is often much higher than the sum of the losses attributed by pure corrosion 'C' and pure erosion 'E' mechanisms in isolation and it is recognised that a synergistic contribution 'S' is involved (Bjordal et al., 1995b; Bardal et al., 1995; Rogne et al., 1996). Similar to that recognised to be relevant to metals (Neville et al., 1995).

1.2 Outline of the thesis

As erosion, corrosion and interactions all contribute to material degradation that often results in premature failures of many engineering components, there is a need of a detailed literature review on corrosion as well as erosion-corrosion mechanisms.

Chapter 1 gives an introduction to an existing erosion-corrosion problems in a wide variety of industries and modern surface engineering as a potential remedy. Chapter 2 comprises a short introduction on corrosion principles and control techniques with a short overview of corrosion of stainless steels.

In Chapter 3, flow induced corrosion and basic liquid hydrodynamics have been explained. Also the basics of solid-liquid erosion, erosion-corrosion interaction mechanism and the general material characteristics have been illustrated.

A review of thermal spray techniques as a potential surface engineering option for many industrial applications, the-state-of-the-art HVOF process and coating properties, morphology etc. is given in Chapter 4.

In Chapter 5, a detailed literature review on general corrosion and erosion-corrosion in both liquid and solid-liquid conditions of several HVOF sprayed coatings is presented.

Experimental techniques used in this research such as electrochemical monitoring by DC potentiodynamic tests, free corrosion tests; weight loss tests, test materials as well as various examination techniques such as SEM, XRD, AFM and Talysurf have been briefed in Chapter 6.

The experimental results are presented in Chapter 7, 8 and 9. The mechanisms are discussed in Chapter 10 with concluding remarks and recommendations for the future work in Chapter 11.

CHAPTER 2. CORROSION

2.1 Background

It is a fact that material degradation is not only a problem in engineering applications but is as well a problem for society. Corrosion represents a huge waste of our natural resources, which has a direct impact on our environment. Material degradation is a waste of money as material is expensive and it causes inconvenience to us and some times in extreme cases loss of life. The term *Corrosion* is derived from the Latin, *rodere*, which means 'to gnaw'.

The expense of corrosion to our society is very high. The approximate annual cost of corrosion in the United States was first estimated in 1949 by Uhlig (1949) to be $5 billion, 2.1% of GNP. According to Government Committee on Corrosion and Protection, in 1971, it was estimated that the cost of corrosion in UK was around £1,365 million, about 3.5% of the GNP (Hoar, 1971). Recent surveys claim UK corrosion losses to be exceeding £10 billion per year. The enormity of these corrosion costs also depends on additional factors known as indirect costs. Tretheway and Chamberlain (1995) have defined these costs as following:

- Lost production shut down or failure.
- High maintenance costs.
- Compliance with environmental and consumer regulations.
- Loss of product quality in a plant owing to contamination with corrosion products.
- High fuel and energy costs as a result of steam, fuel, water or compressed air leakage from corroded pipes.
- Extra working capital because of increased labour requirements and larger stocks of spare parts.

One recent spectacular disaster in which corrosion involved a short circuit, caused due to a corroded wire resulting in fire ignition of Boeing 747 in 1996 that flew from

Kennedy Airport, and made the explosion of the biggest flight in the world, that was considered to be the worst air disaster in history (Black Box, 1996). Figure 2.1.1 below gives some examples of material degradation due to corrosion.

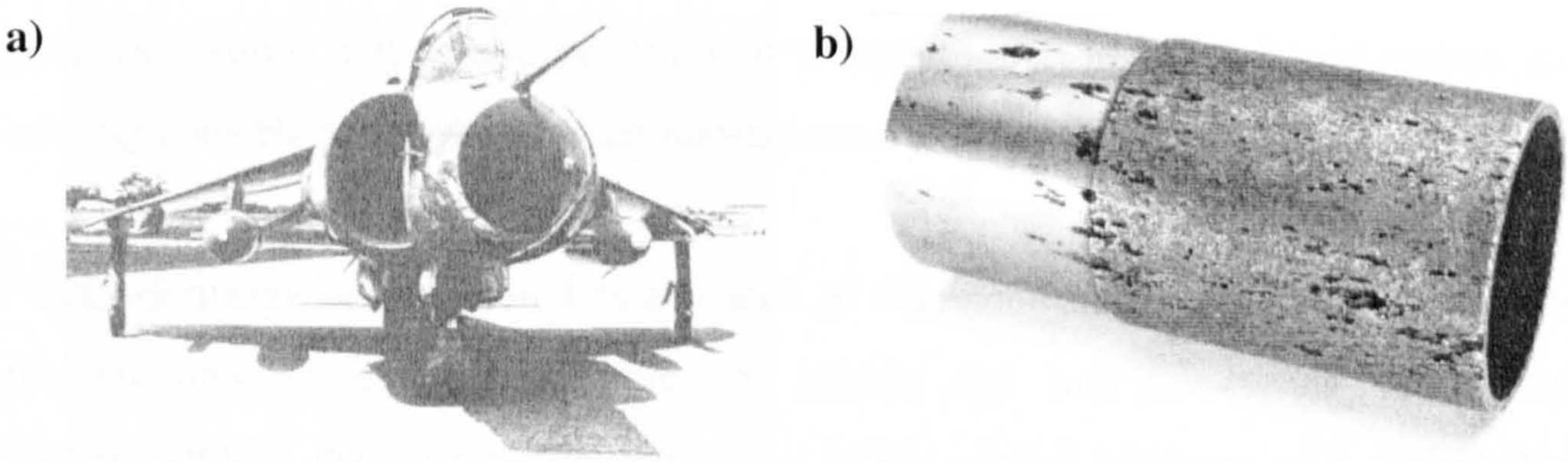


Figure 2.1.1 a) collapse of a nose wheel of a Royal Navy Sea harrier due to bi-metallic corrosion between the stainless steel bearing and the magnesium alloy wheel b) Pitting corrosion in a pipe component.

The marine and offshore industry

Corrosion (as well as erosion-corrosion) is a major problem in the marine and offshore industry. Deep-water platforms of huge steel structures in offshore oilfields have to operate in violent seas and should operate efficiently and safely for several decades in harsh environments. Corrosion of ship hulls is also often a serious issue (Trethewey and Chamberlain, 1995). It has been speculated that the loss of 170,000 tonne Derbyshire in 1980 with all 44 crewmembers resulted due to major structural failure of the ship as a result of corrosion fatigue. Also components working in marine systems such as piping, condensers and heat exchangers, pumps and valves often undergo rapid deterioration due to both corrosion and erosion-corrosion problems associated with impingement attack and cavitation resulting in their premature failure. Deterioration as a result of corrosion is an unavoidable fact of life whenever metals are used and the adverse effect of corrosion is immense to many industries. However, it is estimated that 25-30% of the total corrosion cost in the UK only can be saved using existing techniques of corrosion prevention (Gellings, 1976) which will be discussed in Chapter 2.3.

2.2 Theoretical considerations of Corrosion Behaviour

Different authors have viewed corrosion from different angles. According to Fontana and Staehle (1970): "Corrosion will include the reaction of metals, glasses, ionic solids, polymeric solids and composites with environments that embrace liquid metals, gases, non-aqueous electrolytes and other non-aqueous solutions".

"Corrosion may be considered as a branch of chemical thermodynamics or kinetics, as the outcome of electron affinities of metals and non-metals, as short-circuited electrochemical cells, or as the demolition of the crystal structure of a metal" (Evans, 1981).

Based on thermodynamic laws, a strong tendency for high energy states to transform into low energy states also applies in metals to recombine with components of the environment leading to the phenomenon known as 'corrosion' (Trethewey and Chamberlain, 1995). The principle of aqueous corrosion is generally defined as (Trethewey and Chamberlain, 1995; Shreir, 1963b):

> *Corrosion is the deterioration (degradation) of a metal by an electrochemical reaction with its environment.*

Virtually all metals have an inherent tendency to corrode. All interactions between elements and compounds are governed by the free energy change 'ΔG' available to them, which should be negative for a spontaneous reaction (Trethewey and Chamberlain, 1995). *Corrosion* is practically dependent upon temperature. The value of ΔG can be calculated by using the formula as (Trethewey and Chamberlain, 1995):

$$\Delta G = \Delta G^{\circ} + RT \ln J \qquad \text{Eq. (1)}$$

where, ΔG - free energy change, ΔG°- standard free energy change in $kJmol^{-1}$, R - 8.3143 $Jmol^{-1}K^{-1}$(universal gas constant), T – absolute temperature in K, J – a constant.

where, for a given reaction

$$jA+kB = lC+mD$$

where, C, D are product concentrations and A, B are reactant concentrations, and then

$$\boldsymbol{J} = [C]^{l}[D]^{m}/[A]^{j}[B]^{k} \qquad \text{Eq. (2)}$$

The relation with electrode potential and free energy is given by *Faraday's Law*, expressed as:

$$\Delta G = (-zF)\, E_o \qquad \text{Eq. (3)}$$

where, F= 96494 coulombs/mole; E_o- equilibrium electrode potential; z- the number of electrons transferred in the corrosion reaction. Also for the standard state,

$$\Delta G^{\circ} = (-zF)\, E_o^{\circ} \qquad \text{Eq. (4)}$$

From equations 1,2,3 and 4, we get

$$E_o = E_o^{\circ} - RT/zF * \ln \boldsymbol{J} \qquad \text{Eq. (5)}$$

where, E_o° - standard equilibrium electrode potential. Equation (5) is known as the *Nernst equation.*

Aqueous corrosion is basically an electrochemical process in which the actual metal loss occurs by dissolution of charged metal ions, M^{n+} (where 'n' is the valency, commonly 1, 2 or 3) and releasing electrons, e^- at the anodic site.

Anodic oxidation: $M \Rightarrow M^{n+} + ne^-$

or $Fe \Rightarrow Fe^{2+} + 2e^-$ Eq. (6)

which is further oxidised into

$$Fe^{2+} \Rightarrow Fe^{3+} + e^- \qquad \text{Eq. (7)}$$

The cathode plays an essential complement to the anode by consuming the electrons generated by the anode. Both cathodic and anodic reactions occur simultaneously. A schematic representation of a metal corrosion is shown in Fig. 2.2.1.

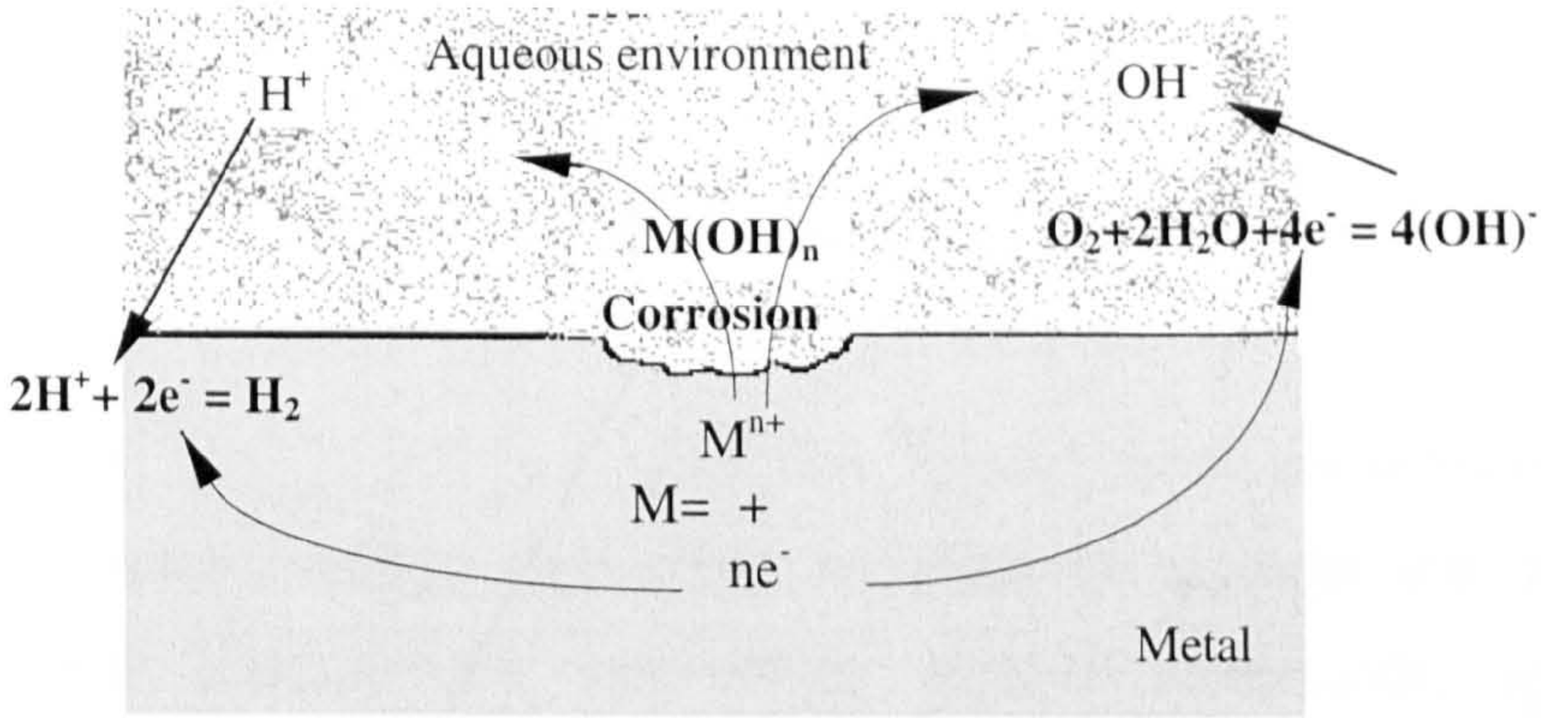


Figure 2.2.1 Metal corrosion at the surface in aqueous environment.

The most common cathodic reactions occurring in acidic environments, where pH < 7 at temperatures of 25°C and in neutral or alkaline environments, where pH ≥ 7 are represented below.

In acidic environments (pH < 7)

$$2H^+ + 2e^- \Rightarrow H_2 \text{ (hydrogen ion reduction)} \qquad \text{Eq. (8)}$$

Absorption of the hydrogen atoms into the metal, i.e. diffusion of hydrogen into the interior metal can cause so called phenomenon of Hydrogen-embrittlement.

In neutral or alkaline environments (pH ≥ 7)

In such environments oxygen-reduction is the most favourable reaction, that consumes dissolved oxygen to liberate hydroxyl ions.

$$O_2 \text{ (aq.)} + 2H_2O + 4e^- \Rightarrow 4(OH)^- \qquad \text{Eq. (9)}$$

This reaction is mostly dependant upon the level of dissolved oxygen in the solution, which in well aerated solution is approximately 5-10ppm but quite sufficient for the cathodic reduction to occur.

Combining equation (7) and (9), we get

$$Fe^{3+} + 3(OH)^{-} \Rightarrow Fe(OH)_3\ _{(rust)} \qquad \text{Eq. (10)}$$

The formation of brown scale, $Fe(OH)_3$ is called rust, formed due to corrosion of iron in an aqueous environment. Factors that affect corrosion in seawater are oxygen content, chloride, pH, calcium and magnesium, organic compounds, specific conductivity, biological activity, temperature and flow velocity (Ijsseling, 1989).

In aqueous corrosion, four components: anode, cathode, electrolyte and electrical connection play an essential role where anode and cathode are the two sites of the metal interface in which electrons are produced and consumed respectively. Removal of any one of these four components can stop the corrosion process (Trethewey and Chamberlain, 1995). An electrically conducting solution may work as an electrolyte whose conductivity mainly depends upon the salt contents of that solution. The electrical connection is required for a current to flow in the corrosion cell.

The mixed potential theory, for a metal surface exposed to homogeneous aqueous environment, dictates that in immersed conditions the metal will attain an electrode potential *E*, the value of which is determined by the subsequent anodic and cathodic reactions (kinetic factors) at the electrode surface. It is this "mixed potential" that will be observed when an electrode potential of a metal is measured with a reference electrode. In a corroding metal, the mixed potential is often more positive than equilibrium potential E_o for the metal-dissolution reaction (anodic oxidation). Similarly, the mixed electrode potential E is more negative than equilibrium potential E_o for the cathodic reduction reaction.

A metal corroding freely in an aqueous solution exhibits a mixed potential E_{corr} at which the subsequent corrosion current density i_{corr} is used to determine the rate of metal dissolution in that particular environment by using *Faraday's Law of Electrolysis*. Thus monitoring of i_{corr} provides a powerful means of monitoring the corrosion rates of metallic components.

From Faraday's law (Shreir, 1963a) the weight loss per unit area is

$$m/S = M.i.t/z.F \qquad (gcm^{-2})$$

where, m - Mass of metal corroded (g)

M- Molecular mass ($gmole^{-1}$)

F - Faraday's constant 96500, coulombs (1A ~ 1 coulomb s^{-1})

I - Current (A)

i - Current density (Acm^{-2}) and i = I/S

t - Time (s)

z - Number of electrons involved in the corrosion reaction.

S - area of metal involved (cm^2)

Aqueous corrosion monitoring

Aqueous corrosion monitoring by a variety of electrochemical techniques is firmly established for corrosion research and practice (Strutt et al., 1981). These monitoring methods also are extremely useful (in conjunction with other experimental approaches such as weight loss, surface profilometry, microscopy) for the study of erosion-corrosion but for this latter phenomenon they have seen rather less application. Some of the electrochemical methods that can be employed in this type of research are described below.

Potentiodynamic Polarisation measurements

The determination of the corrosion current density i_{corr} by accelerated polarisation tests involves a procedure in which sample under investigation is polarised from its free corrosion potential, E_{corr} by means of a potentiostat in a three electrode cell as shown in Fig. 2.2.2. A Saturated Calomel Electrode (SCE), which is a stable reference electrode 'R', measures the potential across the working electrode 'W'. The inert auxiliary electrode 'A' (normally platinum) acts as an electrical connection for the current to flow between itself and the working electrode when the working electrode potential is shifted from the E_{corr} value.

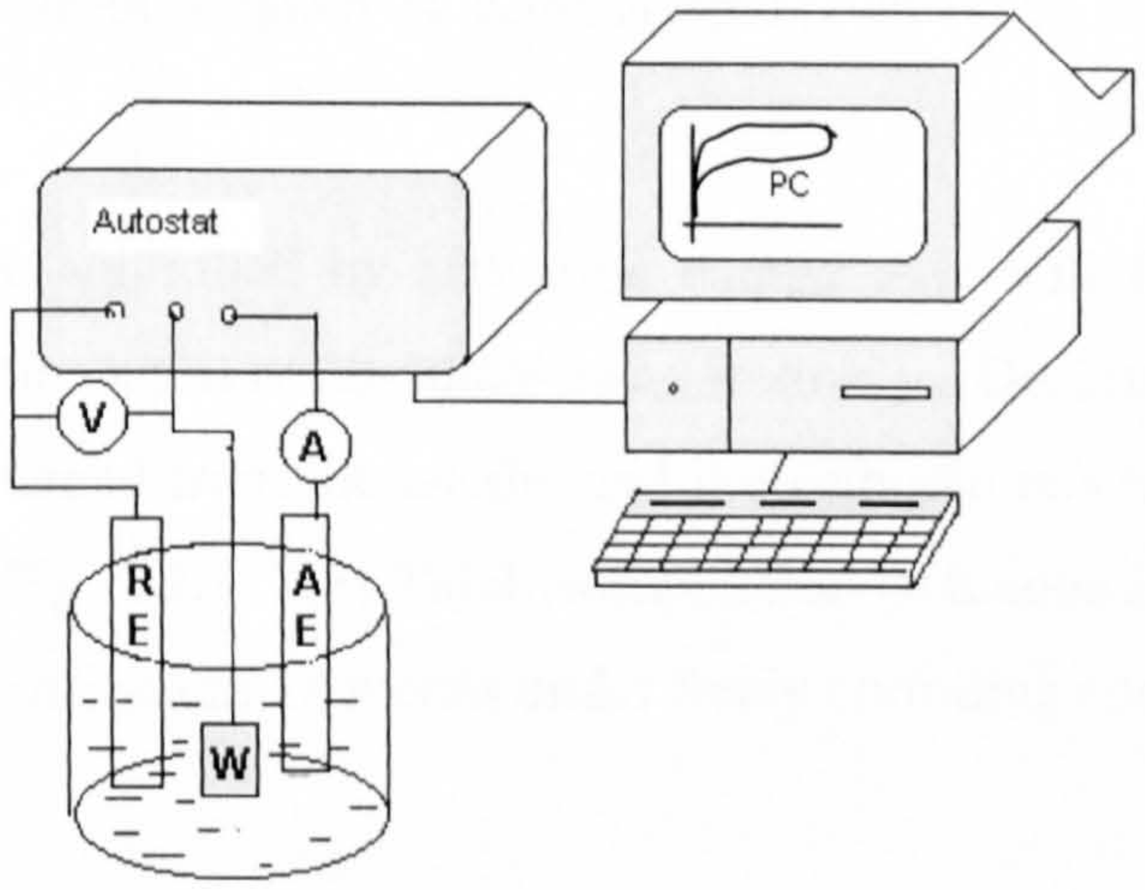


Figure 2.2.2 Schematic diagram of a three-electrode electrochemical cell: R-reference electrode, W-working electrode, A-auxiliary electrode.

The process of polarisation involves shifting the potential of the working electrode in the anodic direction, i.e. to a more positive potential than E_{corr} or in the cathodic direction, i.e. to a more negative potential with respect to the E_{corr} and the potential-current relationship is plotted for both anodic and cathodic reactions.

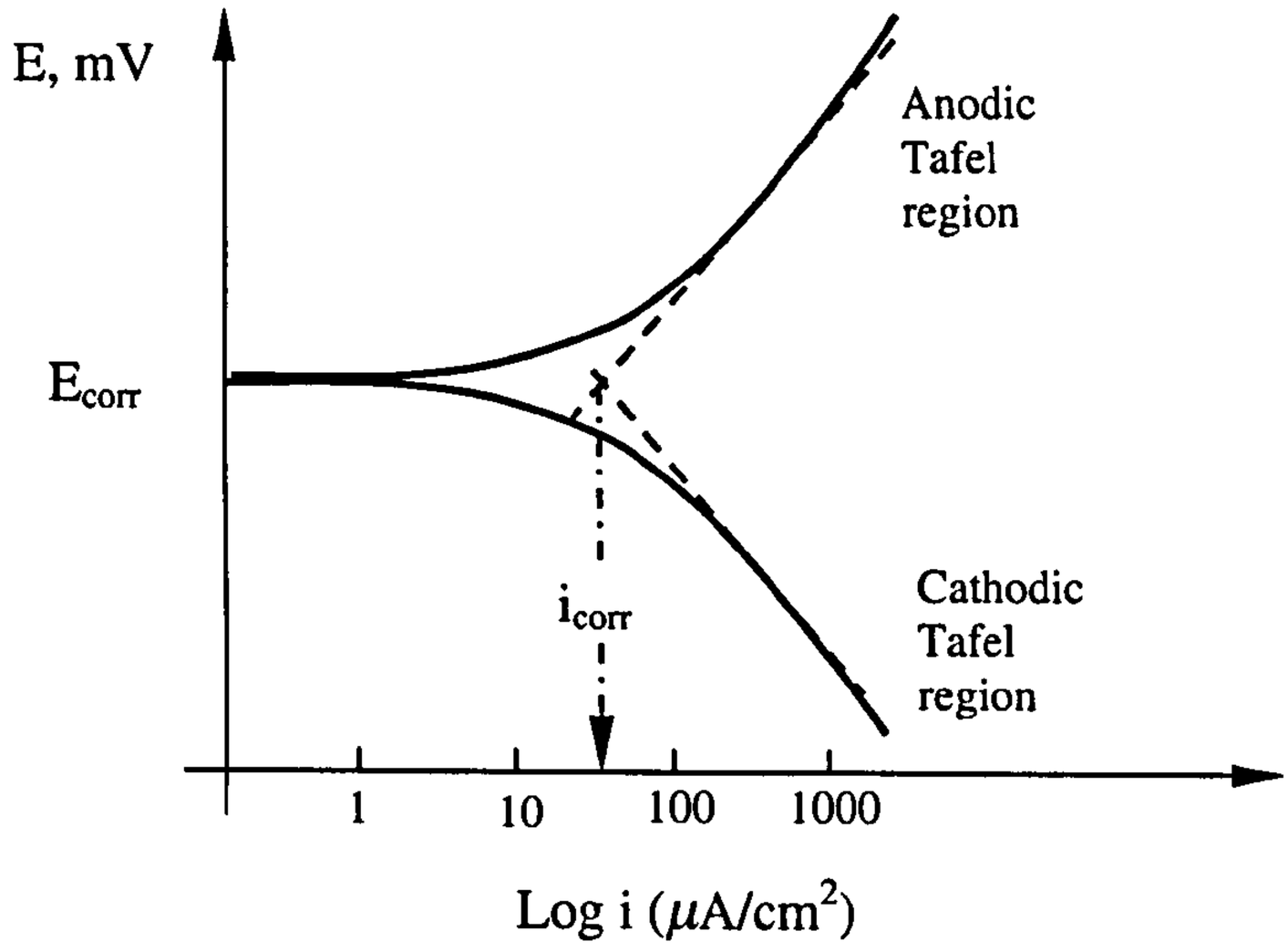


Figure 2.2.3 A schematic diagram of determining i_{corr} by Tafel extrapolation method.

When both reactions are controlled by activation energy they will follow the Tafel relationship at potentials in excess of 20-30mV away from E_{corr}. On extrapolation of the linear E-log i curves obtained from the anodic and the cathodic reactions, i_{corr} can be established as shown in Fig. 2.2.3. This Tafel extrapolation technique is generally used to quantify the actual corrosion rate of metals under freely corroding conditions.

Polarisation resistance

Another method of corrosion monitoring through establishment of i_{corr} is achieved by *polarisation resistance* also called *linear polarisation technique*, primarily developed by Stern and Geary (1957), which involves manipulation of the Tafel equations and certain approximations which are reasonably valid for shifts of potentials, ΔE, from E_{corr} of no greater than about ±25mV. The measured i_{corr} is calculated by using the mathematical relation:

$$i_{corr} = B.\Delta i / \Delta E$$

and,

$$B = \frac{b_a b_c}{2.3 (b_a + b_c)}$$

where, $\Delta E/\Delta i$ = slope of the polarisation resistance plot

b_a, b_c = anodic and cathodic Tafel constants in mV/decade

i_{corr} = corrosion current density, $\mu A/cm^2$

The corrosion current then can be related directly to the corrosion rate using the following equation.

$$\text{Corrosion rate (mpy)} = \frac{0.13\, i_{corr}\,(E.W.)}{\rho}$$

where, E.W. = equivalent weight of the corroding species (g)

ρ = density of the corroding species (g/cm^3)

i_{corr} = corrosion current density ($\mu A/cm^2$)

Both the methods aforesaid are applicable only in situations for assessing general surface corrosion rates, where a metal component is corroding uniformly over the entire surface and does not yield accurate information on localised corrosion (e.g. pitting, crevice etc.) rates. Determination of corrosion rates by the methods mentioned above is useful only when the electrochemical reactions follow Tafel kinetics. However, there are circumstances when the activation polarisation is predominated by the restriction of supply of cathodic reactants. A typical example is an oxygen-reduction cathodic reaction

$$O_{2\,(aq.)} + 2H_2O + 4e^- = 4(OH)^-$$

in which continuous replenishment of oxygen supply to the metal surface from the bulk solution is restricted in stagnant water. This is associated with the slow diffusion rate of dissolved oxygen molecules in static conditions, thus occurring phenomenon 'concentration polarisation'. A schematic representation of concentration polarisation effect in cathodic reaction is shown in Fig. 2.2.4.

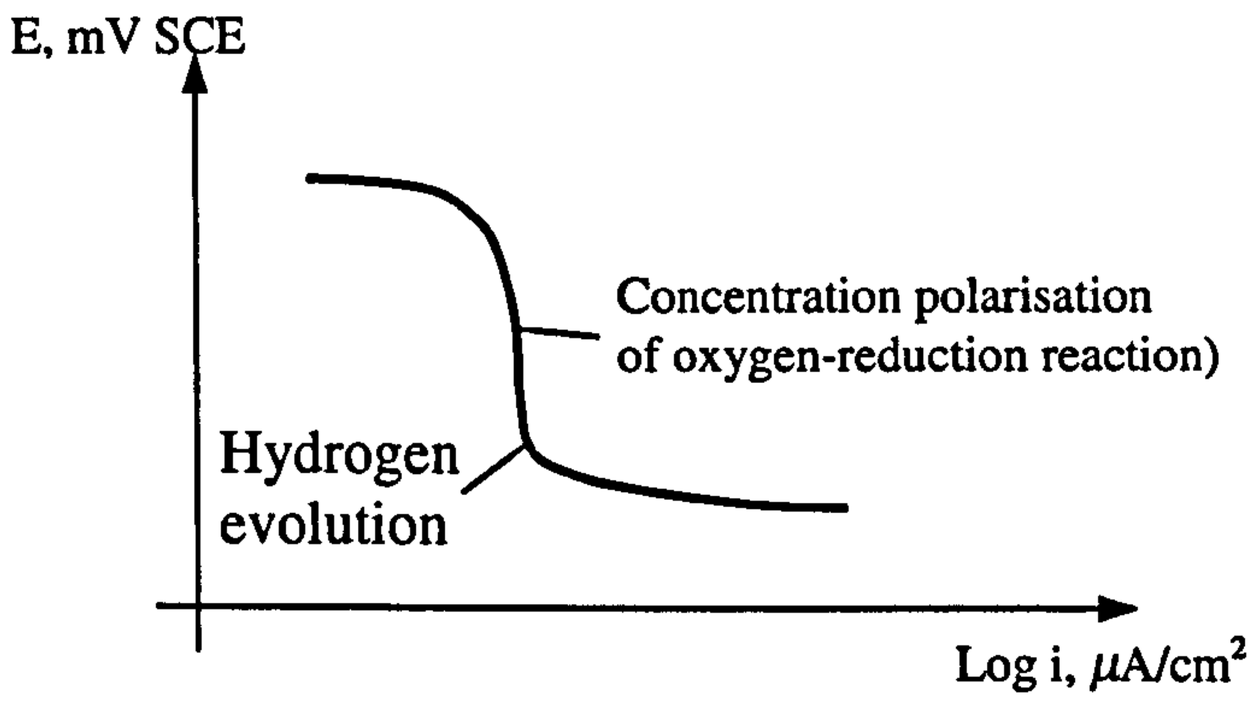


Figure 2.2.4 Concentration polarisation effect slows down the cathodic reaction.

Electrochemical Impedance Spectroscopy (EIS)

In recent years, electrochemical impedance spectroscopy (EIS) has found widespread application in investigations of the corrosion and the passivation mechanisms (Venugopal, 1996; Al-Abdallah, 1996; Wallinder, 1999). The method is rapid, reliable and non-destructive and has become popular for corrosion measurement of different materials including polymer coated metals and anodized Al, which were difficult to study with DC techniques (Mansfeld, 1988).

In this method, a system is considered to have a corroding metal electrode adjacent to a solution containing varying concentration of ions, known as the double layer. If resistance due to film R_f and diffusion effects are neglected, then the remaining resistances, mainly *charge transfer resistance* 'R_p' (also called polarisation resistance, resulting from the separation of charge across the solid interface and the double layer) and the *bulk solution resistance* 'R_s' will form an *equivalent circuit modelling* as shown in Fig. 2.2.5. Determination of 'R_p' enables quantification of the changes in the corrosion rate. C_{dl} is the capacitance value of the double layer.

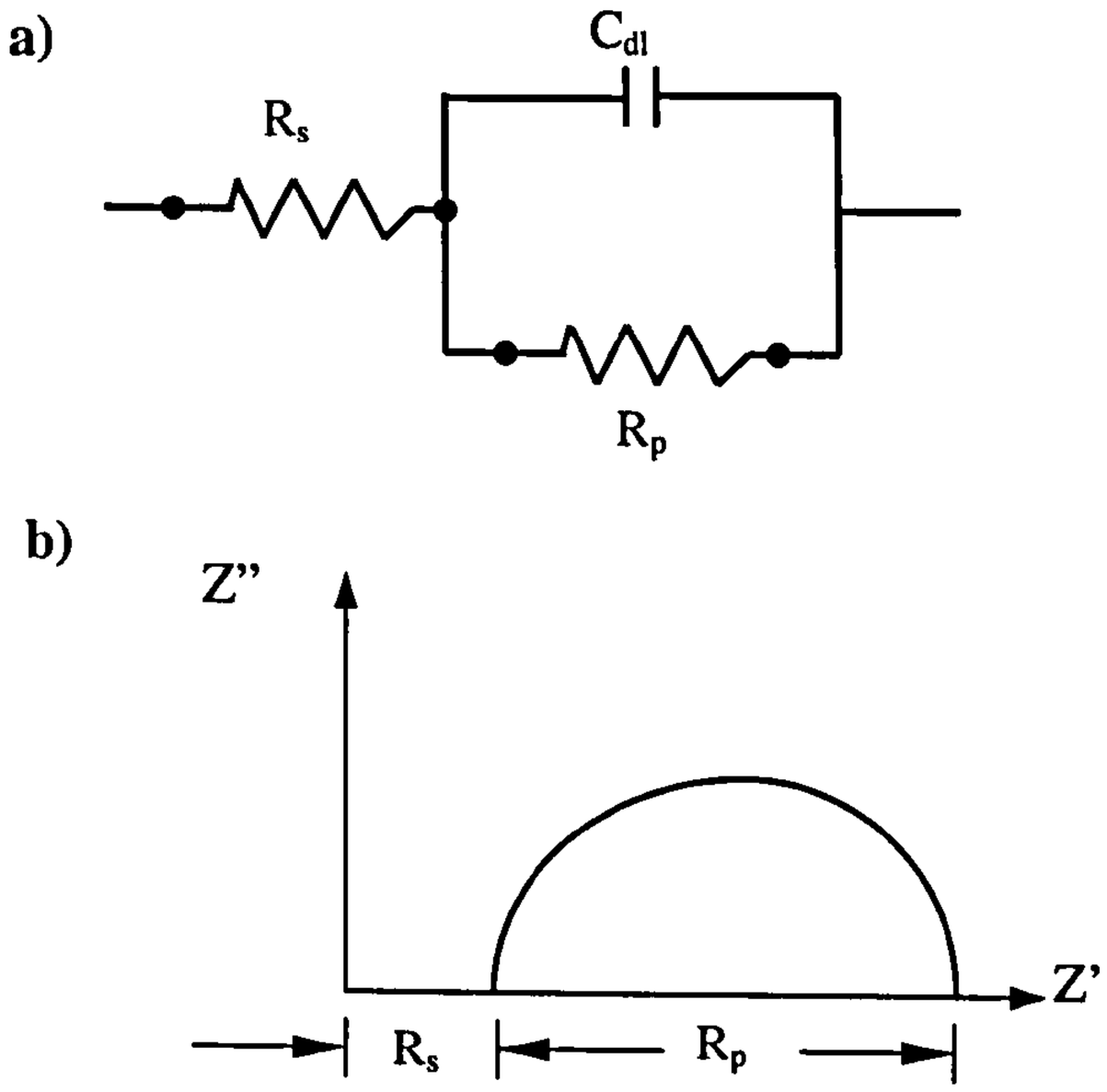


Figure 2.2.5 A schematic model of a corroding electrode. (a) Simple equivalent circuit. (b) A Nyquist plot of impedance data in which real (x-axis) and imaginary (y-axis) components of impedance

The impedance of the sample can be analysed with reference to an equivalent circuit Fig. 2.2.5a consisting of the resistors and capacitors described above. When an AC signal consisting of a series of sinusoidal varying current at frequencies ranging from 10mHz to 20kHz is applied, the impedance, Z, can be determined from the equation

$$E = I \,.\, Z$$

Since the impedance is a complex vector sum of resistance, inductance and capacitance, calculations can be made to determine the real and imaginary components. These vectors can be plotted on a Nyquist plot as shown in Fig. 2.2.5b and can be used to determine the charge transfer resistance (Trethewey and Chamberlain, 1995).

The knowledge of a corrosion system is crucial during corrosion monitoring. The measurement of corrosion promoters such as dissolved oxygen, acidity, dissolved metal levels etc. in a system, selection of material used and the various circumstances under which the system works are vital to predict corrosion rates of a component. Ashworth

(1987) proposed a corrosion system in which the relation between material, environment and circumstance is systematically presented in Fig. 2.2.6.

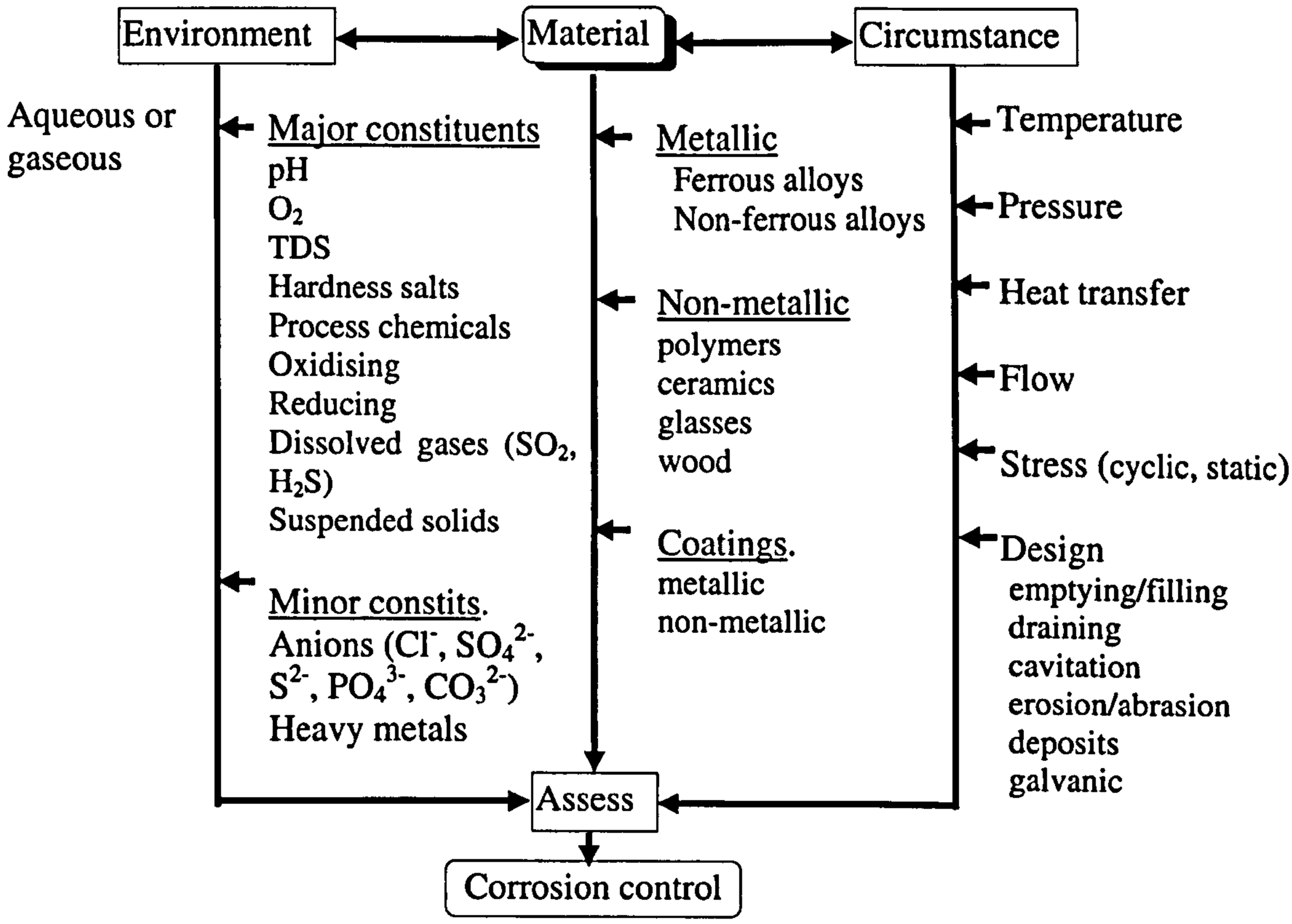


Figure 2.2.6 Ashworth's schematic representation of a corrosion system.

Passivity

"Passivity" of a metal is generally defined as the property of a metal to prevent itself from corroding in a particular environment by restricting the passage of the corrosive electrolyte to the metal substrate surface by forming a thin adherent, non-conducting film basically of an oxide such as Al_2O_3, Cr_2O_3 etc. ASTM defines the "Passivity" as the state of a metal surface characterised by low corrosion rates in a potential region that is strongly oxidising for the metals (Sedriks, 1986). Stainless steels exhibit passive behaviour in a range of corrosive environments due to the formation of a very passive film often supposed to be a complex mixture of Cr_2O_3, Fe_2O_3 and Cr and Fe hydroxides (Neville, 1995). Partial or complete breakdown of passivity (Shreir, 1963b), with the onset of the corrosion, can be brought about by any

factor that produces partial or complete removal of the passivating film. In aqueous solutions at ordinary temperatures, such removal can be affected by electrochemical reduction or oxidation, chemical dissolution at film imperfections or mechanical disruptions (e.g. by bending, stretching, impact scratching, and other forms of mechanical forces).

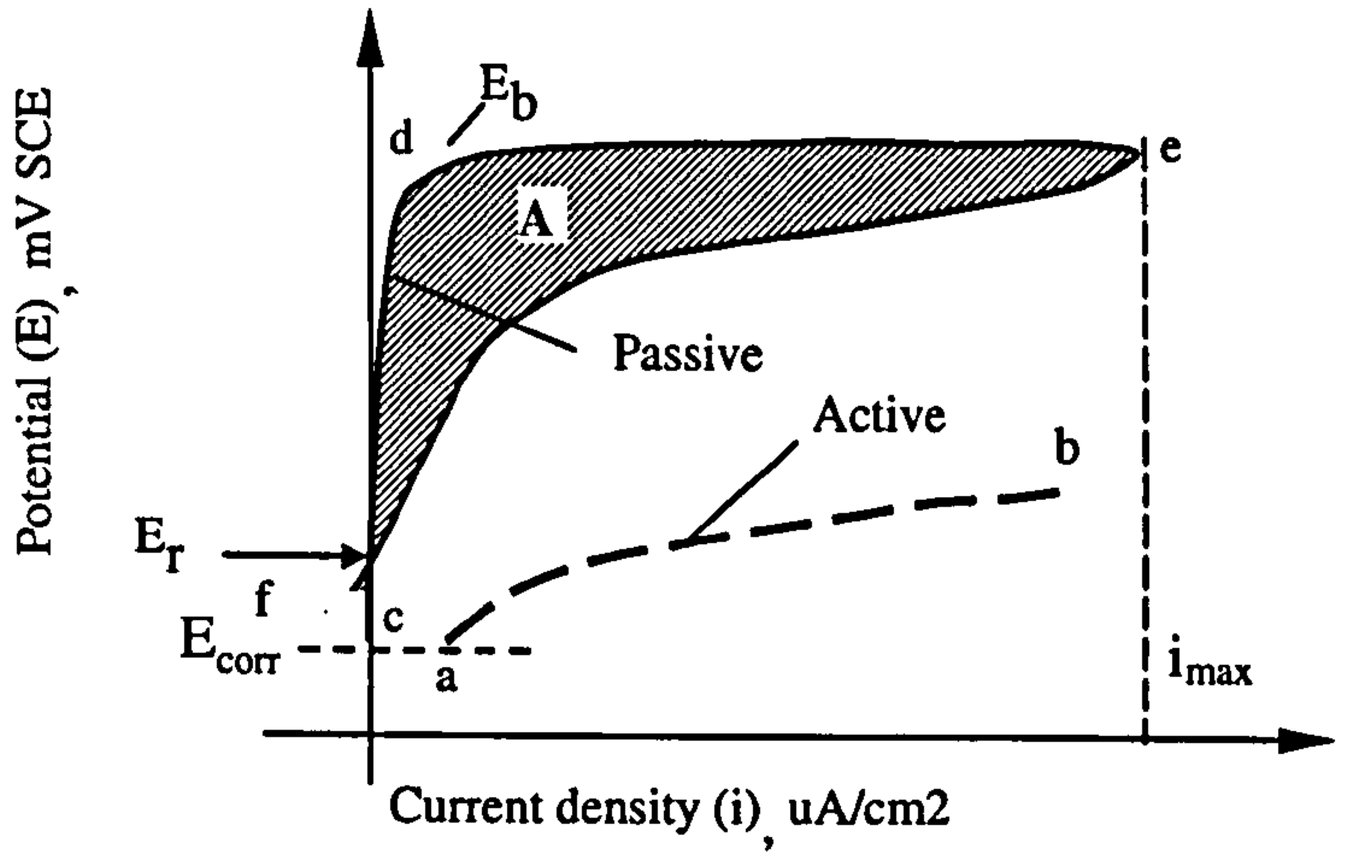


Figure 2.2.7 Electrochemical representation of active passive behaviour and loop formation; E_b - Breakdown potential; E_r - repassivation potential; A- area of hysterisis loop; i_{max} – maximum current density.

The behaviour of a material is manifested by electrochemical methods and often, anodic polarisation is considered as an indispensable tool for evaluating the material's electrochemical performance. An active material i.e. a metal corroding freely in aqueous environment such as a carbon steel shows an anodic curve similar to 'ab' shown in Fig. 2.2.7 with a passage of a substantial amount of current density as soon as the electrode potential value is slightly shifted in the positive direction from its free corrosion potential E_{corr}. A material is passive within a range of potentials positive from E_{corr} that is often shown by anodic curve similar to 'cd' with a very low anodic currents recorded. On reaching the potential 'E_b' often termed as breakdown potential (also known as pitting potential), the material starts registering very high anodic currents. 'E_r' is the repassivation potential (also known as protection potential) when the scan is reversed. The difference between 'E_r' and 'E_{corr}' or the loop area 'A' have been used to assess the danger of localised corrosion occurring e.g. crevice or pitting (Mansfeld, 1988). A smaller loop area means less susceptibility to localised corrosion attacks (Trethewey and Chamberlain, 1995).

Types of corrosion

Uniform corrosion

Uniform corrosion (or 'general corrosion') is characterised by an even, general wasting away of metal from the corroding surface (Gellings, 1976). Virtually all metals are to some extent subject to this type of corrosion under certain conditions (e.g., rusting of carbon steel in the atmosphere or in natural waters, dissolution of steel or zinc in many acids, etc.). If unavoidable, it is sometimes said to be the most desirable form of corrosion, since it allows itself rather well to the life prediction of structures or equipment (in contrast to the localised forms of corrosion).

Localised corrosion

Intergranular corrosion

Intergranular corrosion (IGC), sometimes also indicated as 'IGA' (intergranular attack), is a localised attack at and adjacent to grain boundaries, with relatively little (or virtually no) corrosion of the grains. The particular mechanism of intergranular corrosion in stainless steels (Bain et al., 1933; Greaves and Jackson, 1995) involves the carbide precipitation at the austenite grain boundaries caused by sensitisation (exposure to temperatures around 450-900°C). Corrosion occurs basically due to preferential attack at the carbide/metal matrix interface because of the impoverishment of chromium in the solid solution near the boundaries and as a result of electrochemical cell action (the chromium-depleted region becomes less noble than both the carbide precipitates in the grain boundary and the passive grain interiors). Initially there occurs preferential attack at the anodic site, i.e. at the boundaries and finally dislodgement of whole grain leaving the holes. These carbide particles are stable only below about at 1120K; at higher temperature they either do not form or tend to dissolve if already present (Shreir, 1963b). A schematic representation of a possible mechanism of grain boundary attack is shown in Fig. 2.2.8.

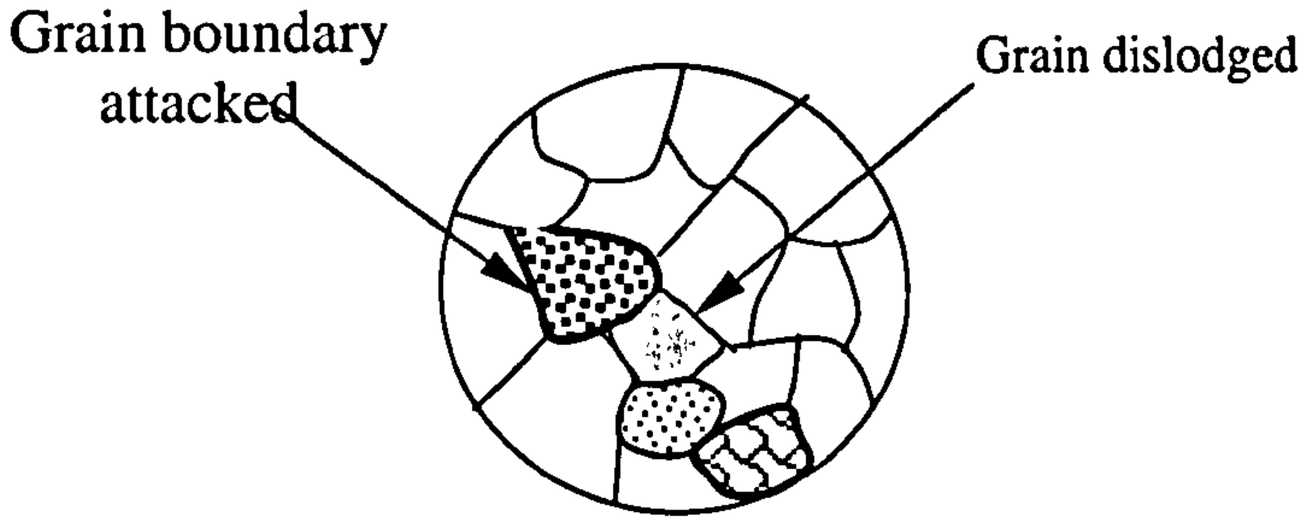


Figure 2.2.8 Localised corrosion attack at grain boundaries of metal.

Crevice corrosion

Crevice corrosion may be defined as an attack at a metal surface in a shielded or restricted environment, compared to the rest of the metal which is exposed to a large volume of electrolyte (Trethewey and Chamberlain, 1995; Ashworth, 1987), e.g. riveted plates, threaded components, welded structures, deposit of sand, corrosion products, interface with non-metal such as plastics, rubber etc. The initiation of crevice corrosion is basically due to environmental factors such as: local depletion of oxygen under a deposit, high chloride content or local drops in pH (Neville, 1995).

A general mechanism of crevice corrosion of stainless steel proposed by Fontana and Green (1978) is as follows:

1. Initially, the electrolyte is supposed to have uniform composition and general corrosion occurs on the whole surface including the crevice zone (Fig. 2.2.9a).
2. Cathodic reaction is stimulated in presence of oxygen. But in the crevice zone where stagnant solution occurs, the oxygen is gradually diminished by its consumption and the depletion starts when oxygen diffusion stops. This slows down the cathodic reaction and the generation of hydroxyl ion is diminished.

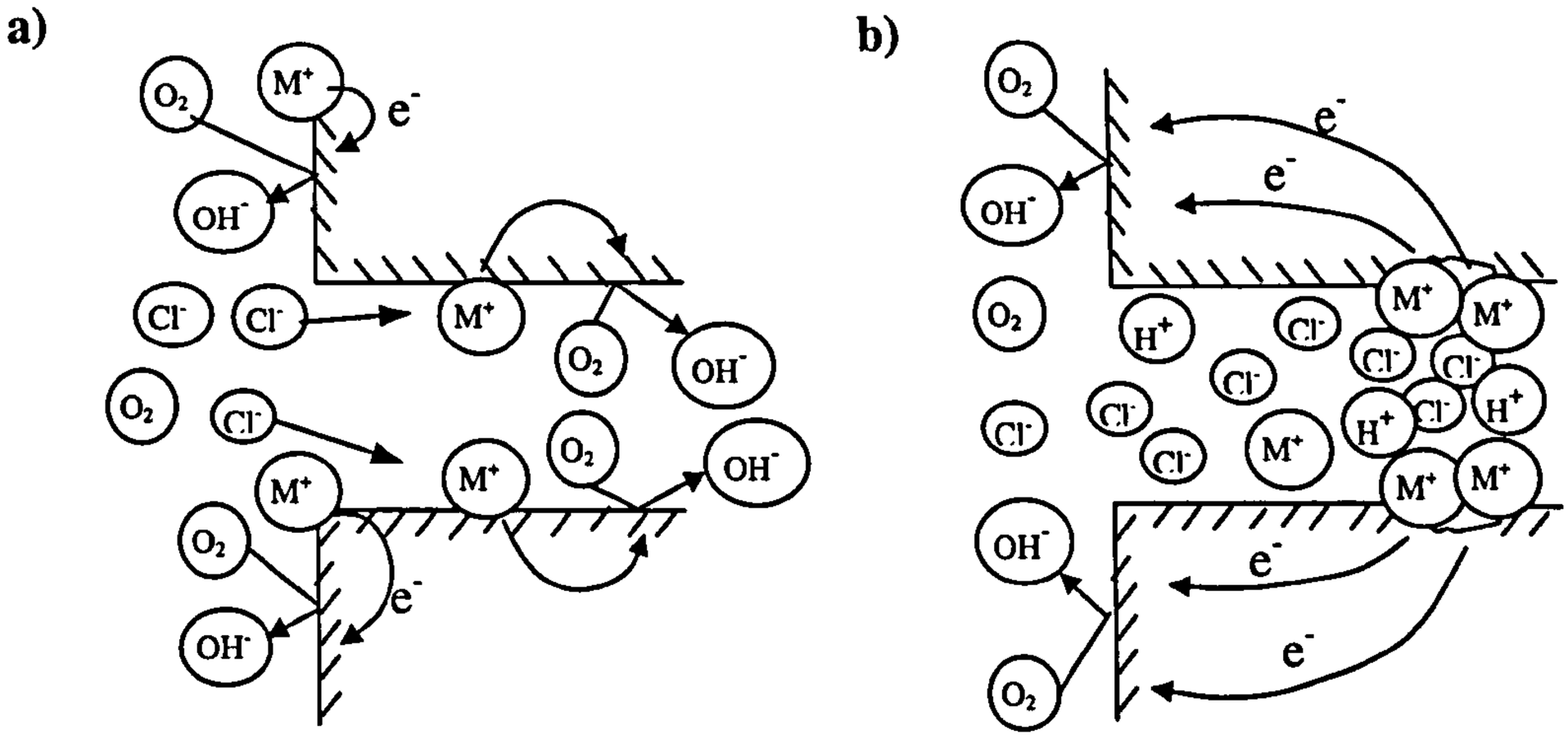


Figure 2.2.9 The Fontana-Greene mechanism of crevice corrosion (a) Initial conditions: corrosion occurs over whole of the metal surface. (b) Final conditions: metal dissolution occurs only inside the crevice where acidity increases, concentration of chloride ion increases, and the reaction becomes self-sustaining (Trethewey and Chamberlain, 1995).

3. Now in the crevice zone starts up the formation of excess of positive metal ions and to counter balance the anodic reaction the negative ions (Cl^- in our case) which is available in sea water migrates to the crevice zone, where complex ions of metal chloride and water molecules are formed. These further undergo hydrolysis forming corrosion product and generating H^+ ions, which reduces the pH at the zone.

$$M^{n+}Cl^-_n + nH_2O \Rightarrow M^{n+}(OH)^-_n + nH^+Cl^-$$

4. The stainless steel, which relies upon the passive film of Cr_2O_3, is affected because of oxygen depletion and eventually this passive film is very unstable in chloride environment (Trethewey and Chamberlain, 1995). The increase of both H^+ and Cl^- ions within the crevice hence accelerates the metal dissolution process. This situation is shown in Fig. 2.2.9b. The dissolution and subsequent hydrolysis of

$$Cr^{3+} + 3H_2O \Rightarrow Cr(OH)_3 + 3H^+$$

Factors affecting crevice corrosion (Mansfeld and Bertocci, 1981):-

1. Bulk solution composition such as Cl^- content, O_2 content and pH
2. Bulk solution environment such as temperature, agitation
3. Mass transport in and out of crevice due to migration, diffusion or convection
4. Crevice solution such as hydrolysis equilibrium
5. Electrochemical reactions such as metal dissolution, oxygen reduction or hydrogen evolution
6. Alloy composition such as major constituents, minor additions or impurities
7. Passive film characteristics such as passive current, film stability
8. Crevice type such as metal/metal, metal/non-metal, metal/ marine-growth
9. Crevice geometry such as gap, depth
10. Total geometry such as exterior to interior crevice area ratio, number of crevices

Pitting

The pits are characterised by the formation of tubercles, small scabs of corrosion products over the hole. Pits are formed where there occurs:-

- a surface scratch or mechanically induced break in protective film.
- an emerging dislocation or slip step caused by applied or residual stresses.
- a compositional heterogeneity such as inclusion, segregate or precipitate.

More recently 'pitting' has been sometimes shown to occur by differential-aeration corrosion. The mechanism of pitting beneath the water droplet occurs preferentially due to the oxygen depletion at the centre of the water droplet as shown in Fig. 2.2.10a, b. where, the central zone becomes anodic to the outer zones which are cathodic. The corrosion products grow over the pit and its surroundings, forming the scab and isolating the environment within the pit from the bulk electrolyte. The autocatalytic process is assisted by an increased concentration of chloride ions within the pit.

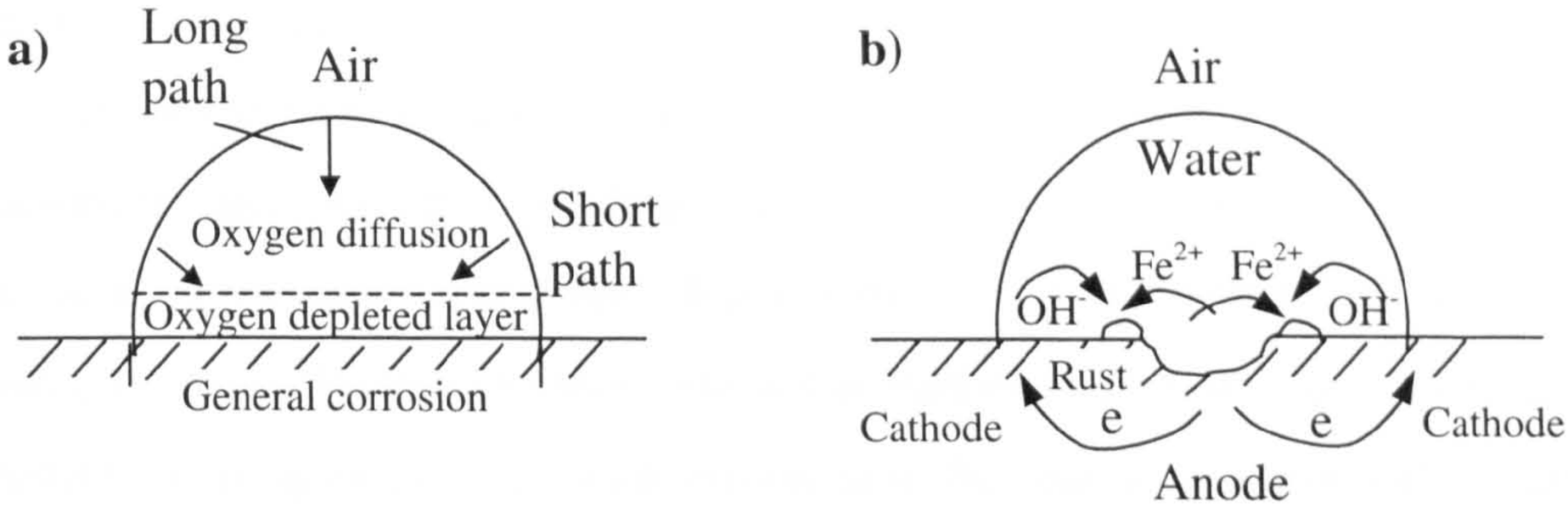


Figure 2.2.10 The pitting mechanism under a water droplet due to differential aeration (a) General corrosion over the whole of the wetted metal surface depletes the oxygen levels in the adjacent electrolyte, (b) Longer diffusion path for oxygen to reach the central area makes this the anode. Metal dissolution occurs in the centre of the droplet and reaction of metal ions with hydroxyl ions formed at the edge generates a ring of rust around the corrosion pit (Trethewey and Chamberlain, 1995).

Bimetallic or Galvanic Corrosion

Galvanic corrosion (also called 'contact corrosion' or 'two-metal corrosion'), occurs when two dissimilar metals in electrical contact are exposed to an aqueous environment and form an electrochemical cell (Robert et al, 1997).

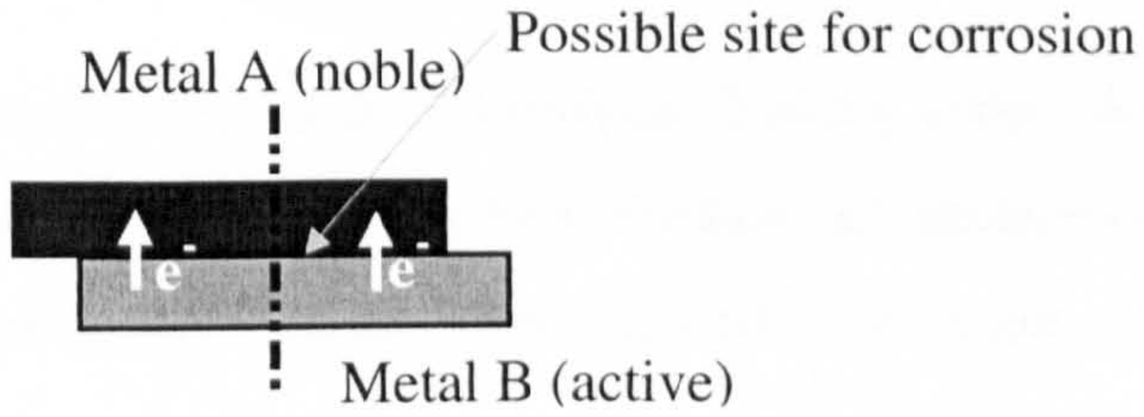


Figure 2.2.11 A possible site for galvanic corrosion within coupling of two dissimilar metals

Figure 2.2.11 shows a schematic diagram of a galvanic cell formed between two different metals *A* and *B*. The metal with the most active potential becomes the anode while the more noble metal becomes the cathode. The driving force for the galvanic corrosion is the difference in electrical potentials of the two dissimilar metals in contact.

Other type of galvanic cells include thermogalvanic corrosion, when a galvanic cell arises from temperature differences. Several other specific types of concentration cells include : deposit corrosion or under-deposit corrosion, 'filiform corrosion' or under-film corrosion, and 'selective leaching' or 'dealloying' corrosion (which is due to galvanic cells on a microscopic scale). 'Electrolysis' or 'stray current corrosion', on the other hand, is caused by an extraneous electrical current, which sets up an 'electrolysis cell', thereby creating similar corrosion effects as in the 'galvanic corrosion' processes.

Hydrogen Damage

All forms of hydrogen damage are caused by the (local) presence of, or the interaction with, hydrogen. Hydrogen blistering and hydrogen embrittlements are caused by penetration of atomic hydrogen into metal. Decarburization (high-temperature attack) is caused by moist hydrogen at high temperatures. The origin of hydrogen is often found in the cleaning, pickling, cathodic protection, welding, treatment and operation (and even in a corrosion process).

Flow induced corrosion

Many engineering systems operate with electrolytes flowing either through or around them. This mode of corrosion which occurs because of predominantly enhanced electrochemical processes, is termed *flow-induced corrosion* (Trethewey and Chamberlain, 1995).

This type of corrosion is based upon three basic conditions:

- Replenishment of oxygen

The replenishment of oxygen can be a mitigating factor for certain metals, which rely on maintaining of a stronger passive film (e.g. stainless steels) under flowing conditions but are adversely affected by stagnant situation often associated with the formation of

differential aeration cells. But this can be possible only when the relative motion is not too great such as not to induce mechanical damage to the surface due to flowing condition. The same situation might be different for an active metal. The liquid flow might constantly remove the corrosion products and subsequently bring a fresh metal to corrosive electrolyte e.g. in carbon steels and cast irons. Figure 2.2.12 shows a schematic diagram of oxygen reduction curves in static and liquid flowing conditions.

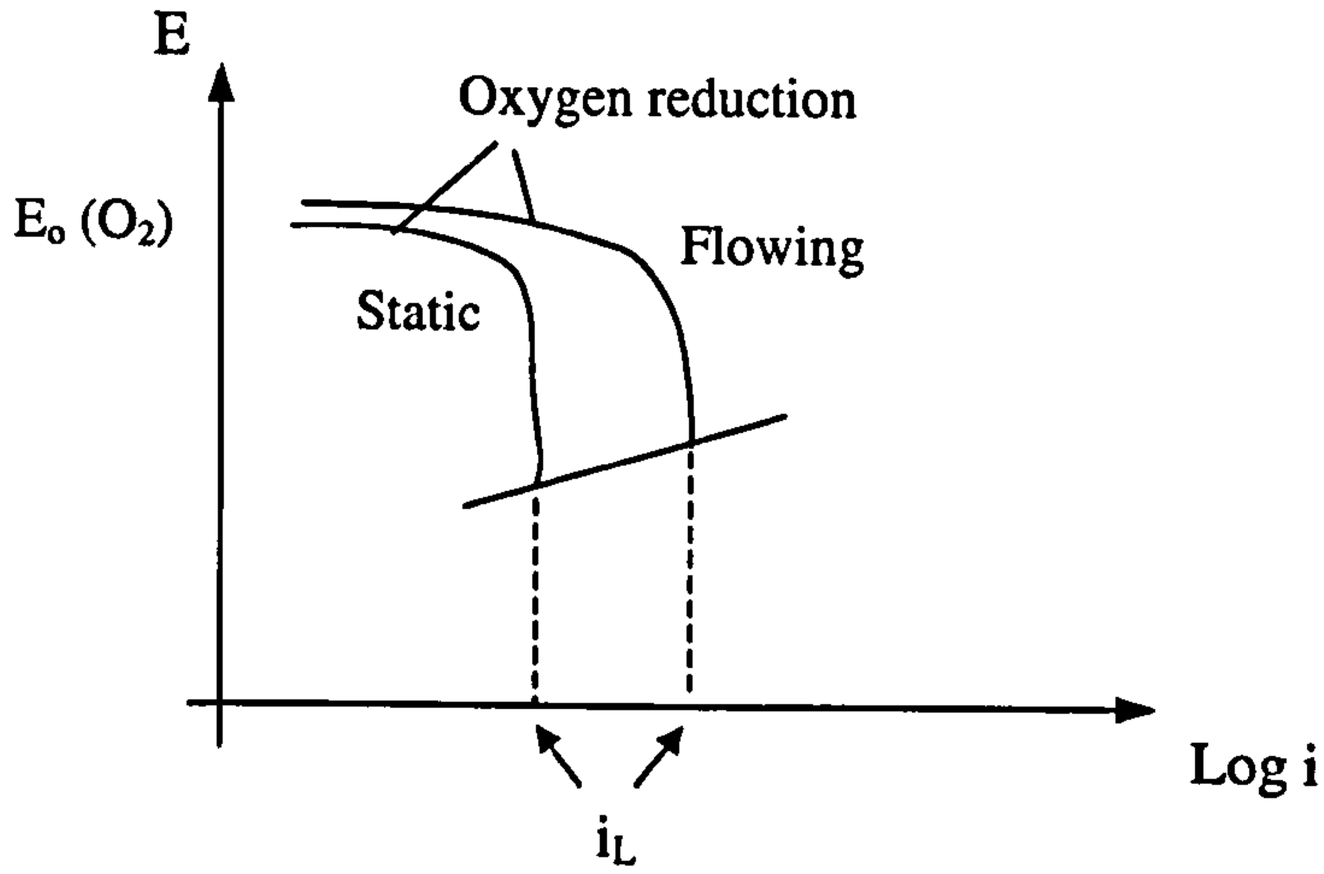


Figure 2.2.12 Schematic polarisation curves showing depolarised oxygen-reduction in flowing systems.

- Replenishment of aggressive ions

A detrimental effect of increased flow rates is the constant supply of aggressive ions such as chloride or sulphide, which might increase the corrosion rate substantially.

- Removal of protective layer

Presence of even the smallest amount of solid particles may induce the mechanical damage to a protective layer and the corrosion is enhanced. Another significant effect occurs when the situation is turbulent causing 'cavitation' and 'impingement attack'. Flow induced corrosion is often called erosion-corrosion and will be discussed later in Chapter 3.

2.3 Corrosion control and prevention

It is natural for most of the metals to corrode unless prevented by human endeavour. Methods of preventing corrosion have been illustrated elsewhere (Gellings, 1976; Shreir, 1963a; Vernon, 1957; Chandler, 1985). Design, material selection, control of environment, application of coatings, protection by electrochemical methods are considered as general methods for preventing corrosion. Corrosion testing and monitoring, supervision and inspection are equally crucial for corrosion control. A corrosion control model by Ashworth (1987) is shown in Fig. 2.3.1.

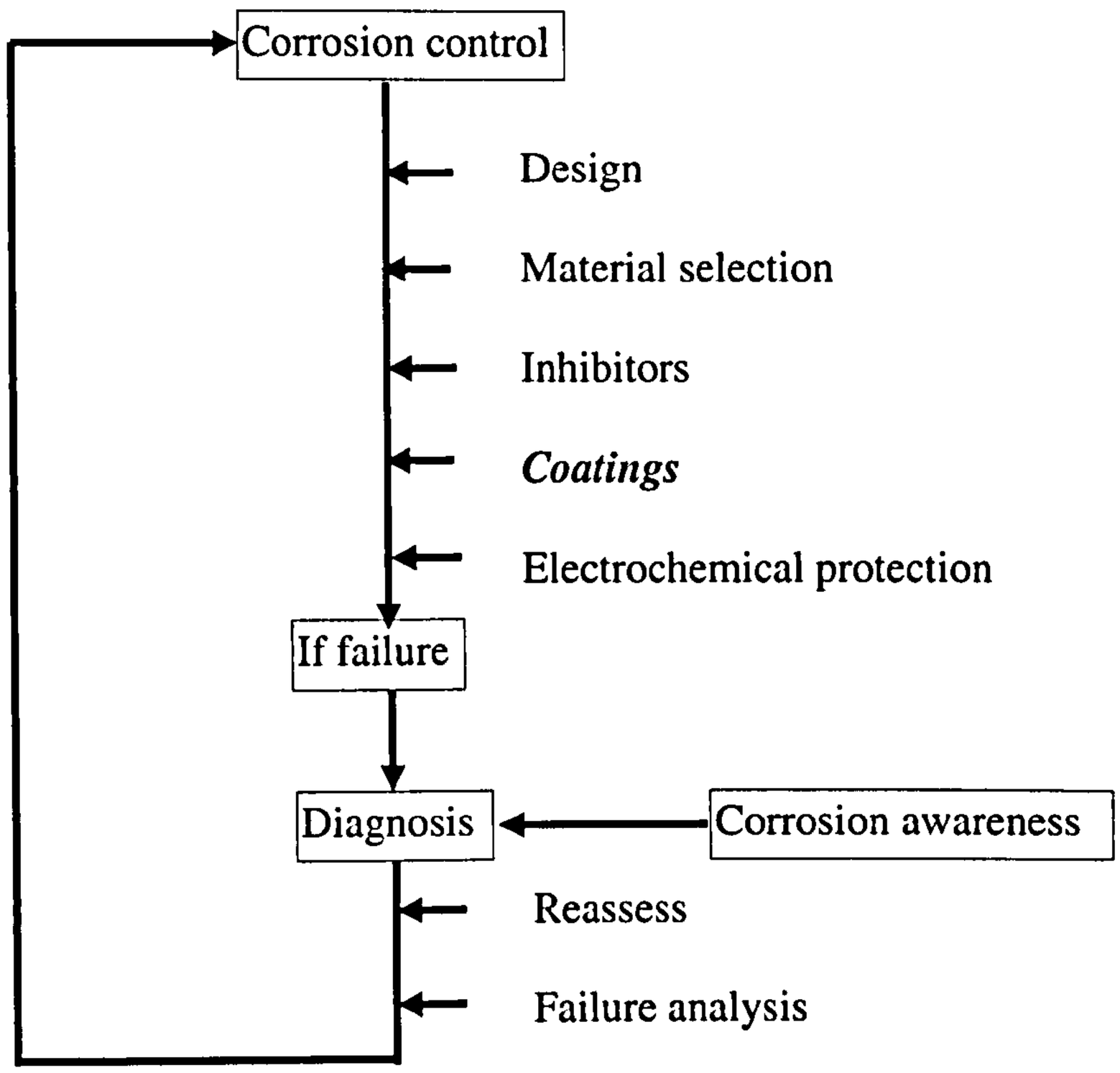


Figure 2.3.1 Ashworth's schematic diagram of a corrosion control system.

Design

A good design can permit the successful use of relatively cheap material in corrosive environment, whereas a bad design might lead even the most exotic materials being at risk of corrosion. Geometrical configurations that facilitate corrosion should be avoided e.g.

- Inadequate drainage and ventilation
- Crevices and situation where deposits can form
- Sharp bends, irregularities, protrusions, roughness etc. that lead to erosion-corrosion such as impingement attack or cavitation damage
- Designs which are inaccessible for periodic maintenance
- Designs with two different metals in the galvanic series which might result in bimetallic corrosion

The working environment such as relative humidity, temperature, pH, oxygen concentration, dissolved pollutants, velocity etc. should be taken into account at the initial stage of the design process.

Material selection

Selection of material as a method of corrosion control is an essential part of the design exercise. Selecting the most corrosion resistant material for a particular environment is not the only principal object, however, meeting many conflicting requirements such as mechanical properties, appearance, ease of fabrication, material availability as well as overall cost are important factors affecting the choice of material. As one indication of the influence of environment on corrosion behaviour of material, the relative resistances of metals to general surface corrosion in low-velocity seawater at ambient temperature are indicated in Fig. 2.3.2 (in which the break in scale between copper and carbon steel represents a relatively large increase in corrosion rate).

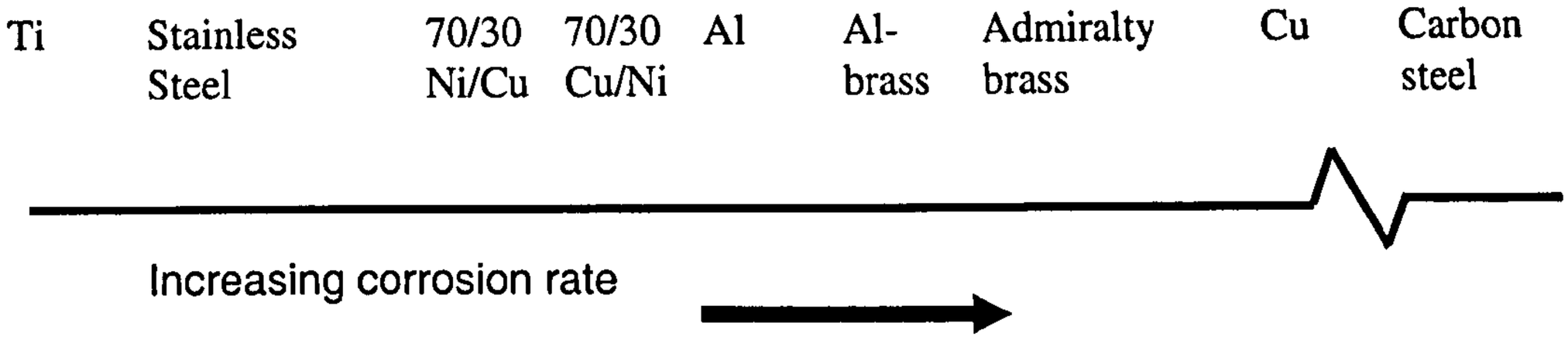


Figure 2.3.2 Relative corrosion rates in moving, aerated seawater at ambient temperature.

However, different situations pertain to localised forms of corrosion with some of the most corrosion-resistant materials listed above which make the selection of material not an easy job.

Inhibitors

The use of inorganic or organic compounds as corrosion inhibitors is quite common. The inorganic inhibitors are generally divided into oxidizing and non-oxidizing compounds. The inhibitors generally produce a marked decrease in corrosion of the metal by affecting either the anodic or cathodic processes. Anodic inhibitors increase the polarisation of the anode by reaction with the ions of the corroding metals to produce either thin passive films, or salt layers which coat the anode. Such anodic inhibitors, used primarily on steel, are soluble hydroxides, phosphates, polyphosphates, nitrites, silicates, and carbonates (Greathouse and Wessel, 1954). Cathodic inhibitors affect the oxygen-reduction and hydrogen-generation cathodic reactions (Trethewey and Chamberlain, 1995). In addition to the oxygen reduction cathodic reaction, one type of inhibitor reacts with the hydroxyl ion to precipitate insoluble compounds on the cathode site, thus blanketing the cathode from the electrolyte and restricting access of oxygen to the site. Magnesium, zinc, or nickel salts serve as cathodic inhibitors for iron and steel under conditions of partial immersion (Greathouse and Wessel, 1954). However, it must be emphasised that the successful use of inhibitors frequently requires substantial knowledge of their action and a thorough understanding of the corrosion process.

Coatings

Protective coatings have been used as a corrosion prevention tool since ancient times and details about the protective coatings can be found elsewhere (Gellings, 1976; Shreir, 1963a). A coating applied to a metal to prevent corrosion may offer a form of sacrificial protection, act as an inhibitor or simply exclude the corrosive environment. For the latter, the coating must be impermeable to the corrosive electrolyte, resistant to subsequent mechanical damage etc. The most common coatings may be categorised as indicated in Table 2.3.1.

Metallic coatings	***Inorganic coatings***	***Organic coatings***
Electrodeposition	Anodizing	Conventional Paints
Hot-dipping	Phosphating	Epoxy coatings
Cladding	Cement	Bitumen
Diffusion	Thermal Spraying	Chlorinated rubber
Laser alloying		Plastic linings
Thermal Spraying		

Table 2.3.1 Types of protective coatings and coating methods.

Thermal Spraying

Thermal sprayed coatings have primarily been developed to combat erosive wear. However, they have been increasingly demanded for applications in very hostile environments where both erosive wear and corrosion occur simultaneously. The environments range from cryogenic temperatures to temperatures exceeding 1500°C, from very low pressures to high pressures, and chemically inert to extremely acidic or basic liquids.

The advanced thermal spray coating processes include detonation gun, high velocity oxy-fuel, and plasma arc spray (Tucker and Ashary, 1995; Pawlowski, 1995). One application of these coatings is to replace coatings such as electroplated chromium, which have environmental problems. In all thermal spray deposition processes, material, usually in the form of powder, is heated to near its melting point, accelerated to a relatively high velocity, and allowed to impact on the surface to be coated. The major

advantages are: greater flexibility to use different coating material, ability to coat the surface without significantly heating it without changing its metallurgical structure or mechanical properties, ability to strip to worn coatings and reapply new coatings. A major disadvantage is the line-of-sight nature of the deposition. Details about this technique will be discussed later in Chapter 4.

Electrochemical protection

The basic corrosion principle in an aqueous environment is already illustrated in section 2.2. As stated in section 2.2, aqueous corrosion is simply an electrochemical process, in which metal tends to corrode due to anodic reaction,

$$M = M^{n+} + ne^{-}$$

which is generally thermodynamically favoured as metals often adopt an electrode potential which is more positive than the equilibrium potential. Metal can be protected by reversing the above anodic reaction by achieving the electrode potential more negative than the equilibrium potential. This method is termed as "Cathodic Protection" and there are generally two methods of achieving this reduction in electrode potential.

i) Impressed current method

This involves using an impressed current from a DC generator or AC power source and rectifier together with an auxiliary electrode (Ashworth, 1987). The negative shift in electrode potential of the component to be protected will be in direct proportion to the magnitude of the current supplied by the electrical source and the larger the surface area to be protected the higher will be the required current for full protection. In pipeline work, the system is generally used in conjunction with a coating aiding to diminish current requirements, as the current is then needed only at the flaws (Greathouse and Wessel, 1954).

ii) Sacrificial anode method

Protecting metallic structures by attaching to them a more electronegative metal (i.e. by creating galvanic cell in which negative charges transfer from base metal to noble metal) is termed sacrificial protection (Ashworth, 1987; Robert et al., 1997). Cathodic protection using sacrificial anode needs no power source and is simple to install. Examples of such protection are used in North Sea oil production platforms (Ashworth, 1987).

Anodic protection

This method in which metal is protected by inducing a positive potential (in which some anodic product is formed which may serve to stifle further anodic reaction and thereby reduce the corrosion rate or by forming passive film at more positive potential) is termed anodic protection. However, the application of this process is quite restricted due to many factors which are described elsewhere (Ashworth, 1987).

2.4 Corrosion of stainless steel

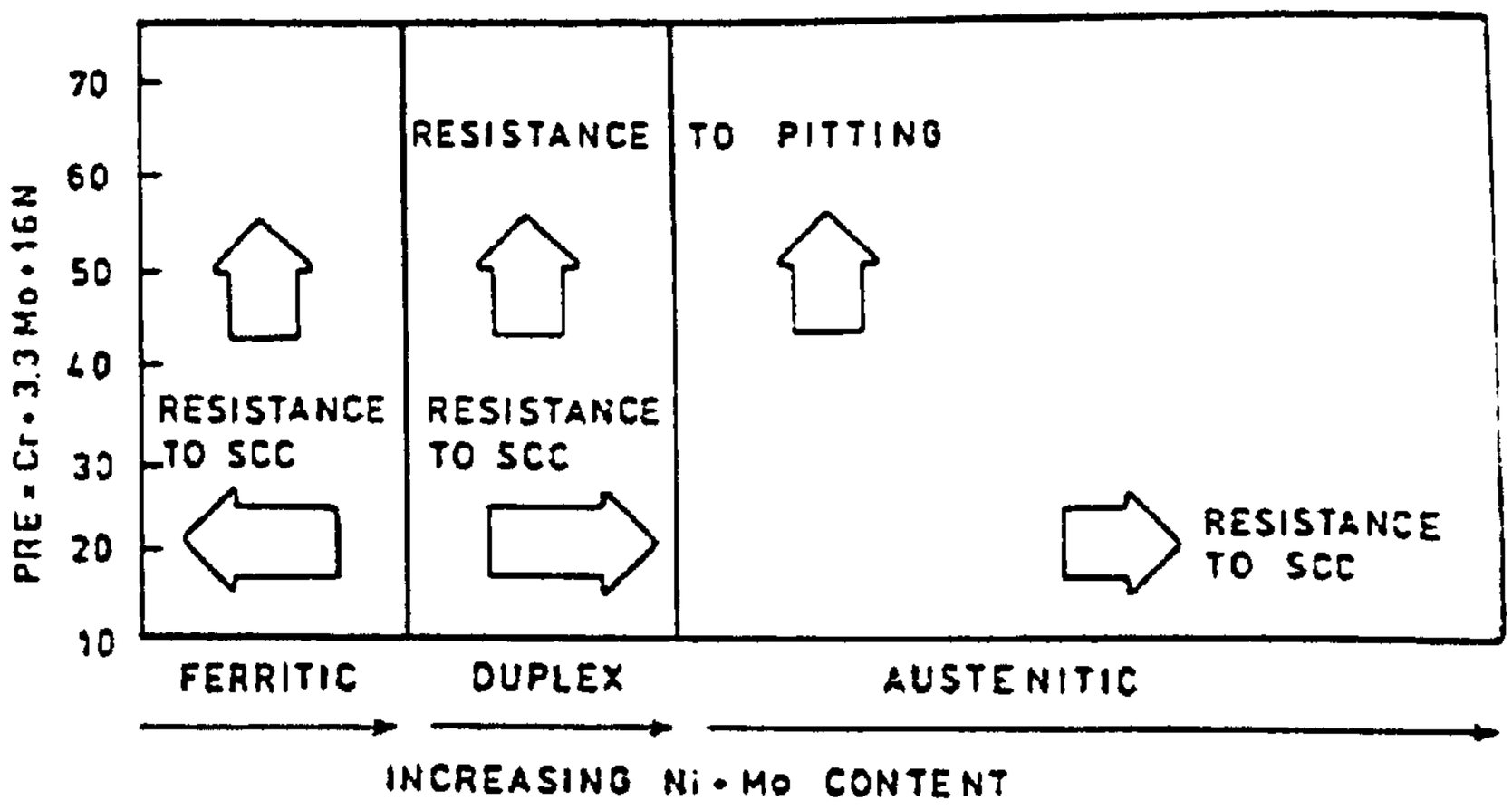
Corrosion of metals has been the matter of concern in industry for many decades. Localised corrosion of stainless steels is generally considered as the main drawback, which limits their suitability for marine applications. Thus, further development in material's resistance, in particular to crevice and pitting is needed to combat the aggressive nature of chloride containing media. Development of new materials is a slow process and needs extensive backup from material's applications e.g., its nature, the working environment, its durability and the cost effectiveness. There has been continuous research and a lot of advancement has been done on stainless steels during the last century. However, increasing demands for marine applications have led to development of new types of stainless steel alloys with more corrosion resistance.

Selection of materials for seawater systems (offshore oil production, power plants, petrochemical plant, desalination and many other coastal industrial plants) is often performed to meet the requirements of two basic systems: a) Low initial cost systems and b) High reliability systems (Todd, 1979). PRE (Pitting Resistance Equivalent) values calculated from the composition of the steel can be used as the first estimate for selection of stainless steels for pitting and crevice corrosion resistance. The PRE value can be estimated by the equation (Alfonsson and Qvarfort, 1992):

$$PRE = \%Cr + 3.3 * \%Mo + 16 * \%N$$

Nitrogen is considered to improve the localized corrosion resistance of the austenite phase.

A schematic diagram of the effect of composition and microstructure on various forms of localised corrosion of stainless steels is shown in Fig. 2.4.1. Increasing the amount of alloying elements, in principle, increases the resistance to all forms of localised corrosion.



SCC-stress corrosion cracking

Figure. 2.4.1 The effect of composition and microstructure on some forms of localised corrosion of stainless steels (Ylasaari et al., 1997).

Ylasaari et al (1997) illustrated a relationship between aggressive anions and temperature and found a more accurate method of material selection using a pass-fail chart in log [X^-]-T domain based on a series of cyclic polarisation curves; where, '[X^-]' is the concentration of an aggressive anion and 'T' is the temperature of the solution.

Dundas and Bond (1985) have shown austenitic, ferritic and duplex stainless steels containing a minimum of 25%Cr-5%Mo, 27%Cr-3.4%Mo and 25%Cr-3.2%Mo to be resistant to crevice corrosion in 25°C seawater. It was shown that austenitic and duplex stainless steels require a minimum of 0.2%N for the crevice corrosion resistance. They found that significant reduction in either chromium or molybdenum content caused substantial attack. Lu et al. (1993) suggested a mechanism by which molybdenum and nitrogen favourably influence the pitting resistance of austenitic stainless steels and was shown that nitrogen is able to prevent the transpassive dissolution of molybdenum from the passive film of these stainless steels. Higher levels of chromium, molybdenum and nitrogen in duplex stainless steels result in greater resistance to passivity breakdown (Sedriks, 1986).

Salvago and Fumagalli (1996) illustrated the application of the breakdown potential (E_b) distribution in corrosion comparisons of several stainless steels and that E_b distribution on the graph of E-vs-log (cumulative breakdown frequency, F) can be used to deduce the localised corrosion resistance of stainless steels.

Other methods of evaluating the localised corrosion resistance of passive alloys include Critical Crevice Index "CCI" and Critical Pitting Index "CPI" criteria. The pitting and crevice indices usually reflect the composition of the alloying elements. Most commonly used values are $CCI = \%Cr + 4.1\%Mo + 27\%N$ and $CPI = \%Cr + 3.3Mo + 13\%N$ based on austenitic stainless steels and also can be used for rolled/forged duplex stainless steels (Steinsmo et al., 1997). The correlation between CCI/CPI and CCT/CPT was shown by the author, where CCT- critical crevice temperature; CPT- critical pitting temperature.

The effect of increased temperature from 25 to 60°C resulted in increased general corrosion, pitting and pit propagation (Saricimen et al., 1994) of UNS S31603 and it has been reported that the stability range of the passive film decreased as the salt solution becomes more corrosive at higher temperature due to increased reaction kinetics. They also postulated that the higher temperature passive film has different structural characteristics than that formed at the lower temperature, which could be attributed to the thermodynamics of hydrolysis reactions between the ions of the alloying elements such as Fe, Ni, Cr, Mo and water molecules.

Mollica et al. (1988) studied the influence of seawater temperature in the range of 25 to 40°C on crevice corrosion of a series of stainless steels. The authors found that the increase in temperature caused an improvement in the resistance to the corrosion initiation and decrease in the propagation rate of localised corrosion primarily due to decrease in the oxygen reduction rate on cathodic surfaces linked to a decrease in activity of aerobic bacteria settled on.

Wang and Akid (1996) recognised that the elongated sulphide-type inclusions in high strength steels were responsible for pitting corrosion in 0.6M sodium chloride (NaCl). Sulphide inclusions or the intervening area surrounding the inclusions are generally

anodic with respect to the matrix and that the H_2S and HS^- ions formed by dissolution of sulphides has the most detrimental effect on the development of the corrosion pits.

Neville (1995) has performed extensive work on corrosion mechanisms of a series of austenitic and duplex stainless steels on marine applications. The study has assessed the increased complexity due to the effect of elevated temperature compared to that at ambient temperature on the electrochemical processes and mechanisms of corrosion attack in static seawater. Increased temperature in static seawater resulted in higher susceptibility of the materials to localised corrosion initiation and propagation. However, the extent of attack and the electrochemical behaviour is different for each material. At ambient temperature, duplex stainless steels (SAF 2205, 25Cr duplex) were found to exhibit significantly better corrosion resistance than the austenitic stainless steel (UNS S31603), as predicted by PRE value. But this superiority no longer exists as the temperature was increased up to 60°C.

Hodgkiess and co-workers (1987) have studied galvanic currents and potentials for bimetallic couples of three different grades of stainless steels, carbon steel, 90 Cu/10Ni and titanium when exposed to seawater in the laboratory at temperatures 18°C and 60°C and varying oxygen contents. It was shown that an intermediate air exposure could cause transient positive shifts in couple potentials and increases in galvanic current when couples are returned to the seawater but without any major long-term effects. Protection of stainless steels to pitting and crevice corrosion could be significantly achieved when electrically coupled with carbon steels. The effect of higher temperature in seawater in the galvanic corrosion rates seemed to be less after the first few hours exposure. The authors have also found that the galvanic-corrosion problems are not likely between electrically coupled, corrosion resistant materials such as 90Cu/10Ni, stainless steels (316L or higher grades) and titanium. Higher corrosion rates in carbon steels were confirmed when coupled to copper-nickel alloys than when coupled to stainless steels (Hodgkiess and Lim, 1993).

CHAPTER 3. EROSION-CORROSION

3.1 Introduction

The need to maximise efficiency in handling fluids demands higher flow rates with the inherent risk of flow-induced corrosion. Flow-induced corrosion can be defined as a complex form of material deterioration by an electrochemical corrosion reaction, which is accelerated by the relative movement (flow hydrodynamics) between a corrosive fluid and the metal surface (Internet 1; Shreir, 1963a). The increased corrosion rate caused by a high-velocity fluid is associated with the transport of species to and from the metal surface-in particular stimulating the oxygen-reduction cathodic reaction. Moreover, rapidly flowing water can have additional mechanical effects, in causing the tearing away of corrosion products (including protective oxide film that will result in localised attack at the areas at which the film is removed) and direct mechanical damage to the metal surface (Shreir, 1963a; Engel and Klingele, 1981). The four basic types of flow-induced corrosion are: 1) *mass transport controlled corrosion,* 2) *phase transport controlled corrosion,* 3) *erosion-corrosion* and 4) *cavitation corrosion.*

Research on flow induced corrosion has been concerned with single-phase flow (liquid or gas). Modern research and development focuses on multiphase flow that can be encountered in oil and gas production (which consists of several phases such as hydrocarbon condensate, water vapour, gas and sand) and on two phase flow in sea water handling systems (which comprises mainly of liquid and solids). A schematic model of flow induced corrosion by Heitz (1991) is shown in Fig. 3.1.1.

Mass transfer (particularly in single-phase flow) plays a crucial effect in controlling the extent of material deterioration, which involves convective diffusion as a rate-determining step (Heitz, 1991). Mass transport corrosion is generally more or less uniform. However, in contrast, increased mass transport can reduce the corrosion rate (especially for material such as stainless steels) provided low velocities exist which can cause passivation and also by minimising differential-aeration cells by preventing the development of critical pit chemistry (Internet1; Ashworth, 1987). Similarly, the flow

may be sufficient to prevent deposition of silt or dirt, which might otherwise cause differential-aeration cells in the crevices beneath.

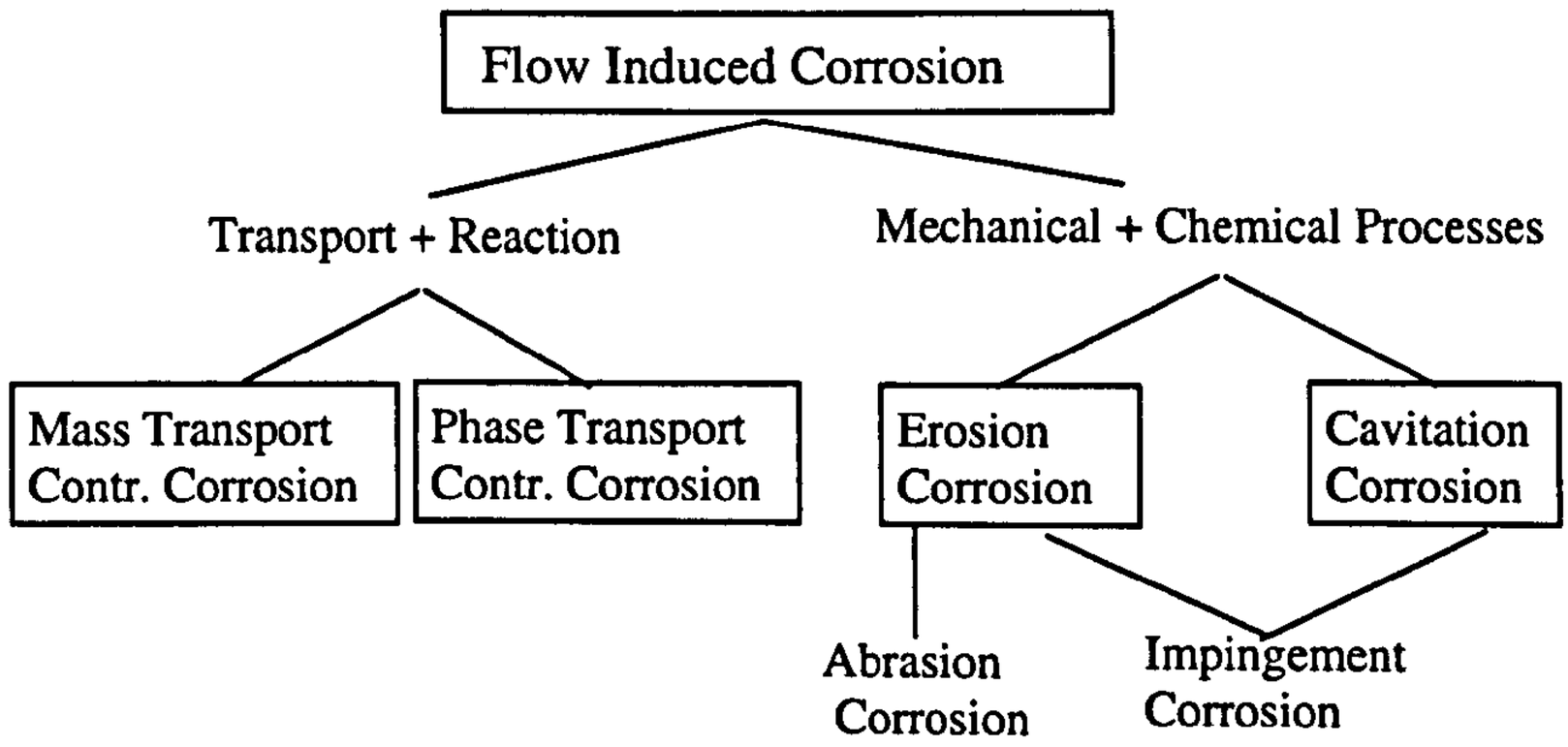


Figure 3.1.1 Classification of flow-induced corrosion.

Phase transport controlled corrosion implies that the wetting of the metal surface by a corrosive phase contained in a multiphase fluid is dependent on flow such as water droplets containing hydrocarbon with dissolved corrosive component. These droplets on contact with the metal surface adhere and corrode by developing a rough surface in the corroded area.

There is sometimes a problem in differentiating unambiguously between erosion-corrosion and mass transport-controlled corrosion because hydrodynamics influences momentum transfers (mechanical action) and mass transport in the same way. Generally erosion-corrosion can be distinguished phenomenologically by its appearance in the form of shallow pits, horseshoes, or other local phenomena correlated with direction of flow (Heitz, 1991).

In a single-phase flow, the crucial parameters, which influence the deterioration rate are pressure and shear stresses variations of the liquid whereas it is the direct particulate impact in two phase flow (Heitz, 1991). Precisely, erosion-corrosion plays a detrimental role in most of the engineering components by the conjoint action of both electrochemical corrosion and mechanical wear. Quite often the material loss due to erosion-corrosion is much higher than the sum of pure corrosion and mechanical wear

due to the factor so called "synergy" which will be discussed later. In most systems the rate of attack increases with velocity and data on effect of velocity of seawater on corrosion of metals can be found elsewhere (Shreir, 1963b). Erosion-corrosion in the widest sense of the term is often taken to include cavitation and impingement attack.

Chapter 3 in general will be split into several sections. Section 3.2 contains review on basic hydrodynamics of liquid erosion. Basics of solid particle erosion in dry condition will be detailed in section 3.3 following the solid-liquid erosion in section 3.4. Section 3.5 gives a brief review on methods for evaluating wear rates. The erosion-corrosion interaction mechanism is described in section 3.6 with general materials characteristics in section 3.7.

3.2 Basic hydrodynamics of liquid erosion, mass transfer, cavitation and impingement attack

To understand liquid erosion-corrosion mechanisms, it is important first of all to understand basic hydrodynamics. Much of the work done in this project considers a free turbulent liquid jet (ranging from 1 to 4mm in diameter) expelled from a fine nozzle (at velocities ranging from 12 to 107ms^{-1}), and impinging perpendicularly on a metallic surface stationed in a mass of miscible fluid similar to that shown in Fig. 3.2.1.

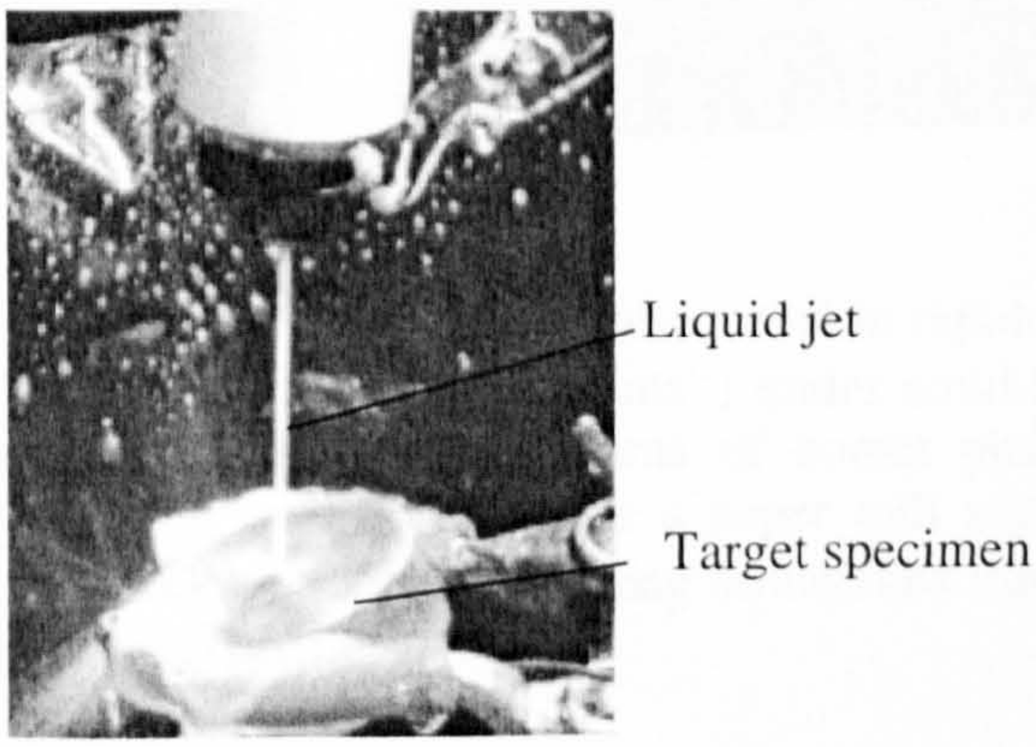


Figure 3.2.1 A fine liquid jet impinging on a metallic surface (in laboratory test).

Many laboratory tests reported in the literature have been based on rotating disc apparatus developed in the 1950's, which operates under clearly defined hydrodynamic parameters and can be used for fundamental studies of mass transfer characteristics and kinetics of anodic and cathodic processes. Another approach to fundamentals of liquid erosion-corrosion is based on a flow loop model where a fine jet of liquid stream is incident on the specimen (Giralt and Trass, 1975; Meyer et al, 1994; Neville, 1995). This approach has been commonly used in recent years and reflects impingement in real applications. Figure 3.2.2 shows an interesting example of attack observed due to erosion in flowing conditions in the laboratory and comparable damage on a pipe. Several other techniques have been successfully used to assess corrosion under hydrodynamic conditions including rotating cylinder (Silverman, 1984, 1988; Holser et al., 1990), flow through pipes (Kastner et al., 1993; Sakamoto et al., 1995b), vibratory horns (Sakamoto et al., 1995a; Brijesh and Hansson, 1990; Kreye et al., 1998), flow through nozzles and orifices (Auret et al., 1993), annular flow channels (McDonald et al., 1988). Vibratory horns are useful in cavitation studies that produce bubbles, which subsequently collapse when the pressure recovers at the low-pressure region.

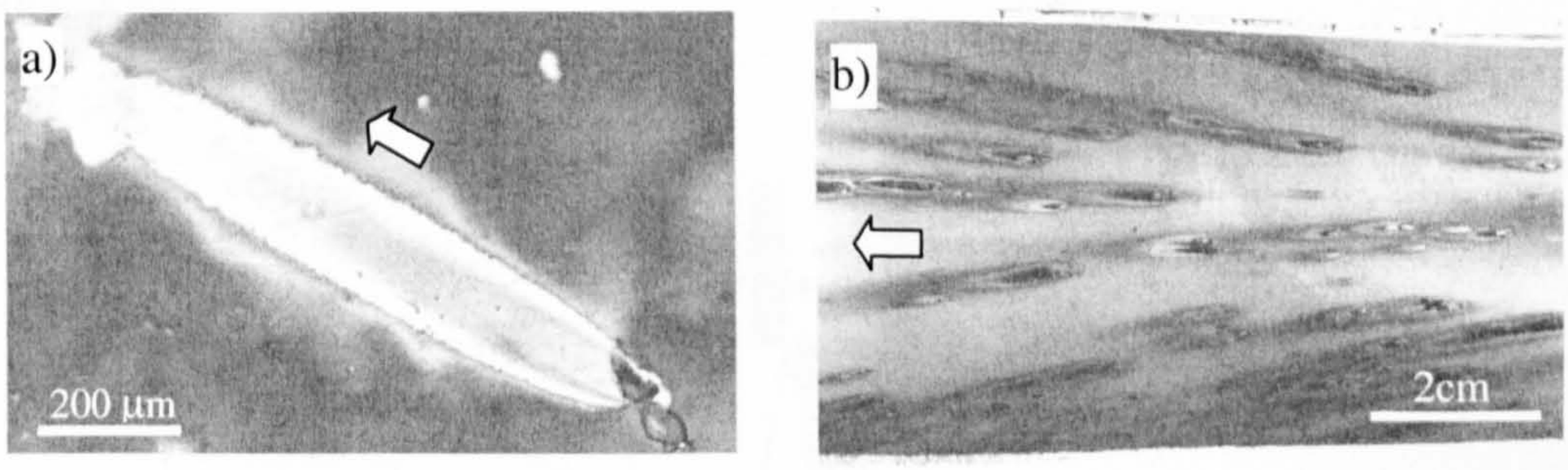


Figure 3.2.2 a) Comet pit attack on UNS S31603 stainless steel in rapid laboratory test (after anodic polarisation at 50°C, pH = 8.2, 72ms^{-1}) under solid-free liquid (artificial seawater) impingement test; and b) streams of comet pits on UNS S31603 stainless steel pipe after 4 weeks' service in a paper mill starch line at 80°C, pH = 9.1, 0.6-1ms^{-1} flow velocity, arrows showing liquid flow directionality (with permission of Hodgkiess and Neville, 1999).

The impinging test technique usually comprises a fine submerged liquid jet striking a stationary flat specimen. The free jet spreads out through a cone of half-angle about 10° (Davies, 1972), entraining a considerable amount of surrounding fluid in the outer part of the jet (Fig. 3.2.3). This simple method allows a precise study of the influence of

flow variables on the erosion-corrosion behaviour including 1) single phase liquid flow, 2) two phase liquid plus solid flow, 3) two phase liquid plus vapour flow (Meyer et al., 1994).

Turbulent jet geometry

Silverman (1988) has reviewed the impinging jet flow geometry. In cases where the corrosion is mass transfer limited, the corrosion rate is considered to be a function of the wall shear stress. Giralt and Trass (1975,1976) have proposed that, at the wall jet region (Fig. 3.2.3) away from stagnation point, the shear stress 'τ_w' follows the equation for ratio r/d > 2-3 and Reynolds number '*Re*' ranging from 2.5×10^4 to 1.25×10^5:

$$\tau_w = 0.0447 \rho \mathbf{u}^2 \, Re^{-0.182} \, (r/d)^{-2}$$

where, 'u' is the nozzle exit velocity (ms^{-1}); 'd' is nozzle diameter (m); 'r' is the distance from the stagnation point (m); 'ρ' is the liquid density ($kg.m^{-3}$); τ_w is the shear stress (Nm^{-2}); v_{str} is the velocity of the main stream of the jet at the appropriate part of the solid plate.

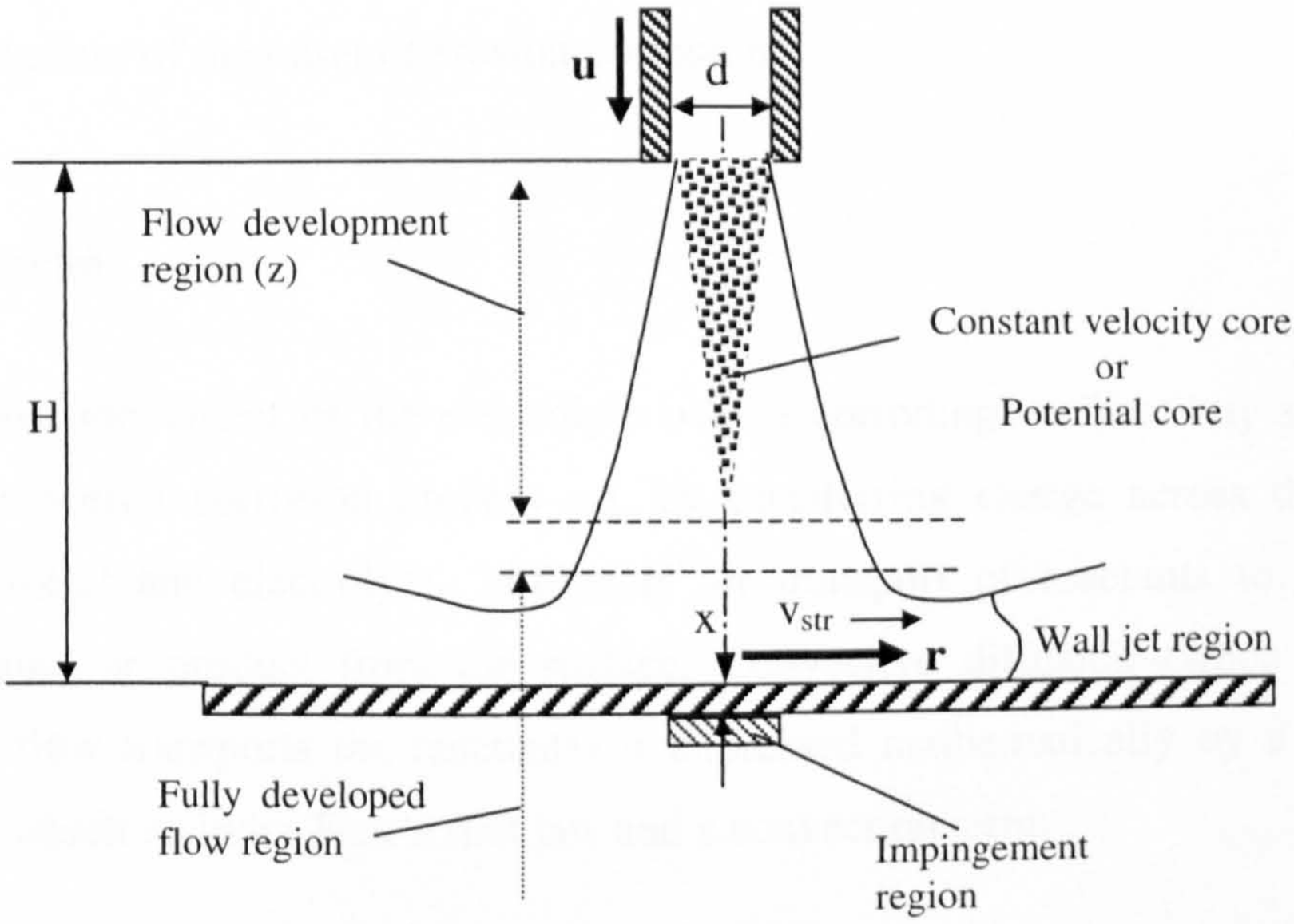


Figure 3.2.3 Submerged jet also called as free turbulent jet impinging onto a horizontal solid plate, showing typical velocity profiles in the main stream and the radial wall jet region (Davies, 1972; Rajaratnam, 1976).

A free turbulent jet usually possesses four flow regimes (Davies, 1972):

1. A regime of flow development, where the flow extends up to 6.4 nozzle diameter i.e., $0 < z < 6.4d$, where "*d*" is the nozzle diameter. The fluid in this region has a core velocity similar to the nozzle exit velocity "**u**".
2. A transition region between $6.4d$ and $8d$.
3. A region of developed flow, extending out to about $100d$.
4. A terminal region where the centreline velocity decreases steeply toward zero.

Rajaratnam (1976) has reported that the wall shear stress increases linearly with '*r*' to a maximum value at $r/H \approx 0.14$ and then decreases as '*r*' increases further. The maximum shear stress 'τ_m' is given by the expression below and is valid only for large impingement heights, i.e., $H/d > 8$.

$$\tau_m = 0.16\ \rho\ \mathbf{u}^2/(H/d)^2$$

where, τ_m – shear stress (Nm^{-2}), ρ - liquid density ($g\ cm^{-3}$)

The relation between shear stress and flow rates is the matter of interest to the critical shear stress necessary for the breakdown of protective surface layers on metals, which can be the cause of the onset of erosion-corrosion.

Mass transfer

The relative movement of the electrolyte over a corroding surface may significantly affect the overall corrosion process e.g. by transferring charge across the interface between metal and electrolyte, "diffusion" or transport of reactants to the surface "convection" or product from the surface. Convective diffusion (when laminar or turbulent flow transports the reactants) is expressed mathematically by a differential equation, which includes Fick's first law and a convection term:

$$n_i = -D_i \text{grad}\ c_i + \mathbf{u}\ c_i$$

where, n_i is the molar mass flux of component i ($mol.m^{-2}.s^{-1}$); D_i, the diffusion coefficient ($m^2.s^{-1}$); c_i, the concentration ($mol.m^{-3}$), and u, the flow velocity (ms^{-1}). The equation shows that the total flux is equal to the sum of diffusional mass transport and convective mass transport. The corrosion process is mostly affected by flow when it is limited by mass transport e.g. transportation of oxygen from bulk solution in flowing waters, enhancing the oxygen reduction reaction.

Another mechanism might include the progressive removal of material by repeated impulse loading at microscopically small areas in the case of impinging turbulent jets. Mechanical effects of a high velocity impinging flow are twofold. The jet generates a high-pressure region at the point of impact and in addition, shearing effects are encountered due to the lateral flow radially outwards from the point of impact.

In fact erosion-corrosion in flowing liquid is controlled by a number of basic mechanico-chemical processes, the most important being mass transfer, momentum transfer, and generation of shear stresses (Weber, 1992). The interrelation of these processes is expressed by a dimensionless relation type:

$$S_h = a\, S_c^{\,b}\, R_e^{\,c}$$

Where, 'S_h' is the Sherwood number (describing mass transfer), 'S_c' the Schmidt number (momentum and mass transfer), 'R_e' the Reynolds number (inertia and friction forces) and 'a', 'b' and 'c' are constants. This relation is also expressed in terms of corrosion rate 'w' as a power function of flow velocity 'u' as

$$w \alpha u^a$$

in which the value of the exponent 'a' indicates the rate controlling mechanism and can have different values for a given metal-fluid system, depending on the flow velocity, the metal and the fluid chemistry. An exponent less than 1 indicates a transport-dependent process. Removal of surface layers gives higher 'a' value. Transport dependent corrosion processes are much influenced by shear stress and for several geometries, the mass transfer coefficient "k" is determined by shear stress at the wall jet region.

$$k = 3.78\ (\tau_w/\rho.u)S_c^{-0.667}\ (r/d)^{0.8}$$

and

$$S_c = \nu/D$$

where, k- mass transfer coefficient (ms^{-1}); ν- the kinematic viscosity (m^2s^{-1});

Investigations by Poulson (1990) revealed that mass transfer correlations are influenced by developing roughness, particularly for geometries such as bends or the region downstream of orifices. It has been suggested that once a surface has roughened the mass transfer is controlled more by roughness than geometry and in particular in bends, which have higher tendency to roughen than straight pipes. Giralt and Trass (1975) revealed that this mechanically generated surface roughness would enhance diffusional transfer rates by increasing wall friction and eddy motion and also might result in loosening surface grains forming additional roughness elements.

The laws of hydrodynamics govern the flow pattern along a given geometry. Various types of flow e.g. laminar, turbulent, attached, separated affect the overall corrosion damage. Practically, laminar flow is rare and it is turbulent flow that has to be considered with respect to corrosion effects. Generally, turbulence is fully established when Reynolds number 'Re' exceeds 4000. Turbulent flow is divided into non disturbed flow with parallel mean velocity vectors and disturbed flow (Heitz, 1991), which is usually caused by boundary variations (e.g. step in a wall or elbow in a pipe) and pressure variations (e.g. due to vibration of pumps). The transfer of material by turbulent eddies is greater than in stagnant systems or laminar flow (Davies, 1972).

Cavitation

This phenomenon exists when pressure variations (resulting from large velocity changes) cause the formation of vapour bubbles in regions of the liquid where the pressure is lower than the vapour pressure of the liquid followed by collapse of these bubbles as the fluid encounters a higher-pressure zone resulting in release of immense energy of the order of 1-2GNm^2 which subsequently leads to the damage of the surface e.g. mechanical "cavitation" damage or to a combined "cavitation corrosion" attack in

corrosive environments. The latter can, for instance, involve protective surface films being disrupted locally, exposing small anodic areas of bare metal surrounded by large surrounding undamaged cathodic areas (Trethewey and Chamberlain, 1995; Chandler, 1985). The surface roughening provides better nucleation sites for new bubble formation and the corrosion process is intensified. Propellers, impellers and hydraulic turbine gear, bends and protrusions (flanges, tees and elbows) are the most common places to encounter corrosion by cavitation. Cavitation depends upon the fluid characteristic, material and fluid velocity. Vapour pressure, air content, surface tension, and fluid viscosity are parameters that influence cavitation wear (Kozyrev, 1980).

Impingement attack

"Impingement attack" is a of form erosion-corrosion generally associated with impingement action (turbulent flow at fairly high velocity resulting in destruction of protective layers or progressive loss of material from a solid surface due to continued exposure to impacts by liquid jet) of liquid often termed as "*liquid erosion*" or "*solid erosion*" if a process results in a continuing succession of impacts between solid particles and a solid surface or "*solid-liquid erosion*" if the flowing liquid jet entrains solid particles.

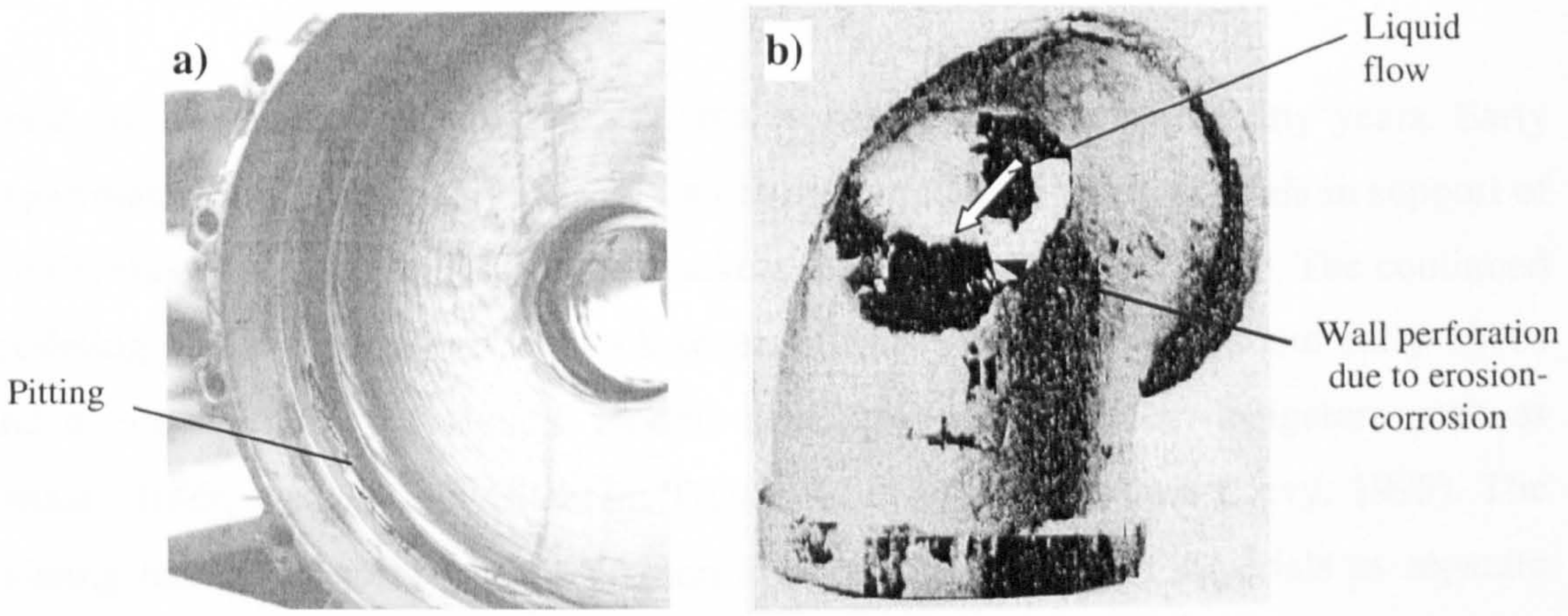


Figure 3.2.4 Erosion-corrosion in a) pump casing, b) pipe elbow.

One situation where impingement attack can be encountered is near the entrance to the tubes, the exact location depending upon the angle of impingement. It takes the form of pitting (Fig. 3.2.4a) or grooving and eventual perforation of the wall (Fig. 3.2.4b) at that location while the remainder of the tube shows no sign of corrosion. Similar attack may occur in the vicinity of an object lodged in a pipe.

Pipe bends, tees, steam-turbine blades are particularly vulnerable to this type of attack. The destructive effect of high velocity impingement of rain upon skins of jet fighter aircraft (Trethewey and Chamberlain, 1995) has been reported. Works by Neville (1995) have demonstrated the high velocity erosion-corrosion performances of high-grade stainless steels such as UNS S31254, UNS S32760 and Copper-Nickel alloys.

3.3 Basics of solid erosion

In section 3.2, the mechanical and mass transfer effects of an impinging single-phase liquid jet stream were considered. This section will consider the effect of hard solid particle erodents on the mechanical removal of the impacting surface layer. This section does not aim to provide a comprehensive review on solid particle erosion but encompasses general guidelines on the wear mechanisms by solid particles to support basics on aqueous slurry "solid-liquid erosion" in section 3.4.

Solid particle erosion or simply solid erosion has been studied for many years. Early experiments of Finnie (1958) proposed an erosion model for ductile metals in support of the development and use of catalytic crackers in the oil-refining industry. The continued modeling of the erosion process took several forms during the 1960s and early 1970s and a compilation of analytical models developed by several investigators such as Finnie, Bitter, Neilson and Gilchrist, Tilly can be found elsewhere (Levy, 1995). The existing models of solid particle erosion treat ductile and brittle materials as separate and distinct, generating two basic theories. The erosion causes material removal by a variety of mechanisms and includes subsurface lateral crack propagation in brittle materials (Engel, 1978; Preece and Brunton, 1980; Slikkerveer et al., 1998) and micro-milling or damage accumulation and fatigue impact in ductile materials (Finnie, 1960; Sundarrajan, 1995).

Most of the works previously have been concentrated on particles carried in a gas flow also referred to as dry erosion. The research has emerged from an inherent requirement of the aerospace industry to develop materials resistant to wear, for gas turbines and compressor components. Other examples of erosive wear are in applications such as tools used to cultivate soils that are inevitably exposed to hard particles. The other possibility of hard particle generation might be due to wear of components of the tribological systems. Particle velocities ranging between 5 and 500ms^{-1} have been reported in erosive wear (Hutchings, 1992).

Solid particle erosion implies the removal of material from component surfaces due to successive impact of hard particles. Material removal due to solid particle erosion is a consequence of a series of impacts, which results in a very short contact between the hard particles and the component surface.

Degradation of materials due to solid particle erosion, either at room temperature (Sundarrajan and Roy, 1997) or elevated temperature (Levy et al., 1986), is encountered in a large variety of industries as illustrated in Table 3.3.1. While usually considered undesirable, erosion process has also been used to advantage in a number of situations like sand blasting of castings, shot peening of rotating components, erosive drilling of hard materials by abrasive jets and rock drilling, abrasive deburring (Sundarrajan and Roy, 1997, Finnie, 1960).

System	*Components*
Chemical plant	Transport tubes carrying abrasives in an air system
Hydraulic mining machinery	Pumps and valves
Propellant systems	Gun barrel, rocket motor trail
Combustion system	Reheater, nozzle, tube tanks
Fluidized bed combuster	Heat exchanger tubes, expander turbine, tube tanks
Coal gasification	Turbine, lock hopper valves
Coal liquification	Throttle valve
Aircraft engine	Compressor and turbine blades
Helicopter engine	Rotor and gas turbine blades

Table 3.3.1 Examples of components subjected to solid particle erosion (Sundarrajan and Roy, 1997)

Erosion rates for a range of materials exposed to sand particles have been compiled by Hutchings (1992). In erosion, the extent of wear depends on the number and mass of individual particles striking the surface and on their impact velocity. Erosion of metals usually involves plastic flow, whereas more brittle materials may wear predominantly either by flow or by fracture.

3.3.1 Influencing factors

Factors that influence erosion processes have been suggested by many researchers (Humphrey, 1990; Heitz, 1991; Hutchings, 1992 and Bjordal, 1995; Levy, 1995) and their combination suggests the following:

- Particle movement - impact velocity, impact angle, kinetic energy of the particles, interference between incoming and rebounding particles
- Erosive particle - hardness, size, shape, concentration and density
- Wall material - hardness, tensile strength, ductility and metallurgical structure

Several factors such as number of particles striking the surface in a given time, the particle velocity and impact angles play crucial role in erosion rates and also these rates are largely affected by carrier medium, flow conditions etc. If the flux rate of erodent is very high then considerations should be taken in to interactions of the impacting particles. Particle shape, size, hardness and density are all very important. Moreover the properties of the target material must be taken into account as ductile and brittle materials show distinctly different behaviour and are always treated separately. Surface characteristics such as stress level, surface morphology, and material properties e.g. fracture toughness and hardness are equally important.

Particle movement

Impact velocity of the erodent particle has been considered to have the most dramatic effect on the erosion rate. The erosion rate (E_R) of a material is often expressed in the form

$$E_R \propto u^n$$

where, 'u' is impact velocity and 'n' is the velocity exponent.

The velocity exponent 'n' is around *2.4* for ductile metals at oblique impact conditions (Hutchings, 1992), around *2.55* for erosion under normal impact (Sundarrajan and Roy, 1997) and values for brittle materials range from *2* to *4* (Humphrey, 1990). Finnie (1960) has found the velocity exponent of *2* for SAE 1020 steel at an impact angle of 20° and remarked that the case might be absolutely different for a brittle material. The effective velocity exponent is lower and in the range of *1-2* if corrosion takes place. The velocity exponent is also influenced by other parameters such as impact angle, particle size etc. Slikkerveer et al. (1998) in his model revealed that erosion efficiency (amount of erosion per amount of kinetic energy of the incidenting particles) is a better parameter to describe erosion processes than the erosion rate. It has been reported that a minimum angle of impact (or a minimum normal velocity) is required to produce material removal (Talia et al., 1999). Earlier experiments used a double disk (DD) technique to measure the particle velocity but most recently laser doppler anemometer (LDA) is widely used (Humphrey, 1990; Hussainova et al., 1999).

Particles with high hardness (high HV) are less likely to shatter on impact with the surface and retaining their full kinetic energy during impact. The kinetic energy of a particle can be given by the expression:

$$k.e. = mv^2/2$$

where, 'm' - mass of a single particle and 'v' – particle velocity

For 'N' number of particles striking the surface where, $N = m_s.a/m$ where, m_s mass of sand, a - surface area, v - particles velocity

$$K.E. = m_s.a.v^2/2$$

The influence of impact angle on the erosion rate has been studied by several investigators (Zu et al., 1991; Sparks and Hutchings, 1991; Stack, 1996; Shimizu et al., 1996; Oka et al., 1997). Dependence of erosion rate on the impact angle is largely determined by the nature of the target material. Fig. 3.3.1.1*a* represents how a ductile material exhibits a maximum erosion rate at intermediate angle (e.g.15°-30°), whereas brittle material exhibits its highest erosion rate at normal impact angle, i.e. at 90° and the rate falls steadily with decreasing impact angle (Humphrey, 1990; Clark, 1992). Recently, it has been noted a maximum erosion rate at normal impact angle, even with ductile materials like mild steel and copper, when a spherical erodent was used and there exists insufficient data regarding the effect of impact velocity, size, hardness etc. of the erodent particle on the variation of erosion rate with impact angle (Sundarrajan, 1991).

Erosive particles

Although erosion by solid particles has been widely studied, comparatively little attention has been paid to the damage which occurs to the particle itself on impact. Salman et al. (1995) investigated the failure mechanism of an aluminium oxide sphere impinged on a mild steel target at a wide range of impact angle and speed.

The erosion rates of a target material largely depend on particle shape, size and hardness (Levy and Chik, 1983; Wang and Geng, 1990; Palasamudram and Bahadur, 1997). Angular and larger particles are more erosive than rounder and smaller particles. It has been illustrated (Levy, 1995) that for AISI 1020 steel, the erosion rate caused by angular steel grit was four times greater than that caused by the spherical shot. The angular erodent caused much sharper, deeper craters to form with a more efficient production of extruded platelets or lips and their removal with repeated bombardment of the stream.

Particle size plays a crucial role in erosion rate of a material. It has been shown in Fig. 3.3.1.1*b*, how erosion rates vary with particle size at different impact velocity (Sundarrajan and Roy, 1997). It has been shown in the figure that the erosion rate increase with an increase in particle size up to a limiting size only beyond which the effect of particle size becomes unimportant. Several other studies on the effect of

particle size were performed by Benchaita et al. (1983), Wang and Geng (1990), Palasamudram and Bahadur (1997).

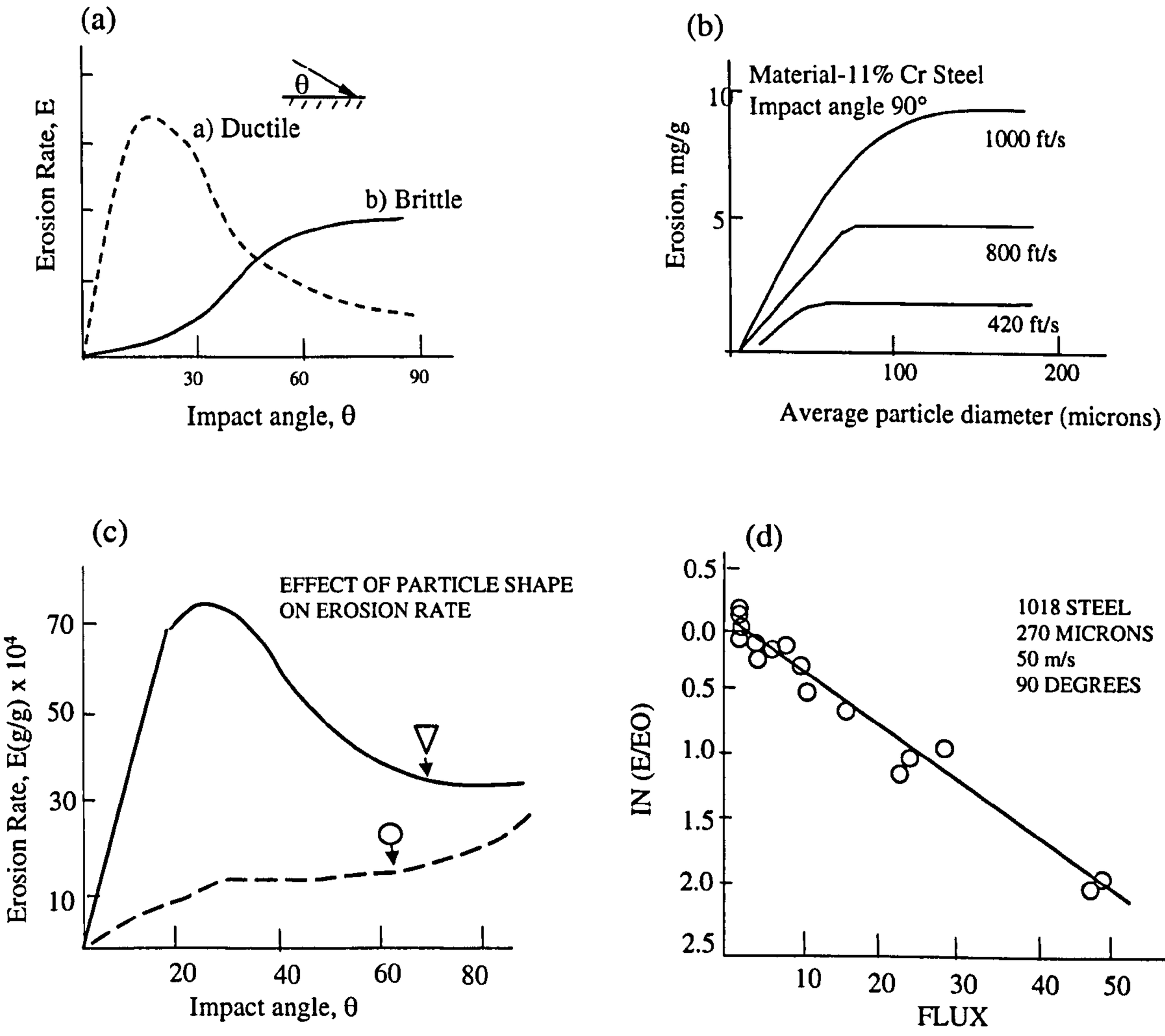


Figure 3.3.1.1 (a) Schematic diagram showing the influence of impact angle on erosion rate in the case of ductile and brittle material; (b) variation of erosion rate with particle size at different impact velocities; (c) influence of impact angle on erosion rate in the case of spherical and angular particles; (d) influence of flux rate on the erosion rate (Sundarrajan and Roy, 1997).

Particle shape often plays a key role in erosion rate and has been studied by several investigators. Wear rates strongly depend on particle shape, with angular particles causing greater wear than rounded particles (Hutchings, 1992; Palasamudram and Bahadur, 1997). As the angularity of the erodent particle increases, the erosion rate increases and in addition, the erosion rate-impact angle behaviour shifts more towards a ductile response (Fig. 3.3.1.1*c*).

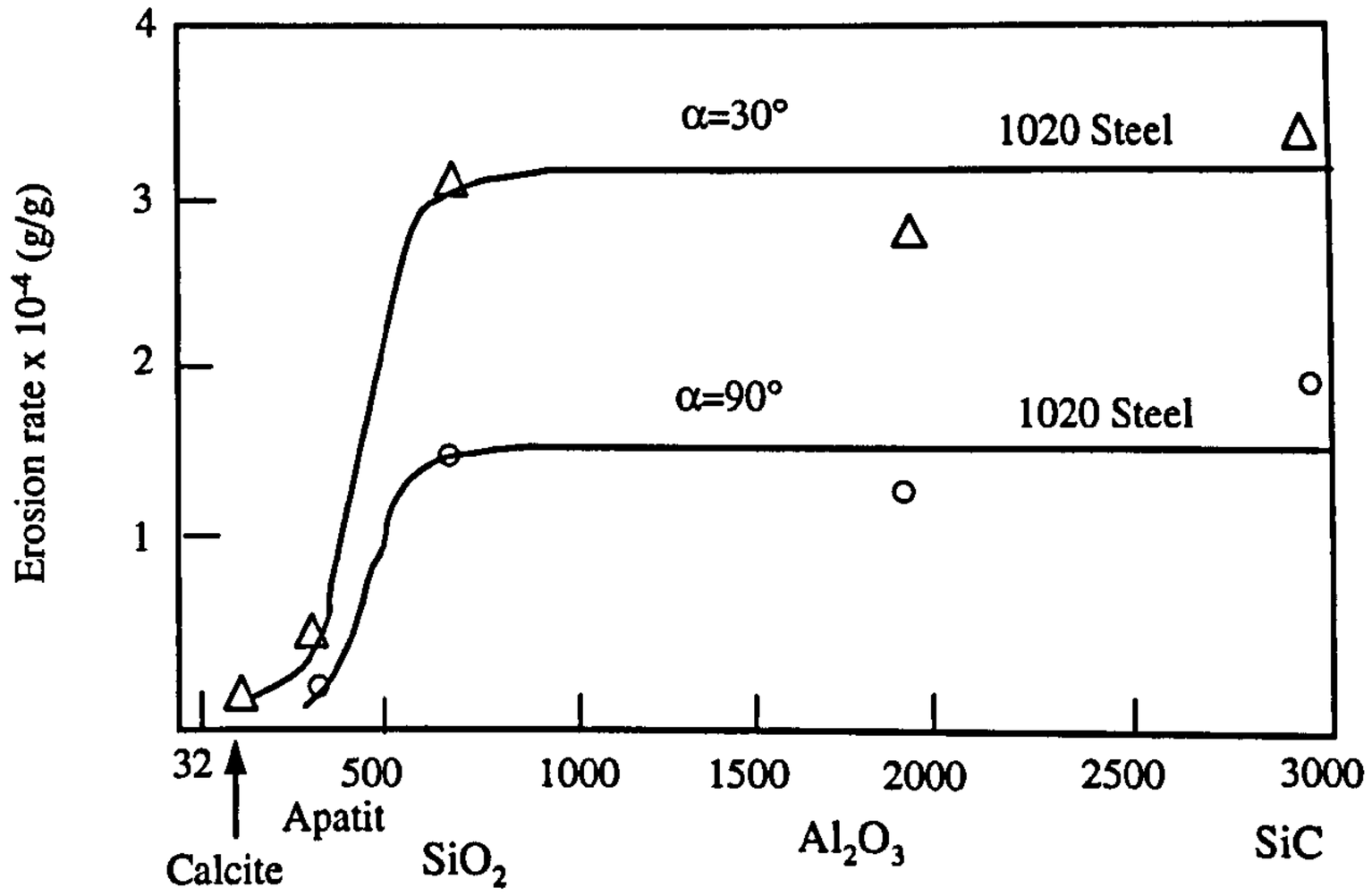


Figure 3.3.1.2 Erosion rates of 1020 steel by calcite, apatite, SiO_2, Al_2O_3 and SiC (Levy, 1995).

The influence of the hardness of the erodent particles is of great importance in the erosion rate of steels. Generally, hard particles cause more erosion than softer particles. Especially, the relation between the particle hardness and the target material is considered crucial. It has been reported that as long as the erodent hardness is at least twice that of the target material, the erosion rate is independent of the particle hardness (Sundarrajan and Roy, 1997). The erosion rate decreased remarkably when the hardness of the erodent particles became comparable to that of the target material. It can be seen from Fig. 3.3.1.2 that the erosion rates are very low for the softest erodent materials, calcite and apatite. Once the Vickers hardness of the particle reaches approximately 700HV, the erosion rates remain constant as the hardness/strength of the particles increases further (Levy, 1995).

Usually, the flux rate of erodent particles does not have a significant influence on the erosion rate of metallic materials. However, at very high feed rates (expressed in terms of $gmin^{-1}$), due to interference with other particles and also with the rebounding particles, the erosion rate decreases. Levy (1995) noticed a large difference between the solids loading effect for spherical particles and for angular particles revealed that increased erosivity of the angular particles is due to reduction of interference between

separate particles. It has been shown (Fig. 3.3.1.1*d*) that erosion rate should decrease with an increase in flux rate.

Wall material

The effect of ductility, strength, toughness and hardness on erosion behaviour of various steels was studied by Levy (1995) and there is considerable evidence in the literature to support the observation that relates higher erosion resistance to increased ductility in a number of single phase alloys rather than to higher strength and hardness. The various strengthening mechanisms such as cold work, grain size hardening and solid solution strengthening for single phase materials has been found ineffective in improving the erosion resistance of the eroding material although in case of multiphase alloys there is a marginal change in the erosion rates (Sundarrajan and Roy, 1997). The general conclusion that alloy selection can be of little benefit in reducing erosive wear is true provided the hardness of the alloy is less than that of the erodent particles themselves (Hutchings, 1992).

Cermets are potentially attractive options for wear resistance. The dominant mechanism of erosion depends on the scale of individual particle contacts. If the erosive particles are small enough, wear can occur by preferential erosion of the metallic binder phase, leading to undercutting and eventual removal of whole carbide grains. If the binder regions are too small to allow this type of localised attack, then overall erosion of the carbide and binder occurs, usually by ductile mechanisms if the erodent particles are small (Hutchings, 1992). Levy (1995) has separated cermets into two different categories such as low carbide content and high carbide content and discussed the mechanisms of material losses.

Silica (quartz) is the most commonly occurring natural abrasive contaminant, constituting about 60% of the earth's crust. Table 3.3.1.1 lists hardness values for some of bulk materials, hard coatings and alloy phases.

Material, phases	*Hardness, HV*
Diamond	6000-10000
Boron carbide, B_4C	2700-3700
Silicon carbide	2100-2600
Quartz(Silica)	750-1200
Chromium carbide, Cr_7C_3	1600
Chromium carbide, Cr_3C_2	1300
Austenite (low alloy)	250-350
Martensite	500-1000
Cementite, Fe_3C	840-1100
Tungsten carbide, WC	2000-2400
Molybdenum diboride, MoB_2	2350
Chromium diboride	1800

Table 3.3.1.1 Hardness values of some of the bulk materials, hard coatings and alloy phases (Hutchings, 1992).

3.4 Basics of solid-liquid erosion

Section 3.3 has given a review on solid particle erosion and encompasses the different factors that influence the overall material loss of the target material during solid impact in dry conditions. Total damage in flowing aqueous liquids containing solids is a complex affair involving both electrochemical corrosion and mechanical wear and will be discussed in section 3.5. This section only reviews erosion in aqueous environments containing solids encountered in fluid handling systems without considering corrosion factor.

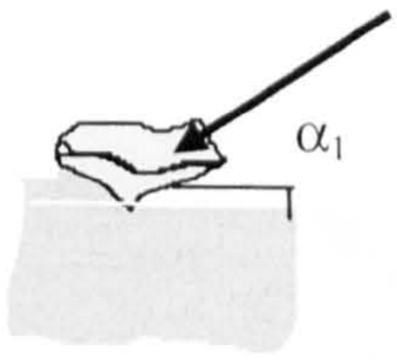
Erosion of metals associated with impingement of solid particles entrained in a liquid stream is quite common in process industry, oil and gas refinery industry and many other multiphase flow industrial devices (Finnie, 1960; Humphrey, 1990; Clark, 1992). Other examples of erosive wear are in applications such as pipelines carrying sand/water slurries in mining operations. Particles may also be contaminants such as fine airborne grit particles mixing into lubricating oil. Metal components in pipelines, nozzles, valves, tees and bends (Fig. 3.4.1) are subjected to severe erosive wear resulting in premature failure of these components (Warman, 1991; Shreir, 1963a).



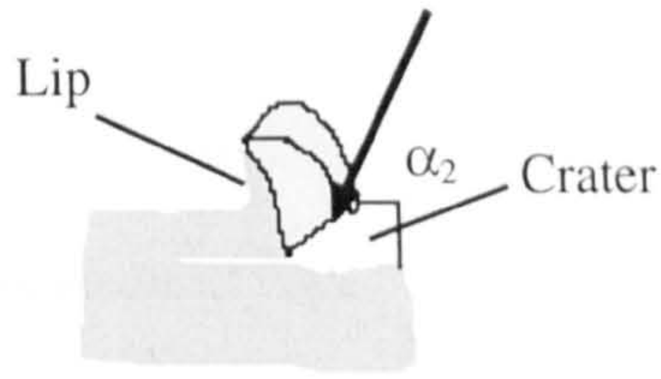
Figure 3.4.1. Solid-liquid erosion in a pipe bend

In the case of ductile metals, impinging particles cause localised plastic deformation in the forms of craters with raised lips. In the case of vertical incidence, the craters are approximately symmetric, whereas for particles impinging at low angles, the impact areas are in the form of furrows, with the area of greatest plastic deformation being located at the end of the furrow. The forms of the impact craters depend upon the shape of the impinging particles. Thus, spherical particles have rounded impressions, whilst sharp-cornered eroding particles produce angular impact craters (Engel and Klinegele, 1981; Hutchings, 1992). It has been reported that the hydrodynamic forcing of particles against surfaces at low-impingement angles has much in common with the relative movement between packed abrasives and surfaces i.e. low stress abrasion (Crook, 1991). Material removal is favoured at the plastically lifted lips. Repeated bombardment at the same point causes severe deformation at this area resulting in spall or fracture. Components exposed to streams of sand particles can be examples of this type of erosive wear. Bombardment of solid particles stream produces high internal stresses in the roughened surface and these can lead to tearing and detachment of portions of metals under impingement. It is also possible that cracks formed during impingement can be initiating sites for fracture during subsequent mechanical loading.

The material loss due to mechanical wear is mainly associated with ploughing or cutting in case of a ductile material and cracking in case of brittle material (Wilson, 1995) by an abrasive action of hard and sharp particles. A schematic representation of ploughing and cutting wear is shown in Fig. 3.4.2.



Ploughing wear: low angle of approach, low wear rate



Cutting wear: high angle of approach, high wear rate

Figure 3.4.2 Effect of approach angle in wear rate of a ductile metal α_1, α_2 being the approach angles (Wilson, 1995).

Materials whose resistance depends upon a protective film are prone to erosion-corrosion attack due to constant removal of the protective films (which may range from thick visible films of corrosion products to the thin invisible passivating films) from the metal's surface (Shreir, 1963b; Chandler, 1985; Trethewey and Chamberlain, 1995).

The general concept of erosion-corrosion involves two interdependent phenomena: the fluid mechanics of the solid-fluid two-phase flow (or momentum exchange between the solid and liquid phase) and the wear of materials by collisions of abrasive particles on the metallic surface (Humphrey, 1990). The material loss of a surface material by solid particles in a fluid stream depends on the number of particles striking the surface, their velocity and their direction relative to the surface. The quantity is largely determined by the flow conditions, in particular pump components and fluid handling units, where the flow direction changes fairly rapidly and that the amount of material removed is related to the work done or energy dissipated by the impacting particles (Finnie, 1960; Lynn et al., 1991). Moreover, several factors e.g. liquid viscosity and density, particle size, density, target shape etc. affect on the rate of material loss (Clark, 1992).

Several forces of different origins may act on a particle in contact with a solid surface. Neighbouring particles may exert contact forces, and a flowing liquid will cause drag force (Finnie, 1960; Humphrey, 1990; Hutchings, 1992). Figure 3.4.3 shows different forces those act on a particle in contact with a solid surface in solid-liquid conditions.

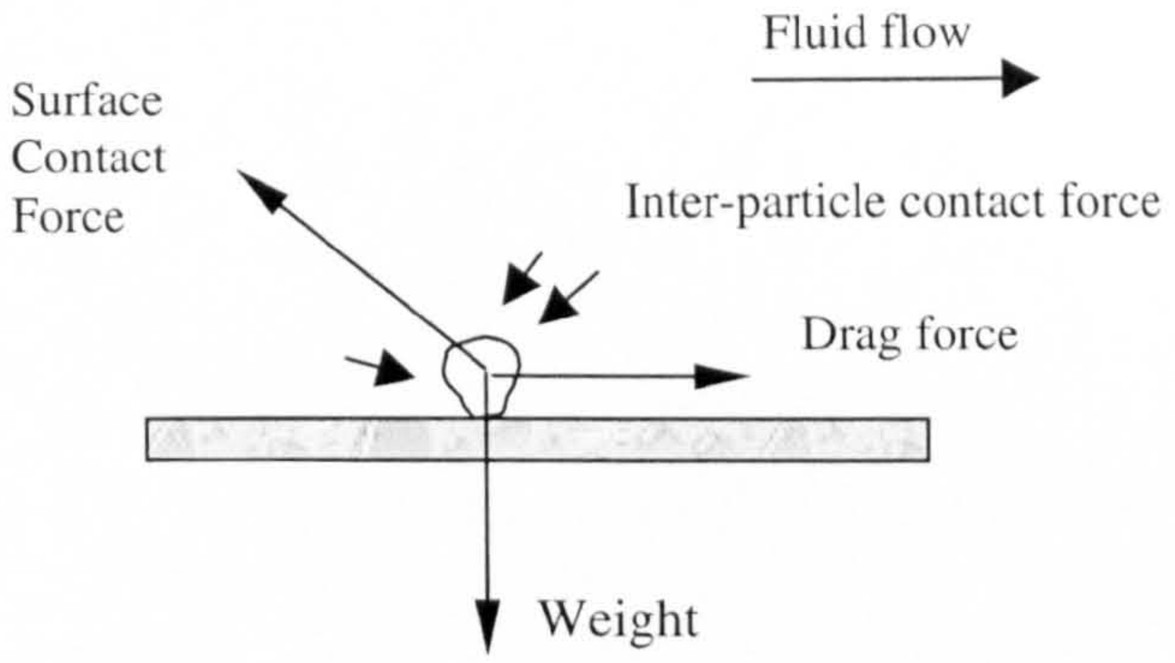


Figure 3.4.3 Diagram showing the forces, which can act on a particle in contact with a solid surface (Hutchings, 1992).

It is to be noticed that the velocity and direction of an abrasive particle in a fluid are not necessarily the same as those of fluid as shown in Fig. 3.4.4. Such phenomenon is encountered in pipe bends or tees when the abrasive trajectories are different from those of the fluid motion, and for a large ratio of inertia force to drag force acting on the solid particles, almost all abrasives impact on the wall (Benchaita et al., 1983).

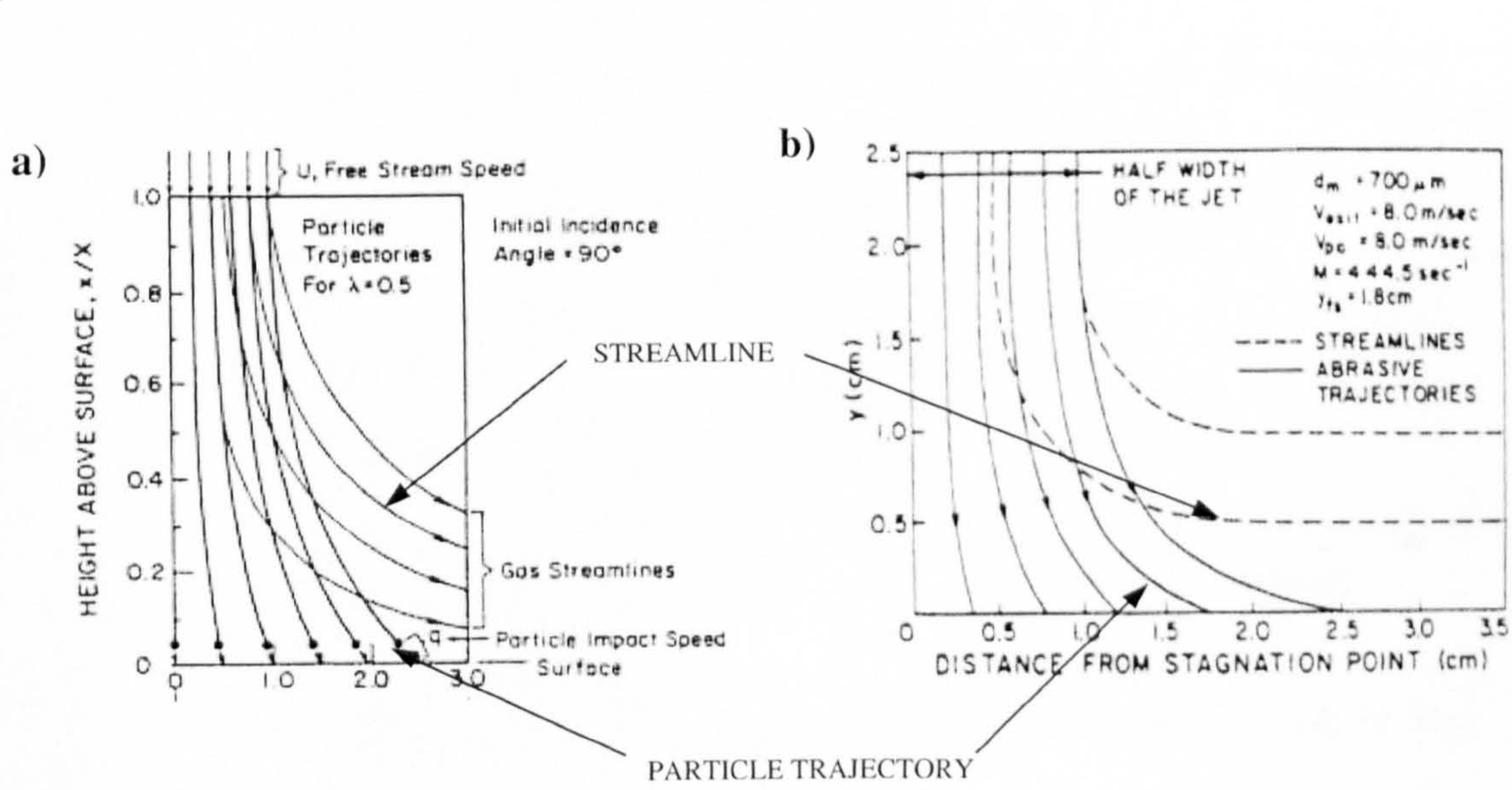


Figure 3.4.4 Solid particle trajectories of two-phase flow a) in gas stream (Humphrey, 1990); (b) in liquid (water) stream (Benchaita et al., 1983).

The particle velocity largely depends on its size and the carrier fluid viscosity. It has been reported that the impact velocities of suspended particles are much less than the

flow velocities and for small particles in viscous liquids can be as low as 10% of the nominal velocities (Clark and Burmeister, 1992). Particularly useful in this regard is the concept of collision efficiency 'η' (also called striking efficiency), which may be defined as the ratio of the number of particles striking unit area of the surface in unit time and the number of particles contained within the volume of suspension swept by that area in unit time (Clark, 1991). Figure 3.4.5 represents a variation of collision efficiency and impact velocity with respect to viscosity of the bathing fluid.

Low values of collision efficiency will result in a low value of erosion rate. Also a liquid of high viscosity will exert a greater drag force on a particle than a liquid of low viscosity, which in turn has more effect in moving the particles laterally. As a consequence, at high viscosities, relatively few particles will be able to collide with the contacting surface. The impact velocity as reported (Humphrey, 1990; Clark, 1991) depends upon interactions between particles, liquid and the specimen and the prevailing flow regime.

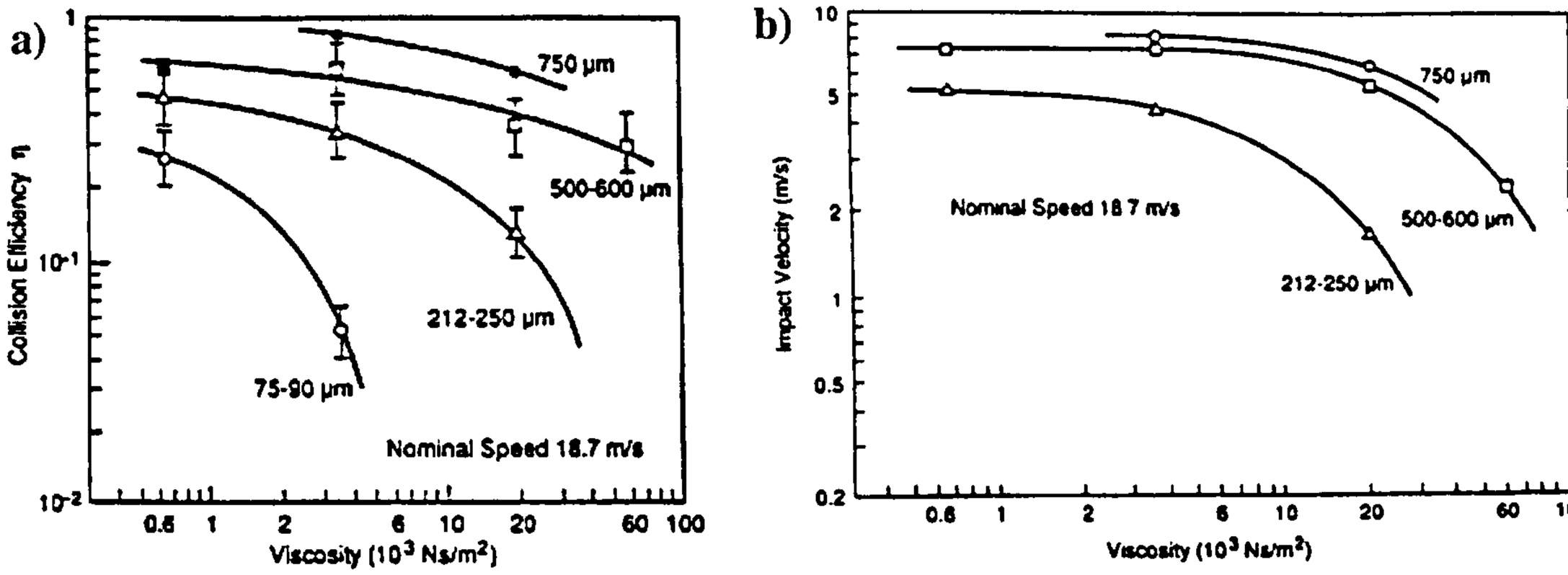


Figure 3.4.5 a) The variation of collision efficiency with viscosity and; b) The variation of impact velocity with viscosity (Clark, 1991).

The final impact velocity with which the particle hits the surface largely depends upon the squeeze film or the boundary layer existing in between the planar target surface and the liquid that provides a cushioning effect. Significant retardation prior to impact and approach velocities due to the film in solid-liquid erosion has been discussed by Clark (1991) and Clark and Burmeister (1992), in particular when a high speed particle

penetrates a lower speed boundary layer governed by the particle inertia number 'λ' (Humphrey, 1990).

A different mechanistic approach was studied by Zu et al. (1991), comparing the difference between the slurry erosion and dry erosion of aluminium by silica sand particles at a velocity of 4.5ms^{-1}. It has been reported that erosion rate by aqueous sand slurries proceeds by several times that of airborne erosion and the ratio of two rates depending strongly on the impact angle. The reason was confirmed to be sand particles being embedded in the metal surface during dry erosion, forming a surface hardened composite layer of metal and silica which resulted in significant reduction of the wear rate. In contrary, water inhibited the embedment of fragments of erodent particles into the metal surface. Figure 3.4.6 shows erosion rate of aluminium in aqueous sand slurry and air-borne sand erosion at different impact angles.

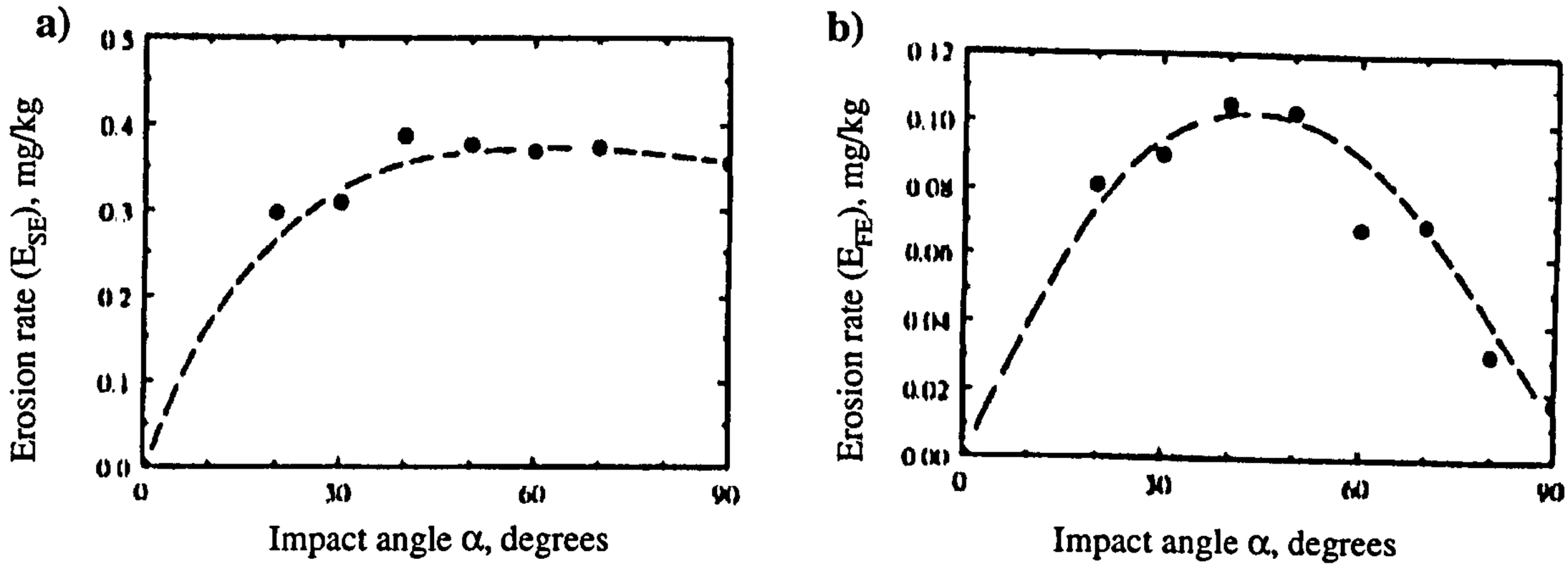


Figure 3.4.6 Erosion rate of aluminium at an impact velocity of 4.5ms^{-1} as a function of impact angle α: (a) aqueous sand slurry erosion; (b) air-borne sand erosion (Zu et al., 1991).

A recent approach for solid-liquid erosion was investigated by aqueous erosion-corrosion map controlled by elastic rebound (defined by coefficient of restitution '*e*'), that has been shown to have significant effect for the low velocity conditions such as in pipe flows (Stack et al., 1998). It has been stated that the effects of fluid drag may retard or accelerate rebound behaviour and depending upon other factors such as component geometry, result in an enhancement or a reduction in the wastage rate.

It is however a very difficult task to identify and assess fluid mechanics phenomena that can significantly influence the erosion of material surfaces by impinging particles, some factors listed in Table 3.4.1 can be readily controlled or measured although most are interrelated in a rather complex manner (Humphrey, 1990).

For particles	*For surfaces*	*For the carrier fluid*
• Impact and rebound angles • Impact and rebound speeds • Rotation before and after impact • Shape and size • Volume concentration and surface flux • Physical properties (hardness, strength and density) • Fragmentation • Interactions (with surfaces, fluid or other particles) • Temperature • Presence of additives • Electrical change	• Physical properties • Change in shape caused by erosion • Stress level • Temperature • Presence of oxide (or other) coatings • Simultaneous occurrence of corrosion	• State of motion (laminar vs. turbulent) • Velocity • Temperature • Chemical composition and physical properties

Table 3.4.1 Factors that affect erosion of surface by solid particle impact (Humphrey, 1990).

3.5 Aqueous erosion-corrosion interactions

Conventionally, the ranking of different materials in erosion-corrosion conditions has been done using the material loss (mass, volume, depth etc.) basis, and after the actual mechanism of degradation was not considered. Only recently, it has been recognised that, material loss by erosion-corrosion in aqueous systems is often governed by complex mechanisms, which include electrochemical corrosion and mechanical wear interactions. The actual material loss in a corrosive aqueous environment is often much higher than the sum of the losses attributed by pure corrosion and pure erosion mechanisms in isolation and is recognised as the synergistic contribution. Table 3.5.1 summarises two approaches for defining the synergistic components existing in erosion-corrosion.

No.	*Investigators*	*Approach*
1.	Madsen, 1988 Wood and Hutton, 1990 Neville et al., 1995 Zheng et al., 1995 Bardal et al., 1995 Neville and Hodgkiess, 1997b Hodgkiess et al., 1998 Shrestha et al., 1999	$TWL = E + C + S$
2.	Wood and Fry, 1989 Bjordal, 1995 Stack et al., 1995a Zhou et al., 1996 Bjordal et al., 1996 Rogne et al., 1996 Berget, 1998 Stack et al., 1999	$TWL = E + C' + dC_e + dE_c$

Table. 3.5.1 Two approaches defining the synergistic factor.

In the first approach, *TWL* is the total loss (weight, volume, penetration depth etc.); E is loss due to pure erosion in the absence of corrosion; C is loss due to pure corrosion only

but under erosion-corrosion condition, and *S* is the synergy which represents an indirect involvement of corrosion processes in enhancing erosive material loss. Synergisms up to 55.3% and 62.3% of the total wear rate (at 26°C and 60°C, 2% solids of 50-70 mesh, 0.06M Na_2SO_4 solution and 5.8ms^{-1} of impeller speed) have been reported for 316 stainless steel (Madsen, 1988). Neville and Hodgkiess (1997c) have reported up to 18 and 37.3% of synergism in solid-liquid impingement (25ms^{-1} normal impingement, 0.1% silica sand, 3.5% NaCl solution, 30°C temperature) for stainless steel type UNS S31603 and graphite cast iron respectively. Zheng et al. (1995) have reported 32-99% of synergism for carbon steels and stainless steels in 10% H_2SO_4 in distilled water + 15% corundum sand (60mesh) slurry.

In the second approach some workers define the synergy effect as split into two separate components:

$$Synergy = dE_c + dC_e$$

Where, dE_c is corrosion enhanced erosion and termed as "synergistic" effect and dC_e is erosion enhanced corrosion and termed as "additive" effect (Stack et al., 1999). The increased corrosion rate due to particle erosion dC_e is determined as the difference between the measured corrosion rate under erosion $C' + dC_e$ and the corrosion rate during flow without particles C' (Bjordal, 1995). It is to be noticed that $C' + dC_e$ in the second approach is equivalent to C in the first approach and that $dE_c = S$.

TWL is often measured as the erosion-corrosion loss under free corrosion potential; E is obtained by applying cathodic protection to a material under erosion-corrosion condition at a sufficient negative potential in order to suppress the corrosion factor; C is calculated by Tafel extrapolation method from an anodic polarisation curve as stated earlier in Chapter 2.

Attempts have been made to define whether the erosion-corrosion mechanism is "synergistic" i.e., $TWL = E + C' + dE_c$ or "additive" i.e., $TWL = E + C' + dC_e$ (Stack et al., 1995) but it has been recognized that dE_c is the dominating factor in slurry erosion (Bjordal, 1995). However, it remains a very complicated task and still not well understood and there exist several thoughts about these combined interactions and their dominance in the overall material loss.

Particle erosion can influence the corrosion rate by different mechanisms, such as: increased mass transport by high turbulence levels caused by surface roughening (Poulson, 1990), removal of protective oxide or corrosion product films exposing fresh reactive material and local acidification in erosion pits that accelerates corrosion rates and prohibits film formation. Similarly, corrosion can affect the erosion rate by removing work hardened surface, by preferentially attacking at grain boundaries resulting in loosened and eventual lost grains, by lowering the fatigue strength of the material and by introducing micro-pits that act as stress-concentrating defects (Wood and Hutton, 1990). However, in situation where hard oxides can reduce erosion at elevated temperatures, corrosion can also be considered to "inhibit" erosion (Stack and Bray, 1995).

3.6 Methods for evaluating wear rates

Erosion damage results in unexpected facility downtime, loss of income, and high repair cost. Therefore, a better understanding of the factors that cause erosion and the level of erosion associated with each other is needed. Performing experimental tests to simulate the real conditions is one way to obtain this information, however, is costly and time consuming. "If results are desired for nine impingement angles, seven particle impingement speeds, five particle sizes, three particle types, seven target materials, three carrier fluids, and three duplicate points for each conditions, the time required to obtain this information, barring any mechanical failure of the apparatus, is over 32 years" (Chase et al., 1992). Evaluation of wear rates can principally be obtained using prediction methods, models, lab measurement methods and industrial measurement methods.

Estimation of wear rate of components in flowing conditions in the industry can in principle be calculated by applying conservative "band method" and more realistic "blanket method" (Chandra et al., 1994). The band method usually takes a circumferential band around the component and assumes that the largest wall thickness reading is the original wall thickness and the smallest is the worn area of the component. The wear is then largest reading minus the smallest reading. This method is considered to be conservative, as it does not account for the manufactured wall

thickness variation. In the "blanket" method UT (ultrasonic testing) data from the component is divided into zones or "blankets" and a series of calculations are performed on the data in each blanket to evaluate maximum and minimum thicknesses.

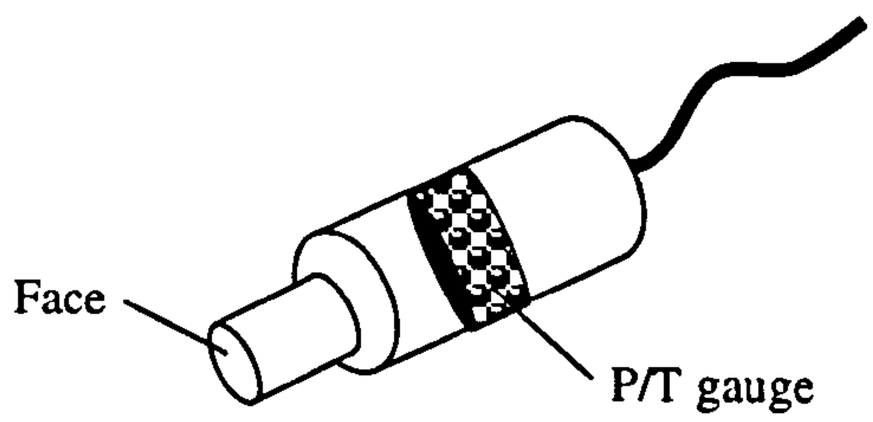


Figure. 3.6.1 A schematic diagram of a sand and erosion probe.

CorrOcean (Trondheim, Norway) has a developed a multi-functional sand and erosion probe for subsea or topside use (Circle 202, 1999). The probe is fitted with erosion elements facing the flow (Fig. 3.6.1), which can read cumulative erosion directly. A spike resistant pressure and temperature (P/T) gauge is integrated on the midsection of the probe.

'American Petroleum Institute (API) recommended practice 14E (API-RP 14E) erosion velocity limit' has been suggested to limit the flow velocity to the maximum flow erosion velocity in offshore production platform piping systems to avoid erosion damage (API, 1991). The API-RP-14E is formulated as:

$$V_e = \frac{C}{\sqrt{\rho_m}}$$

where,

V_e – fluid erosion velocity, ft/s

C – empirical constant (150-200 when the corrosion is controlled by inhibition or by using corrosion resistant alloys and 100 for corrosive systems), attention should be given to reducing the value if solid particles are anticipated.

ρ_m – gas liquid mixture density at flowing pressure and temperature, lb/ft^3 calculated by the equation:

$$\rho_m = \frac{12409 S_l P + 2.7 R S_g P}{198.7 P + RTZ}$$

P – operating pressure, psi;
S_l – liquid specific gravity (water = 1)
S_g – gas specific gravity (air = 1)
R – gas /liquid ratio, ft^3/bbl
T – operating temperature, °R (degrees Rankine = 460 + °F)
Z – gas compressibility factor, dimensionless

However, the API recommendation can be overly conservative under certain conditions and can result in early failure under others and hence, should not be used without consultation (Salama, 1993). Moreover, the RP 14E does not account for the type of material, flow geometry (coupling, elbow, choke, valve), particle characteristics (size, shape, hardness) and the corrosivity of the medium.

An alternative method DNV RP 0501 similar to API RP14E has been defined for dimensioning of piping systems exposed to erosive wear (DNV, 1996). The erosion rate was expressed as:

$$E_L = \frac{m_p \,.\, K \,.\, U_p^{\,n} \,.\, F(\alpha)}{\rho_t \,.\, A_t} = \frac{E_m}{\rho_t \,.\, A_t}$$

where, E_L – erosion rate (mm/yr.); E_m – erosion rate (kg/yr.); m_p – mass flow of sand (kg/s); K- material constant $(m/s)^{-n}$; U_p – particle impact velocity (m/s); n – velocity exponent; $F(\alpha)$ – function characterizing ductility of the material; ρ_t – density of liquid phase (kg/m^3); A_t – area exposed to erosion (m^2).

However, this model also completely ignores the corrosion and erosion-corrosion factors and thus lacks the much reliable data for the proper application.

Chase et al. (1992) proposed a model for the effect of velocity on erosion of N80 steel tubing due to normal impingement of solid particles. The erosion ratio (ER) was defined as the ratio of the mass of target material removed to the mass of impinging particles required to remove that mass of target material using 5 semi-empirical models. Each

model contains a single unknown parameter that is determined from a data point. The model then can be used to predict erosion behaviour for other conditions. All models included plastic deformation of the target material.

Benchaita et al. (1983) developed a model for erosion of metallic materials by solid abrasives, combining the fluid mechanics of particle suspension in a liquid and weight removal from the plate (by a single abrasive particle) to determine the distribution and amount of erosion along the metallic plate and revealed that small particles about 200μm have the tendency to follow the streamlines, and consequently, some of them do not impact the metal plate. The larger particles > 200μm hit the metallic plate at approximately the same impact angle as the jet itself. This model assumes that abrasive particles are rigid (or harder than the metallic plate); the abrasive impinges with a sharp leading edge; the oxide layer which generally develops at any metallic surface is neglected; the metallic surface deforms plastically; the fluid flow surrounding the plate is two dimensional and so is the motion of the abrasive itself; the boundary layer, vorticity and secondary flow effects are neglected. Influences of jet velocity and abrasive size were taken into account in this model. Moreover corrosion processes and erosion-corrosion interactions are fully ignored.

Earlier methods for evaluating wear rates included Finnie's model of micro milling (Finnie, 1960) and Bitter's model (Bitter, 1963a, 1963b). Another method includes theoretical erosion model based on the plastic zone around an indentation and dynamic mechanical properties in order to derive a predictive equation for erosion damage (Sundarrajan, 1991, 1995). Other methods are Hutchings model by normal impinging spheres based on the concept of a critical plastic strain under repeated plastic loading and wear maps showing the transitions between the erosion-corrosion regimes usually defined as erosion-dominated, erosion-corrosion dominated, corrosion dominated-1, corrosion dominated-2 (Stack and Bray, 1995).

The widely used methods to calculate erosion-corrosion rates are volume loss (Madsen, 1988; Auret, 1993; Kumar et al., 1997), mass loss or total weight loss '*TWL*' (Bjordal, 1995; Neville et al., 1995; Neville and Hodgkiess, 1997c; Stack et al., 1999), thickness loss (Wang and Geng, 1990), erosion depth (Benchaita et al., 1983; Wood and Hutton,

1990) and also penetration depth for cavitation tests (Wood and Fry, 1989). Most of the above methods are based on measuring the actual wear parameter during the entire experimental duration and then finding the actual wear rate.

3.7 General material characteristics

Liquid flow systems

Liquid erosion-corrosion is a complex process and is influenced by a number of factors. It is generally accepted that the erosion-corrosion rate of steels in aqueous media is affected by:

- the composition of the material, principally the alloying elements of chromium, copper and molybdenum.
- the water chemistry in use – pH, salinity, dissolved oxygen, and temperature, corrosivity
- the flow variables – fluid velocity, diameter, fitting geometry, upstream influences, and void fraction (if two-phase flow).

Corrosion data on materials tested in the high velocity seawater jet up to $43ms^{-1}$ showed that stainless steel type 316 has the least corrosion rate about $0.005mmyear^{-1}$ compared to other materials tested such as Monel alloy 400, NiAl bronze, Gun metal, 70/30 CuNi + Fe, 70/30 CuNi + Cr (Todd, 1979). It has been reported that the minimum velocity of $1.2ms^{-1}$ is required to prevent pitting corrosion of 316 stainless steel in seawater.

Within the last 2 decades, studies of the chemo-mechanical effects during flow-accelerated corrosion have increased the knowledge of the basic processes, parameters and mechanisms. The phenomenon of flow accelerated corrosion must be approached from consideration of flow mechanics, electrochemistry, material degradation, transport processes and inorganic chemistry (Neville, 1995).

Sakamoto et al. (1995a) carried out several erosion-corrosion tests on various copper alloys used for valve seats in water taps. Cavitation erosion-corrosion test was

performed in a vibratory facility (frequency of 20kHz) with eccentric stationary specimen. Flow induced localized corrosion test was also performed in which, solution of copper II chloride (12.7g $CuCl_2.2H_2O$/1000ml H_2O) was injected normally with a flow velocity of 3.3ms^{-1} on to the specimen. They concluded that the damage originated on the valve seat was associated mainly due to flow-induced localised corrosion. It has been reported (Sakamoto et al., 1995b) that in the two vibratory tests (a vibratory unit with a vibrating specimen; a vibratory unit with a stationary specimen), the ranking order of the materials investigated (aluminium, brass, armco iron, carbon steel and stainless steel) according to their durability to cavitation attack evidenced a complete coincidence with that of performance in the field. However, the ranking based on the water tunnel test (a rectangular 40x30mm test section with semicircular columns by which the fluid was accelerated to generate cavitation) was different from those of the vibratory units with sudden acceleration of damage of some materials (in particular stainless steel and carbon steel) in the middle of the tunnel. The test liquid was deionised water (0.2μS cm^{-1}) for the vibratory units and tap water for the water tunnel.

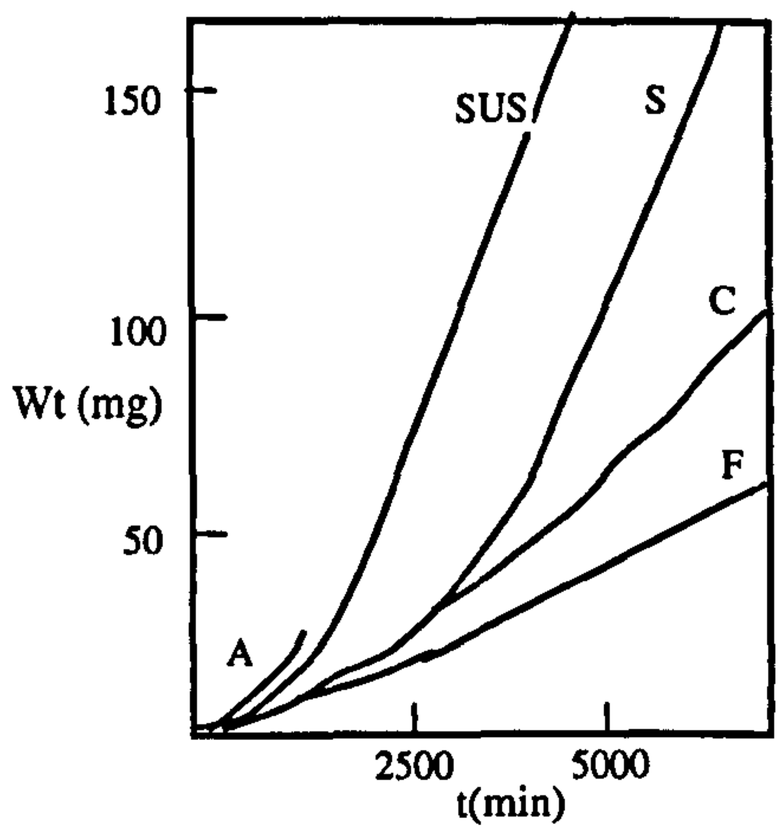


Figure 3.7.1 Mass loss vs. exposure duration in a water tunnel (SUS-stainless steel; S-carbon steel; C-brass; F-armco iron; A-aluminium) (Sakamoto et al., 1995b)

In the water tunnel test both stainless steel and carbon steel exhibited large amounts of mass loss (Fig. 3.7.1). They concluded that the cause of a sudden increase in erosion rate occurring during the test depends upon the test conditions.

Chexal et al. (1996) investigated the impact of chromium on flow-accelerated corrosion of carbon steel (ASTM/ASME A106 Grade B). Generally, it has been demonstrated that addition of chromium approximately 0.1% substantially reduces the rate of flow-accelerated corrosion. It has been recognised that during the impingement material with high chromium content will follow a non-linear wearing of the surface.

Al-Hashem et al. (1997) aimed at identifying the relative susceptibility of the ferrite and austenite phases of a duplex stainless steel to cavitation damage in seawater. Cavitation attack concentrated in the austenite phase but spread to the ferrite phase and was associated with ductile tearing, cleavage-like facets, river patterns, and crystallographic steps resulting in a significant increase in mass loss. It has been reported that the mechanical factor was the most dominant factor in cavitation corrosion of the duplex stainless steel. Application of CP reduced the mass loss up to 19%. Figure 3.7.2 shows that the application of cavitation shifted the corrosion potential in the active direction by ~140mV. Potentiodynamic results have shown that cavitation resulted in a decrease in breakdown potential by 50mV contrary to the work by Brijesh and Hansson (1990), where the breakdown potential of a stainless steel type 304 SS in 3.5% NaCl also in the cavitation condition has been reported to be raised. The latter also concluded that cavitation decreases the probability of pitting of stainless steel in chloride solutions. Moreover, cavitation decreases the rate of pit growth by destroying the film over a pit, thus preventing the formation of a high concentration of corrosive solution within the pit.

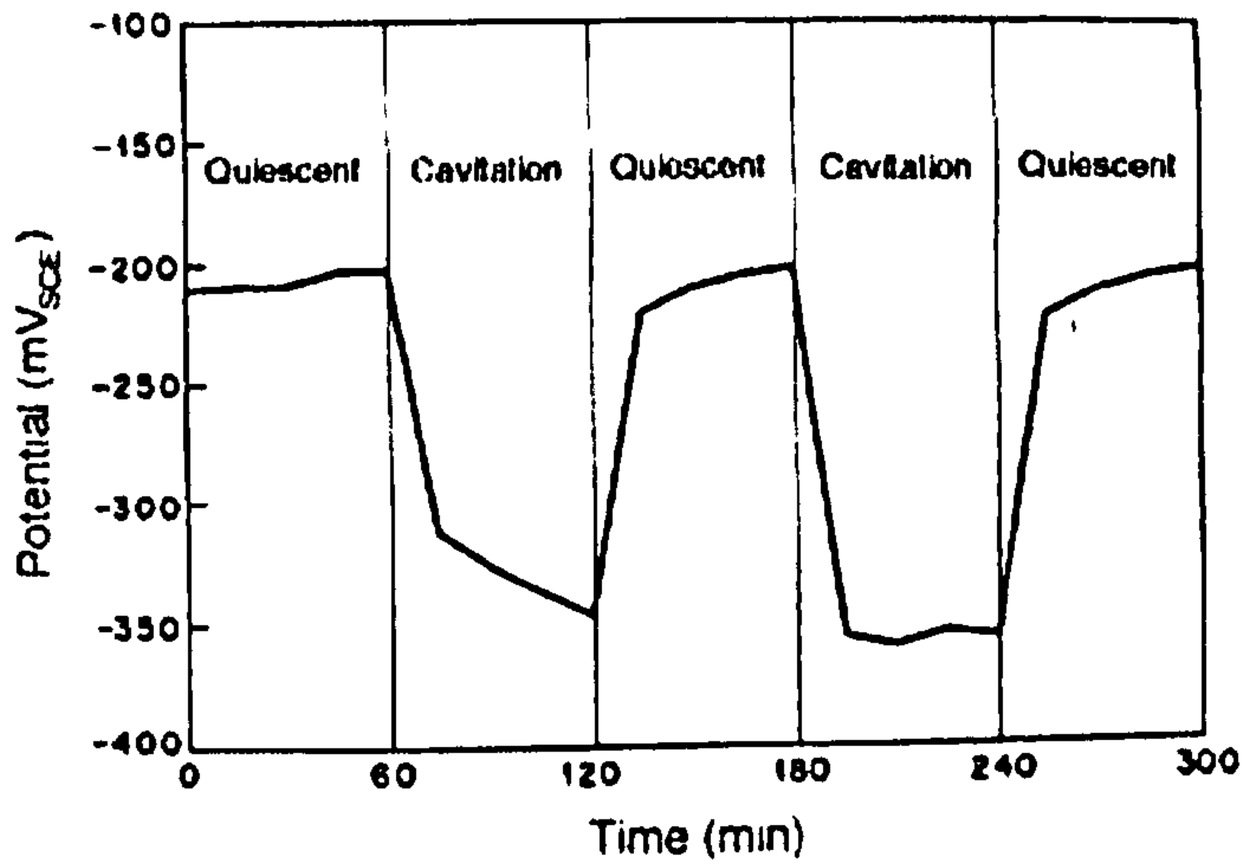


Figure 3.7.2 Effect of cavitation on free corrosion potential of duplex stainless steel in seawater (Al-Hashem, 1997).

Auret et al. (1993) studied the relation between the velocity, pressure, cavitation erosion and damage characteristics and confirmed the existence of a peak erosion rate (PER) as a function of pressure and increased erosion rate with increasing velocity for aluminium alloy type BS 1C. A study was performed by Momma and Lichtarawich (1995) on A6063 aluminium alloy and found correlation between PER and upstream pressure, indentation count and indentation diameter.

Di Vernieri Cuparri et al. (1999) tried to study the correlation between microstructure and cavitation resistance of high chromium cast steel. It was shown that for high-chromium steel, the increase of the austenite content decreases cavitation resistance. However, it has presented a superior performance, as compared to the austenitic steel AISI 304 in similar test. They also observed that finer carbide particle morphology has a beneficial effect on the cavitation resistance.

Neville et al. (1995) studied the erosion-corrosion behaviour of three generic materials (C-Mn steel, an austenitic and a duplex stainless steel) under a high velocity ($100ms^{-1}$) saline liquid jet impinging perpendicularly on to the target material. This velocity is representative of upper velocities encountered in geometrical irregularities where impingement may occur and is the same magnitude as the estimated micro-jet impinging velocity which exists during cavitation bubble explosion. The observations revealed that the passive film on stainless steel has a crucial role in conferring protection against mechanical removal of material with its much superior resistance to degradation than the C-Mn steel. The observations also indicated a mixed mode of material deterioration in such environment due to the complex array of incident angles imposed by the hydrodynamic conditions. Material ranking of various austenitic, superaustenitic, duplex and superduplex stainless steels in high velocity liquid impingement conditions at ambient temperature by Neville (1995) has illustrated reduced corrosion resistance of all materials except Inconel 625 and Ultimet. It was also shown that increased temperature (50°C) resulted in decrease of erosion-corrosion resistance of all materials tested. The attack mechanisms in liquid flow conditions were due to formation of pits in the forms of "comets" and was postulated that corrosion products emanating from these pit-heads are likely to act as abrasive particles during subsequent impacts of liquid jet.

Solid and Solid-liquid flow systems

Many of the studies regarding solid-erosion emphasize the various factors such as particle movement, particle properties and wall material properties and these have been already discussed in section 3.3. In solid-liquid erosion the liquid flow characteristics play an important part in addition to the solid particles presence in material degradation (section 3.4) and is more accentuated by liquid corrosivity (section3.6) involving a high synergistic effect.

Dry erosion

Levy et al. (1986) reported the accelerated temperature erosion behaviour of several commercial ferritic and austenitic stainless steels over a range of temperatures from room temperature to 900°C with nitrogen as carrier gas and silicon carbide particles as erodent. It was determined that all the steels had constant or decreasing erosion rates as the test temperature was increased until a temperature was reached where a sharp increase in erosion rate began to occur with temperature. Austenitic steels were found to have lower erosion rates than ferritic steels and their hardness had no correlation with their erosion rate. All the steels were eroded by the platelet mechanism of erosion.

Wang et al. (1992) conducted erosion-corrosion tests on hot-rolled 1018 plain carbon steel at 25 and 450°C, at particle velocities of 10 and 20ms^{-1}, and at an impact angle of 30°. The erodent particles (SiO_2, CaO 250μm size) were obtained from circulating fluidized bed combustors (CFBC). It was found that the particles must be strong enough not to shatter upon impact in order to be erosive and that more angular and larger size particles have higher erosivities. The erosion-corrosion mechanism by FBC bed material particles impacting on a steel alloy is the erosion of a bed material-iron oxide mixture from the surface and its replacement by the diffusion of metal atoms into the scale layer where replacement oxide forms. Levy and Man (1985) observed that the erosion-corrosion mechanism and rates and the resulting scale morphologies of 9Cr1Mo steel at an impingement angle 30° (temperature 850°C) were considerably different than those occur at impingement angle of 90°. At 30° impingement angle the primary mechanism of scale loss is chipping at all particle velocities through 70ms^{-1}. At 90° impingement angle, the mechanism changes from chipping to periodic spalling at

velocity of $35ms^{-1}$. It has been reported that the mechanism consists of a "V" notch configuration in the centre and further away from the centre a halo zone.

Sundarrajan (1995) in his paper assessed the influence of various strengthening mechanisms (e.g. dislocation strengthening, grain size, dispersion, precipitation, transformation and second phase hardening) in metallic materials on their erosion resistance. It is reported that in the case of Cu, addition of solutes like Zn and Al increases the hardness/strength and the erosion rate whereas in the case of Ni, addition of 20wt% of Cr increases the strength/hardness but decreases the erosion rate. Erosion rates of the dispersion-strengthened alloys are generally higher compared to the same alloy without the dispersion despite the fact that, strengthening mechanism results in a substantial improvement in material strength. He concluded that none of the parameters (strength, ductility etc.) could be utilized to correlate the erosion rate on a consistent basis and that erosion is a complex phenomenon involving not only material deformation but also its fracture.

Liquid-solid erosion-corrosion

The influence of applied potential on the erosion-corrosion behaviour of AISI321 stainless steel in 10%H_2SO_4 + 15% corundum sand (60 mesh) acidic slurry ($5ms^{-1}$) was investigated using a modified slurry pot apparatus (Yao et al., 1995). The results showed that cathodic protection 'CP' could significantly decrease erosion-corrosion '*EC*' rate, and the cathodic protection efficiency could be 73.6% (Fig. 3.7.3). The cathodic protection efficiency η is defined as

$$\eta\ (\%) = (\text{EC rate without CP} - \text{EC rate with CP})/\ \text{EC rate without CP} \times 100$$

It has been reported that the more negative the cathodic potential, the greater is the protection efficiency and the effect of "hydrogen cushion" but the potential should be suitable not to cause hydrogen embrittlement. The influence of applied anodic potential on the erosion-corrosion behaviour has been determined in terms of three different zones: at potential a little more positive to free corrosion potential; stable passive and transpassive regions and their relation to particle impingement frequency was defined.

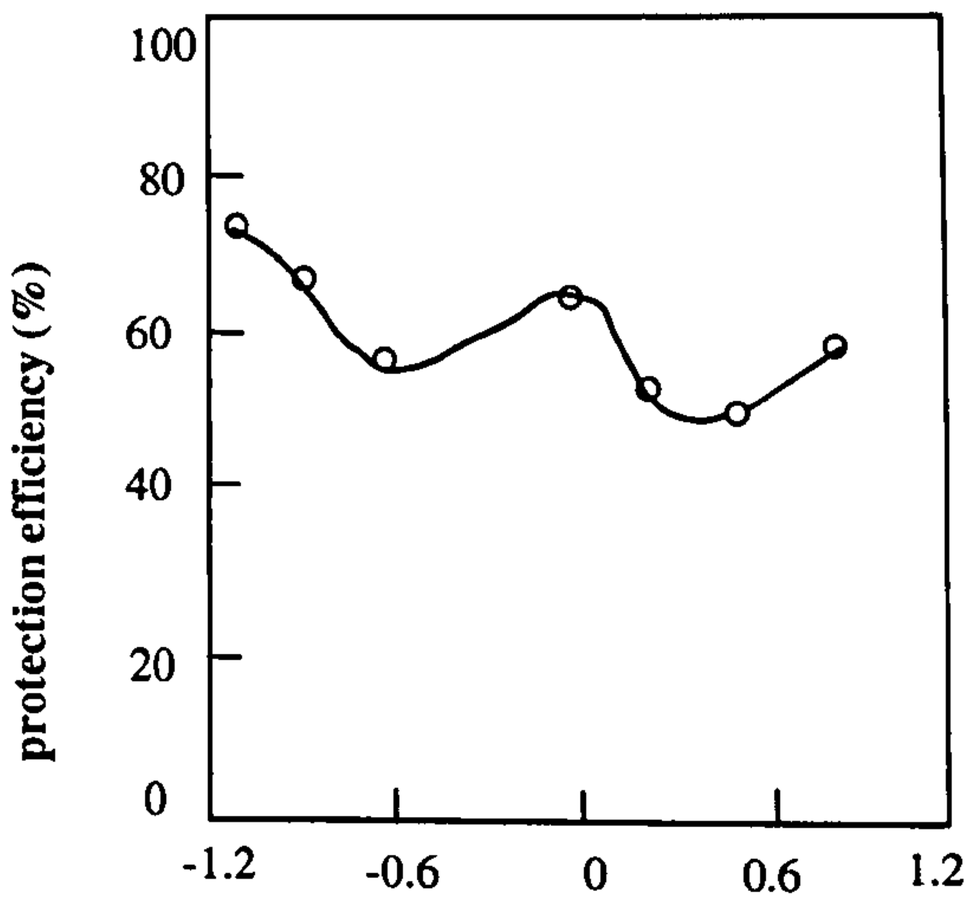


Figure 3.7.3 Variation of protection efficiency of AISI321 as a function of applied potential in 10%H_2SO_4+15% corundum sand (60mesh) at 5ms^{-1} (Yao et al., 1995).

Madsen (1988) found that at the lower impeller speed of 5.8ms^{-1} (the experiment being performed with 2% solids and 0.06M Na_2SO_4), the wear rates were only 2.73% or less of those attained at higher speeds. An increase in temperature from 26 to 60°C caused the wear rates to increase 25-30% for all three alloys at 15.6ms^{-1}. At the lower speed of 5.8ms^{-1} the increase in temperature caused an increase of 46%, 2.7% and 74% for the A514 steel, 316 stainless steel, and low alloy steel (REM 500) respectively. Wear rates and synergism for all tested alloys are listed in Table 3.7.1.

Alloy	Wear rate (mm^3/h)							
	26°C				60°C			
	TWL	E	C	S	TWL	E	C	S
A514 steel								
15.6ms^{-1}	28.12	18.57	0.277	9.27	35.68	22.98	3.86	8.84
5.8ms^{-1}	0.494	0.248	ND	ND	0.722	0.022	ND	ND
316 SS								
15.6ms^{-1}	31.32	20.52	0.841	9.96	39.34	23.74	0.876	14.72
5.8ms^{-1}	0.781	0.267	0.082	0.432	0.802	0.217	0.085	0.500
REM 500								
15.6ms^{-1}	16.56	12.53	0.099	3.93	21.58	14.52	0.720	6.34
5.8ms^{-1}	0.339	0.041	0.062	0.236	0.589	0.016	0.381	0.192

Table 3.7.1 Wear rates and synergism of three different steels as a function of impeller speed and temperature with 2% silica sand in a Na_2SO_4 solution (Madsen, 1988) ND - not determined.

Shadley et al. (1996) studied the erosion-corrosion of carbon steel. The test was performed at 93°C in a deoxygenated 3%NaCl solution saturated with CO_2, pH 5 to 6, flow velocity up to 5.2ms^{-1} and sand particles of size 155μm between 0.5 wt% and 4 wt%. Experimental results revealed three typical types of behaviour. At low velocities less than 1.5ms^{-1}, a protective iron carbonate ($FeCO_3$) scale formed over all surfaces of the elbow, and corrosion rates were very low. At higher velocities, impingement on elbow surfaces by sand particles entrained in the flow prevented protective scales forming in the elbow. Corrosion rates were fairly high and uniform over the entire surface. At intermediate velocities, protective scales formed all over the elbow surface except at very localized points, where impinging sand particles prevented scale formation. Deep pits formed at these points, and wall penetration rates were very high.

An erosion-corrosion map was constructed for PVD coated and uncoated steels (mild steel type BS6323 and stainless steel type AISI 304) in aqueous carbonate/bicarbonate slurry containing alumina particles (Stack et al., 1999). The effect of velocity at various applied potentials was assessed for the tested materials. The results showed that increases in specimen rotational velocity and applied potential have a significant effect on the erosion-corrosion rates for both the coated and uncoated steels.

Neville et al. (1995) studied the erosion-corrosion behaviour of three generic materials, a C-Mn steel, an austenitic and a super duplex stainless steels commonly used for marine pumping applications. Tests were performed in a slurry jet comprising of 3.5% NaCl and 0.1% silica sand at a normal impingement velocity of 25ms^{-1}. It has been reported that the percentage contribution of corrosion to the total weight loss on SAF 2205 was greater than on UNS S31603 and so was the synergistic component. Hence corrosion directly or indirectly attributed to 19.3 and 24.4% of the total weight loss on UNS S31603 and SAF 2205 respectively. In the case of C-Mn steel the figure was up to 40%. The results have demonstrated that a lower erosion resistance of a duplex stainless steel can outweigh a greater role of corrosion resistance to the overall material loss. It has been shown in this study that the effect of the solid particles was to render the surface of the stainless steels susceptible to active corrosion, hence signaling the removal of the protective oxide layer. As an extension of this work, later Neville and Hodgkiess (1997c) experimented on graphite cast iron, grade 250 and an austenitic

stainless steels type UNS S31603 to study the effect of liquid corrosivity on the components of deterioration owing to corrosion, erosion and synergism in the overall material loss. The tests were conducted in 3.5% NaCl solution at temperatures 30 and 50°C and also in 0.05% TDS at normal jet impingement, 25ms^{-1} jet velocity and 0.1% silica sand. The breakdown of the total weight loss, pure corrosion, pure erosion and synergistic components are shown in Table 3.7.2.

	Cast iron		**UNS S31603**	
	3.5% NaCl	**0.05% TDS**	**3.5% NaCl**	**0.05% TDS**
***TWL*, mg**	57.4	55.9	25.9	24.0
***E* /*TWL*, %**	52.4	87.2	81.2	99.0
***C* /*TWL*, %**	5.3	1.4	2.0	0.4
***S* /*TWL*, %**	42.3	11.4	16.8	0.6

Table 3.7.2 Total weight loss distribution under solid-liquid impingement at 50°C after 1 hour (Neville and Hodgkiess, 1997c).

Lowering the TDS of the carrier fluid had the effects of increasing the proportions and magnitude of the total weight loss attributed to pure erosion *E* and reducing the synergistic factor *S*. Increased synergism is supposed to be associated with the interfacial attack that occur at the graphite boundaries in the cast iron in 3.5% NaCl. Another possible factor accounting for the increased amount of erosion *E* in the low TDS water has been suggested to be associated with the decreased viscosity and density of the liquid medium, which would confer reduced drag forces on the impinging particles and increase their kinetic energy. For the stainless steel high chloride content in solid-liquid stream substantially increased the corrosion rate and synergistic component of the total weight loss.

CHAPTER 4. SURFACE ENGINEERING

Introduction

"Surface engineering is an enabling technology widely applicable to a range of industrial sector activities. It encompasses techniques and processes capable of creating and/or modifying surfaces to provide enhanced performance such as wear, corrosion and fatigue resistance and bio-compatibility" (Datta and Gray, 1993). Coating techniques among the methods of surface engineering have clearly a considerable industrial/economic potential for the protection of advanced materials during operations and for extending their working life, especially of valuable components (Hondros, 1993). A range of methods used in surface engineering is summarised in Fig. 4.1 (Hutchings, 1992).

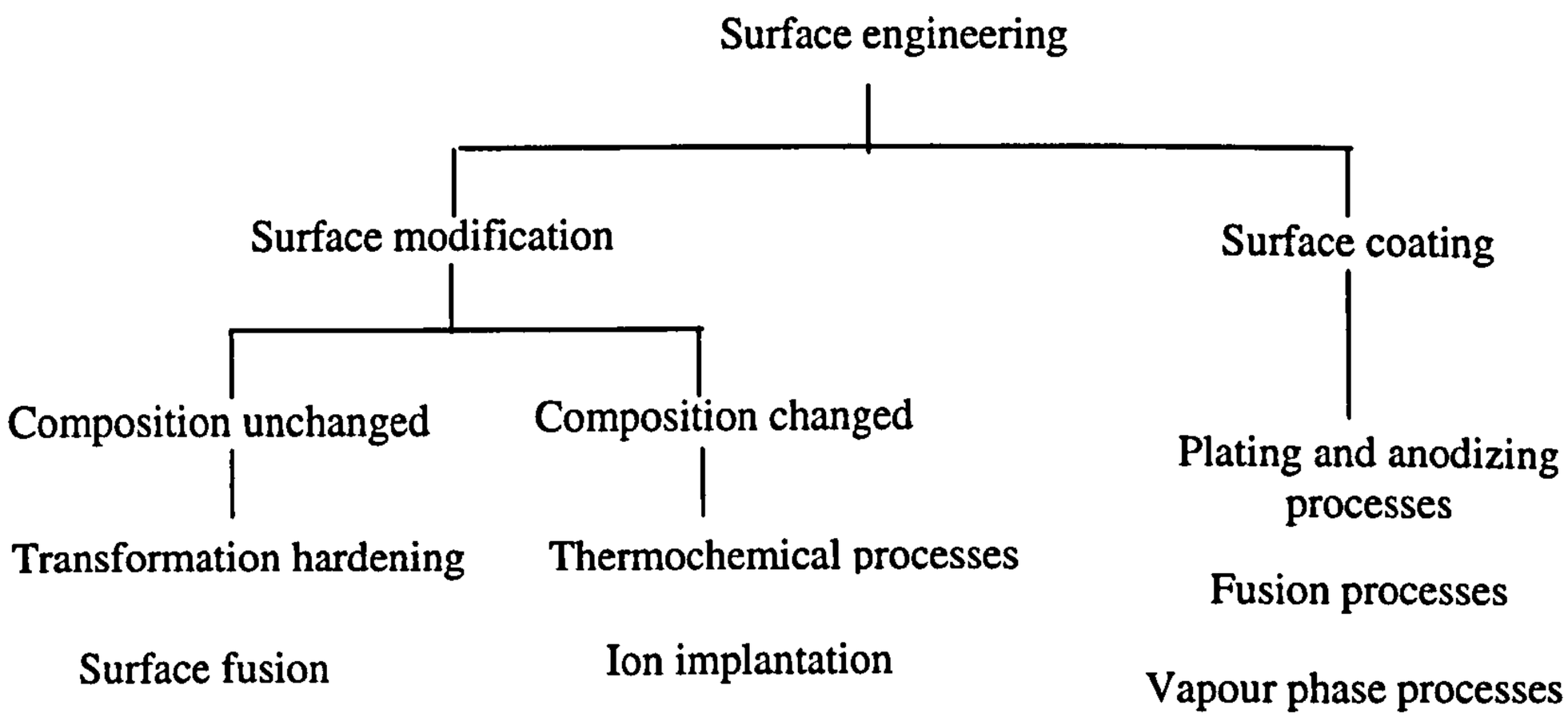


Figure 4.1 Methods of surface engineering (Hutchings, 1992).

Details of the surface modification techniques are described by Hutchings (1992). This chapter of the thesis will encompass only to surface coatings in general. More details of the HVOF coatings of relevance to this thesis will be given in section 4.3. It is important to appreciate the breadth of coatings available such as coatings obtained by plating and anodizing such as chromium, nickel and composite coatings (Hutchings, 1992; Ebdon, 1993). Vapour phases processes such as physical vapour deposition *PVD* and chemical vapour deposition *CVD* (Duret and Pichoir, 1983; Hutchings, 1992, Mathews, et al.,

1993) and fusion process in which coating material is applied in the molten state such as *welding* and *thermal spraying* are primarily developed for wear resistance. Thermal spraying which is considered in depth in this thesis is detailed in section 4.1.

4.1 A brief review of general thermal spray processes

The various processes of thermal spraying are primarily based on methods, which require metallic, non-metallic or cermet wire or powder (Steffens, 1983; Berget, 1998). In all thermal spray deposition processes material, usually in the form of powder or wire is heated to near its melting point, accelerated to a relatively high velocity depending on the process, and allowed to impact on the surface to be coated. The molten or nearly molten droplets flow into thin overlapping and interlocking lamellar particles 'splats' forming the coating (Nicoll et al., 1992). The three important factors that affect the coating properties are velocity, temperature of particles on impact and the extent to which they have interacted with the surrounding environment (air) during the deposition process. The major advantages of thermal spraying are: greater flexibility to use different coating material, ability to coat the surface without significantly heating it without changing its metallurgical structure or mechanical properties, ability to strip worn coatings and reapply new coatings. The coating is achieved to required thickness by repeatedly spraying on to the same area. The coating is applied to a pre prepared surface, which is achieved usually by grit blasting or mechanical preparation such as by lathe turning. The concept of thermal spray consists of a spray gun, in which either wire or powder is fed. The coating material is melted and is accelerated towards the substrate material by a propellant air or gas (Bjordal, 1995).

Early thermal spray techniques have been illustrated by Berndt and Kowalsky (1996) in which the thermal spray is simply declared as feeding a solid body of the fusible substance towards a melting appliance and blowing the melted substance against the surface. Conventional thermal spray techniques include flame spraying, electric arc spraying. The advanced thermal spray processes include detonation gun, high velocity oxy-fuel (HVOF) and plasma spray (Tucker and Ashary, 1995).

Thermal spray coatings are widely used to combat wear and corrosion. The service environments range from cryogenic temperatures to temperatures exceeding 1500°C,

from very low pressures in vacuum to high pressures, and from chemically inert to extremely acidic or basic. The use of thermal spraying in recent years is increasing due to: a) its cost effectiveness b) because of the value of longer lasting surfaces in terms of higher productivity and the higher quality of produced goods.

Flame Spraying (FS)

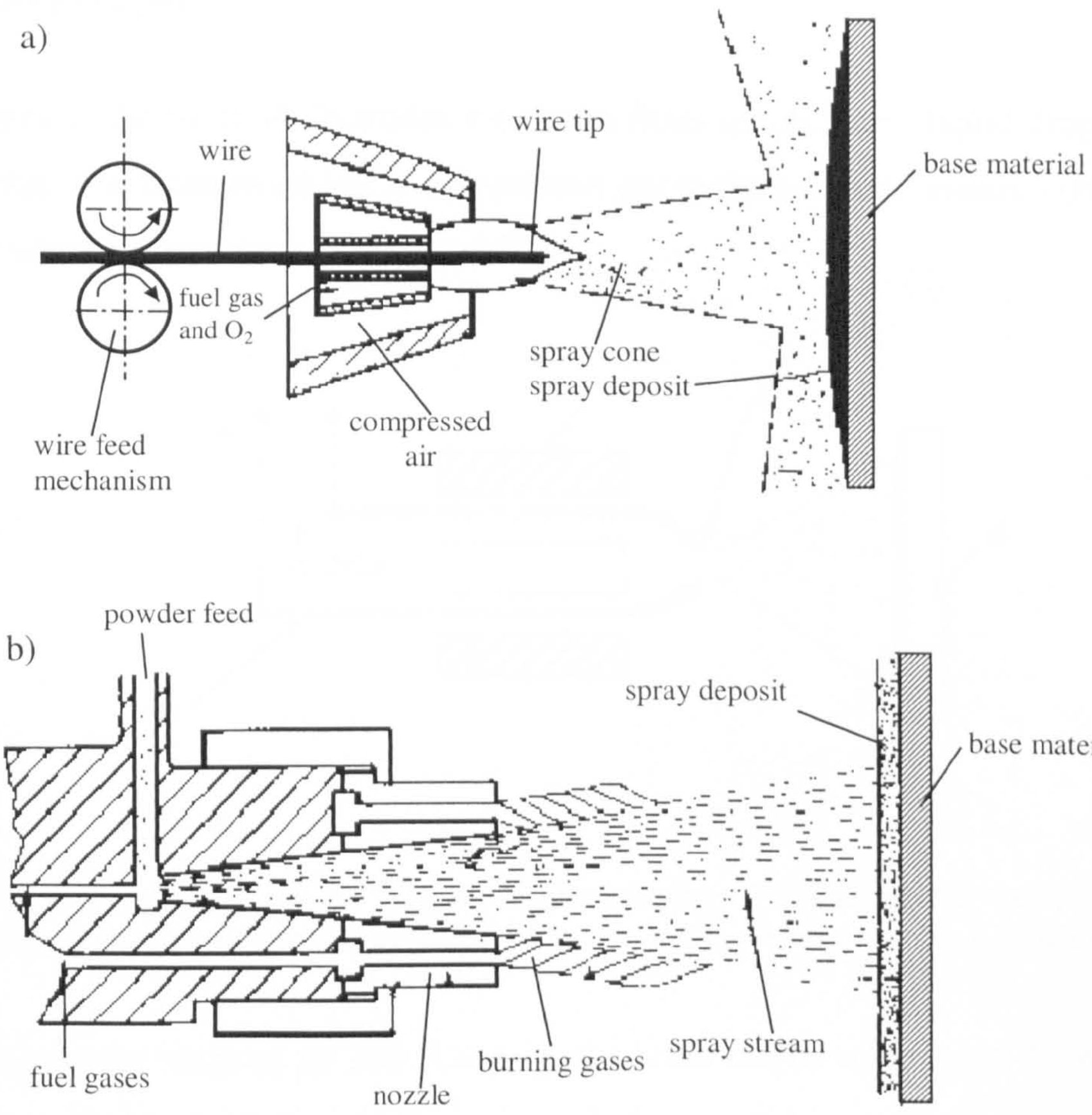


Figure 4.1.1. Schematic diagrams of flame spraying process (a) wire form (b) powder form.

In flame spraying, an oxygen-fuel gas (Fig. 4.1.1) melts the combustible wire or powder. Fuel gases commonly used are acetylene, propane or hydrogen. The carrier gas may be oxygen, fuel gas or some other inert gases (Steffens, 1983; Lugscheider and Jokiel, 1993). The combustion flame consists of a stream of compressed air or inert gas, which can be convergent, divergent or parallel in flow. Process parameters for a

particular material define the choice of gases, the geometry of the spray head, gas and powder flows etc. Much about the process parameters can be found elsewhere (Pawlowski, 1995). The powder flame spray process allows using various carbides, oxide ceramics, cermets etc. to be sprayed. Typical bond strength values are in the range of 15MPa for ceramic coatings to 30MPa for other materials. Porosity is in the range of 10-20% and typical thicknesses are in the range 100-2500μm.

Arc Spraying (AS)

Two wires in the form of electrodes are drawn from spools, form liquid droplets upon arc heating which are propelled by compressed gas to the substrate material (Fig. 4.1.2). The particle velocities can reach up to 150ms^{-1}.

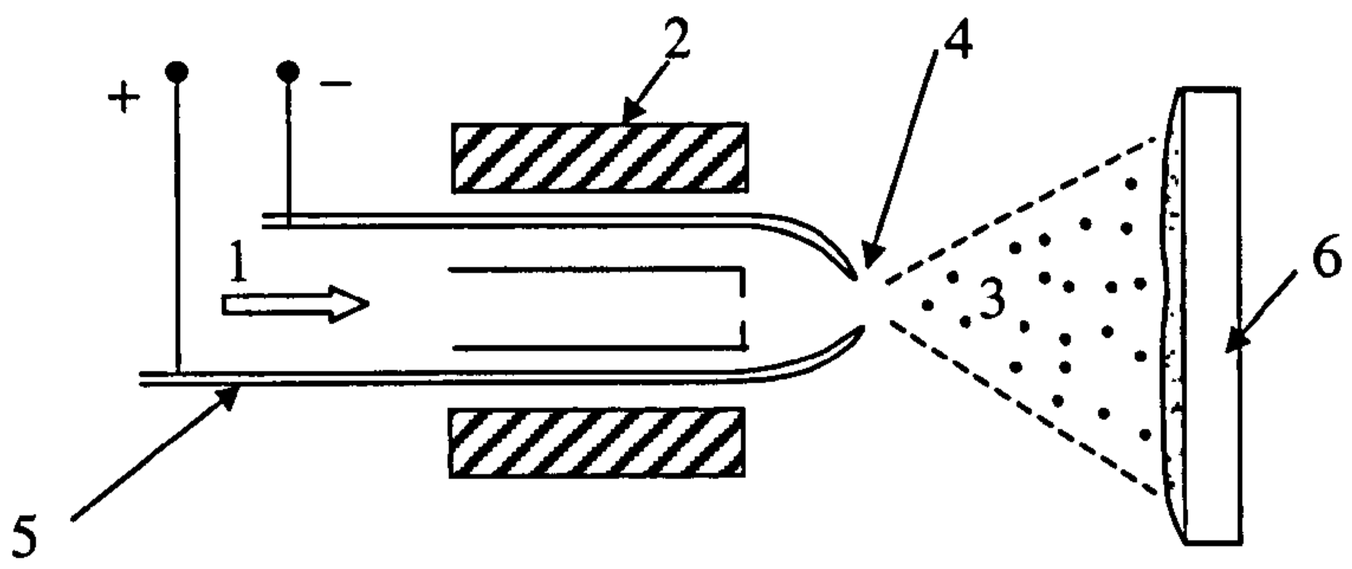


Figure 4.1.2. A schematic diagram of arc spraying; 1, carrier gas; 2, torch outer shield; 3, stream of molten particles; 4, electric arc; 5, electrode wires; 6, substrate.

Porosity is in the range of 10-20%. Coatings thickness can be achieved in the range 100-1500μm. All electrically conductive materials (e.g. metals or metallic alloys) can be applied by this technique. Cored wires, wrapping for example hard materials into a metallic sheath are in extensive use. Both atmospheric arc spraying and vacuum arc spraying have been well illustrated in the literature (Steffens et al., 1994).

Atmospheric Plasma Spraying (APS)

Atmospheric plasma spraying (Fig. 4.1.3) comprises an anode usually made of copper, and cathode of thoriated tungsten. The electric arc discharge heats up the working gas typically Ar or a mixture of Ar+H_2, Ar+He or Ar+N_2. The temperature of the plasma (ionised gas) can be typically at a maximum of about 14000K and the nozzle exit velocity can reach above 800ms^{-1} (Pawlowski, 1995).

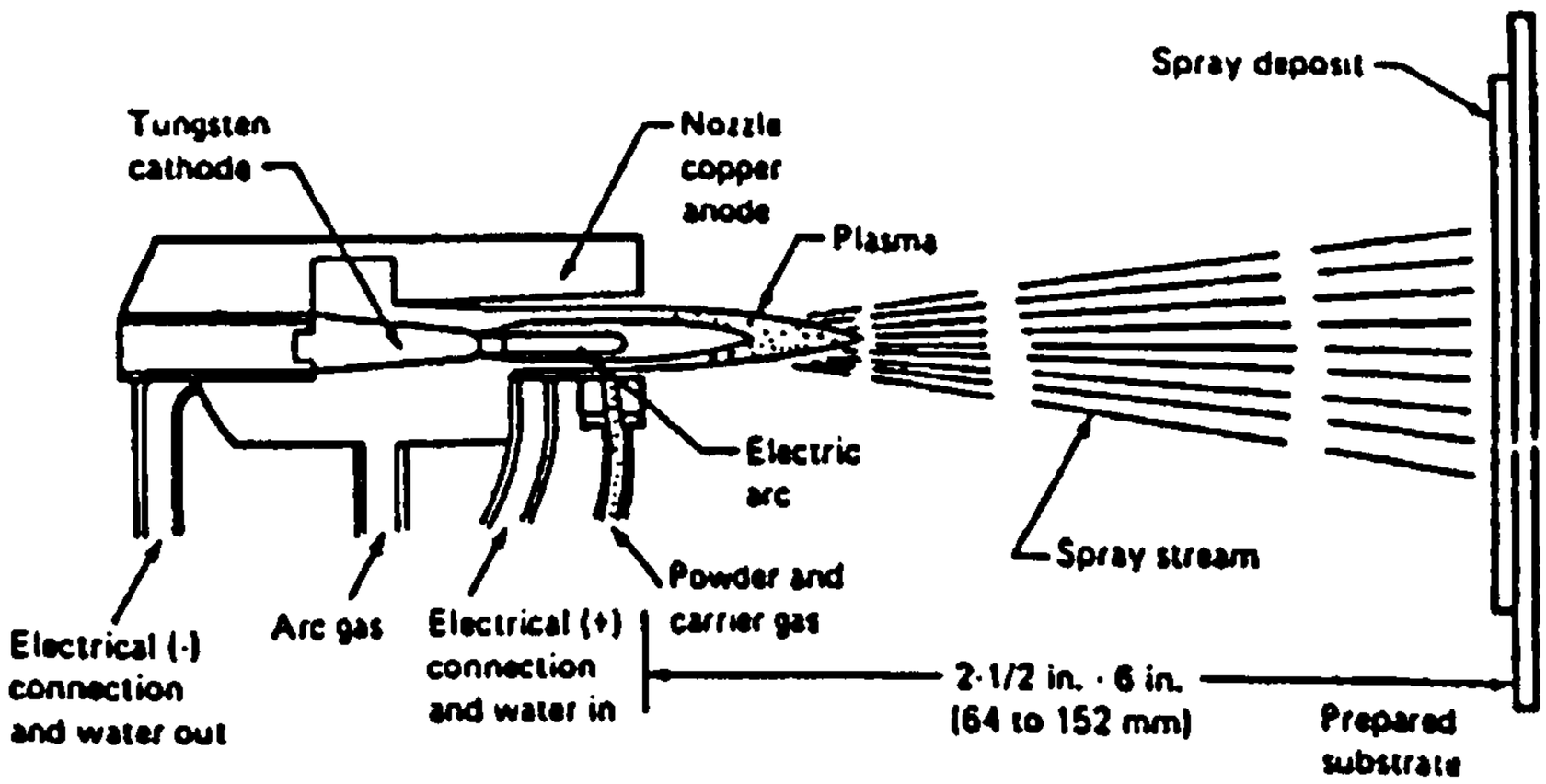


Figure 4.1.3. A schematic diagram of a plasma spraying gun.

The angle of spraying is usually perpendicular to the substrate being sprayed. The porosity can be in the range of 1-7% and greater. The thickness of the coating can be in the range 50-500μm. Combustion sensitive materials (e.g. nitrides and carbides) and also reactive materials (e.g. titanium and tantalum) can be sprayed by this method (Steffen et al., 1994).

Vacuum Plasma Spraying (VPS)

Vacuum plasma spraying also called low-pressure plasma spraying (LPPS), consists of a plasma torch with a vacuum nozzle. A port feeds the powder to a plasma jet working in vacuum Fig. 4.1.4. Additional transferred arc is used to clean and heat up the surface prior to spraying (Pawlowski, 1995).

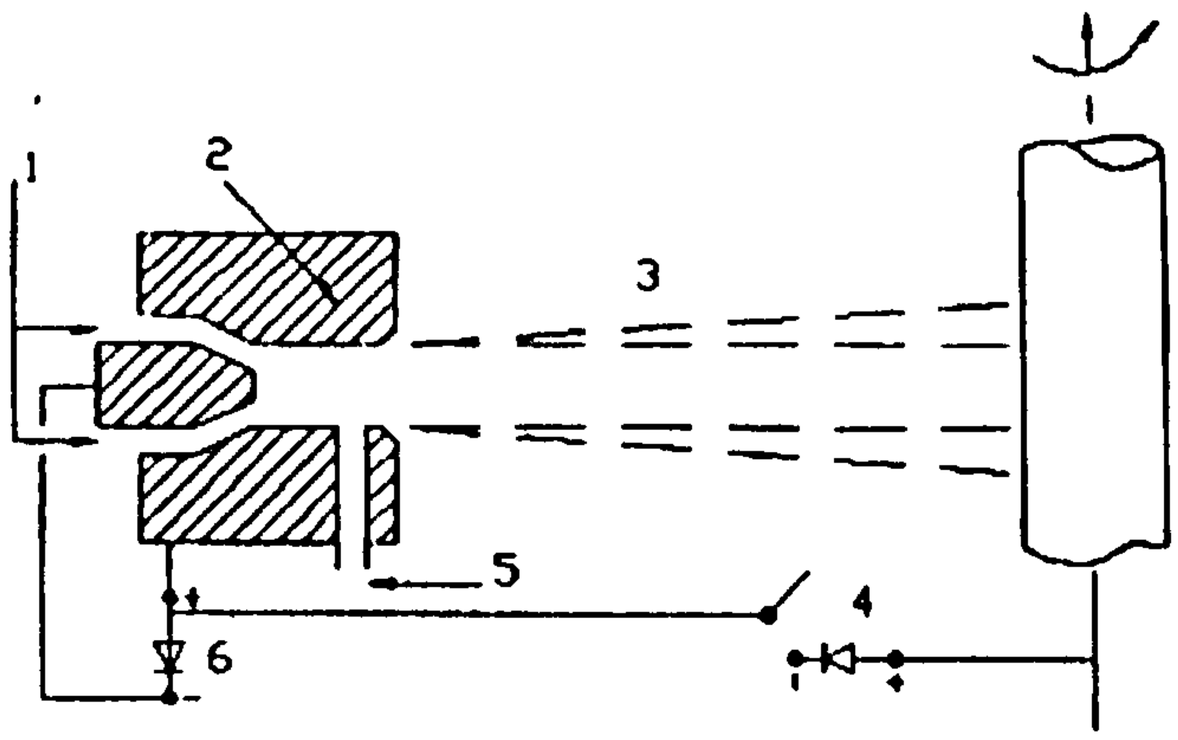


Figure 4.1.4. A schematic diagram of a vacuum plasma spraying. 1, working gases inlet; 2, anode; 3, vacuum environment; 4, transferred arc generator; 5, powder injection port; 6, plasma arc generator.

Detonation Gun Spraying (DGS)

The detonation gun (Fig. 4.1.5) comprises oxygen and fuel (acetylene) gases with uniformly dispersed fine powder (primarily metallic and non-metallic hard metals), which are repetitively injected into the barrel. A spark is used to ignite the mixture and the pressure rises resulting in a detonation wave.

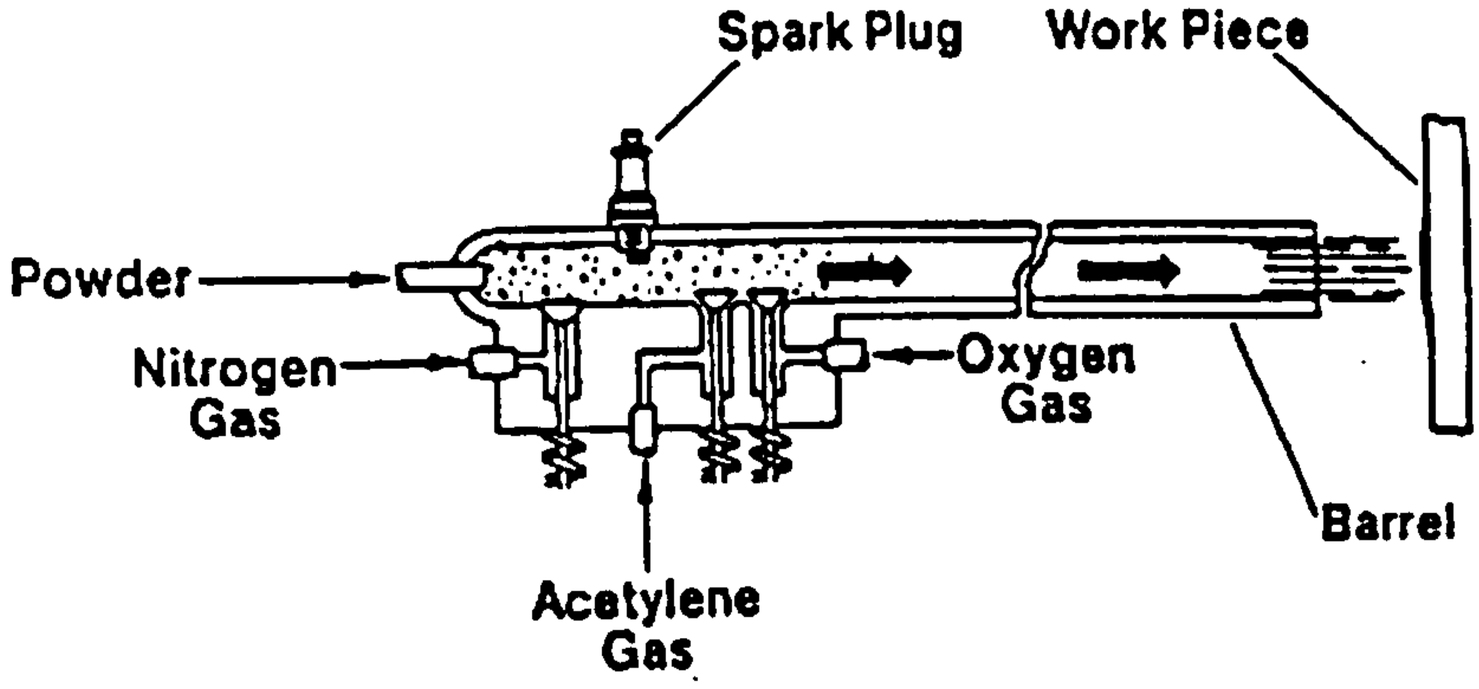


Figure 4.1.5. A schematic diagram of oxygen-fuel detonation gun, D-Gun™ (Tucker and Ashary, 1995).

This wave propagating down the barrel heats the powder particles near or above their melting point and accelerates the heated particles to a velocity of about 750ms^{-1} in the D-Gun^{TM} (Irving et al., 1993) and about 1000ms^{-1} in more advanced type Super D-Gun^{TM} (Tucker and Ashary, 1995). The barrel is then purged with nitrogen and the detonation process is repeated 1-15 times per second (Berget, 1998). The porosities of D-Gun^{TM} coatings are about 0.5% for WC-Co and about 2% for Al_2O_3 coatings and the bond strength, correspondingly greater than 83MPa and 70Mpa. The thicknesses of the D-Gun^{TM} coatings are typically about 300μm (Pawlowski, 1995).

High Velocity Oxy-Fuel (HVOF) Spraying

Developments of HVOF guns were started at the end of the 1970s and beginning of the 1980s. The HVOF process represents the state -of-the art for thermal sprayed coatings. In HVOF process particles with high kinetic energy and controlled thermal input are impacted onto a surface to produce a dense coating with very low porosity (< 1%), high bond strength up to 40MPa and low residual stresses. Substrates that can be sprayed include metals and alloys, non-metals, plastics. Possible coating materials include pure metals (e.g. Ni, Cu, Al, Mo, Ti), metal alloys (e.g. steels, brasses), ceramics (e.g. Cr_2O_3, Al_2O_3, ZrO_2), cermets (e.g. WC/Co, WC/CoCr, Cr_3C_2/NiCr, NiCrSiBC) and others e.g. AlSi/thermoplastic/graphite (Kumar and Modi, 1995; McIntyre, 1996).

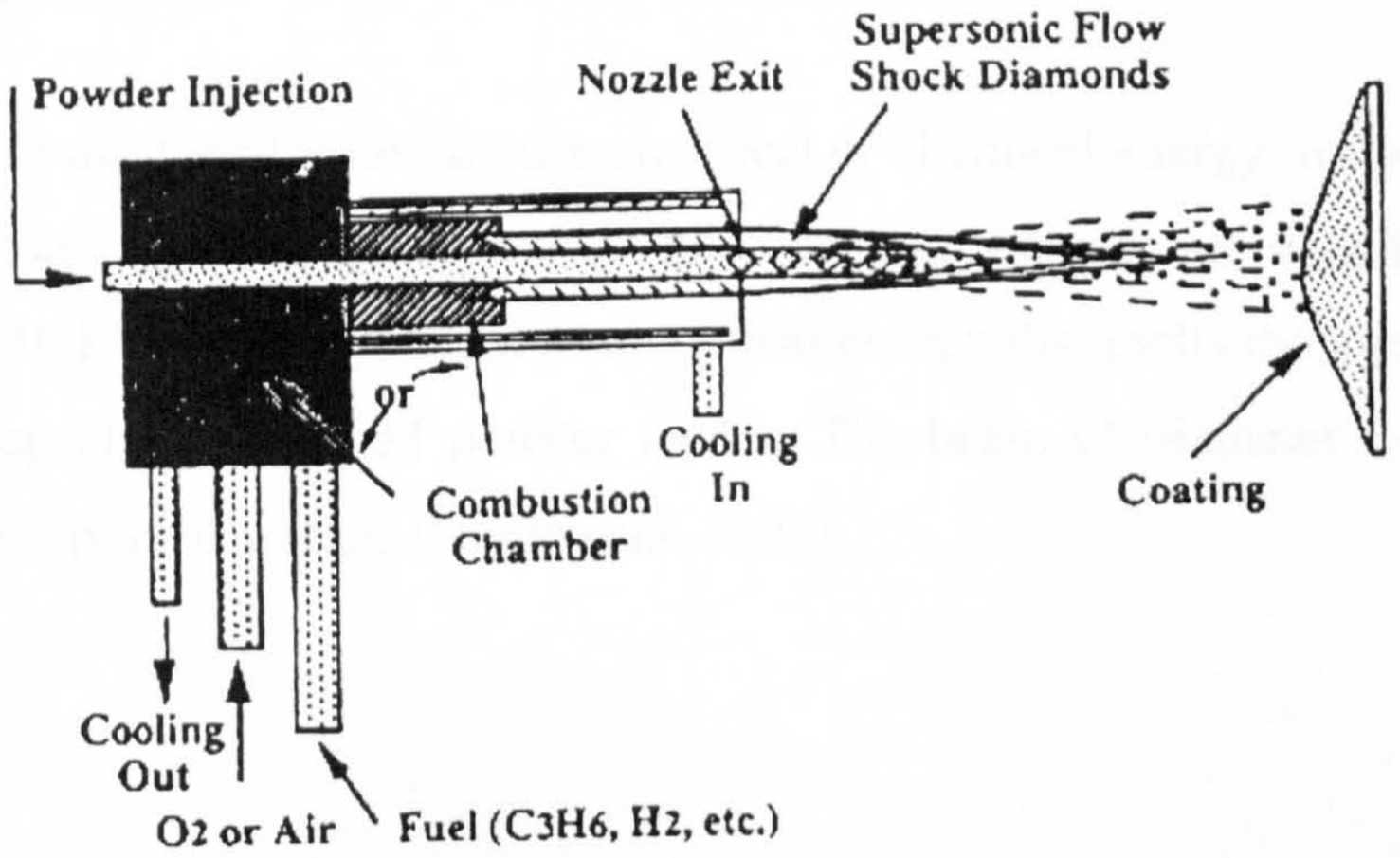


Figure 4.1.6 A schematic diagram of a High Velocity Oxy-Fuel (HVOF) gun (Irving et al., 1993).

The schematic diagram in Fig. 4.1.6 represents a high velocity oxy-fuel gun. The basic principle of HVOF process is one in which, fuel such as acetylene (C_2H_2), kerosene, propane (C_3H_8), propylene (C_3H_6) or hydrogen (H_2) gas is burnt with oxygen depending upon coating requirements, at a very high pressure with a formation of high velocity exhaust jet (Berjet, 1998; Parker and Kutner, 1991). The powder is injected axially into the jet. The gases are burnt in the combustion chamber and flow through the nozzle. The combustion chamber and the nozzle are air or water-cooled. In most HVOF systems particles reach 25-55% of gas velocity (Thorpe and Thorpe, 1993). Gas temperatures greater than 2,760°C are produced in HVOF systems (Parker and Kutner, 1991).

Another type of thermal spray technique is a Hypersonic Velocity Impact Fusion (HVIF) flame spraying (Browning, 1992), which operates using much the same principle as its oxy-fuel counterparts with the exception that, the static temperature of the expanded combustion product gases is held low enough to prevent softening of even the smallest particles (i.e. the sprayed particles are kept in temperatures below melting points). Another type of newly developed thermal spray system is a High-velocity-air-fuel (HVAF) system introduced by Browning Thermal Systems Inc. (Irving et al., 1993), which uses air instead of oxygen.

New Spraying Techniques

Laser Spraying (LS)

All techniques discussed primarily use electrical or chemical energy to fuse the sprayed particles. Laser spraying represents a new coating process in which, the system comprises a 10 kW CO_2 laser beam as an optical energy that melts the injected particles fed from a specially designed powder feeder. The beam of diameter 2-3mm is kept parallel to the sprayed surface (Pawlowski, 1995).

Underwater Thermal Spraying

Underwater thermal spraying has been developed viewing the application of protective coatings to offshore structures, particularly in the splash zone (Ohliger et al., 1990). The Jet-Kote-System was the first commercially available equipment. In under-water plasma spraying, the component is sprayed under the water and thus reducing exposure to dust, noise and radiation. It has been reported that the quality of the sprayed coating increases with water depth (Steffens et al., 1994). Reports on HVOF/PS technique under shallow water (0.5m) and deep-water (25m) have been illustrated (Kim et al., 1996). A schematic diagram of underwater spraying is shown in Fig. 4.1.7.

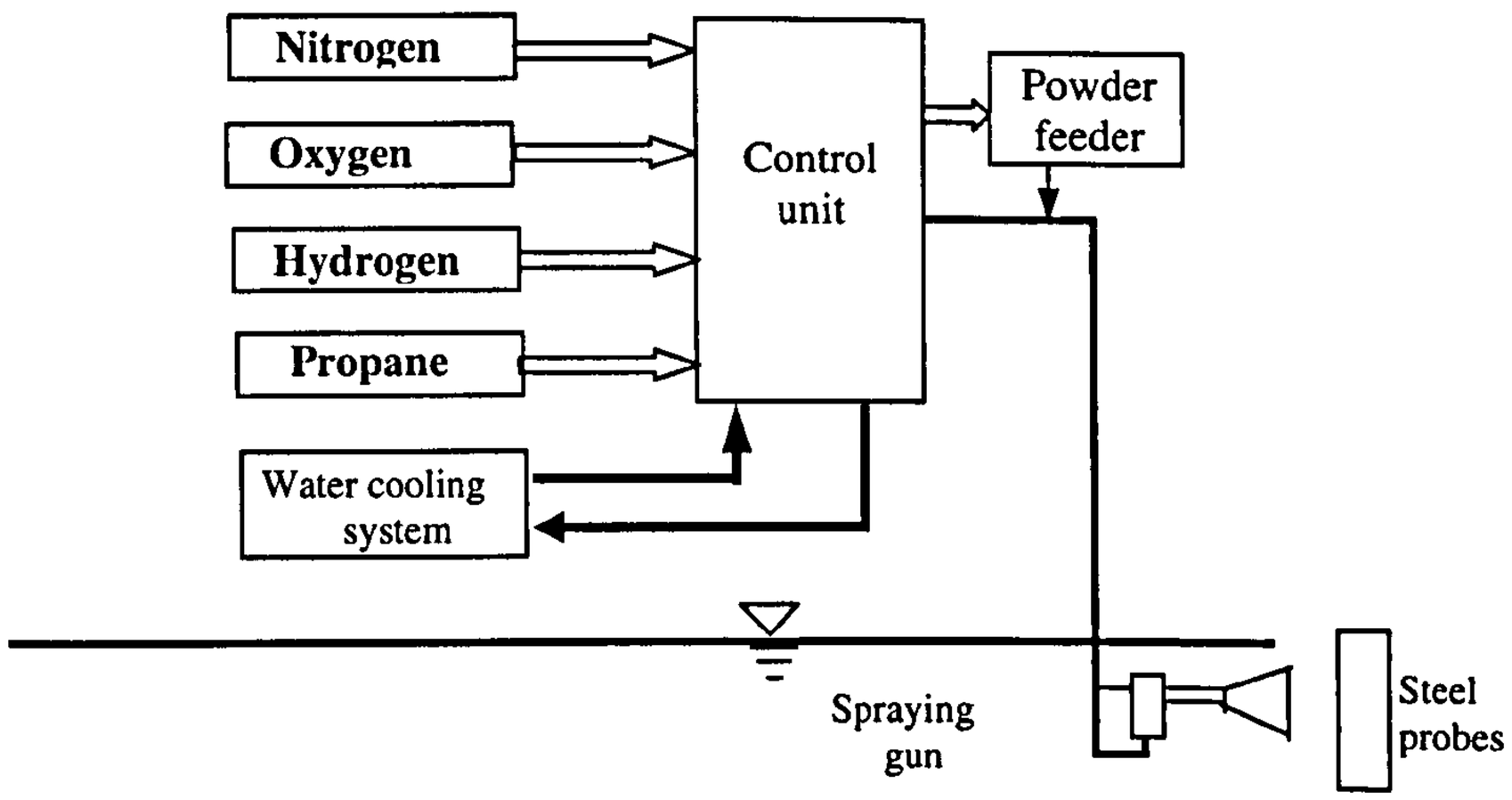


Figure 4.1.7 A schematic diagram of underwater spraying with the HVOF Gun.

4.2 Application and Industrial Relevance

The number of applications of thermal sprayed coatings has been growing steadily in the last two decades due to increased use of surface engineering. Equipment and plant shutdowns, both planned and unplanned can be extremely costly. Relatively fast and effective repair can be very valuable. Thermal spray processes have been offering attractive potential solutions to many of these problems due to the speed, portability, and low heat input.

Primarily developed for wear resistance and mainly used in aerospace industry, thermal sprayed coatings have now been a focus point for many industries. Principal applications of this technology are based on corrosion and wear protection, electrical and thermal insulation, decoration, and repair of worn component (Steffens et al., 1994). Such repair and Overhaul Base for Rolls-Royce aero-derivative, industrial gas turbines have been provided by *Rolls Wood Group* (Naisbitt et al., 1997). One of the first shipyard level, major component repairs with HVOF process (tungsten carbide coating) was performed on the rudder rams of the US Saipan (LHA-4) in 1994 and these coated rudder rams have been in service over 2 years with an estimated savings of over $1,000,000 (Rigney et al., 1998). Thermal sprayed coatings may be machined, milled, ground, polished and sealed in order to achieve the finish dimensions and the required surface quality (Steffens et al., 1994).

In the petrochemical industry, the coating is applied on tools such as drill bit cones, on vessels in chemical refinery, on ends of gas well tubing in gas research drilling. In situ refurbishment of pressure vessels, risers, pipelines and structural components in oil and gas industry coated with Nickel based alloys by thermal spray process have been detailed (Price, 1998). Metal seated ball valves with carbide coatings manufactured by Valvtechnologies have been reported to serve routinely for four years in a severe catalyst service without any maintenance (Manuel and Yung, 1994). These valves operate in a wide range of petrochemical applications, which include severe service to actuate at around 68MPa with zero leakage, in purifying kerosene by dewaxing at 482°C and many others. In the automotive industry the coating is used in valve lifter and internal parts of diesel engines e.g. piston rings, cylinder bores (Pawlowski, 1995;

Delaet and Coddet, 1997; Barbezat et al., 1997; Huchin, 1998; Barbezat et al., 1998). Recent developments of such coatings are widely used in production of car combustion engines, on the internal surfaces of synchronising rings in gearboxes, on crankshaft pins and on diesel engine injection nozzles and pistons (Fig. 4.2.1).

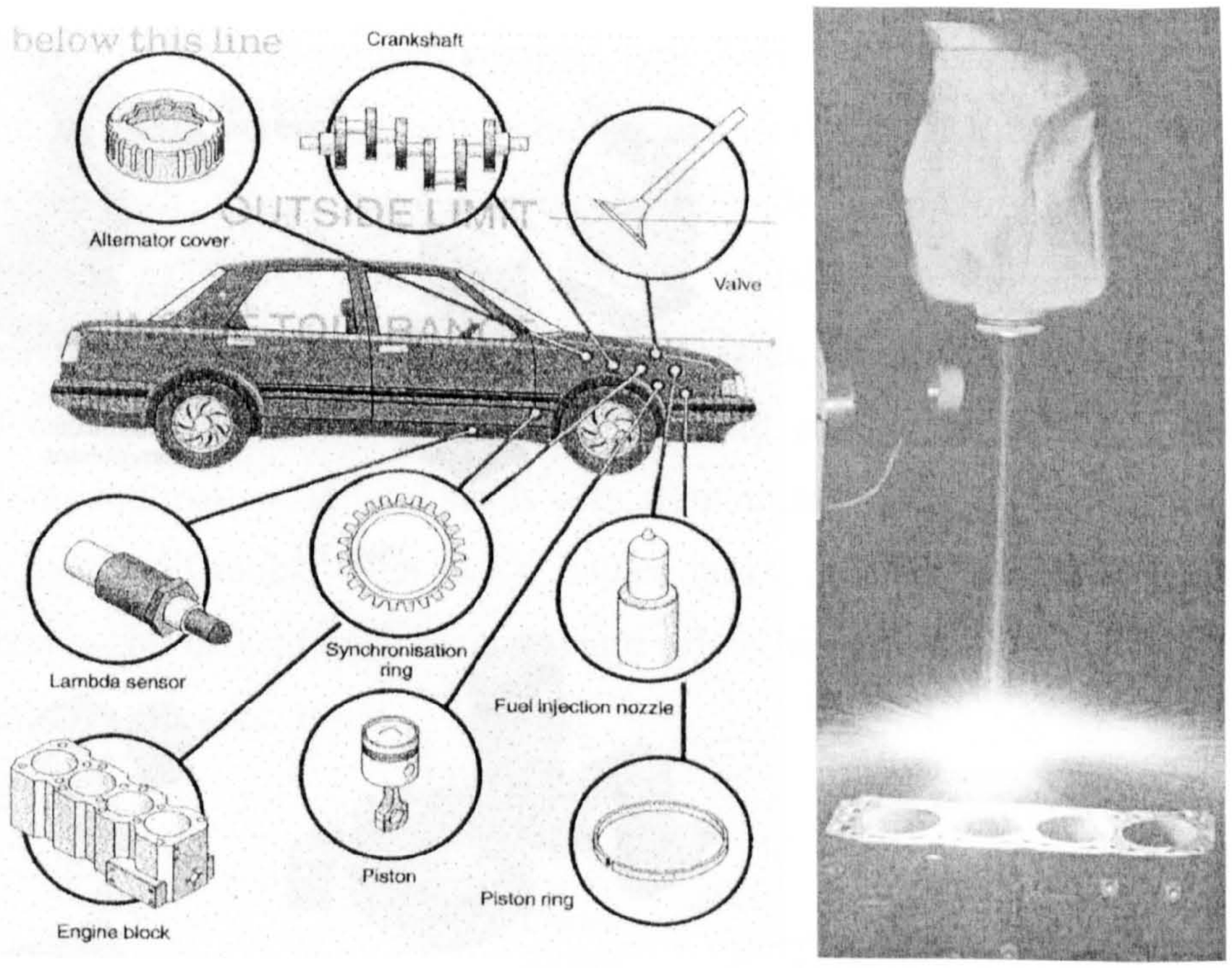


Figure 4.2.1 Application of thermal spray coating on automotive component (left) (Huchin, 1998) and a plasma gun spraying a cylinder (right).

Plasma spraying with metal powder (Brit. Corr. J., 1996) was recently used by Sultzer Metco (UK) on the Euro Fighter 2000 on metal panels for protection against plume thermal effects. The aerospace industry is probably the largest user of such coatings accounting for approximately 65% of the total powder production (Saywell, 1996) widely used in aero-engine components (Amos, 1996), aircraft landing gear (Bodger et al., 1997; Nestler et al., 1998), helicopter components (Guillemette, 1998) and many others such as fan-blade clappers, stator blades, turbine vanes, turbine blades, combustion cans, subsea piping (Wolfson, 1996) etc. In utilities and paper mills, high temperature corrosion and particle erosion are real problems on the boiler tubes. It has been reported that the life expectancy of the tube walls has increased up to five times by applying arc sprayed or plasma sprayed coating (Gardega et al., 1986). Application of

HVOF sprayed WC cermet coating in paper mills for wear and corrosion resistance has been reported (Tani and Nakahira, 1998). Other applications in paper and printing industries include drying rolls, sieves, filters, roll pins etc. In the textile industry the coatings are applied on thread guiding elements, guiding and distribution rollers, ridge thread brakes, distribution plates gallets, tension rollers. Protection of steam valves on board of naval and merchant vessels has been another successful use of thermal sprayed coatings. HVOF thermal sprayed coatings type 316L and Hastelloy C-276 have been used in many environments, which include acetic, sulphuric, hydrochloric, hydrofluoric and carbonic acids, molten sulphur, hydrogen sulphide and sodium hydroxide and have been reported to exhibit corrosion resistance equal to or slightly inferior to the performance of their wrought counterpart (Moskowitz, 1992). A significant reduction in material cost can be achieved by applying a thin coating on a cheap substrate. In shipbuilding thermal spraying of steels with aluminium coating on applications, such as weather decks, oil tanks, bilge tanks, ballast tanks, sanitary spaces, sewage holding tanks, fresh water tanks, fuel tanks and steam valves has provided testimonial success of the technology (Rogers, 1995).

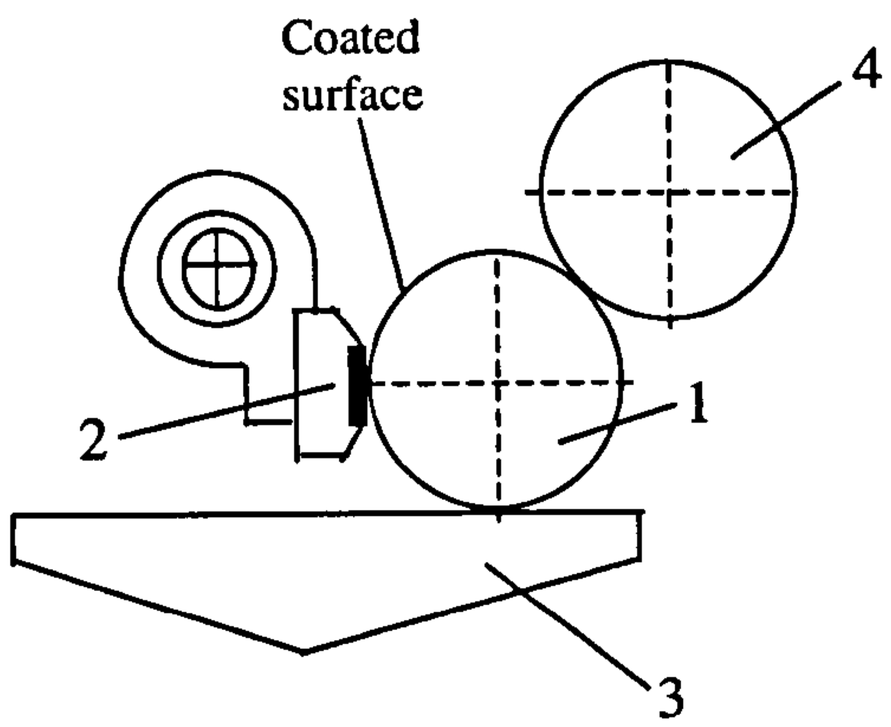


Figure 4.2.2 Part of a flexographic machine. 1, anilox roll; 2, doctor blade; 3, ink container; 4, printing roll.

Parker and Kutner (1991) have reported the use of HVOF spray processes for improved wear and erosion-corrosion resistance, clearance control, and restoration for various components such as compressor blade, compressor stator vane and bearing housing. Recent advancement of thermal sprayed coatings is applicable also in medicine e.g. coating on to prostheses "orthopaedic and dental" (Magome et al. 1998; Gross et al.,

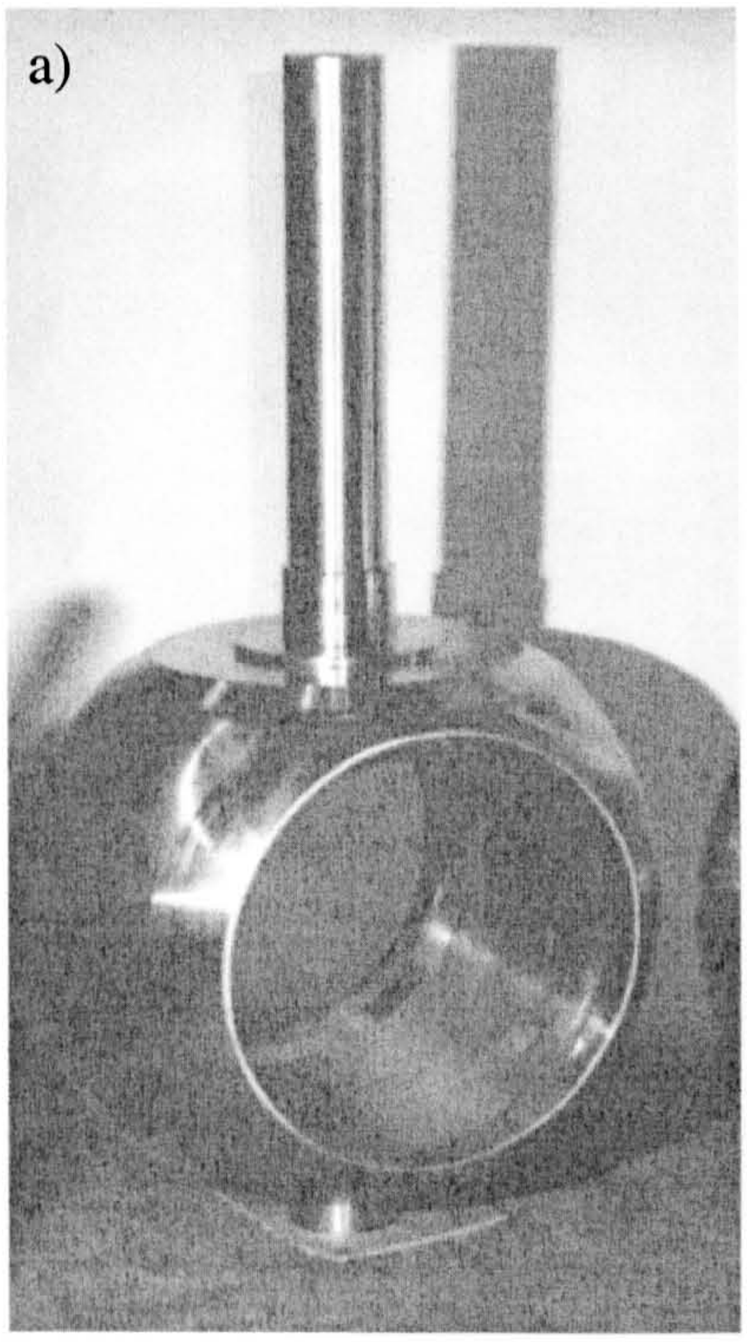
1998), electronic industry e.g. microwave integrated circuits (MIC), capacitors etc., paper and printing industry e.g. Corona rolls, Anilox rolls (Fig. 4.2.2.) etc. (Pawlowski, 1995; Groc et al., 1997, Irons et al., 1995).

High Velocity Oxy-Fuel (HVOF) coatings

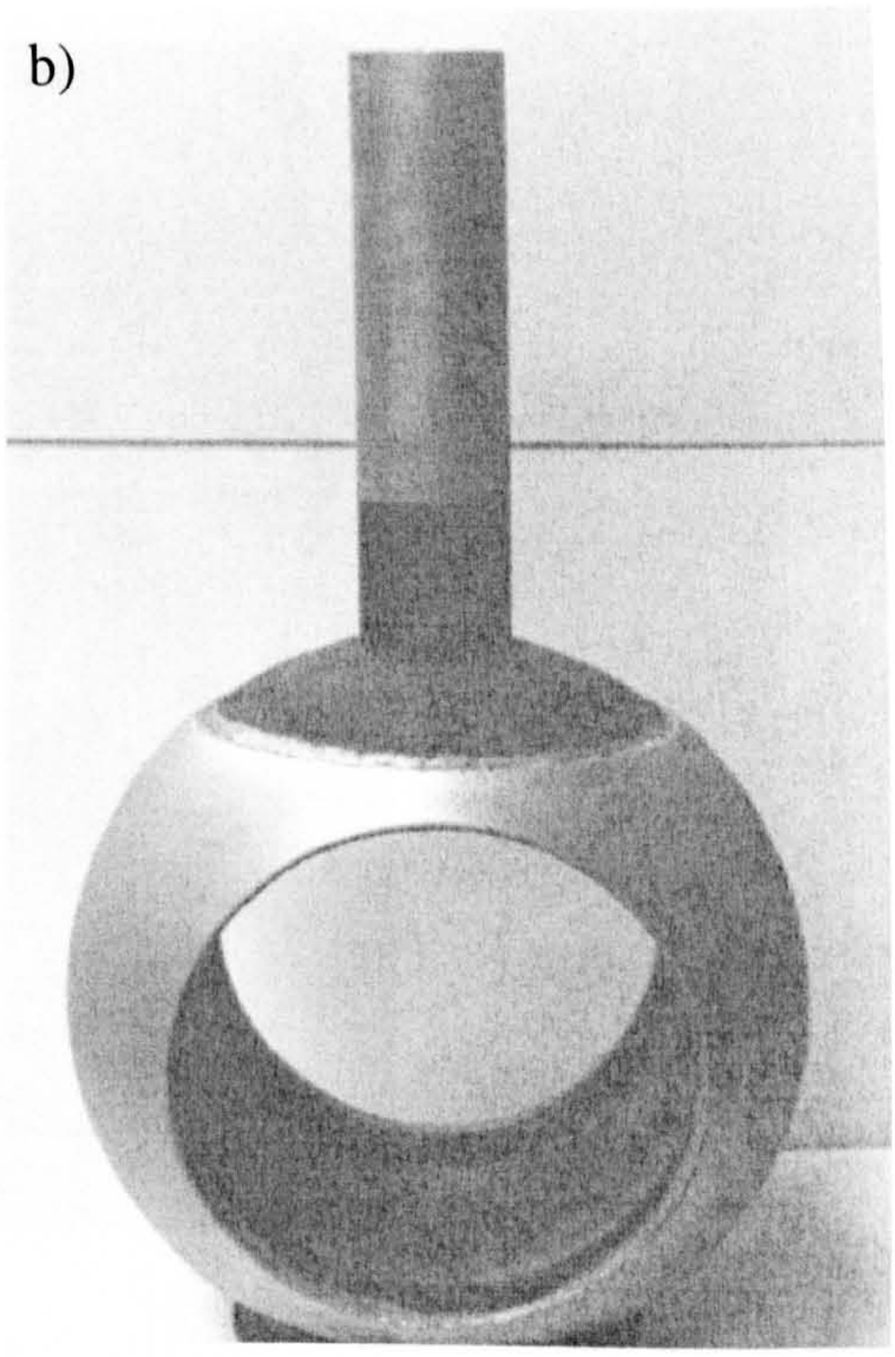
Ceramic-base materials represent attractive prospects for service in high-wear conditions and there has been extensive consideration of thermal-sprayed cermets as surface coatings on conventional metallic materials. Thermal spray application techniques have been the subject of steady development in particular the high-velocity oxy-fuel (HVOF) process (Siitonen et al., 1994; Kumar and Modi, 1995; Parker and Kutner, 1991) and has been in use in the industry since 1985 (Huchin, 1998). Cermet coatings applied by HVOF spraying have been developed primarily for wear resistant properties in dry (sliding) or pure tribological conditions (Bhagat et al., 1996) and for thermal barrier applications (Wigren et al., 1997) but their potential for service in aqueous erosive conditions has also recently received attention and study (Kembaiyan, and Keshavan, 1995; Bjordal et al., 1995a; Karimi et al, 1995; Rogne et al., 1996).

Several applications of the HVOF coatings include subsea pump internals, impeller wear rings, valve plugs and seats, slurry pump internals, extruder dies and tips, audio recording equipment, valve balls and seats, wire drawing equipment, butterfly valve discs, rock drill internals, etc. Moreover, manufacturing of thin walled hollow cylindrical objects from pre-shaped cores by HVOF spray using WC/Co, Nickel-chromium alloy and stainless steel has been reported (Helali and Hashmi, 1996). Some of the components sprayed by HVOF process are shown in Fig. 4.2.3.

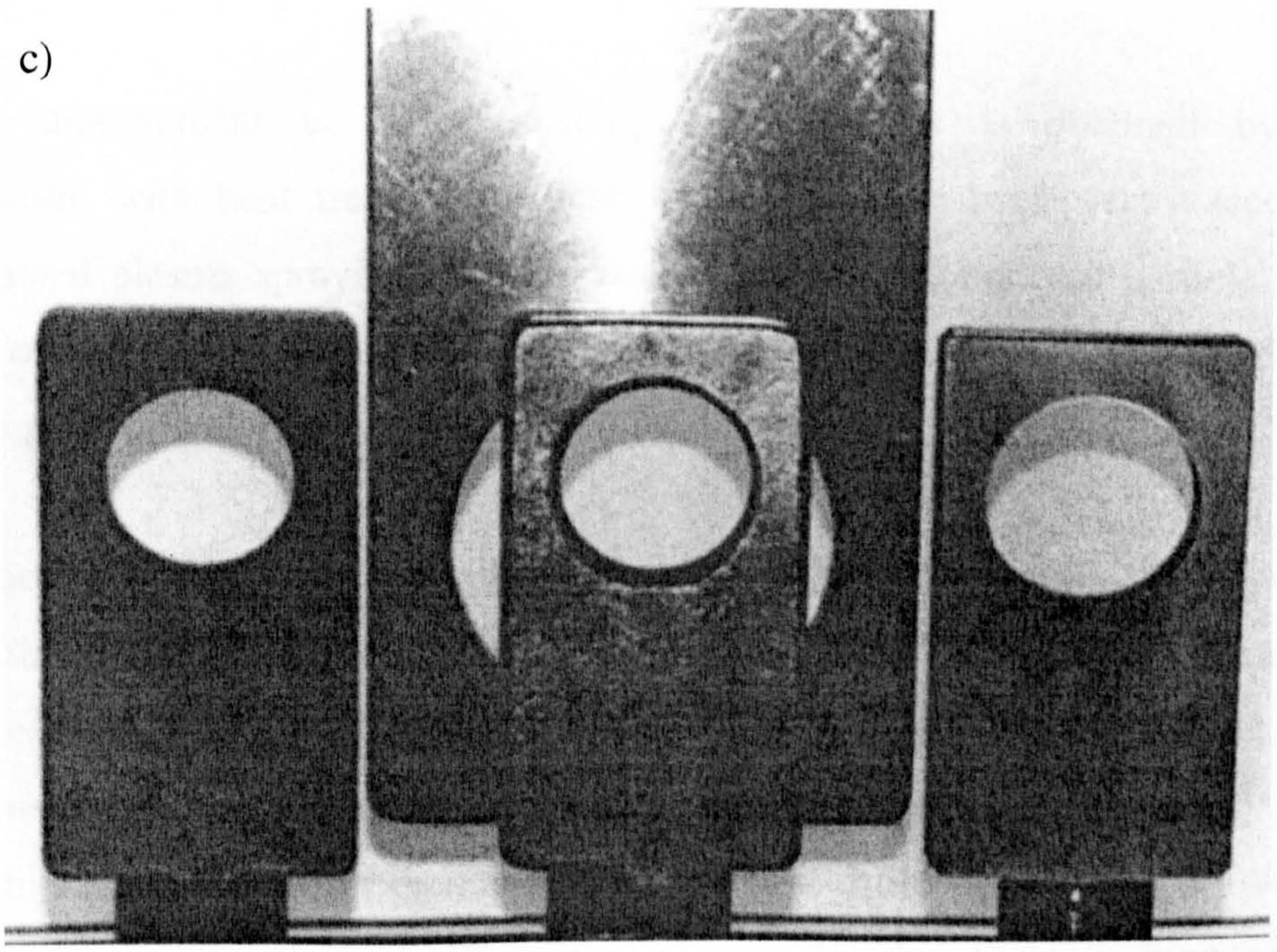
a)



b)



c)



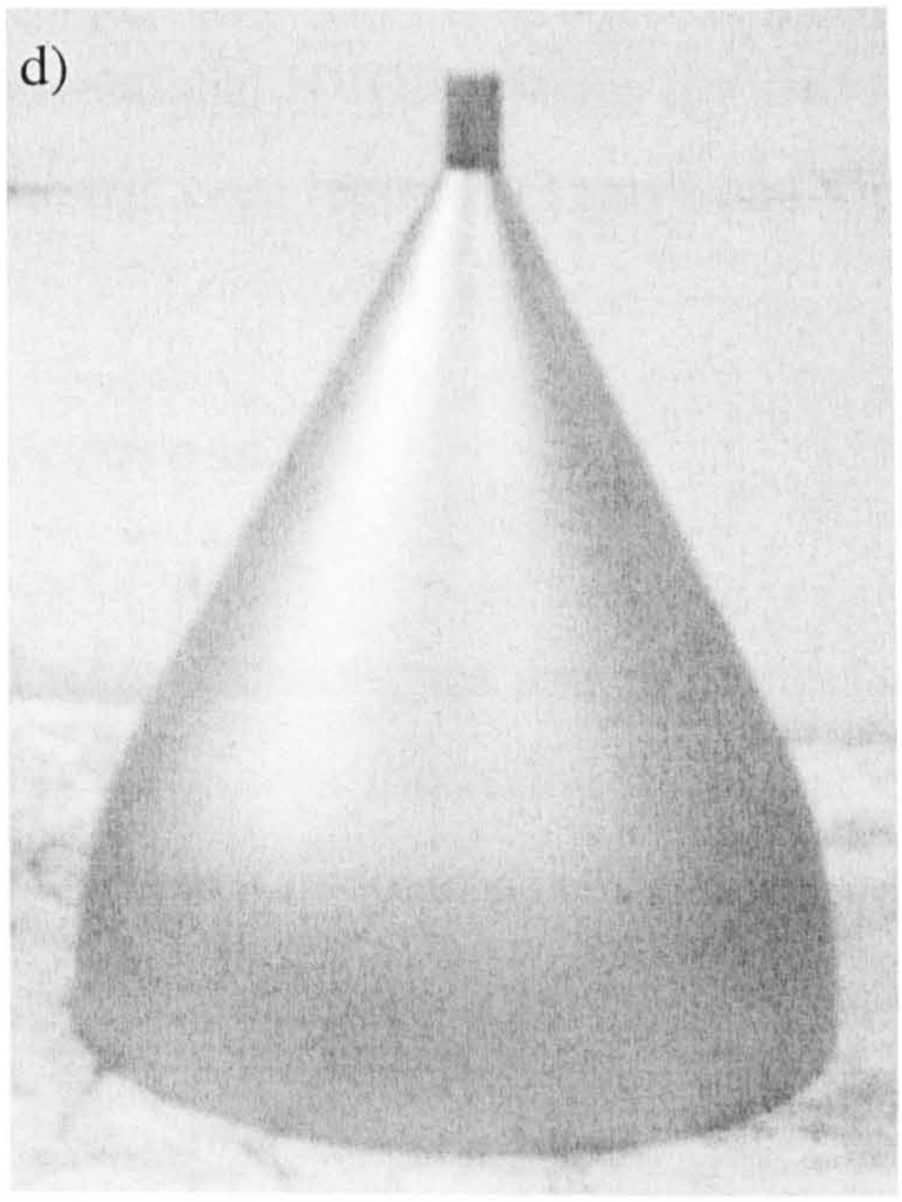


Figure 4.2.3 Valve balls, flow bore up to 300-400mm a) uncoated and b) coated in Co-based alloy, HRC 45; c) valve gates with flow bore up to 165mm coated in Ni-based alloy, HRC 50; d) valve needle for use in steam generation coated with Ni-based alloy containing WC, using a dual process of high pressure HVOF and subsequent vacuum furnace fusion (Courtesy of Pro-Vacuum Ltd.)

Further improvement in HVOF coating characteristics is obtained by surface modification with heat treatment. These treatments have been very successful for conventional plasma spraying coatings as they modify the sprayed particle structure, remove oxides formed during flight with air contamination and fill up pores formed in between grain boundaries by remelting the particle grain.

In addition to HVOF's better coating technology it is also successful in obtaining the desired thickness of the coating. The next advantage of HVOF powder coatings is due to their easiness in repair of damaged coatings. The TAFA Water Jet Coating Removal System uses supersonic jet of water, which completely removes thermal spray coatings. The jet hits the coating with such a great force that it causes the coating to fracture and spall, eliminating the coating without causing part damage. Water is pumped through specially designed laser drilled sapphire orifices at pressure up to 376MPa (Internet 1). Water jet has significant advantages over other coating removal procedures such as grit blasting, machining or grinding, chemical or molten baths.

Lower operating cost and higher spray rates are achieved by using higher oxygen flow rates and improved particle heating in the barrel. The spray cost of $6.45/kg using hydrogen-oxygen with conventional HVOF systems lowered to $0.5/kg using kerosene-oxygen for tungsten carbide has been reported (Thorpe and Thorpe, 1993).

4.3 HVOF technology, process

The principles of thermal spray technologies and in particular the High Velocity Oxy-Fuel (HVOF) thermal spray have been illustrated in section 4.1. Fig. 4.3.1 illustrates a closed system of integrated research in coatings technology.

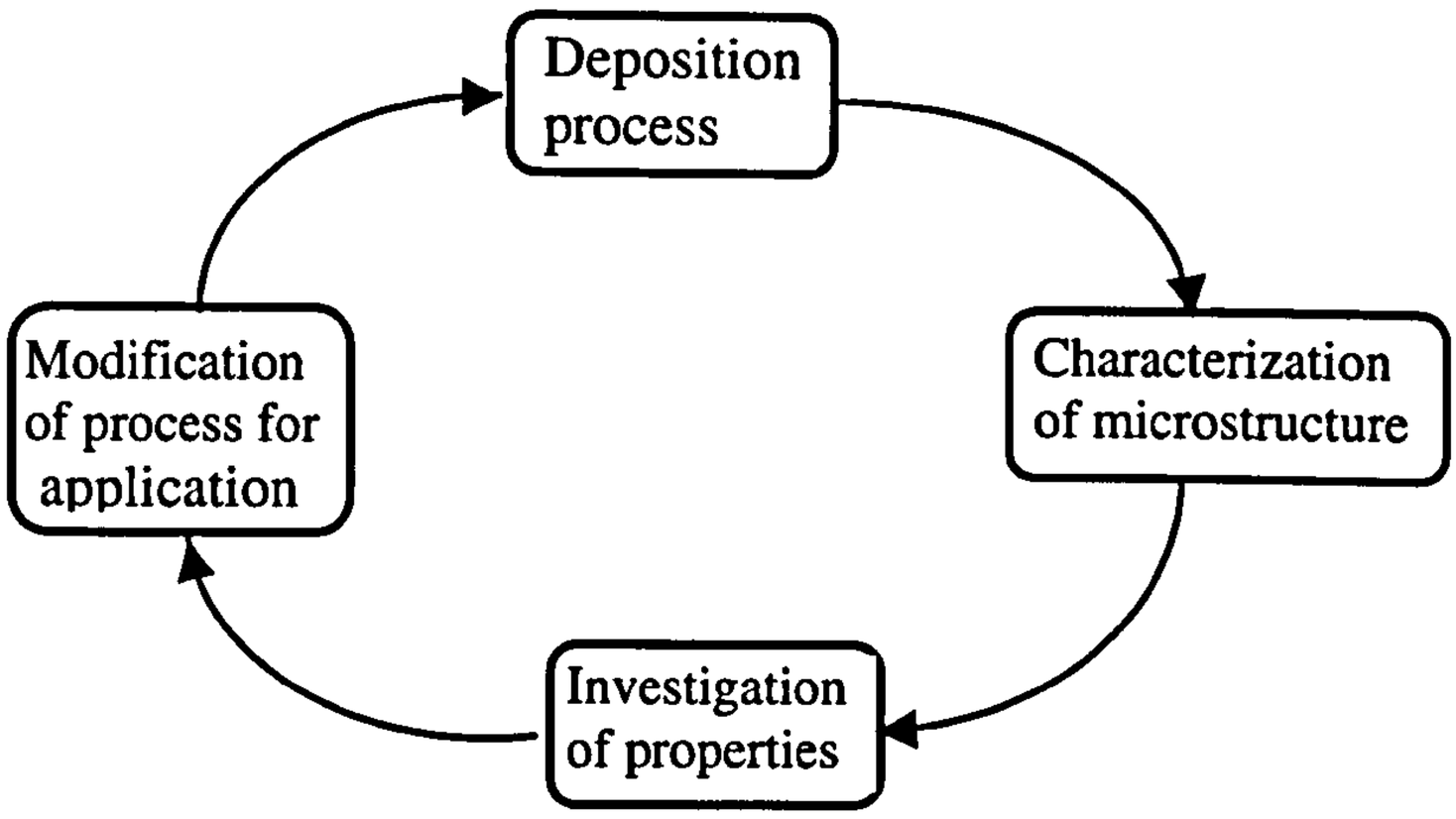


Figure 4.3.1 The closed loop of integrated research in Coating Technology (Jacobson and McGuire, 1983).

HVOF thermal spraying is the most significant development in the thermal spray industry since the development of the plasma spraying and is a rapidly evolving field (Parker and Kutner, 1991; McCartney, 1998), that interacts with a broad industrial community and has a wide range of practical applications. The diverse range of applications has already been illustrated in section 4.2. HVOF sprayed coatings are extremely complex in nature and their properties and microstructure depend upon numerous processing variables. Despite the inherent complexity, thermal spraying is widely used for the protection of conventional engineering materials which allows them to function under extreme conditions of aggressive wear, corrosion and high temperatures (McCartney, 1998). Different patented HVOF processes are Diamond Jet from Sulzer Metco (Rogne et al., 1998), JP-5000 from Hobart Tafa Technologies (Arsenault et al., 1997, 1998), Jet Kote from Browning Thermal Systems Inc. (Mohanty et al., 1996), Top Gun from UTP (Khan et al., 1997; Hearley et al., 1998), D-Gun from Union Carbide (Niemi et al., 1992; Vuoristo et al., 1994; Kembaiyan and Keshavan, 1995) and HV-2000 from Miller Thermal Inc. (Irving et al., 1993).

The HVOF process is entering into the next phase of development stemming from: additional competitive devices; more fundamental studies on the properties of the coatings and ways of improving them through gun design; new coating and process parameters such as fuel type, injection techniques and gun operating pressures. The evolution of HVOF spray guns is illustrated in Fig.4.3.2.

New HVOF systems such as JP-5000 high pressure HVOF can deliver spray rates four times higher than typical HVOF systems due to their exceptionally high chamber pressures over 0.8MPa against 0.1-0.4MPa in other HVOF systems and superior gas velocities exceeding 2,190ms^{-1} versus 1,460-1,800ms^{-1} in other systems (Internet 2). Thorpe and Thorpe (1993) have reported that Hobart/Tafa's JP-5000 high pressure HVOF system produces twice the gas velocity within the barrel of the spray gun compared with other HVOF systems.

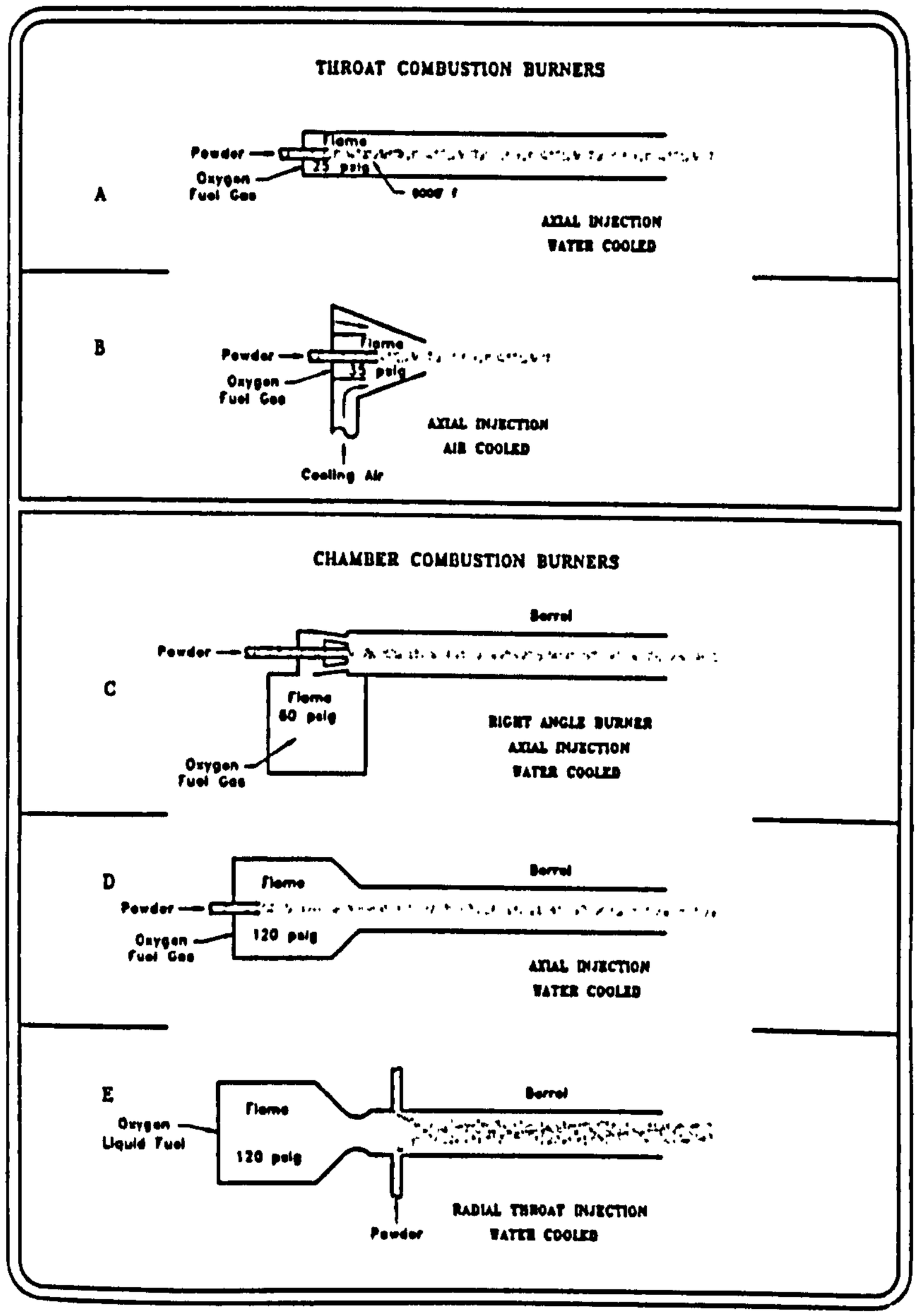


Figure 4.3.2 The evolution of HVOF spray guns (Thorpe and Richter, 1992).

The JP-5000 HP/HVOF gun consists of a new design with its radial powder injection system (Fig. 4.3.3). The powder is injected down stream of the combustion nozzle. Injection to this lower pressure area promotes better powder mixing, more even heating, less oxidising, more uniform and higher particle velocities. The design feature allows powder with a larger particle size to be used (Internet 2). Fuel and oxygen mix and atomise after passing through orifices into the combustion chamber, thereby creating stable, clean and uniform combustion. The combustion chamber pressure is monitored to assure the proper combustion mode and constant pressure.

JP-5000

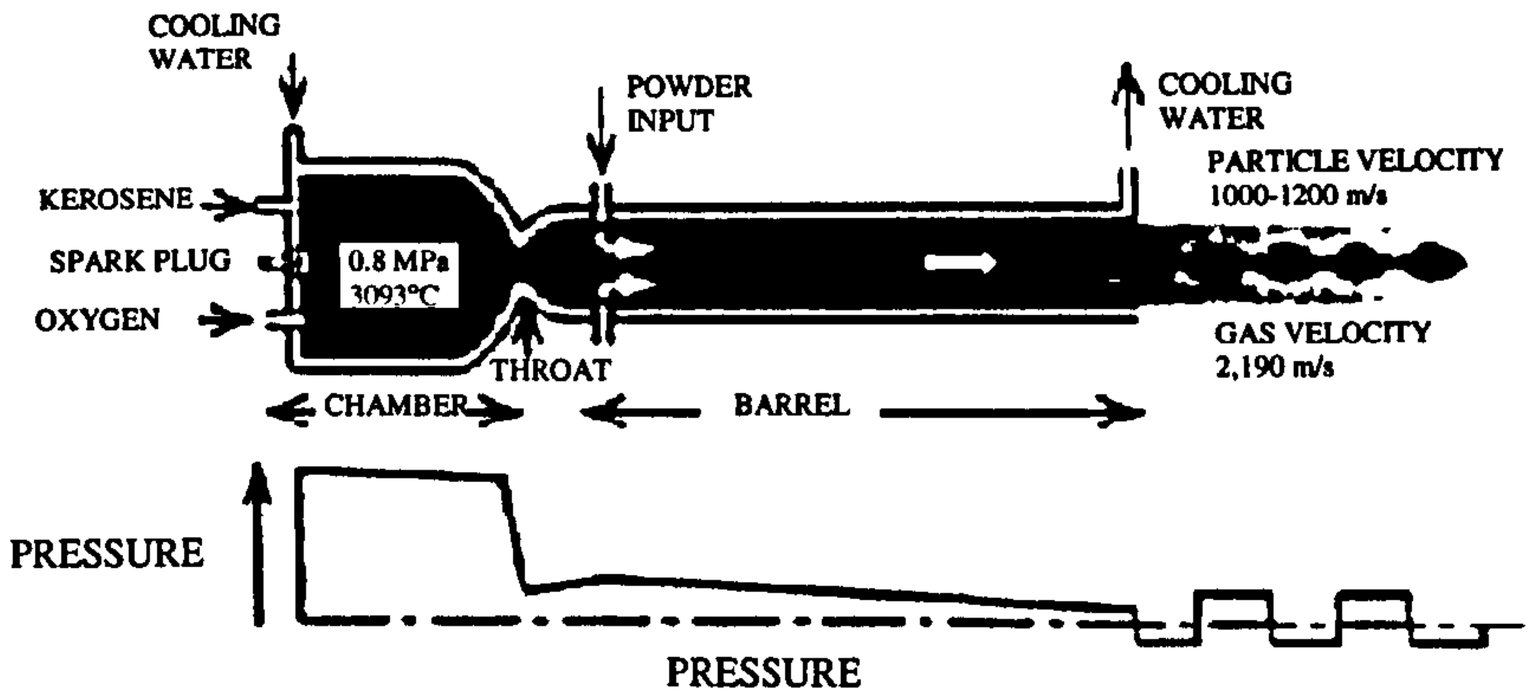


Figure 4.3.3 JP-5000 high pressure HVOF system.

The unique converging/diverging exit nozzle of the combustion chamber is sized and shaped to create a supersonic jet that maintains a low-pressure area where the powder is radially injected through multiple ports. Unique compressive stresses in this new spray system allow coating thickness 10 times those of other spray systems (Thorpe and Thorpe, 1993) exceeding 12.7mm (Internet2).

Recent developments in thermal spray processes have brought significant technological advancement. The major differences between current commercial systems include the use of water or air cooling, axial or radial powder injection, fuel flows, combustion chamber pressure and configuration, nozzle design and length. Operational differences comprise combustion pressure, gas types and flow rates and nozzle length which will eventually determine particle dwell/heating time, flame/particle temperatures, particle velocities and acceleration attained (Irving et al., 1993).

HVOF Spray Processing

HVOF spray comprises 4 basic stages as shown in Fig. 4.3.4.

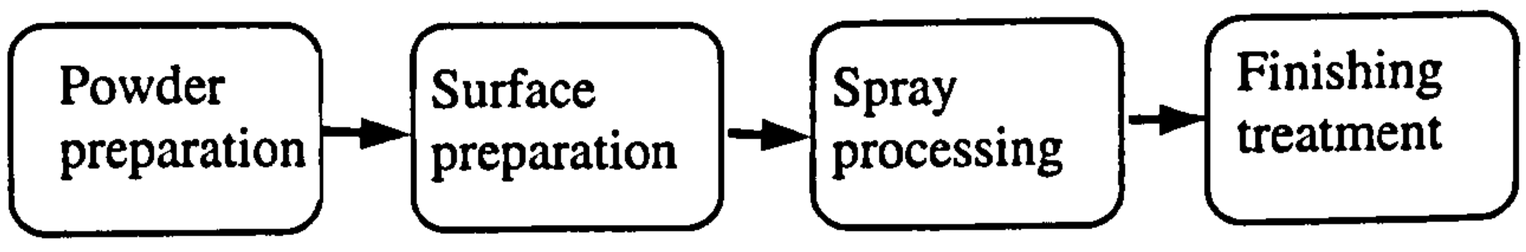


Figure 4.3.4 Principal stages in HVOF spray processing

1. Powder preparation

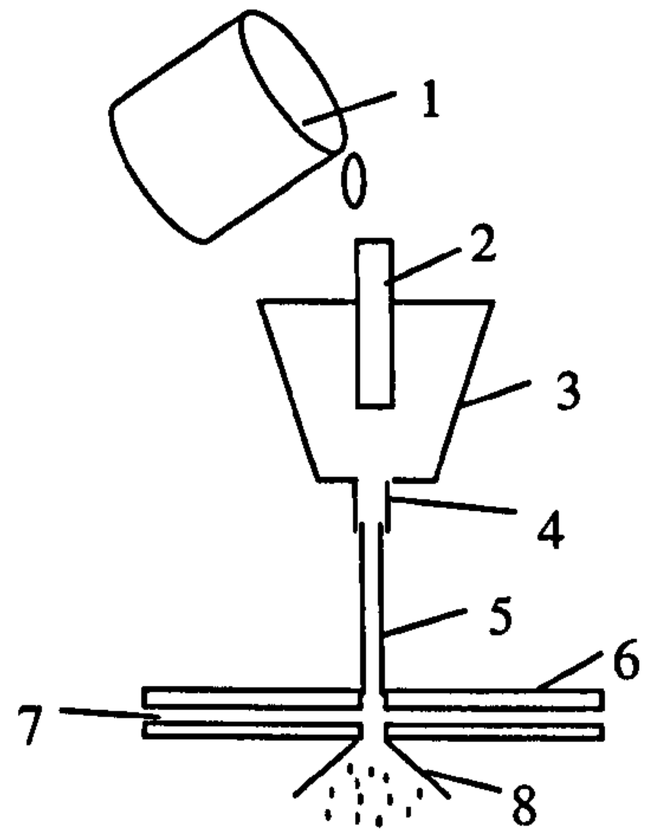


Figure 4.3.5 A schematic diagram of the atomisation process.

The powders of metals and alloys are usually prepared by atomisation methods or sometimes sintering. Carbide and oxide ceramics are generally manufactured by fusing followed by crushing. More about the various powder production methods can be found elsewhere (Pawlowski, 1995).

A common atomisation process (Fig. 4.3.5) consists of melting the alloy in a heater (1), the melt is poured into the previously heated funnel (3) through a calibrated outlet (4) and exits as a liquid jet (5) on the nozzle (6) and finally through the atomising medium (7). The alloy particles (8) solidify during the free fall and finally reach the powder collector. The most important powder parameters for spraying are grain size, chemical and phase composition, shape, and internal porosity.

2. Surface preparation

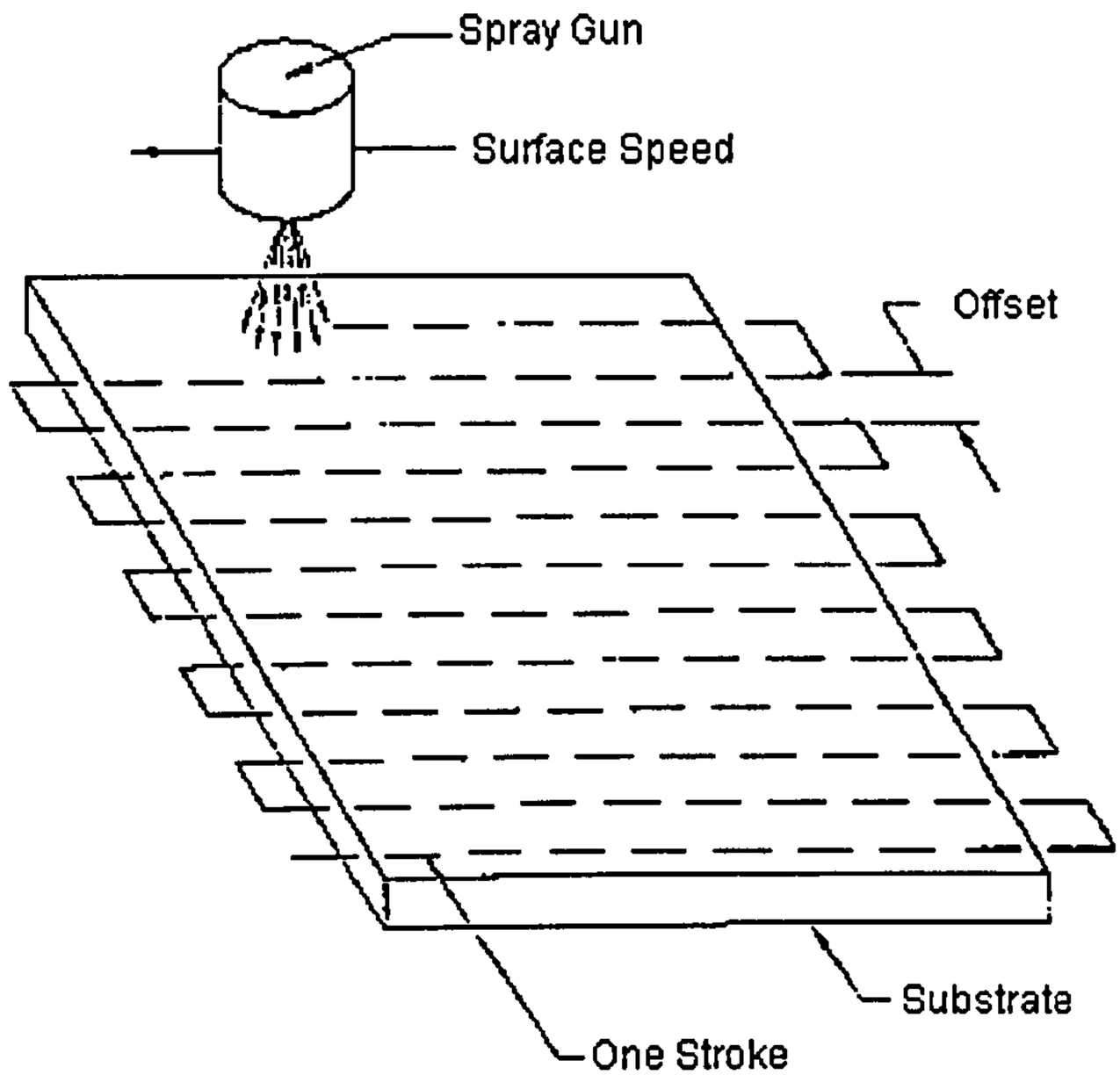
Adequate preparation of the surfaces to be sprayed is crucial for all thermal spray techniques. Degreasing using common organic solvents, shaping the object to be coated to required dimensions, surface roughening are typical operations before spraying. Grit blasting is considered as the standard technique of surface roughening. Commonly used grits are metal grits, silica grits, alumina or silicon carbide. The grit blasting leads to the generation of compressive stresses at the roughened surface. Due to this reason finer grit

and low blasting pressure is recommended. Different grit sizes can be used to roughen the surface according to the required thickness and adhesion. Grit blasting installations are often automated, especially if used for long series of products.

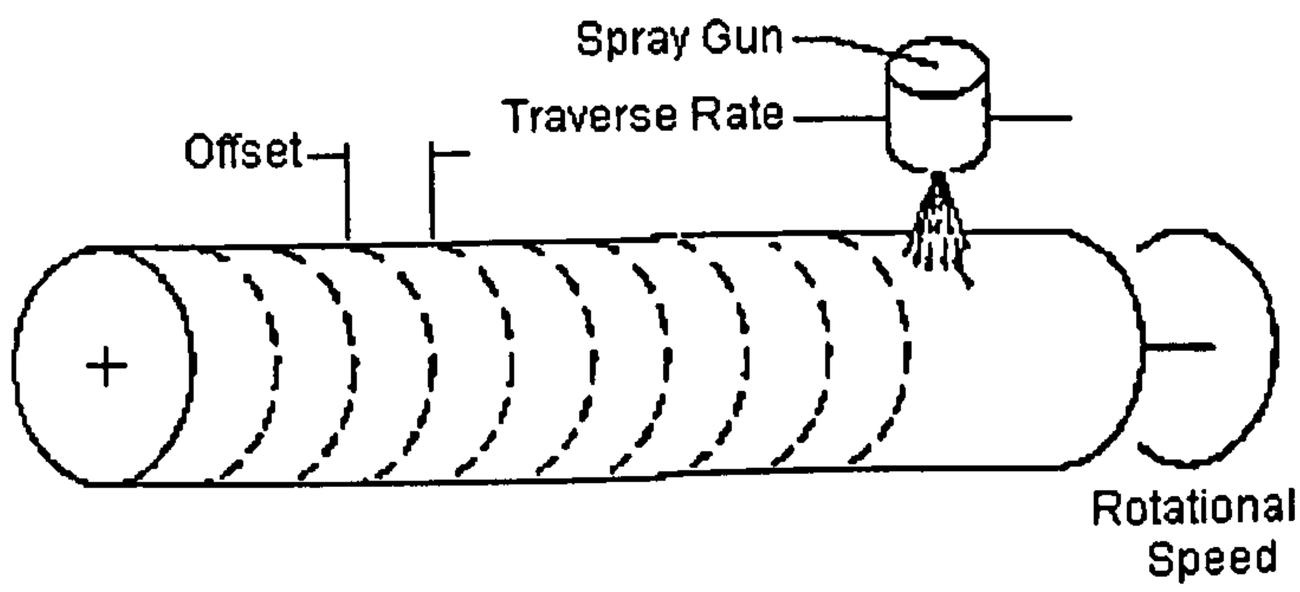
3. Spray process

HVOF guns consist essentially of an internal combustion chamber into which a gaseous or liquid fuel and oxygen or air are injected at 0.5-3.5MPa pressures and high flow rates, up to 0.016m^3s^{-1} (Irving et al., 1993).

a)



b)



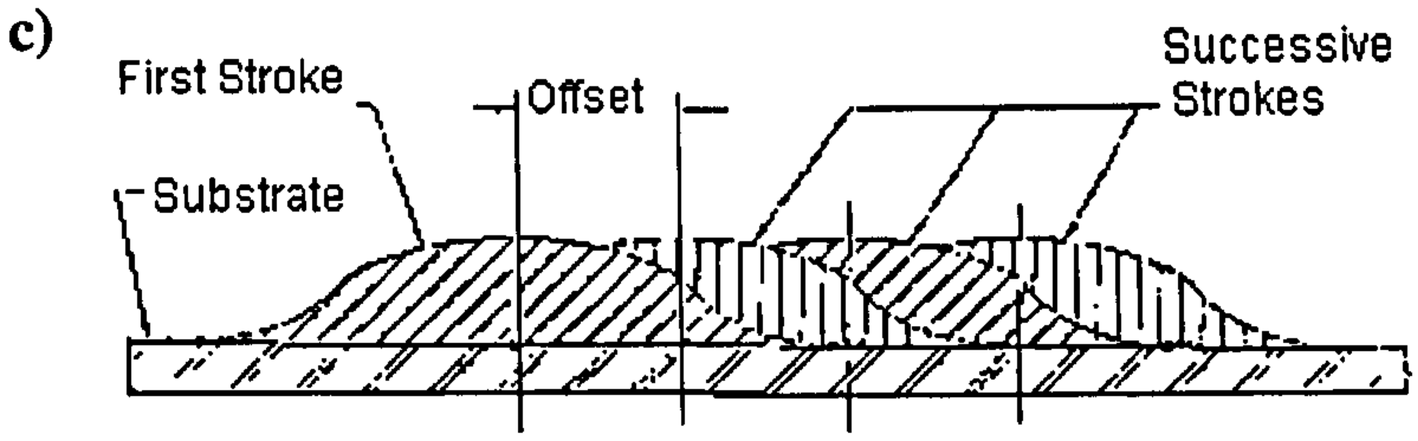


Figure 4.3.6 Schematic diagrams of automated HVOF spray a) on static component, b) on cylindrical component and c) formation of lamellar splats.

The mixture is ignited and continuously combusted, the resulting flame being allowed to accelerate supersonically and exit to atmosphere through a nozzle similar to that of a rocket motor with presence of characteristic "shock diamonds" in the flame (Fig. 4.1.6). Powder is injected into the combustion chamber and the particles in molten or nearly molten state are bombarded on to the pre-prepared substrate (workpiece). The particles with high kinetic energy are flattened in layers (lamellar splats) to form an integral coating Fig. 4.3.6c.

Modern HVOF spray techniques are generally automated. A single layer is applied on a flat work piece as shown in Fig. 4.3.6a. or as in Fig. 4.3.6b if the component is cylindrical by a series of gun traverses (strokes) back and forth, each with a certain offset from the previous stroke, until the entire surface is covered. The process is repeated until the desired coating thickness is achieved.

The HVOF spray technique has emerged as the most versatile technique and has proved superiority over many other thermal spray techniques with respect to better bond strength, lower porosity, less oxide content, higher hardness value, better wear resistant properties and cost effectiveness. HVOF offers fewer restrictions to the size and weight of components that can be coated. The cost of the capital of a HVOF equipment has been reported to be six times less than that of a comparable vacuum plasma spray system (McIntyre, 1996). Moreover, HVOF systems are convenient for repair and on site spraying and are more user friendly. Table 4.3.1 shows comparative process parameters of HVOF system with other thermal spray systems and the benefits of HVOF process are illustrated in Table 4.3.2.

Attribute	Flame Spray	HVOF	D-Gun	Wire Arc	Air Plasma
Jet temp. K	3500	5500	5500	< 6100*	15000
Jet velocity, m/s	50-100	500-1200	> 1000	50-100	300-1000
Gas flow, Slm	100-200	400-1100	N/A	500-3000	100-200
Gas types	O_2, C_2H_2	CH_4,C_2H_2, H_2, C_3H_6, O_2	O_2, C_2H_2	Air, N_2, Ar	N_2, Ar, H_2, He
Power input, kW	20	150-300	N/A	2.5	40-200
Particle temp. °C	2500	3300	N/A	> 3800	> 3800
Particle velocity, m/s	50-100	200-1000	N/A	50-100	200-800
Material feed rate, g/min	30-50	15-50	N/A	150-2000	50-150
Coating density, %	85-90	> 95	> 95	80-95	90-95
Bond strength, MPa	30-60	> 150	> 170	60-85	> 150
Oxides	high	moderate, dispersed	small	high	moderate, coarse

Table 4.3.1 Comparison of HVOF with other thermal spray processes (Kumar and Modi, 1995), the original value* quoted was 25000K. Value* corrected from Pawlowski, 1995.

Coating benefits	Main causes
Higher density (lower porosity)	Higher impact energy
Improved corrosion barrier	Less through porosity
Higher hardness	Better bond, Less degradation
Better wear resistance	Harder, tougher coating
Higher bond and cohesive strengths	Improved particle bonding
Lower oxide content	Less in-flight exposure time
Fewer unmelted particle content	Better particle heating
Greater chemistry	Reduced time at temperature
Thicker coating	Less residual stresses
Smoother as sprayed surfaces	Higher impact energy

Table 4.3.2 Benefits of HVOF process (Thorpe and Richter, 1992).

HVOF spray processes are separated into four major designs (Kumar and Modi, 1995): (i) internal combustion type with the hot gases directed into the chamber where a mixture of carrier gas and powder particles are heated, (ii) simultaneous injection of

powder into a combustion chamber where the mixture continuously burns and heats the particles, (iii) confined combustion into which a stream of powder with carrier gas is injected, (iv) high pressure liquid systems with radial injection of powders downstream of the combustor exit. Much about the dynamic processes (combustion, fluid and particle dynamics and heat and mass transfer) of HVOF spray techniques for Cr_3C_2-NiCr powder particles can be found elsewhere (Sobolev et al., 1995).

Hackett et al. (1993) studied the gas dynamics behaviour of HVOF thermal spray process using optical flow visualisation techniques (Fig. 4.3.7) and concluded that the rapid turbulent mixing of the hot supersonic jet with the surrounding atmosphere (which concerns coating quality due to contamination) appears to be merely a function of the density ratio between the hot jet and the cold atmosphere, rather than depending upon such parameters as combustion chamber pressure or barrel length. He found that the jet dissipates rapidly and no longer remains supersonic when it impinges upon the target surface. Other issues also observed in this study include strong jet noise radiation from the HVOF plume and the entrainment and induced bulk motion of the surrounding atmosphere, which much concerns on gas dynamics of HVOF spray process.

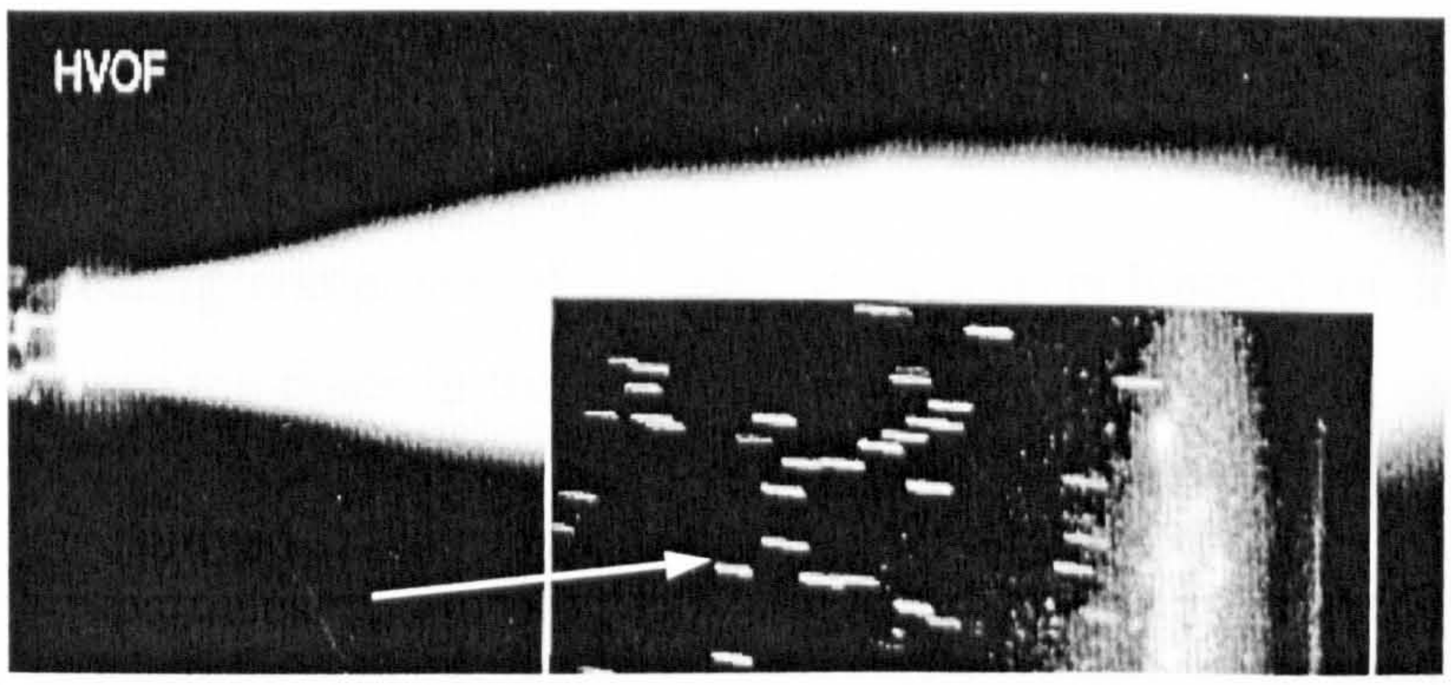


Figure 4.3.7 LaserStrobe ™ used for flow visualisation in HVOF spraying process.

HVOF parameters

HVOF parameters play crucial role in improving coating quality. The various processing parameters are:

- Chamber size (mm)
- Stand off distance (mm)
- Traverse rate (ms^{-1})
- Total gas flow ($lmin^{-1}$)
- Oxygen/fuel gas ratio
- Powder feed rate ($gmin^{-1}$)
- Carrier gas flow ($lmin^{-1}$)

Finishing Treatment

In most practical applications sprayed coatings have to be ground and polished to get the required surface roughness. Grinding is used to achieve the desired dimension and polishing to get the required roughness. Surface treatment also improves the aesthetic view of the material coated. Other post spray finishing techniques include polymer impregnation with organic polymers sealing (Lugscheider et al., 1993); heat treatment by a flame torch or in a furnace (Bell, 1984); and by laser melting (Potzl, 1994; Sridhar et al., 1998).

Polymer sealing process:

The process of sealing comprises of a sealer (basically polymers) of low viscosity, which penetrates into the pores in the sprayed metal by capillary action and seals them off, without necessarily adding to the total thickness of the coating (Internet 3; Lugscheider et al., 1993). The sealer is generally low viscous (3 poise or less to facilitate good penetration into the pores), low water absorbent, and electrochemically compatible with sprayed material. Some other features of sealing are smooth surface texture, possibility of pigmenting to provide colour for decorative effect. For high corrosion protection of thermal sprayed coatings, it is recommended to seal after final mechanical treatment such as grinding (Wielage et al., 1998). Tobe (1998) reported that in the case of HVOF coatings the sealant might not be very effective due to their very little porosity and that the choice of sealant is rather difficult. Neville and Hodgkiess (1996) demonstrated similar case, where the influence of a polymer-sealing post

treatment on HVOF sprayed WC-Co-Cr and WC-NiCrSiB coatings has been found to be minor.

Heat treatment:

Heat treatments have proved to be very successful in obtaining better coating quality with improved corrosion and wear resistance. After the treatments the coating microstructure changes with change in particle structure, phase transformation and its matrix. Moreover, such treatments help to remove oxide contents formed during flight with air contamination. The post surface heat treatment techniques such as torch or furnace fusing should eliminate interparticle boundaries and increase the overall density of the overlay as the powder particles coalesce. Self-fluxing alloys are generally common for this purpose. The inbuilt fluxing potential permits the alloy to be fused to a dense, coherent coating which is metallurgically bonded to the substrate metal, by heating to a temperature between the solidus and liquidus, usually between 1050 and 1150°C, depending upon the material (Bell, 1984). One of the major problems with fused coatings is that as the alloy liquates, there is a tendency for the liquid to "run" or "sag". This can be a problem if the coatings are heavy (greater than 1.3mm) or the components being fused have complex shapes (Moskowitz, 1997). Attempts to torch fuse very thin coatings fail, as too much oxide is produced at the interface and the hot gas impingement produces excessive oxidation of the powder particles leading to a non-continuous coating. In case of furnace fusion, uniform temperature in a non-oxidising environment ensures the highest quality in the coating with minimum distortion of the component. The absence of any oxidising element in the furnace atmosphere offers the possibility of fusing very thin coatings, 0.05-0.2mm, to dense, coherent films. This advantage has been used widely for the repair of gas turbine components (Bell, 1984). Post heat treatments of plasma sprayed NiCrAlY coatings under vacuum condition have resulted in lowered residual stresses and increased adhesion (Richard et al., 1996). Also Lugscheider and Jokiel (1993) have reported that vacuum furnace fusion of NiCrBSi-alloy has resulted in increased wear resistance than the same alloy after flame fusion. Bond strengths of various thermal spray techniques are shown in Fig. 4.3.8.

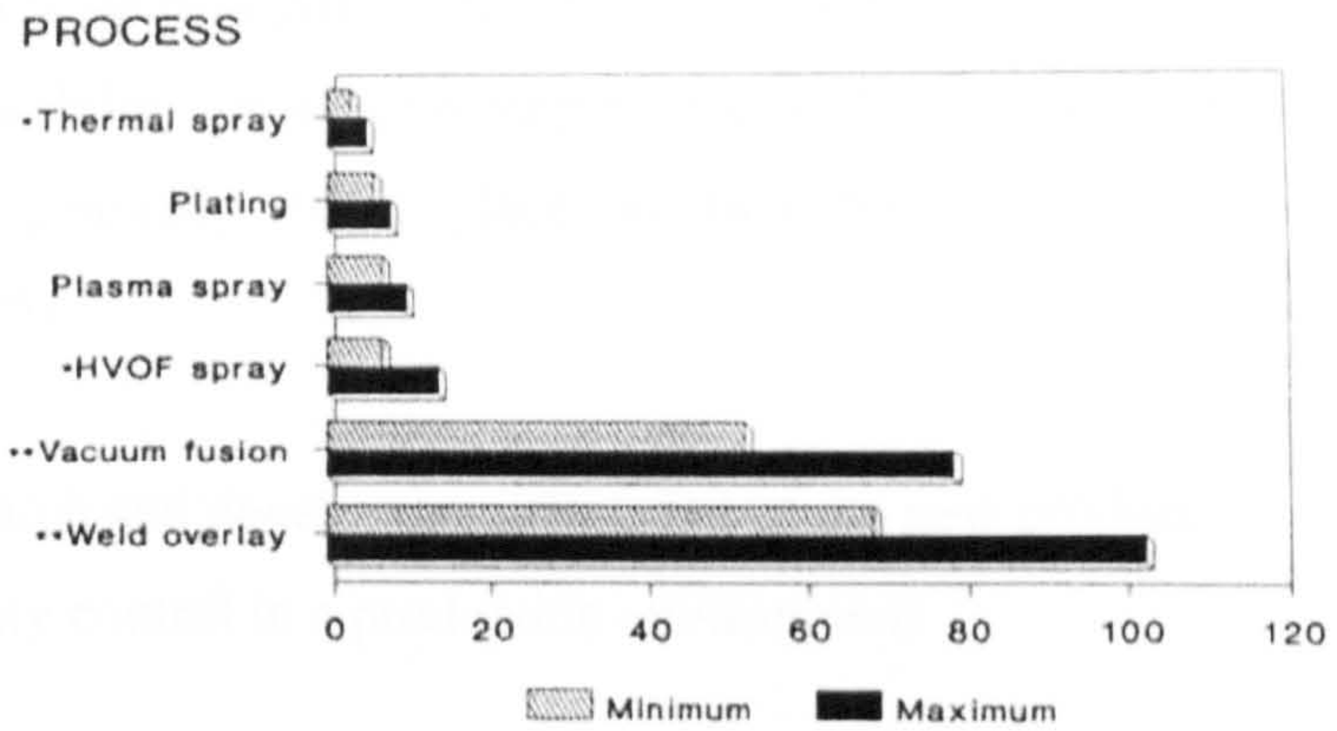


Figure 4.3.8 Bond strengths of various thermal spray techniques (Pro-Vacuum Ltd.), figures in thousand psi (1 MPa ~ 145 psi)

4.4 Coatings property, morphology

The performance of thermal spray coatings (TSCs) including HVOF sprayed coating is dependent on several characteristics such as coating thickness, surface finish (roughness), microstructure and hardness, service conditions etc. Premature failure of the coatings can occur due to interactions between service conditions (such as abrasion, thermal cycling, corrosion, the environment) and coating defects. Defects that result in coating failure (Shah et al., 1994) include: 1) disbonds at the coating/substrate interface and inter-splat boundaries; 2) the occurrence of pores within the coating; 3) formation of oxides within the coating; 4) residual stress build-up. Figure 4.4.1 shows metallurgical characteristics of a thermal spray coating. A schematic representation of the coating formation by thermal spraying is shown in Fig. 4.4.1.

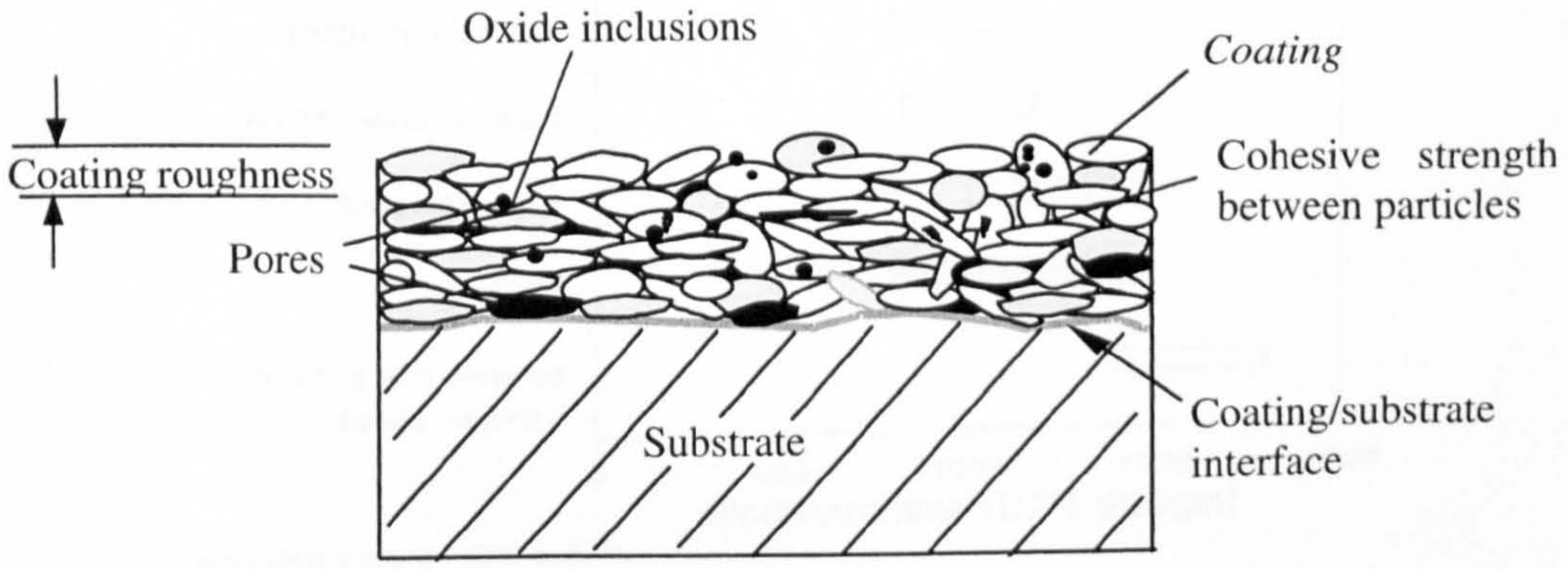


Figure 4.4.1. A schematic diagram illustrating material characteristics of a thermal spray coating.

Powder parameters such as grain size, chemical and phase composition, shape, internal porosity and flowability are of great importance for the coating properties. The coating characterisation generally takes place in two stages in the coating production (Pawlowski, 1995):

- Research and development (R & D) of the new product
- Quality control in a production environment

The properties of the coating determine its behaviour during service. Generally coatings are characterised by their physical and chemical properties. The mechanical properties such as micro-hardness, tensile strength, fracture strength, toughness, wear resistance, elastic moduli are of significant importance. Thermo-physical properties such as thermal conductivity, diffusivity are often important such as in application of zirconium oxide for the thermal barrier coatings (TBC). The electric and magnetic properties are of great importance in applications for electric and electronic industries. Chemical property such as corrosion resistance is of significant importance.

Microstructural characterisation includes chemical composition, grain morphology and orientation, defects such as density and porosity, heterogeneity, micro-defects such as dislocations etc. Micro-hardness of WC-Co coating obtained by different spray techniques is illustrated in Fig. 4.4.2.

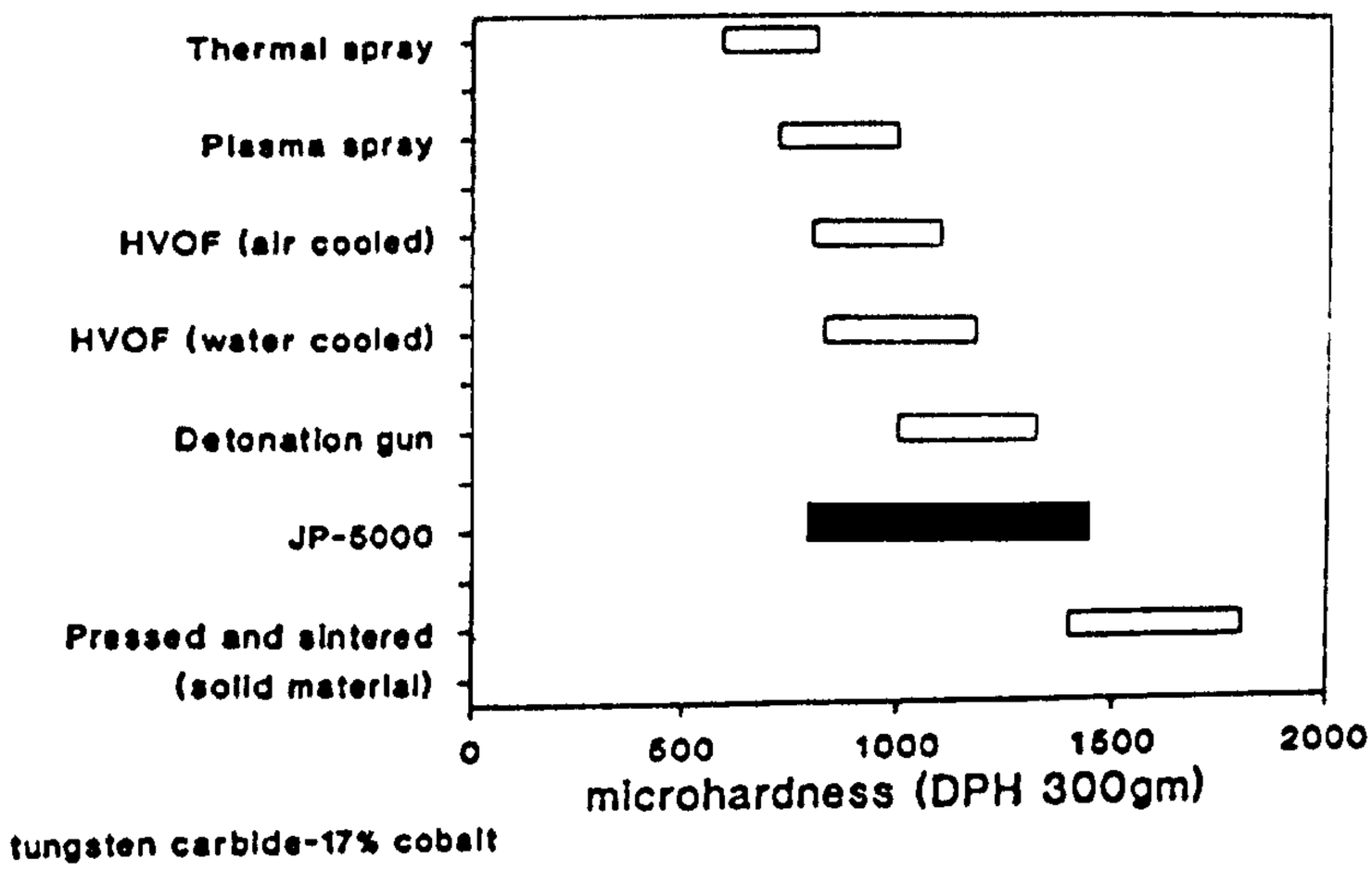


Figure 4.4.2 Microhardness of various thermal spray systems

Density and porosity

Porosity is one characteristic feature and structural index of thermal sprayed coatings and is inevitable despite of the advanced thermal spray techniques. The degree of porosity depends on the spraying method used, the coating material and the spraying conditions (Siitonen et al., 1992). The amount of porosity in the coating is one of the mostly used criteria for evaluation of the coating quality. The density of the sprayed coating is lower than the theoretical density of the same but compact material.

The micro-porosity of the coatings is associated with the liberation of dissolved gases such as oxygen, nitrogen and hydrogen due to their reduced solubility during temperature decrease. The dissolved gases can either escape into free atmosphere (open porosity) or into the micro-voids (enclosed porosity) distributed along inter particles boundaries. Formation of different types of pores possible in a thermal sprayed coating is shown schematically in Fig. 4.4.3.

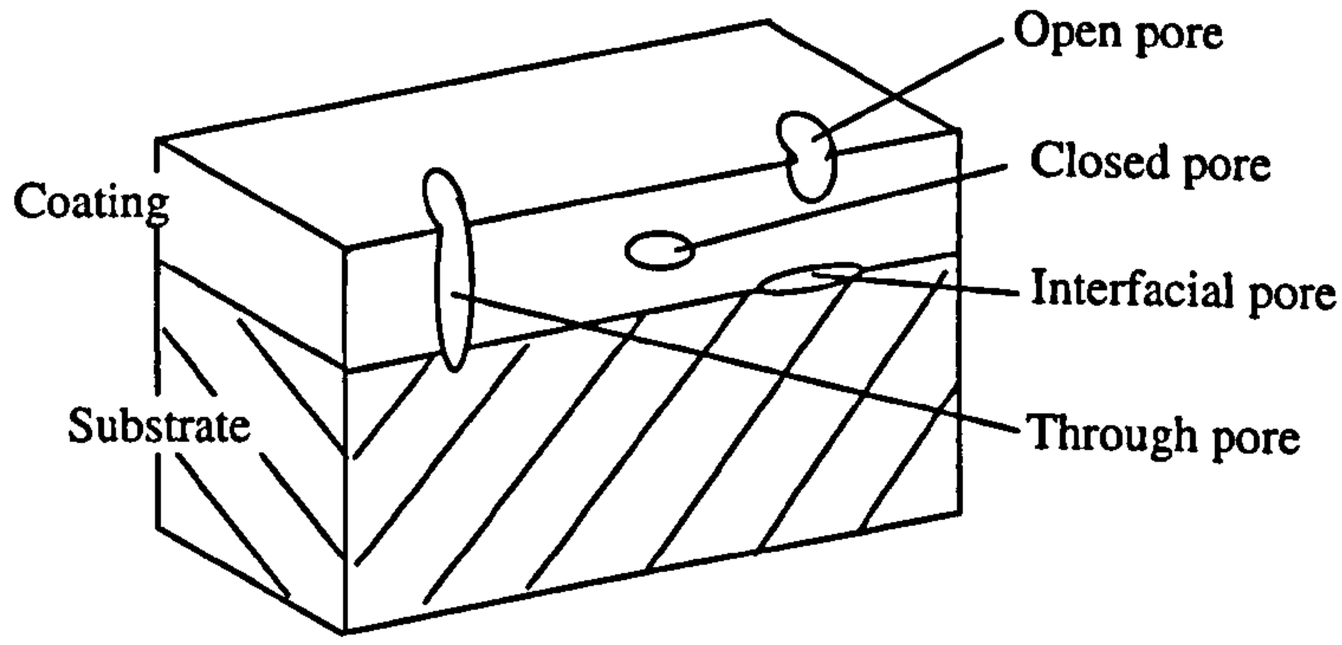


Figure 4.4.3 A schematic representation of various types of pores in a thermal sprayed coating.

CHAPTER 5. CORROSION AND EROSION-CORROSION OF HVOF SPRAYED CERMET COATINGS

Introduction

This chapter contains a general literature review on the durability of several thermal sprayed coatings (TSCs) and in particular focuses on HVOF sprayed cermet coatings. Thermal sprayed cermet coatings of major interest to industry as wear resistant coatings are WC-M based (where, M can be Co, Ni, CoCr, NiCr or NiCrSiB) and NiCrSiBC self-fluxing types. For application of relevance to this project, there is a general dearth of information on the erosion-corrosion resistance of these coatings. This is especially so in respect of the NiCrSiBC type with, in fact, more attention having been devoted to the durability of the WC-M coatings. Consequently, this literature review of erosion-corrosion of thermal sprayed cermets will contain a major proportion devoted to WC-M based cermets but will also comprise some references, where appropriate, to HVOF sprayed metallic coatings. The discussion of durability of the WC-M cermets in aqueous condition should throw some light on factors that are likely to be relevant to NiCrSiBC type. The pure corrosion resistance of coatings in various working environments and in particular seawater will be discussed in section 5.1. In section 5.2 the erosion-corrosion behaviour of these materials both in single-phase (liquid) and in two-phase (solid-liquid) systems will be discussed. The much higher rates of material loss of conventional metals in solid/liquid conditions will be illustrated and the increasing demand of more wear resistant coatings and the need for their development as a replacement will be discussed. Section 5.3 will contain a summary and rationalisation for the experimental program involved in this research.

5.1 Corrosion

Thermal sprayed cermet coatings have been primarily developed for wear resistance and not much is known about their corrosion properties. The corrosion characteristics of a cermet coating and the substrate, as well as the inherent general and localised corrosion resistance of each phase can play an important role (Ashary and Tucker, 1991). In the past, the application of thermal sprayed coatings for corrosion protection has been

limited due to their inherent heterogeneous nature and porosity (Costa et al. 1996). The basic three drawbacks of the thermal sprayed coatings are: i) oxide content generated during spraying causing low passivity, ii) porosity and interparticle boundaries possibly allowing the corrosive fluid to penetrate to the substrate, iii) degradation during spraying of coating material due to partial oxidation of elements such as chromium resulting in change of chemical composition of the coating material (Tobe, 1998). Also, thermal sprayed coatings applied to protect cheap base metals may suffer from bimetallic corrosion at the metal/substrate interface, thus undermining the coating. The corrosion property also depends upon grain size and chemical homogeneity. Reduced chemical homogeneity may also result in an increase in galvanic action between various phases.

Development in modern HVOF technique has overcome many of the above problems such as oxidation and interparticle boundaries due its very high kinetic energy and less particle flight time, thus resulting in dense coating with very less porosity. Proper selection of a coating and a coating/substrate combination for a given environment and designing the component as a single integrated system, progress in powder manufacture, process parameters are very important factors that will concern coating quality. This also implies that the overall durability of the components largely depends upon the inherent corrosion resistance of the coating material itself.

Normand et al. (1998) showed that the corrosion behaviour of the coating strongly depends on its microstructure. Interconnecting porosity acting as a passageway to the substrate promotes generally severe galvanic corrosion. Moreover, if the coating material does not possess a passive film, then the porosity might induce localized corrosion. Experiments were carried out on a HVOF sprayed Inconel 690 with varied spray parameters in order to obtain an evolution in the coating morphology. They found that a coating free of unmelted particles exhibits a notably reduced passive current density while the localized corrosion resistance is dependent on the amount of interlamellar oxide.

Dorfman et al. (1993) found that corrosion resistance of 316 (Bal. Fe, 11Ni, 17Cr, 2.4Mo, 0.03C, 2.5 others) stainless steel coating applied onto low carbon steel substrate is inferior to wrought type due to heterogeneous microstructure of the coating compared

to a wrought type where formation of an adherent passive film contributes to its higher corrosion resistance. The corrosion current densities (by the Tafel extrapolation method from the cathodic and anodic polarisation curves intersections) in 0.1M hydrochloric acid measured 163μA/cm^2 versus 9μA/cm^2 for a HVOF sprayed coating compared to a similar type 316-wrought alloy signalling that the former is inferior to the latter. However, they found that HVOF sprayed coating showed better performance compared to other spray processes such as traditional combustion and plasma spray. This shows that the coating performance is much dependent on spray processes. They also remarked that the improvements can be achieved by incorporating deoxidizers into thermal spray powders which will eventually minimize oxidation at interparticle boundaries as these boundaries are active sites for galvanic attack.

Dearnley et al. (1996) carried out an investigation to determine the aqueous corrosion response of a commercial Ni-Fe-Cr-B-Si-C coating thermally sprayed (process not specified) and then oxyacetylene torch fused on to a 317 LMN austenitic stainless steel substrate. The findings showed that preferential corrosion of the coating/substrate interface resulted in coating delamination. Moreover, the corrosion rate of the coating in 0.5M H_2SO_4 + 3 wt%NaCl solution was 15-40 times higher than the uncoated substrate and this was attributed due to hard precipitates (probably Cr_7C_3) which are considered to be anodic relative to the nickel-based matrix.

Alloying with Mo and increasing Cr content might provide a benefit to cermet coatings similar to their well-known effect in wrought metal as have already been discussed in section 2.4. Indeed Kretschmer et al. (1997) have reported that alloying of Mo up to 3% (in some cases up to 5%) in self-fluxing Ni-base alloys and up to 8% in Co-base alloys improves the corrosion resistance in non-oxidizing environments. A new complex self-fluxing alloy with 13% Mo (Ni-18Cr-13Mo-Si-B-Fe-Cu-C) was comparatively evaluated with commercial Ni-based self-fluxing powders e.g. Ni-18Cr-4Mo-Si-B-Fe-Cu-C; Ni-26Cr-Si-B-C; Ni-16Cr-Si-B-Fe-C; Co-27Ni -19Cr-5Mo-Si-B-C, and was found to have improved corrosion resistance in strong mineral acid solutions including oxidizing acids. It has been reported that increasing Cr content of the binder matrix significantly reduces the corrosion rate of cermet coatings in saline environments and sometimes more than 10 times when the Cr content was increased up to 5% (Bardal et

corrosion resistance with increasing Cr and Mo was also shown by Berget et al. (1998) under similar experimental conditions as of the latter.

Other methods of improving corrosion resistance of thermally sprayed coatings include post-spray treatment such as resin sealing (Ishikawa et al., 1997), fusion (Kretschmer et al., 1997) and laser treatment (Garcia-Alonso et al., 1997; Sridhar et al., 1998). Ishikawa et al. (1997) noted that titanium coating by conventional wire flame spraying has no resistance to corrosion in chloride containing solution (3.5% NaCl, 30°C) because of high level of porosity but they observed that after sealing the coated surface with epoxy and silicon resins, the corrosion resistance of the coating was improved as to a comparable level to the wrought one. Garcia-Alonso et al. (1997) have concluded that laser surface treating of Ni-Cr-W-Mo-Cu-C-B coatings resulted in high content of chromium and nickel on the surface which promotes the formation of a passive layer with a good corrosion resistance. Their work included the studies of modifications produced by laser treatment such as dilution, microstructure, possible defects in the surface alloy and the corrosion resistance of laser treated coatings.

Neville and Hodgkiess (1996) have studied the corrosion behaviour of two HVOF sprayed cermet coatings (50WC-50NiCrSiB and 86WC-10Co-4Cr) applied to a superduplex stainless steel (UNS S32760) substrate. The results have shown the evidence of corrosion attack on the coating itself (as opposed to corrosion of the substrate) in both moderate and high salinity aqueous environments and that the attack was significantly enhanced as the temperature was increased from 18 to 50°C. They found that the influence of a polymer sealing post treatment and a corrosion resistant interlayer (Inconel 625 interlayer, applied in between coating and substrate) were minor. Observations revealed that the modes of attack on the two types of coating were extremely complex. The first coating suffered mainly due to pitting and crevice corrosion while general surface attack was predominant for he latter. Detailed analysis revealed this general surface attack comprised of selective attack on a microscale on the different constituents of the coating. Other work by Neville and Hodgkiess (1997a) on a WC/CoCr cermet coating has also shown that the corrosion resistance of the coating material to be critically dependent on the temperature of the solution and similar mechanisms of coating degradation such as crevice corrosion, loss of hard phases due to

interfacial attack (sometimes also called 'micro-galvanic' action between the hard phase and the binder matrix) and pitting attack at elevated temperature have been observed.

Hodgkiess and Neville (1998a) demonstrated that there is a strong dependence on coating durability for coatings (HVOF sprayed WC/CoCr and spray-fused WC-Co, Ni-Cr-Si-B) as a function of temperature but salinity has a lesser effect (salinity varied between 500ppm and 35,000ppm TDS). Spray-fused coatings were found to have undergone principally localized pitting and crevice attack whereas on the HVOF coating the increased temperature accentuated localized attack at the matrix/hard phases interface, thus evidencing the complex nature of these types of cermet coatings.

Another aspect that concerns the durability of the sprayed coatings is the galvanic interactions that occur at the coating/substrate interface and also on a micro scale between separate components of the coating itself (Hodgkiess and Neville, 1997; Neville and Hodgkiess, 1997b). HVOF-applied cermet coatings: WC/CoCr, WC/NiCr, Inconel 625, NiCrBC on both stainless steel and carbon steel substrates were studied in laboratory simulated seawater of TDS 35000ppm. Examples of localized attack in the form of knife-line-cut at the coating/substrate interface were reported, which will lead to premature loss of bond. In addition, localized attack on a micro scale between coating constituents was discussed.

Holcomb et al. (1997) investigated the use of thermal sprayed titanium anodes for impressed current cathodic protection (ICCP) for steel reinforced concrete structures. The primary advantage of using titanium anodes rather than zinc which has been commonly used till now is that titanium anodes are non consumable because of their high corrosion resistance. However, it should be used in conjunction with some other material e.g. a cobalt nitrate catalyst as titanium alone will not work as an effective anode material since the passive layer will prevent significant current flow. Moreover, selection of appropriate process parameters should be incorporated to achieve the most effective result.

Electrochemical methods such as potentiodynamic, potentiostatic and impedance methods are commonly used in evaluating the corrosion resistance and coating quality. Electrochemical interactions such as anodic and cathodic behaviour of thermal sprayed

coatings are generally evaluated by polarization techniques (Ashary and Tucker, 1991; Lester et al., 1997; Neville and Hodgkiess, 1997a). Polarisation techniques are described in Chapter 2. An electrochemical method has been also used for quantitative evaluation of porosity level in thermal sprayed coatings (Siitonen et al., 1992). Often, porosity level in thermal sprayed coatings (TSC) is evaluated by optical or scanning electron microscopy and further examining the coating by *Image Analysis Technique*. The amount of porosity level however, strongly depends upon the sample preparation technique (e.g. mounting, grinding, polishing etc.) and is very time consuming. Siitonen et al. (1992) formulated the connected porosity (P) of a ceramic coating on a steel substrate as:

$$P = I_C/I_B \times 100\%$$

where, I_C - current density of the coated substrate and I_B - current density of substrate without coating (polarized in neutral 3.5% NaCl solution, 30°C). For metallic coatings, the quantitative analysis of porosity may be determined as:

$$i^E_{total} = \Sigma i^E_{anodic} + \Sigma i^E_{cathodic}$$

and,

$$i^E_{total} = i^E_{coating} + p * i^E_{substrate}$$

where, i^E_{anodic} and $i^E_{cathodic}$ - anodic and cathodic current densities; $i^E_{coating}$ - current density of coating without substrate; $i^E_{substrate}$ - current density of substrate (in the passivation zone); p – relative area of substrate connected to the electrolyte by porosity.

5.2 Erosion-corrosion

Most of the research and developments for tribological properties of thermal spray coatings such as Cr_3C_2/NiCr, Mo/NiCrBSi, WC/CoCr, WC/Co are in the field of adhesive and abrasive wear (Niemi et al., 1992; Vuoristo et al., 1994; Mohanty et al., 1996; Khan et al., 1997; Fervel et al., 1998) and in dry erosive wear (Arsenault et al., 1998). High temperature erosion-corrosion and erosion of several thermal spray coatings in detail for fluidised bed combustor (FBC) bed tubes has been reviewed by Levy and Wang (1988), Wang and Geng (1990), Wang (1996c), Wang and Lee (1997). Other studies in dry erosion include the effect of carbide/matrix proportion of HVOF sprayed Cr_3C_2/NiCr coatings using SiO_2 angular quartz, bed and fly ash at test temperature up to 450°C (Wang, 1998) and HVOF sprayed WC, NiC, TiC, WC/CoCr coatings in 300 and 450°C at different velocities and different impact angles (Wang, 1996b). Also effects of alkali chlorides (NaCl, KCl particles) mixed with SiO_2 on erosion-corrosion of HVOF sprayed Cr_3C_2/NiCr coatings have been reported by Wang (1996a). In most cases material wastage was determined in terms of coating thickness only but some mechanistic approaches such as cracking and chipping for hard coatings were reported even at low particle velocity (Wang and Geng, 1990; Levy, 1995; Lee and Wang, 1996). However, a very little is known about the erosive behaviour of such coatings in liquid and solid-liquid "slurry" conditions. The material degradation rate is even much accentuated if the environment is corrosive and the aim of this section is to review some of the recent results, which have enhanced the current understanding in this area.

A recent study on erosion behaviour of a coating by liquid water jet has been performed by Briscoe et al. (1997). Normal tap water jet (jet velocity 40ms^{-1}, jet diameter of 1mm) was normally impinged on a 3mm thick composite coating (made of a mixture of glass Ballotini spheres and polymethylmethacrylate 'PMMA'). The erosion patterns were generally found to be symmetrical about the axis of the jet and majority of the erosion was found to occur in the centre of the tested specimen, directly below the jet axis. It was concluded that the coating sample was eroded by a bulk cohesive mechanism, which led to rapid failures once a critical jet pressure was exceeded.

Kreye et al. (1998) reported that the cavitation resistance of thermal sprayed coatings-plasma sprayed and HVOF is limited-by pores, microcracks and oxides present. HVOF coatings demonstrated the occurrence of the cavitation damage due to formation and propagation of fatigue cracks. The cracks originate from existing microcracks and propagate preferentially along interlamellar boundaries. The presence of pores and brittle phases enhances the formation and propagation of the cracks. Table 5.2.1 illustrates how the HVOF spraying can produce coatings of various materials with resistance to cavitation erosion similar to bulk sample of stainless steel UNS S31603 (the test was done in distilled water).

Coating Process	Material	Hardness HV_{300}	Cavitation Erosion Rate (mg/h)
HVOF JP-5000/Kerosene	UNS S31603	260	6.8
HVOF Jet Kote/Propane	NiCrBSi type 60	670	4.4
HVOF DJ 2700/Propane	Stellite 6	650	3.8
HVOF DJ 2700/Ethylene	WC-Co 83-17	1400	7.2
HVOF JP-5000/Kerosene	Cr_3C_2-NiCr 75/25	1220	3.8
Bulk Material	UNS S31603	165	6.0

Table 5.2.1 Cavitation erosion rates of the coatings investigated (Kreye et al., 1998).

Kumar et al. (1997) evaluated the effectiveness of HVOF and Plasma sprayed cavitation-erosion resistant coatings for hydroelectric turbine and pumps. Testing was performed using a submerged cavitating water jet erosion apparatus utilizing an operating pressure of 27.6MPa. They have found that the cavitation rates of HVOF and plasma sprayed coatings were higher than the welded 308 stainless steel. It has been noticed that HVOF coatings generally had lower cavitation rates than the plasma sprayed coatings. However, no mechanistic approach for the material loss was elaborated. Despite relatively poorer corrosion resistance, it was reported that the cost of the HVOF sprayed Stellite 6 coating is estimated to be one third of weld repair and by HVOF spraying the cost of cavitation repair for the US Army Corps of Engineer's Granite House, WA, Hydroelectric Project could be minimised three times by sustaining the cost at $2012 per sq. meter.

Karimi and Verdon (1993) have performed erosion-corrosion tests on HVOF sprayed WC/CoCr, WC/Ni coatings in a mixture of tap water and 0.3 wt.% sand particles (20-

200μm) at 25ms^{-1} tangential flow velocity. They have reported that cermets of Co matrix resist better than those of Ni-matrix and the addition of Cr improves the erosion resistance of WC-Co coatings by about four to six times. In addition, it has been reported that the wear behaviour of WC-metal matrix cermets has been found to be governed mainly by the carbide grain sizes and by the binder volume fractions. Cermets of fine carbides (1-2μm) showed a relatively lower erosion resistance than those of the coarse carbides (3-4μm) and it was speculated that fine carbides are physically too small to resist and deflect the abrasive particles and their contribution would be limited only to lending hardness to the matrix to reduce scratch depth and related material loss. The same authors under different flow velocities (velocity varied between 20-145ms^{-1}) also reported the improved erosion resistance due to chromium addition under similar conditions (Karimi et al., 1995). The damage mechanism evidenced that at lower velocities the binder phase wears preferentially leading to subsequent loss of carbides, whereas, at higher velocities the carbides also scratched to a some extent and are removed together with the surrounding binder phase. Moreover, local heating of the single impact sites due to friction between abrasive and eroding surface "thermomechanical effects", as well as due to high strain rate deformation of the surface layer affects notably the erosion behaviour of the WC-metal cermets. It was only speculated that the beneficial action of Cr results in the improvement of corrosion resistance of the matrix, or to a smaller degree of internal stresses developed thus suppressing crack propagation.

Arsenault et al. (1997) studied several JP-5000 HVOF sprayed coatings (WC/Co, WC/Ni, Cr_3C_2/NiCr, Ni-W-Cr-Si-Fe-B-C, Co-Cr-Ni-Mo-W-Fe and 316L stainless steel) with an impinging slurry jet (10% alumina and water mixture, 15ms^{-1} slurry velocity, ambient temperature) at different impinging angles (20 and 90°) with different sizes (35 and 200μm diameter) of the erodent particles. Their results concluded that the behaviour of HVOF sprayed coatings is dependent on the erodent particle size, to the impinging angle to some extent and to the corrosion resistance of the cermet matrix and also that the relative erosion resistance of the coatings experimented did not correlate with their respective hardness value. For a large particle erodent size, the relative ranking of erosion resistance of coatings is almost independent of the impinging angle whereas, for slurry erosion with smaller particle size, both the impinging angle and the corrosion

resistance of the metal matrix play a role in the relative ranking of slurry erosion resistance. Later, Arsenault et al. (1998) concluded that, in absence of significant corrosion, target material hardness is an important factor affecting the mechanism of erosive wear and also that the relative hardness of the experimented coatings are in accordance with their relative ranking performance in dry or slurry erosion. This is in absolute contrary with the statement that the authors made in the former report despite of all the experimental conditions and the tested materials being the same. They also indicated that cermet coatings with Co matrix are more susceptible to corrosion than CoCr matrix. Similar case of high corrosion and material losses for HVOF sprayed WC/Co was reported based on experiment performed in a rotating disk (14ms^{-1} rotational velocity) in synthetic sea water and 0.025-2.5% of silica sand of particle size of average 230μm at ambient temperature (Bardal et al., 1993a).

Bardal et al. (1993a) studied the effect of sand concentration on the erosion-corrosion performance of HVOF sprayed WC/Co and WC/CoCr coatings and a duplex steel SAF 2205 as a reference material. The experiment was performed on a rotating disk in aerated synthetic seawater mixed with varied silica sand concentration that ranged between 0.025 and 2.5%. The average grain size was 230μm and the temperature was kept at 20±3°C.

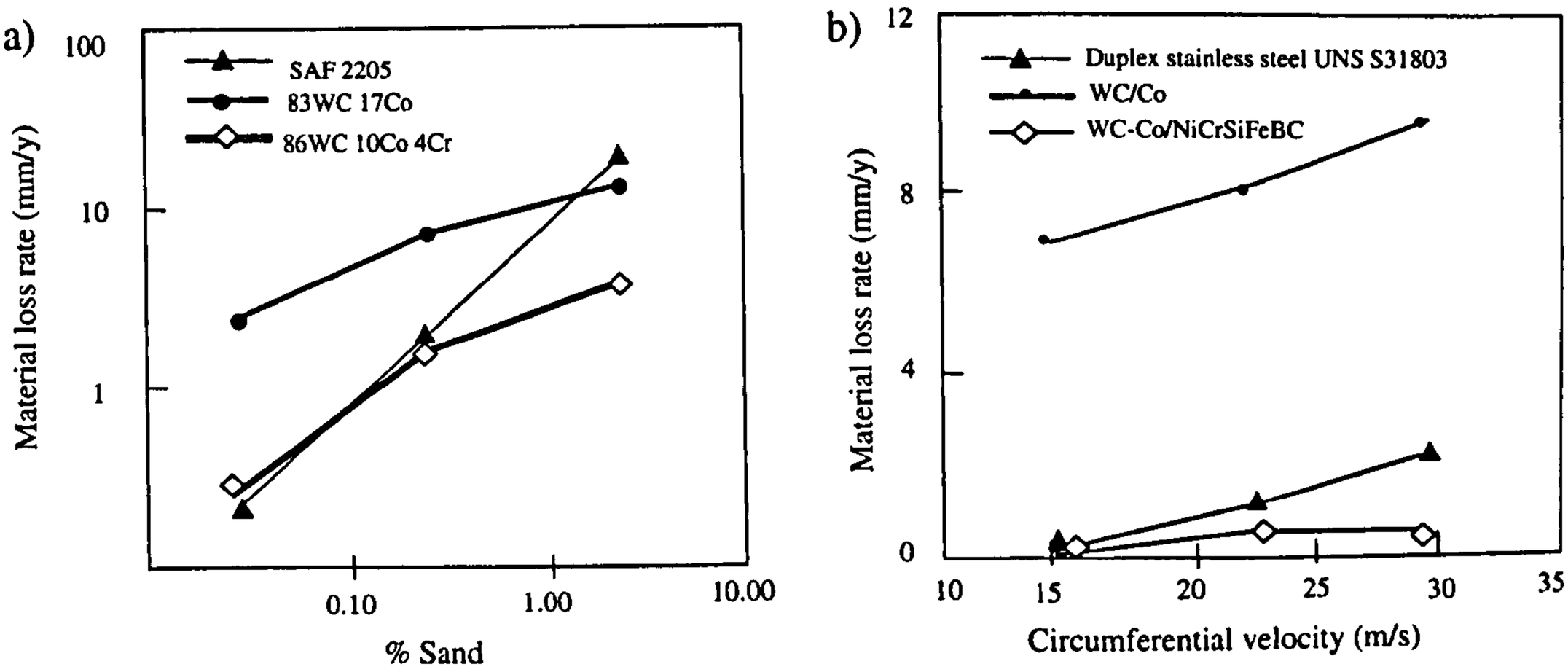


Figure5.2.1 a) Effect of sand concentration on material loss rate at flow velocity 14.3ms^{-1} (Bjordal et al., 1995a); b) Effect of circumferential velocity on material loss (Bjordal et al., 1995b).

Their findings showed that the total material loss for the duplex steel is nearly proportional to the sand concentration, whereas the effect of sand content is much smaller for the coatings. Similar trend was shown also by Bjordal et al. (1995a) in Fig. 5.2.1a. The increase of erosion-corrosion with increasing sand concentration is much less than proportional, for all three materials. At low erosivities corrosion is the most important deterioration mechanism, whereas at high erosivities erosion will dominate over the corrosion, and the corrosion properties become less important.

Bjordal et al. (1995b) studied the effect of flow velocity on the erosion corrosion behaviour of three different materials (Duplex stainless steel UNS S31803; WC/Co and WC-Co/NiCrSiBFeC) and found that the coating with Co-NiCrSiBFeC binder had the least material loss at different velocities tested Fig. 5.2.1b. The tests were performed in synthetic seawater, pH 8.2, 0.25% silica sand, 20±3°C. Such material loss has been related to velocity exponent and that the velocity exponent in pure erosion conditions is 3±0.25 for similar coatings and stainless steels experimented in similar environments. For materials with high corrosion rate, like the WC-Co coatings, the exponent is much lower (Bardal et al., 1995).

Berget et al. (1998) has reported that erosion and erosion-corrosion resistance of HVOF sprayed WC/CoCr increases with decreasing WC particle size. The test was performed with a rotating disc in a slurry of substitute seawater and silica sand (0.25wt%) at peripheral velocity of 22.9ms^{-1} at 20°C.

The study of combined mechanistic effect of erosion and corrosion of thermal spray cermet coatings has been a matter of prime interest during the past few years. The major concern is that, although these coatings were developed to possess a high wear resistance, such coatings with a highly corroding matrix such as Co will suffer significant material loss than coatings with less corroding matrix even though the erosion resistance is the same due to a high "synergistic" effect (Bjordal et al., 1995a, 1995b). It has been reported that corrosion can lead to a "synergism" of up to 90% and has been speculated that such mechanism of corrosion of the binder matrix leads to undermining of the hard carbide particles leaving them unsupported and eventually in the removal of these particles leading to excessive material loss (Bardal et al., 1995;

Bjordal et al., 1996). Similar wear mechanism involving preferential attack of the binder phase in WC/Co coating which leads to eventual "pullout" of the poorly supported carbide particles has been reported by Knapp and Nitta (1997). The authors have also noted that the increased mean free path between the carbide particles as well as the volume fraction of the binder phase increases the wear rate. The importance of carbide fracture and fragmentation in the wear mechanism of multiphase materials has also been discussed by the same authors. The experiment was performed in water and zirconia particles slurry at the flow rate of 30-40cm^3min^{-1}.

Other factors that might affect the coating integrity are the corrosivity of the medium and any galvanic interaction with the surrounding material. This is especially important when the surrounding materials are corrosion resistant alloys such as stainless steels, where the coatings otherwise will act as an anode (Rogne et al., 1997). Increasing the Cr content in the metal phase by replacing Co increases the corrosion resistance of the WC/CoCr type coatings. At low erosive and high corrosive conditions increased Cr improves the erosion-corrosion resistance, but at high erosive conditions increased Cr has a negative effect (Rogne et al., 1998).

Erosion-corrosion resistance ranking of WC based cermet coatings with different binder metals in tap water and synthetic seawater environment is illustrated in Table 5.2.2.

Comparative erosion-corrosion resistance	Medium	Reference
WC/CoCr > WC/Co > WC/Ni	Tap water	Karimi et al., 1993 Rogne et al., 1997
WC/CoCr > WC/Co	Synthetic seawater	Bardal et al., 1993a; Bardal et al., 1995; Bjordal et al., 1995b
WC/CoCr > WC/Co	Water	Arsenault et al., 1998
WC/CoCr > WC/NiCr	Synthetic seawater	Rogne et al., 1997; Rogne et al., 1998
WC/Co > WC/Ni	Synthetic seawater	Berget et al., 1998

Table 5.2.2 Erosion-corrosion resistance of HVOF sprayed cermet coatings with different binder metals.

What the data in Table 5.2.2 reveals is a generally-observed benefit in erosion-corrosion resistance associated with alloying the binder phase with Cr and that the Co matrix has

superior corrosion resistance than Ni matrix that affects the combined erosion-corrosion performance.

5.3 Summary and rationalisation for the experimental program

The literature review demonstrates unambiguously that HVOF sprayed cermet coatings represent attractive options for wear protection in aqueous slurry environments. Uniform distribution of hard ceramic particles within a skeletal net work of a soft metal matrix gives cermet coatings a unique property of ductility and high hardness. But these coatings seem to be prone to corrosion degradation that enhances excessive material loss resulting in substantial amount of 'synergism'.

However, much of the works described in the literature review encompassed on WC based cermet coatings, a very little is known about the self-fluxing NiCrSiB cermet coatings. This project has focused on one generic type of HVOF sprayed NiCrSiB coating. The durability of such a coating obtained from two different commercial thermal spray companies has been studied in detail. The findings in relation to these two coatings are described and discussed in two separate chapters following the experimental techniques in Chapter 6.

CHAPTER 6. MATERIALS, EXPERIMENTAL AND EXAMINATION TECHNIQUES

6.1 Specimen preparation

Specimens investigated in this programme included two types of the same generic coating (type NiCrSiBC) supplied by two different commercial thermal spray companies and will be considered as *Coating A* and *Coating B* and their results will be treated separately. Both coating types *A* and *B* were HVOF sprayed either onto a carbon steel substrate (BS970 En8) or onto a stainless steel substrate (UNS S31603). Coating A was studied in detail without any post-spray treatment (except for polishing), whereas, *Coating B* was subjected to post-spray treatments such as *vacuum sealing* with polymer impregnation and high temperature *vacuum furnace-fusion.*

Substrate preparation

Substrate samples either in the form of plates (100x60x10mm) or in the form of discs (∅25x10mm) were prepared. The disc samples in the quantity of 15-20 pieces were either grit blasted, cleaned with acetone and glued using a strong adhesive (type F2015 from Ciba) or screwed on to a separate thick (~5mm) metallic plate as shown in Fig. 6.1.1. The specimen samples attached to the plate were sent to the coating companies for spraying.

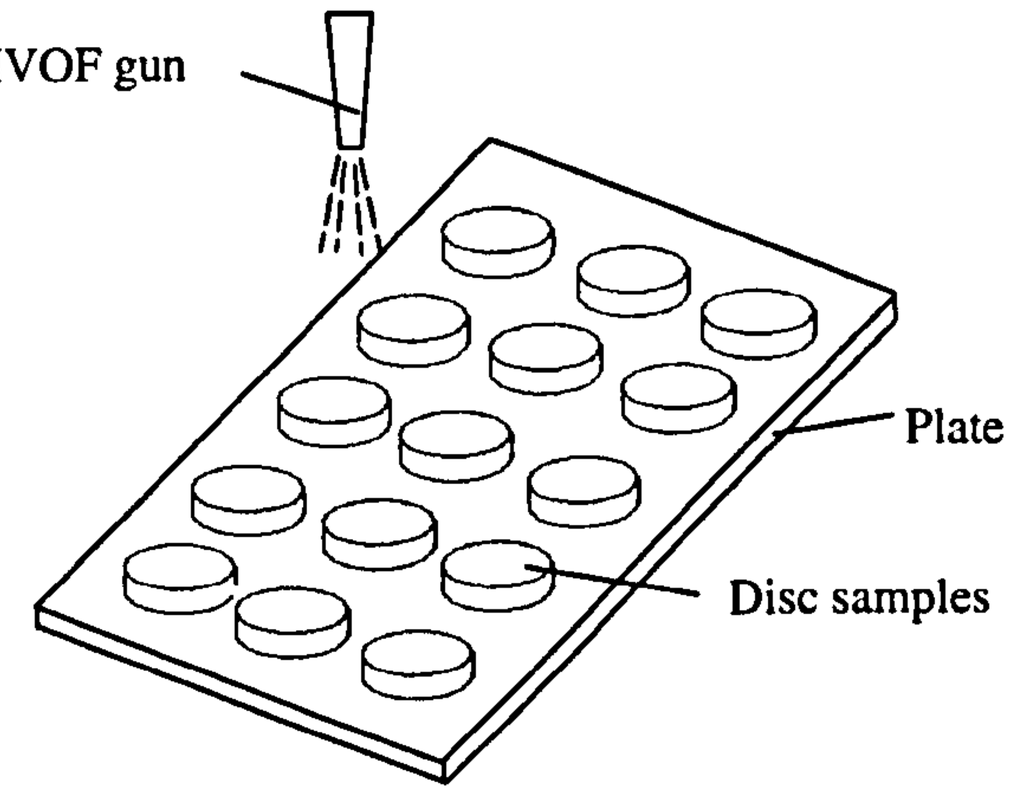


Figure 6.1.1 Samples assembled for HVOF spraying.

6.1.1 Coating manufacture, spray process and parameters

Coating A

The specimens in the form of plate or discs assembled as in Fig. 6.1.1 were sprayed utilising a Hobart Tafa HVOF gun. The coating material was a premium grade NiCrSiBC alloy *Diatec1060*, whose characteristics were as follows (manufacturer's detail):

Chemical composition:	Ni balance Cr17% Si4% B3.5% C1%
Hardness:	58-60 HRC
Porosity:	< 1%
Service temperature:	815°C
Bond strength:	> 83MPa (low carbon steel, grit blasted)
Surface finish as sprayed (R_a):	7.85μm

The process details were not available for this coating.

Coating B

The specimens were cleaned with a vapour degreaser and subsequently roughened by blasting with angular steel grit. The self-fluxing alloy powder *1275*H as shown in the Table 6.1.1.1 was applied to the specimens by spraying. The spray system utilised the Hobart Tafa JP-5000 high pressure HVOF gun as shown in Fig. 4.3.3.

Coating Material	*Powder Type: Chemical Compositions are Nominal*	*Applications and Properties*
1275 H	Ni balance 16Cr 3.5Si 3.5B 3Mo 4Fe 0.8C 3Cu Water Atomized	Resists abrasive grains, hard surfaces, cavitation, particle erosion and fretting; corrosion resistant Dense, hard, fusible, oxide-free coatings (55 HRC)

Table 6.1.1.1 Powder characteristics of *Coating B* (manufacturer's data).

The following spray parameters were used for the spraying:

Spray System:	JP-5000 HP/HVOF
Spray Rate:	46 $gmin^{-1}$
Gun Barrel:	203mm
Feeder Speed:	86 rpm
Fuel:	Kerosene No. 1K
Spray Distance:	355mm

After spraying, the specimens were also subjected to sealing by resin impregnation under vacuum. Coating thicknesses for both as-sprayed and vacuum-sealed coatings were about 250±25μm.

Vacuum furnace-fusion

After spraying specimens to be fused were loaded into a vacuum-furnace. During the fusion cycle, the furnace temperature was controlled with regard to the physical properties of the substrate and the coating material. The furnace vacuum was maintained at around $1x10^{-4}$ millibar during the cycle. This removed gaseous contaminants and allowed for better "wetting" of the substrate by the coating material. Process parameters were maintained at fusion temperature to allow sufficient time for the counter diffusion of elements between the coating layer and the substrate material. Furnace cooling rates were controlled with particular reference to the substrate material property. The coating thickness of vacuum furnace-fused coating was 260±10μm.

Experiments were also performed on the substrate materials without the coating. The austenitic stainless steel type UNS S31603 was studied in more detail than the carbon steel for comparative purpose. The chemical analyses of the substrate materials are given in Table 6.1.1.2.

Material	Cr	Mo	Ni	Mn	N	S	C	Cu	Si	Fe
UNS S31603	16.7	2.4	11.7	1.7	-	<0.01	0.03	-	0.3	bal.
BS 970 En 8	-	-	-	0.60-1.0	-	0.06 max.	0.35-0.45	-	0.05-0.35	bal.

Table 6.1.1.2 Compositions of substrate materials.

6.1.2 Mounting and polishing techniques

Specimens of either plates of 10x10mm size (sectioned using a precision diamond saw type ISOMET 2000 from Buehler Ltd.) or discs of ∅25mm were mounted in a non-conducting epoxy resin type Metset FT with an electric wire soldered to the rear side of the specimen. Schematic representations of specimens encapsulated in a cold mount epoxy are shown in Fig. 6.1.2.1. The plate specimens were primarily used for static corrosion tests whereas disc specimens were used for impingement tests.

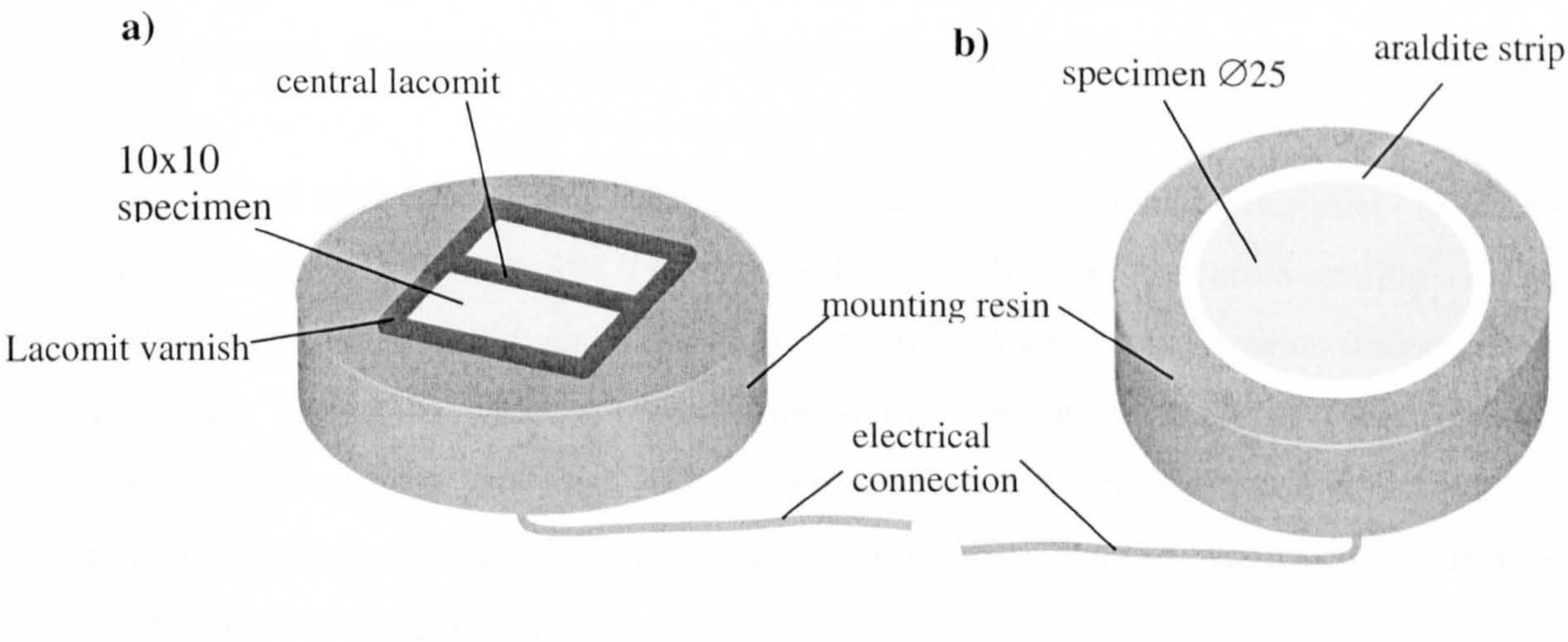


Figure 6.1.2.1 Schematic diagrams of a working electrode a) for static corrosion test painted with lacomit varnish; and b) for impingement test with an araldite strip to seal the coating/substrate interface.

Polishing

All specimens were investigated in the as-polished condition unless stated "as-received". The polishing process comprised successive grinding on 240, 400, 800, 1200 SiC grit papers and finally 6-micron diamond polishing. The equipment used was a polishing disc type Metaserv Universal Polisher and the specimen was polished on a polishing cloth (Microcloth®) using a diamond abrasive type Meta-D from Buehler Ltd. The polished surface was first washed with methanol and air-dried. The metallographic preparations are in accordance with the references (Bjerregaard et al., 1996; Sauer, 1997; Blann, 1997; Blann and Voort, 1997; Nelson and Voort, 1997).

6.1.3 Metallographic investigation

The powder morphology and its microstructure was studied by embedding the powder particles into the cold setting epoxy resin and then successive grinding and polishing as illustrated above in section 6.1.2. The coating microstructure was revealed by examining the coating in both plan and cross section using the various techniques, which are mentioned in section 6.4.

Porosity in the coating was determined by *image analysis* technique. It consists in separating the image into 256 grey levels, and extracting a phase (pores) by grey levels discrimination. Then the percentage of the phase is equal to the percentage of the pores.

The coatings were investigated with Vickers indentations (Buehler Micromet^{R} II Micro hardness tester, ASTM E-384-73* standard) on both plan and cross-section of the coating under loads of 200 and 500g to give microhardness measurements. Indentations were also performed under a macrohardness machine under loads of 10 and 30kg. Measurements under low load (0.2-0.5kg) describe the microhardness of individual lamellae and measurements under a larger load (10, 30kg or more) describe the hardness of the whole coating (Pawlowski, 1995).

6.2 Corrosion measurement

Electrochemical polarisation tests were performed using a three-electrode cell arrangement attached to a computer controlled potentiostat type Autostat as shown in Fig. 2.2.2 of Chapter 2, manufactured by Sycopel Scientific Ltd, Boldon, Tyne and Wear, England. Experiments were carried out at 18 and 50°C either in a 3.5% NaCl solution (made from distilled water) or artificial seawater made from a commercial salt 'Instant Ocean' mixed with distilled water to obtain the electrical conductivity of 53000μScm^{-1} at 25°C. The conductivity of the solution was measured using water analyser type JENWAY PWA1.

For the anodic scan the sample potential was shifted from E_{corr} (free corrosion potential) in the positive direction until a current of 500μA/cm^2 measured in the external circuit

between the working and auxiliary electrodes was reached. The scan rate was 15mVmin^{-1}. Once 500μA/cm^2 was reached the scan was reversed and the potential was shifted in the negative direction back to E_{corr}. Cathodic scans were carried out by shifting the potential to a value -1400mV, measured using the saturated calomel reference electrode (SCE). The specimens were immersed for 1 hour prior to the polarisation so as to settle the free corrosion potential 'E_{corr}'. The substrate material was fully isolated from the working fluid by applying a non-conductive lacomit varnish at the specimen-resin interface as shown in Fig. 6.1.2.1a, which also shows a central lacomit strip over the exposed surface. This central lacomit strip allows assessing the crevice effect more accurately than the lacomit strip applied at the specimen-resin interface as at this region, there is more likely that corrosion product from the substrate material may easily come out if the working fluid penetrates into the substrate.

Free corrosion tests were also performed by simply immersing the specimens in the electrolyte in a beaker under free corrosion potential and examining after certain intervals of time. The conductivity was maintained by regularly checking the solution and diluting with distilled water as the conductivity increases due to evaporation.

6.3 Erosion-corrosion measurement

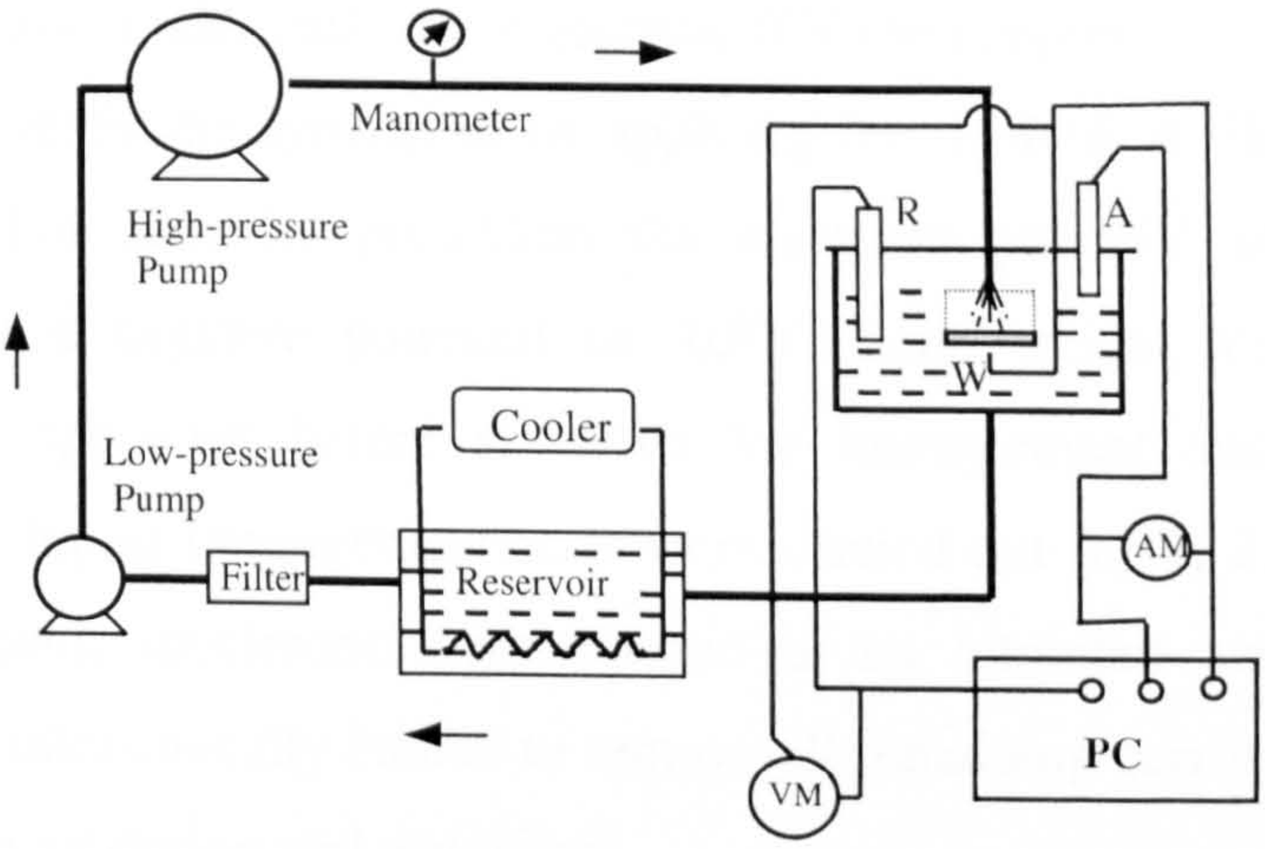
6.3.1 Liquid erosion-corrosion measurement

The liquid erosion-corrosion tests apparatus comprised an electrochemical monitoring (three-electrode cell) attached to an impinging jet rig where saline water was directed at 90° angle to the working electrode surface 'W' at a range of velocities (17 to 72ms^{-1}). The liquid erosion rig was similar to one used by Neville et al. (1995). Figure 6.3.1.1a, b show the liquid jet impingement rig of closed circulating loop comprising a low-pressure centrifugal pump, which feeds saline water from the reservoir to a higher-pressure pump.

The circulating water was constantly filtered to provide a liquid-jet free from suspended solids. The system comprised stainless steel pipes with the exit nozzle diameter of 1mm. The velocity of the system was varied by changing the pressure of the high-pressure

pump. The distance between the nozzle and the specimen was kept constant for all impingement tests at 5mm in order to maintain the flow development region unless otherwise stated.

a)



b)

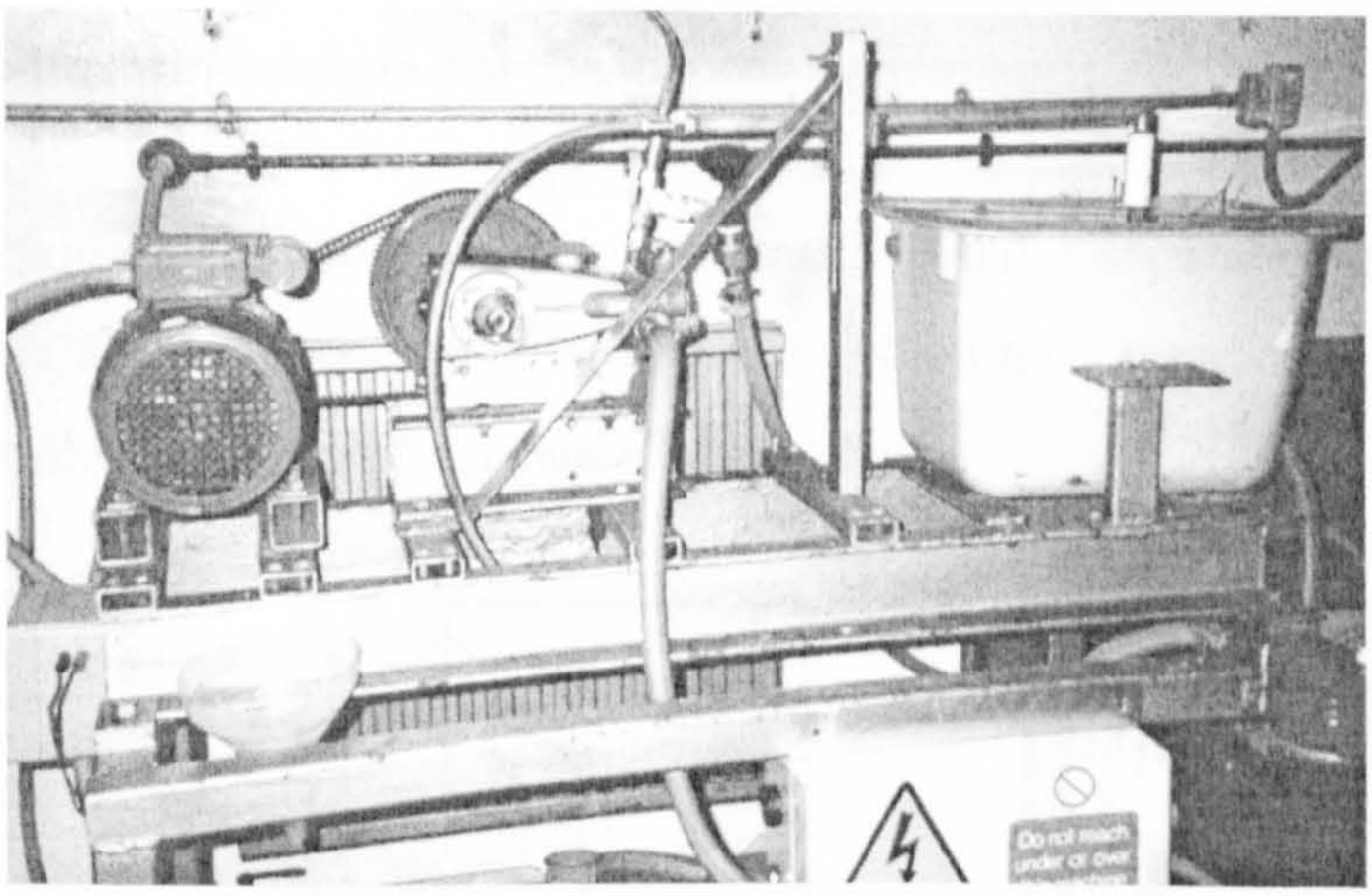


Figure 6.3.1.1 a) a schematic diagram of a liquid jet impingement rig comprising a three-electrode cell: where, R-reference electrode; A-auxiliary electrode, W-working electrode; VM-voltmeter, AM-ammeter; and b) same liquid jet impingement rig.

The temperature of the system was maintained by using a commercially available thermostat-controlled cooling device for experiments performed at higher temperature (50°C). For experiments at ambient temperature (18°C), a water-cooling coil of stainless steel was used. Anodic and cathodic scans were conducted for different velocities and

different temperatures. Commercially available araldite type F2015 was used to seal the coating/substrate interface during electrochemical tests.

Weight loss tests were carried out under liquid impingement both at the free corrosion potential and also under cathodic protection (CP) to suppress the corrosion component and hence quantify the synergism by applying the method as illustrated in Chapter 3 section 3.5. For cathodic protection the electrode potential of the specimen was maintained at a negative potential of -0.8V. Total weight loss was measured by weighing the specimen before and after the impingement tests to an accuracy of 0.0001g. The liquid impingement tests were carried out for 1, 2, 4 and 6 days. After each experiment, specimens were washed in an inhibited acid solution (Clarke's solution) and ultrasonically bathed to remove all remaining corrosion products from the surface before air drying and weighing.

6.3.2 Solid-liquid erosion-corrosion measurement

The solid-liquid erosion-corrosion experiments utilised a separate rig as shown in Fig. 6.3.2.1, which also comprised a closed loop in which tests were conducted either for 1-hour or multiples thereof with change of fluid hourly.

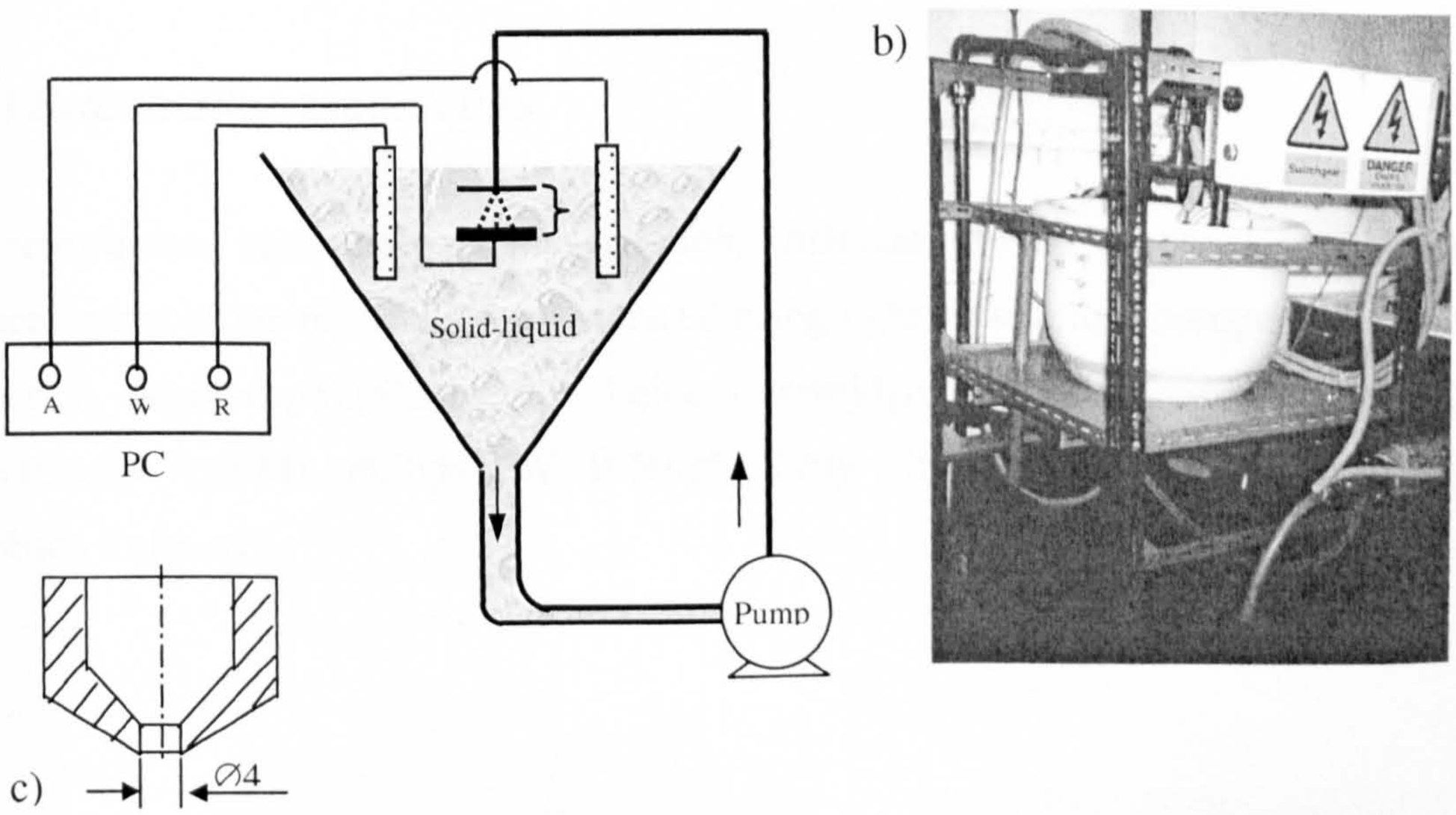


Figure 6.3.2.1 a), b) Solid-liquid impingement rig, where A-auxiliary; W-working; and R-reference electrodes; c) schematic view of a nozzle made of high wear resistant Nylon.

The nozzle diameter of the solid-liquid rig was 4mm and the solid-liquid slurry jet was subjected to 90° impingement at jet velocity of 17ms^{-1}. The stand off distance was kept at 5mm. The solid-liquid slurry was made of 3.5% NaCl solution plus 800ppm of silica sand as erodent. The size distributions of the two types of sand particles used as erodent are shown in Tables 6.3.2.1 and 6.3.2.2 respectively.

size, μm	> 425	300-425	250-300	180-250	106-180	< 106
Wt, %	6.8	20.0	20.5	36.2	15.9	0.6

Table 6.3.2.1 Particle size distribution of sand type A.

size, μm	1000	710	500	355	250	180	125	90	63
Wt, %	Trace	0.1	1.0	5.6	29.6	41.6	21.0	1.0	0.1

Table 6.3.2.2 Particle size distribution of sand type B (Congleton HST60).

All solid-liquid impingement tests were carried out at temperature18-20°C. Tests were also carried out under cathodic protection (CP) as in liquid impingement conditions at electrode potential being held at -0.8V. In solid-liquid impingement tests, the specimens were subjected to 5 minutes impingement prior to polarisation in order that the surface is not severely damaged before starting the polarisation experiment.

6.4 Examination techniques

Microstructure and phase characterisation, different modes of attack and damage mechanisms of the materials were assessed using light optical microscope and scanning electron microscope (SEM) type Leica Cambridge Stereoscan 360, atomic force microscope (AFM), Philips PW 1050/35 X-ray diffractometer (XRD) and Taylor Hobson Talysurf.

6.4.1 Scanning electron microscopy (SEM)

Sample Preparation

The samples to be examined under the SEM should be handled very carefully after the experiment, since the evidence of damage mechanism can be destroyed during transportation from the place of experiment to the SEM laboratory. The samples were dried and carbon coated in an evaporative coater to make the surface conductive. The coating is very thin (approx. 20nm) so that it does not hinder the identification of the underlying material.

Principle of operation of SEM

The coated SEM sample is first placed in a chamber and evacuated to very high vacuum about 2 x 10^{-6} torr. A fine electron beam (diameter approx. 10nm) from a tungsten filament is accelerated by a 20kV accelerating voltage which when impinges on the sample produces various forms of radiation, such as secondary electrons, back-scattered electrons, characteristic X-rays etc. The secondary and back-scattered electrons are used for SEM micrograph, whereas the characteristic X-rays are processed electronically to produce on energy dispersive X-ray (EDX) spectrum.

The SEM image is formed by collecting the secondary electrons generated by the primary beam. The secondary electrons are collected by a secondary electron detector mounted in a SEM chamber and are further processed by the electronics console in to the familiar SEM image and then displayed on a TV screen and photographed with an attached camera (Welton, 1984). Electron emissions are also dependent on the atomic weight of the atoms in the sample. Heavy elements emit more electrons than light ones. Different phases can be differentiated as a result of the contrast in the back-scattered image (Engel and Klingele, 1981).

Elemental analysis on a sample is performed by collecting the characteristic X-rays produced as the electron beam scans the sample. Each element in a sample produces X-rays with characteristic energies and wavelengths, which can be analysed by an energy

sensitive Si (Li) detector in an energy dispersive system (EDX). This EDX system is useful to obtain analysis of elements above atomic number (Z) = 11 (for Sodium). The primary electron beam in the SEM ionises the atoms in the metal by exciting and ejecting electrons in the inner shells of the atom. Electrons from the outer shells replace the inner shell vacancies to regain the stability. During this transition period, specific amount of energy in the form of X-rays is released, which is determined by the energy difference between the electron shells involved.

X-ray microanalysis

Average analysis

The general analysis of the sample is done at a very low magnification of 20, and with a flat specimen inclined in the SEM at an angle of 45°, the incident beam scans a small area. Large area scanning provides a general analysis of a specimen.

Spot analysis

A spot analysis of the sample is obtained by positioning the electron beam at a particular point, in which the primary electrons cause the excitation of characteristic X-rays (Fig. 6.4.1). The spot analysis is particularly done at very high magnification so as to obtain the elemental distribution at that point.

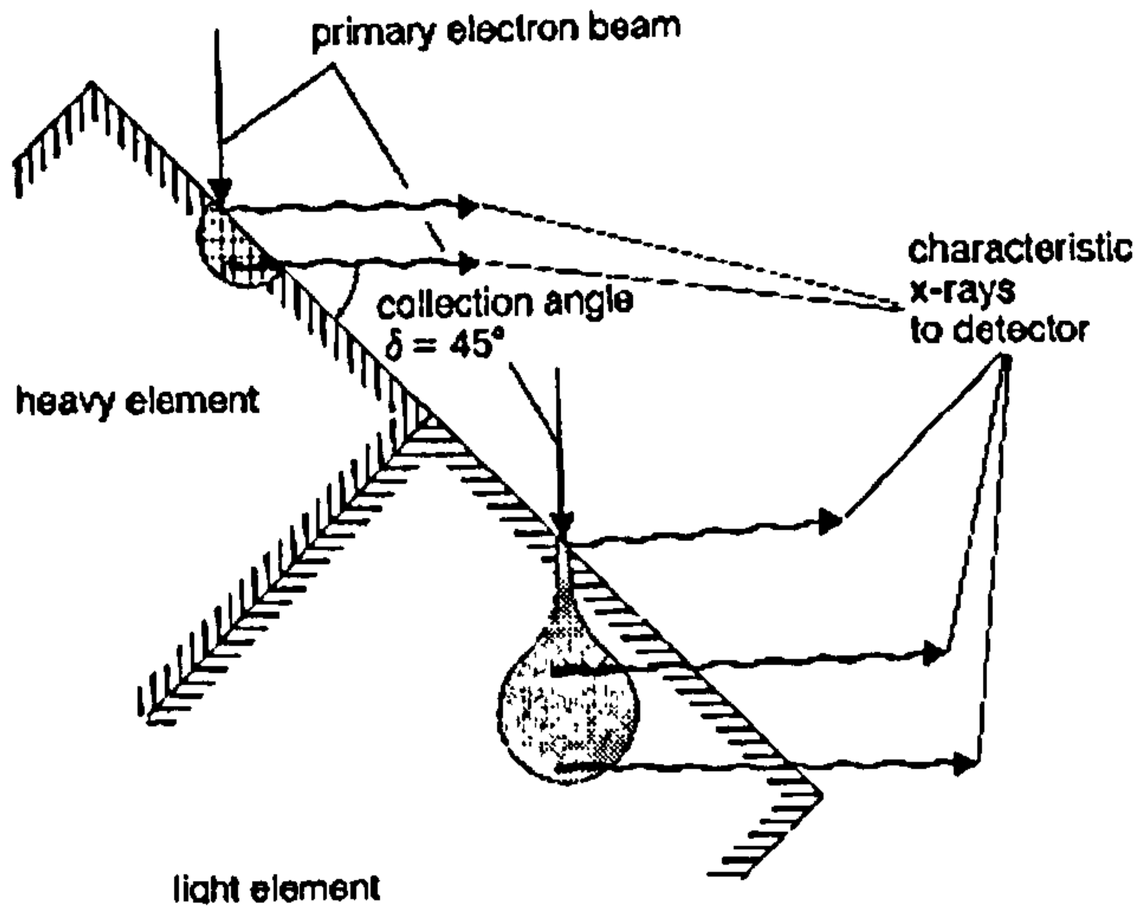


Figure 6.4.1 Point analysis of the sample (Engel and Klingele, 1981).

The elemental analysis is mainly performed on the basis of ZAF correction, which is undertaken by a computer programme built-in to the SEM data-handling facility. The program corrects the 'raw X-ray data' for effects on X-ray emission due to atomic number (Z) of the elements present plus X-ray absorption (A) and fluorescence (F) phenomena.

6.4.2 Atomic Force Microscopy (AFM)

AFM was used to characterise the coatings microstructure in an atomic level and also to identify the hardness values of different phases of the coatings. The AFM operates by measuring the forces between a stylus probe and the sample. These forces depend on the nature of the sample, the distance between the sample and the probe, the probe geometry, and any contamination on the sample surface. AFM consists of a very sharp, fractured diamond tip mounted on a small, cantilevered beam that acts as a spring.

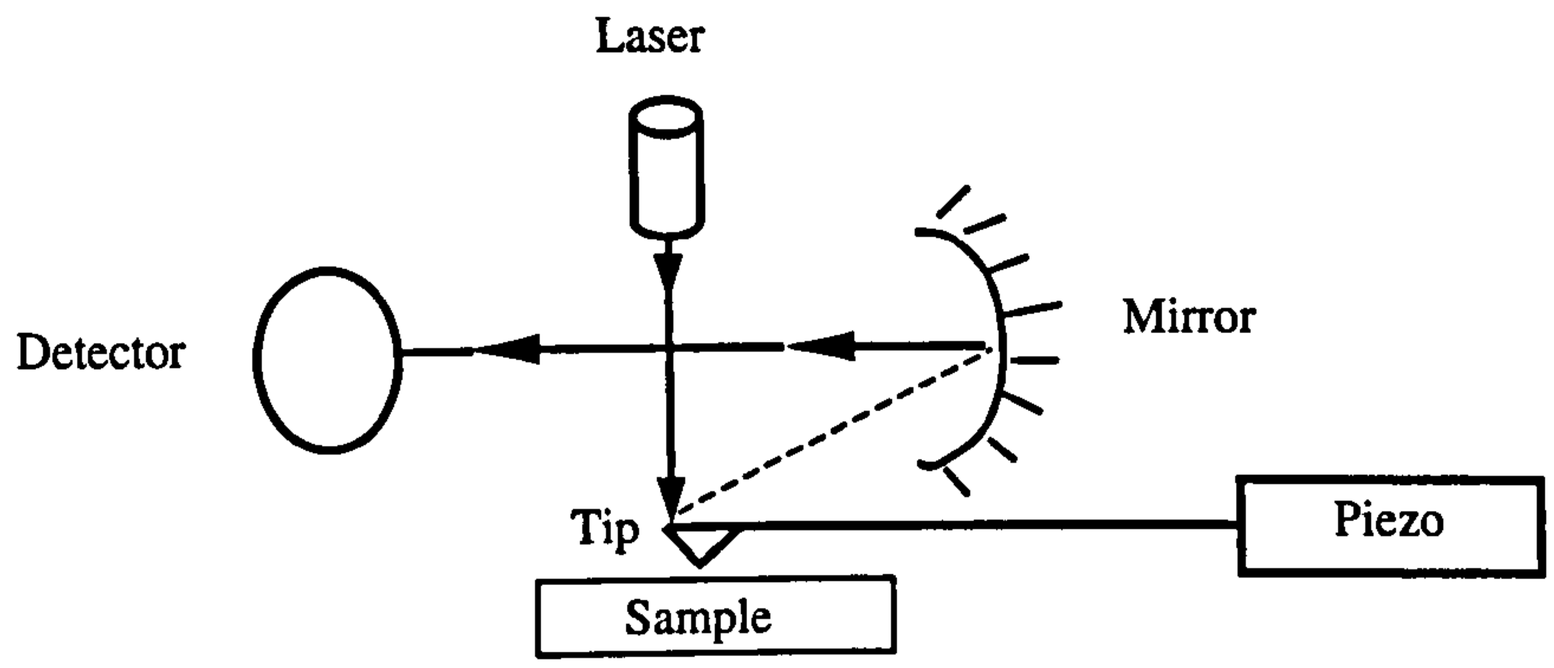


Figure 6.4.2 A schematic diagram of atomic force microscope (AFM).

Piezo-electric elements move the tip towards the sample until interatomic forces between the tip and the sample deflect the cantilever. The AFM monitors the amount of deflection (using optical interferometer) to sense the amount of force acting on the tip (Burleigh, 1991). A schematic diagram of an atomic force microscope is illustrated in Fig. 6.4.2.

6.4.3 Talysurf

Talysurf instrument by Taylor Hobson was used to measure the surface texture of the wear scars produced under erosion tests. The principle of the instrument is to move a stylus over a representative length of the surface under examination.

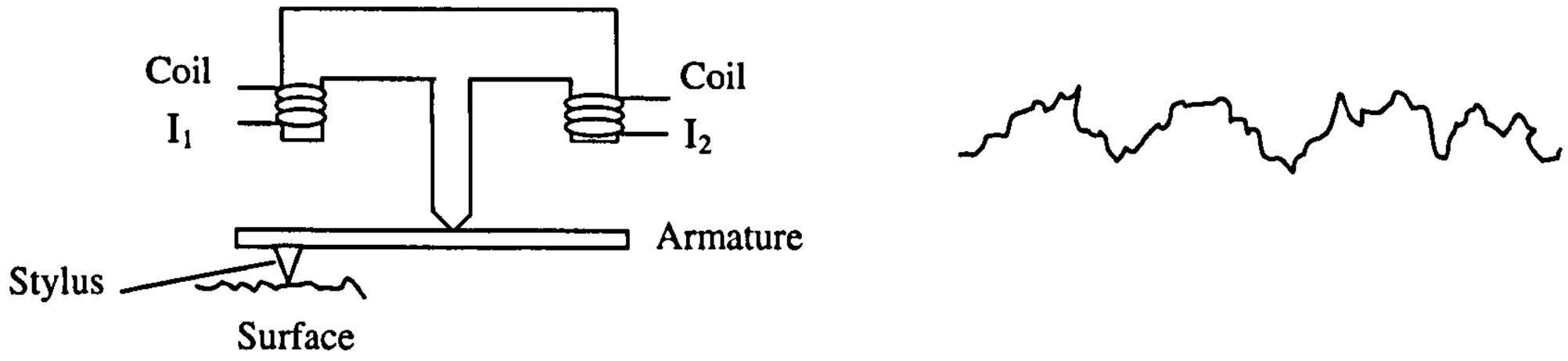


Figure 6.4.3 a) Principles of a Talysurf; b) profilometric trace of a surface, where the peaks and spacing between them are distorted due to difference in horizontal and vertical magnifications (Sarkar, 1977).

Figure 6.4.3a shows a stylus moving over a surface with the result that the oscillatory movement cause the armature to tilt. The armature supports the pole pieces around, which are two coils I_1 and I_2, each carrying a high frequency current. The air gap between the armature and the pole pieces varies as the stylus traverses the surface under investigation. This results in a variation of the impedance of the coils and hence the magnitude of the high frequency current that actuates the pen recorder and the surface texture is obtained in the form of a trace. A profilometric trace of a surface as obtained with a Talysurf is schematically shown ion Fig. 6.4.3b.

6.4.4 X-ray diffraction (XRD)

X-ray diffraction measurement is used for the identification of the various 'phases' of compounds present in powder and coating samples. Identification is achieved by comparing the X-ray diffraction pattern or 'diffractogram' obtained from a powder or coating sample with an internationally recognised database containing reference patterns for more than 70,000 phases. Modern computer-controlled diffractometer

systems use automatic routines to measure, record and interpret the unique diffractograms produced by individual constituents in even highly complex mixtures (Jenkins and DeVries, 1993). Phase structures of the coatings are studied using monochromatized CuK_{α} radiation. The X-ray diffraction patterns are scanned between the 2-Theta values of 0-120° using a scanning speed of 1° min^{-1}.

CHAPTER 7. *Coating A* Results

7.1 Powder characterisation

The self-fluxing NiCrSiBC powder particles are generally spherical with size ranging from 5 to 45μm. However, a few non-spherical particles can also be seen in Fig. 7.1.1 and this might presumably be associated with either contamination or formed during powder manufacturing. Area analyses on these non-spherical particles gave 1.9% Fe 53% Ni 11%Cr 3.2% Si and 3.5% Mo but existence of such evidence was very rare. The powder particles differentiated from one another mainly in smooth and rough texture. Microanalysis of smooth and rough textured powder particles showed a slight variation in the nickel content. The EPMA results of powder particles are shown in Table 7.1.1.

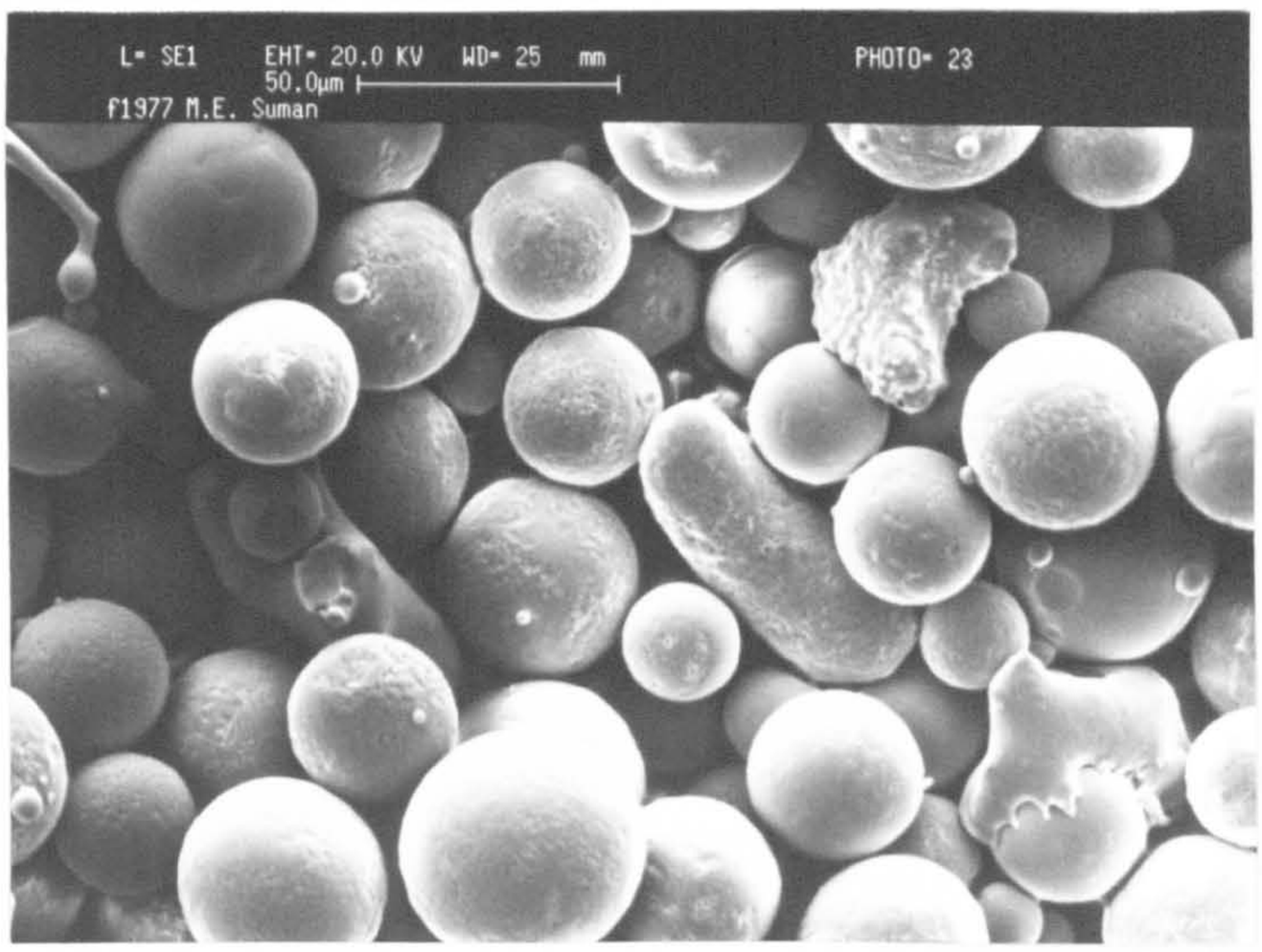


Figure 7.1.1 SEM micrograph showing gas atomised powder particles possessing rough and smooth textures

Powder particle	Fe	Ni	Cr	Si	Mo	Cu	Total
Smooth textured	2.9-3.2	63.6-68.4	11.5-13.7	2.9-3.4	< 0.1	< 0.1	83.4-88.12
Rough textured	3.2-3.4	55.5-61.0	12.3-16.7	3.0-3.3	< 0.2	< 0.1	79.6-82.5

Table 7.1.1 SEM microanalysis of 20x20μm powder particles (average wt. % of 4 analyses)

The split (secondary and back-scattered) SEM image (Fig. 7.1.2) of a polished powder particle revealed pore-free dense powder particle with a good distribution of larger black and smaller grey hard phase particles dispersed within the Ni rich matrix which are shown with atomic number contrast. SEM microanalysis on these black (low atomic number) particles showed very high Cr content (up to 50%). Exact analysis of the smaller grey particles in the powder was difficult. The black particles were generally 2-4μm size whereas grey particles were of sub-micron size.

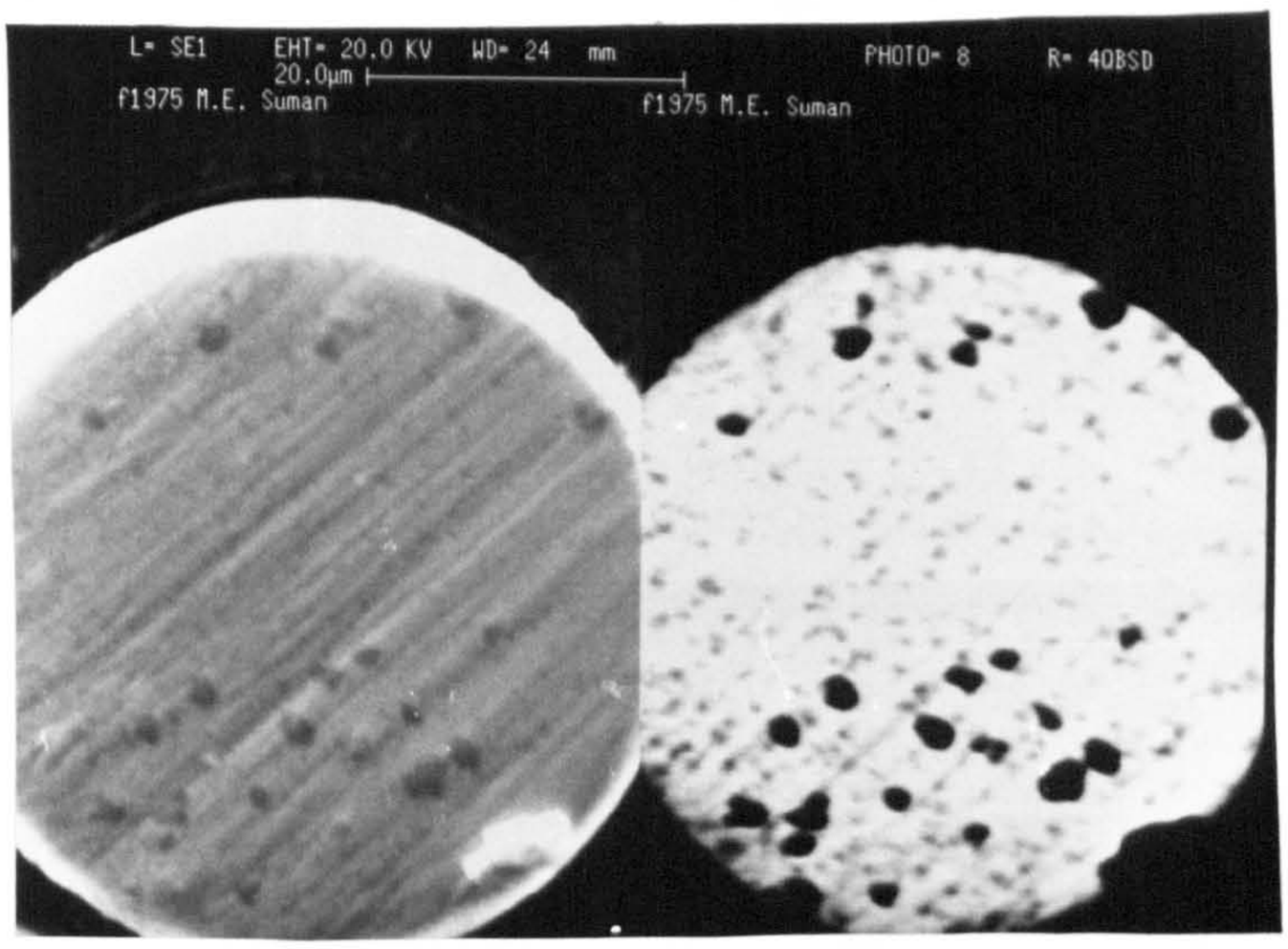


Figure 7.1.2 Split SEM micrograph of a polished single powder particle (left) secondary electron and (right) back scattered electron images.

The X-ray diffraction XRD patterns recorded for the powder particles revealed the presence of different phases shown in Fig. 7.1.3. The binder phase i.e. the matrix consists of a complex compound NiCrFe (74.95% Ni 15.47% Cr 8.8% Fe) shown by four major peaks, as such also reported by Ahn and Lee (1998). The hard phases, which form a skeletal network, comprised complex compounds of nickel chromium silicide '$Ni_{16}Cr_6Si_7$' and chromium carbide '$Cr_{23}C_6$'. Berget et al. (1998) have reported existence of similar $Cr_{23}C_6$ in 85WC-6.5Co-8.5Cr powder. The XRD database was examined closely in an attempt to correlate any of the peaks with borides but no significant correlation was found.

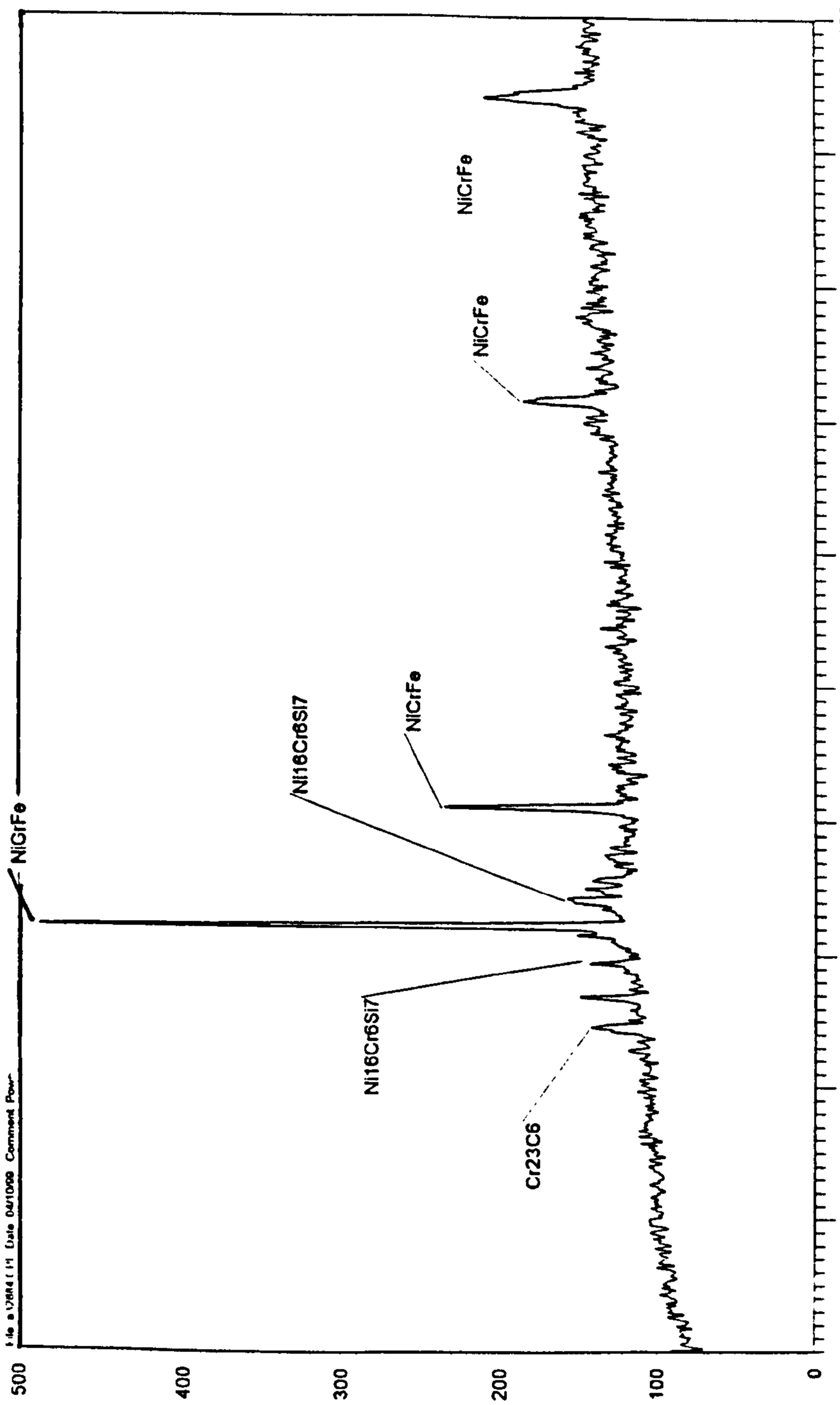


Figure 7.1.3 XRD pattern of *Coating* A powder

7.2 Pre-microscopy of coating

Coating A was supplied in two different batches and each batch was examined separately. Hereafter, each will be designated as '*Coating* AI' and '*Coating* AII'. The substrate type will be designated as '*Coating* A_i/ss' for stainless steel substrate and '*Coating* A_i/cs' for carbon steel substrate, where 'i' is the batch number. Coating characterisation was performed by examining the coatings both in plan and cross section. Microscopic observations confirmed that the coating sprayed on a stainless steel substrate is very similar to that sprayed on a carbon steel substrate and hence only micrographs of the former will be shown. Cross sectional examination revealed (Fig. 7.2.1) very low coating porosity (closed porosity 1.7-1.9% quantified by Image Analysis) and very low interfacial porosity for coatings of both batches. The coating thicknesses were found to be 300±20μm. Several splat lamellae without any hard particles were clearly distinguishable in Fig. 7.2.2a. Close examination of the coating in cross section has exhibited few coating defects. Formation of a void due to poorly adhered splat 'intersplat porosity', a possible pull out during polishing 'polishing void' and a defect around fully unmelted splat particle 'splat boundary gap' are clearly shown in Fig. 7.2.2b.

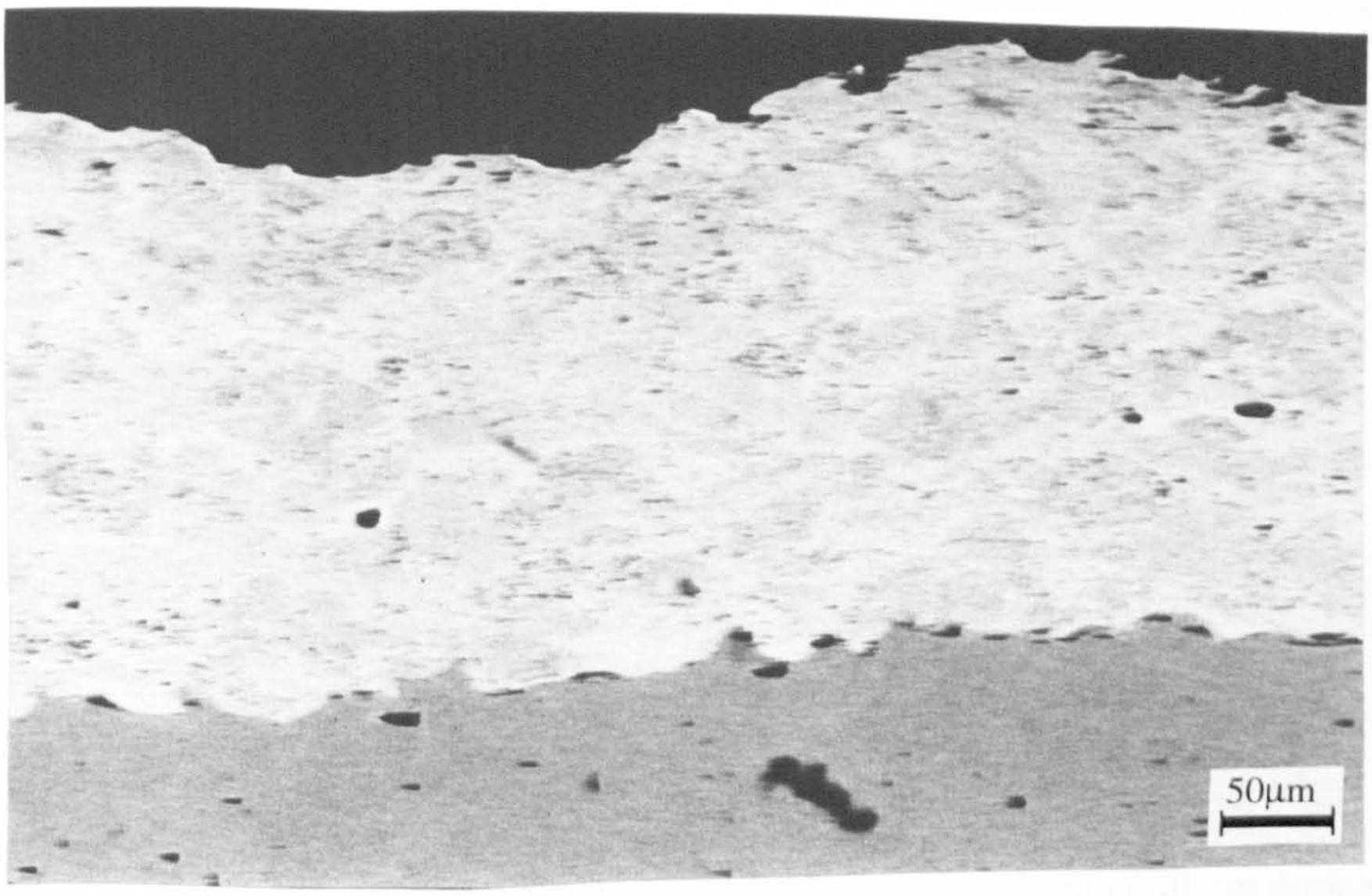


Figure 7.2.1 Back-scattered SEM cross sectional image of a polished as-received *coating A*, showing splat lamellae, micro roughness of the as-sprayed layer and a very little coating porosity.





Figure 7.2.2 Optical micrographs: a) abundance of several splats with metal matrix; b) showing: (top left) intersplat void; (bottom left) possible pull out during polishing; and (right) boundary void of fully unmelted powder particle.

Figure 7.2.3 shows a highly porous WC/CoCr coating as a cross reference to illustrate that such can possibly be resulted in a cermet coating obtained by similar thermal spray process presumably due to wrong spraying process parameters.

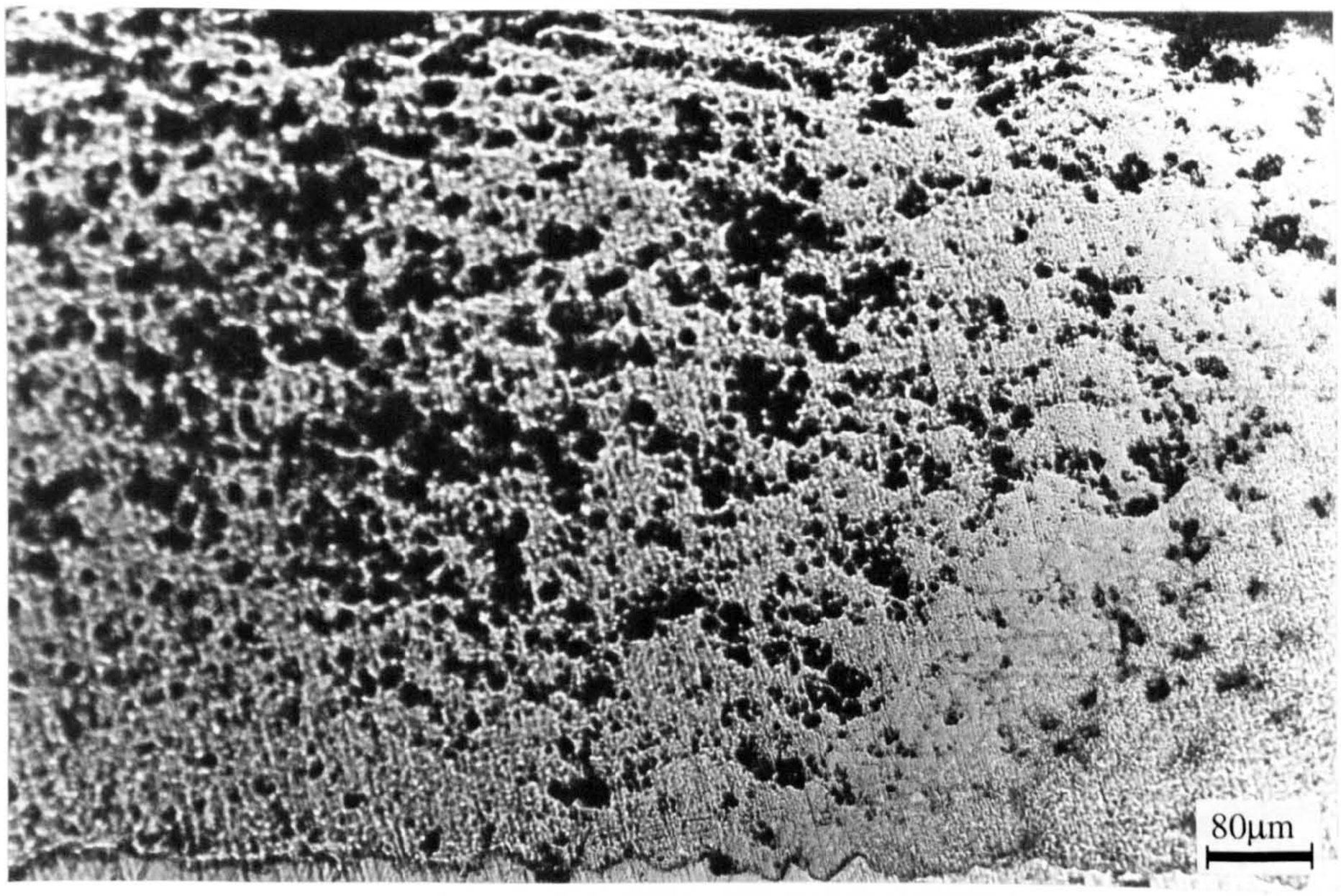


Figure 7.2.3 A highly porous WC/CoCr coating with a slight interfacial separation.

The back scattered SEM image (Fig. 7.2.4) of the polished specimen of *Coating* AI in plan showed clear abundance of black (low atomic number) globular hard phase particles and smaller particles of grey appearance similar to those shown in the powder particle. The particles were generally well distributed but with some regions containing a lower amount. Spot analyses were undertaken on hard-phase particles and the intervening metallic matrix. The ranges of many analyses are quoted in Table 7.2.1 - the range of the figures reflecting the difficulty in obtaining accurate analyses on such microscopic features of micron-size dimensions. Nevertheless, the data in Table 7.2.1 demonstrate that the black particles are highly rich in Cr. Table 7.2.1 also contains a "bulk" analysis which was obtained by analysing a relatively large area ($200\mu m^2$).

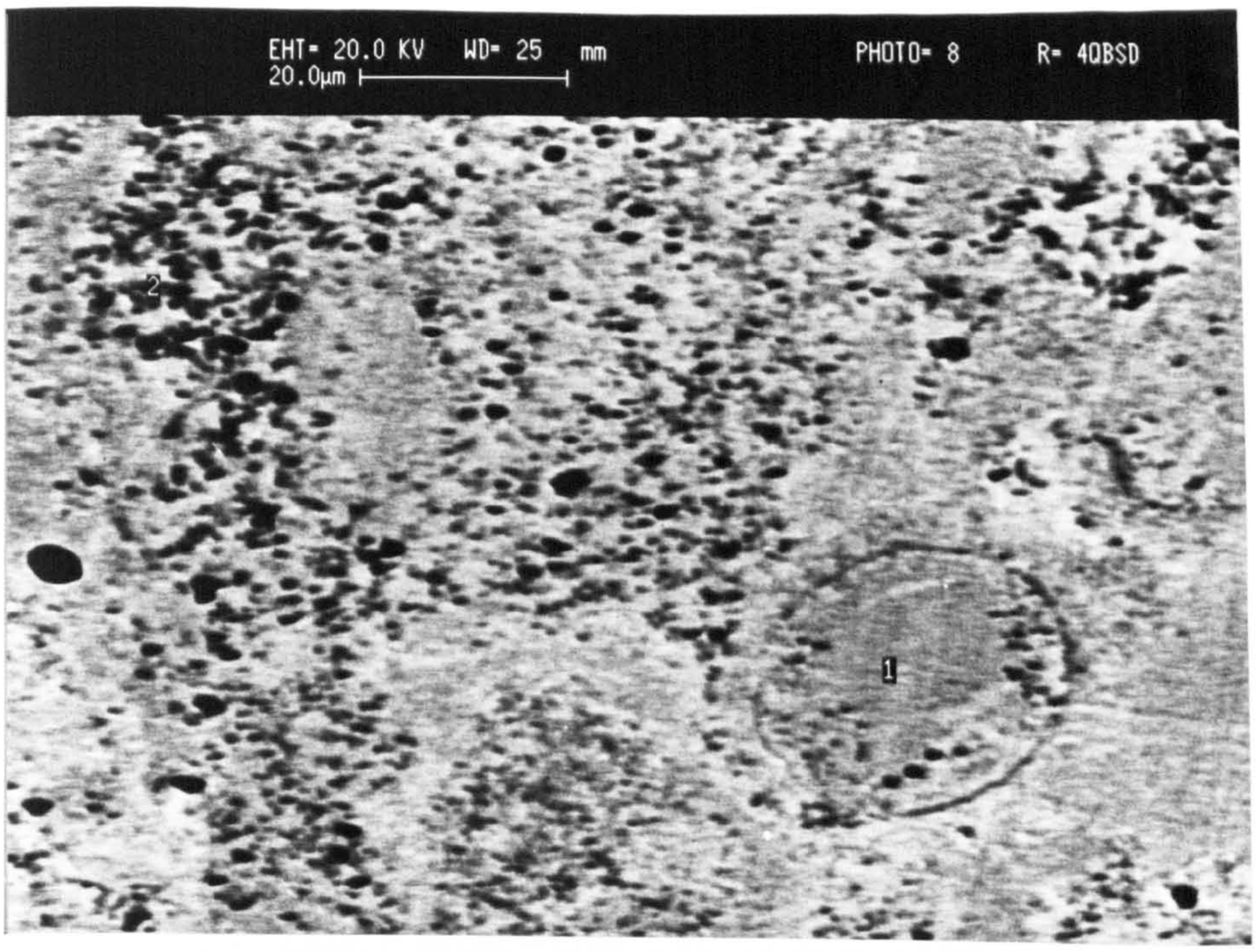


Figure 7.2.4 Back scattered SEM image of polished surface of as-received coating AI.

Elements	Matrix	Tiny grey hard phase	Black globular hard phase	Bulk
Fe	3.8-4.2	3.7-3.9	3.1-3.6	3.6-3.7
Ni	75.6-77.4	64.7-68.5	26.4-51.3	71.5-72.0
Cr	14.6-15.2	21.0-22.5	35-57.1	17.7-18.2
Si	3.8-4.0	2.6-3.0	2.5-3.8	3.5-3.7
Mo	0.0	0.0	0.0	0.0
Cu	< 1.5	< 0.3	< 0.02	1.2-1.8
C, B	not measured	not measured	not measured	not measured
Total	98.3-100.2	92.3-98.0	88.2-93.1	98.4-99.2

Table 7.2.1 Microanalysis on polished surface of as-received *Coating* AI (values shown in wt. %).

SEM observations revealed both batches were very much identical in their microstructures but EPMA results exhibited abundance of Mo in *Coating* AII accounting up to 6.4 wt% taken from the bulk analysis. Split SEM micrographs of *Coating* AII show clear abundance of black globular (Fig. 7.2.5a) and tiny grey (Fig. 7.2.5b) hard phase particles. EPMA results of black hard phase '1', matrix '2', grey hard phase '3' and area analysis of 100μm^2 taken are shown in Table 7.2.2. Figure 7.2.5c shows splat '1' containing mainly black particles, splat '2' and '3' containing mainly tiny grey particles. EPMA analysis of a 10 x 10μm area was taken on each particle, which showed variation in Ni and Mo contents (Table 7.2.3).

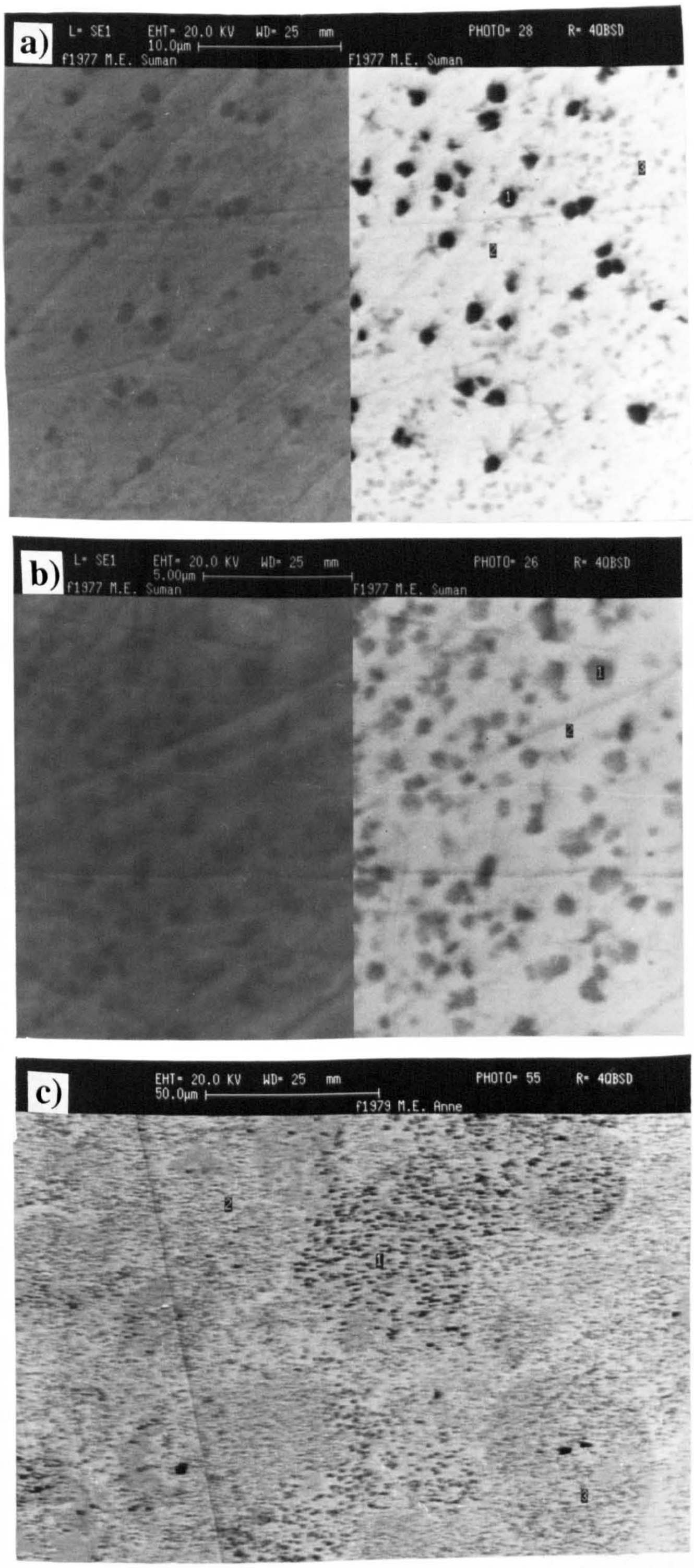


Figure 7.2.5 a) Split SEM image of *Coating* AII showing black globular and tiny grey hardphase particles embedded in the NiCrFe matrix; b) split SEM image of above tiny grey hard particles; c) back-scattered image showing several clear splats (1) containing many black hard phase particles (2, 3) containing mainly tiny grey hard phase particles.

Elements	Matrix	Tiny grey hard phase	Black globular hard phase	Bulk
Fe	2.6-2.9	2.1-2.4	3.1-3.6	2.8-3.2
Ni	79.0-82.0	40.1-44.2	35.2-51.4	69.0-71.3
Cr	8.7-9.8	29.0-35.3	28.1-50.3	18.2-18.5
Si	4.6-5.0	2.0-2.3	2.7-3.4	3.9-4.0
Cu	2.3-2.6	1.1-1.3	0.0-0.1	1.5-1.9
Mo	1.9-2.3	13.7-15.7	0.0-0.5	4.5-6.4
Total	98.6-101.2	92.3-94.8	94.7-100.5	99.3-100.4

Table 7.2.2 Microanalysis on polished surface of as-received *Coating* AII (values shown in wt. % taken from 5 analyses)

Elements	Area 1	Area 2	Area 3
Fe	3.2	2.6	2.5
Ni	70.2	62.7	62.5
Cr	16.5	17.9	17.5
Si	3.4	3.7	3.7
Cu	1.1	1.9	1.6
Mo	1.0	5.9	6.8
Total	94.9	95.4	94.5

Table 7.2.3 Average area (10 x 10μm) analyses of different splats (Fig. 7.2.5c) on polished surface of as-received *Coating* AII (values shown in wt. % taken from 3 analyses).

The bulk hardness of *Coating* AI and *Coating* AII were measured to be quite similar. The values measured in plan on a polished surface under indentation load of 500g are shown in Table 7.2.4. The range of microhardness was rather wide because of the different types of hard phase particles present in the coating and possibly due to porosity as well (Karimi and Verdon, 1993) and this range may account up to 15% (Reiners et al., 1998). The hardness value of UNS S31603 is also tabulated for the comparative purpose of this project. Kreye et al. (1998) have found slightly higher microhardness value for similar type of coating, which is listed in the table below.

Material	Process	HV (Indentation load, gms)	Porosity %	Density g/cm^3
Coating AI	HVOF	513 – 591 (500)	1.9	5.9
Coating AII	HVOF	527 – 587 (500)	1.7	6.2
NiCrBSi (Kreye et al., 1998)	HVOF JetKote	670 (300)	-	-
UNS S31603 (Kreye et al., 1998)	Bulk	165 (300)	-	7.97

Table 7.2.4 Properties of the coatings and a stainless steel.

Figures 7.2.6 and 7.2.7 show X-ray diffraction patterns for the coatings AI and AII respectively. As also indicated by SEM images, it has been confirmed that there are no phase transformations during the spraying process and the major peaks retained as in the powder form. The actual structural form of the Mo and Cu detected by microanalysis in coating AII could not be identified by XRD. Also, a peak at $2\theta = 47°$ in Fig. 7.1.3 of the powder seems to have slightly transformed to another phase resulting in different peaks in both coatings during spraying (Fig. 7.2.6 and Fig. 7.2.7) but could not be detected.

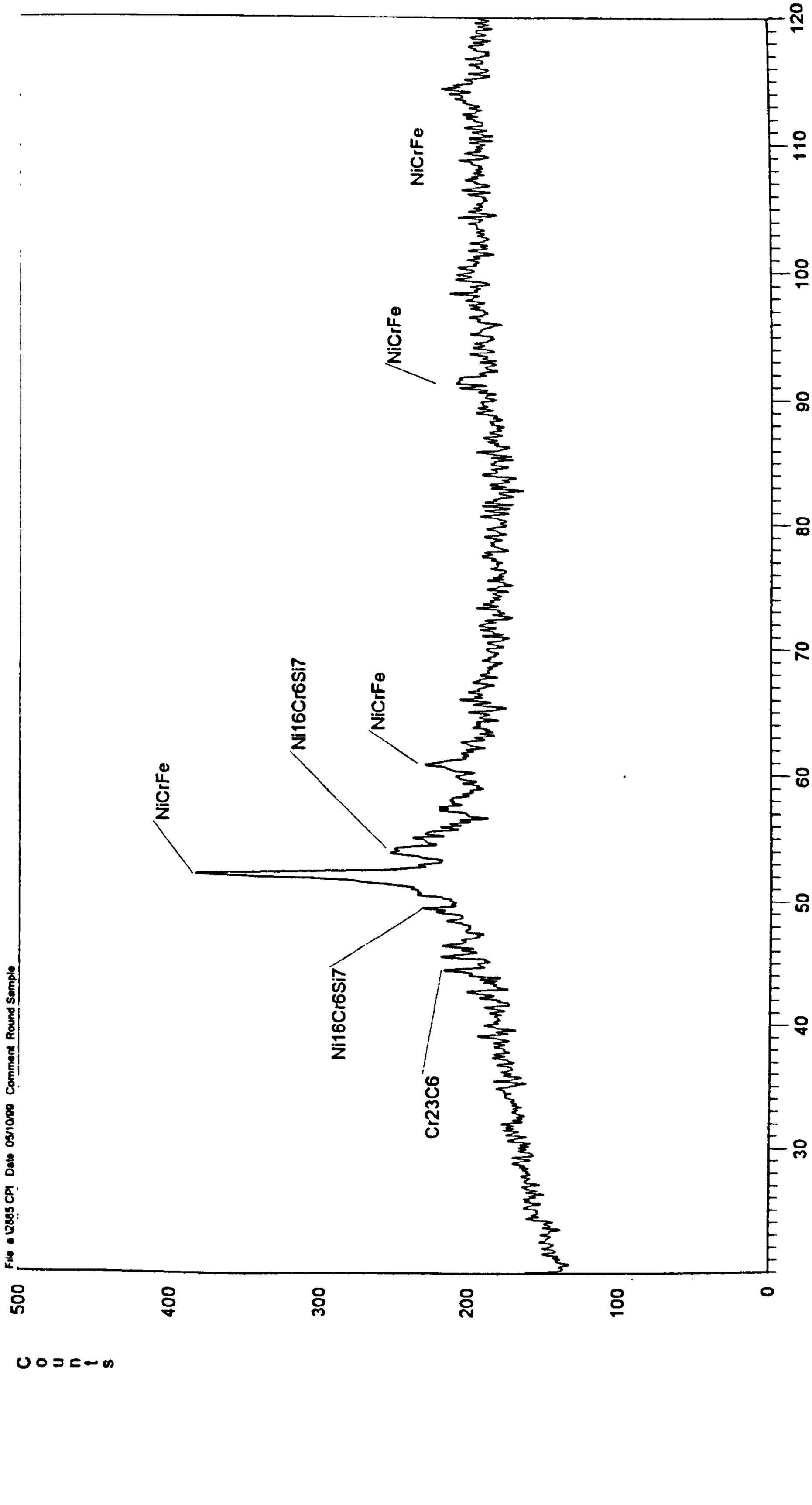


Figure 7.2.6 XRD patterns of *Coating* AI

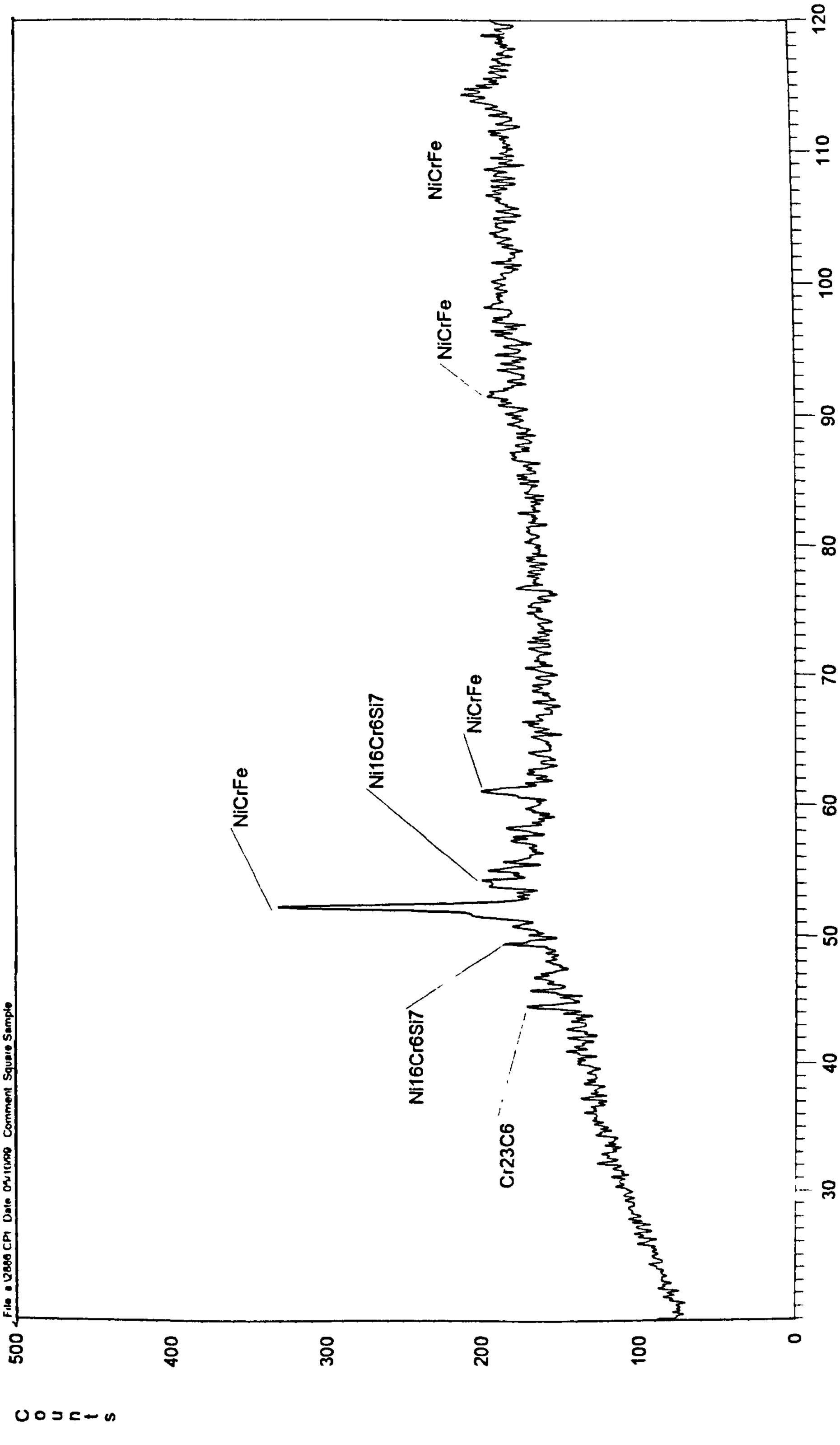


Figure 7.2.7 XRD patterns of *Coating* AII

The atomic force microscopy (AFM) image in Fig. 7.2.8 shows the surface roughness and micro-topographic detail of the polished surface (area 100x100μm) of the Coating AI. The image shows hardphase particles protruding out from the binder matrix.

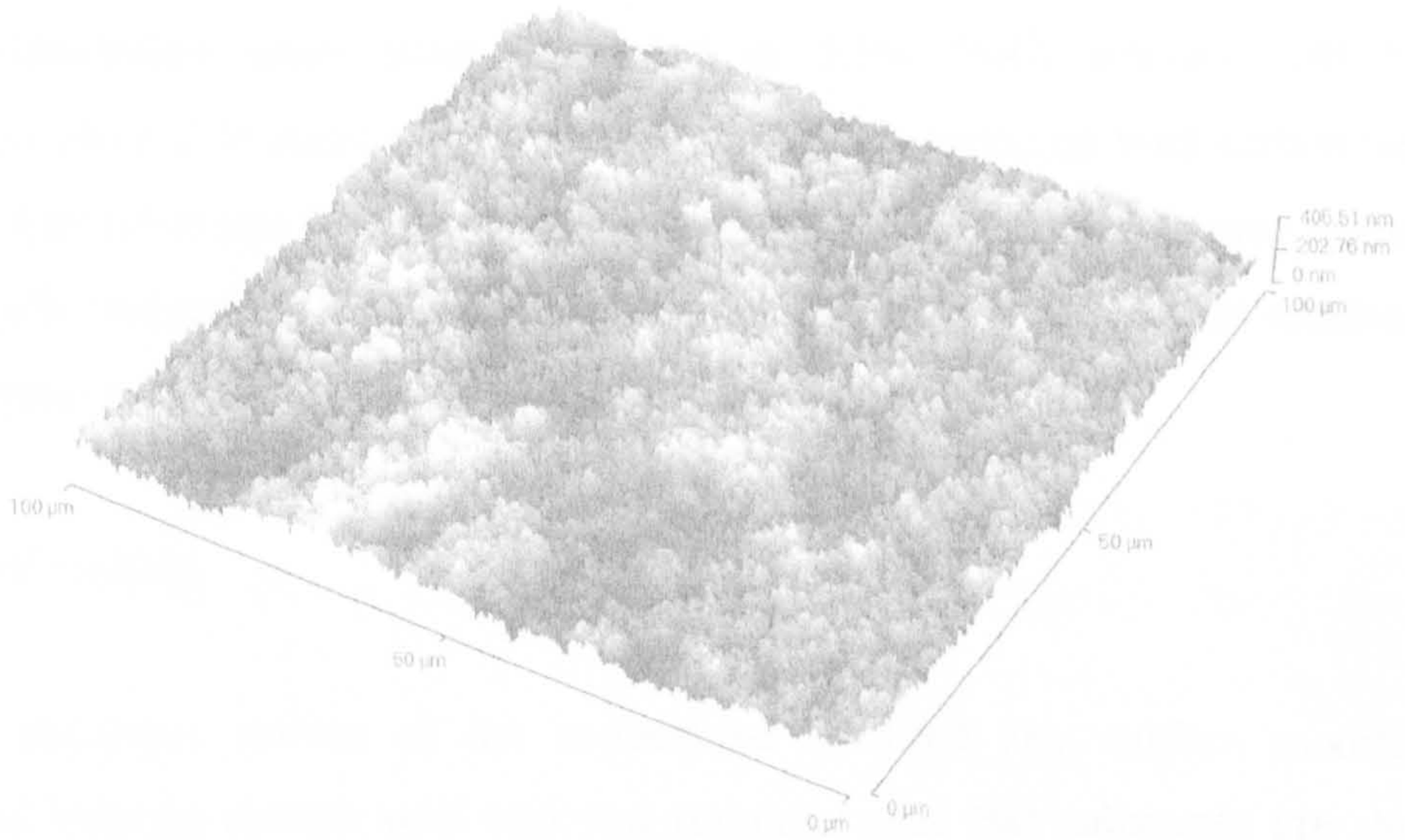


Figure 7.2.8 AFM image of Coating AI showing hardphase particle protruding out from the surface.

Quantification of the relative hardness of the hardphase particles with respect to the binder matrix has been attempted by using AFM. The force spectroscopy measurements were taken on the binder matrix and the hardphase particle and the slope in the form of deflection per distance travelled was recorded. A difference in the slope was obtained as shown in the Table 7.2.5.

No.	Area indented	Slope nA/nm
1	Hardphase	0.114
2	Hardphase	0.116
3	Matrix	0.120
4	Matrix	0.121

Table 7.2.5 Force spectroscopy measurements of matrix and hardphase particle.

7.3 Corrosion of coating Al and stainless steel

Anodic Polarisation

Anodic polarisation scans were conducted in 3.5% NaCl solution (pH 8.2) at temperature 18±2°C in static condition. The coating was tested on both carbon steel and stainless steel substrates to assess if there is significant effect of substrate material on the corrosion resistance. Moreover, coating surfaces were tested on 'as-received' and after polishing to 6μm diamond 'polished' conditions.

As received coating

Anodic polarisation curves of the as-received (without any surface modification) *coating* Al both on carbon steel (cs) and stainless steel (ss) substrates are shown in Fig.7.3.1 which also displays for comparative purposes plots for uncoated carbon steel (BS970 En8) and stainless steel (UNS S31603) specimens.

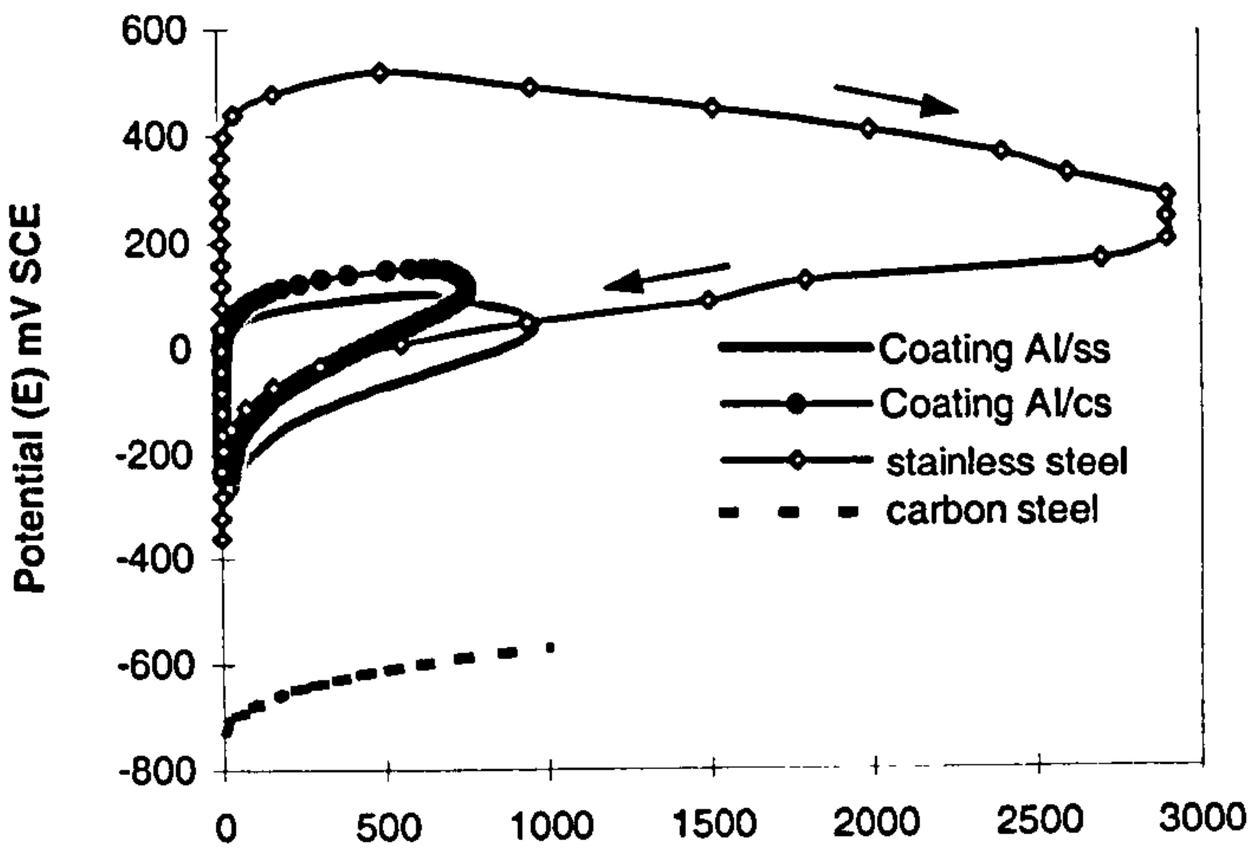


Figure 7.3.1 Anodic polarisation of a stainless steel UNS S31603 (ground to 1200 grit) and as-received coating compared to 'active' corrosion behaviour of carbon steel in 3.5% NaCl at 18±2°C (arrows showing forward and reversed scan of the polarisation curve).

The results in Fig.7.3.1 demonstrate the contrasting behaviour of the coating compared to uncoated carbon steel. On increasing the potential from E_{corr}, an immediate increase in current was measured on carbon steel. In contrast the coating followed classic passive behaviour by transmitting only very small currents comparable with the stainless steel (UNS S31603). On the coating, potentials beyond -10÷0mV labelled the breakdown potential 'E_b' (Fig. 7.3.2) the current increases rapidly, signifying a rise in the anodic activity and the onset of corrosion attack. However, stainless steel displayed passive behaviour until breakdown at significantly higher potential 'E_b' of about 350mV (SCE). An interesting feature of the coating was that its corrosion behaviour was very reproducible with a negligible scattering of E_{corr}, E_b and i_{max}. The E_{corr} values were between -240 and -285mV for as received coatings. The breakdown potential scattering was 0±14mV unlike the stainless steel whose E_b value showed scattering in a range exceeding 100mV. The coating was also shown to have difficulty in repassivating, displayed by its no intersection between the forward and reversed scans.

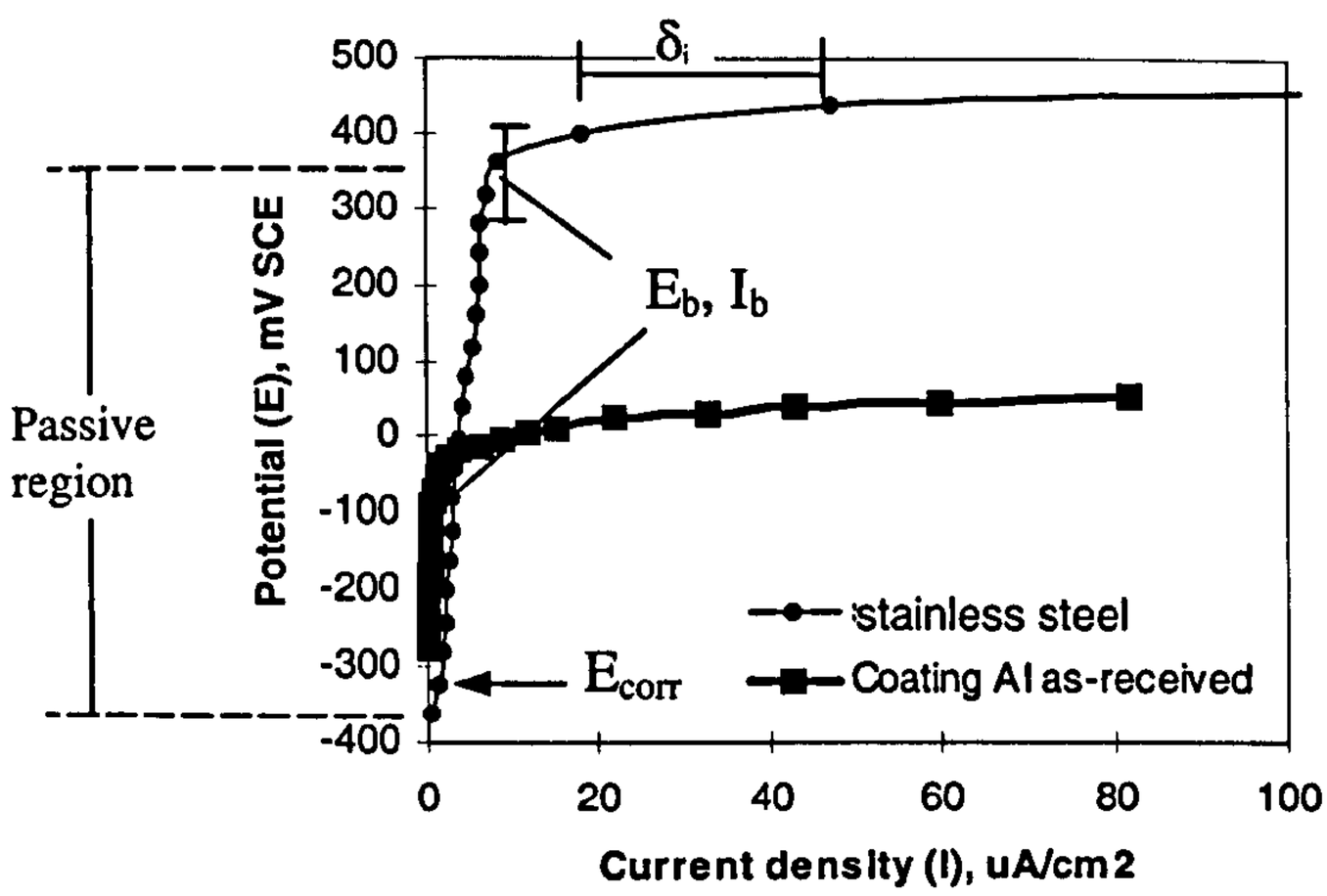


Figure 7.3.2 Stainless steel showing higher initial current density in a passive region E_b-E_{corr} and a scatter in breakdown potential (E_b is defined such as the current density increment $(i_n-i_{n-1}) \geq 5\mu A/cm^2$).

Coating AI revealed quite similar trend of the hysterisis loop as the stainless steel with greater difficulty to repassivate but with significant smaller loop mimicking the coating's susceptibility to localised attacks. A bigger hysterisis loop in Fig. 7.3.1 of the stainless steel compared to a smaller loop of the coating generally signifies that stainless steel is more prone to severe rate of localised attacks such as crevice or pitting corrosion

(Fig. 7.3.8 and Fig. 7.3.9). Despite the fact that stainless steel has retained its passivity to much higher positive potential, it registered a very large increase in current steps denoted by 'δ_i' for identical potential increment as shown in the Fig. 7.3.2, where 'δ_i' is a current increment after the breakdown current 'I_b' during the forward scan. Moreover, stainless steel recorded an enormous amount of current reaching maximum current density exceeding 2800μAcm^{-2} after which it started the reversed scan. This might signify the rapid propagation of localised attacks once they have been initiated. A very noticeable behaviour shown in Fig. 7.3.2 was that stainless steel which indeed is regarded as a passive material due to presence of a protective oxide film exhibited the passage of a small amount of initial current in the passive region unlike the coating which registered a very negligible amount of current with in the passive range as manifested by its forward scan.

Effect of polishing

Significant changes in the anodic polarisation characteristics were observed on the coating once it was subjected to polishing. The E_b value has significantly lowered with reduction in E_{corr}. Figure 7.3.3 shows the replicate experiments on polished surfaces of the coating under similar experimental condition.

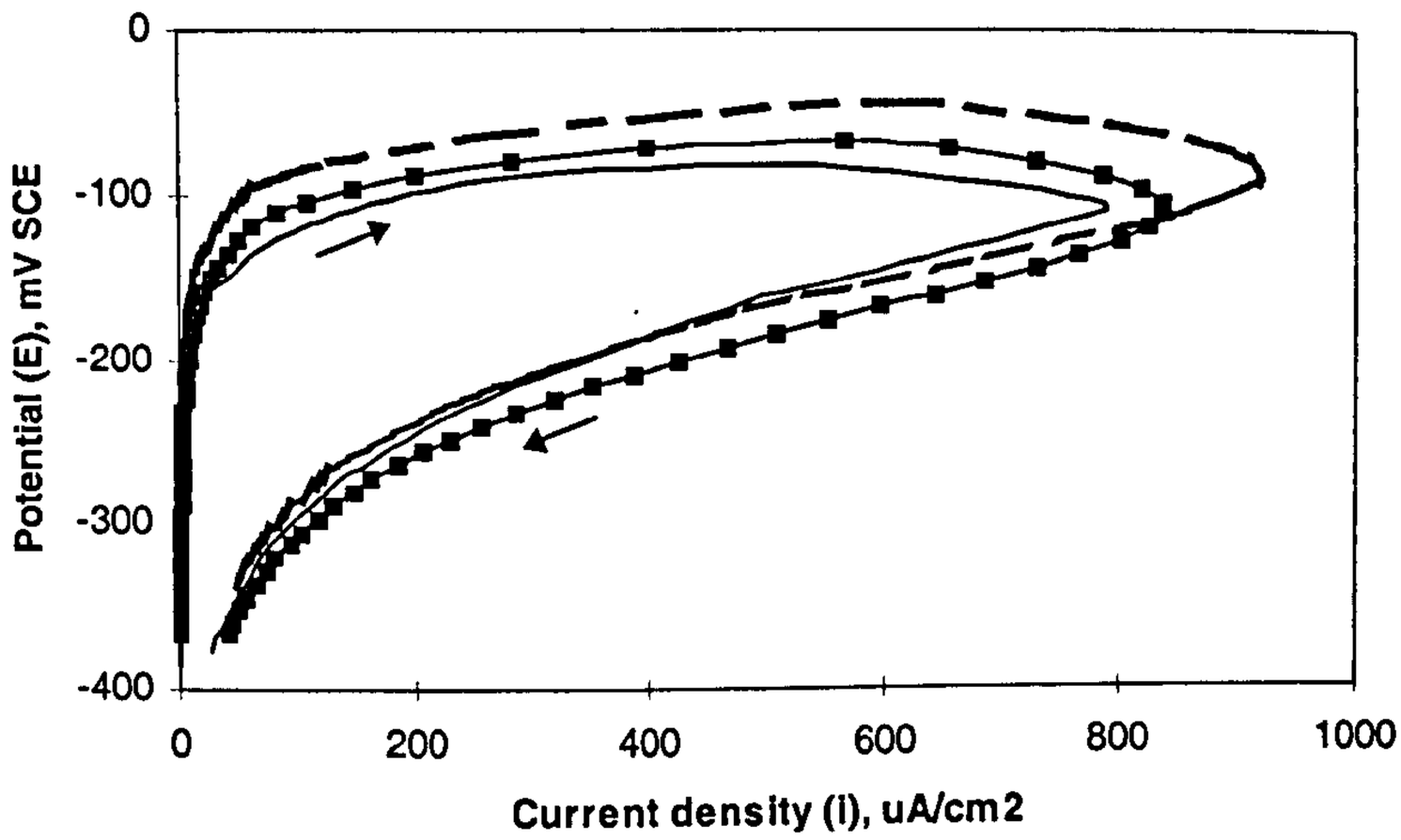


Figure 7.3.3 Replicate experiments on polished surfaces of Coating AI on a stainless steel substrate showing no repassivation behaviour manifested by no intersection between the forward and reversed scans shown by arrows.

Figure 7.3.4 is an expanded plot of the forward scan showing a small amount of initial current recorded within the passive region for coating AI/ss, which might suggest a semi-passive behaviour once it is subjected to polishing compared to a classic passive behaviour manifested by the as-received coating. Coating AI/cs showed similar effect and so only the former is shown in the figure below.

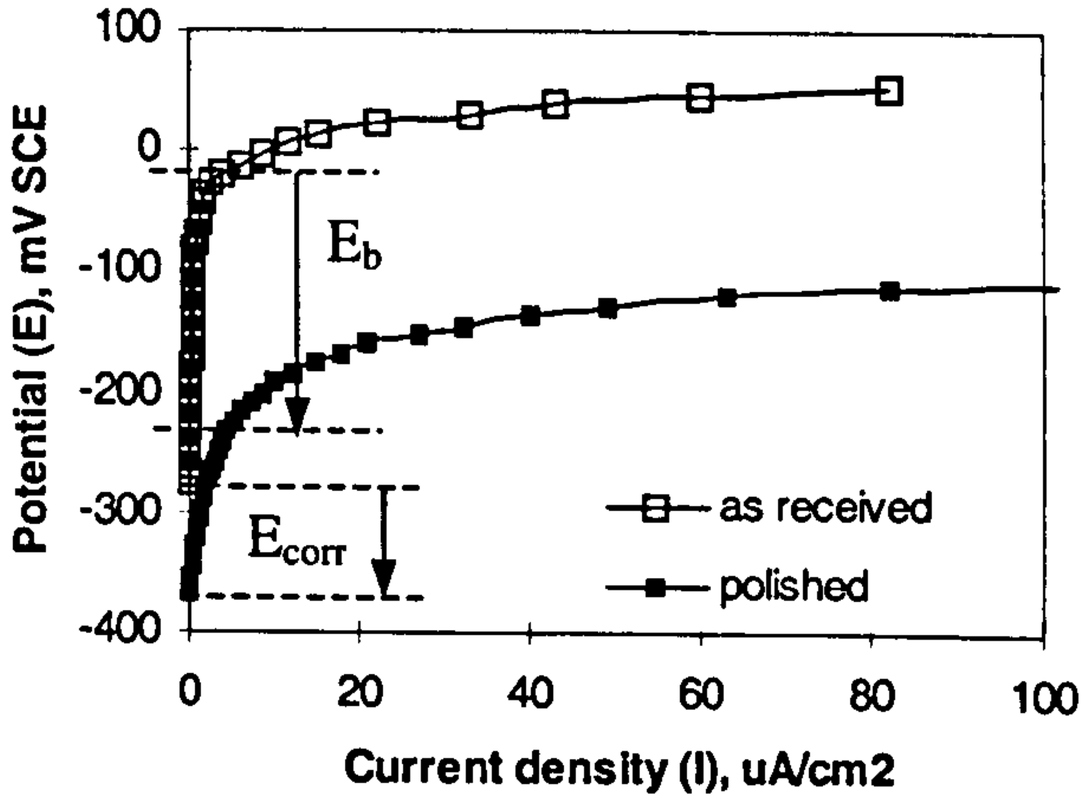


Figure 7.3.4 Effect of polishing on coating AI/ss, resulting reduction in E_b and E_{corr}.

Effect of substrate material

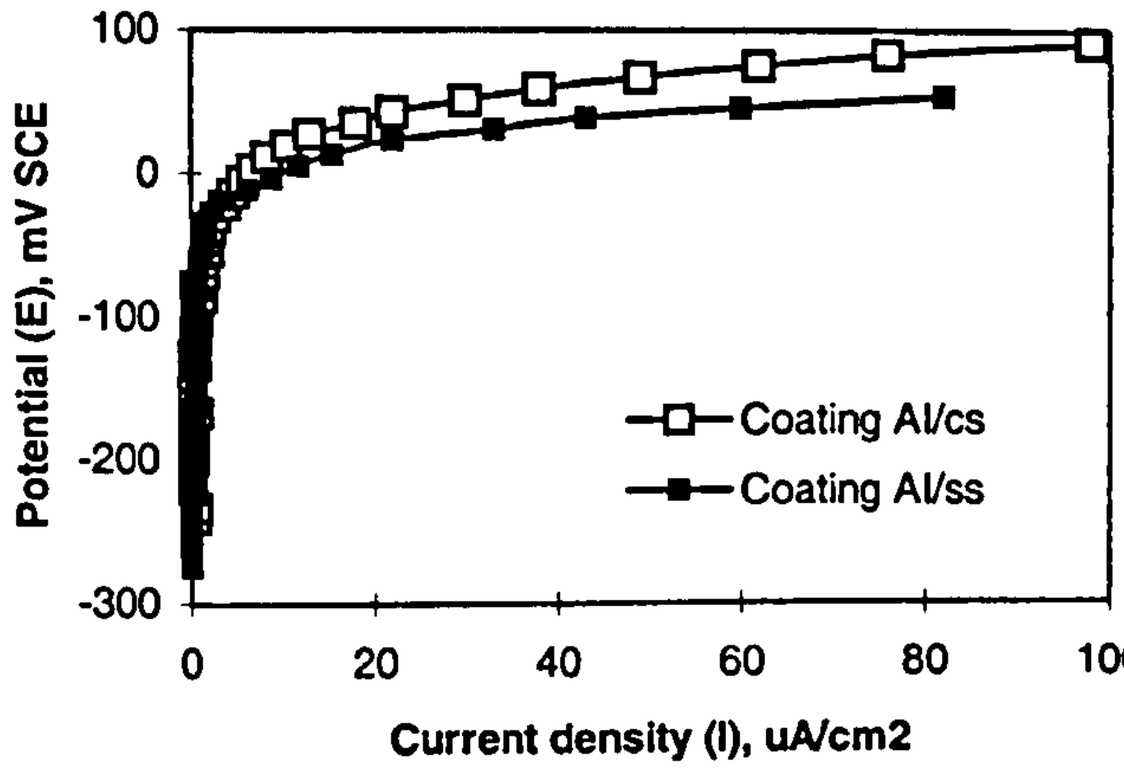


Figure 7.3.5 Expanded forward scans of as-received coating AI with carbon steel and stainless steel substrates.

Several experiments were performed on the coating with both carbon steel and stainless steel substrates. Coating on either substrate displayed very similar polarisation curves as shown in Fig. 7.3.1. The forward scans of the coatings in Fig. 7.3.5 displayed very identical corrosion behaviour of the coatings. This indicates the very important point that in these tests it is the coating itself, which is under scrutiny and not the substrate. The parameters such as 'E_b', 'E_{corr}', 'E_b-E_{corr}' and 'i_{max}' for the coating are listed in Table 7.3.1 below.

Coating	E_b, mV	E_{corr}, mV	E_b-E_{corr}, mV	i_{max}, $\mu A/cm^2$
AI/ss as-received	0	-240	240	759
AI/cs as-received	-5	-273	268	969
AI/ss polished	-153	-352	199	917
AI/cs polished	-164	-384	220	759

Table 7.3.1 Average values of 'E_b', 'E_{corr}', extent of passive range 'E_b-E_{corr}' and maximum current density 'i_{max}' of *Coating* AI (Values are average of 3 measurements with scattering of ±7%).

Cathodic Polarisation Test

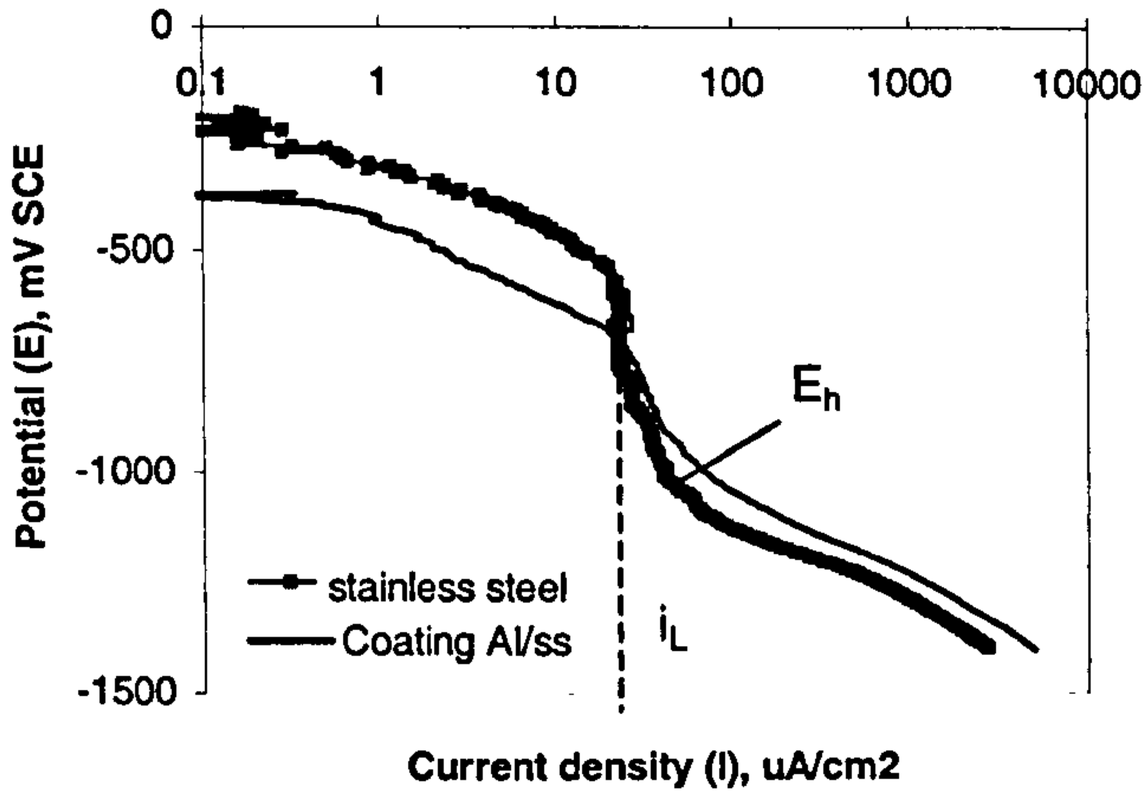


Figure 7.3.6 Cathodic polarisation of as-received *Coating* AI and UNS S31603 (1200 grit) at 18°C

A cathodic polarisation curve for the coating AI is shown in Fig. 7.3.6 in comparison to the stainless steel. The oxygen reduction cathodic reaction is clearly under diffusion control on the stainless steel as shown by the sharp limiting current density 'i_L'. However, on the coating the reaction appears to be under more activation control. Hydrogen evolution started once the potential reached a sufficient negative value of

about -1000 ÷ -1100mV, after which the cathodic currents increased very rapidly and exhibited Tafel behaviour again - typical of the onset of the alternative cathodic reaction, e.g. hydrogen evolution occurring at these relatively negative potentials. Stainless steel had similar cathodic polarisation curve but with a larger effect of concentration polarisation – due to more positive E_{corr}. In summary theses results demonstrate that the cathodic polarisation characteristic of the coating is similar to those of the stainless steel.

Post experimental examination

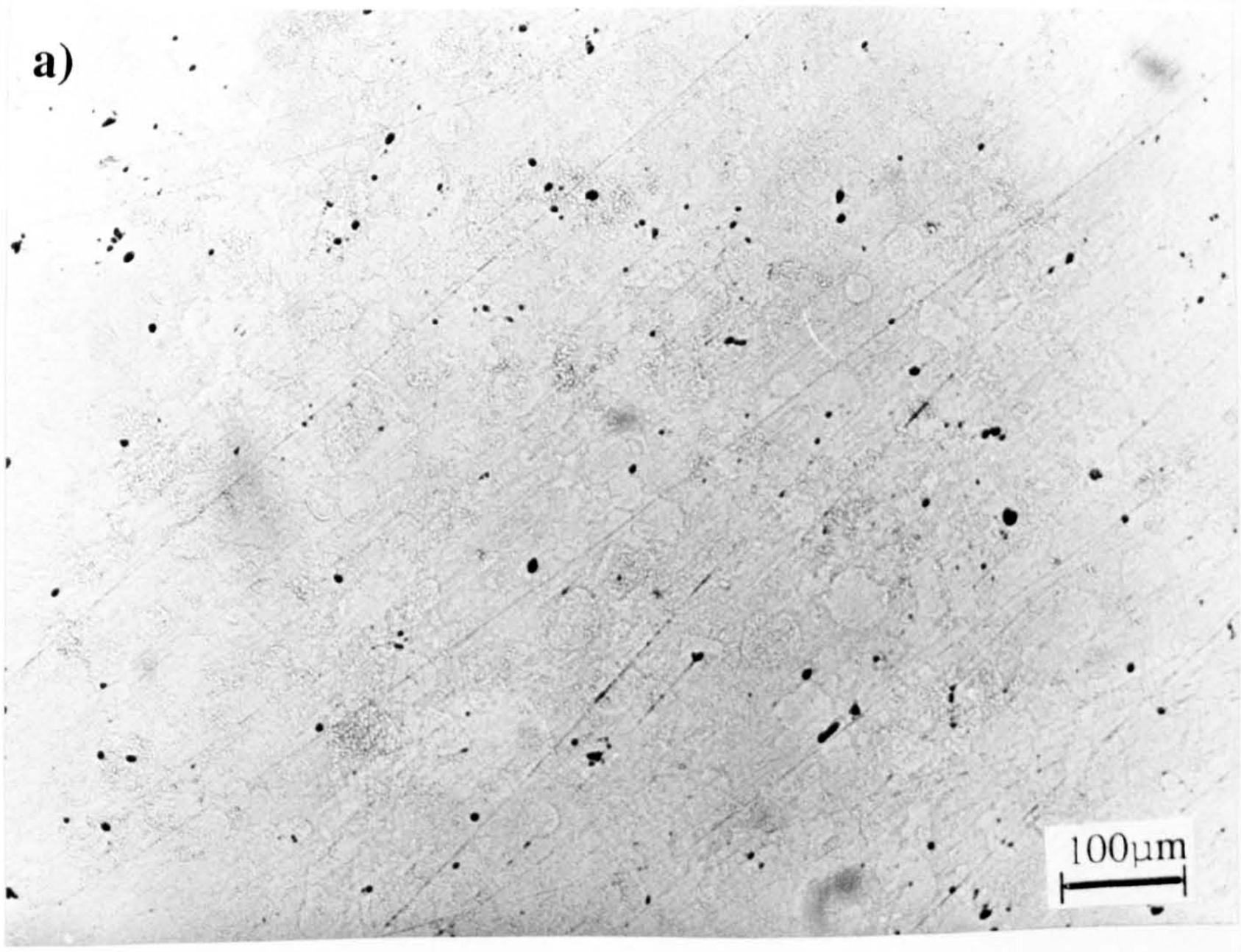
Examination using light and scanning electron microscopy was used to identify the corrosion mechanisms of the coating. Localised attack in the form of pitting and crevice corrosion occurred on the coating surface on a macro scale and is comparable with the types of attack seen on the stainless steel in saline environment. Another mechanism encountered was 'general' attack associated with attack that affects more extensive areas of the exposed surface. In addition, attack on a more micro scale was clearly evidenced on the cermet coating. These aspects are described in detail in the following paragraphs.

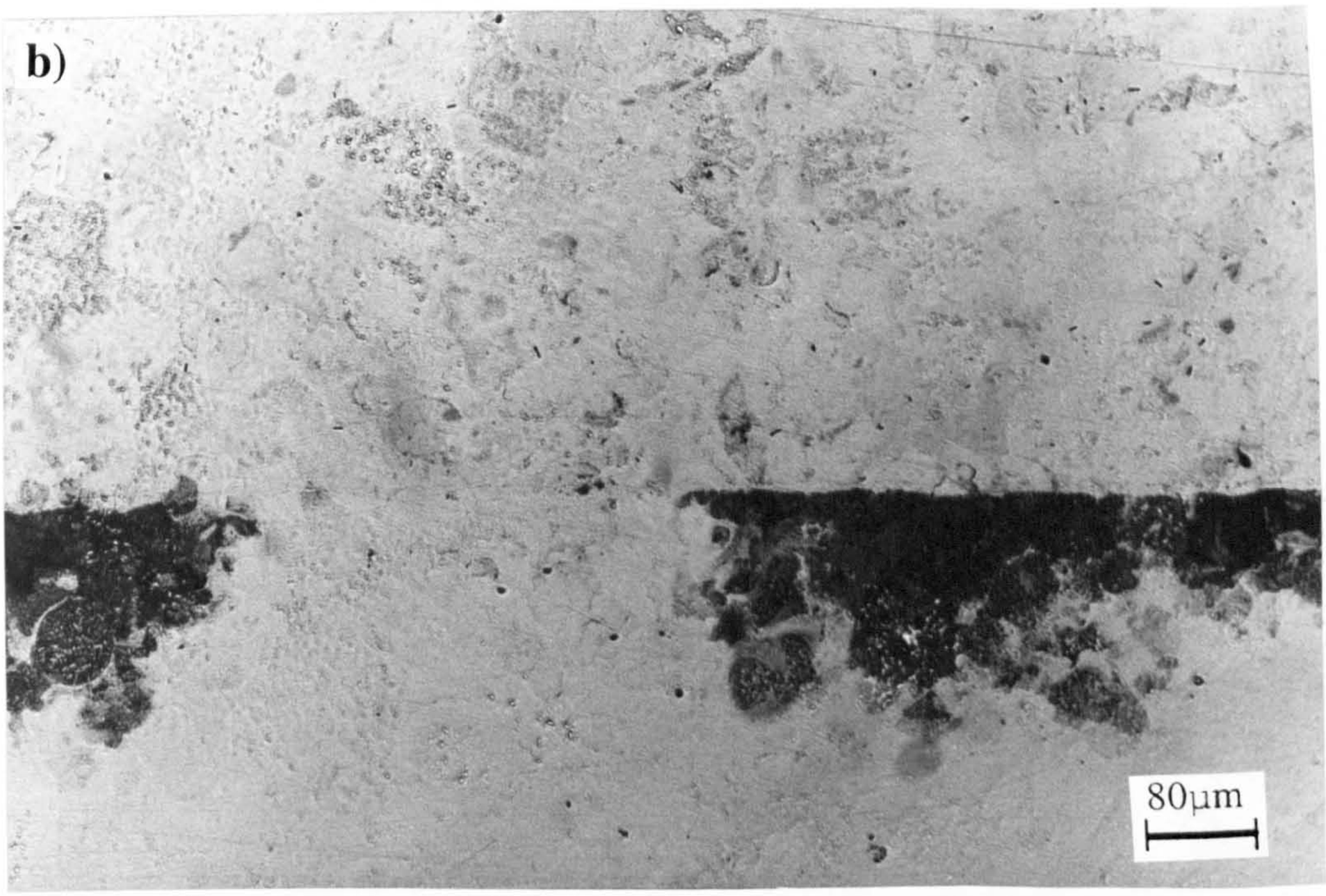
Examination after anodic polarisation

Microscopic examinations revealed that corrosion of the coating specimen with either carbon steel or stainless steel substrate is identical and hence only specimen surface of the latter is considered for microscopic results. Figure 7.3.7a shows a light micrograph of a polished surface of coating AI prior to the experiment. Particle splats of different sizes, which contain tiny hard phases and few with pure matrix, are quite clear. A small amount of black dots were present primarily resulting from the polishing effect. The complexity of corrosion mechanism of such a multiphase coating is shown in Fig. 7.3.7b after anodic polarisation in static saline solution at ambient temperature, which clearly shows localised attack in the form of crevice corrosion beneath the lacomit varnish. The lacomit strip, which was used to seal the coating/substrate interface, was carefully removed after the polarisation test. The darker strip in the picture represents severe crevice attack with several isolated splats being fully corroded. The upper area that was exposed to the saline solution during polarisation, shows remarkably less attack

than the crevice region but general attack was noticeable all over the exposed area. The bottom area away from the crevice region, which was fully covered with the lacomit paint, showed virtually no attack after the test. The crevice length ranged in between 11-15% of the total perimeter of the lacomit applied. Further examination under higher magnification (Fig. 7.3.7c) shows the following attack mechanism:

- Severe crevice was associated with corrosion of the matrix leaving the unsupported hardphase particles to fall eventually.
- On the exposed area macro-pit formation in the form of splat boundary attack and the eventual fall (flaking) of the whole splat leaving macro pit shown by dark areas. The pit depths were in the range of 3-6μm, which suggests the removal of individual splats. The circular black pit was associated with the flaking of a single splat after the splat boundary has corroded and pits of irregular shapes were formed due to removal of much smaller splat particles.
- Higher corrosion of the matrix in areas where hard particles were distributed densely.
- Micro-galvanic attack around the hardphase/matrix interface that results in the fall of tiny hard particles leaving micro-pits (Fig.7.3.7d).




b)
80μm

c)
20μm

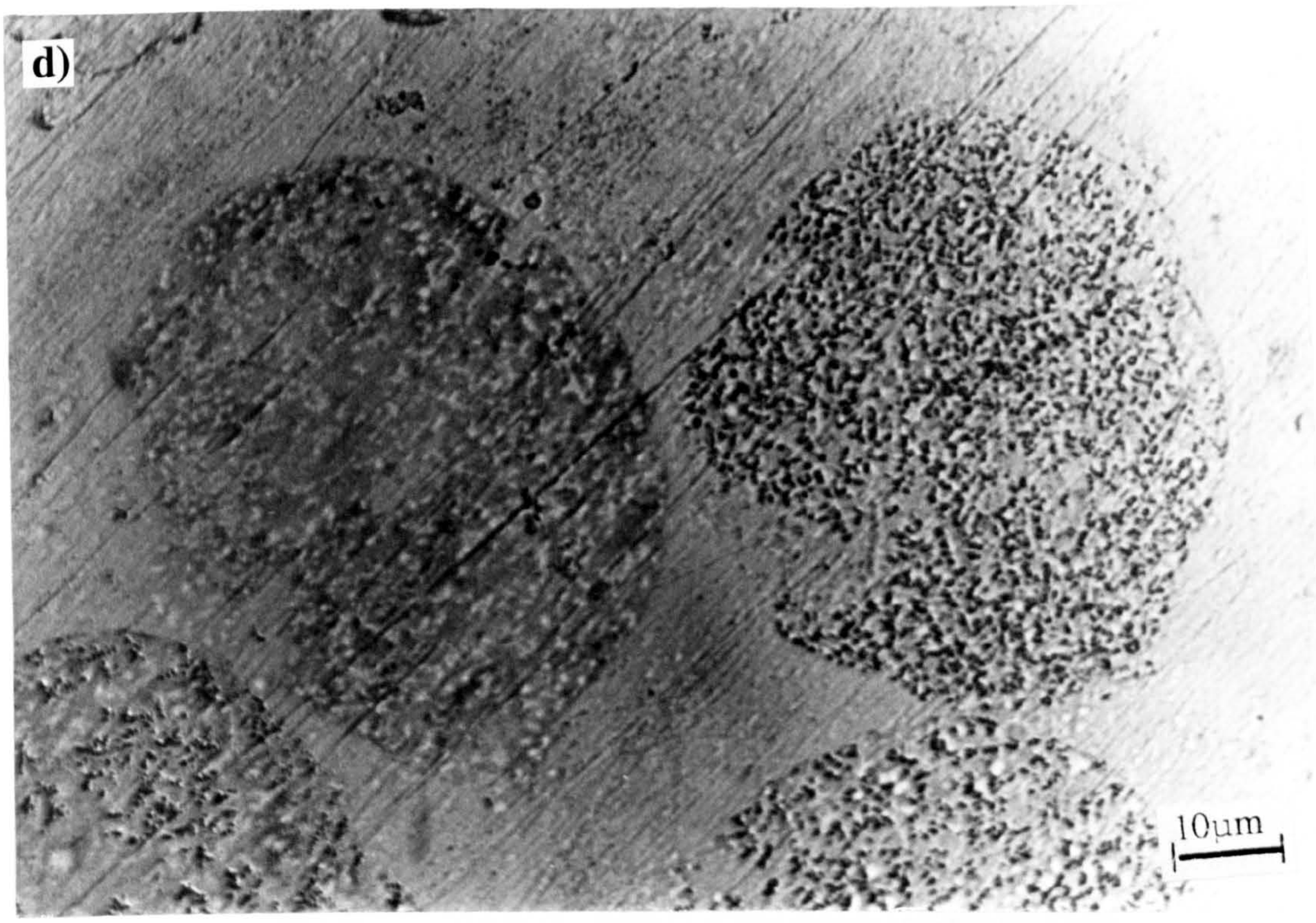


Figure 7.3.7 Corrosion mechanism of the *Coating* AI: a) polished surface of the surface prior to polarisation test; b) crevice corrosion after anodic polarisation in 3.5%NaCl at 18°C; c) macro-pit due to splat dislodgement; and d) micro-pits due to removal of hard particles after polarisation

In the case of stainless steel as shown in Fig. 7.3.1 with a very high current density achieved during anodic polarisation and with a very large loop area exhibited much severe localised attack in the form of severe crevice and pitting corrosion was observed. Figure 7.3.8a shows extensive crevice corrosion of the stainless steel surface at the lacomit/surface interface. Almost 80% of the total length of the applied lacomit showed a very severe crevice attack, which had been further propagated as the onset of the corrosion increases. This crevice corrosion was found to be associated with intergranular attack at the grain boundaries (Fig. 7.3.8b). On further examination at higher magnification, extensive pitting was found under the crevice itself (Fig. 7.3.8c) which also consisted of several intergranular attacks within the pit itself and finally falling out individual grains.

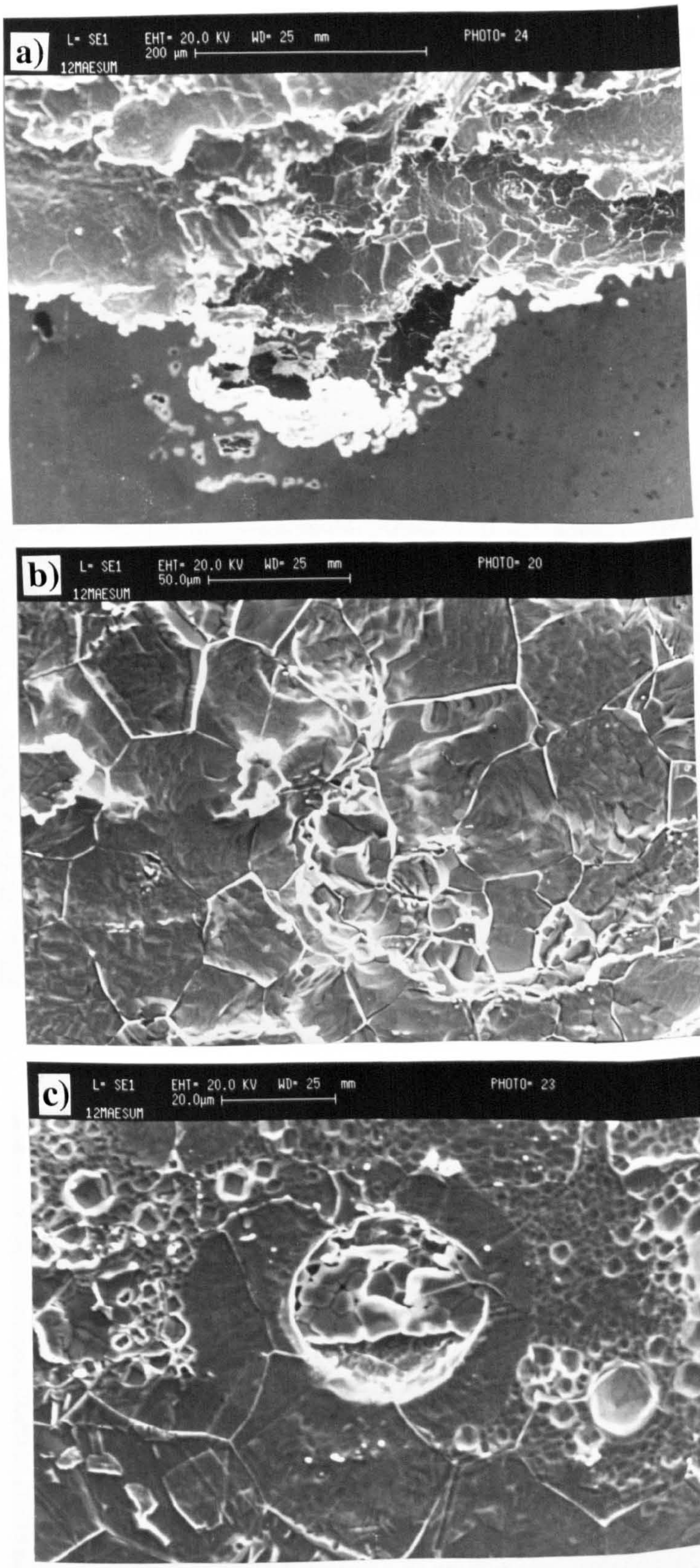
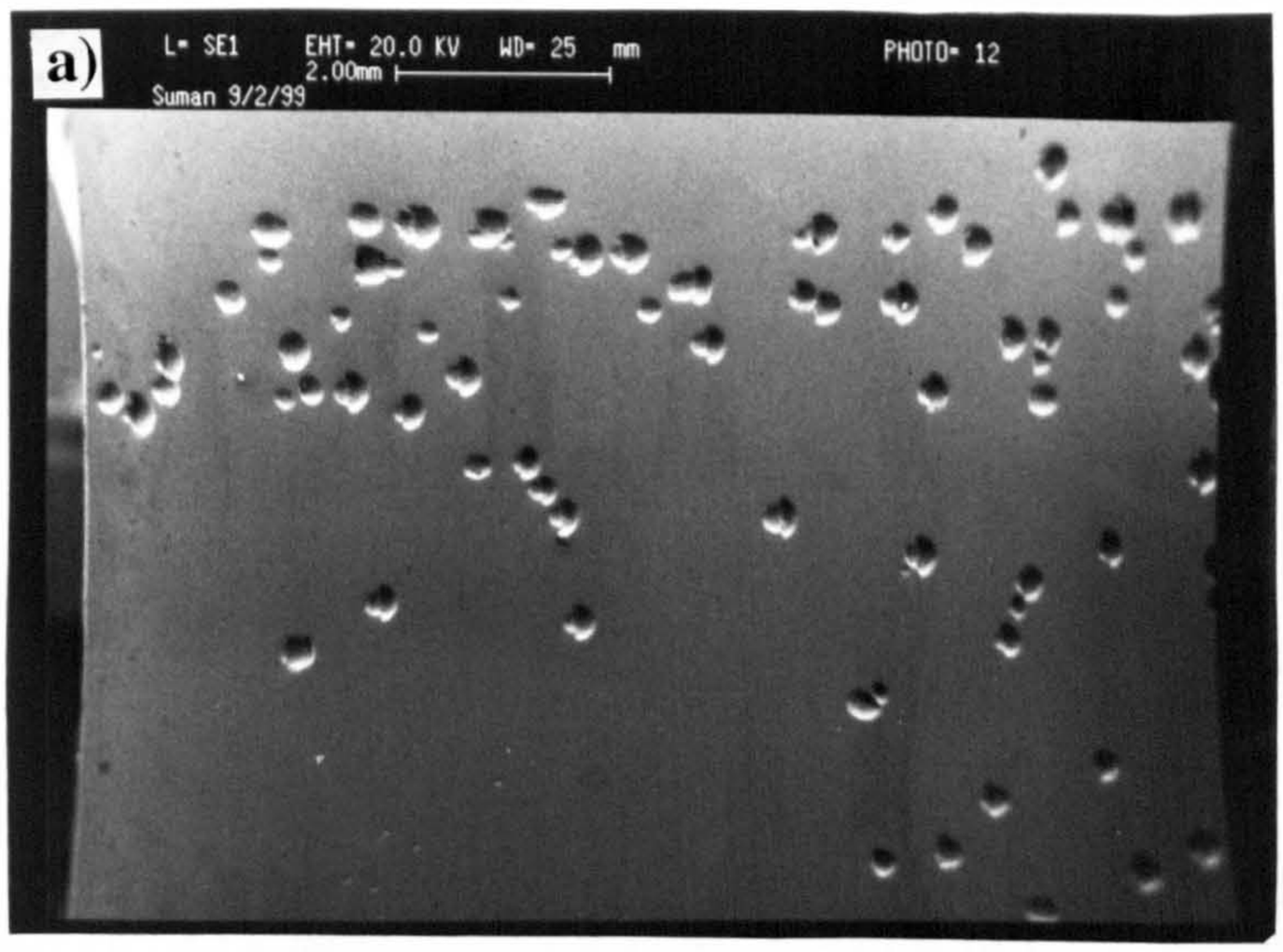
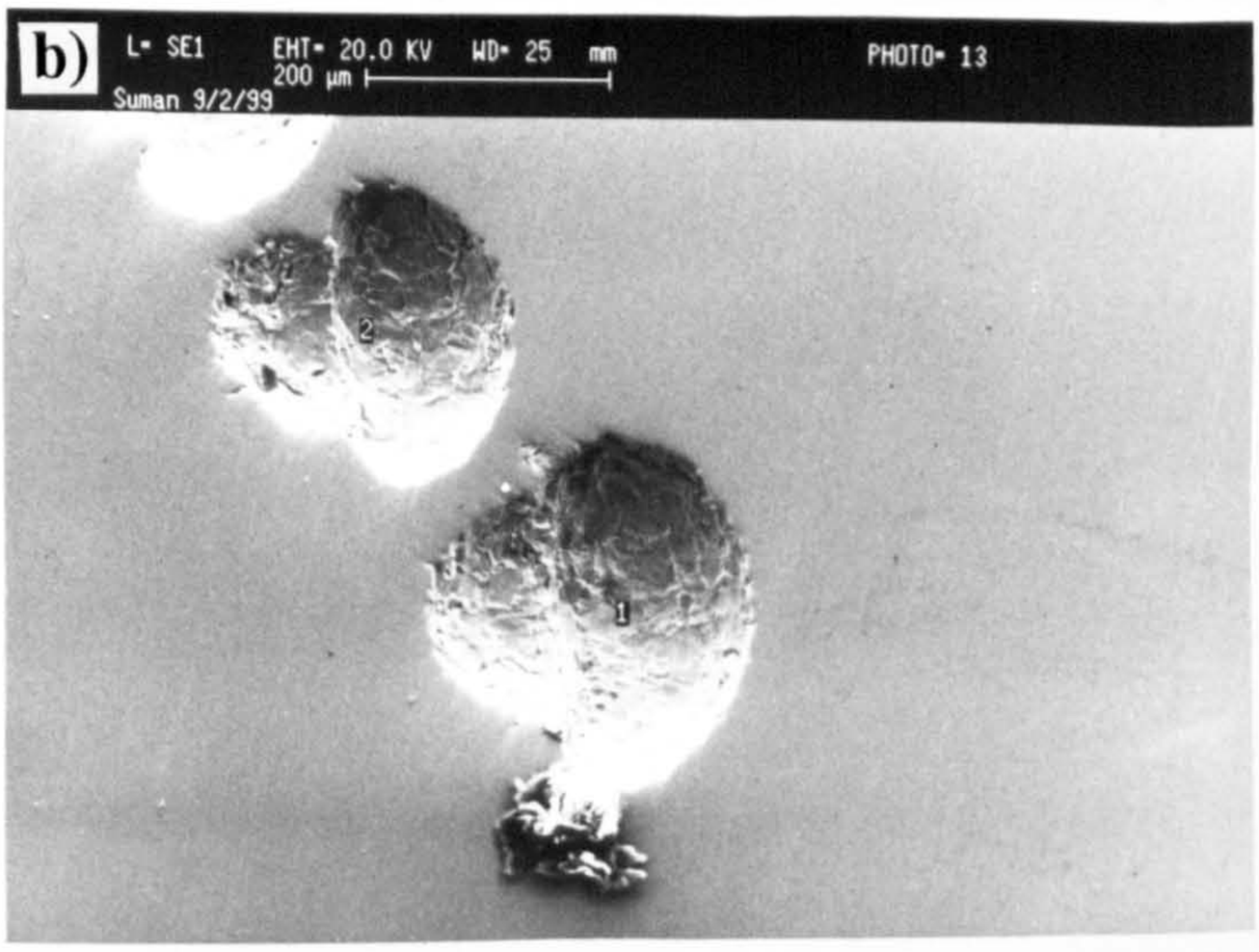


Figure 7.3.8 Crevice corrosion mechanism in the stainless steel: a) severe crevice under the lacomit strip; b) higher magnification of the crevice showing intergranular attack; c) pitting inside the crevice.

Figure 7.3.9 shows another stainless steel specimen, which was polarised without the lacomit varnish that seals the surface/mounting resin interface. There was an evidence of a small amount of corrosion product coming out of the interface but was not clearly shown in the picture. However, an immense damage to the entire surface had occurred shown by a large number of deep pits (Fig. 7.3.9a). SEM micrograph in Fig. 7.3.9b shows corrosion product flowing out of the pit. Higher magnification of this pit in Fig. 7.3.9c shows intergranular attack around grain boundaries within the pit itself and spalling out of some of the grains very similar to that shown in the crevice.





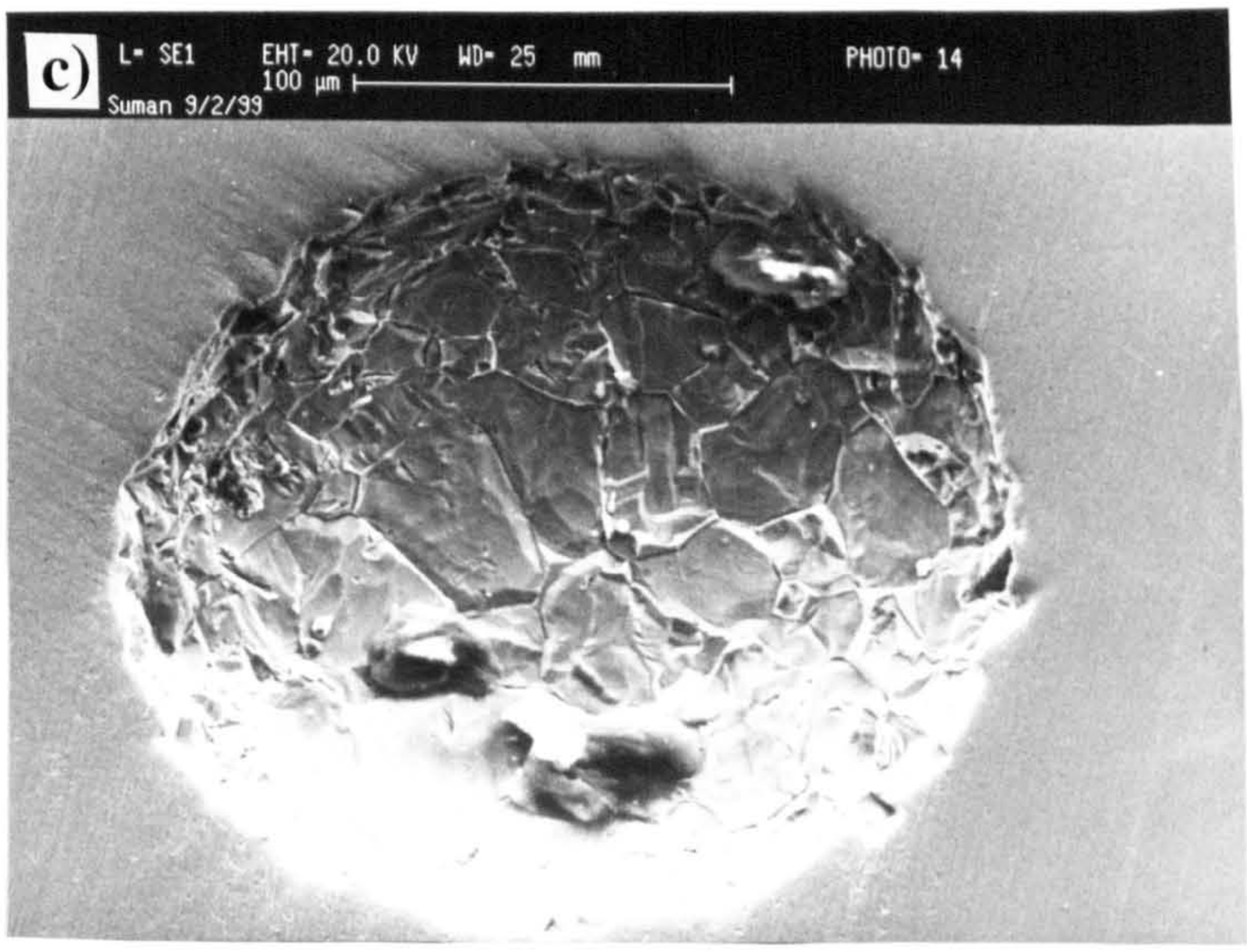


Figure 7.3.9 Pitting in a stainless steel: a) low magnification SEM image showing several pits on the surface after anodic polarisation at ambient temperature; b) higher magnification of the above pits; c) intergranular attack within the pit.

Table 7.3.2 illustrates the EPMA results taken inside and out side the pit. The result shows reduction of Fe and other alloying elements such as Ni, Cr and Mo within the pit.

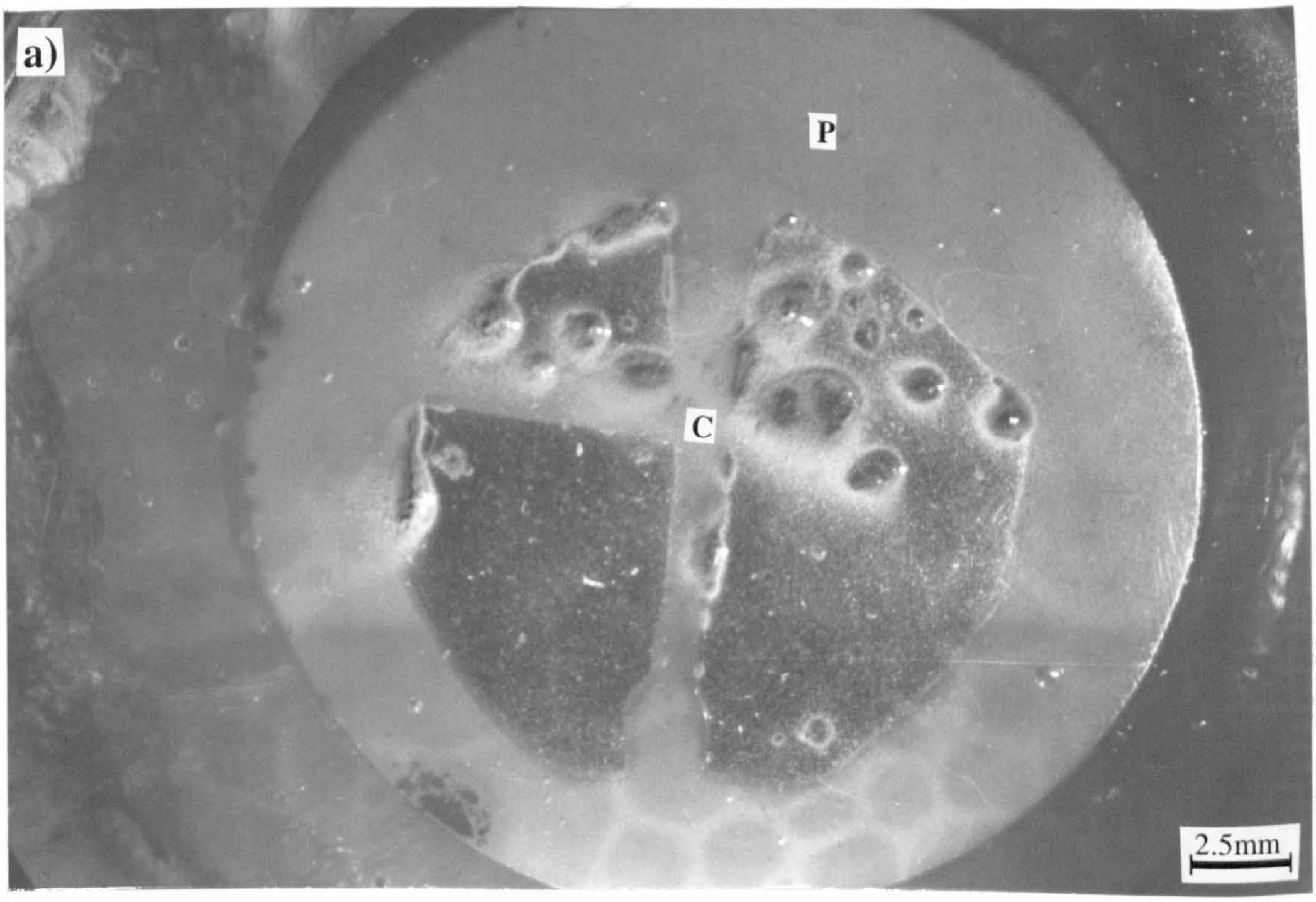
Area	Fe	Ni	Cr	Mo
Outer	67.6-69.1	11.3-11.5	17.6-18.1	1.9
Inside pit	54.4-55.9	9.0-9.2	15.0-15.8	1.2-1.3

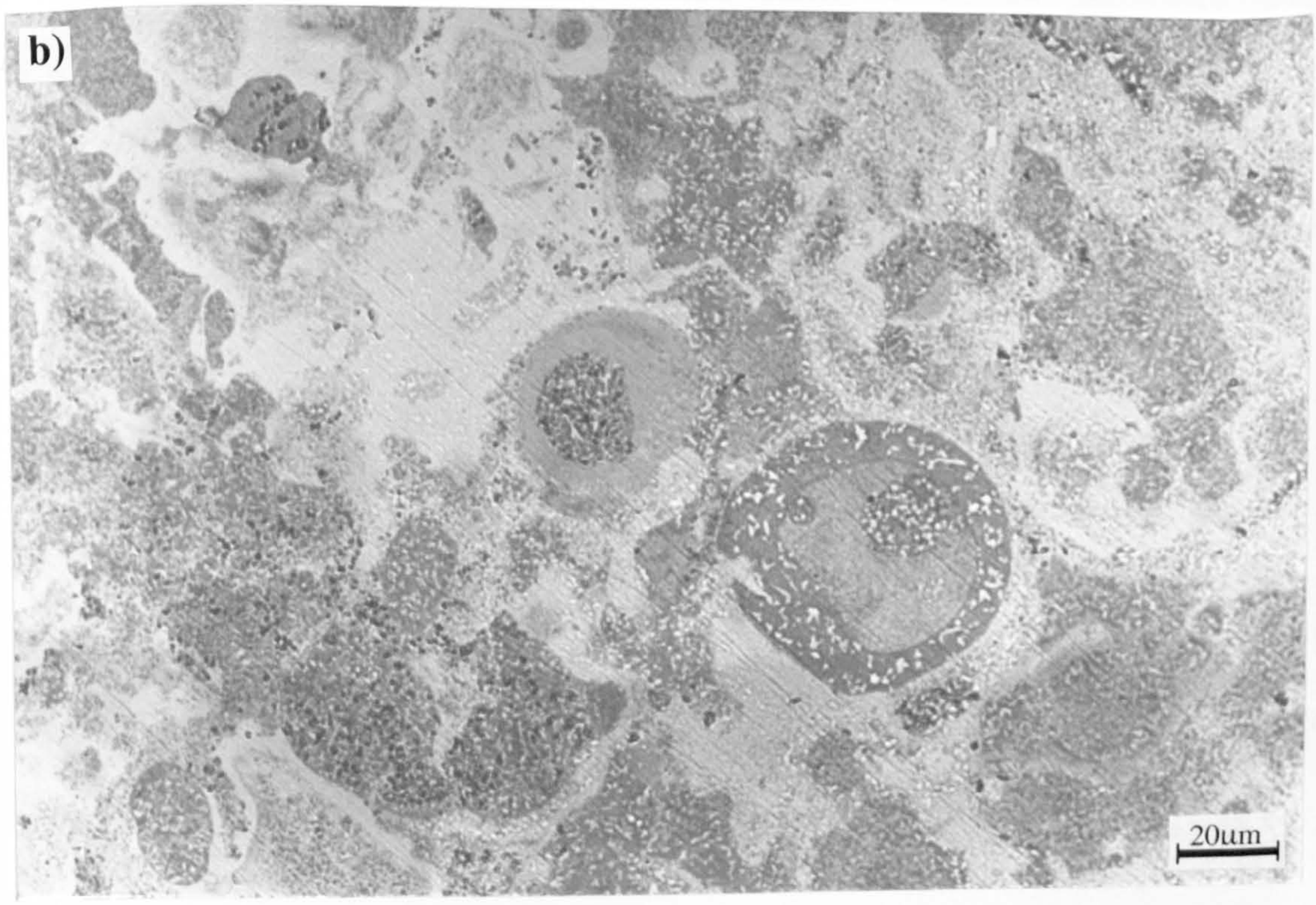
Table 7.3.2 50 x 50μm area analysis (wt.%) inside and outside the pit of Fig. 7.3.9b.

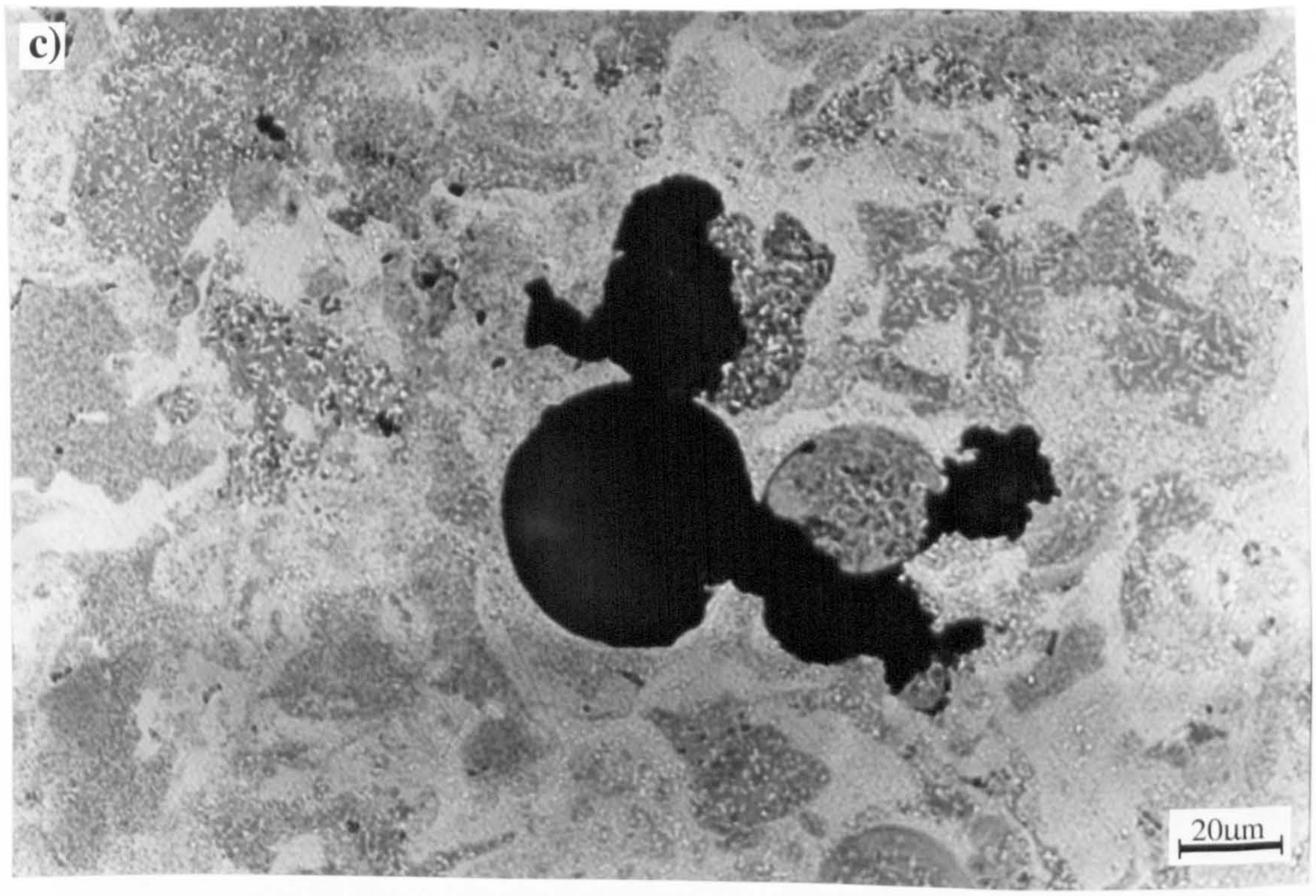
Extended exposure test

Long-term corrosion tests were performed by simply immersing the coating in a beaker with salt solution (3.5% NaCl) at ambient temperature. The extent of corrosion damage incurred after natural exposure was correlated with those obtained after rapid electrochemical tests. The polished surfaces were examined prior to the experiment and then inspected regularly for visible signs of corrosion. The conductivity and the temperature of the solution were maintained constant throughout the test period.

Periodic examination showed a slight dullness of the polished surface just after 2 days, which further increased after 4 days. Brown-coloured corrosion products started to appear on the surface after a week immersion, which increased substantially after the specimen had been left for 2 weeks. Figure 7.3.10a shows a low magnification picture of the coating after 2-weeks exposure to saline environment in naturally corroding condition. Dark exposed area and brown-coloured corrosion products were readily visible on the surface. The clear outer perimeter and central clean strip was under the lacomit varnish paint. The corrosion mechanism was difficult to assess as the surface was covered with the corrosion product and so was cleaned with Clarke's solution to remove the excessive corrosion product and then finally cleaned in an ultrasonic bath. The exposed area in Fig. 7.3.10b shows some areas virtually unattacked, whereas most of the area suffered general corrosion on a macroscopic level. The picture also shows three particle splats overlapping each other with different corrosion mechanisms. The smallest splat (18μm diameter) has most of the matrix being corroded leaving the hard particles unaffected. The middle splat (40μm diameter) has less corrosion, while the outer splat (60μm diameter) has the corroded matrix as well leaving the hard particles unaffected. A few splat particles in the exposed area (Fig. 7.3.10c) have fallen out leaving macro-pits. The maximum pit depth was measured to be 10μm. Crevice corrosion was once again much more severe than the exposed area, which is clearly shown in Fig. 7.3.10d with loss of several splats. Crevice corrosion occurred at about 22% of the covered length under lacomit strip. Figure 7.3.11a shows crevice attack of the stainless steel after being exposed to similar environment after 1-month period under freely corroding condition. The crevice corrosion length was approximately 40%. Most of the exposed surface has a very dull appearance. Further microscopic observation revealed a large amount of pits over the entire exposed area as shown in Fig. 7.3.11b.


a)
P
C
2.5mm


b)
20um



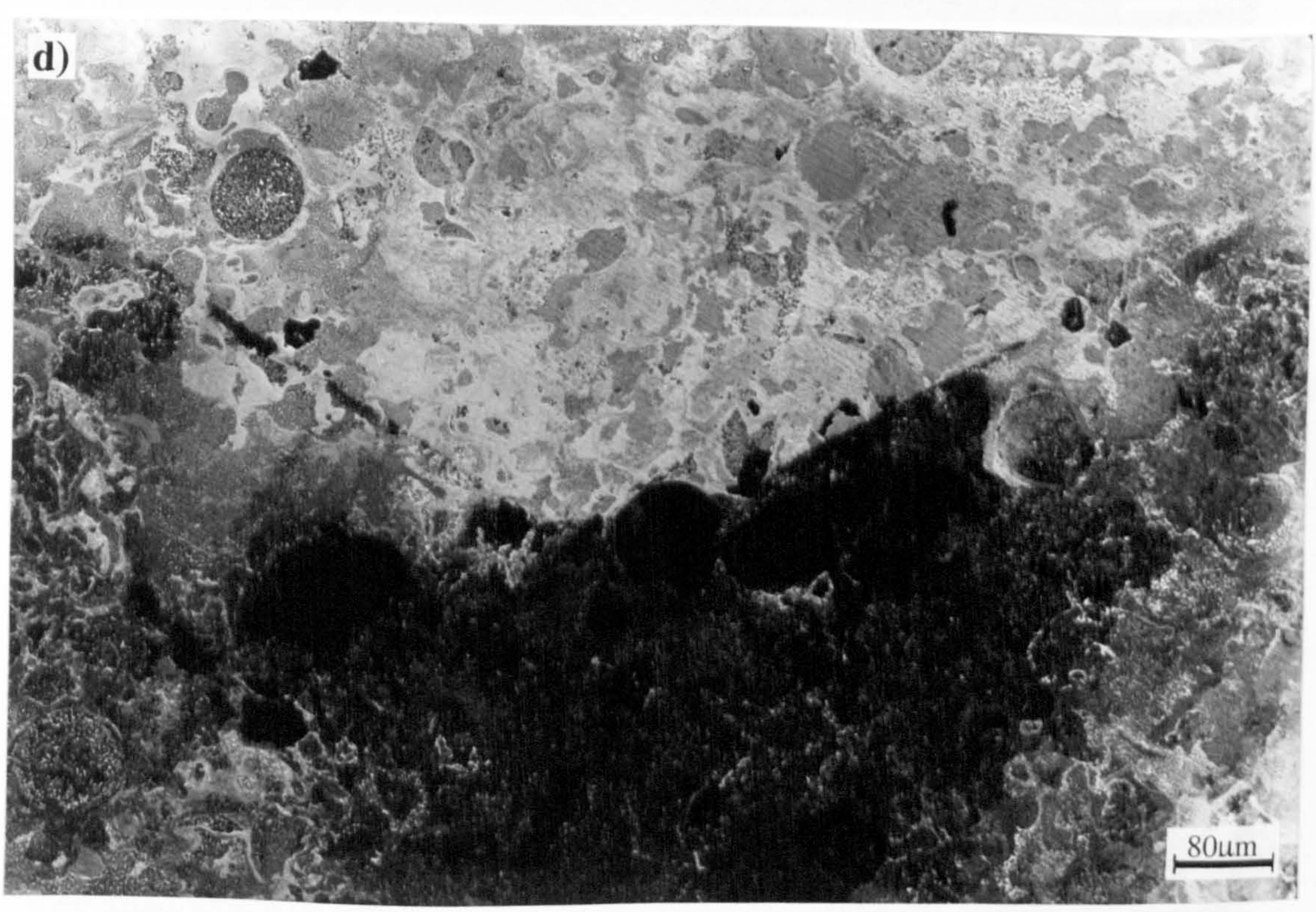


Figure 7.3.10 a) Corrosion of the coating AI after 2-weeks exposure to 3.5% NaCl solution; b) several splats corroded in the exposed area; c) spall of splats after corrosion attack around the splat boundary; d) severe crevice corrosion of the coating under the lacomit strip.

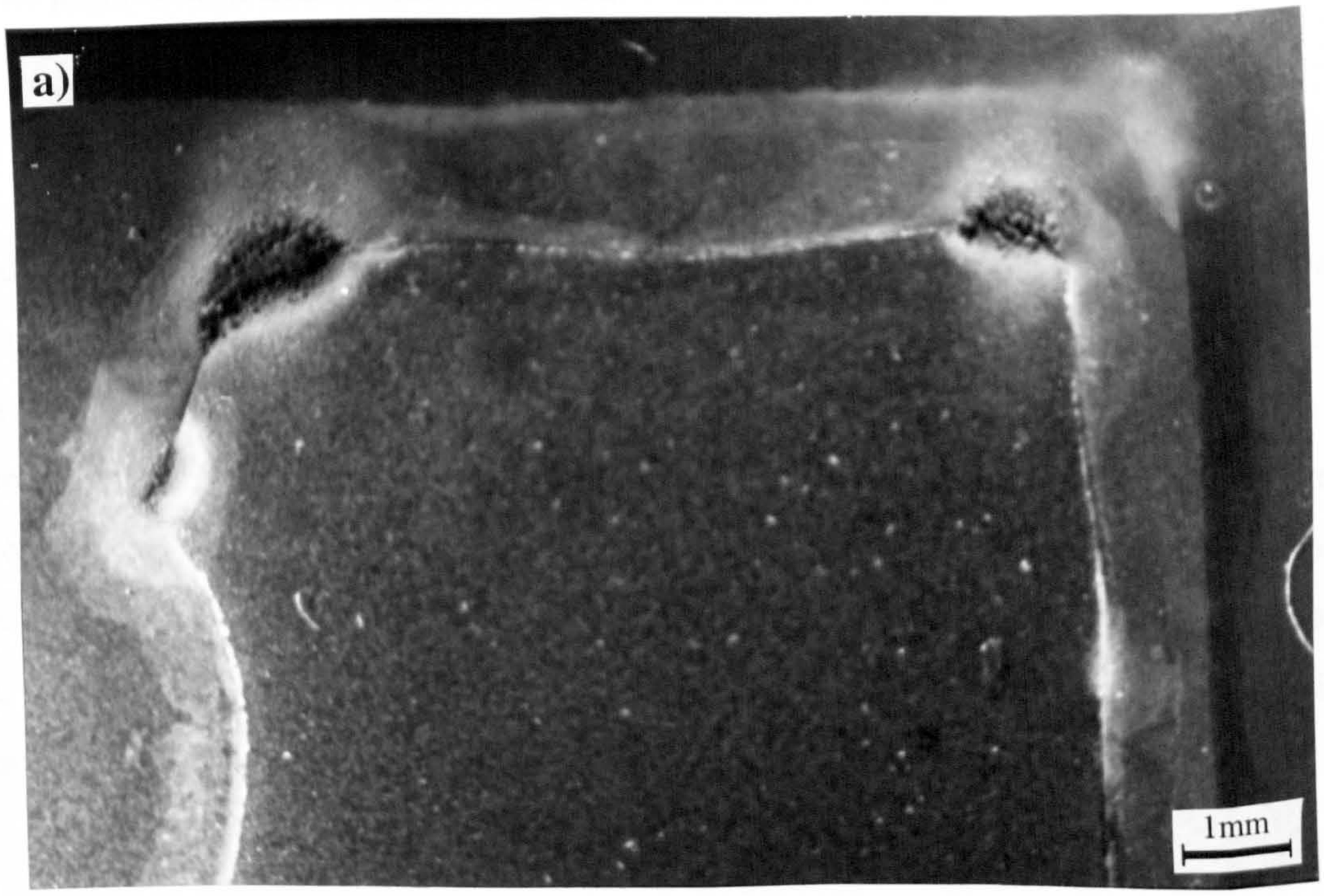


Figure 7.3.11 a) Crevice corrosion; and b) pitting at exposed area of stainless steel UNS S31603 after 1 month natural exposure to 3.5% NaCl solution at ambient temperature.

7.4 Corrosion of coating AII

Anodic polarisation under static condition

As received coating

Anodic polarisation curves of as-received coating AII (Fig. 7.4.1) on both stainless steel (ss) and carbon steel (cs) substrates exhibited once again likeness with a distinct passive behaviour demonstrated by their very low current density within a wide range of potential positive from their free corrosion potential E_{corr}. Coatings with stainless steel and carbon steel substrates had very similar breakdown potentials about +90 to +100mV SCE. The hysterisis loops for both coatings are very much alike with very similar loop area. The maximum current density recorded was no more than 700μA/cm^2 after which the scan started to reverse its direction.

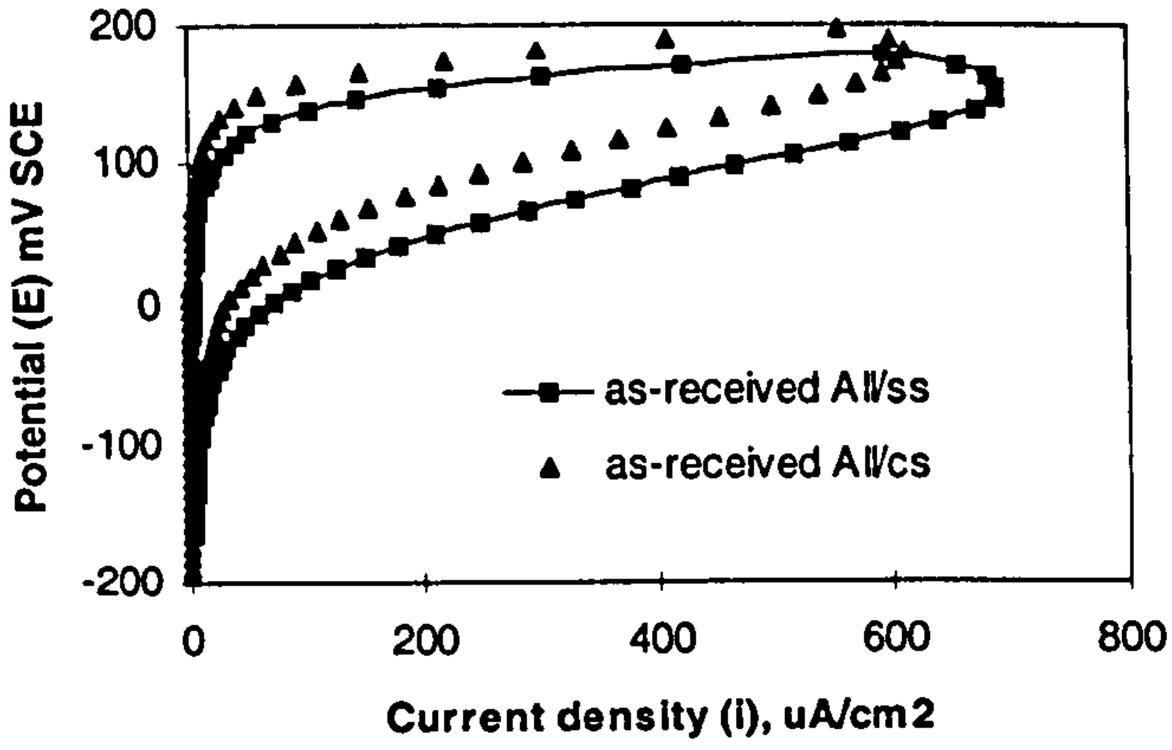


Figure 7.4.1 Anodic polarisation of as-received Coating AII in static 3.5% NaCl at 18°C.

Effect of polishing

Polishing of the surface once again resulted in much lower breakdown potential E_b for the coating with either substrate as shown in Fig. 7.4.2. Reductions of E_b by almost 80mV were recorded for the coatings AII/ss and AII/cs. Despite the reduction in breakdown potential of polished coatings once again they showed similar anodic

polarisation curves with similar loop sizes. Both coatings still retained their passive behaviour with their breakdown potentials at about +20mV SCE. Free corrosion potential 'E_{corr}' of both coatings were found to have more negative value of the electrode potential after polishing.

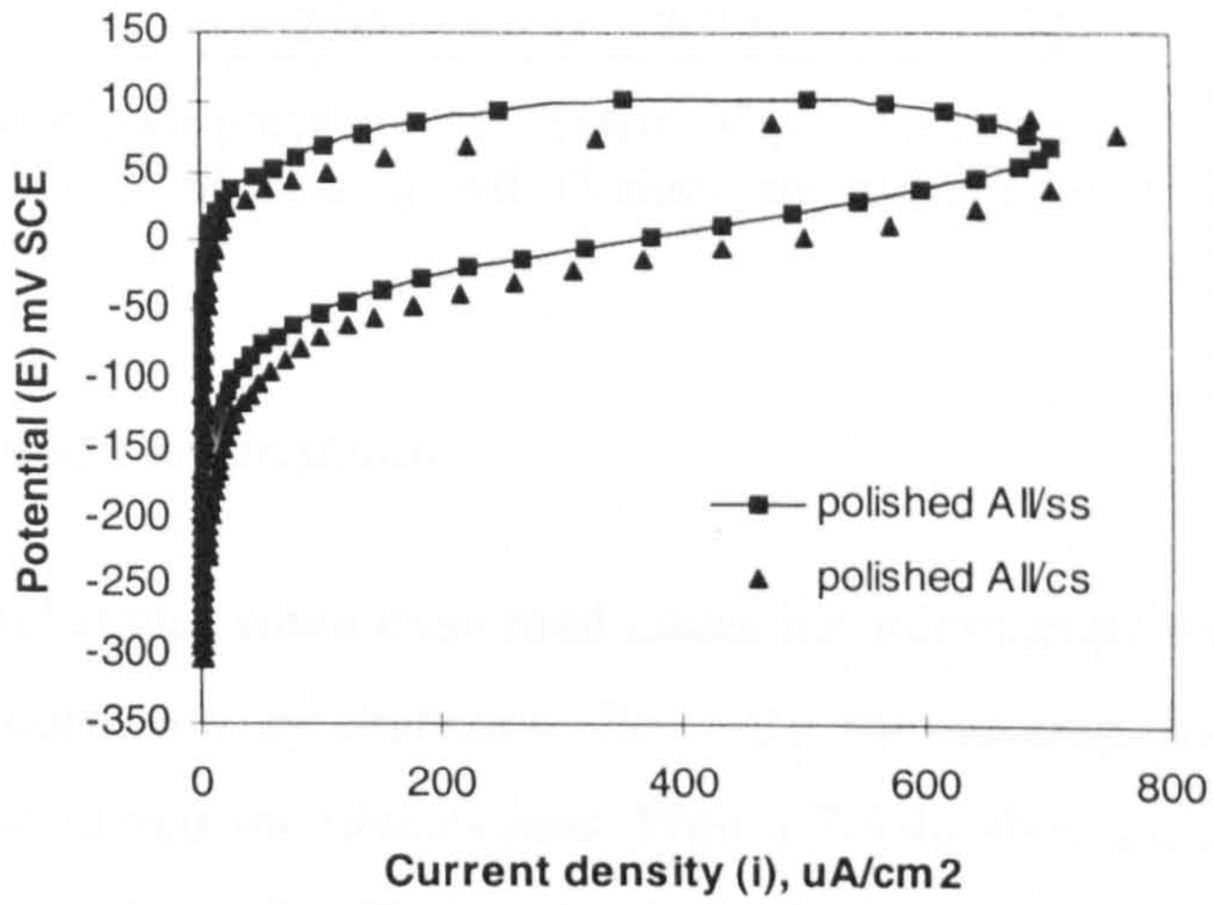


Figure 7.4.2 Anodic polarisation of coatings AII/ss ans AII/cs after polishing.

Figure 7.4.3 illustrates the reduction in breakdown potential of the coatings polished to 6μm diamond suspension and after anodic polarisation in 3.5% NaCl at ambient temperature.

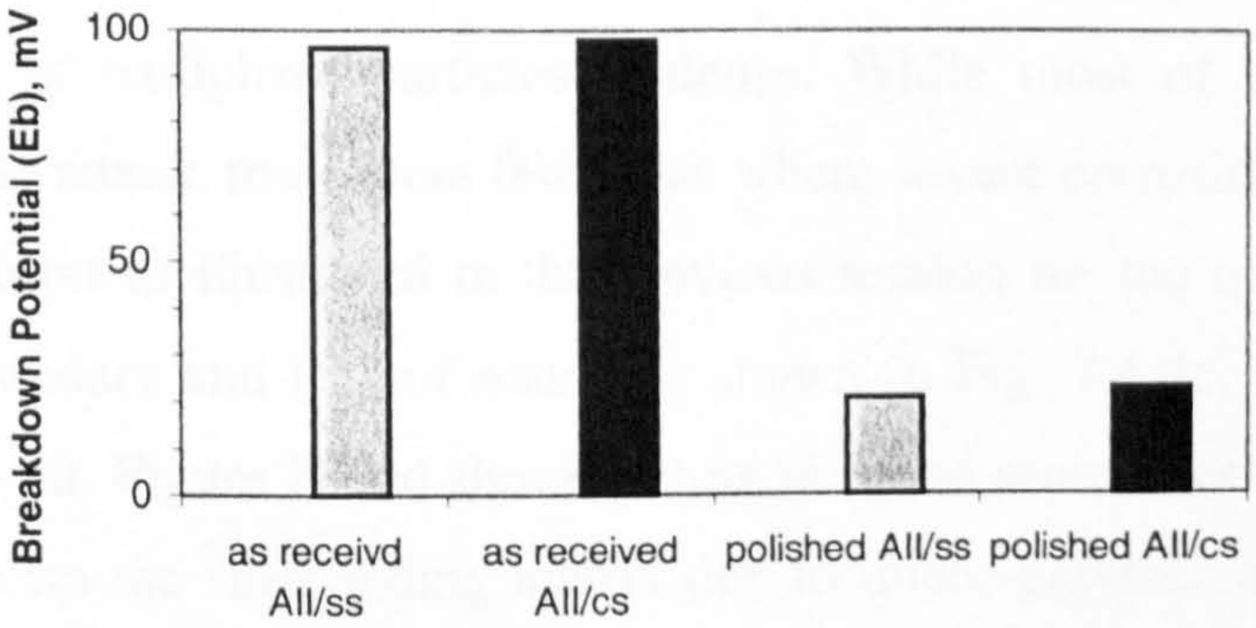


Figure 7.4.3 Comparison of breakdown potentials of as-received and polished surfaces after anodic polarisation in 3.5% NaCl solution at 18°C (The scattering of E_b is about ±5mV).

Table 7.4.1 shows E_b, E_b-E_{corr} and i_{max} of coating AII with different substrate materials and in as-received and polished conditions.

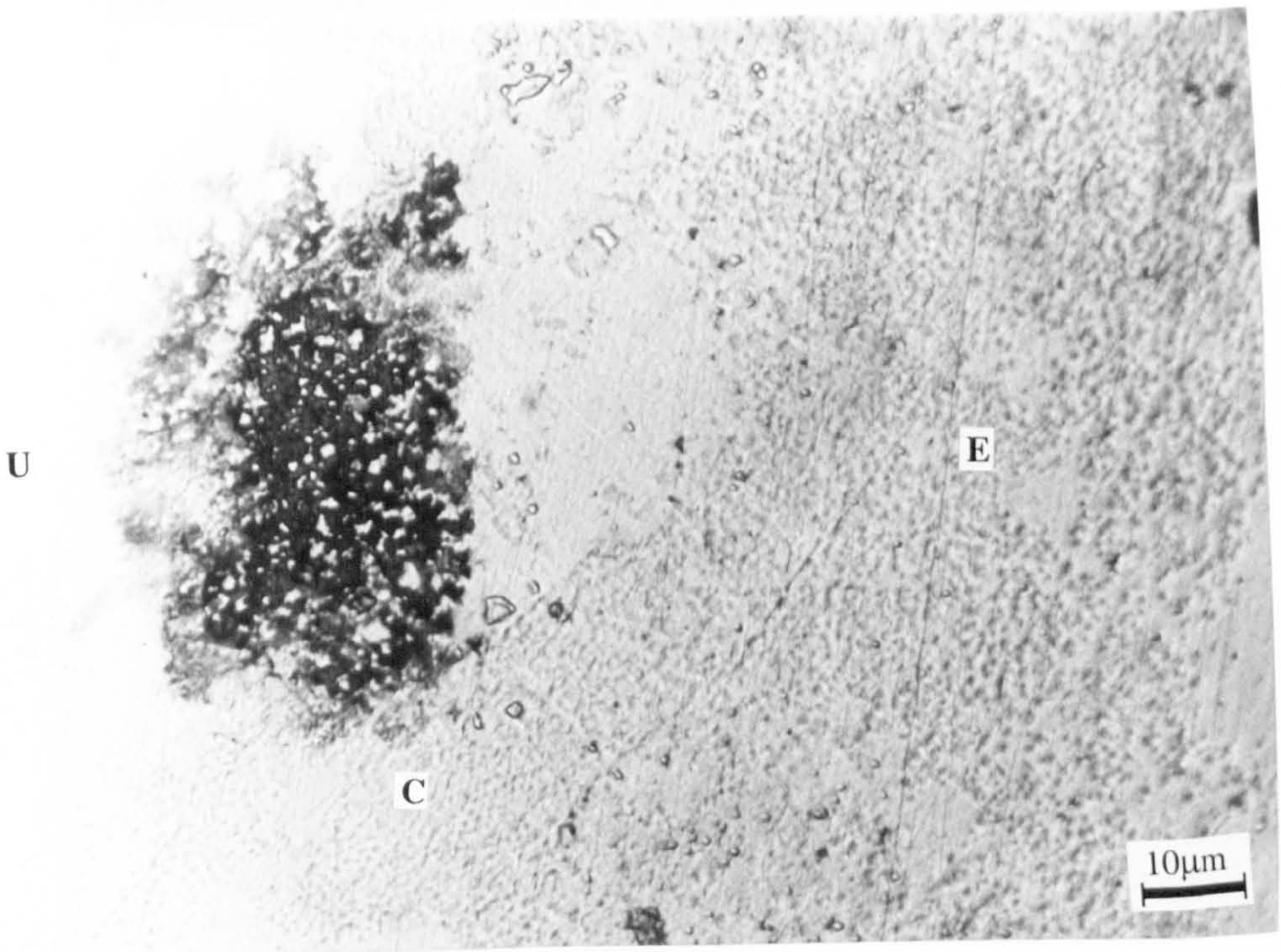
Coating	E_b, mV	E_{corr}, mV	E_b-E_{corr}, mV	i_{max}, $\mu A/cm^2$
AII/ss as-received	96.0	-197.0	293.0	706.0
AII/cs as-received	98.0	-222.9	323.9	871.0
AII/ss polished	20.8	-291.0	311.8	694.0
AII/cs polished	23.0	-301.0	324.0	759.0

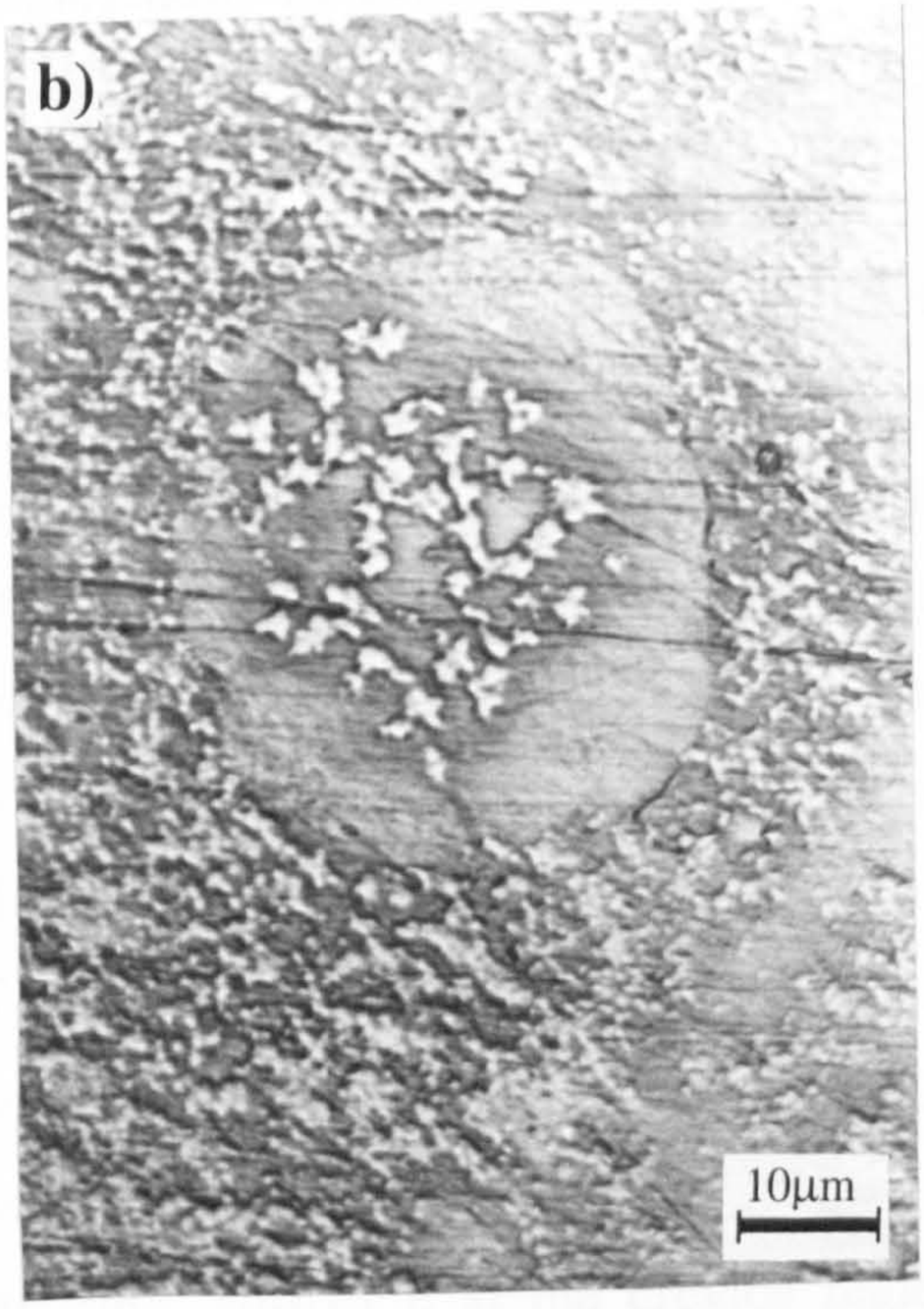
Table 7.4.1 Breakdown potential 'E_b', extent of passive range 'E_b-E_{corr}' and maximum current density 'i_{max}' of coating AII (Values are average of 3 measurements with scattering of ±5%).

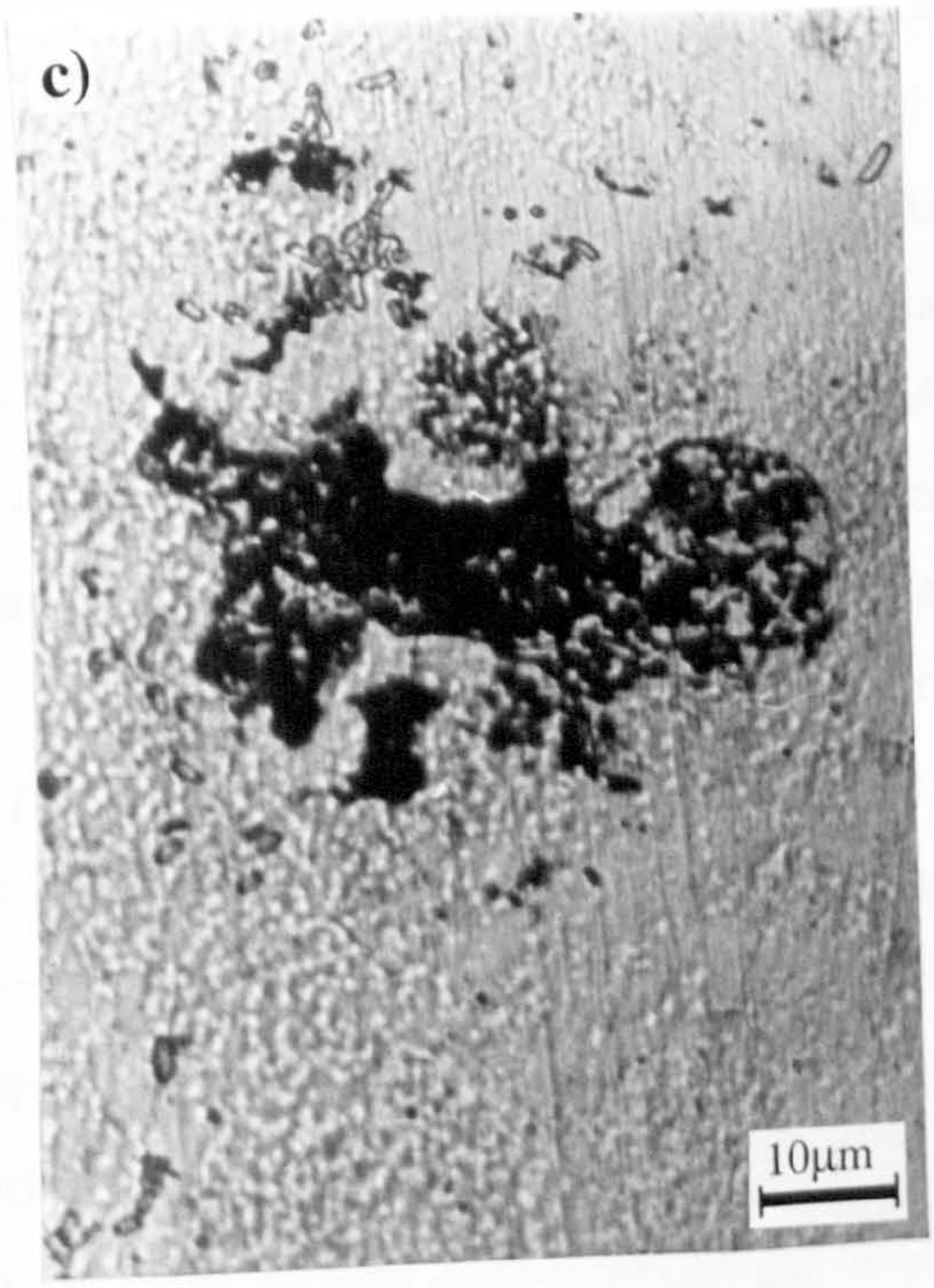
Examination after anodic polarisation

Coatings on either substrate, when examined under the microscope were found to have undergone similar corrosion mechanisms. So, only the coating with stainless steel substrate will be considered for illustrations. Figure 7.4.4a shows crevice corrosion at the lacomit/coating interface 'C'. The mechanism of attack was associated with severe corrosion of the matrix shown in black colour leaving the white hardphase particles unaffected. It seems that only half of the single splat was affected which was under the lacomit strip. The total crevice corroded length was about 8-11% of the total lacomit varnish strip applied. The area 'U' under the lacomit strip virtually remained unaffected, whereas slight corrosion of the matrix has initiated all over the exposed surface 'E' about surface area of $1cm^2$, which was visible only under the magnification of 1000 times. Figure 7.4.4b demonstrates initiation of matrix corrosion (shown by light brown colour) within a splat. It seems to be clear that corrosion has taken place mainly at areas where abundance of hardphase particles is dense. While most of the exposed area showed a very little attack, there were few areas where severe corrosion has occurred in the form of macro pit as illustrated in the previous section for the coating AI. Attack around a splat boundary and loss of matrix is shown in Fig. 7.4.4c, which eventually will lead to macro pit. Figure 7.4.4d shows pitting in micro scale after the hard particles being dislodged from the surrounding matrix due to micro-galvanic attack at the hard particle/matrix interface.

a)







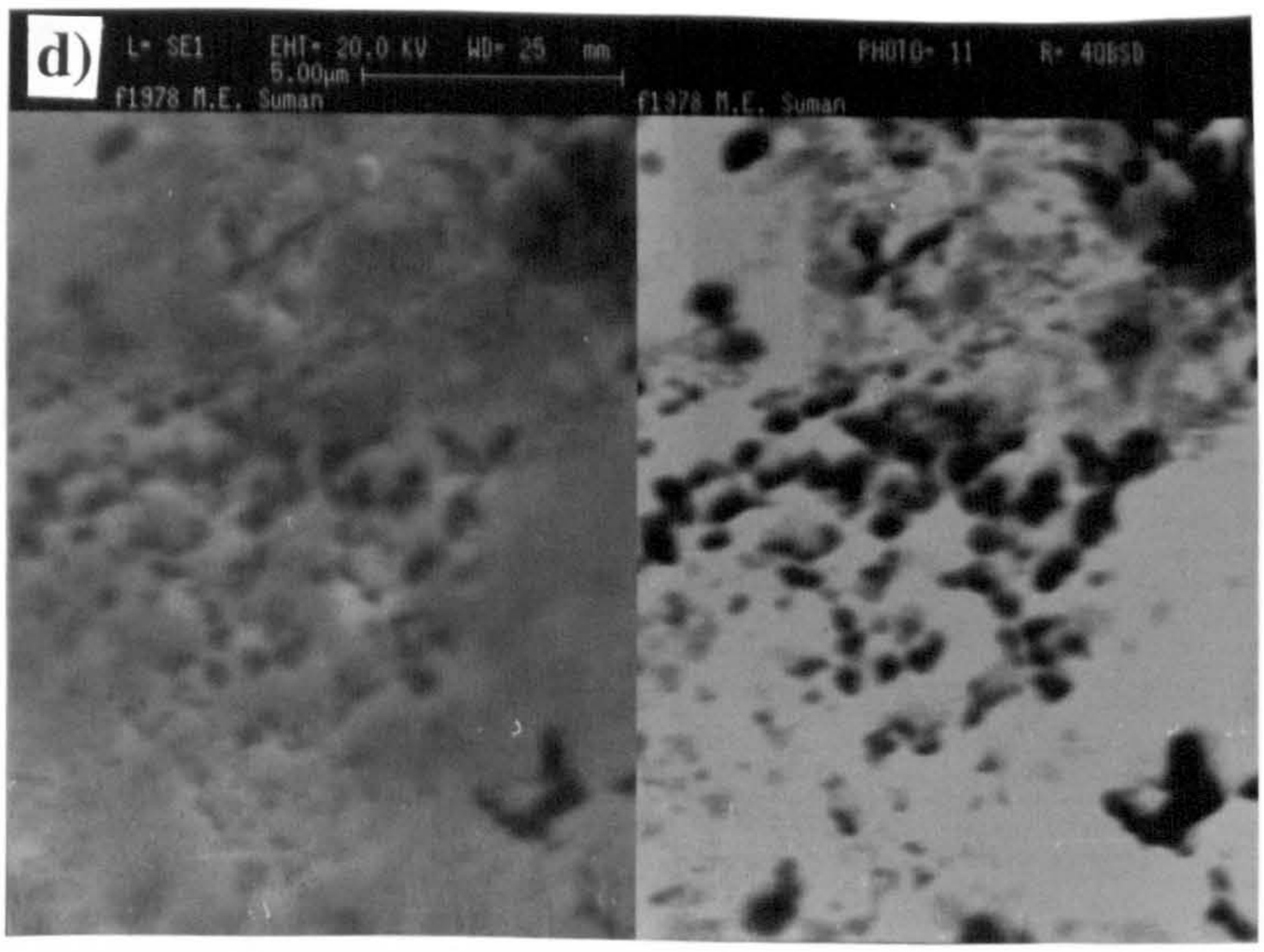
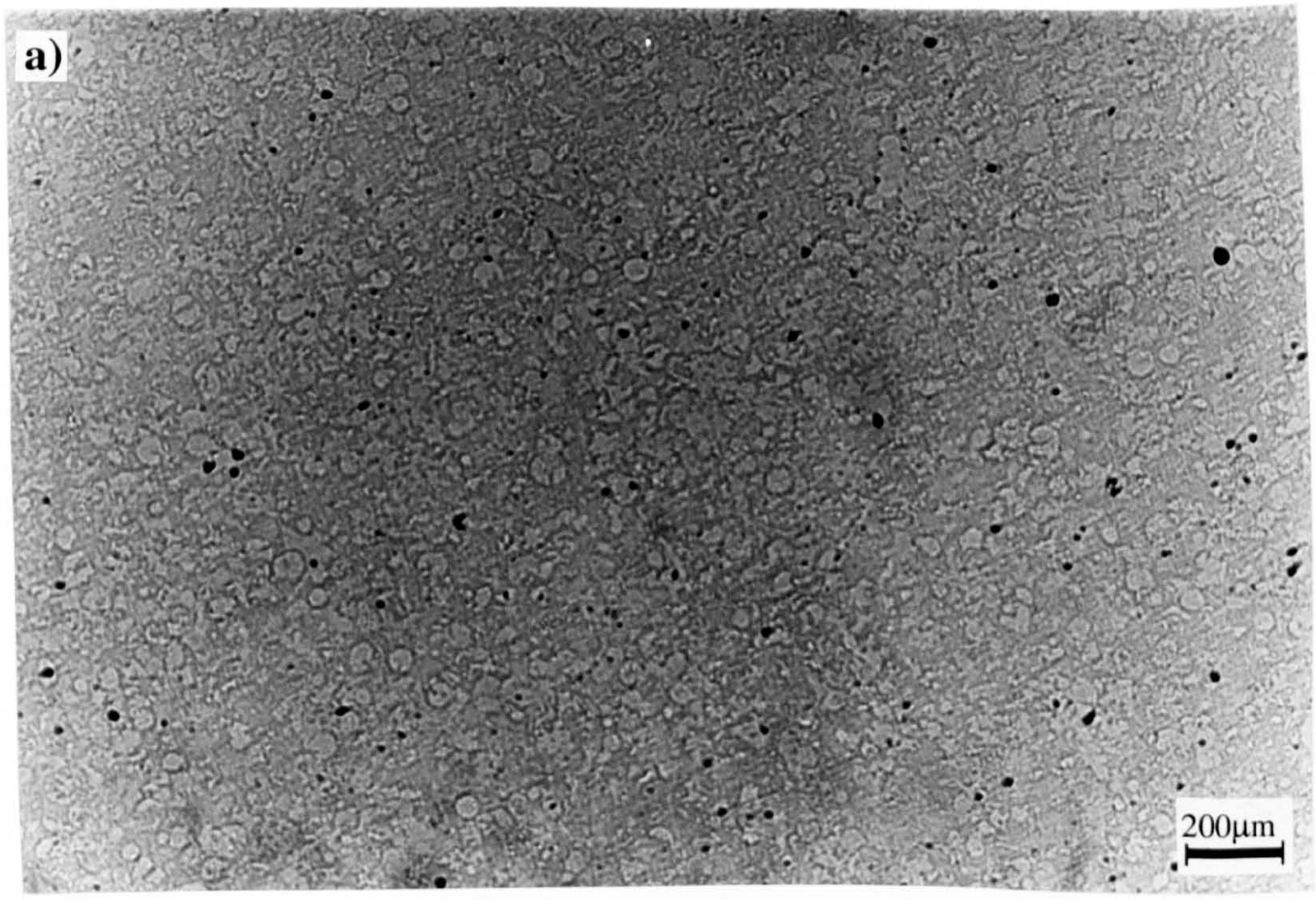
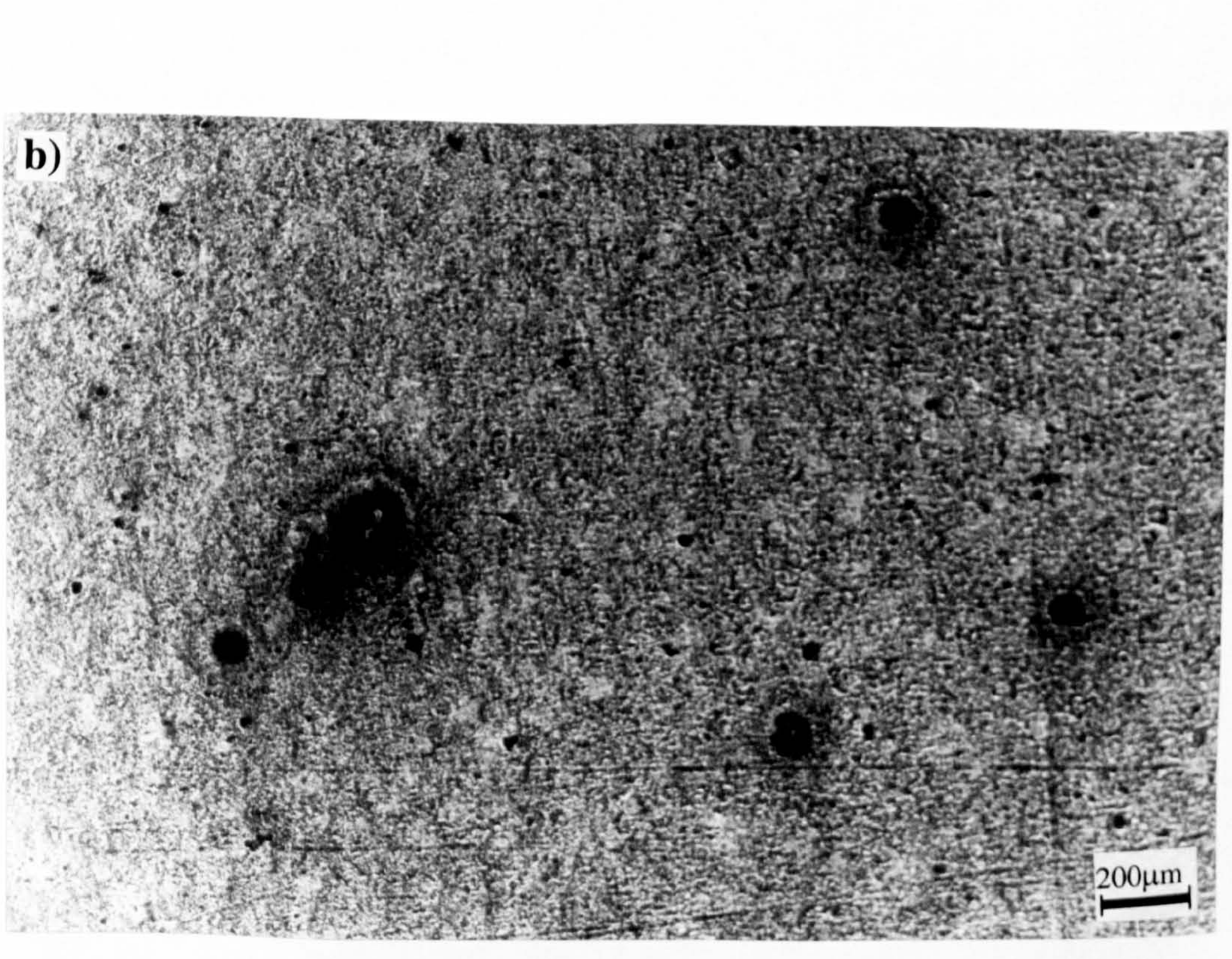


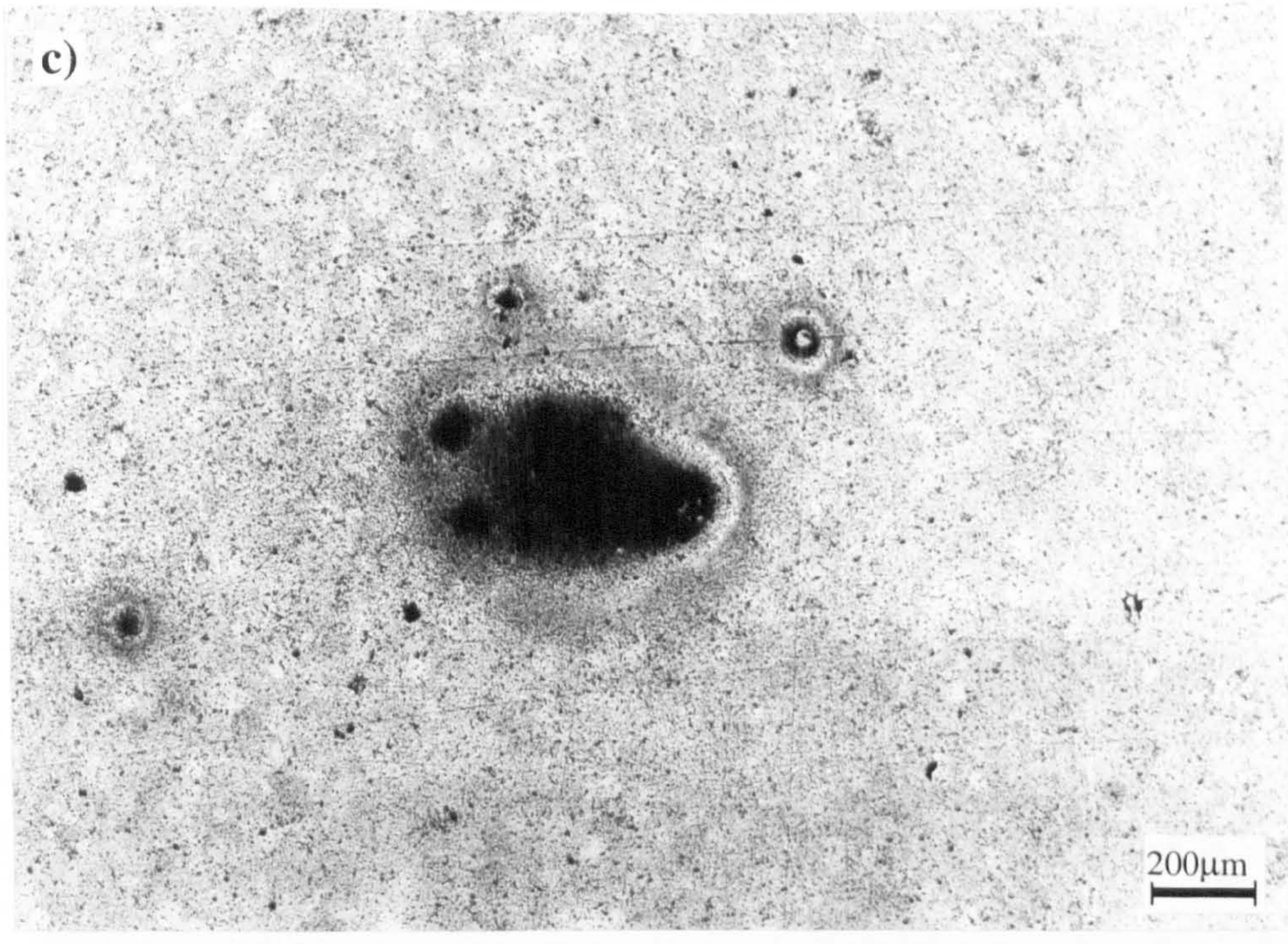
Figure 7.4.4 a) Crevice attack at the lacomit/coating interface; b) corrosion of matrix more pronounced near hard particles; c) macro-pitting after splat loss; and d) micro-pitting due to hard particles dislodgement of coating AII after anodic polarisation in 3.5% NaCl solution at 18°C.

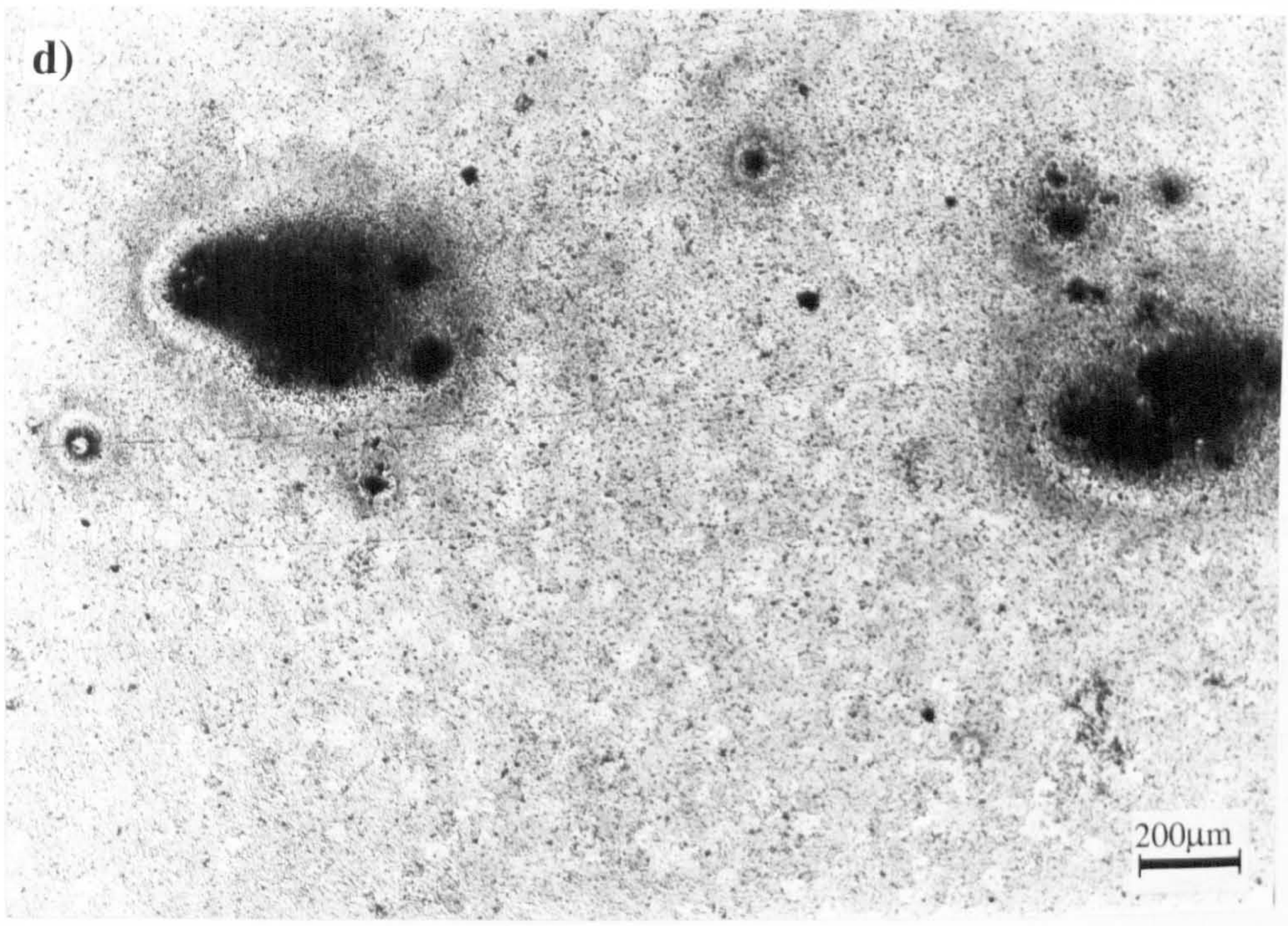
Extended exposure test

A long-term experiment was accomplished by immersing the coating sample as illustrated previously. However, this time microscopic observations were recorded in a series of time to establish an evolution of corrosion mechanism. Figures 7.4.5a to. 7.4.5e illustrate development of corrosion attack of coating AII in a freely corroding environment but without any rapid electrochemical test. The polished surface of the coating (Fig. 7.4.5a) at low magnification shows abundance of flattened splat particles clearly visible in circular shapes, which also shows a few pores (black dots). After 1-week immersion in 3.5% NaCl solution, corrosion products in the form of brown circular patches have appeared at various places of the exposed surface (Fig. 7.4.5b). Moreover most of the surface area had a dull appearance. These patches became larger after 2-weeks and also the surface became duller as shown in Fig. 7.4.5c. More increased corrosion had been evidenced after 3 weeks of immersion (Fig. 7.4.5d) but no crevice attack at the lacomit/coating interface was noticed. However, after 1-month exposure, corrosion at the crevice region 'C' was severe and most of the exposed surface 'E' became very dull, covered with corrosion products (Fig. 7.4.5e).


a)
200μm


b)
200μm


c)
200µm


d)
200µm

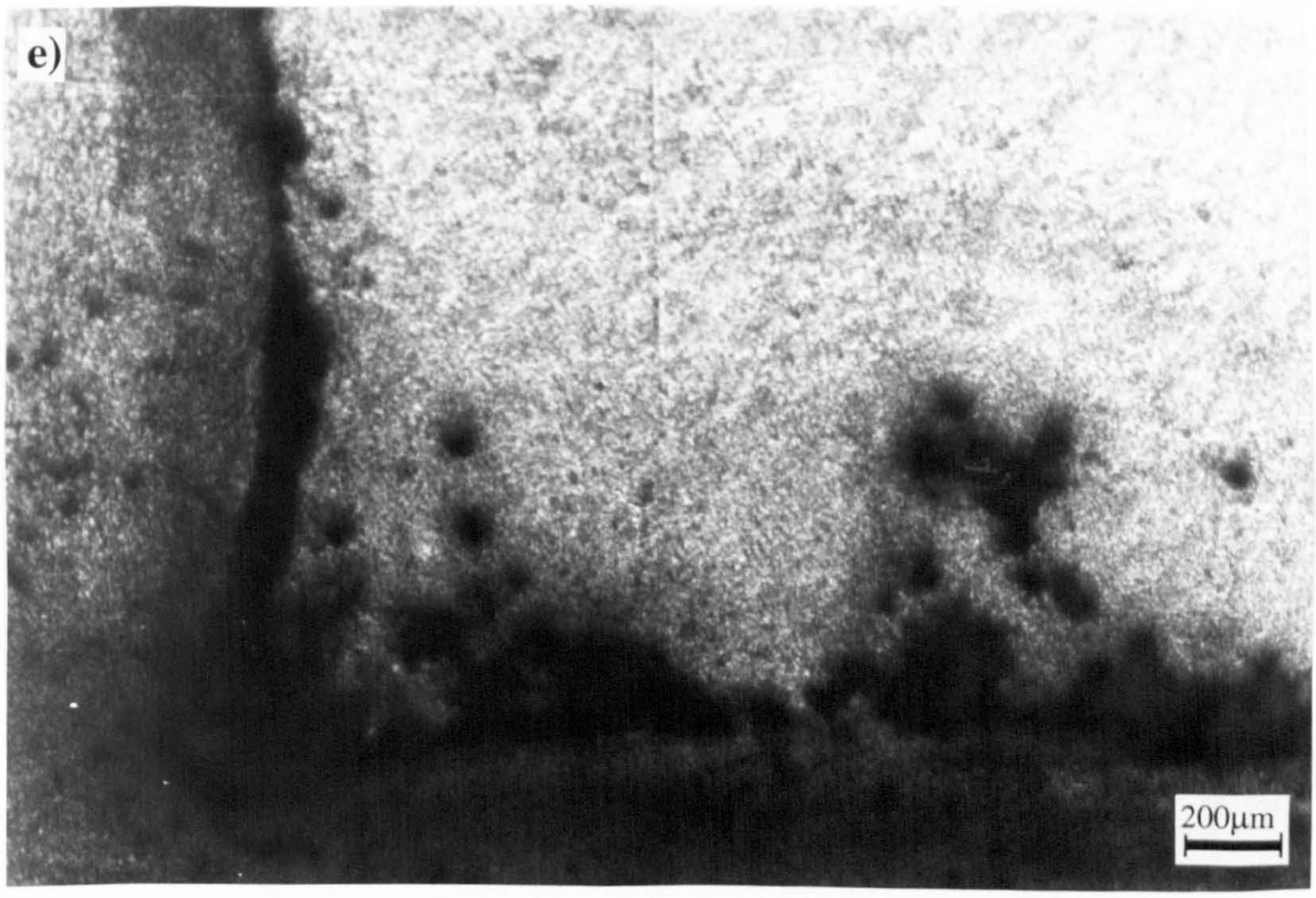


Figure 7.4.5 a) Polished surface of *Coating* AII before experiment; b) corrosion attack after 1-week; c) 2-weeks; d) 3-weeks; and e) 1-month of free immersion in 3.5% NaCl solution at 18°C.

Exact identification of the corrosion processes was difficult as most of the surface was covered with corrosion products. After the experiment, lacomit strip was removed from the surface and the corroded specimen thereafter was cleaned with Clarke's solution and washed in ultrasonic bath. Corrosion in the form of splat particle attack was visible all over the surface that covered 75-80% of the total exposed area (Fig. 7.4.6). SEM observation revealed severe crevice corrosion attack at the lacomit/coating interface that has resulted due to loosening of the splat boundary (Fig. 7.4.7a) and eventual dislodgement of individual splat (Fig. 7.4.7b) forming macro pit (pit depth ranged between 5-12μm). Inspection in the macro pit showed clear evidence of initiation of further attack at the splat boundary of particle splats within the local pit (Fig. 7.4.7c).

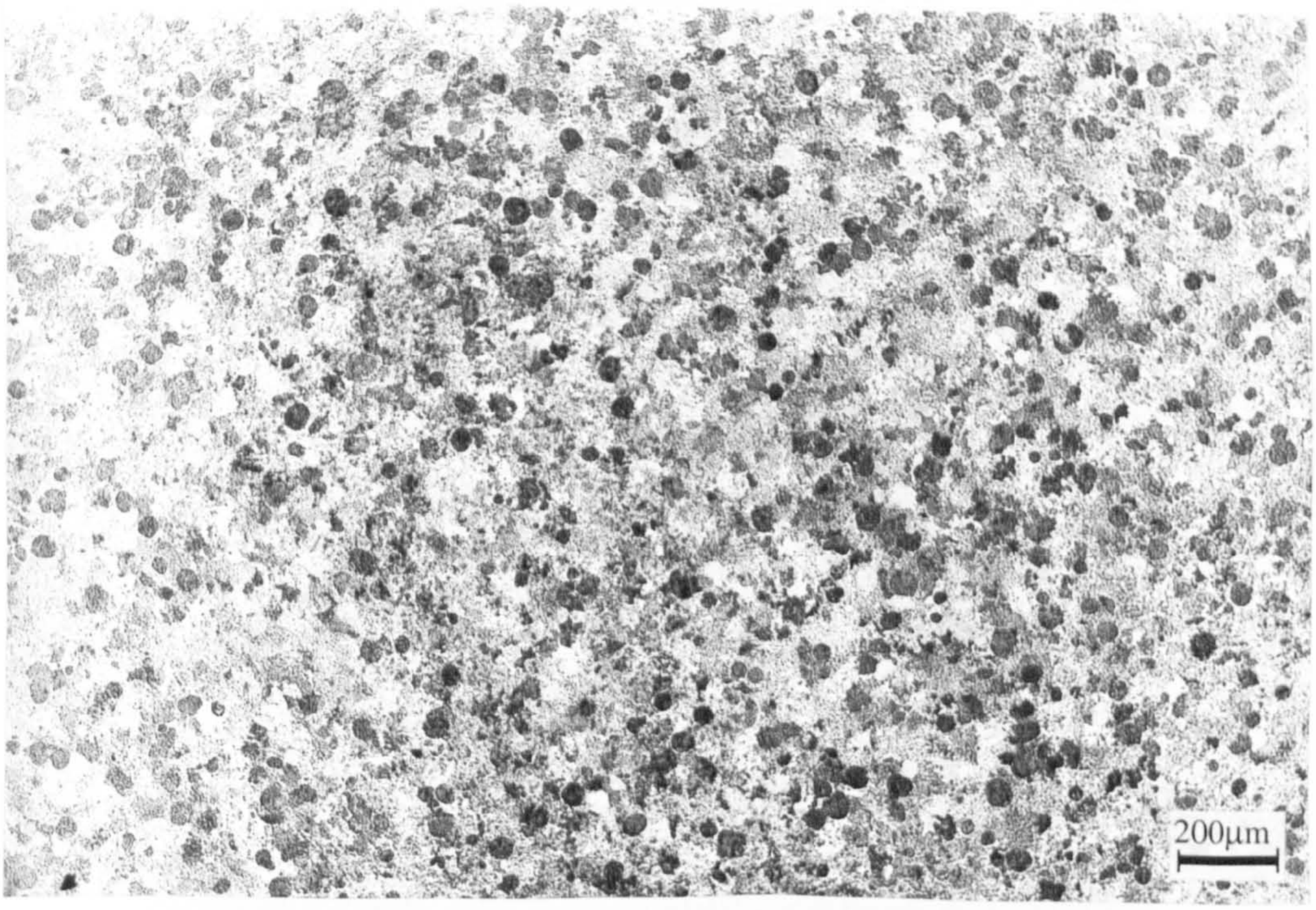
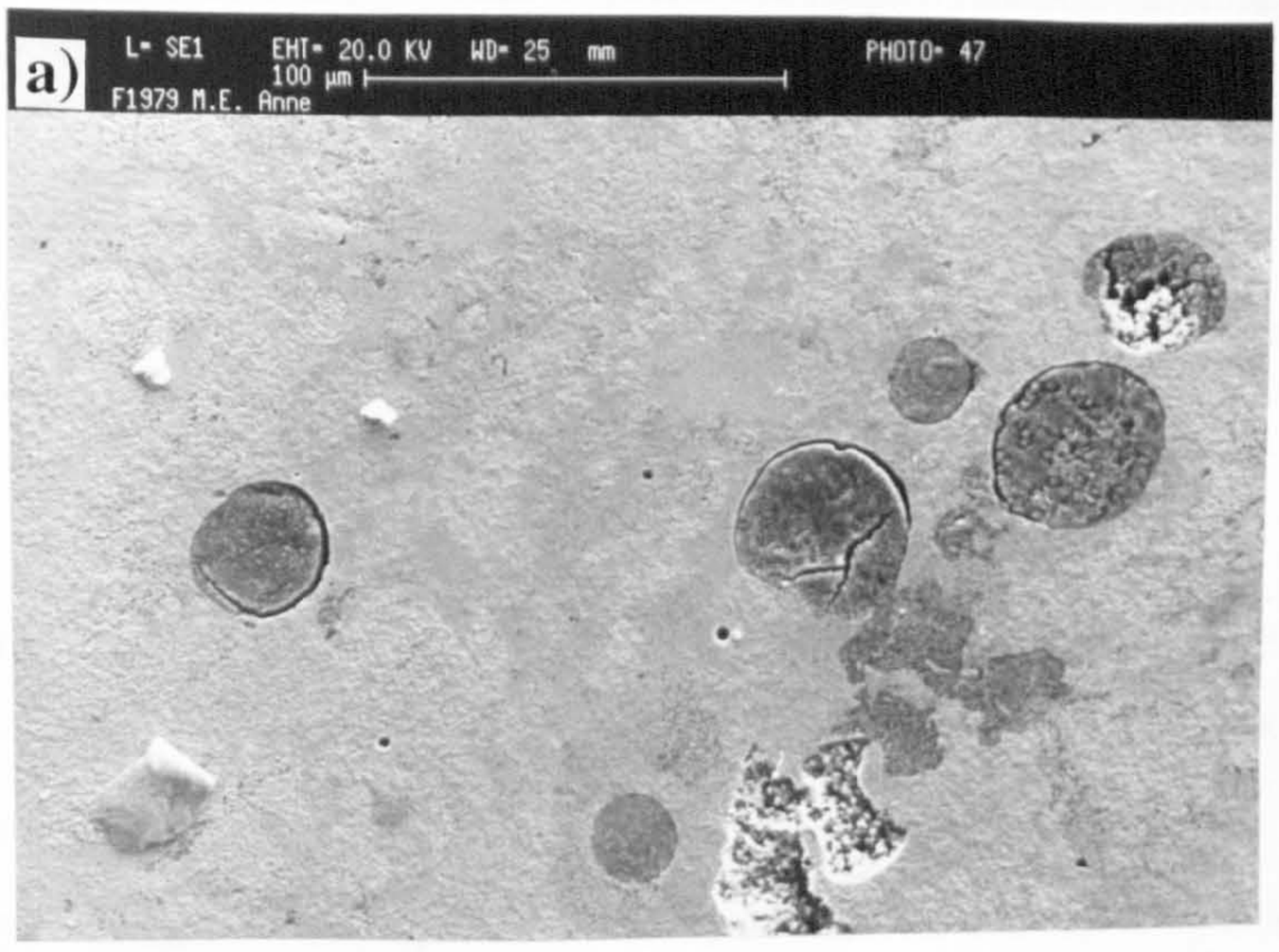
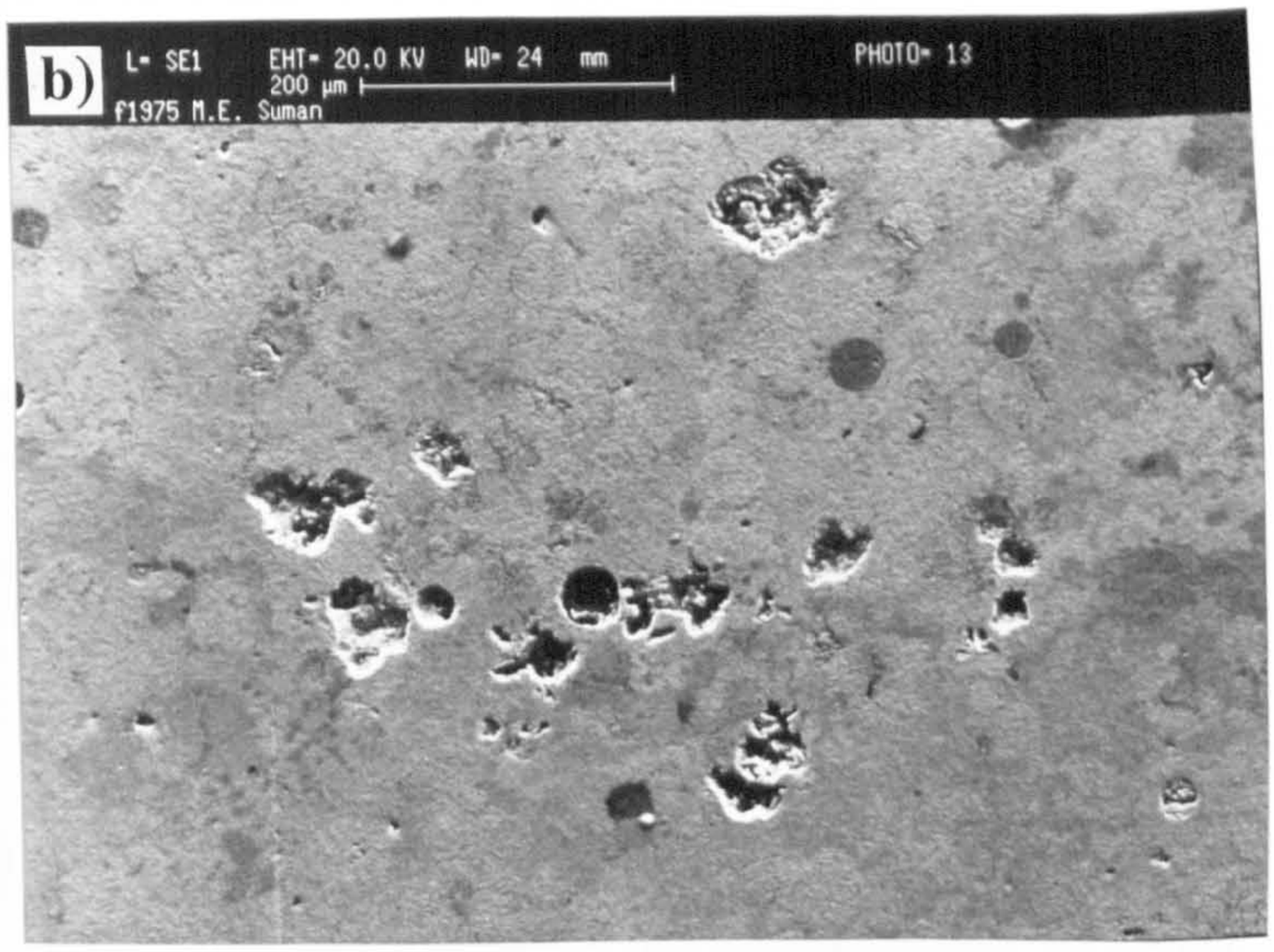


Figure 7.4.6 General corrosion of exposed surface after 1-month exposure in 3.5% NaCl solution at ambient temperature (specimen was cleaned with Clarke's solution and washed ultrasonically).





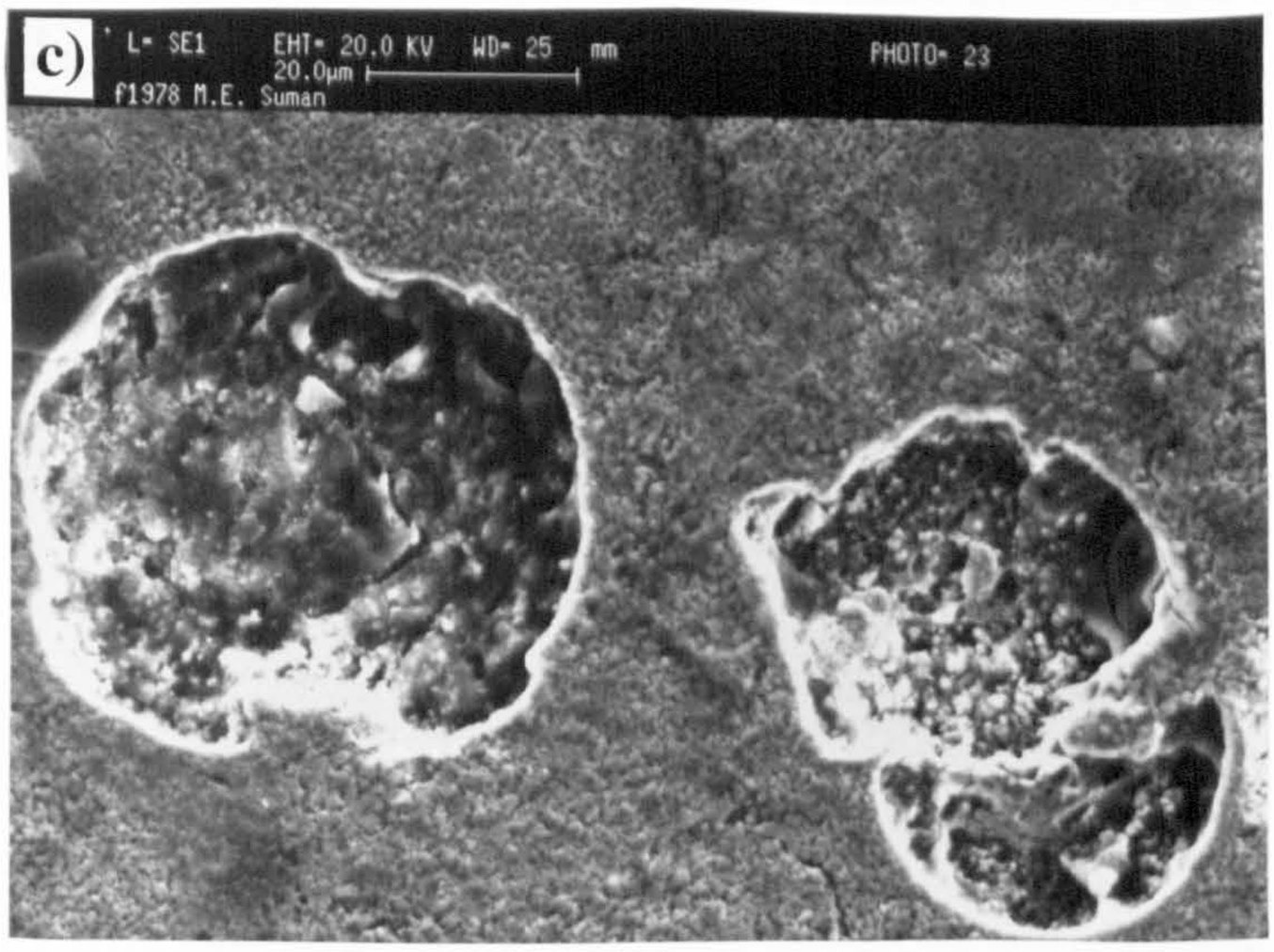


Figure 7.4.7 Crevice region under the lacomit strip showing: a) Splat boundary attack around individual splat particle; b) macropits left after dislodging of above splats; c) undermining splat boundary attack of next layer particle.

The exposed area suffered significantly at the microscopic level but rather general than crevice region, which exhibited, localised but macroscopic level attacks with individual splat losses. Figure 7.4.8 shows attack associated with micropitting at exposed area, however, attack initiated with splat boundary attack has been evidenced at few sites. Moreover, attack is readily pronounced in particle splat where tiny grey hardphase

particles are abundant (Fig. 7.4.9a). Higher magnification of the splat (Fig. 7.4.9b) shows preferential dissolution of brighter matrix '2' around tiny grey hard phase particle '1'.The picture also shows an indication of most of the binding matrix being removed leaving the hard particle unsupported.

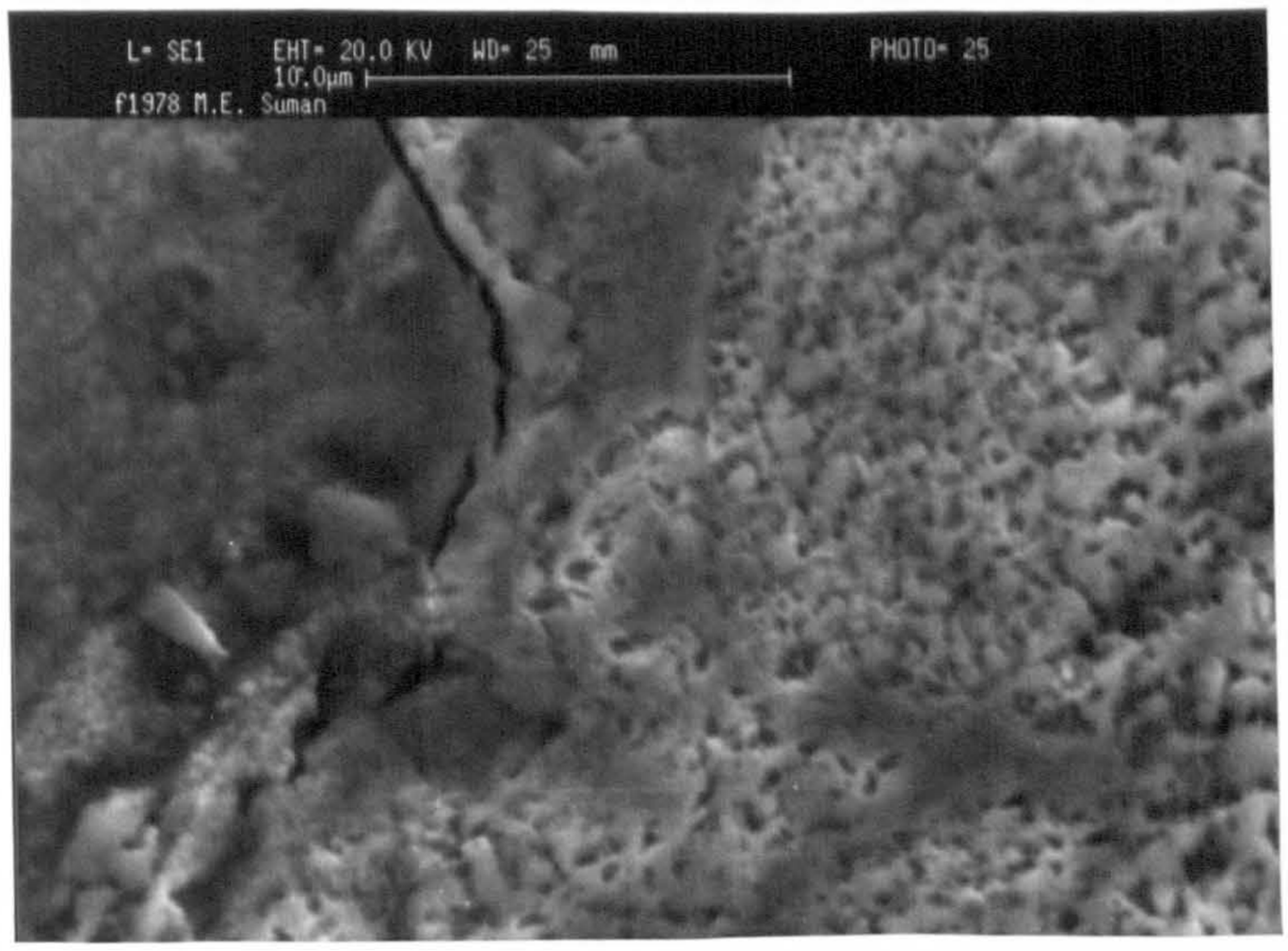
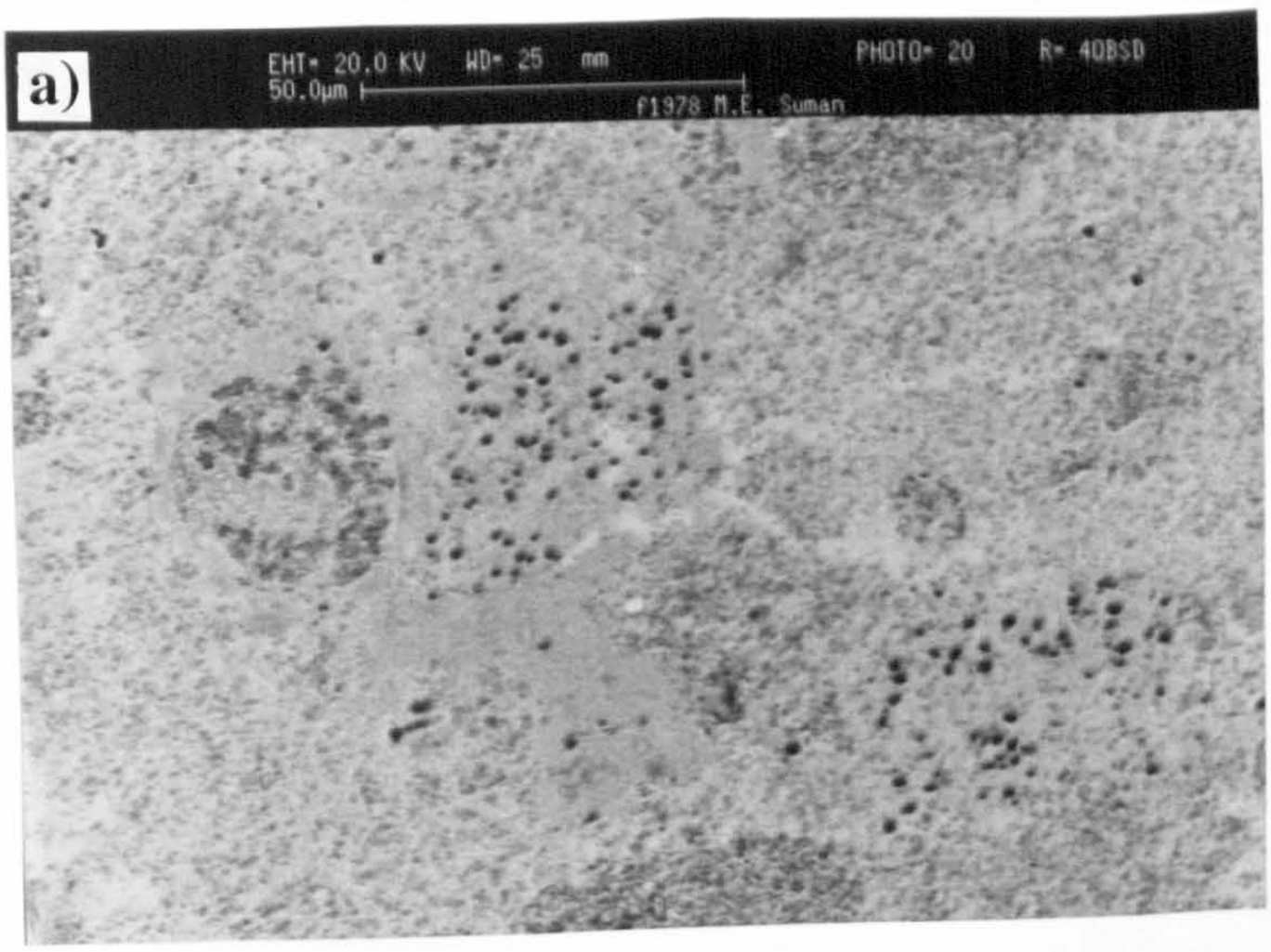


Figure 7.4.8 Micro pitting due to loss of hard particles and dislocation around splat boundary at exposed area of the sample after 1-month free corrosion.



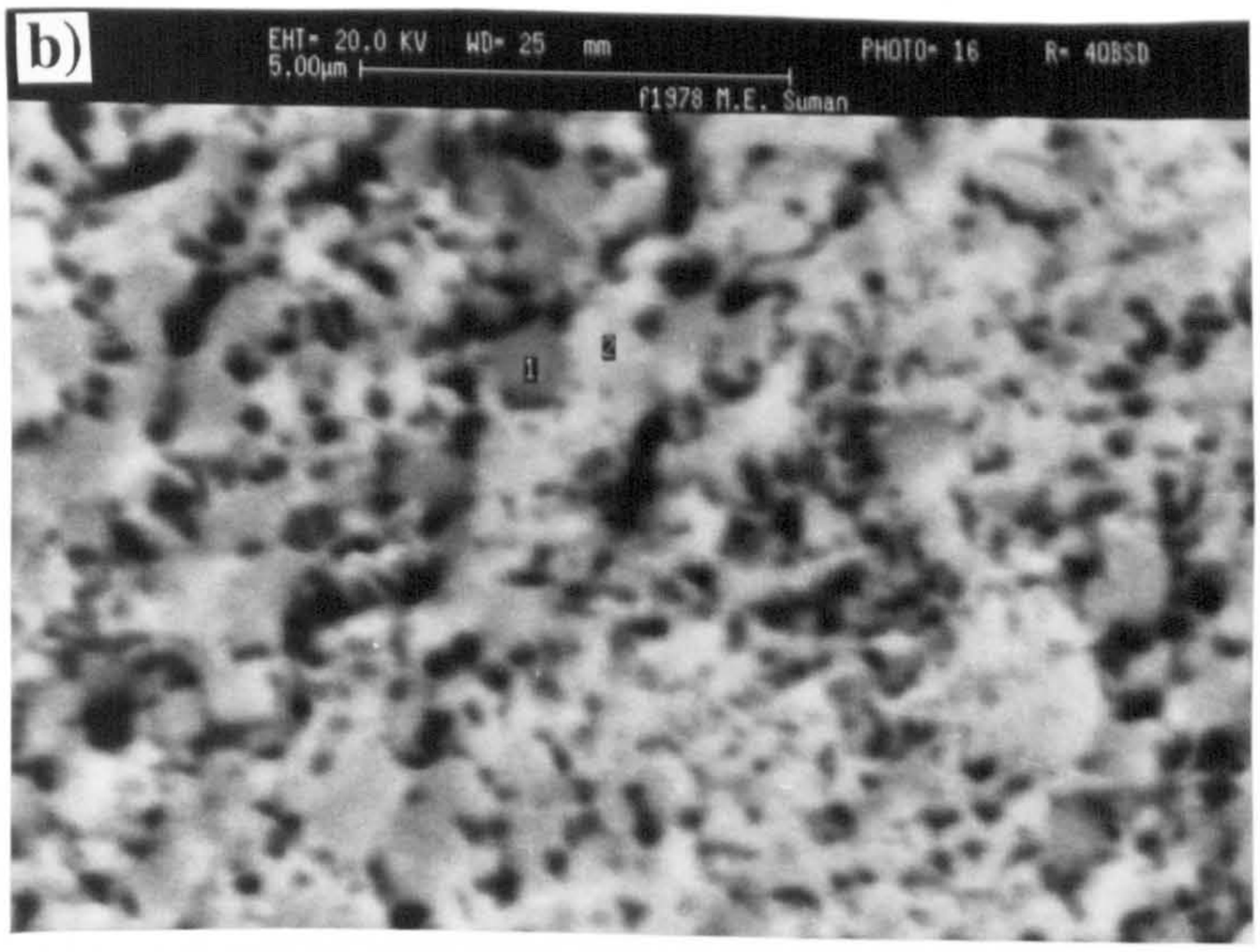


Figure 7.4.9 a) Corrosion attack initiated in a particle with abundant tiny grey hardphase particle; and b) higher magnification of above splat showing preferential dissolution of matrix '2' around grey Mo rich hardphase particle '1'.

Anodic polarisation under liquid impingement

Anodic polarisation tests were performed on *Coating* AII under normal impingement of liquid jet at $17ms^{-1}$. Coating AII on stainless steel and carbon steel substrates displayed once again very similar results.

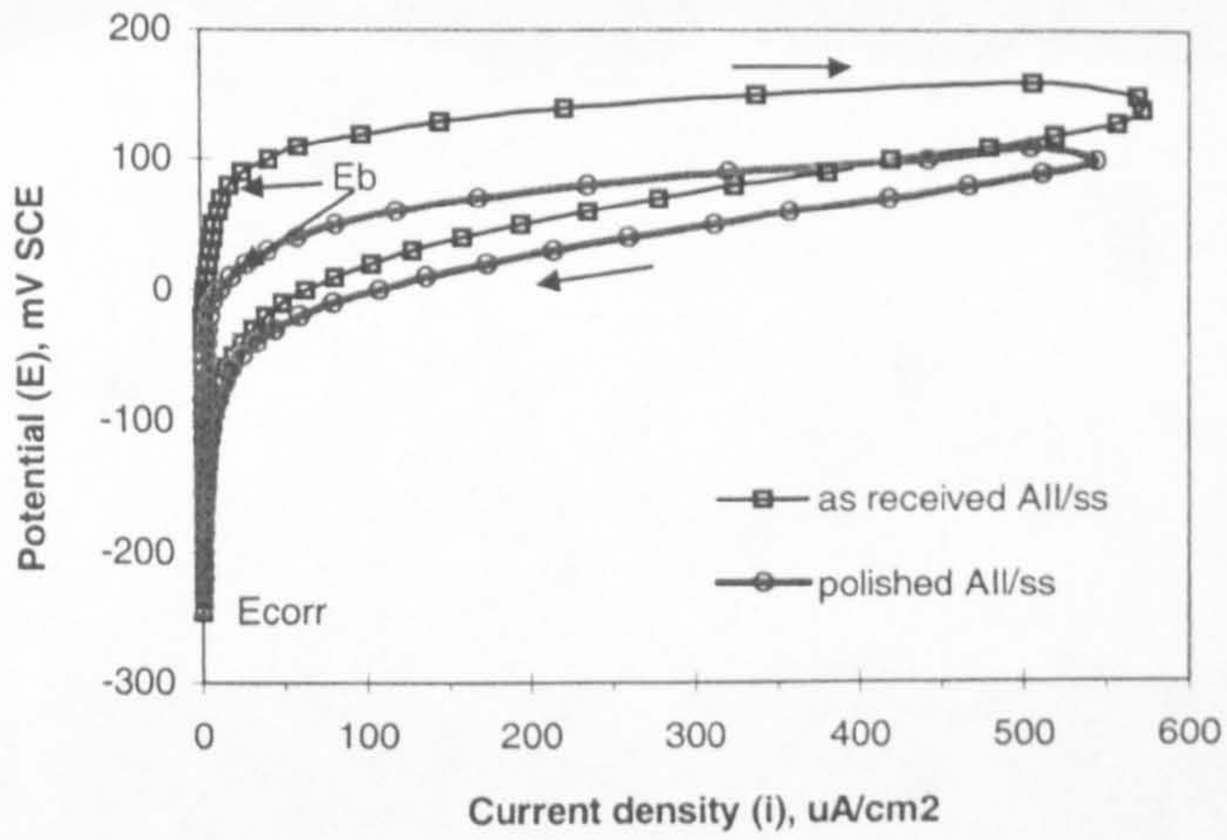


Figure 7.4.10 Anodic polarisation of as-received and polished surfaces of the *Coating* AII under liquid impingement (3.5% NaCl, $17ms^{-1}$, 18°C).

Thus only the coating on stainless steel substrate 'Coating AII/ss' will be presented in this result. Figure 7.4.10 shows anodic polarisation curves of the coating in as-received and polished conditions. Under liquid impingement condition, once again the coating demonstrated a classic passive behaviour shown by its very low current density within a passive range denoted by 'E_b-E_{corr}'. The breakdown potential 'E_b' was about +65mV compared to about +100mV in static polarisation. Polishing again had a similar effect of reducing the breakdown potential 'E_b' to about zero mV. However, this time no shift of E_{corr} in the negative direction was observed after polishing the as-received surface. Microscopic observations showed that the damage mechanism such as splat boundary attack, micro and macropitting, matrix corrosion etc., under impingement condition is very similar to that of *Coating* AI under similar impingement condition whose microscopic results are fully illustrated in a later section 7.5.

Galvanic Interaction between Coating and Substrate

Tests to assess the galvanic effects at the coating/substrate interface were performed on the coating with both carbon steel and stainless steel substrates. The coating specimens, mounted in a non conducting epoxy resin with the cross sections exposed, were allowed to corrode naturally at their free corrosion potential E_{corr}.

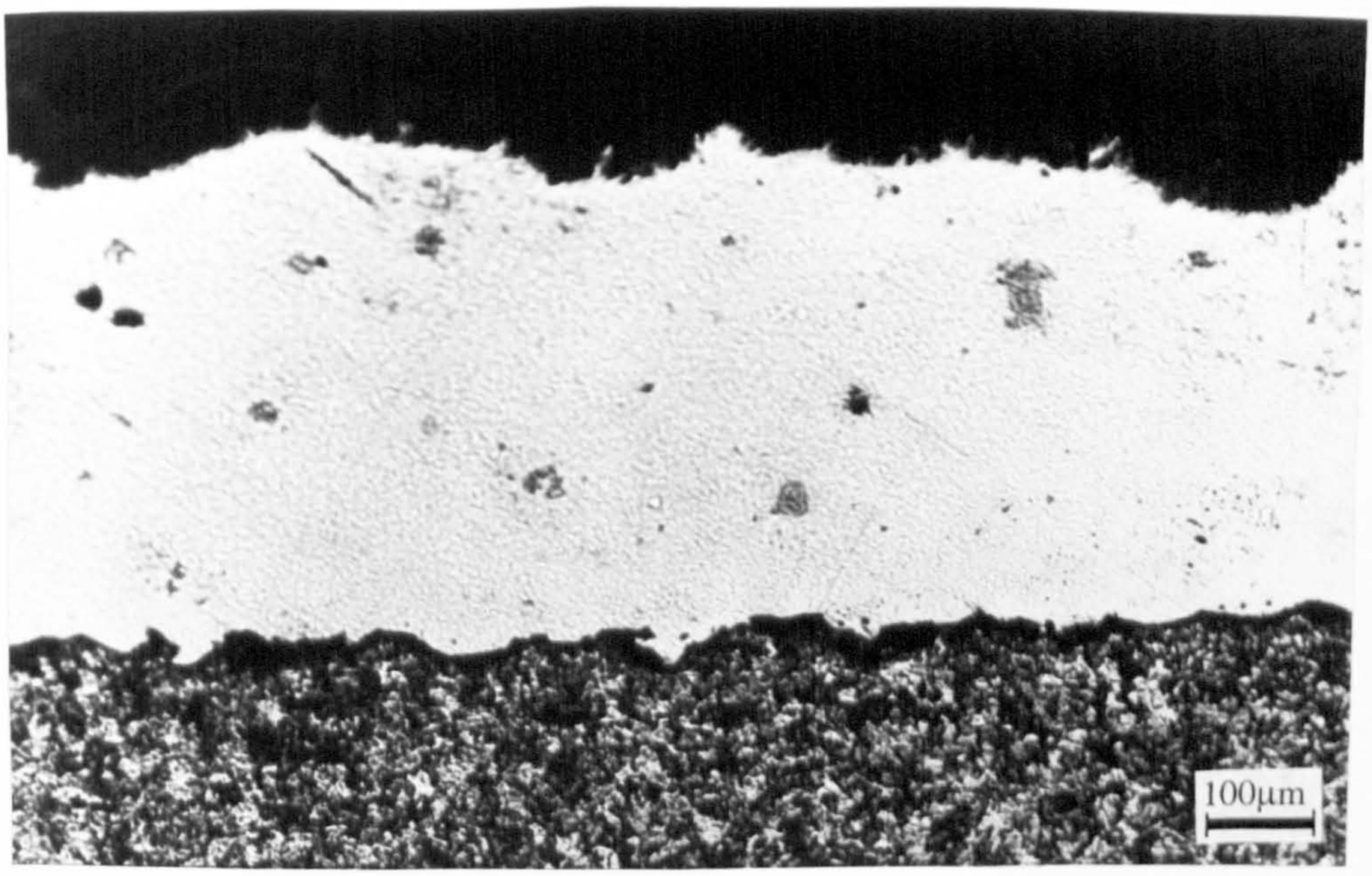


Figure 7.4.11 Severe corrosion attack at coating/substrate interface after 1-week immersion in 3.5% NaCl solution at 18°C.

The exposed area of the coating/substrate ratio was 1:3. After a week immersion, the specimens were removed from the electrolyte made of 3.5% NaCl solution. The coating on a stainless steel substrate showed no evidence of corrosion attack at the coating/substrate interface. The coating on a carbon steel substrate was cleaned with Clarke's solution to remove the corrosion product from the coating. No visible corrosion had occurred on the coating during the 1-week immersion. A few patches on the coating surface in Fig 7.4.11 represents the corrosion product from the substrate that were not removed during the cleaning process. The substrate had corroded extensively as expected. However, there was a distinct zone of relatively excessive attack near to the interface on the substrate as shown in Fig. 7.4.11 with its 'knife line attack'. This attack appeared to form a channel at the interface thus separating the coating from the substrate.

Corrosion of splat particles

Microscopic observations revealed the complexity of corrosion degradation on the coating. Corrosion in the form of 'general' attack as illustrated before was associated with corrosion of particle splats in a random process. The exact reason, why one type of particle splat was attacked and yet the adjacent splat remained virtually unaffected was not clear. Thus the polished Coating AII/ss was marked with diamond indentation 'd_6' (Fig. 7.4.12) and EPMA area analyses were taken for splat particles '1-7' before the coating was subjected to corrosion test. The marked coating sample was then allowed to corrode naturally in 3.5% NaCl at 18°C at its free corrosion potential 'E_{corr}' for two weeks. After this long-term exposure, splat particles were again analysed to assess if any compositional heterogeneity might have affected the different corrosion process of such a multiphase coating. The elemental compositions of the splats are shown in Table 7.4.2. Values in the bracket indicate composition after two weeks corrosion test.

Area	Fe	Ni	Cr	Si	Cu	Mo	Total
1	2.7 (**3.5**)	65.8 (**63.7**)	17.5 (**18.9**)	3.2 (**3.5**)	2.0 (**1.6**)	5.6 (**6.9**)	98.9 (**98.6**)
2	2.8 (**3.5**)	63.7 (**60.8**)	17.6 (**20.5**)	3.3 (**3.1**)	2.2 (**1.5**)	6.8 (**8.2**)	98.3 (**98.2**)
3	2.9 (**3.5**)	67.3 (**72.1**)	16.8 (**17.4**)	3.2 (**3.6**)	1.5 (**0.5**)	3.7 (**2.2**)	97.5 (**99.8**)
4	3.0 (**3.5**)	67.3 (**68.3**)	17.0 (**18.8**)	3.9 (**3.6**)	1.4 (**1.0**)	3.2 (**3.2**)	98.7 (**98.9**)
5	3.1 (**3.6**)	68.0 (**69.6**)	17.5 (**19.3**)	3.2 (**3.4**)	1.6 (**0.5**)	3.9 (**2.6**)	99.2 (**99.3**)
6	3.0 (**3.5**)	68.6 (**73.4**)	17.1 (**18.0**)	3.1 (**3.8**)	1.1 (**0.4**)	3.0 (**1.9**)	98.5 (**101**)
7	2.7 (**2.9**)	65.9 (**65.3**)	17.4 (**19.1**)	3.3 (**3.7**)	2.4 (**1.7**)	5.9 (**7.1**)	98.6 (**100**)

Table 7.4.2 Area analyses of particle splats around indentation 'd_6' (Fig. 7.4.12) before and after the 2-weeks free corrosion test (values in brackets) in 3.5% NaCl solution at 18°C.

Figure 7.4.12a shows clear particle splats of a polished coating prior to exposure to saline solution. Splats '1' and '2' clearly indicate abundance of tiny grey hardphase particles, whereas splat '3' exhibited no hardphase particles. Splats '4' and '5' have mainly black larger hardphase particles with some of similar hardphase particles also in the splat '6'. Splat '7' appears to have tiny grey hardphase particles in much less amount. After immersion of the polished coating sample for 2 weeks, all labelled splats showed clear indication of corrosion attack as shown in Fig. 7.4.12b. Splats '1' and '2' had the largest corrosion attack, which is quite distinguishable and associated mainly with corrosion of matrix surrounding the hardphase particles.

The severe attack was presumably due to presence of a large number of tiny grey hardphase particles containing molybdenum and such results were consistent. Perhaps, there exists a galvanic cell with higher charge transfer from the matrix (less noble) to the hard phase particle, which is nobler. Table 7.4.2 shows that there is a reduction of Ni in splats '1' and '2' as might be expected since the Ni has corroded from the matrix. The increase in Cr and Mo might have resulted due to more hard particles standing out on the surface, which have not yet dislodged during the 2 weeks corrosion period. Splat '7' exhibited a similar trend. However, splats '3', '4', '5' and '6' behaved differently with increased Ni content but reduction in Mo. Cr content has also increased in these splats. Reduction of Cu and increase in Fe content after the corrosion was evident for all splat particles. Another interesting evidence was that splats '1', '2', '3', '4', '5' and '6' showed initiation of splat boundary attack.

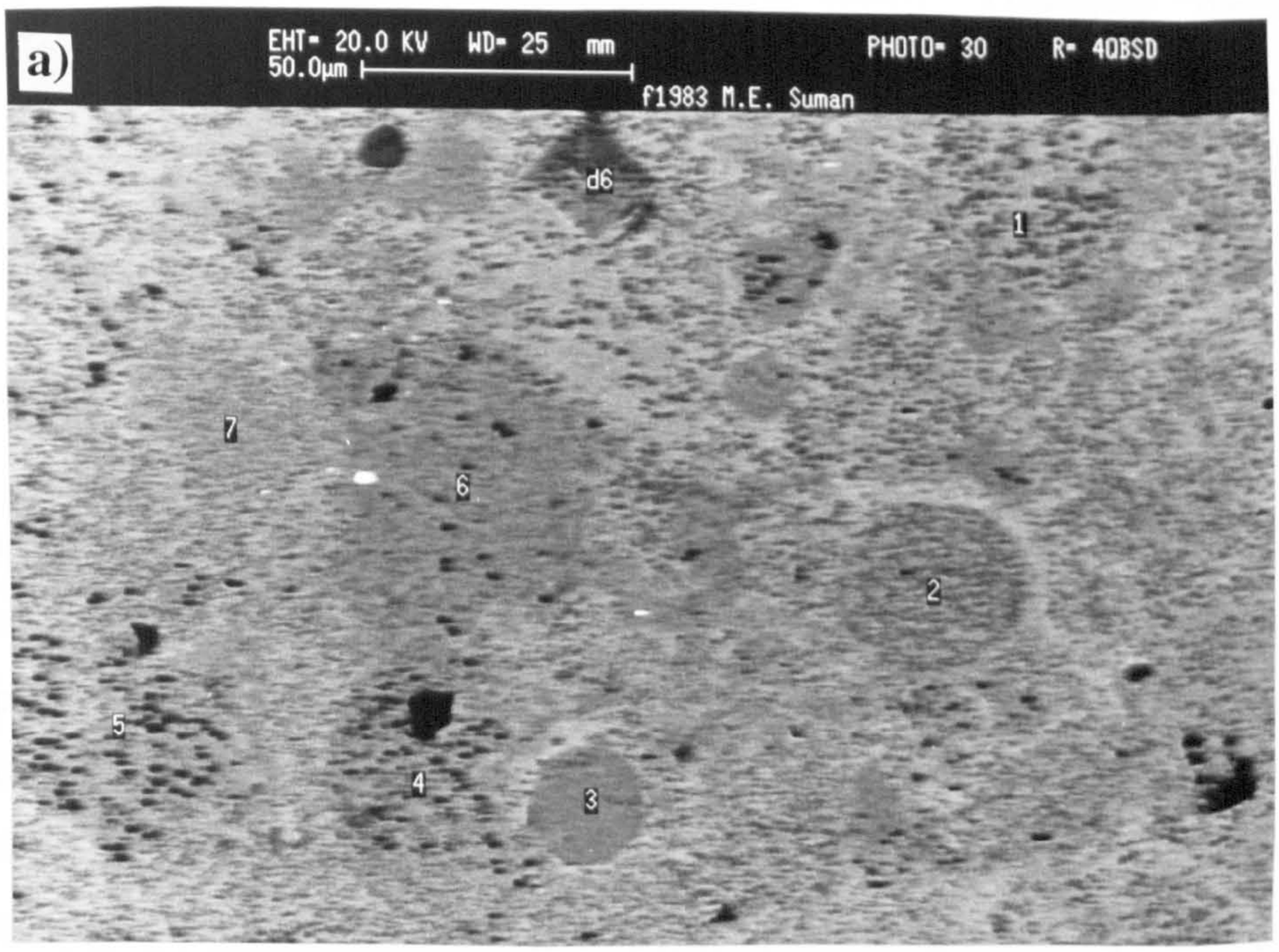


Figure 7.4.12 a) Particle splats of a polished specimen prior to corrosion test marked with diamond indentation 'd_6'; and b) same particle splats after 2-weeks free corrosion in 3.5% NaCl solution at ambient temperature.

Summing up, splat boundaries are more prone to initiate preferential corrosion attack. Generally, it was found that particle splat containing tiny grey hardphase particles (rich in Mo) seemed more likely to corrosion attack possibly due to large potential difference between the hardphase particles and surrounding matrix. Moreover, the higher abundance of hardphase particles in a splat appears to accentuate corrosion. This might signal a huge charge transfer from the matrix to a large number of hardphase particles acting as cathodes.

Corrosion of powder particles

The complexity of the corrosion mechanism of a multiphase coating has been demonstrated. A new attempt was tried to study the corrosion behaviour of such a discrete powder particle. A few powder particles were injected with a syringe and embedded into a cold mounting resin. The particles were then polished and analysed and labelled by SEM (Fig. 7.4.13) prior to corrosion test. The powder particles were carbon coated in order to facilitate SEM analysis. When the polished powder particles were washed with methanol to remove the carbon coating, the particles fell off from the mounting resin. This indicated a difficulty in performing experiment at the micro level of such powder particles.

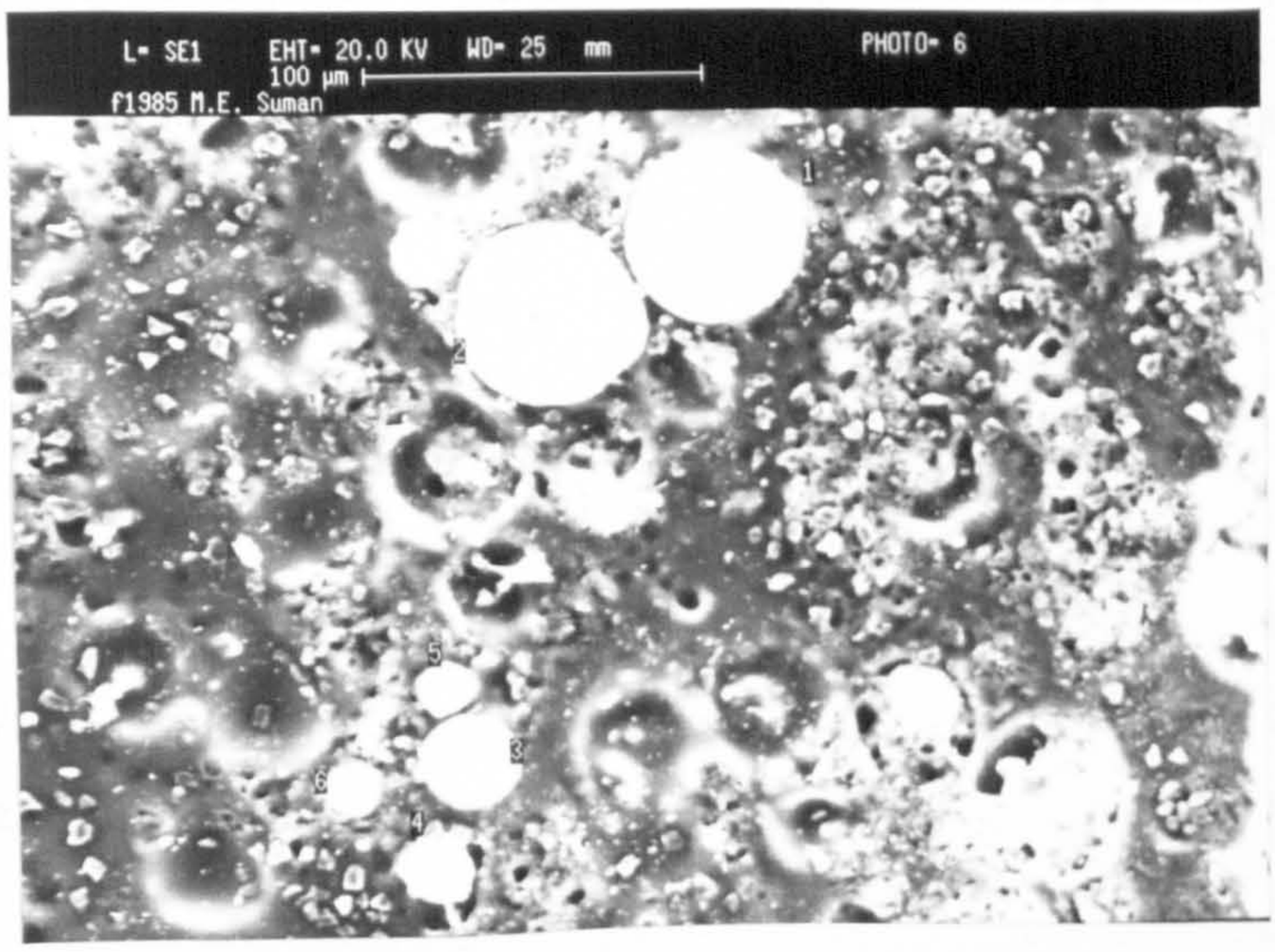


Figure 7.4.13 Individual powder particles embedded in a cold mounting resin.

7.5 Liquid and solid-liquid erosion-corrosion of Coating AI

Erosion-corrosion tests in both solid-free liquid and solid-liquid impingement conditions were carried out for coating AI (mainly with ss substrate) at an impingement velocity of $17ms^{-1}$, 18°C and 90° impingement angle. A few anodic polarisation tests under liquid impingement were carried out also on the coating with cs substrate. Tests were also carried out for uncoated stainless steel specimen for comparative purpose. Experiments were carried out on polished surfaces unless mentioned 'as-received'. Details of the experimental procedure were already mentioned in section 6.3.

Weight loss measurement

Under solid-free liquid impingement at $17ms^{-1}$, both materials (coating AI/ss and stainless steel) exhibited no detectable weight loss during a three-hour test. Further experiments were conducted for a total of 6 days with the sample coupons being weighed after 2, 4, 6 days and observed under the microscope to visualise the weight loss mechanism. The results obtained are given in Table 7.5.1 and reveal higher material losses for the coating compared to stainless steel.

Material	***TWL, mg***						***Weight. loss under CP, mg***					
Coating AI	2 days	*Avg*	4 days	*Avg*	6 days	*Avg*	2 days	*Avg*	4 days	*Avg*	6 days	*Avg*
	0.7 1.0 1.3	***1.0***	1.2 2.1 1.7	***1.7***	1.9 2.6 2.7	***2.4***	0.1 0.2	***0.15***	0.5 0.5	***0.5***	0.4 0.3	***0.35***
Stainless steel	0.5 0.3 0.6	***0.5***	0.7 0.4 0.9	***0.7***	0.9 0.8 1.1	***0.9***	0.1 0.1	***0.10***	0.6 0.5	***0.55***	0.4 0.2	***0.30***

Table 7.5.1 Weight loss results under solid-free liquid impingement of $17ms^{-1}$.

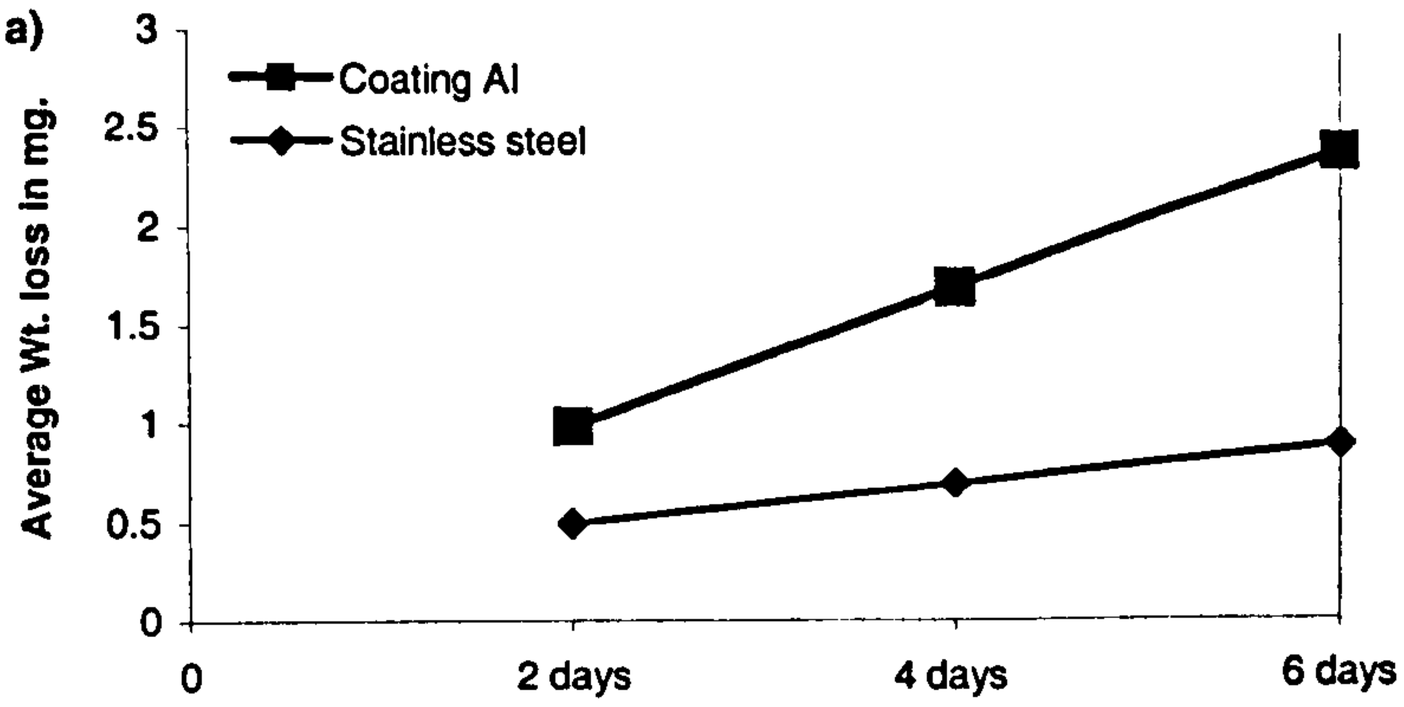
Tests in which the sample was cathodically protected while under impingement were conducted. It was found that application of CP reduced the weight loss of both materials essentially to zero after 2 days since the sensitivity of the weight measurement was 0.1mg. After 4 days and 6 days of CP weight losses were evident in both materials, but the weight losses were much lower than those found without the application of CP.

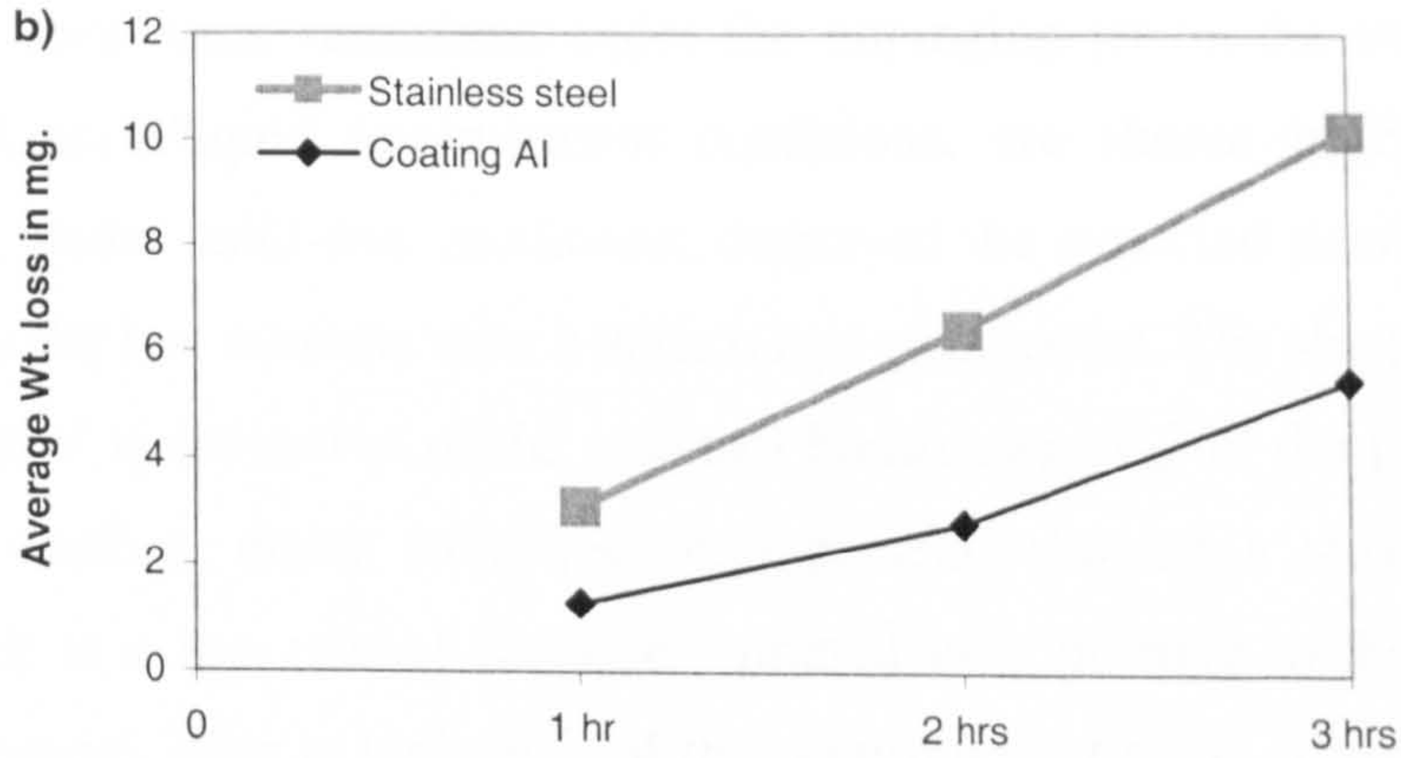
Measured weight loss data for the solid-liquid experiments with a solid loading of 800ppm are presented in Table 7.5.2. The comparative results obtained in solid-liquid erosion were opposite to those displayed under pure-liquid impingement with the stainless steel exhibiting much higher material loss than the polished coating. Again the application of CP resulted in a substantial reduction in weight loss from both materials.

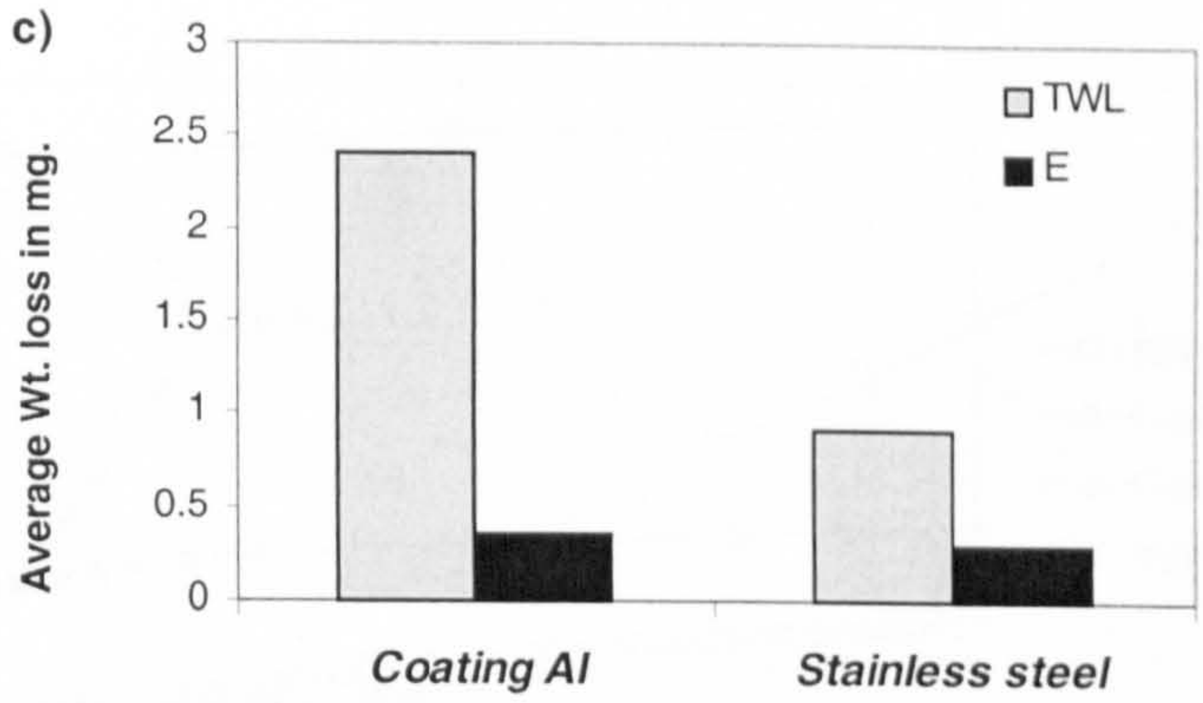
Material	*TWL, mg*						*Wt. loss under CP, mg*	
	1 hr	*Avg.*	*2 hrs*	*Avg.*	*3 hrs*	*Avg.*	*1 hr*	*Avg.*
Coating	1.3 1.5 1.2 1.3	***1.33***	2.9 2.8	***2.85***	5.7 5.4	***5.55***	0.9 1.1 0.9 0.8	***0.93***
Stainless steel (316L)	3.3 3.1 2.9 3.1	***3.1***	6.2 6.7	***6.45***	10.5 9.9	***10.2***	2.3 1.9 2.2 2.0	***2.1***

Table 7.5.2 Weight loss under solid-liquid impingement at $17ms^{-1}$.

The average weight loss trend in both solid-free liquid impingement and solid/liquid impingement are shown in Fig. 7.5.1a and b. The steeper curve in Fig. 7.5.1a might signal that the material loss rate of the coating progresses as a function of time, while the weight loss rate for the stainless steel is not very significant. Figures 7.5.1c and d show in column charts the total weight loss 'TWL' and weight loss due to pure erosion 'E' under CP in liquid and solid/liquid impingement conditions respectively. Much pronounced effect of CP was displayed by the coating in liquid impingement condition as shown in Fig 7.5.1c with reduction in weight loss by almost 7 times.







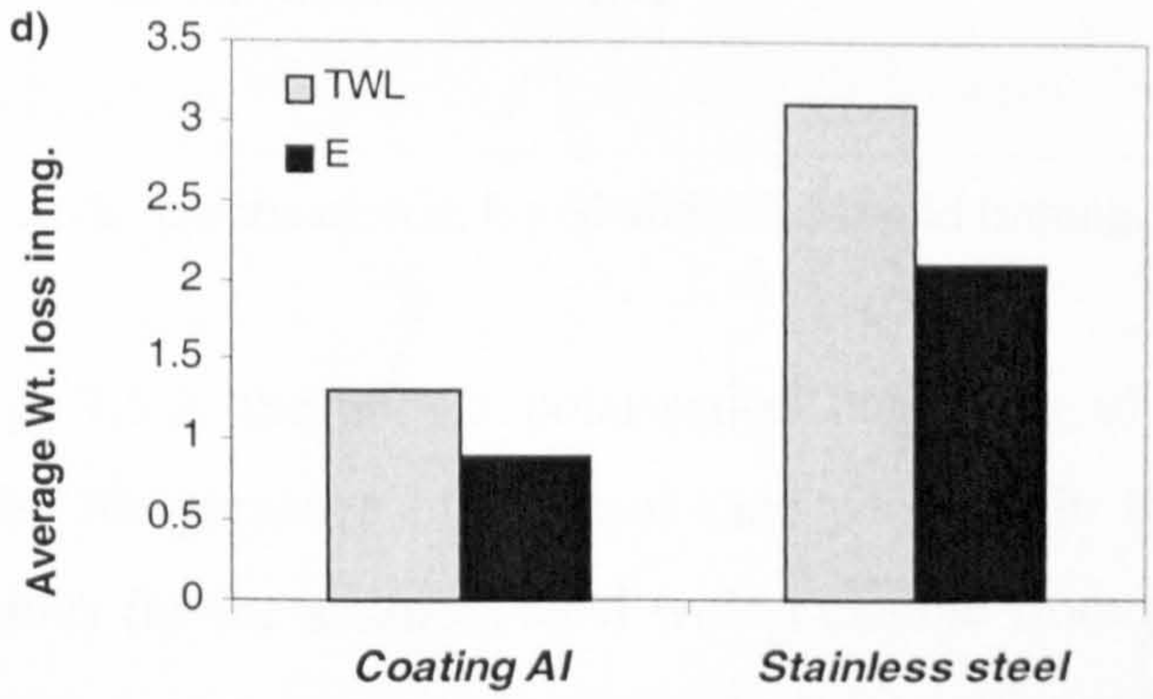


Figure 7.5.1. Average weight loss trend during a) solid-free liquid; b) solid/liquid impingement at 17ms^{-1}, 18°C and 3.5% NaCl solution; and column charts showing total weight loss 'TWL' and weight loss due to pure erosion 'E' under CP; c) after 6 days of liquid impingement; d) after 1 hour solid/liquid impingement.

Anodic polarisation

Anodic polarisation tests conducted under the impinging jet on the two materials in solid-free and solid/liquid impingement conditions, are shown in Fig. 7.5.2. The stainless steel, under solid-free conditions, displayed the expected passive behaviour - represented by the low currents over a wide range of potential. The sharp rise in current at about +420mV is indicative of the eventual breakdown (E_b) of the passive film. In contrast, the coating, under solid-free impingement, showed a steadily increasing current - albeit at a low rate of increase - immediately positive to the starting (free-corrosion) potential. This is indicative of the occurrence of some corrosion activity on the surface under free-corrosion circumstances.

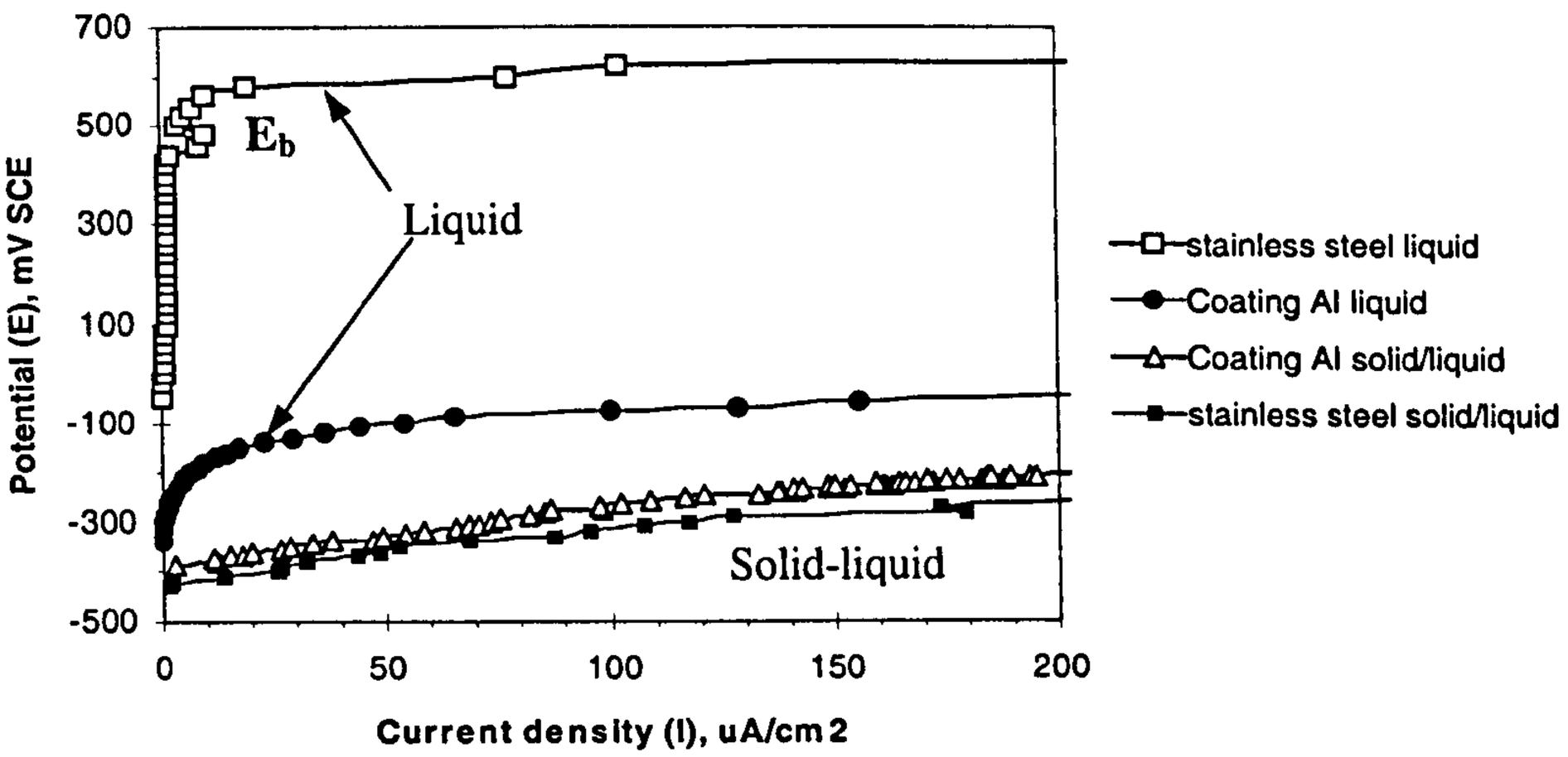
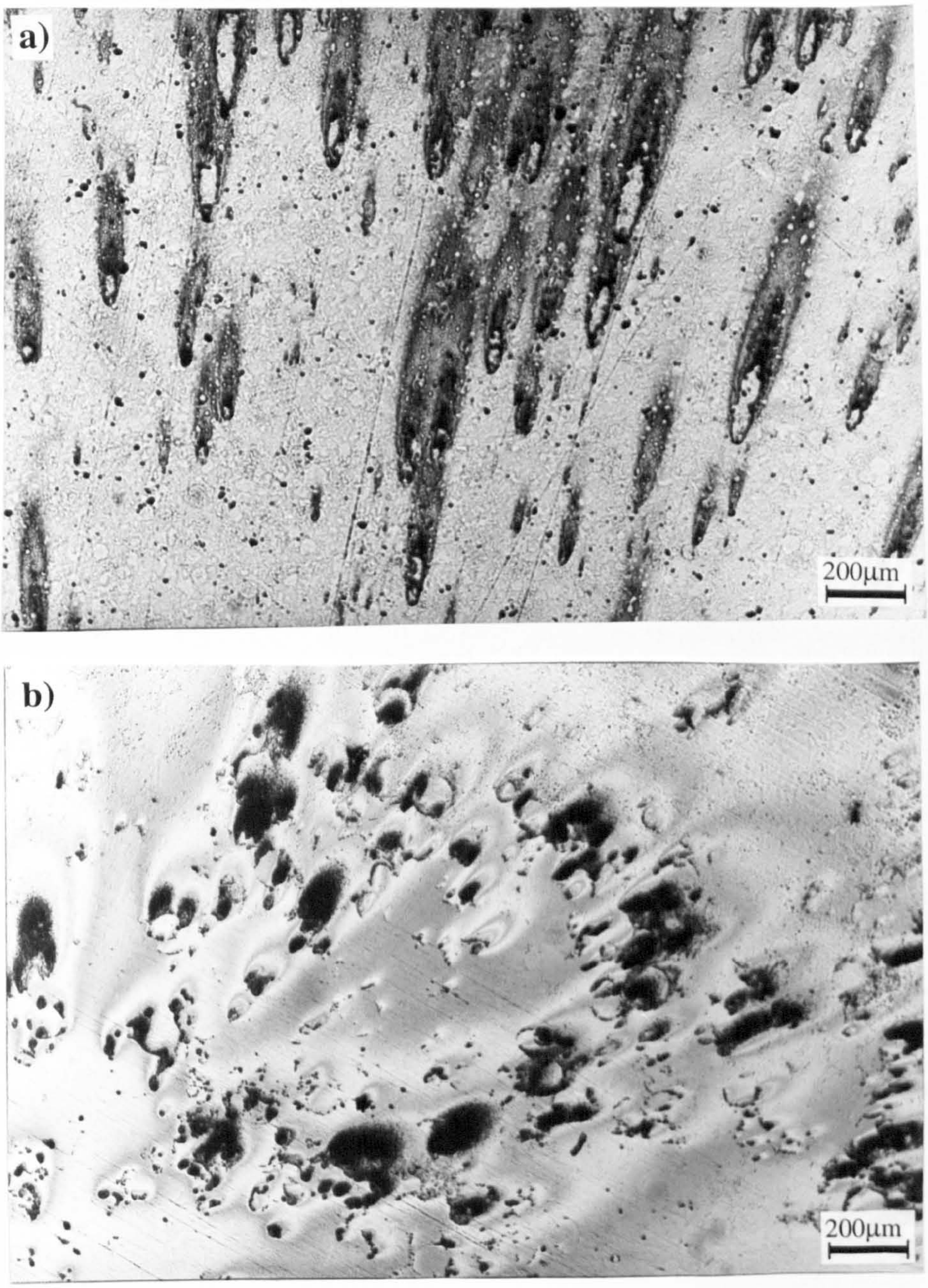


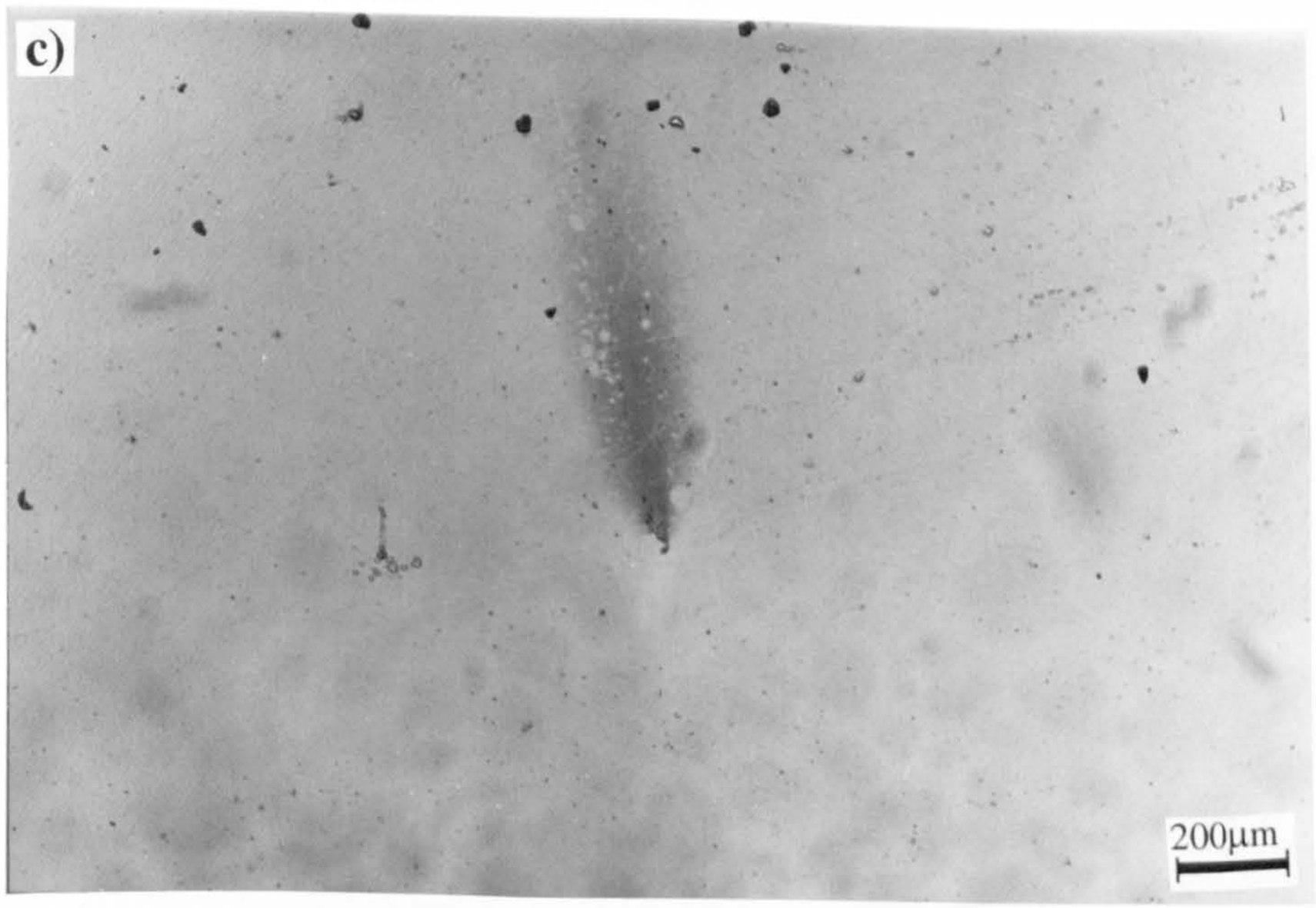
Figure 7.5.2. Anodic polarisation in liquid and solid-liquid impingement tests.

As is shown in Fig. 7.5.2, the anodic polarisation behaviour of both materials was altered drastically by the presence of 800ppm sand particles in the impinging liquid. This was most obvious for the stainless steel with a change from passive behaviour to active corrosion. It was also substantial for the coating as evidenced by the considerably higher rates of current increase, for the solid/liquid case, immediately positive to the free corrosion potential.

Microscopic observations after solid-free liquid impingement.

Corrosion products were much more clearly visible on the coating surface than on stainless steel under both free-corrosion impingement and impingement with anodic polarisation. Corrosion in the form of comet-shaped streams of corrosion product was readily distinct after just two days of liquid impingement on the coating and this attack was significantly increased after 6 days. Stainless steel only started to show such localised attack after 6 days (Fig. 7.5.3). The comet-shaped attack was associated with the flow directionality in the higher shear zone and was not observed in the central area directly under the jet.





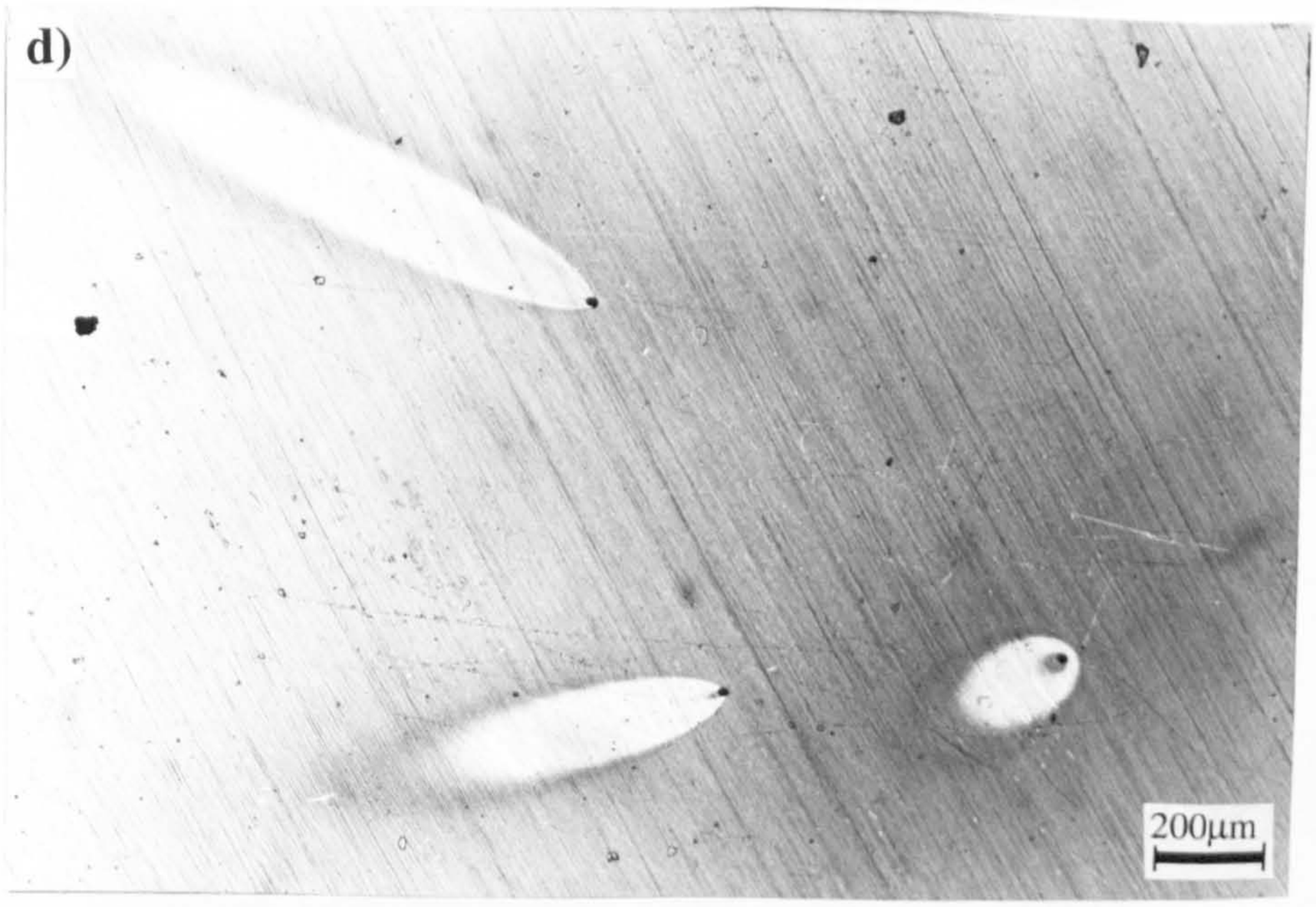
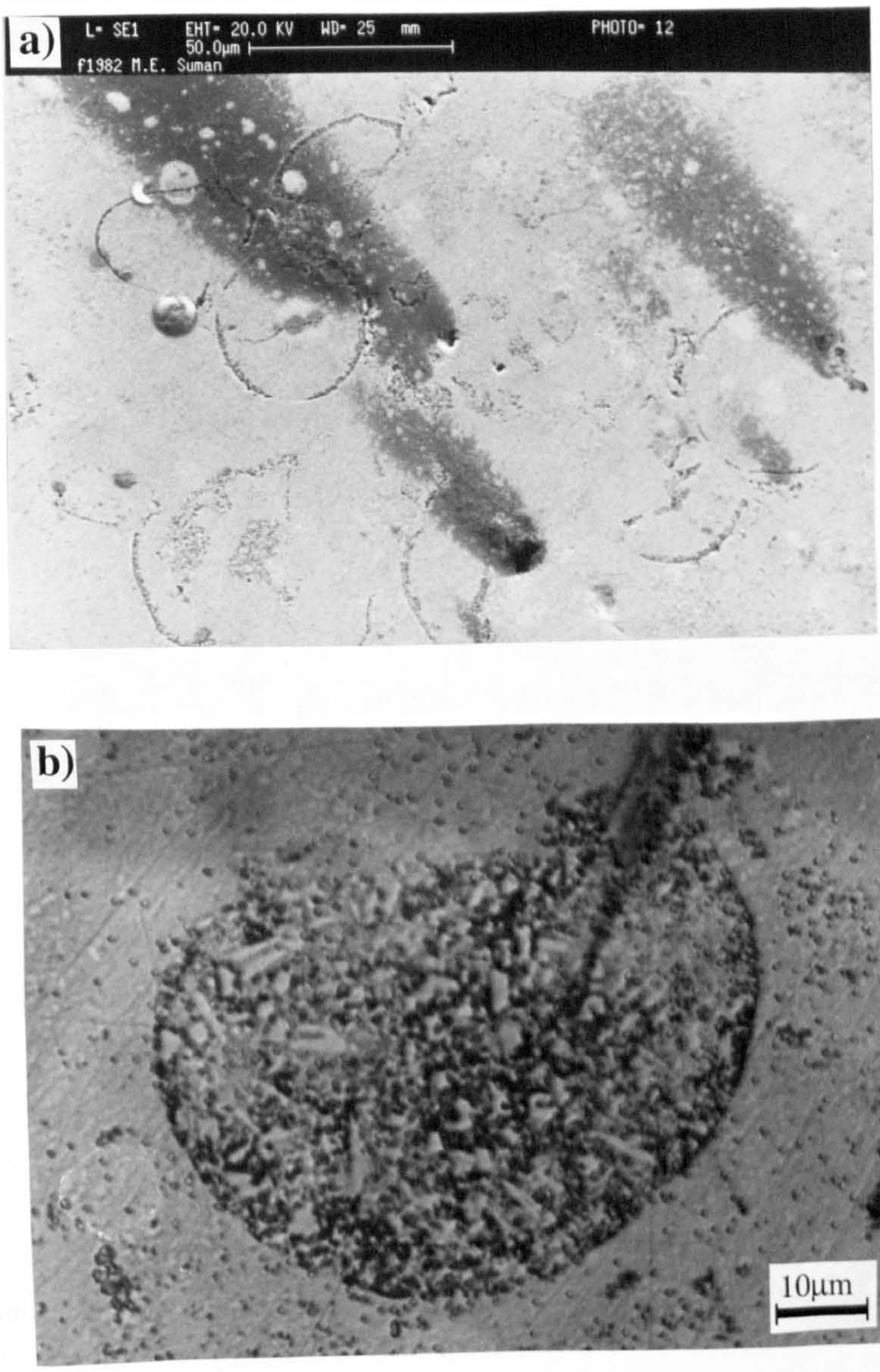


Figure 7.5.3 Comet pits on coating (a) after 6-days solid-free liquid impingement; (b) after anodic polarisation and stainless steel (c) after 6-days solid-free liquid impingement; (d) after anodic polarisation.

On a microscopic level, it was obvious that erosion-corrosion attack on the coating was occurring generally over the specimen surface by very complex corrosion mechanisms associated with general corrosion of the matrix, micro-galvanic attack at the hard particle/matrix interface together with more-severe preferential attack around some of the sprayed particle 'splat' boundaries (7.5.4a, b).

A very small amount of crevice corrosion, approximately 1% of the total length of the polymeric sealant (which was used to seal the coating/substrate interface) was also evident. The comets on the free surface comprised streams of corrosion product emanating from relatively deep pits at the comet head (Fig. 7.5.4c) resulted due to excavation of sub-layers of the coating within the local pit.



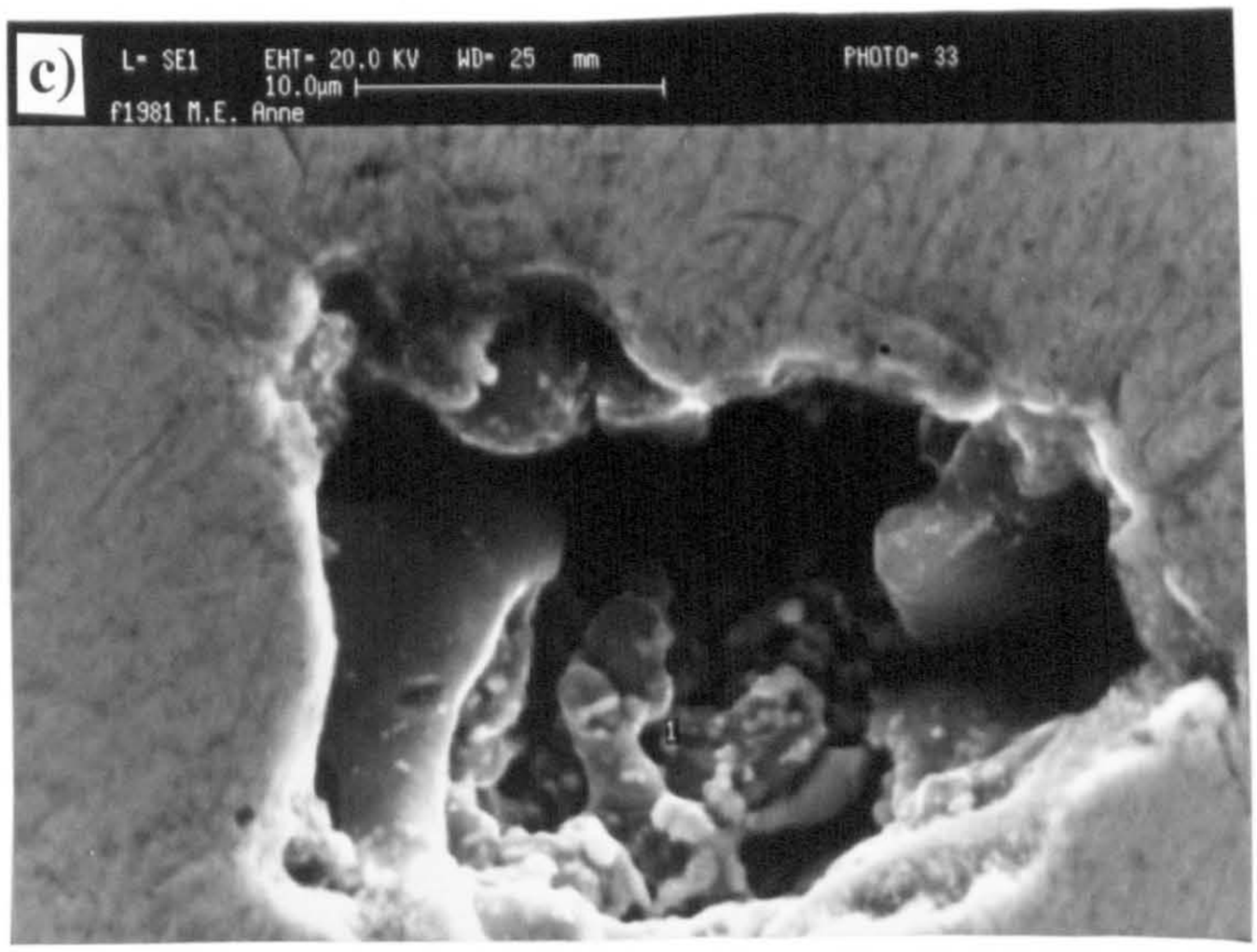


Figure 7.5.4 a) Coating showing comet pits, splat boundary attack and preferential attack around hard phase particles after 6-days liquid impingement; b) comet stream emanating from hard particle/matrix interface; and c) deep pit at head of one of above comets after removing corrosion product with Clarke's solution.

In contrast, exposure of the stainless steel, under similar conditions of liquid impingement, resulted in much less deterioration with a much smaller concentration of comets (Fig. 7.5.3) some of which were associated with pitting and dislodgement of sulphide inclusions at the comet head (Fig. 7.5.5). EPMA results unveiled high sulphur concentration (max. 22.4%) of the inclusion '1' shown in the Fig. 7.5.5, which also showed several other tiny pits surrounding the comet head.

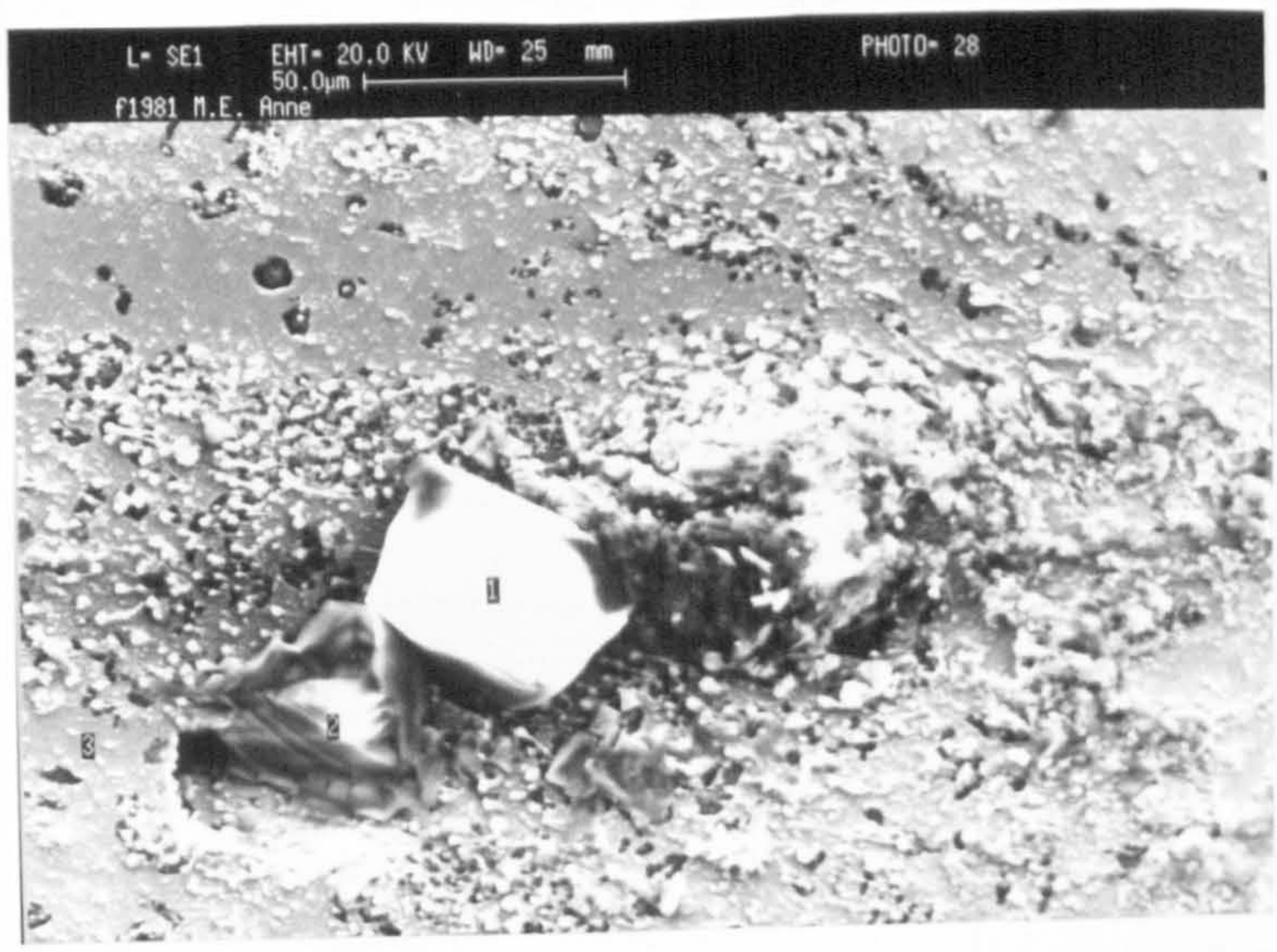
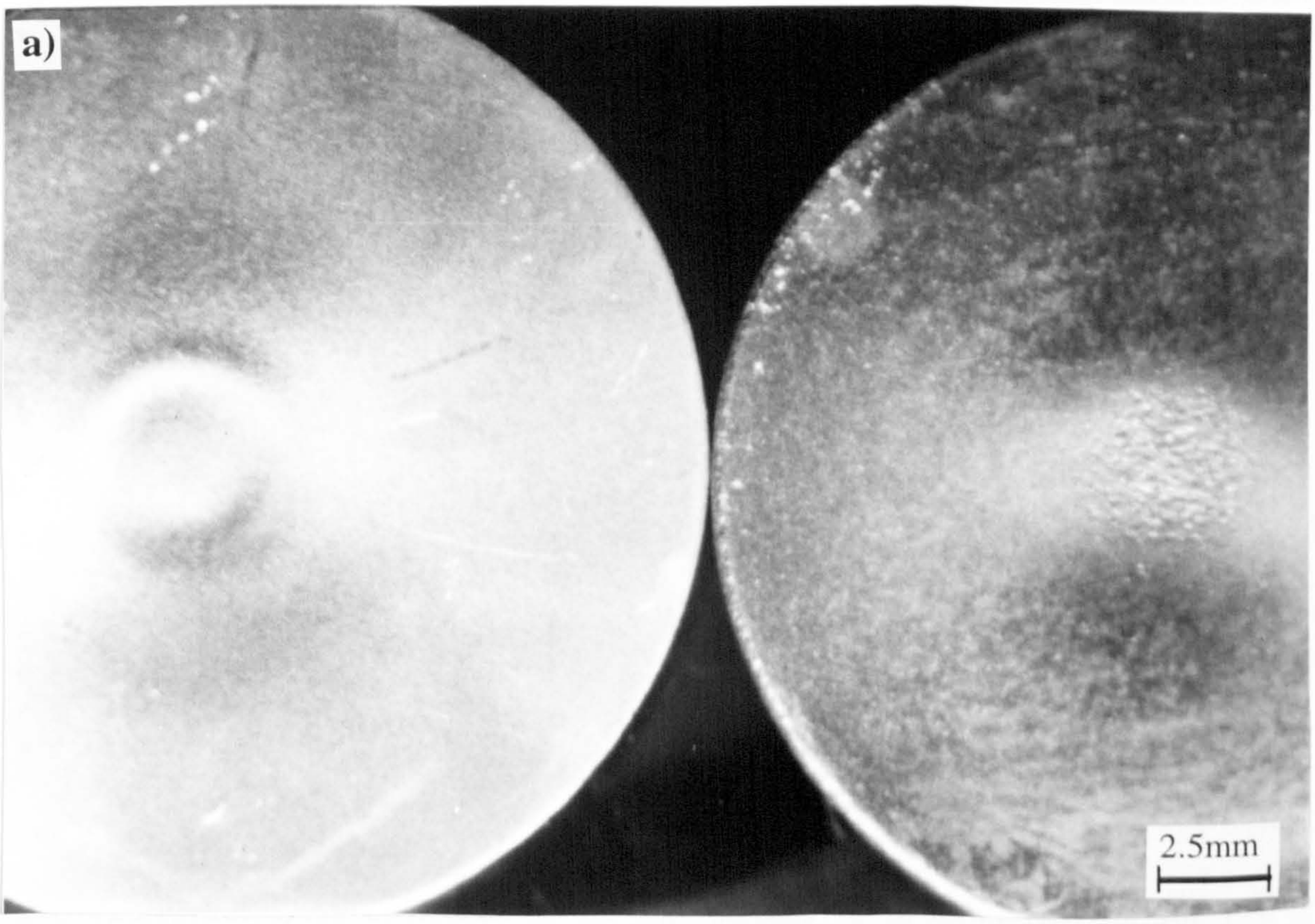


Figure 7.5.5 Sulphide inclusion emanating from the comet head directing towards the liquid flow and several tiny pits surrounding it on the free surface of the stainless steel specimen.

Microscopic observations after solid-liquid impingement

Examination of specimens after solid/liquid impingement showed clear wear scars (Fig. 7.5.6) after just a one-hour test, demonstrating much higher material loss when solids are present. It is also evident from Fig. 7.5.6a that the damage to stainless steel was greater than to the coating and that there were major differences between the two materials with the stainless steel having an eroded surface with smoother features (Fig. 7.5.6b) as opposed to the rougher surface, containing relatively-large holes formed by drilling actions of impinging slurry, on the coating (Fig. 7.5.6c).



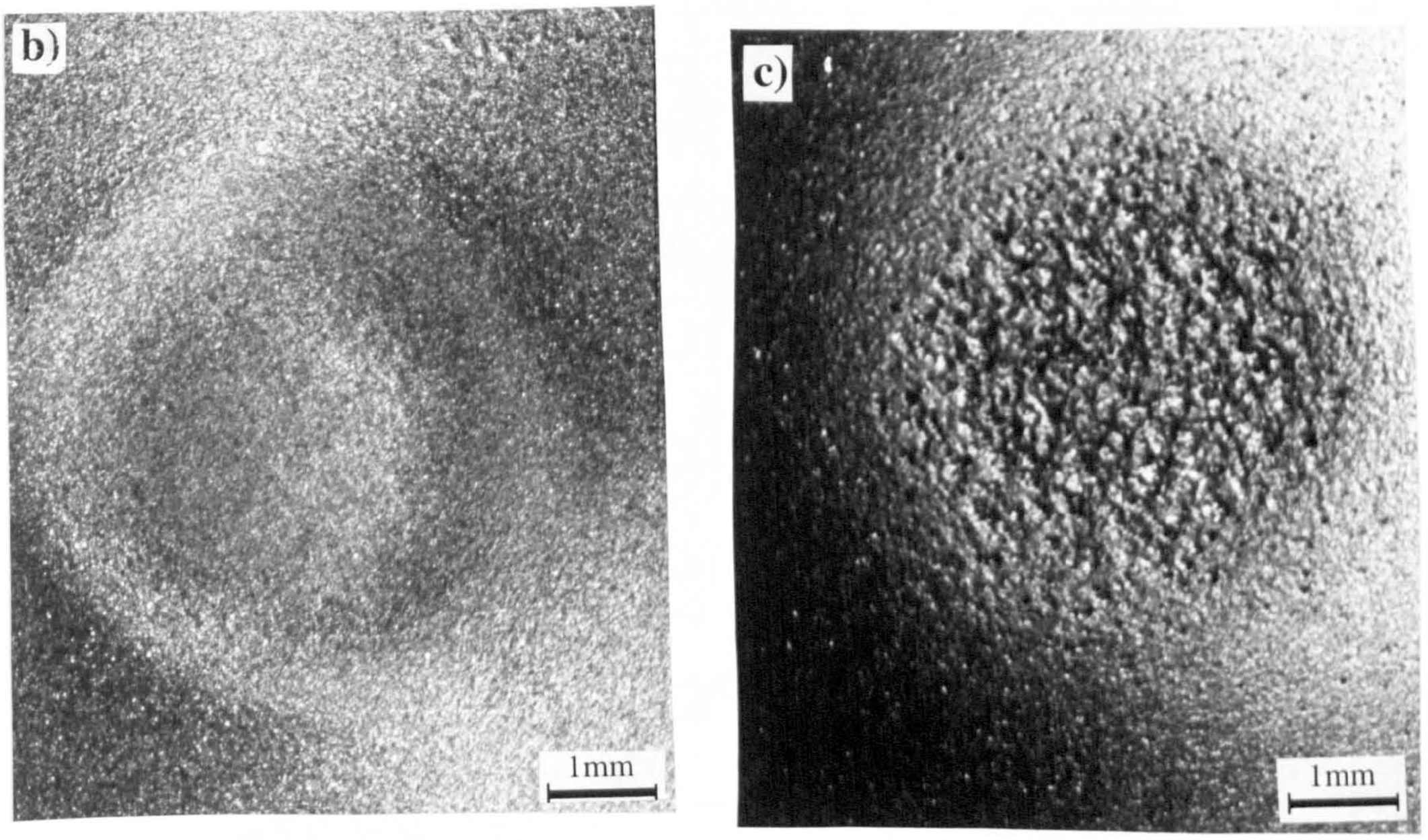


Figure 7.5.6 a) Wear scars after 2-hours solid/liquid impingement on *Coating* AI (right) and stainless steel (left); b), c) Higher magnifications of above wear scars of stainless steel and coating respectively showing smooth and rough surfaces

The higher material loss of the stainless steel was confirmed also by examining the cross section through the central wear scar of the eroded sample. Figure 7.5.7 shows Talysurf traces of the wear scars under the impinging jet after 2 hours of free solid/liquid impingement, which clearly demonstrate the higher material loss for the stainless steel specimen. The material loss of the central region directly under the 4mm jet for the stainless steel specimen was 1.4 times higher than that for the coating (measured by Image Analysis). The remaining higher material loss for the stainless steel compared to the coating after the same 2-hours impingement as displayed in the Table 7.5.2 was confirmed in the outer region away from the central area. Moreover Fig. 7.5.7 also demonstrated the difference in the mechanisms of material loss for the two materials investigated. As seen from the Talysurf traces, stainless steel displayed a ductile nature of material ploughing with smooth surface, whereas the coating showed a brittle behaviour with a rough surface associated with localised damage in the form of several deep peaks and valleys inside the groove.

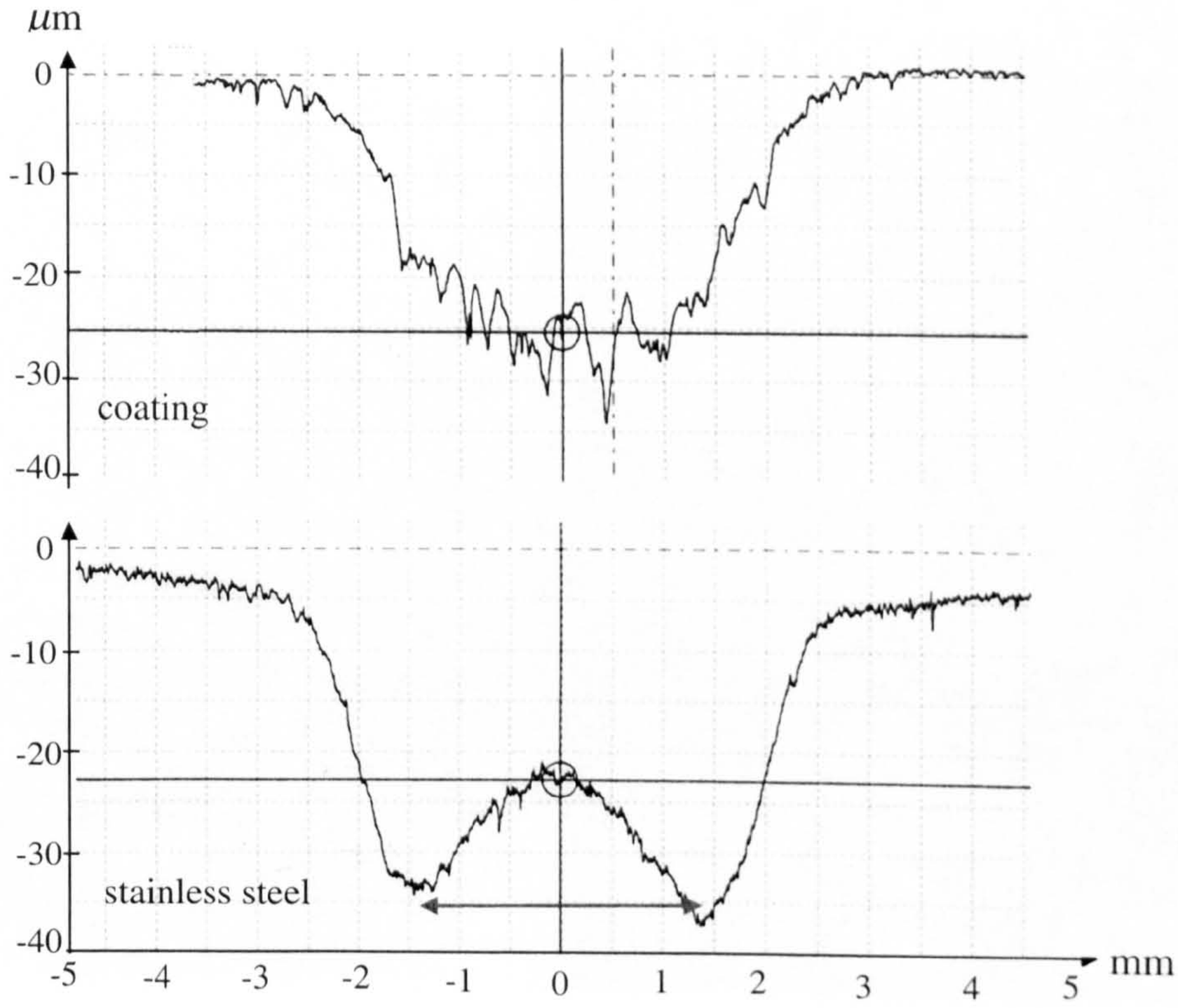


Figure 7.5.7 Talysurf traces of *Coating* AI and stainless steel after 2-hours of free solid/liquid impingement (800ppm silica sand).

The removal of material from the coating under the jet was mainly associated with the drilling action forming macro-pits (Fig. 7.5.8). However, the higher material loss of stainless steel involved severe ploughing (usually associated with low-angle attack) of material just out from the central region of the specimen. The region further away from the centre had well defined grooving and the outermost region was found to have large numbers of deep tracks resulting from ploughing by the particles impinging at low angles and lower velocities. Figure 7.5.9 shows the comparison of individual particle wear tracks of the coating and the stainless steel at a distance of 8mm away from the centre of the specimen with more ploughing on the stainless steel clearly evident. Figure 7.5.10 shows an outer region (low angle cutting) of a cross sectional view of the eroded stainless steel specimen after 1-hour solid/liquid impingement evidencing craters in the form of plastic deformation.

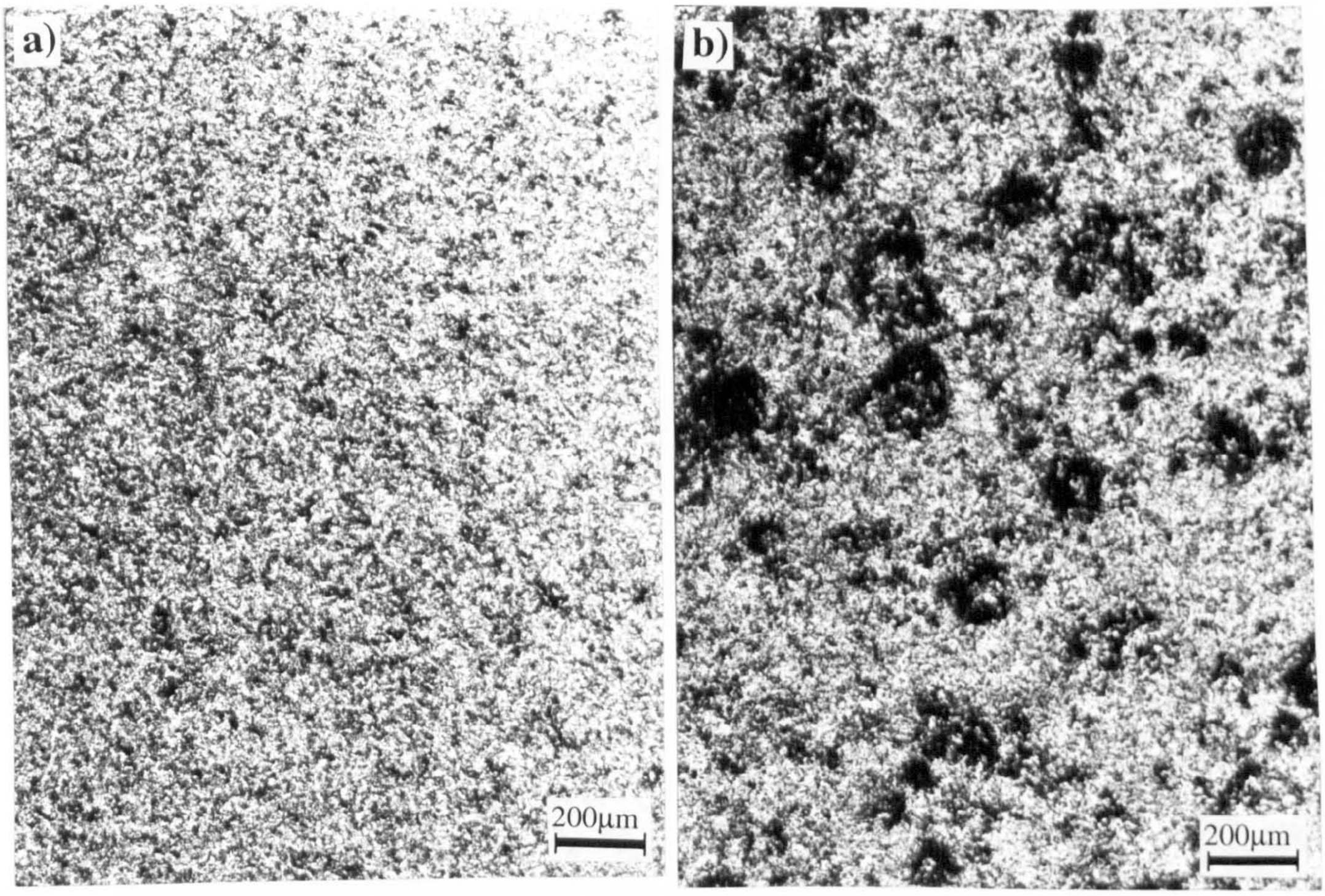
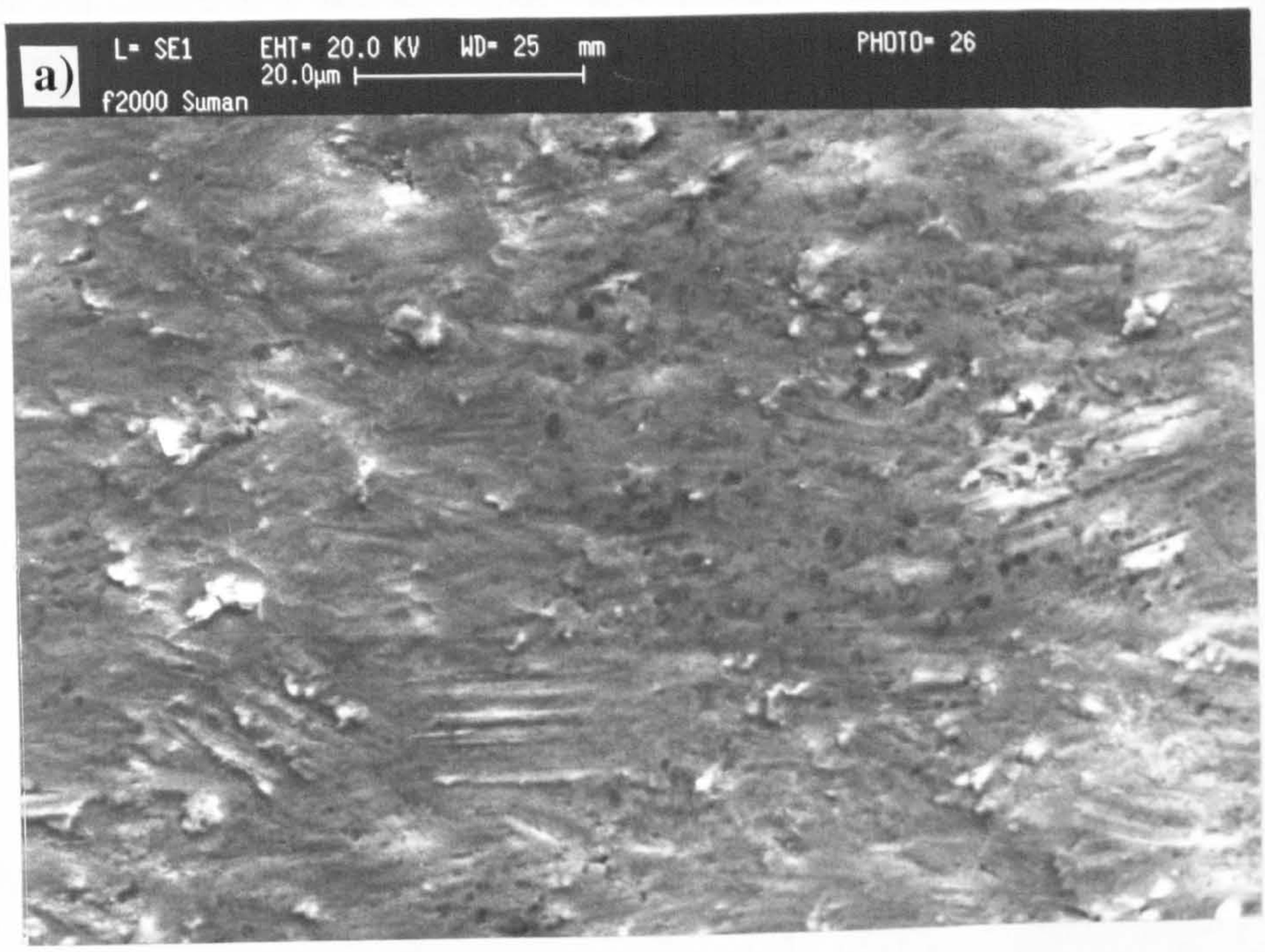


Figure 7.5.8 In central wear scars of (a) stainless steel; and (b) coating AI after 1-hour solid/liquid impingement.



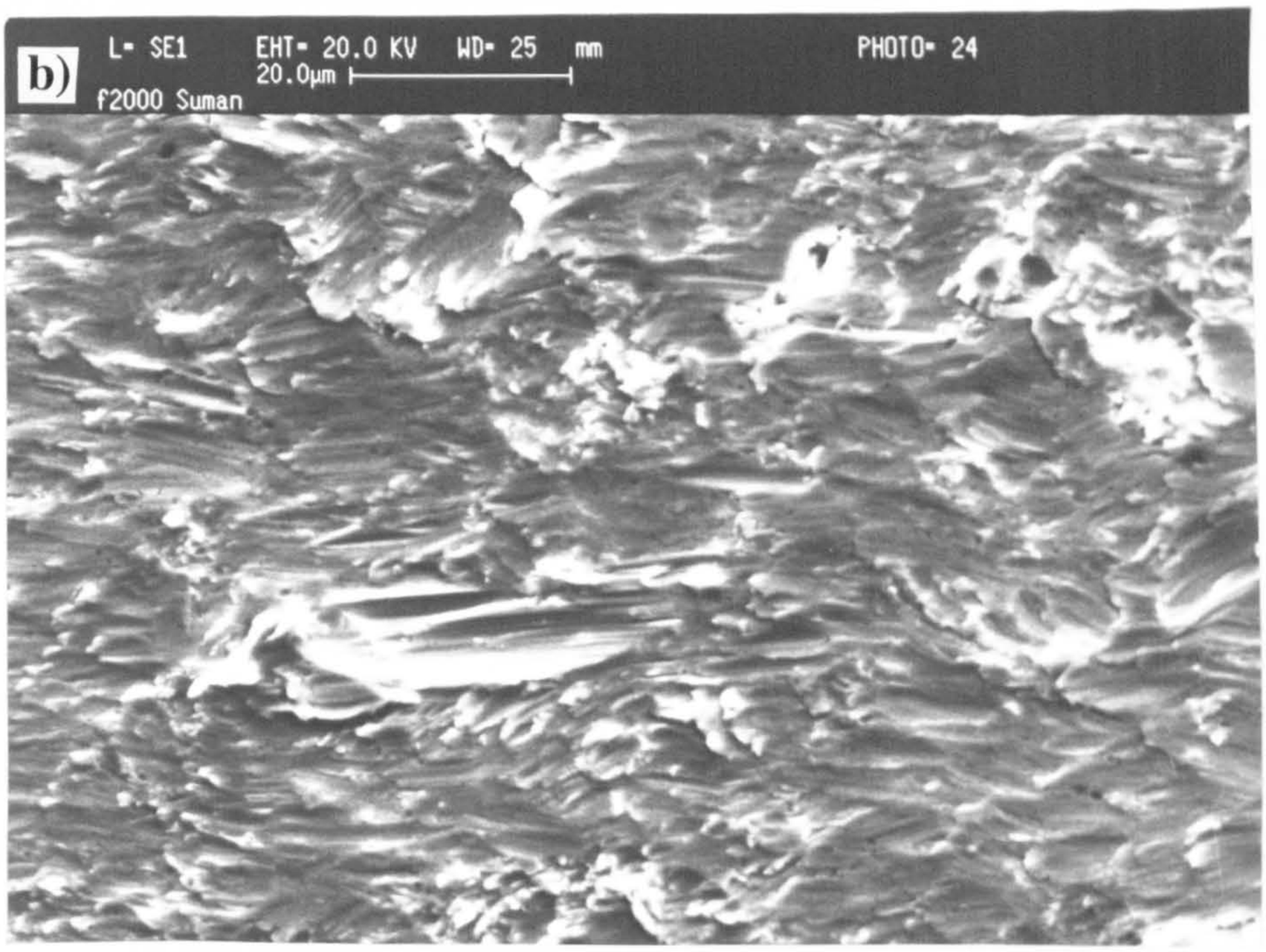


Figure 7.5.9 SEM micrographs of outer region; a) coating and b) stainless steel.

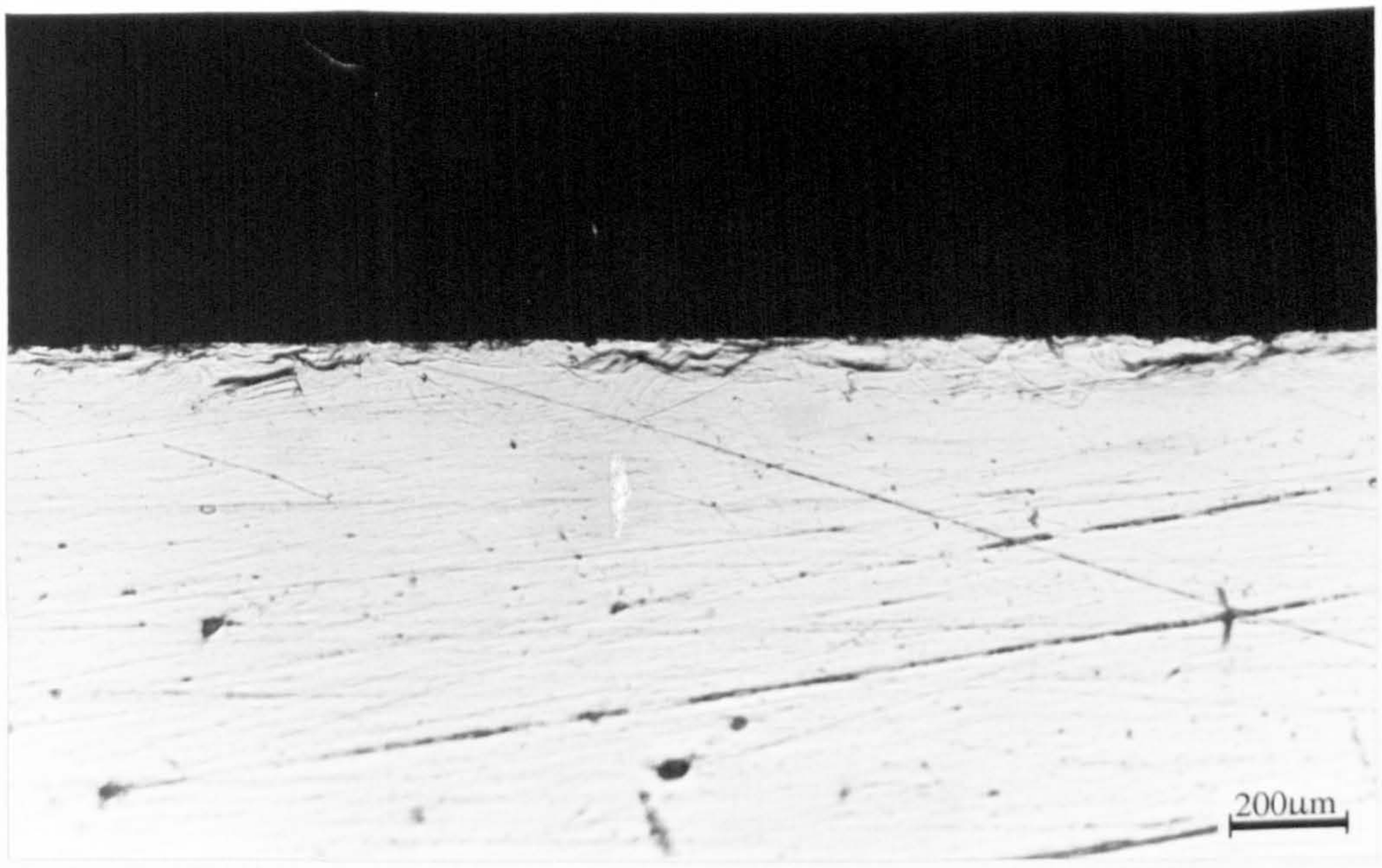


Figure 7.5.10 Optical micrograph showing cross-sectional view of outer region of a stainless steel specimen after 1-hour solid/liquid impingement showing plastically deformed craters.

However, Fig. 7.5.2 shows more or less similarity with their anodic scan curves for both materials (*Coating* AI and stainless steel) under solid/liquid impingement, distinct features of the two materials were clearly visible from the light microscopy. Fig. 7.5.11 shows more corrosion product on the coating surface than on the stainless steel surface after anodic polarisation under solid/liquid impingement, whereas stainless steel suffered higher erosion evident from a large number of skidding tracks due to particle impingement at a region 5mm away from the centre.

Much detailed observations of the central wear region revealed distinction between the material loss mechanisms of the two materials investigated. Macropits formed by drilling action as shown in Fig. 7.5.8b were found to have been resulted due to loss of large chunks of material presumably due to both electrochemical corrosion attack around particle splat and mechanical action which could help the crack initiation at the particle splat boundary, thus weakening the inter particle bonding (Fig. 7.5.12a). On a more micro scale, micropitting was clearly visible under the central jet associated with spall of hardphase particles due to micro-galvanic corrosion attack between the hardphase particle and the binder matrix (Fig. 7.5.12b).

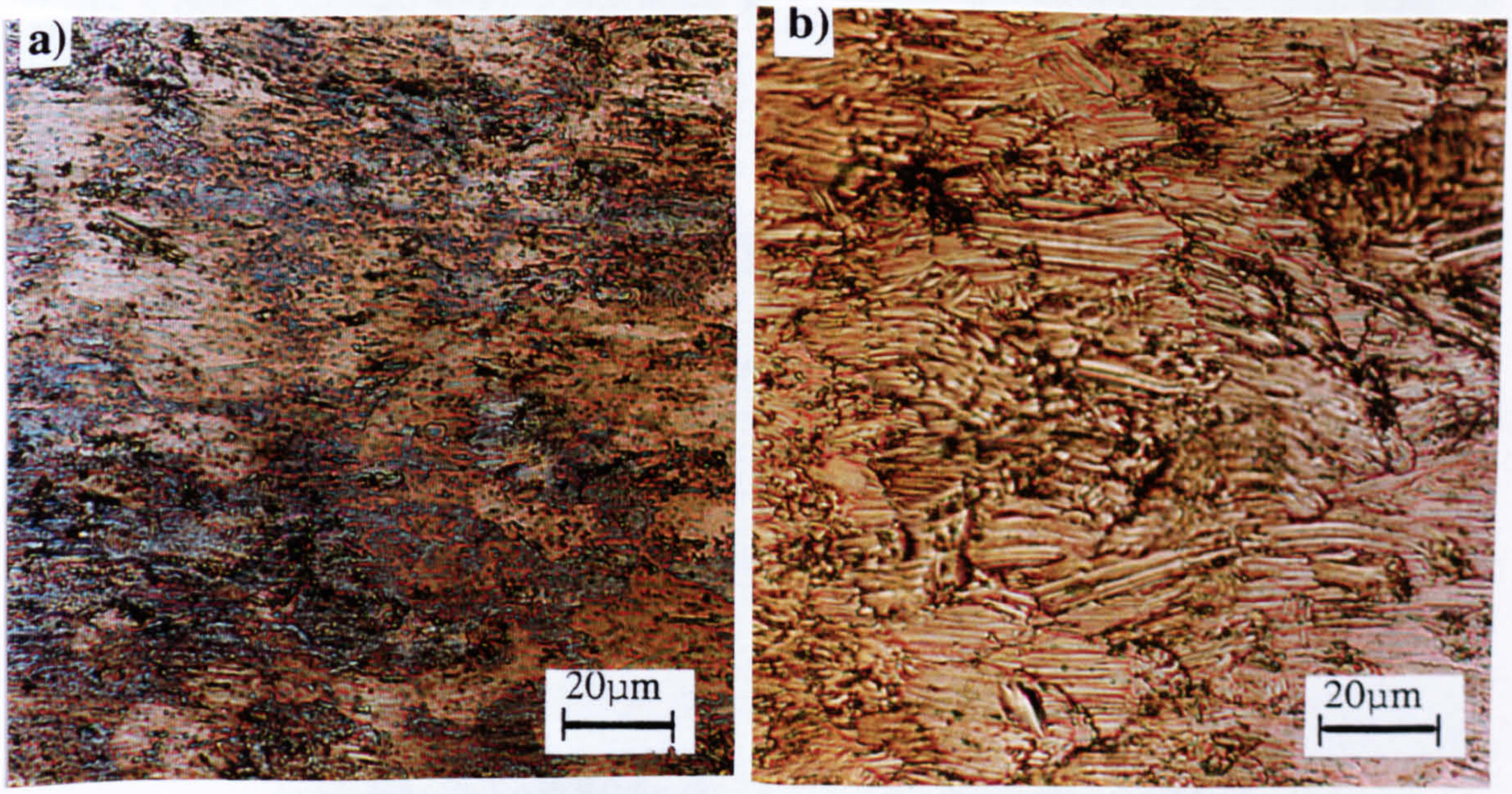


Figure 7.5.11 Micrographs of a) coating AI; and b) stainless steel at a distance of 5mm away from the centre after anodic polarisation under solid/liquid impingement

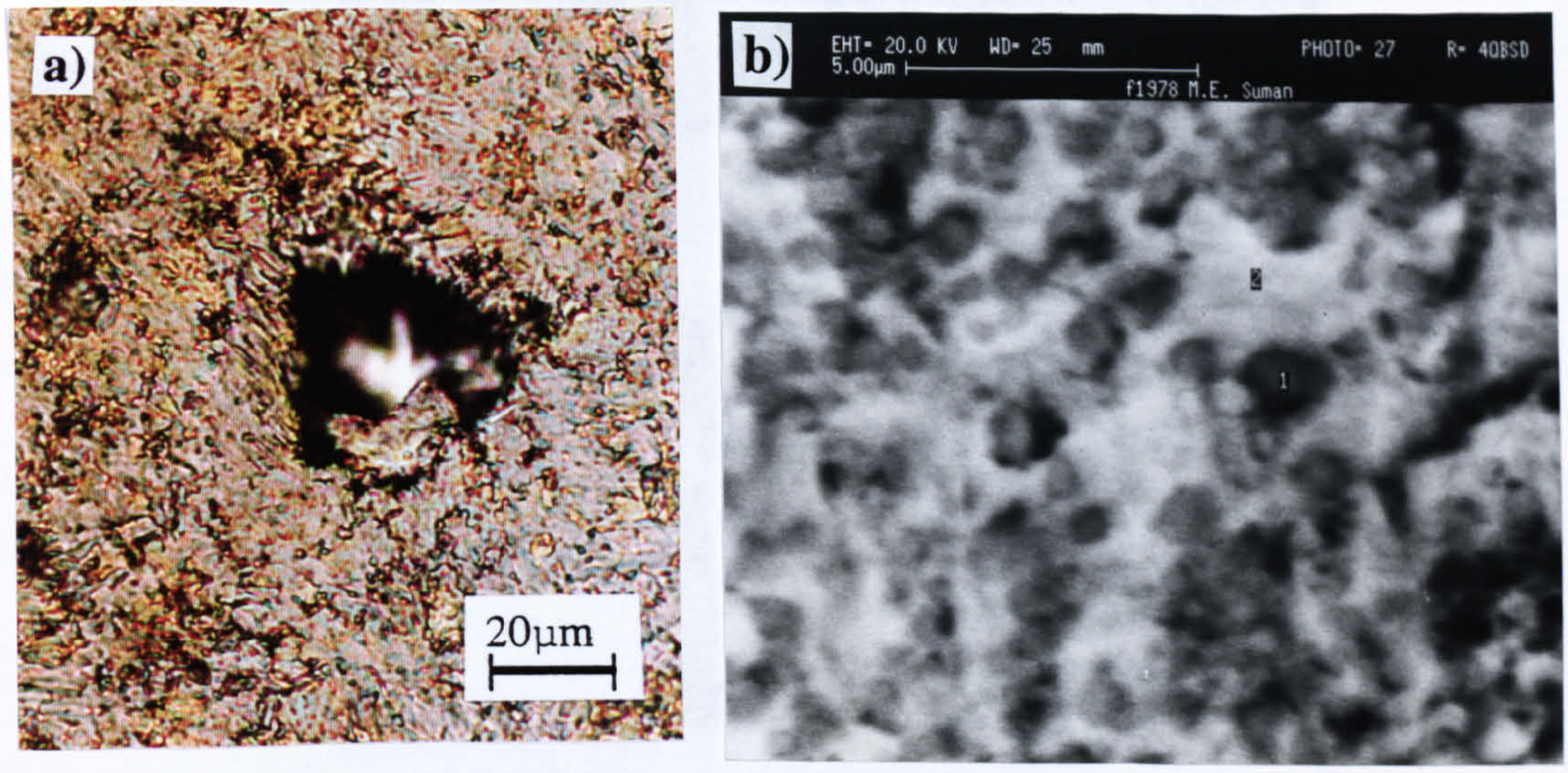
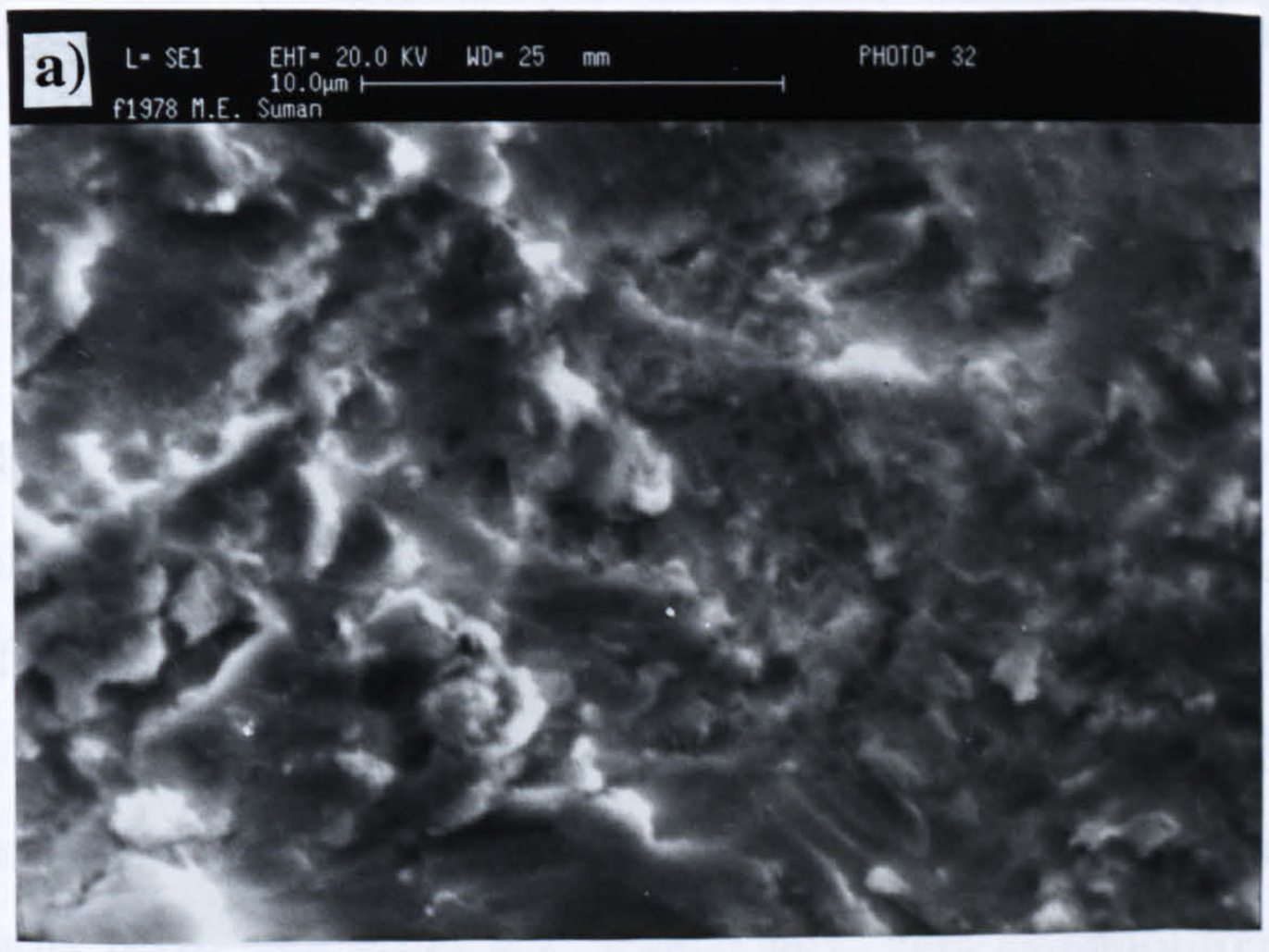


Figure 7.5.12 a) Optical micrograph showing macro pitting due to chunk removal; and b) SEM micro graph showing micro pitting due to micro-galvanic attack at the hard particle/matrix interface

Stainless steel however as said previously showed mainly ductile material degradation. Examination after anodic polarisation under solid/liquid impingement exhibited at the central wear region, severe ploughing forming craters with raised lips (Fig. 7.5.13a). These lips eventually break and fall during subsequent impacts. Figure 7.5.13b also shows a deep grooving under the central wear region. At higher shear zone, material removal in the form of deep skidding tracks were evident (Fig. 7.5.13c).



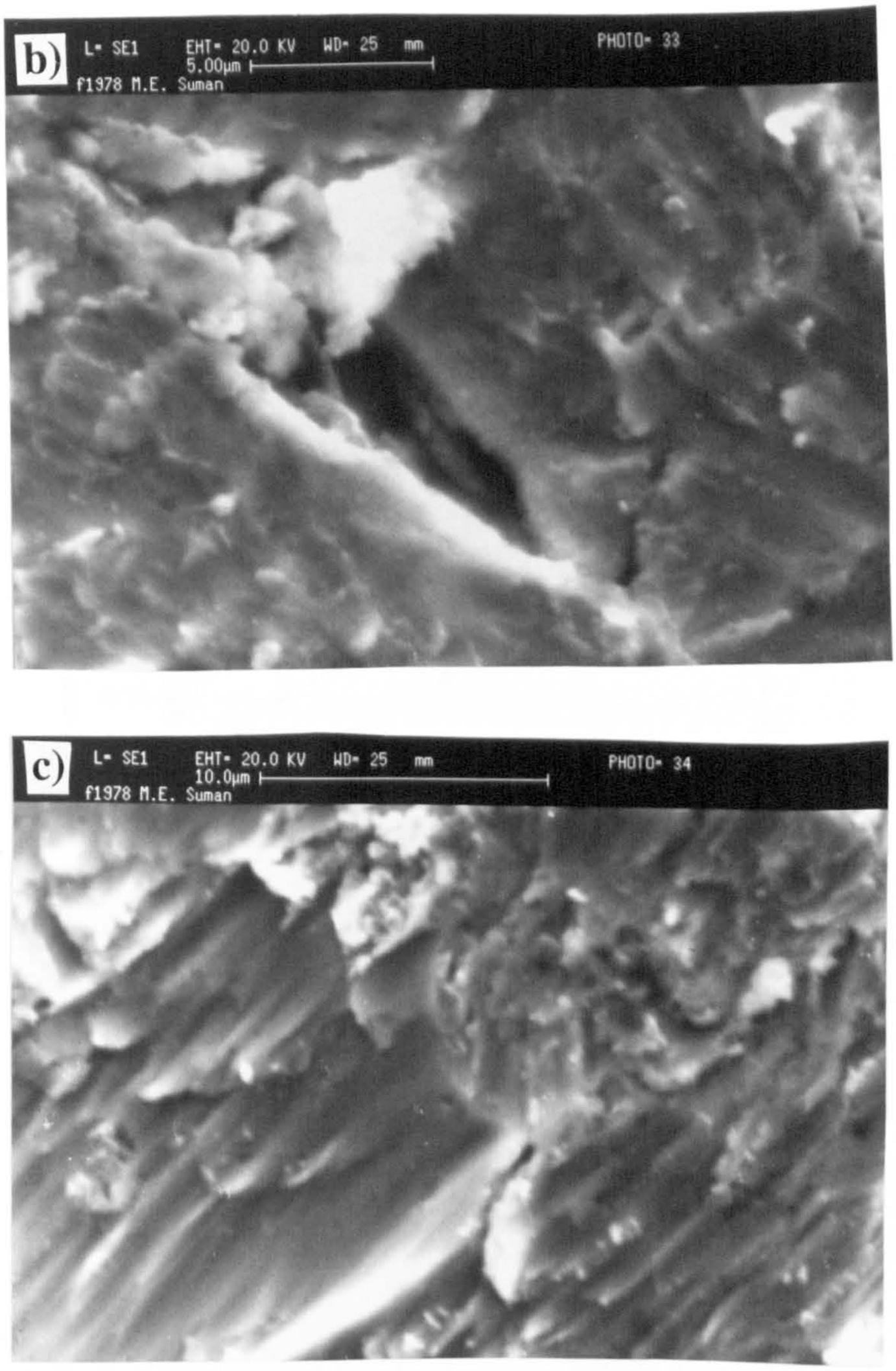


Figure 7.5.13 SEM micrographs a) craters with raised lips; b) deep groove at central wear region; and c) severe skidding tracks at higher shear zone of stainless steel after anodic polarisation under solid/liquid impingement.

As received coatings

The results in the preceding section were obtained on the specimen, which had been abraded and polished to 6μm diamond suspension. In addition the received coating without the surface being subjected to polishing was investigated for both solid-free liquid and solid/liquid impingement tests. Anodic polarisation tests for the as-received coatings were carried out in liquid impingement condition only, whereas weight loss tests were primarily performed under solid/liquid impingement conditions. As-received

coating AI/ss on stainless substrate exhibited higher (more positive) breakdown potential 'E_b' by almost 150mV with a typical passive behaviour compared to polished surface of the same coating shown by their anodic scans in Fig. 7.5.14a under liquid impingement of jet velocity 17ms^{-1} showing superiority of as-received surface. Experiments performed on coating with carbon steel substrate are exactly similar to that performed on stainless steel substrate.

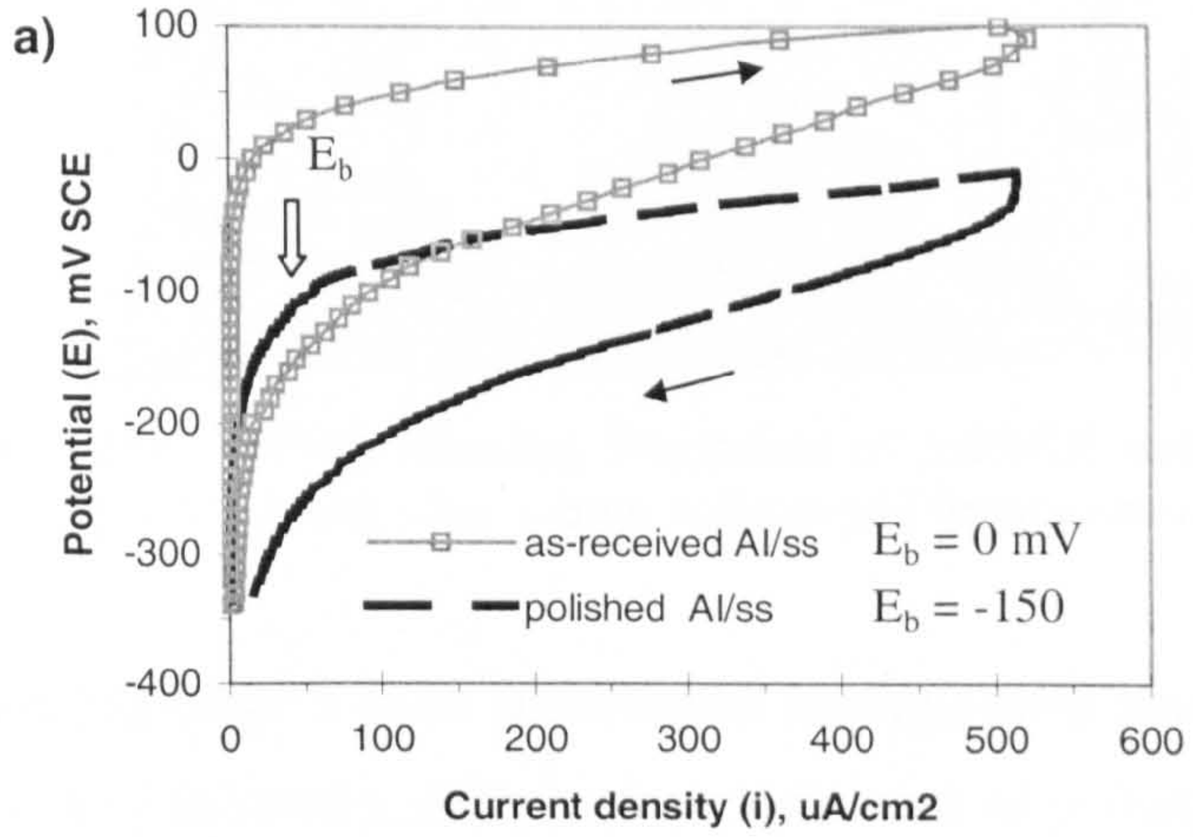


Figure 7.5.14 a) Anodic polarisation curves of as-received and polished surfaces under liquid impingement; b) Average weight losses from replicate experiments of as-received and polished surfaces after 1-hour solid/liquid impingement in 3.5% NaCl, 18°C, 17ms^{-1}.

In contrast, performance of as-received surface was inferior to polished surface under solid/liquid impingement condition, which was shown by its much higher weight loss compared to that of polished surface (Fig. 7.5.14b) by almost fourfold. This was evident in cross sectional view of Fig. 7.5.15 with fragments of material being detached from the rough surface in the outer region.

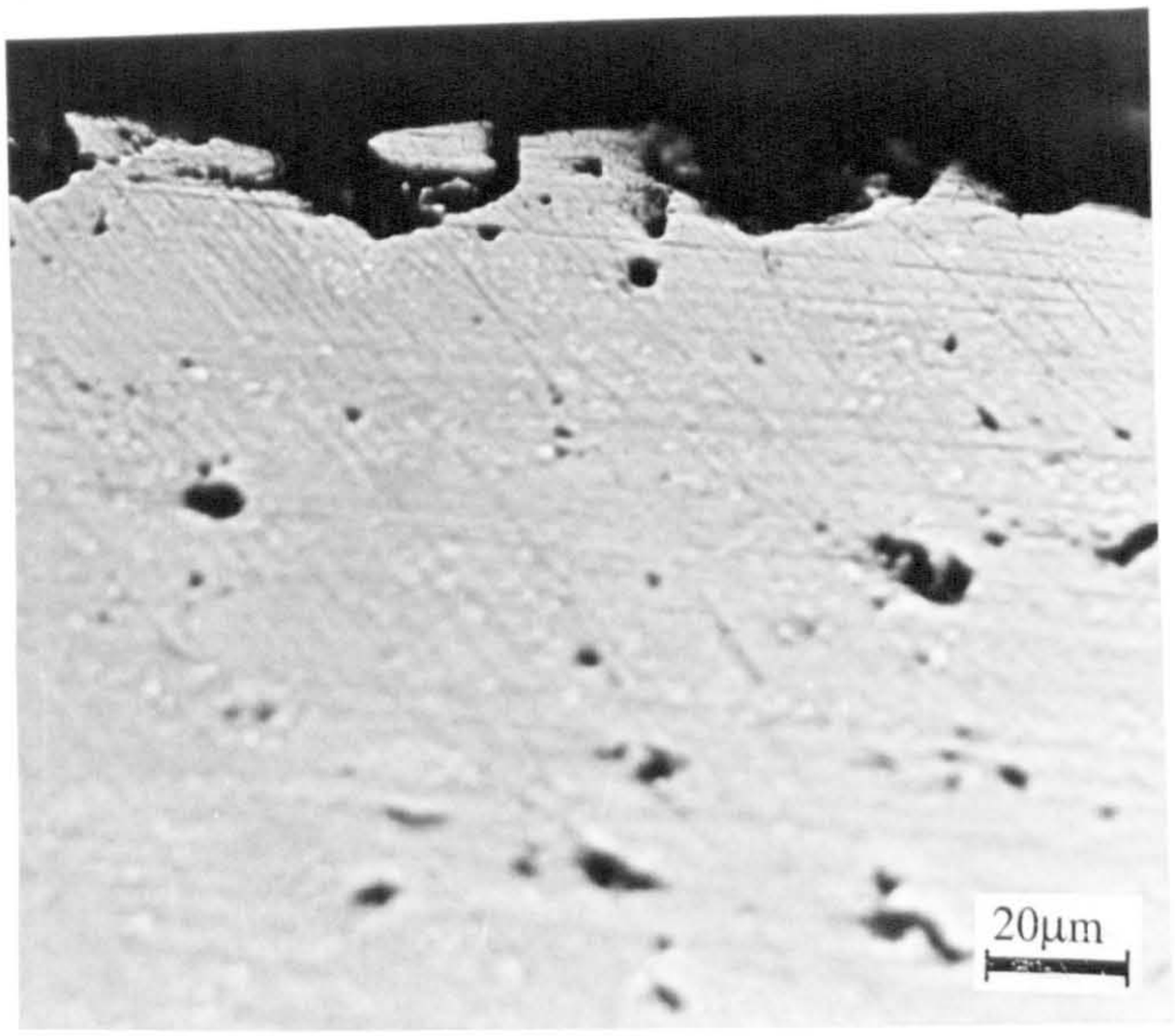


Figure 7.5.15 Cross section showing fragments of material detaching from the surface of as-received coating after 1-hour solid/liquid impingement.

The as sprayed coating after 1-hour solid/liquid impingement was observed under the optical microscope and showed a shiny surface indicative of polishing due to erosion by sand particles. Moreover, the central wear region of the as-sprayed surface was smoothened by impinging sand particles after being exposed for 1-hour test (Fig. 7.5.16).

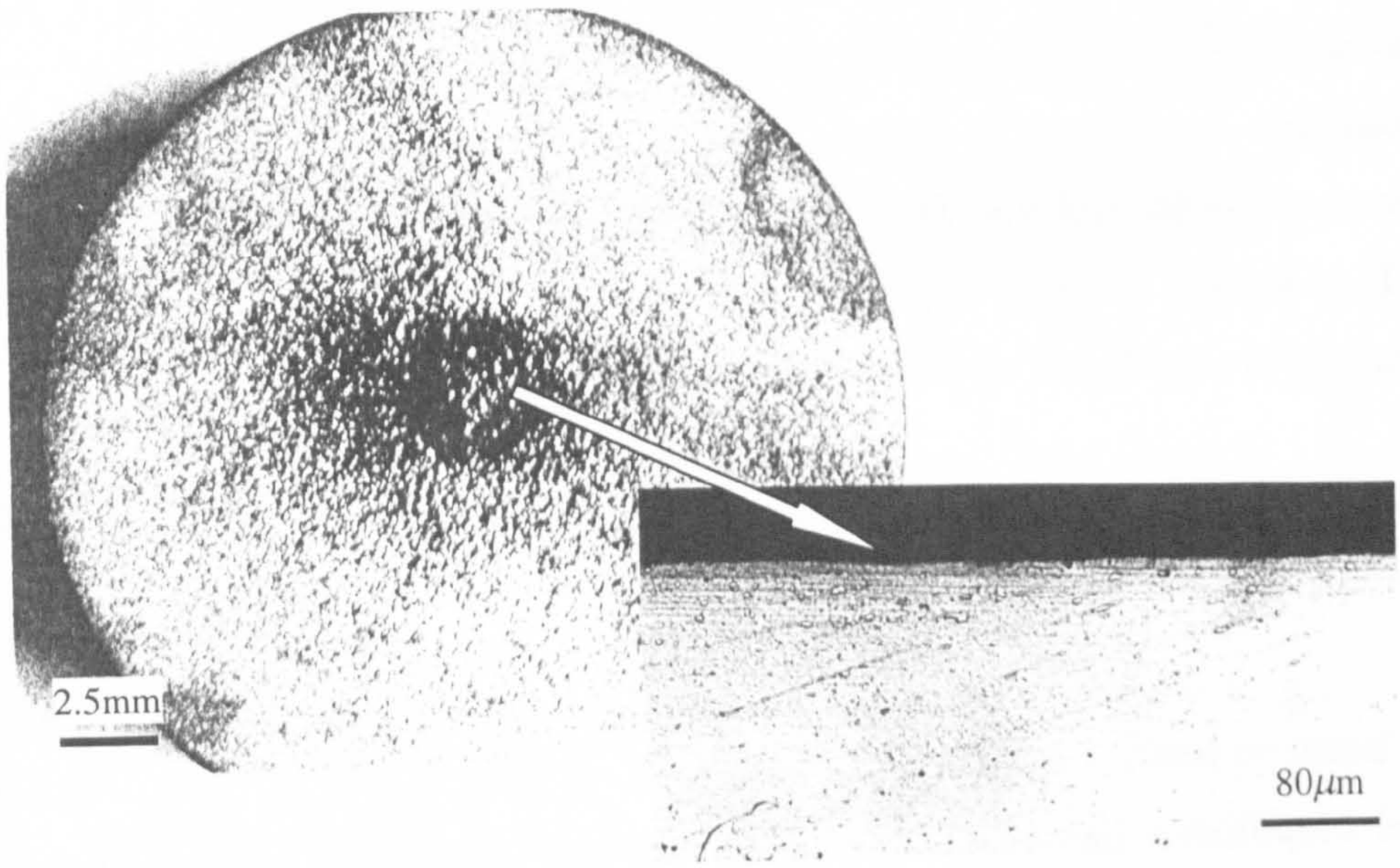


Figure 7.5.16 Polishing of as-sprayed surface by sand particles and smoothening of central wear region of as-sprayed surface after 1-hour solid/liquid impingement.

Cathodic polarisation

Cathodic polarisation tests were undertaken on coating AI/ss while the solid/liquid slurry being impinged on the specimen surface.

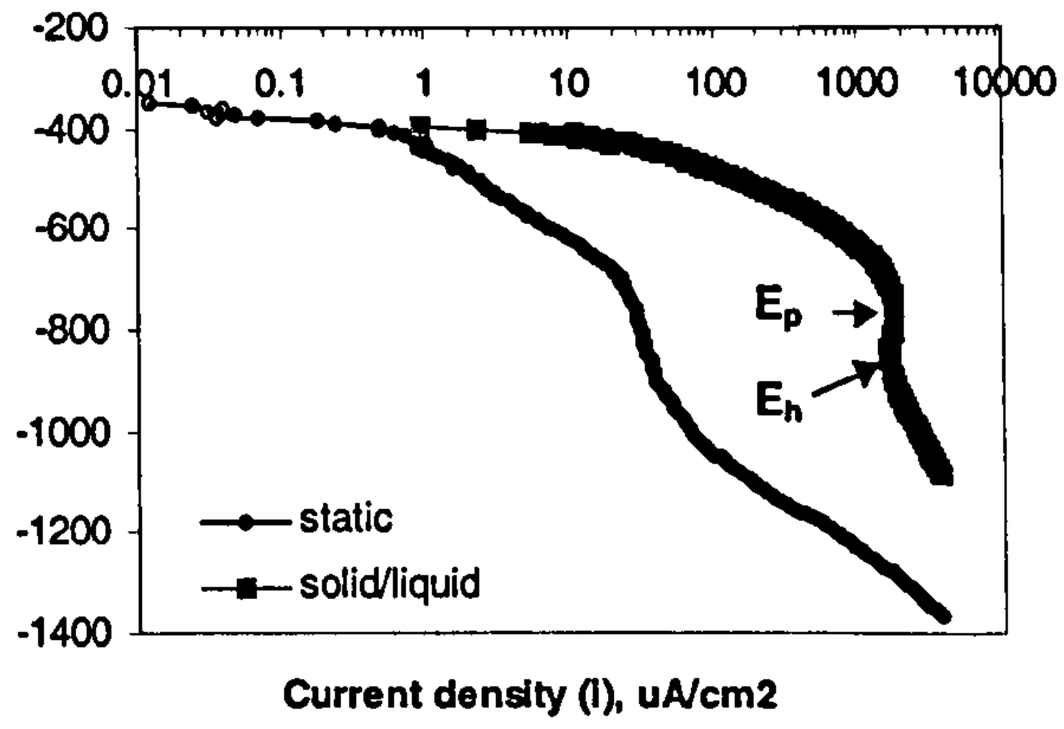


Figure 7.5.17 Cathodic polarisation of coating AI under static and under solid/liquid impingement conditions (E_h - hydrogen evolution potential; E_p - cathodic protection potential).

The result of the cathodic sweep revealed (Fig. 7.5.17) that the cathodic oxygen reduction reaction under solid/liquid impingement condition can occur extremely faster (much higher current density) than in static conditions as expected. At a potential at about -760mV the current started to stabilise (typical of concentration polarisation) until it reaches potential value of about -875mV indicative of hydrogen evolution potential 'E_h', which is relatively at much higher potential than that of static condition. The hydrogen evolution potential 'E_h' is about -1000mV in static condition. The limiting current density of the cathodic polarisation curve is about 1700μA/cm^2 under solid/liquid conditions.

Potentiostatic tests

Potentiostatic tests were carried out for both materials at a fixed potential of -800mV SCE (cathodic protection potential) under both liquid and solid/liquid impingement conditions. Potentiostatic tests under liquid impingement were carried out for 2, 4 and 6

days whereas solid/liquid impingement tests were carried out only for 1 hour and the currents attained as a function of time were recorded for the test period.

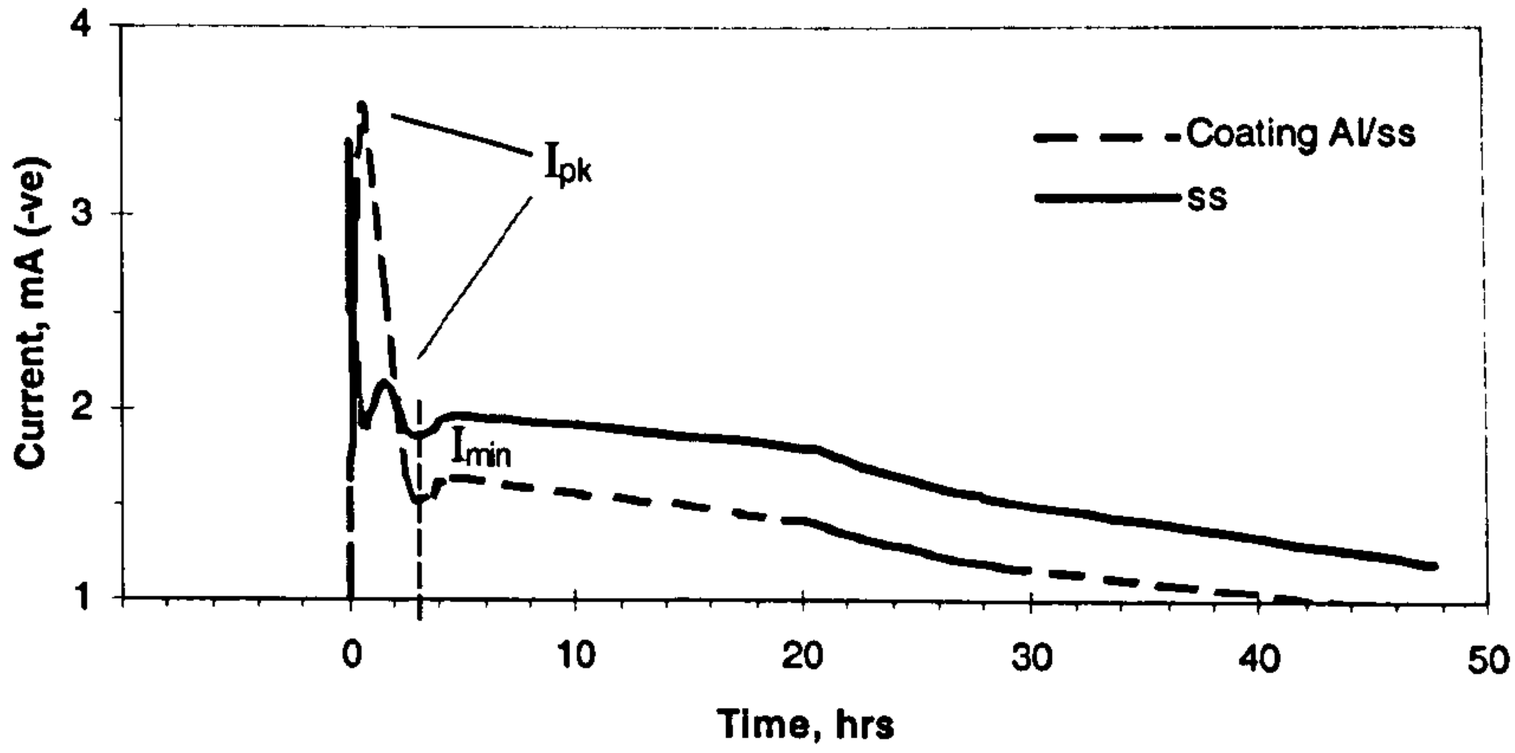


Figure 7.5.18 Cathodic currents of *Coating* AI and stainless steel under liquid impingement with 2-days CP.

Figure 7.5.18 shows cathodic current curves under 2-days liquid impingement at a fixed potential of -800mV. Immediately after the impingement the current started to increase steadily from its very low initial current in case of the coating and attained its maximum value 'I_{pk}' at about 3.5mA after which it showed a steady fall until it reaches the minimum current value 'I_{min}' after 2.67 hours. On reaching 'I_{min}' the current started to rise again for few hours and then after gradually declined. In contrast stainless steel exhibited a high initial current immediately after the impingement started, which fell to its lowest value during the first hour and then increased to its maximum value 'I_{pk}'. After this stainless steel exhibited very similar trend to the coating.

Under solid/liquid impingement condition both coating and stainless steel behaved in much similar way as in liquid impingement condition. Nevertheless, the currents are much higher in more severe condition when solids are present as shown in Fig. 7.5.19.

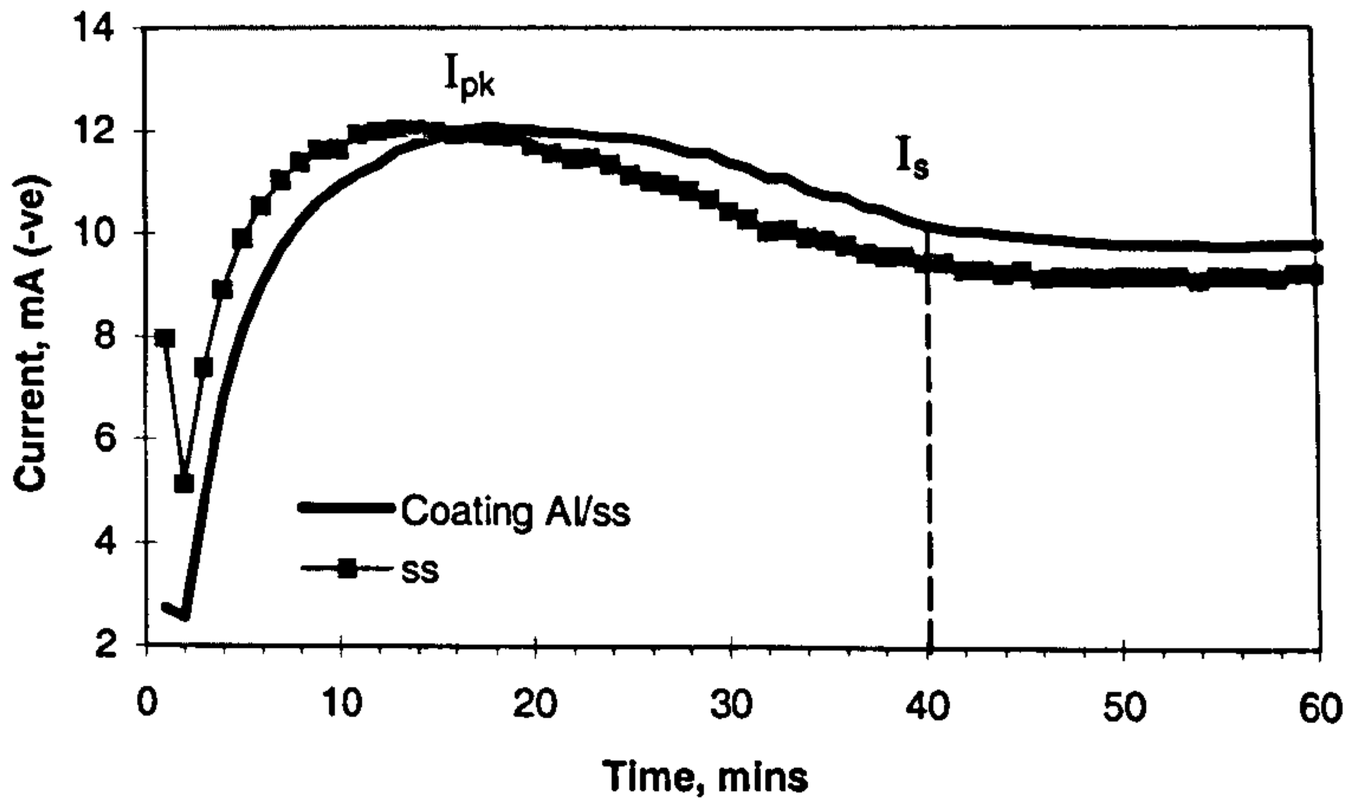


Figure 7.5.19 Cathodic currents of coating AI and stainless steel under solid/liquid impingement

Stainless steel in solid/liquid condition as in liquid condition started with much higher initial current. On reaching its lowest current value it again gains the current till it achieves 'I_{pk}'. After reaching the peak current 'I_{pk}', both curves showed lowering of the cathodic current value and then after 40 minutes both curves exhibited steady current 'I_s', however, this time the currents recorded for the coatings were higher that that exhibited by stainless steel. A very noticeable thing is that both curves showed very much similar trends of the cathodic currents.

Microscopic observations after potentiostatic tests.

Post experimental microscopy after 2-days cathodic protection under liquid impingement revealed the formation of a multicoloured film over the entire surface. The film formed was multi-coloured and deposited concentrically as shown in Fig. 7.5.20. SEM analysis revealed this film deposit to be made of granules rich in Ca (Fig. 7.5.21a). The very small weight loss under the CP was associated with mechanical damage by the liquid jet that results in the formation of comets (as under free corrosion potential and anodic polarisation) emanating from the pits (Fig. 7.5.21b). Thickening of the deposit (Fig. 7.5.21c) was observed after 6-days liquid impingement under CP and such cases were evident in both materials investigated.

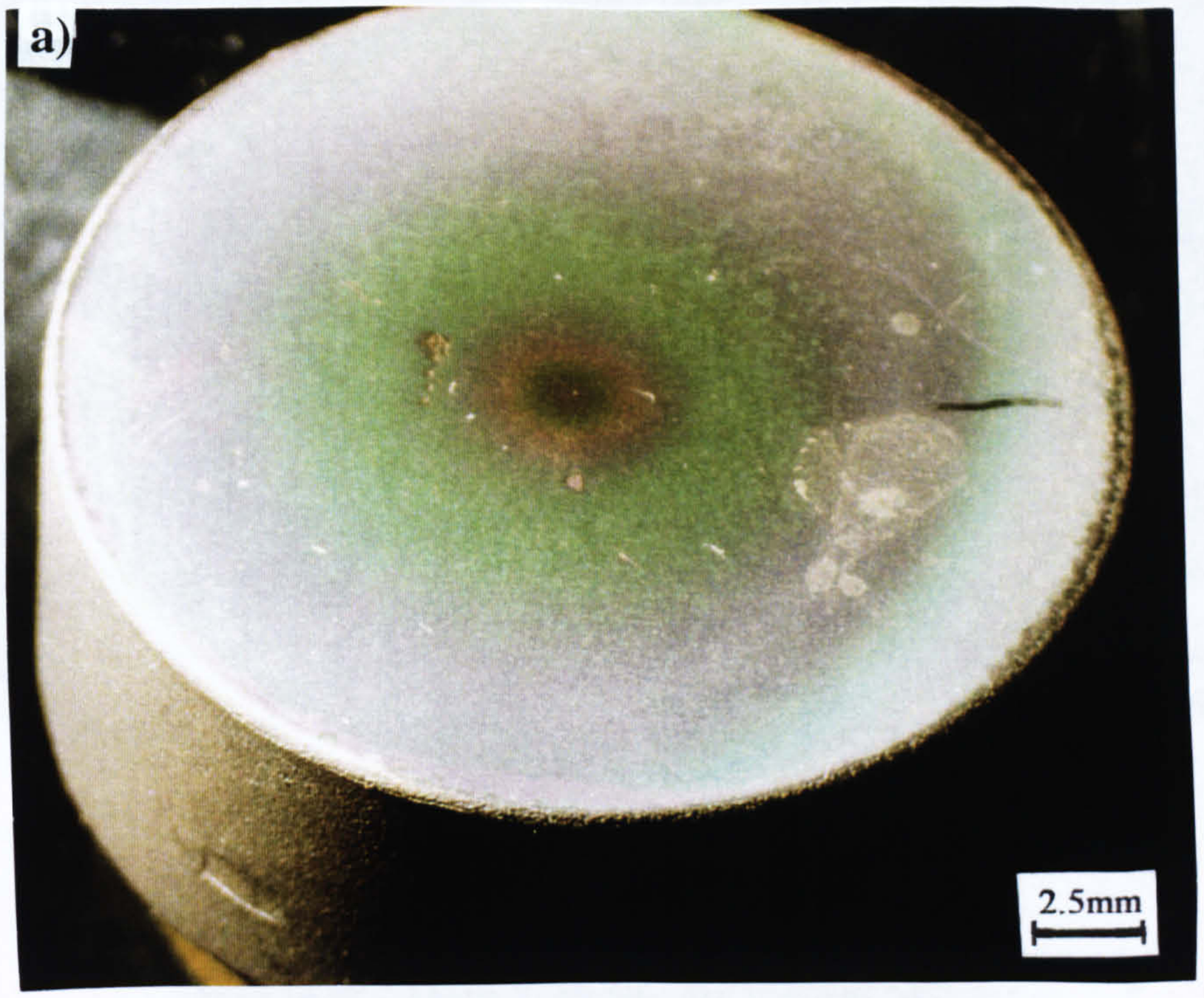




Figure 7.5.20 Colour film formed on a) *Coating* AI; and b) stainless steel after 2 days of CP under liquid impingement.

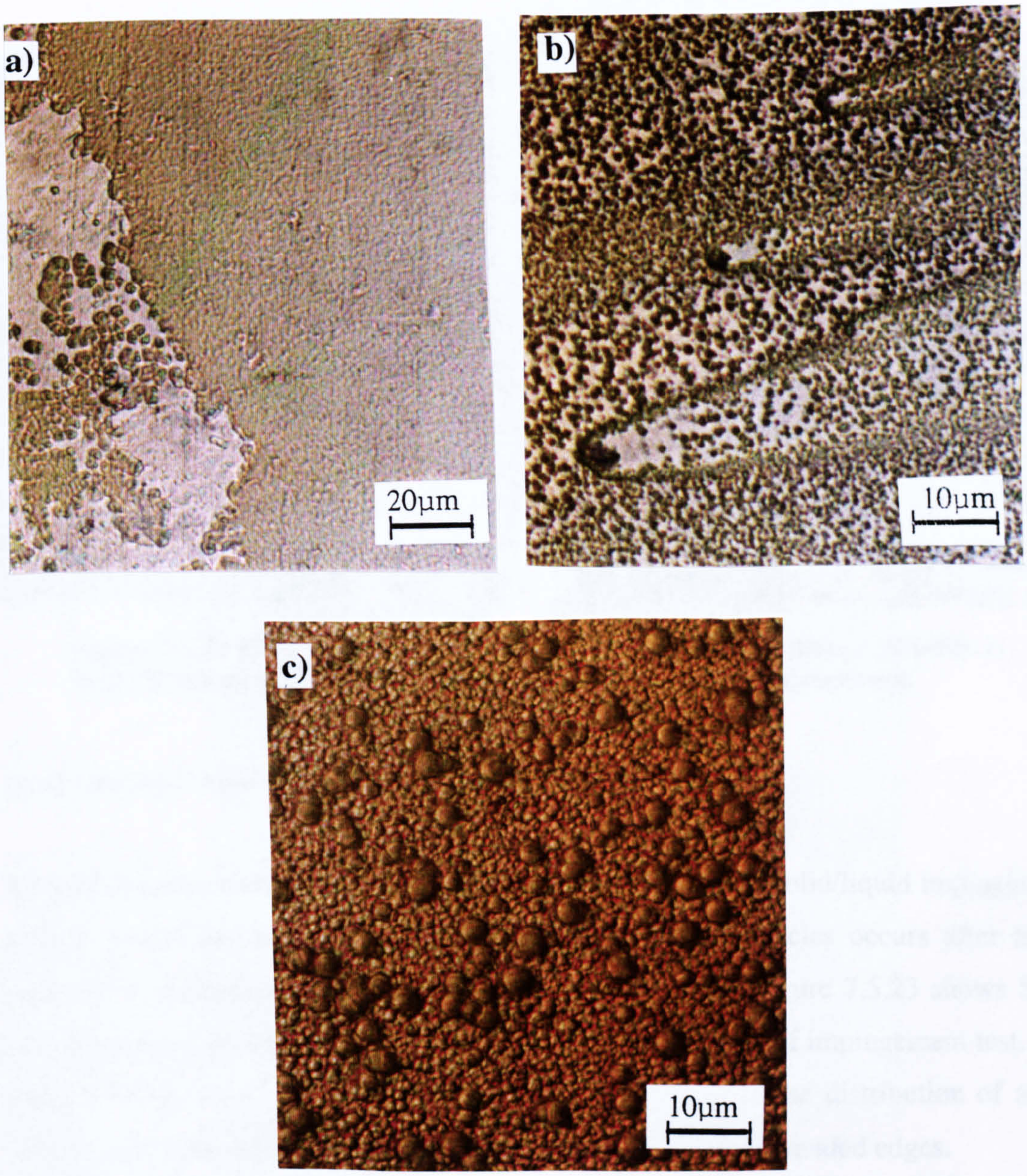


Figure 7.5.21 a) Calcium rich deposit formed during liquid impingement under CP of 2 days; b) comets emanating from the surface beneath the deposit at the outer region and; c) thickening of deposit after 6 days of CP.

Microscopic observations after 1-hour solid/liquid impingement under CP revealed formation of coloured films on both coating and stainless steel surfaces during cathodic protection at -800mV and these films were appeared to have broken during continuous solid impacts (Fig. 7.5.22). It is apparent that there was more film on coating than on stainless steel.

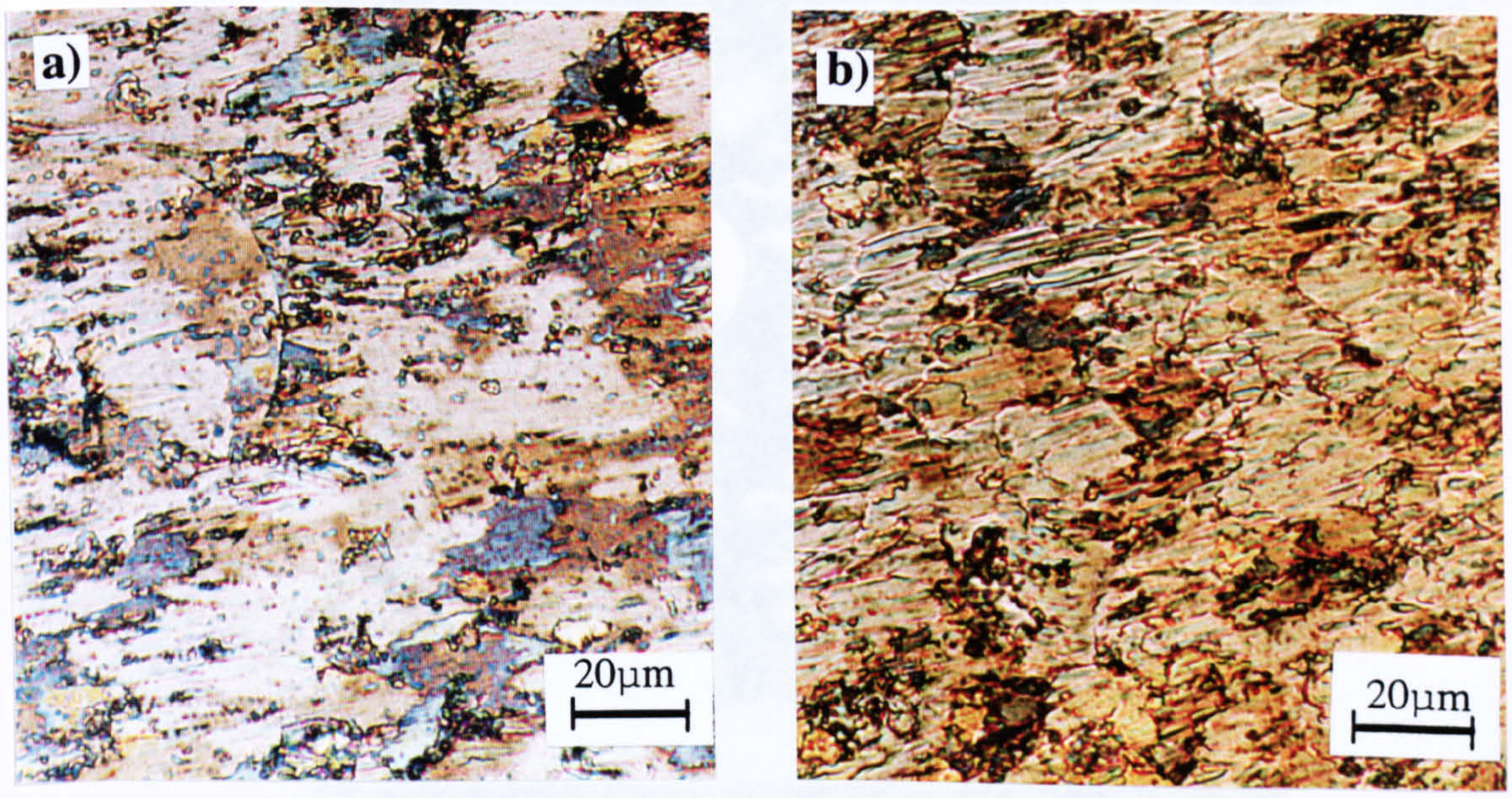
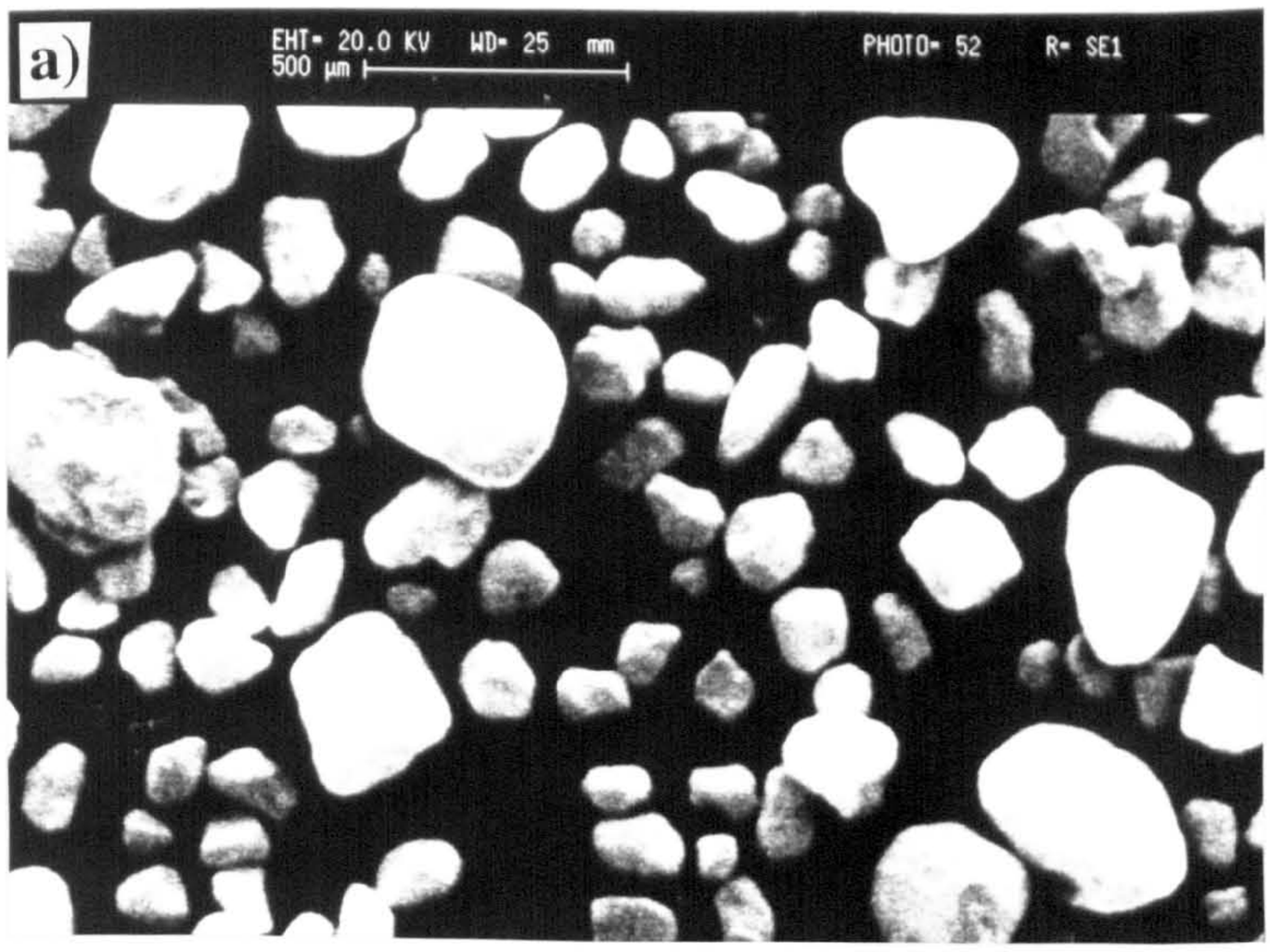


Figure 7.5.22 Breaking of coloured films a) coating; and b) stainless steel under 1-hour CP at a distance of 5mm from centre during solid/liquid impingement.

Examination of solid (erodent) particles

Erodent particles were carefully examined before and after the solid/liquid impingement tests to see if any physical change (size, shape) of the particles occurs after being exposed to continuous bombardment on the target surface. Figure 7.5.23 shows SEM micrographs of the silica sand type A before and after 3 hours of impingement test. The sand particles are of varying sizes with almost one third of the distribution of about 180μm size. The particles are of irregular shapes with slightly rounded edges.

It is likely that a small percentage of the larger sand particles on impact with the solid surface converted their shape to more rounder after the edges being broken as shown in Fig. 7.5.23b, which might eventually increase the distribution of the smallest sand particles but was not clearly evident in Fig. 7.5.24. Such rounding of particles during erosion has also reported been by Bjordal (1995). However, SEM micrographs in Fig. 7.5.23 reveal that there is not much change in the sand particles after the test.



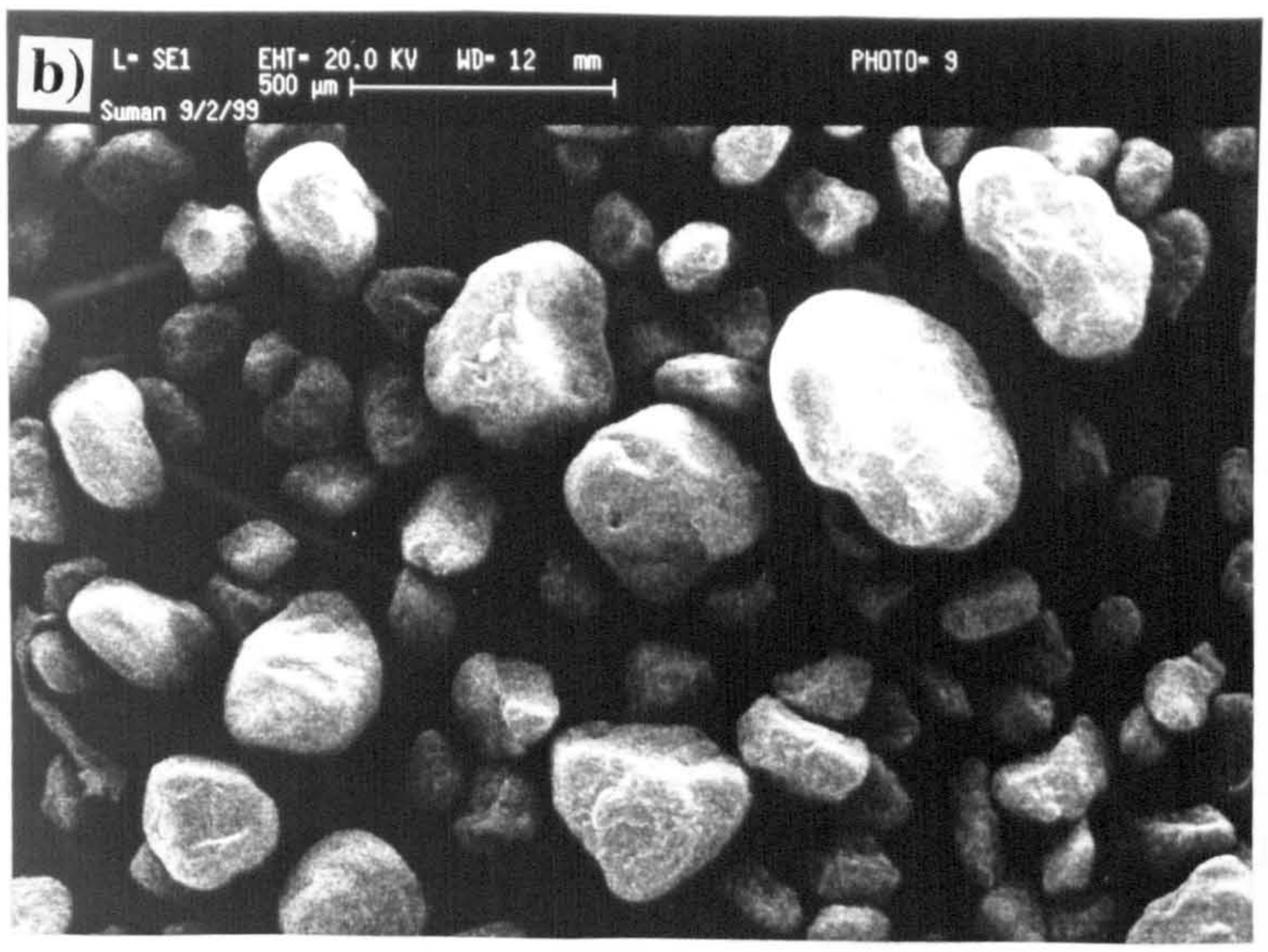


Figure 7.5.23 Silica sand type A: a) before test; and b) after 3 hours of solid/liquid impingement in 3.5% NaCl solution.

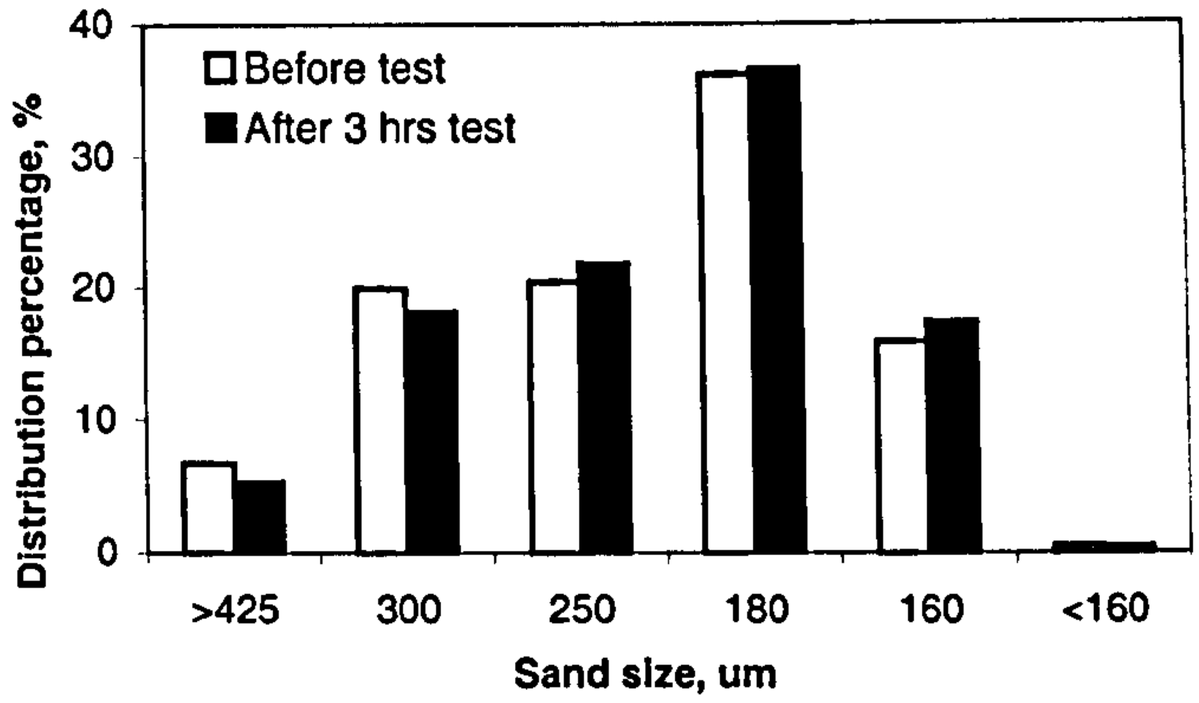


Figure 7.5.24 Distribution of sand particle type A before and after 3-hours test.

Calculation of pure corrosion 'C' and synergy 'S' values

Physical properties of the elements that constitute *Coating* AI and stainless steel are shown in Table 7.5.3.

Elements	Fe	Ni	Cr	Si	Cu
Density (ρ), g/cm^3	7.9	8.89	7.2	2.3	8.9
Atomic wt. (M), g/mol	55.84	58.71	52.01	28.08	63.54
Free electron number	2	2	3	4	2
Atomic number	26	28	24	14	29

Table 7.5.3 Physical properties of the alloying elements of *Coating* AI and stainless steel.

Considering bulk composition of the coating from Table 7.2.1 we can find average atomic weight and average charge of the coating.

	Average atomic wt.	Average charge
Fe	55.8 x 0.036 = 2.01	2 x 0.036 = 0.07
Ni	58.7 x 0.72 = 42.26	2 x 0.72 = 1.44
Cr	52.0 x 0.18 = 9.36	3 x 0.18 = 0.54
Si	28.1 x 0.036 = 1.01	4 x 0.036 = 0.14
Cu	63.5 x 0.015 = 0.95	2 x 0.015 = 0.30
	55.59	2.49

We get from the Faraday's law

96500 coulomb ~ 55.59/2.49 = 22.32g

The corrosion current 'i_{corr}' of the *Coating* AI under solid/liquid impingement was found by Tafel extrapolation as shown in Fig. 7.5.25 from the intersection of the anodic and cathodic Tafel curves with the E_{corr}, which gave a value of about 20μA/cm^2. 'i_{corr}' of the stainless steel was found by similar method.

For coating corrosion rate can be expressed as,

$$C = \frac{23.32}{96500} * 20 * 10^{-6} * 60 * 60$$

$$= 17.4 * 10^{-6} \text{ g/hr/cm}^2$$

$$= 0.0174 \text{ mg/hr/cm}^2$$

$$= 0.0174 * 5 = 0.09 \text{ mg/hr}$$ (where, 5 cm^2 is the specimen surface area)

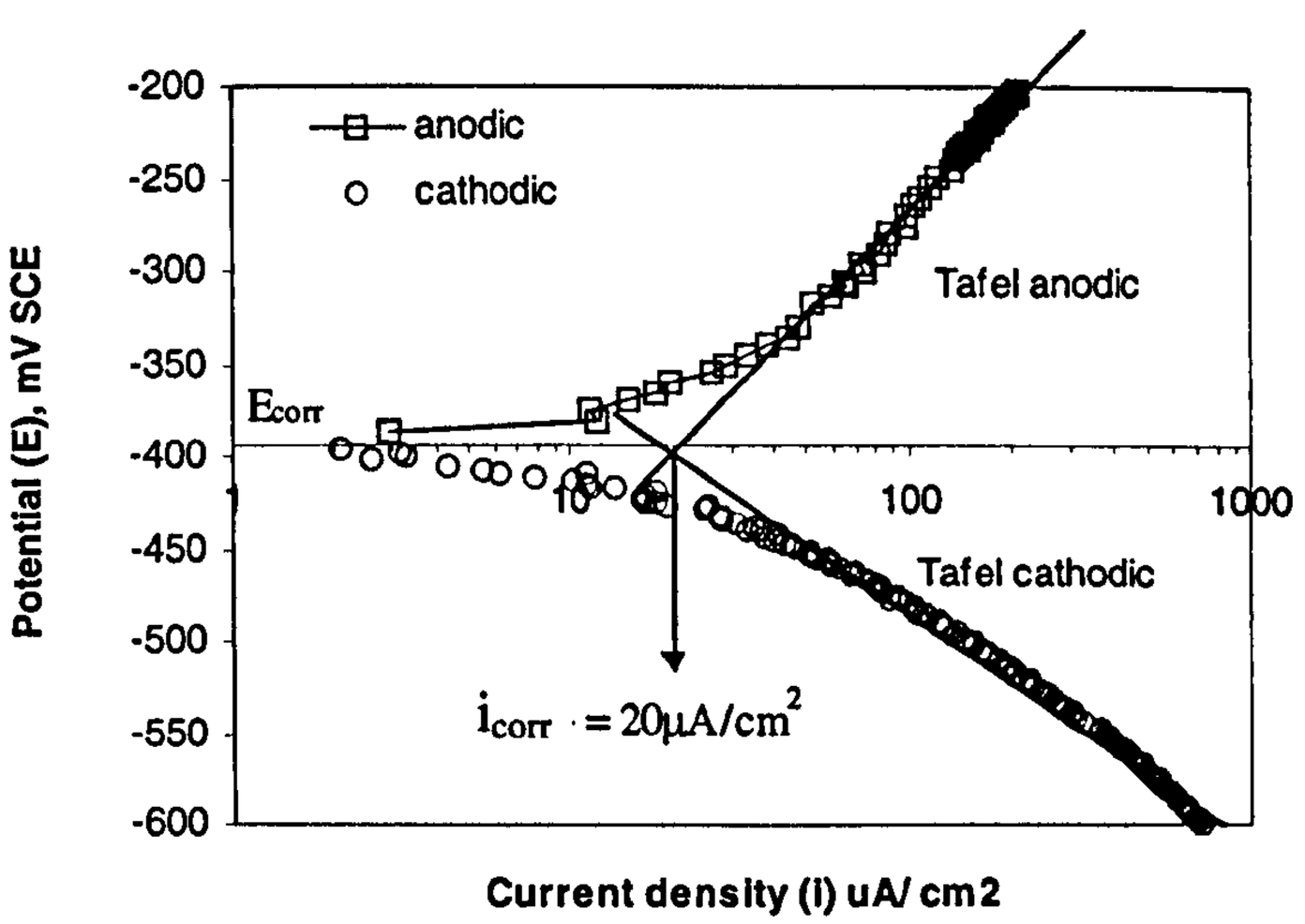


Figure 7.5.25 Cathodic and anodic polarisation curves of *Coating* AI under solid/liquid impingement.

Total weight loss due to erosion-corrosion 'TWL'; pure erosion 'E' with applied CP; pure corrosion 'C' and synergy 'S' components for the *Coating* AI and stainless steel under solid-free liquid and solid/liquid impingement are shown in Tables 7.5.4 and 7.5.5.

Material	TWL mg/hr	E mg/hr	i_{corr} $\mu A/cm^2$	C mg/hr	S mg/hr
Coating AI	0.033	0.0049	1.0-1.5	0.006	0.022
Stainless steel	0.013	0.0042	0.1-0.3	0.001	0.01

Table 7.5.4 Breakdown of 'E', 'C' and 'S' under solid-free liquid impingement

Material	TWL mg/hr	E mg/hr	i_{corr} $\mu A/cm^2$	C mg/hr	S mg/hr
Coating AI	1.33	0.93	20	0.09	0.32
Stainless steel	3.10	2.1	10.5	0.05	0.94

Table 7.5.5 Breakdown of 'E', 'C' and 'S' under solid/liquid impingement.

In the above tables, E, C and S degradation rates (mg/hr) are all calculated as average values over the entire specimen surface of area of $5cm^2$. In fact, degradation rates are greater at the central region directly under the jet. However this is true for all the measured parameters 'TWL', 'E' and 'C'. Consequently, comparisons of the relative proportions of 'E', 'C' and 'S' to the overall erosion-corrosion rates are still valid.

7.6 Effect of pre-erosion and effect of pre-corrosion

A preliminary study of the effect of pre-erosion on the pure corrosion behaviour and also the effect of pre-corrosion on the erosion-corrosion behaviour of *Coating* AII was studied using a separate rig as shown in Fig. 7.6.1.

Experimental procedure

The rig used in this experiment (Fig. 7.6.1) comprised a reservoir containing 3.5% NaCl solution. The liquid alone was circulated in a closed loop through a pump, while the temperature being maintained at 18±2°C. The sand particles (type B) were sucked through a doubled-walled glass injection tube and sand/liquid mixture was impinged normally at 90° angle onto the specimen of 1cm^2 surface area at 7.9ms^{-1} impact velocity. The sand loading was 1000ppm. The specimen was connected with a wire at its rear side for electrochemical monitoring as described in Chapter 6 of experimental techniques. The nozzle diameter of the injection tube was 5mm and the stand-off distance between the specimen and the nozzle exit was kept constant at 5mm.

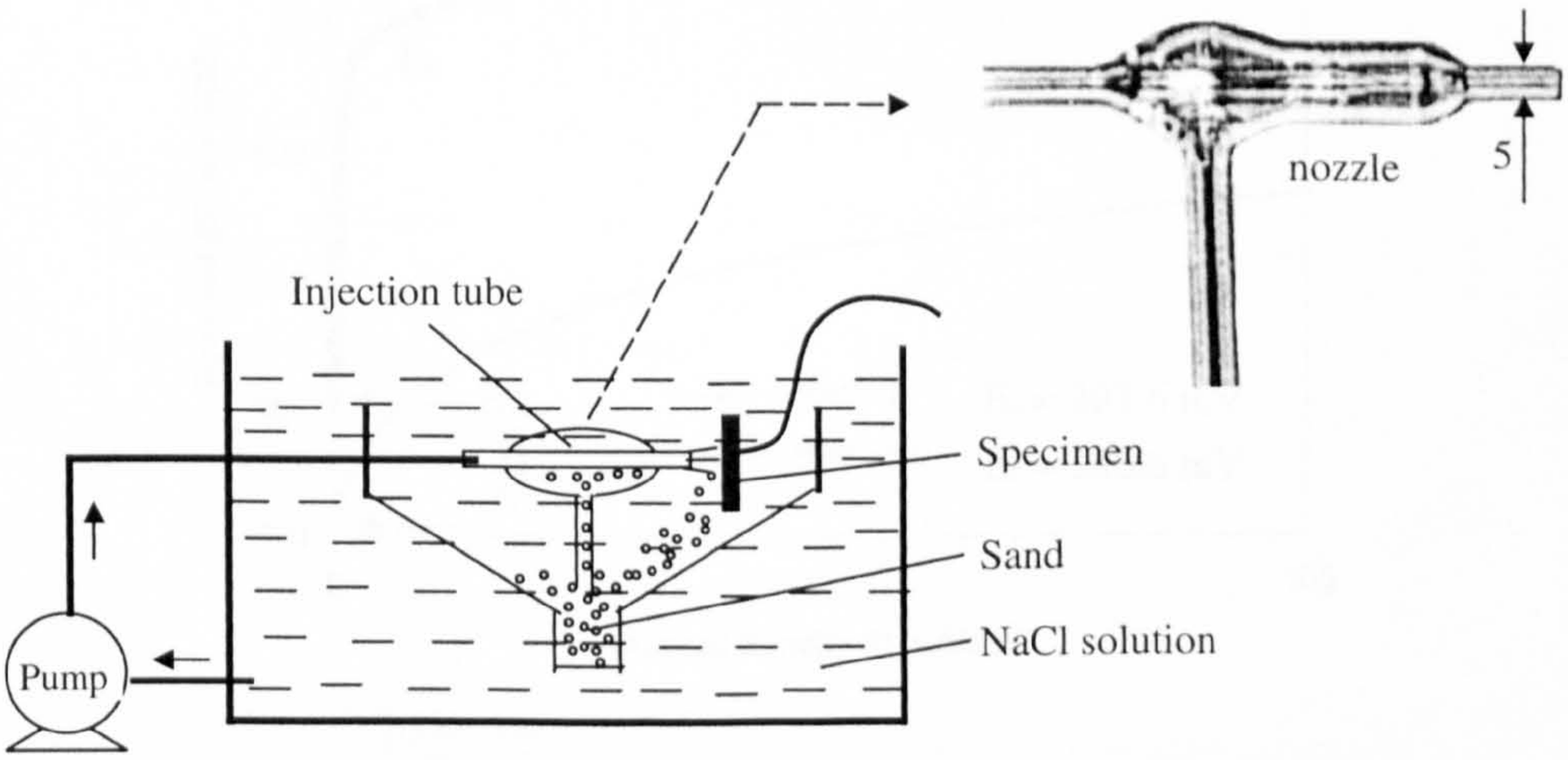
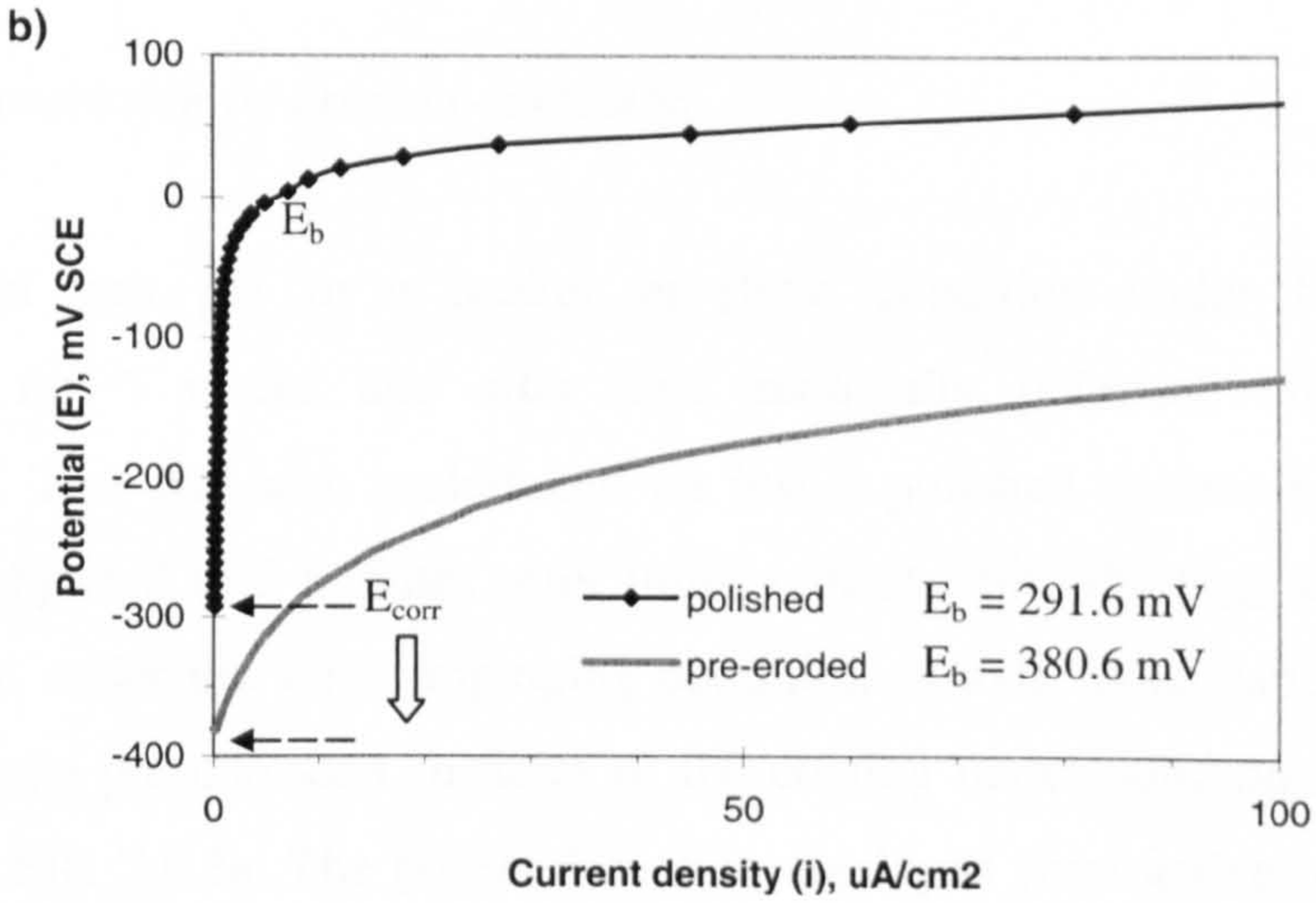


Figure 7.6.1 A schematic diagram of solid/liquid impingement rig.

Effect of pre-erosion on corrosion

The polished surface of the coating was subjected to sand/liquid impingement for 1 hour at E_{corr} prior to static anodic polarisation as the test being conducted on the eroded surface. The specimen polarised in polished condition was immersed in the electrolyte solution for 1-hour prior to the test so as to settle the E_{corr}.



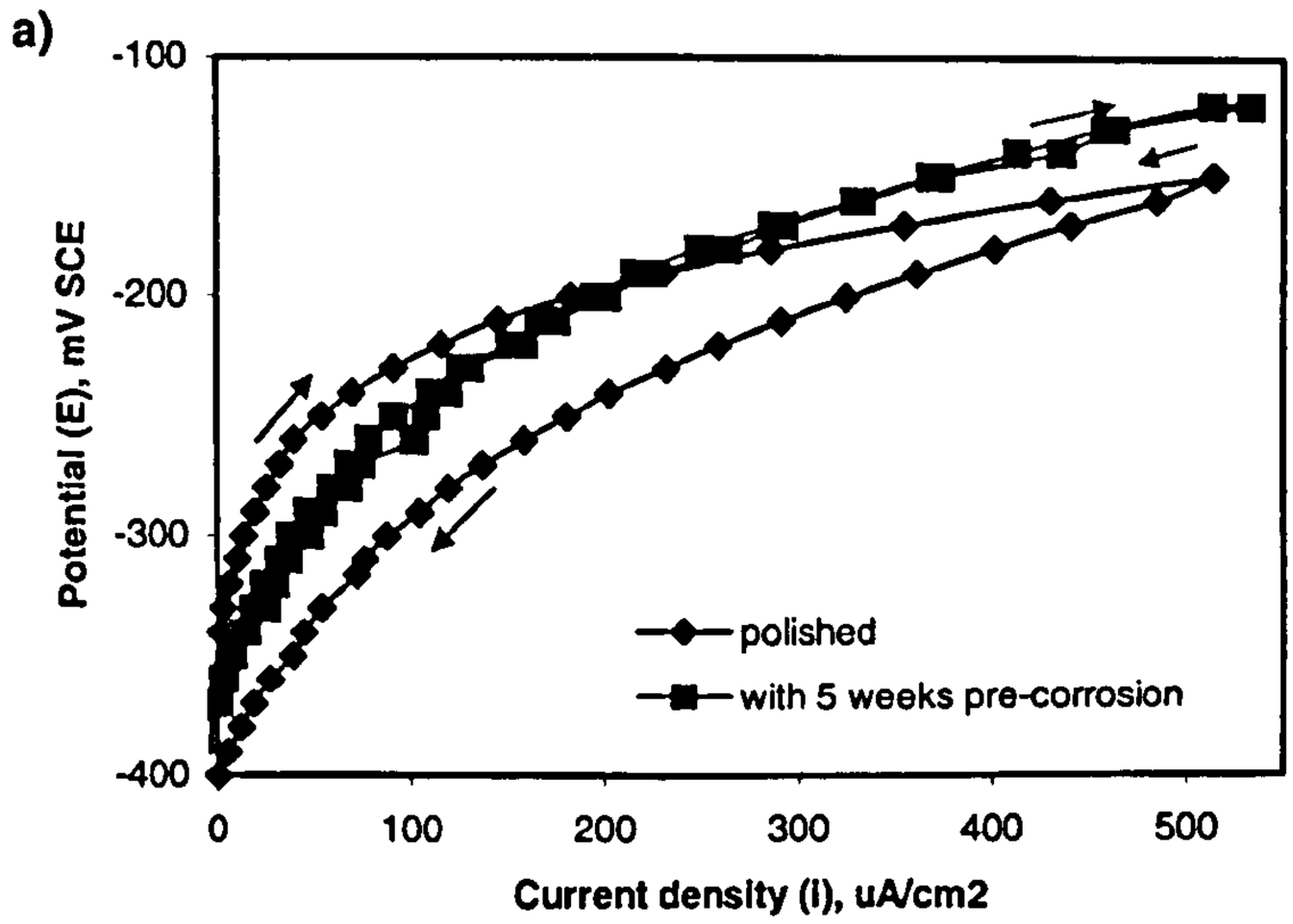
b)
100
0
-100
-200
-300
-400
Potential (E), mV SCE
E_b
E_{corr}
polished
pre-eroded
E_b = 291.6 mV
E_b = 380.6 mV
0
50
100
Current density (i), uA/cm2

Figure 7.6.2 a) Static anodic polarisation curves of polished and pre-eroded surfaces of *Coating* AII; and b) the same expanded to a current density of $100\mu A/cm^2$

The anodic polarisation curves in Fig. 7.6.2 clearly demonstrate the effect of 1-hour prior sand/liquid impingement on the static corrosion behaviour of the coating exhibited by its no passive range 'E_b-E_{corr}'. The steady increase of the current was displayed just above the free corrosion potential 'E_{corr}' and did not show any breakdown potential 'E_b'. The polished surface had a distinct 'E_b' showing a classic passive behaviour as reported previously. Another interesting feature evidenced was that there was a consistent lowering of E_{corr} value by 50+80mV once erosion had occurred as shown in Fig. 7.6.2b.

Effect of pre-corrosion on erosion-corrosion

The specimen was put in a beaker in static condition under freely corroding environment for 5 weeks and after then anodically polarised under solid/liquid impingement. Test was also undertaken on just a polished surface of the specimen, which was subjected to 5 minutes prior impingement while the E_{corr} settled down and then polarised under the same impinging condition. Anodic polarisation results of the polished and the pre-corroded surfaces of the coating under solid/liquid impingement are shown in Fig. 7.6.3a. The polished coating displayed semi-active behaviour with a steady increase in the current within a small range of potential (about 50mV) positive from E_{corr} after which the current increased rapidly. The specimen with 5 weeks pre-corrosion exhibited relatively larger current densities than the just polished coating, mimicking rather an active behaviour, which is clearly shown in Fig. 7.6.3b.



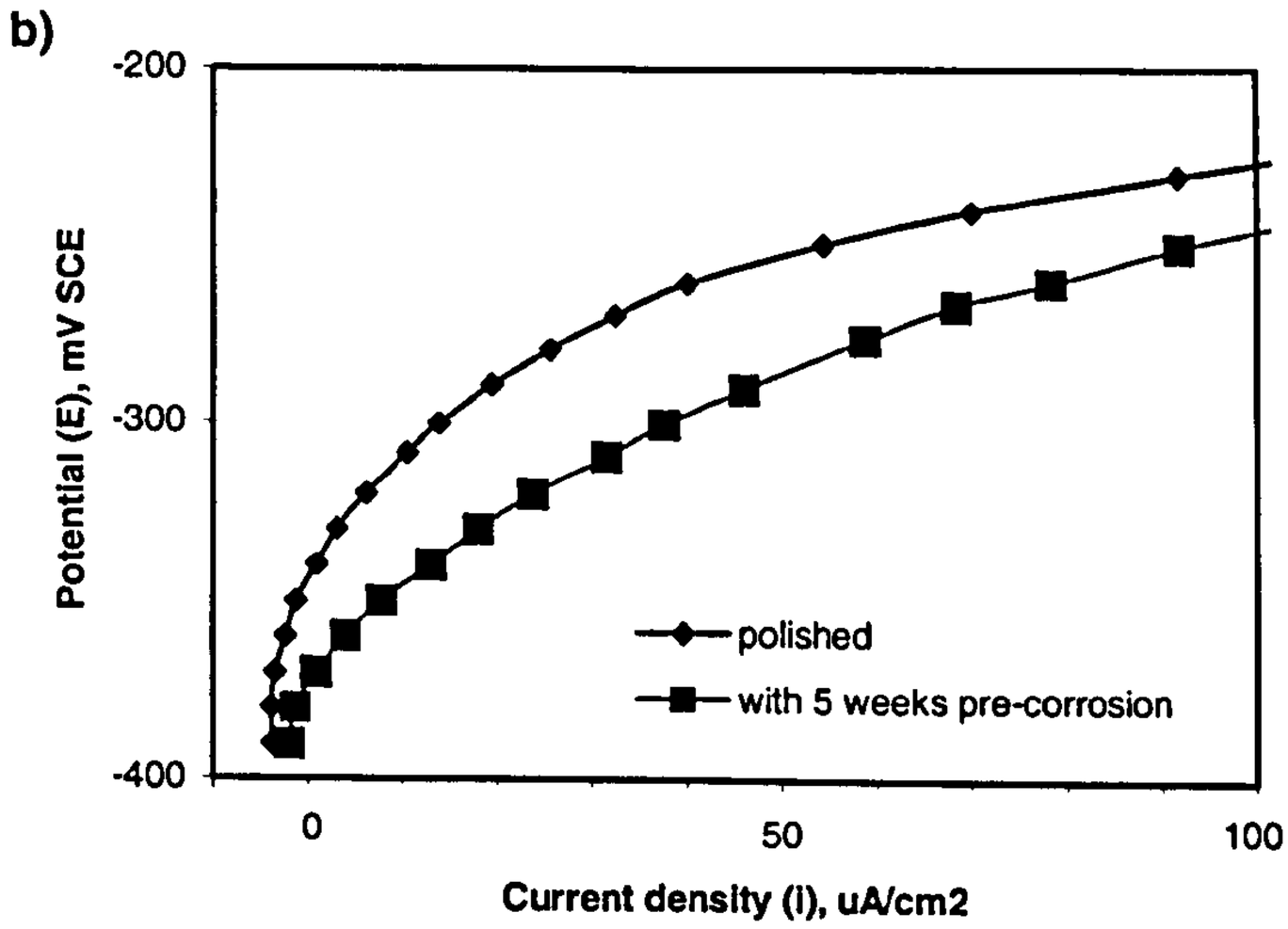


Figure 7.6.3 Anodic polarisation curves under solid/liquid condition of as-polished and 5-weeks pre-corroded surfaces of Coating AII.

An interesting thing that was demonstrated by the pre-corroded surface was that both forward and reversed scan curves of the anodic polarisation test had overlapped on each other showing almost no hysterisis loop. The corrosion current densities and the corrosion rates of the coating are shown in Table 7.6.1. The table also clearly indicated that there were significant effects of pre-erosion and pre-corrosion on the overall durability of the coating.

Condition	i_{corr} $\mu A/cm^2$	*Corrosion rate* $mg/yr/cm^2$
Static polished	0.1-0.15	0.98
Static pre-eroded	1.8-2.3	15.3
Solid/liquid impingement polished	5.0-7.5	51.0
Solid/liquid impingement pre-corroded	10.0-11.5	85.7

Table 7.6.1 Corrosion current densities and corrosion rates of coatings.

Microscopic observations of pre-erosion test

The central wear scar under the impinging jet was clearly visible on the coating specimen just after 1-hour solid/liquid impingement Fig. 7.6.4a. Higher magnification

of the wear scar revealed a drilling effect of the impinging slurry (as shown in the previous section 7.5) with a large number of macropitting as shown in Fig. 7.6.4b.

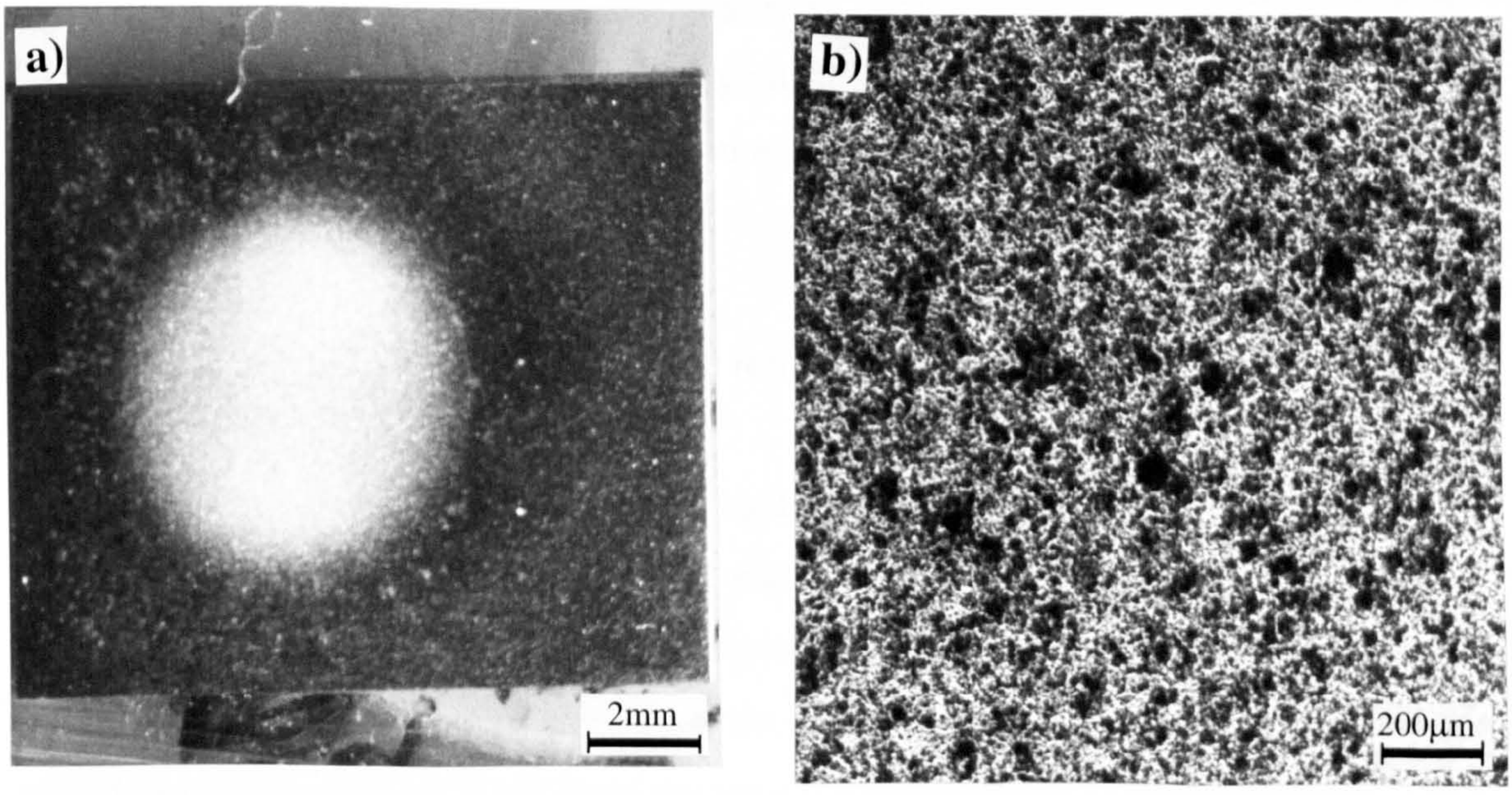


Figure 7.6.4 a) Central wear scar after 1-hour free solid/liquid impingement; and b) same at higher magnification showing macropitting.

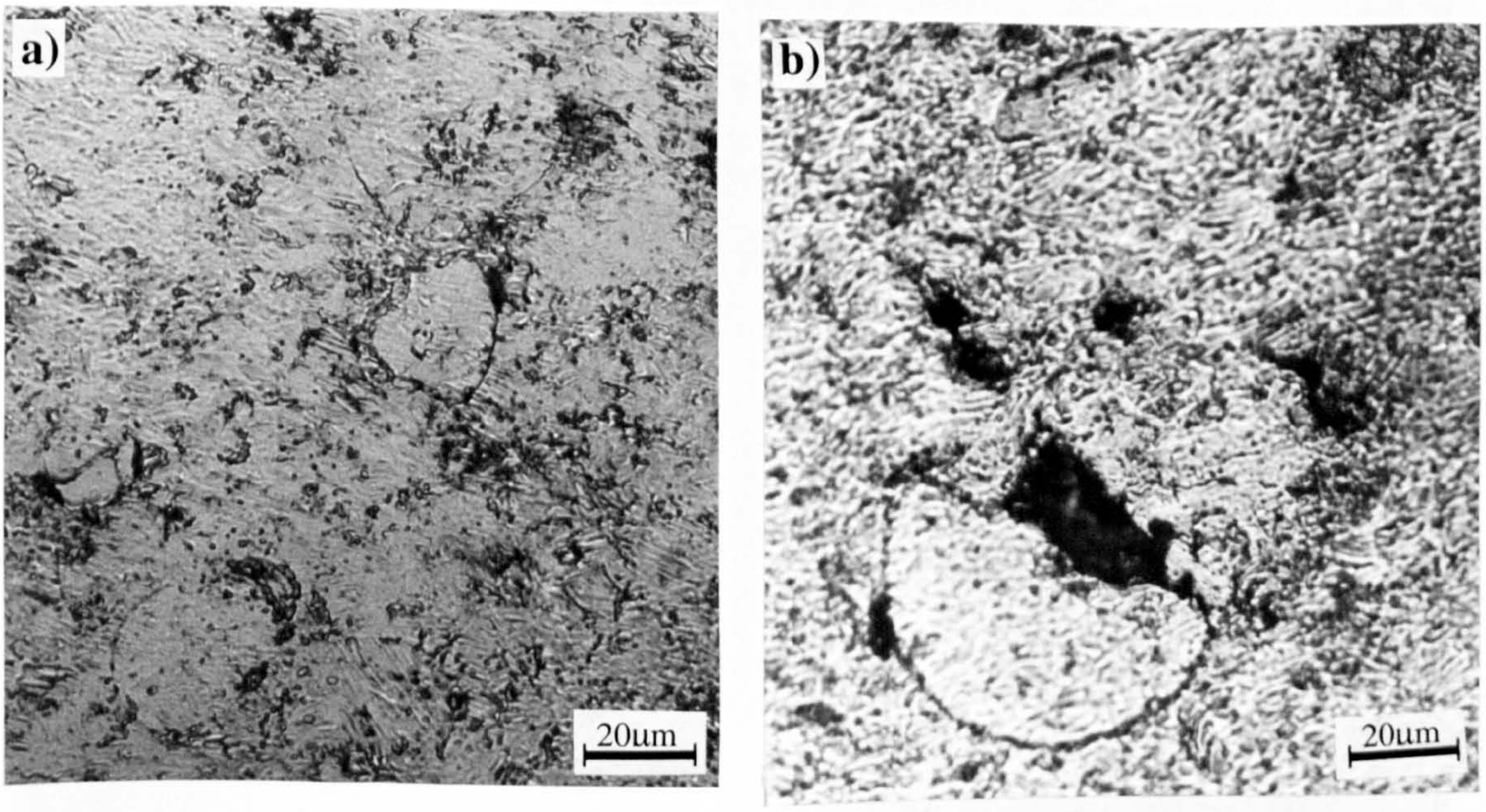


Figure 7.6.5 Region 2mm away from the centre: a) after 1-hour solid/liquid impingement without polarisation; and b) same region after anodic polarisation in static condition.

Some skidding tracks at the region 2mm away from the central area and initiation of splat boundary attack were already evident after the 1-hour pre-erosion period (Fig. 7.6.5a). After anodic polarisation enhanced corrosion attack was evident at regions where corrosion attack had already initiated in the form of more severe corrosion of the splat boundaries and their eventual dislodgement as shown in Fig. 7.6.5b. There were some areas as well with corrosion attack on a micro scale with micro-galvanic attack at the hard particle/matrix interface.

Microscopic observations of pre-corrosion test

Figure 7.6.6 shows macro-scale wear scars of the coating after anodic polarisation under solid/liquid impingement of as-polished and 5-weeks pre-corroded surfaces, which demonstrate the effect of pre-corrosion on extensive material loss of the coating. Figure 7.6.6b clearly shows material loss in the form of a severe drilling action imposed by the solid/liquid jet at the central region of the pre-corroded surface.

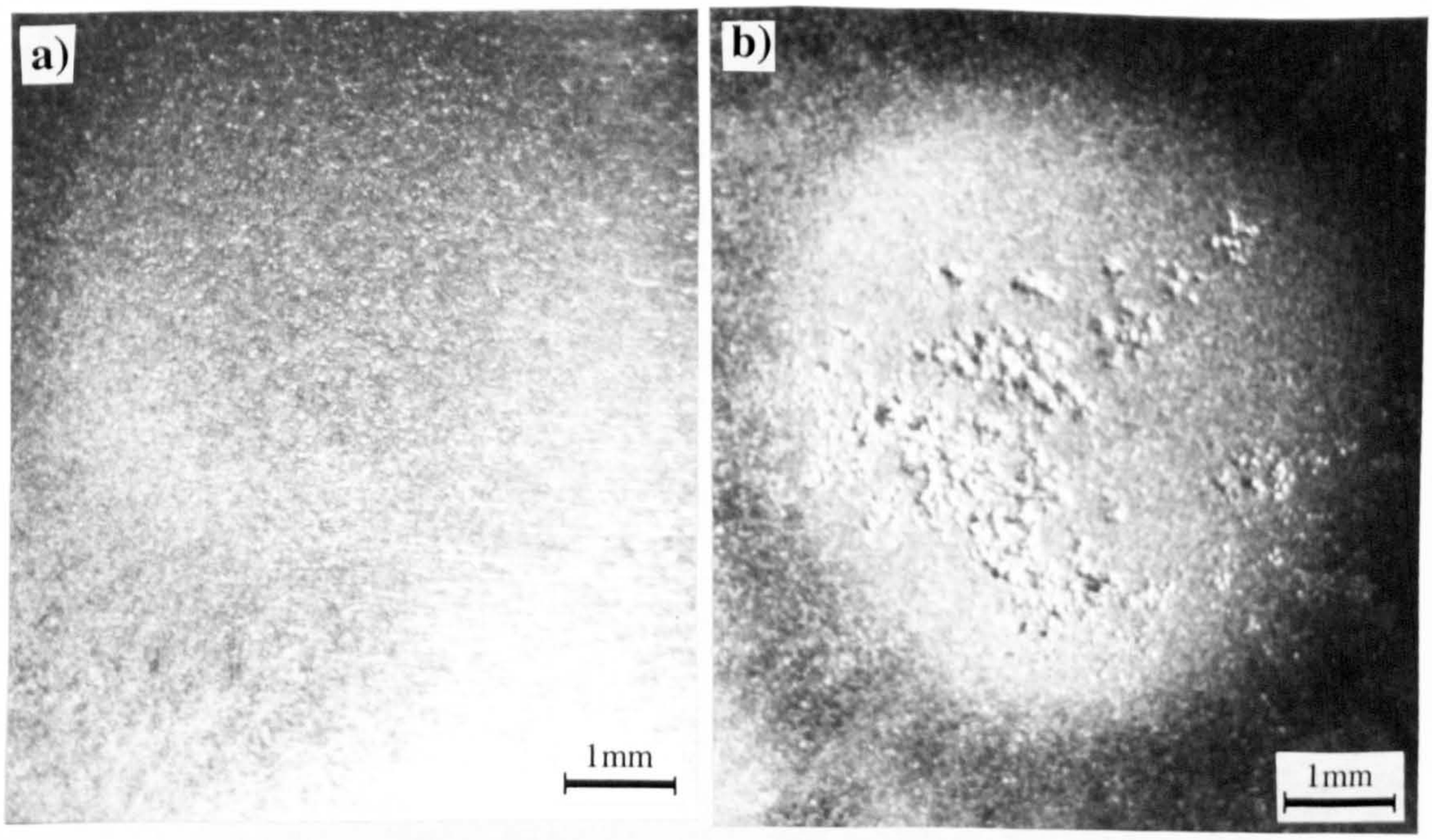
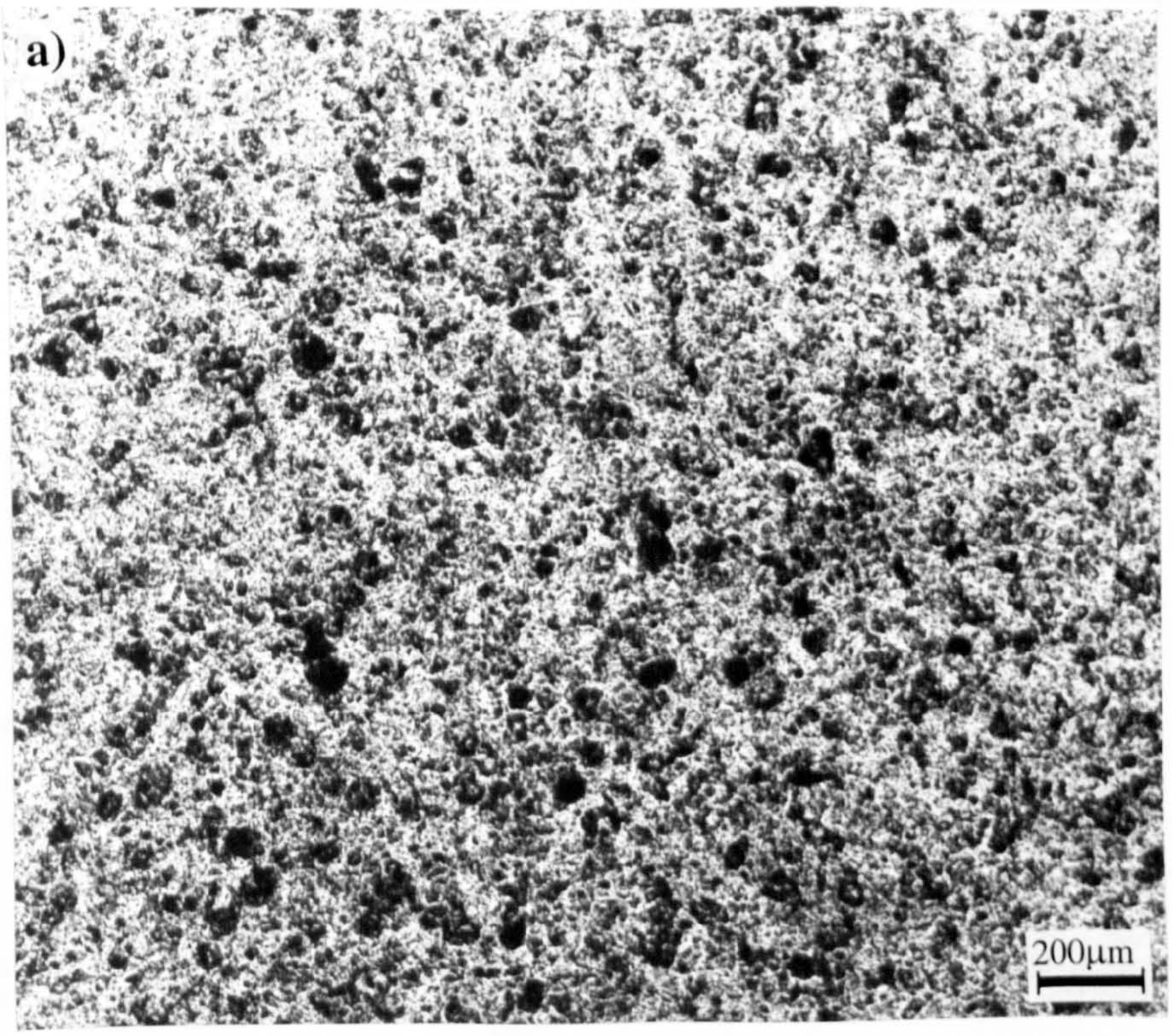


Figure 7.6.6 Wear scars of the coating after anodic polarisation under solid-liquid impingement of a) as-polished; and b) 5-weeks pre-corroded surfaces.

Anodic polarisation under solid/liquid impingement showed a similar wear scar as in 1-hour free solid/liquid impingement at E_{corr}. However, some distinctions were observed under the microscope with a relatively large amount of macropitting under the central jet after anodic polarisation (Fig. 7.6.7a). Moreover, attack in the form of splat boundary corrosion was quite distinct after the polarisation test. The specimen left for 5 weeks free immersion evidenced corrosion product on the surface, which after 1 hour free solid/liquid impingement promoted excavation of already loosened splat particles resulting in more macropitting (Fig. 7.6.7b) under the central wear region.

The outer region had shown some particle skidding tracks typically seen after solid/liquid impingement. The severity was much more pronounced when the pre-corroded specimen was polarised under solid/liquid impingement. Figure 7.6.7c shows the central wear region of pre-corroded surface of the coating being severely attacked after anodic polarisation under solid/liquid impingement. Corrosion in the form of splat particle losses was quite distinct in Fig. 7.6.7c. The region away from the centre had very less attack. It is very clear that large localised regions of material loss exist after pre-corrosion, which illustrate how exposure to a corrosive environment can affect the material integrity in solid/liquid erosion-corrosion conditions.



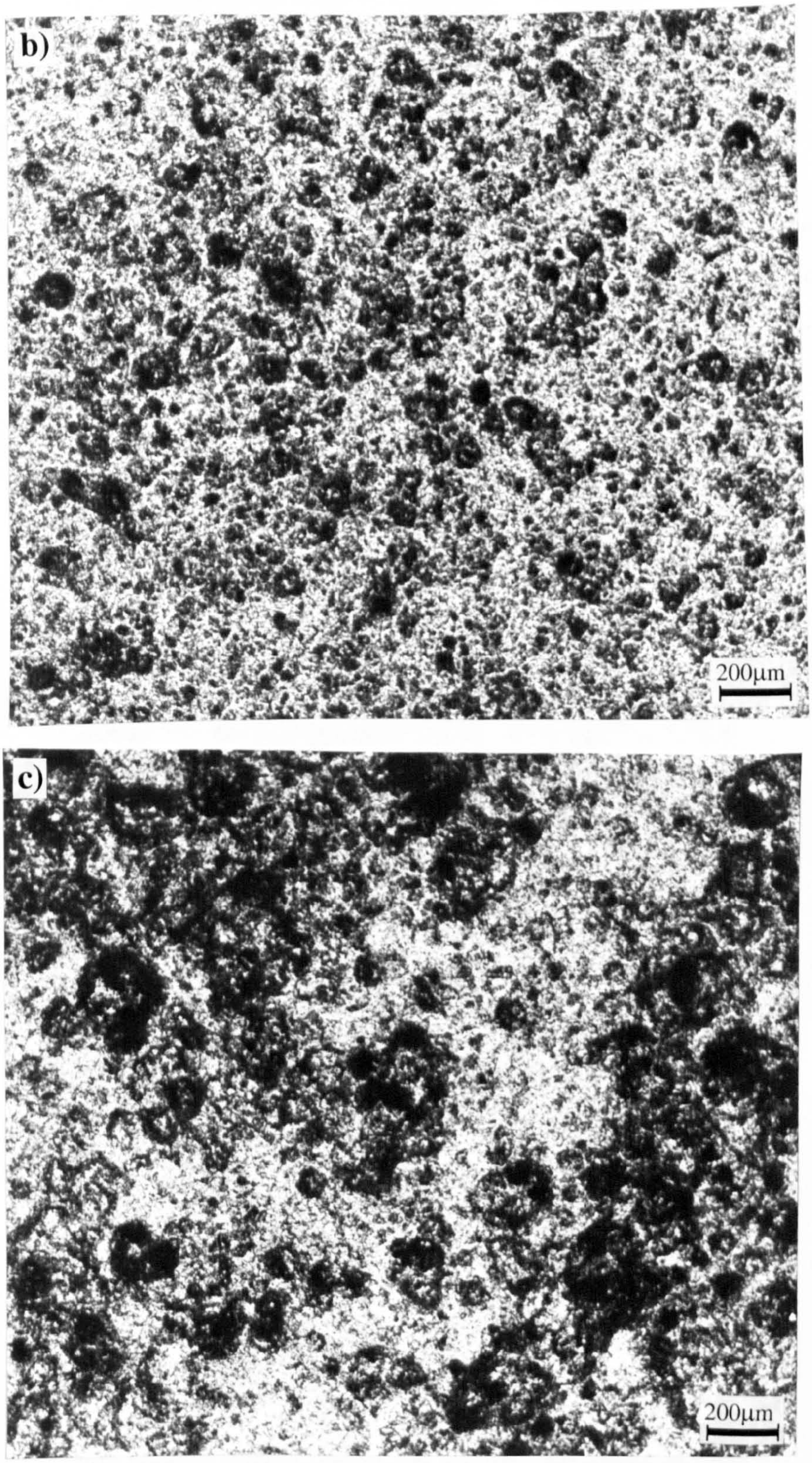


Figure 7.6.7 a) Central wear region of the coating after anodic polarisation under solid/liquid impingement; b) Central region under the impinging jet of 5-weeks pre-corroded surface after 1-hour free solid-liquid impingement; and c) the central region of the 5-weeks pre-corroded surface after anodic polarisation under solid/liquid impingement.

CHAPTER 8. *Coating* B Results

8.1 Powder characterisation

The self-fluxing NiCrSiBMoC (*Coating* B) powder particles are almost identical to the particles of *Coating* A, comprising spherical shapes with a grain size distribution from 3 to 40μm (Fig. 8.1.1a). Figure 8.1.1b shows a higher magnification back-scattered SEM image of the cross section of a powder particle.

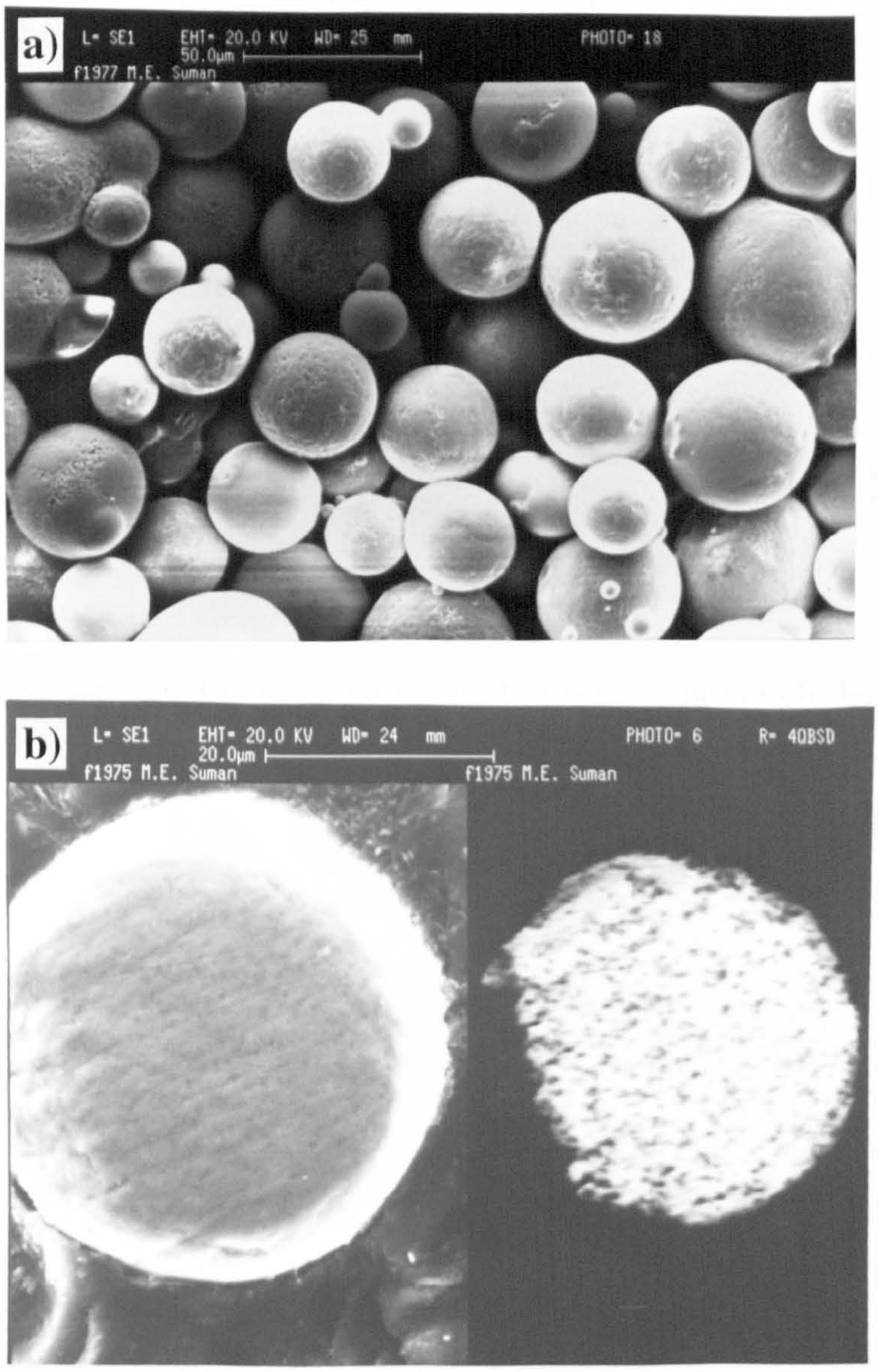


Figure 8.1.1 a) SEM micrograph showing water atomised powder particles possessing rough and smooth textures; b) back-scattered SEM image of a polished powder particle.

SEM observation revealed some differences between the powder particles from one another mainly in smooth and rough texture. Microanalysis of smooth and rough textured powder particles showed slight variations of elemental composition primarily in nickel, chromium and molybdenum contents. The particles having smooth texture showed higher average Ni content, however, displaying reductions in Cr and Mo. The EPMA results of several powder particles are shown in Table 8.1.1. SEM observation of polished powder particles revealed that there existed density variation of the hardphase particles content on the different particles observed.

Element, %	Powder particles (20x20μm)						
	rough				smooth		
	1	**2**	**3**	**4**	**5**	**6**	**7**
Fe	2.5	2.9	2.5	2.9	2.9	3.2	2.7
Ni	62.8	62.7	61.6	59.1	67	74.2	65.2
Cr	16.1	17.4	17.3	20	13	11	12.4
Si	3.8	3.6	3.6	3.6	4.0	4.4	4.4
B	-	-	-	-	-	-	-
Mo	5.8	6.1	6.7	8.1	2.7	2.9	3.5
Cu	1.8	1.9	1.7	1.8	1.8	2.0	1.8
C	-	-	-	-	-	-	-
Total	**93**	**95**	**93.4**	**95.8**	**93**	**98.2**	**96.7**

Table 8.1.1 Average SEM microanalysis of as-received powder particles.

EPMA analyses of individual powder particles showed that although the Fe, Si and Cu content were relatively consistent, there were variations in the Ni, Cr and Mo contents such that particles enriched in Ni were denuded in Cr and Mo. The differences in the totals in Table 8.1.1 could have been affected due to the surfaces of the powder particles being not flat.

The XRD pattern for the powder particles (*Coating* B) is shown in Fig. 8.1.2. The binder phase i.e. the matrix comprised mainly a solid solution of complex compound NiCrFe, which is very much identical to that of *Coating* A, however, some new phases Nickel Silicide 'Ni_5Si_2' and ChromiumNickelBoride 'Cr_3NiB_6' were identified.

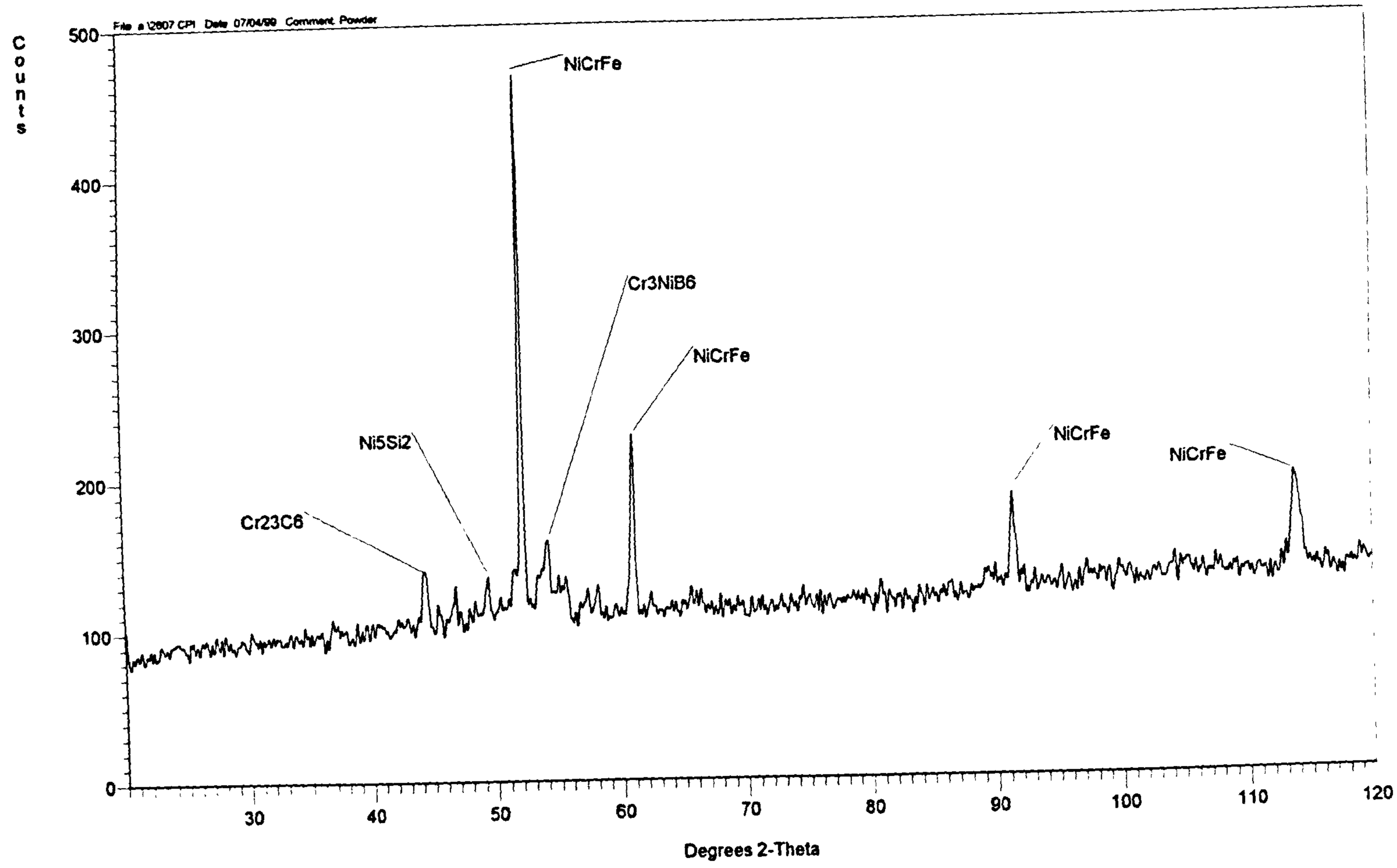


Figure 8.1.2 XRD pattern of *Coating* B powder

8.2 Characterisation of Coating B

Coating B was received in three different conditions; as-sprayed, vacuum-sealed and vacuum-fused. These were obtained on carbon steel and stainless steel substrates. Coatings on the carbon steel substrate will be referred to as *Coating* BI and those with the stainless steel substrate will be referred to as *Coating* BII. Both coatings BI and BII displayed identical microstructural characteristics and hence micrographs of only coating BII will be shown in this section. Moreover, both as-sprayed and vacuum-sealed coatings exhibited identical microstructures and thus only micrographs of the as-sprayed coating will be displayed in this section. Some distinctions were identified between the coatings sprayed on the different substrate materials mainly at the coating/substrate interfaces after being subjected to high temperature vacuum furnace fusion.

Visual examination of as-received coatings

Visual examination of the as-sprayed and vacuum-sealed coating showed a dull darker appearance of the coating surface. In contrast, the vacuum-fused coating showed a dense shiny surface.

As-sprayed/vacuum-sealed coating

Cross sectional examination of sprayed/sealed coating revealed very low coating porosity amounting to around 1.5-2.7% quantified by image analysis and low interfacial porosity. The back scattered SEM image of the cross section showed a dense dispersion of individual splat lamellae overlapped onto one another and not very smooth as-sprayed surface as shown in Fig. 8.2.1a. Higher magnification SEM displayed fewer coating defects typical for thermal sprayed coating such as 'inter lamellae void', fully not adhered splat particle showing 'splat boundary separation' and few 'micro-pores' within the particle splat itself (Fig. 8.2.1b). The back scattered SEM image (Fig. 8.2.1c) of the polished plan surface showed a clear abundance of black (low atomic number) globular hardphase particles of sizes varying 0.2-1.5μm. EPMA analyses taken on both hardphase particles and the binding matrix are listed in Table 8.2.1.

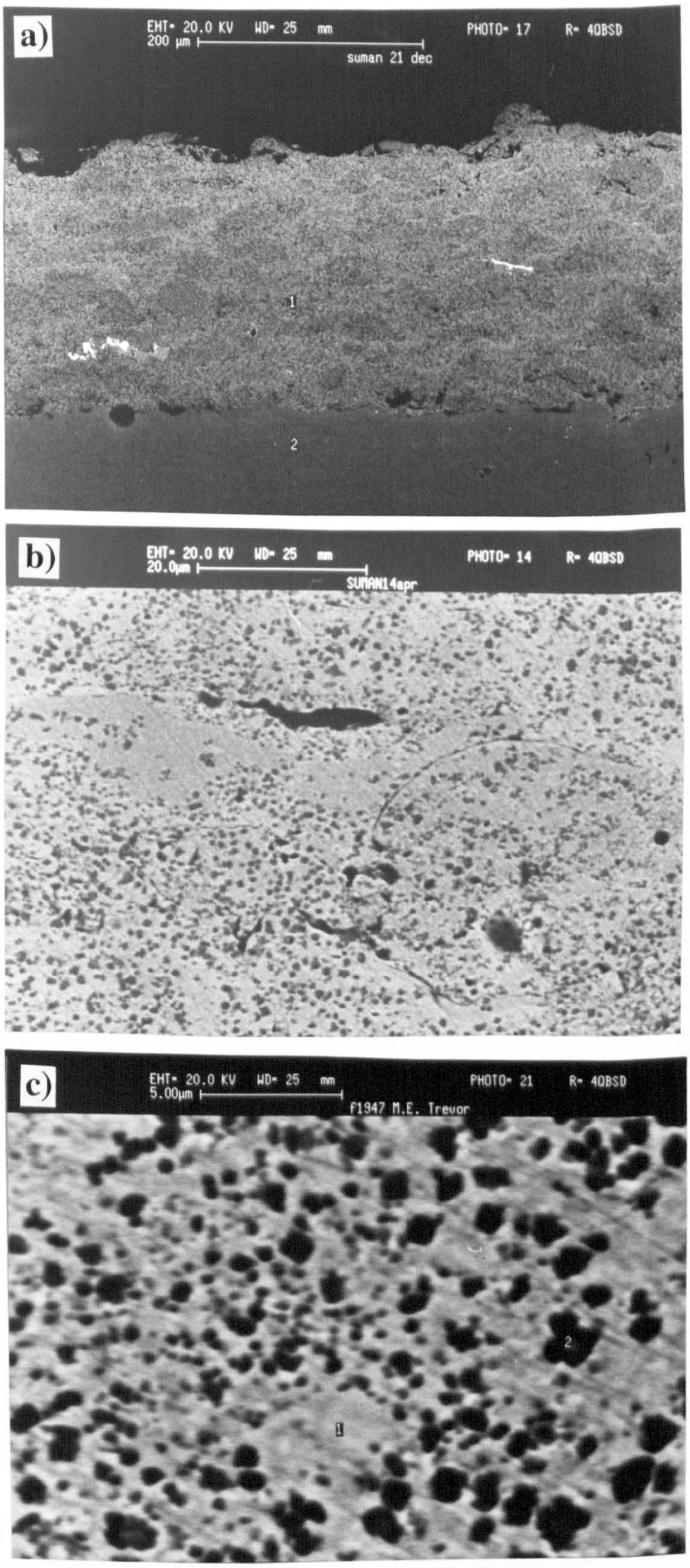


Figure 8.2.1 a) Back scattered cross sectional SEM image of sprayed/sealed coating; b) coating defects due to inter lamellae void, splat boundary separation, micro-void in the particle splat; and c) back scattered image of polished surface showing black globular hardphase particles.

Elements	Matrix	Globular hard phase	Bulk (100 x 100μm)
Fe	3.0-3.3	1.9-2.3	2.7-3.0
Ni	77.7-81.9	25.1-32.5	62.7-67.7
Cr	9.8-14.3	38.8-42.2	16.9-17.7
Si	4.8-5.2	1.2-1.6	3.6-4.0
Cu	1.6-2.3	0.49-0.5	1.6-2.0
Mo	2.2-4.1	17.5-19.2	5.9-6.7
Total	104.3-106.3	90.3-93.6	95-101

Table 8.2.1 Microanalysis on polished surface of as-received sprayed/sealed coating (values shown in wt. %)

Accurate analyses were difficult on the hard phase particles due to their sub-micron size. Nevertheless, analyses taken on a range of such particles revealed that these hard particles comprise a significant amount of Cr amounting up to 42.2%. This feature, taken with the relatively low 'total analysis' and their appearance in the back-scattered SEM image, is indicative of these particles being Cr-rich carbides and borides (as also indicated by the XRD results). The particles were generally well distributed but with some regions containing mainly Ni rich matrix. Table 8.2.1 also shows a 'bulk' analysis of the coating, which was obtained by analysing an area of 100x100μm.

Vacuum fused coating

Significant changes in microstructure were observed in the coatings that had been subjected to post-treatment by vacuum furnace fusion, which was clearly discernible in cross sectional view shown in Fig. 8.2.2a. Reductions in both coating and coating/substrate interfacial porosities were observed after the fusion process. The fusion process also resulted in the removal of the clear coating/substrate interface, which was visible in sprayed/sealed coating. Moreover, the as-sprayed surface was significantly smoothened (Fig. 8.2.2a).

Examination of a polished plan surface revealed an abundance of dark hard phase particles (Fig. 8.2.2b) which were clear under the back-scattered SEM image. Furthermore these hard phases were significantly bigger than on the as-sprayed coating and were relatively large acicular shapes. In addition, bright (higher atomic-numbered) hard phase particles were visible, which were found to be rich in molybdenum (Fig. 8.2.2c).

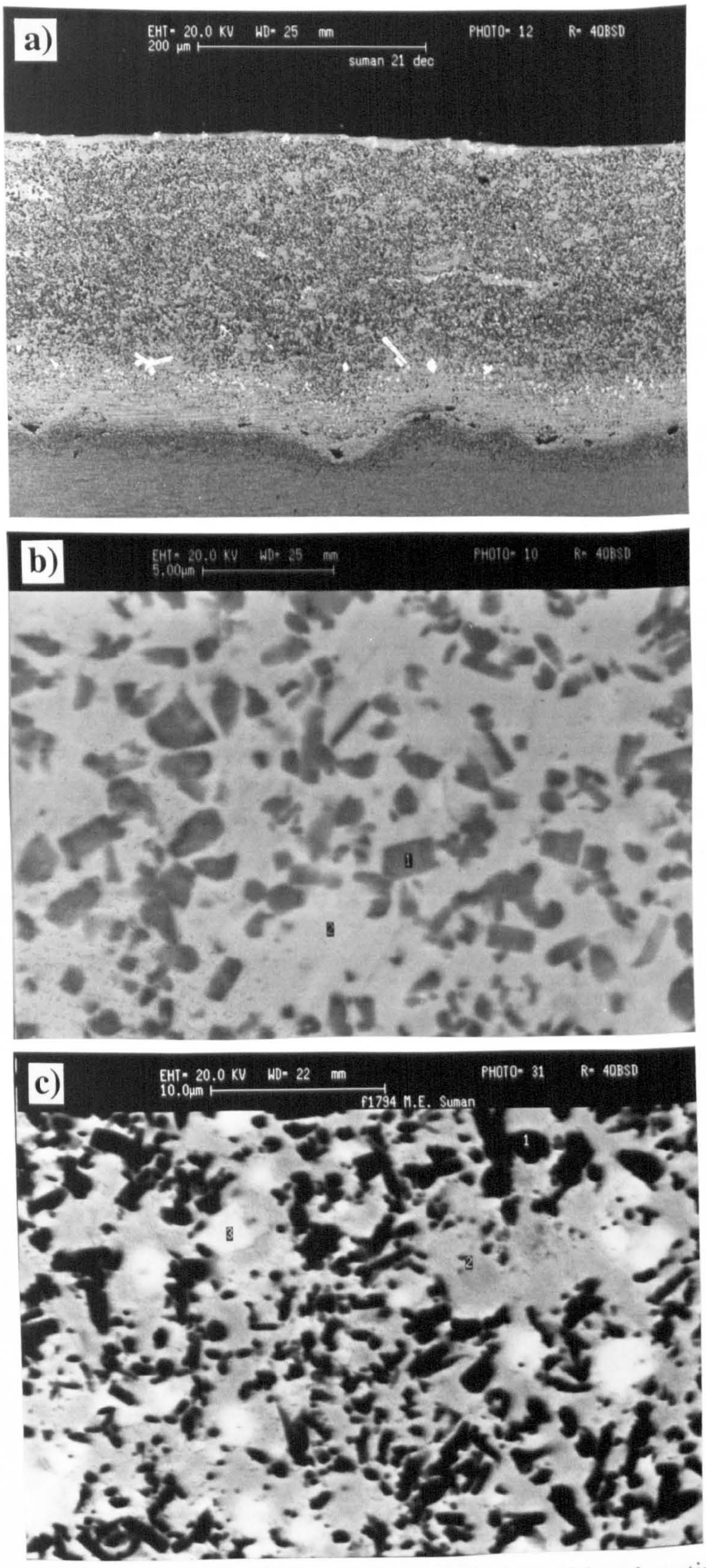


Figure 8.2.2 a) Back scattered cross sectional SEM image of fused coating BII; b) distribution of dark acicular hard particles; and c) distribution of Mo rich blocky white '3' particles.

Black acicular and globular hard particles '1' were rich in chromium accounting up to 60.1% Cr, 12.9%Mo, 34%Ni. Matrix '2' comprised up to 84.9%Ni, 6.8%Cr, 1.2%Mo and blocky white '3' was enriched in molybdenum accounting up to 62%Mo, 32.8%Cr, 39.2%Ni (Fig. 8.2.2c). EPMA results taken on both spot and area analyses are displayed in Table 8.2.2.

Ele-ment	Matrix	Dark acicular HP	Blocky white HP	Area analyses				
				Zone T (3x3μm)	Zone 1 (100 x100μm)			Zone 2 (20x20μm)
					50μm in	100μm in	150μm in	
Fe	2.6-5.4	0.8-2.2	1.0-1.3	4.9-5.2	2.9-3.2	3.0-3.4	3.2-3.8	12.3-13.4 ***(20-22)***
Ni	78-84.9	18-34	37.7-39.2	84-86	60-61.7	62.9-64	64-68.1	71.5-73.8
Cr	4.9-6.8	48-60.1	27.2-32.8	7.5-7.0	23-24	21.8-22.8	20.2-22	7.96-8.02 ***(5.2-6.1)***
Si	4-8-5.6	0.8-2.8	6.2-6.5	5.5-5.1	4.0-4.2	3.8-4.0	3.4-3.6	3.5-3.8
Cu	1.97-3.1	0.2-0.3	0.2-0.4	3.4-2.0	1.0-1.4	1.2-1.3	1.5-1.5	1.0-1.2
Mo	0.08-1.2	9-12.9	37.3-62	0.6-1.1	8.1-9.7	7.8-8.1	4.9-6.4	1.9-2.0
Total	93-99	89-91.1	103-105	108	101-102	101-102	101-102	98.1-99.4

Table 8.2.2 Microanalysis of as-received *Vacuum fused* BII coating representing Fig. 8.2.2, Fig. 8.2.3 and Fig. 8.2.4 (values shown in wt. %). Values in bold italic numbers represent for coating BI with carbon steel substrate; analyses in all other zones for BI are similar to BII (HP - hardphase particle).

A cross sectional schematic representation of the as-sprayed and vacuum fused coatings is shown in Fig. 8.2.3, which also disclosed interfacial diffusion at the coating/substrate interface. The major distinctions found between *Coating* BI and *Coating* BII were only at the interface as shown in Fig. 8.2.4.

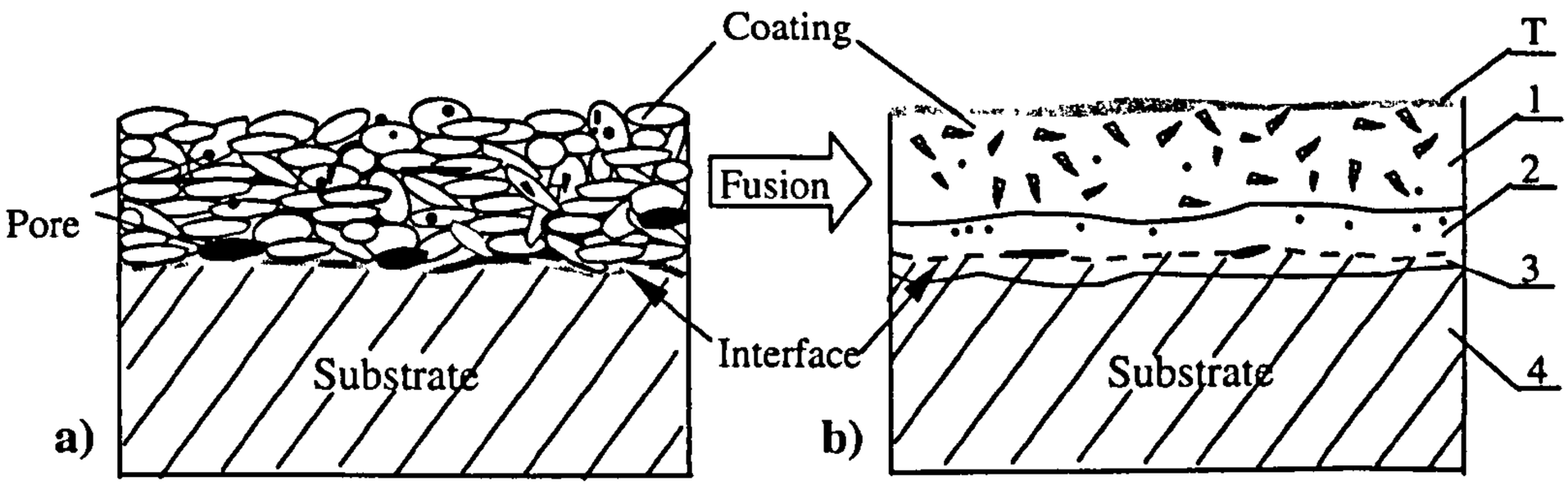


Figure 8.2.3 A schematic diagram of (a) As-sprayed; and (b) Vacuum-fused coating showing different coating/substrate interfaces (T-top white layer; 1-main coating; 2-diffusion zone of coating (basal white layer); 3-diffusion zone of substrate; 4-substrate).

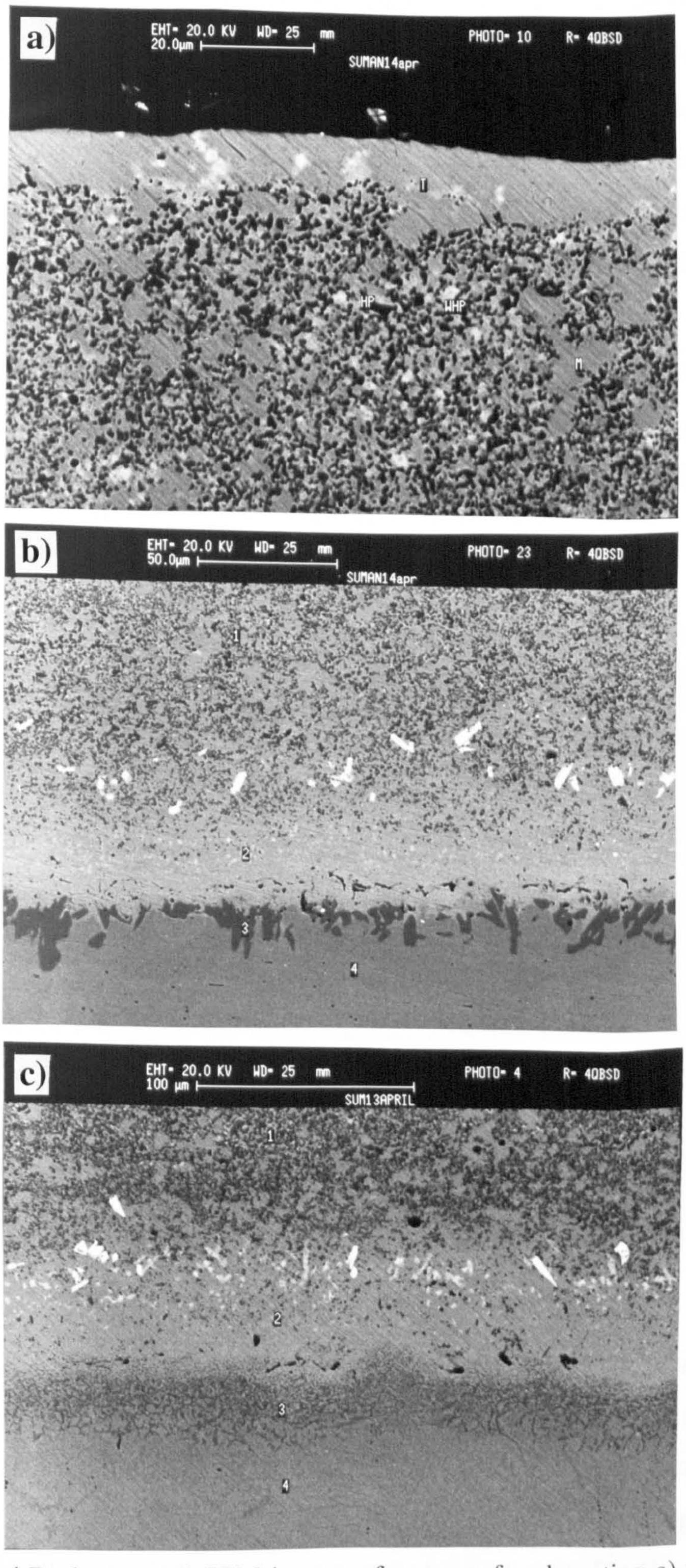


Figure 8.2.4 Back-scattered SEM images of vacuum fused coating a) white top layer 'T'; b) diffusion and basal keys at the interface of coating BI; and c) diffusion of coating BII at the interface.

The EPMA analyses in Table 8.2.2 taken at various areas of the cross sections for both coatings BI and BII (Fig. 8.2.3b, Fig. 8.2.4) signal that there occurred a significant amount of counter diffusion of elements clearly shown by a change in composition near the substrate, resulting in the formation of a basal white layer. This basal white layer had less amount of Cr compared to other areas analysed, thus resulting decreased Cr and Mo in the layer. However, there was an increase in Ni compared to the rest of the coating amounting up to 73.8%. Diffusion zone '3' of the substrate of the coating BII showed 64.6%Fe 17.3%Ni 19.4%Cr. Moreover, both coatings showed a uniform top white layer 'T' as shown in Fig. 8.2.4a of thickness about 8-10μm, rich in Ni amounting up to 86%Ni. Also, a band of white needle like particles (Fig. 8.2.4b, c) was found near the basal white layer in the coating. Spot analysis revealed these particles enriched in Mo amounting up to 60.6%.

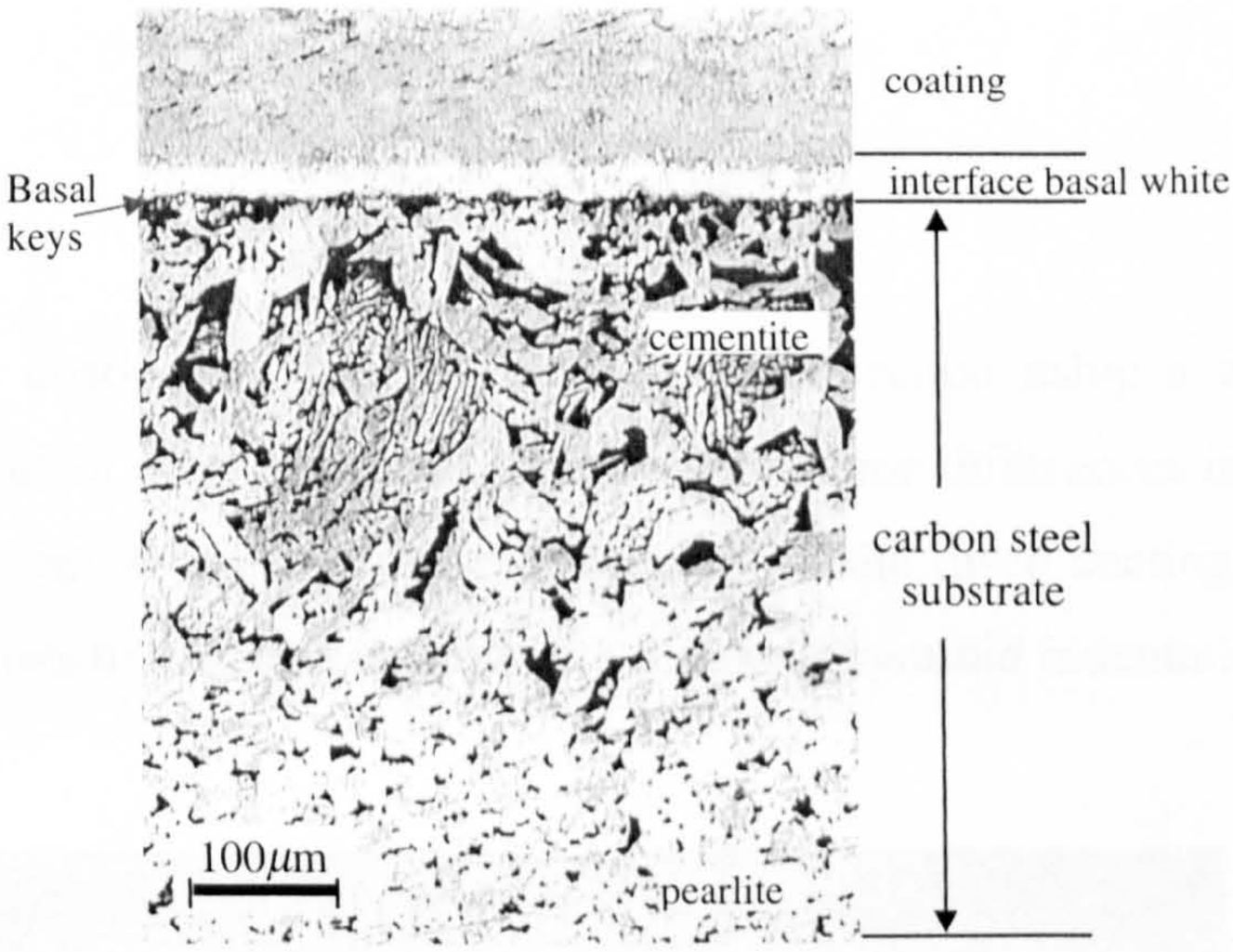


Figure 8.2.5 Vacuum fused coating BI displaying two layers of substrate near interface after etching in 2% Nital.

Analyses on Coating BI were identical to that of coating BII, but there was slightly higher amount of Fe in the basal white layer '2' of coating BI amounting up to 22% as can be expected from the carbon steel substrate. Moreover, a distinct band in the form of 'black basal keys' was visible in the coating BI as shown in Fig. 8.2.4b. Spot analyses on these 'black basal keys' found 94%Fe 0.3%Ni 0.2%Cr. Figure 8.2.5 shows a polished cross sectional view of coating BI etched in 2% Nital revealing

microstructural change of the substrate at the interface. Analysis on the upper layer of the diffused zone on the substrate showed trace amounts of Ni and Cr.

The post fusion process also resulted in reduction of coating porosity, increased coating density, and higher hardness value, which are listed in Table 8.2.3. The coalescing of splat particles due to the high temperature fusion process also resulted in removal of inter-splat boundaries.

Coating type	Coating porosity, %	Hardphase distribution, % area (25 x 25μm)	Vickers Hardness (500g) Plan	Thickness (μm)	R_a, μm	Density, g/cm^3
Sprayed	1.5 - 2.73	14 ± 5	612 - 692	240±25	8.7	6.60
Sealed	1.7 - 2.41	14 ± 5	546 - 716	240±25	8.5	6.65
Fused	0.23 - 0.33	28.54 ± 3	816 - 876	260±10	3.5	8.30

Table 8.2.3 Characterisation of coatings properties

Hardness measurement

Microhardness for coating BI was measured in cross section using a microhardness indenter under a load of 300g revealed that there were some differences in the hardness value measured at various areas of the cross section of the fused coating. Figure 8.2.6 shows various regions in the cross section with diamond pyramid indentations.

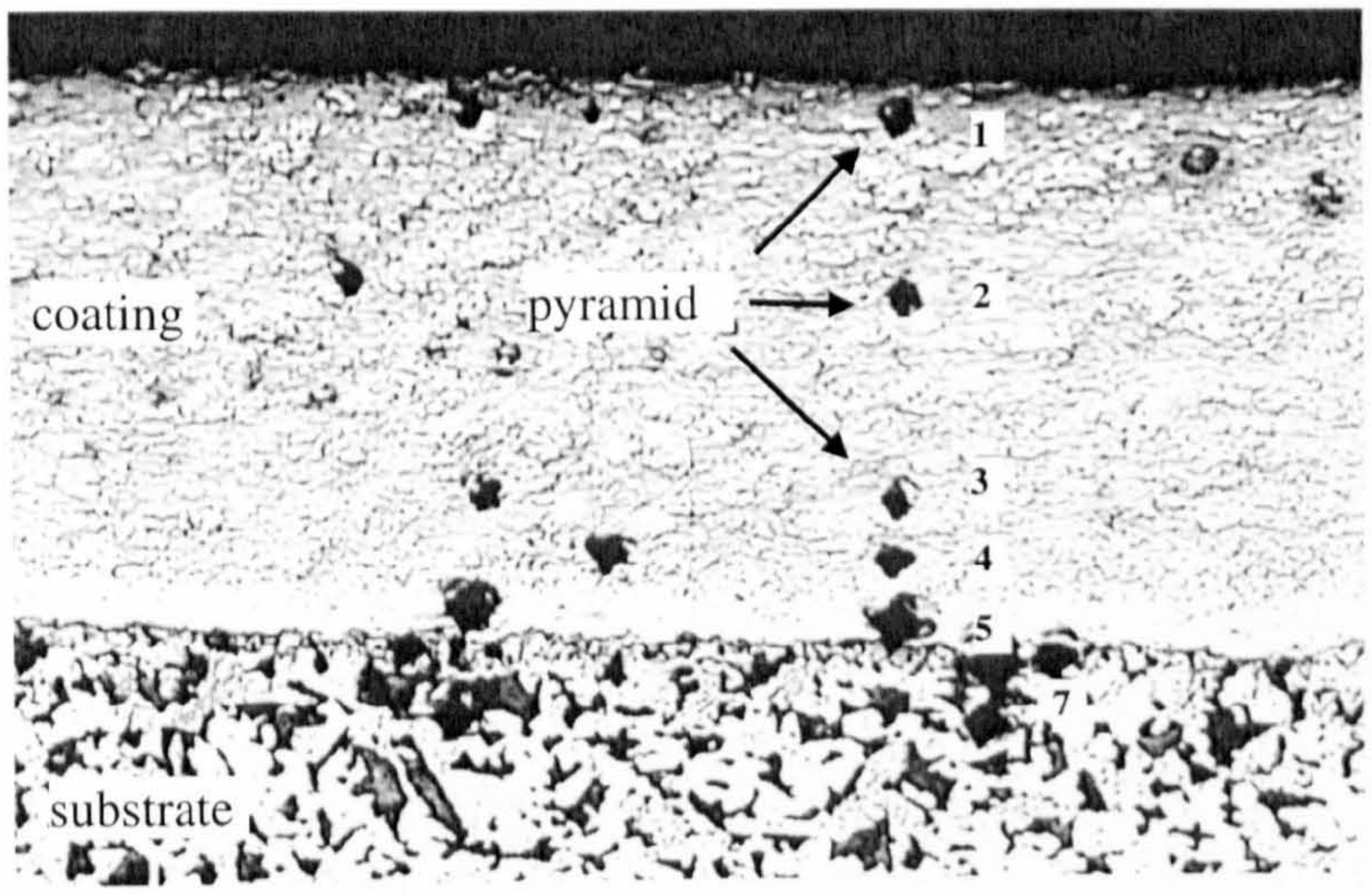


Figure 8.2.6 Fused coating BI with diamond pyramid indentations.

Region	Top layer	Coating				Basal white	Basal keys	Substrate	
	T	*1*	*2*	*3*	*4*	*5*	*6*	*7*	*8*
Hardness, HV	-	857	816	779	536	276.5	249.5	139	117

Table 8.2.4 Vickers microhardness at different regions of the fused coating BI (Average of 3 readings).

Hardness measurement was difficult on the top white layer due to its very small cross sectional area. Table 8.2.4 clearly indicated that there was a decreasing trend of microhardness at regions further away from the surface.

X-ray diffraction

X-ray diffraction patterns of the sprayed/sealed coating (Fig. 8.2.7) were slightly different to that of the powder particles evidencing some phase transformations. Peaks of Ni_5Si_2 and Cr_3NiB_6 were found to disappear. A new phase $Ni_{16}Cr_6Si_7$ was shown at $2\theta = 88.4°$. The principal hardphase particles within the metal matrix were confirmed to be the carbide compound ($Cr_{23}C_6$) and no Mo-containing crystalline phase was identified.

XRD analyses on the vacuum-fused coating showed the hardphase particles to be carbides ($Cr_{23}C_6$) and borides (Cr_3NiB_6, $FeMo_2B_2$ and Fe_2MoB_4), which were not found in the as-sprayed coating. XRD patterns of the vacuum-fused coating are shown in Fig. 8.2.8.

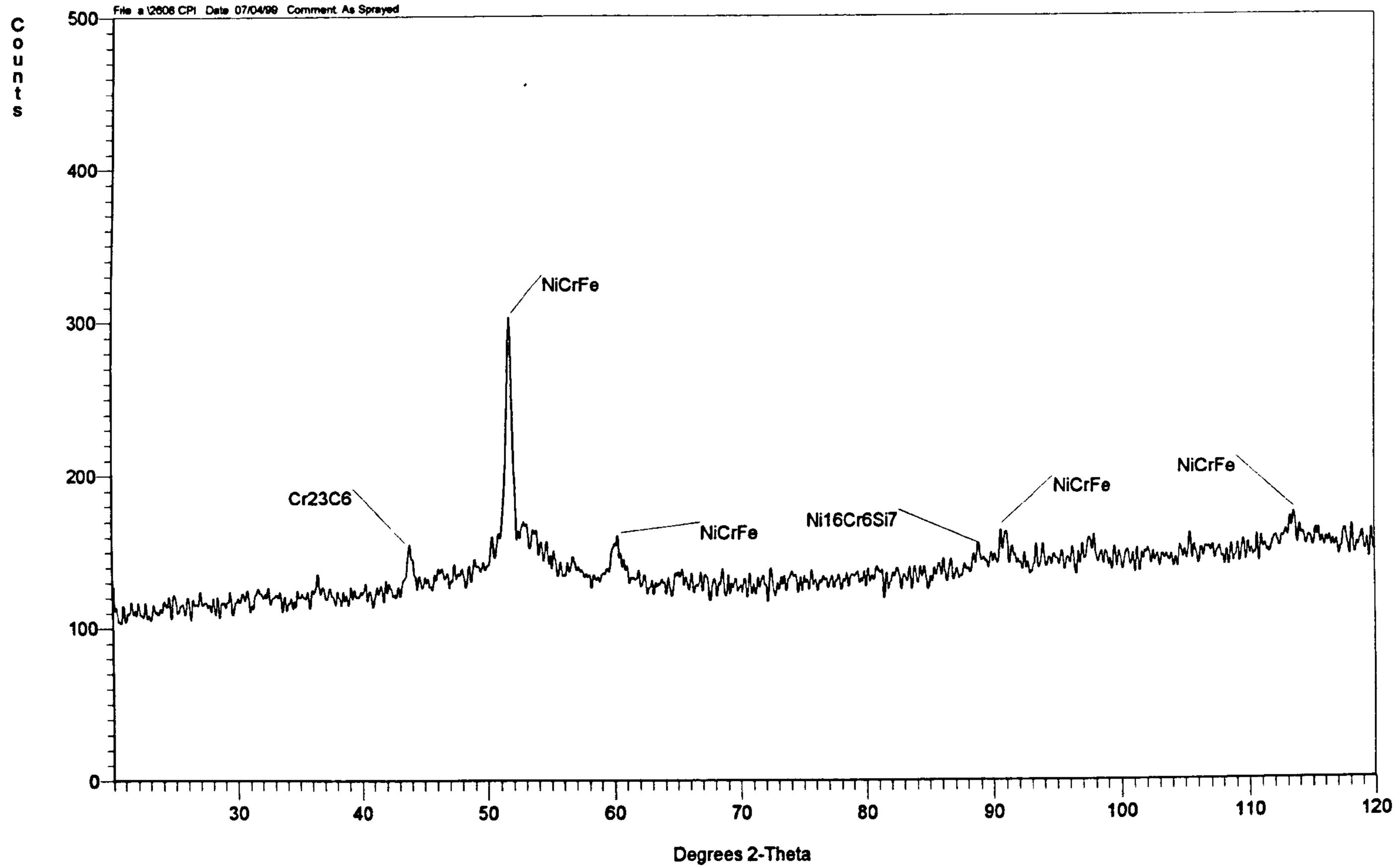


Figure 8.2.7 X-ray diffraction patterns of sprayed/sealed coating

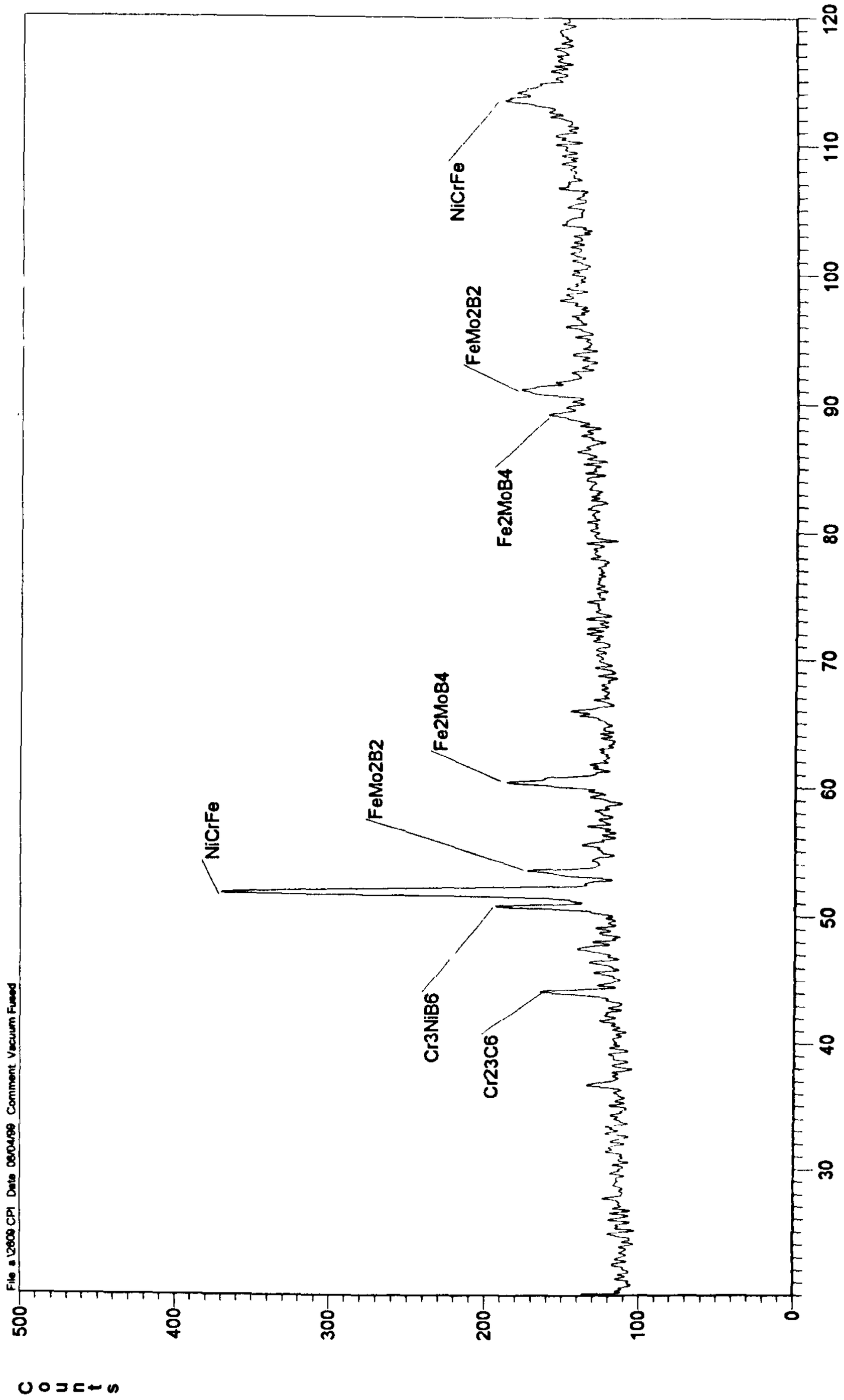


Figure 8.2.8 X-ray diffraction patterns of vacuum-fused coating.

AFM images in Fig. 8.2.9 shows surface textures of the polished surfaces of the as-sprayed and the vacuum-fused coatings exhibiting tiny hardphase particles protruding out of the surface of the coatings. The fused coating revealed a more dense distribution of hardphase particles and smoother texture than the as-sprayed coating.

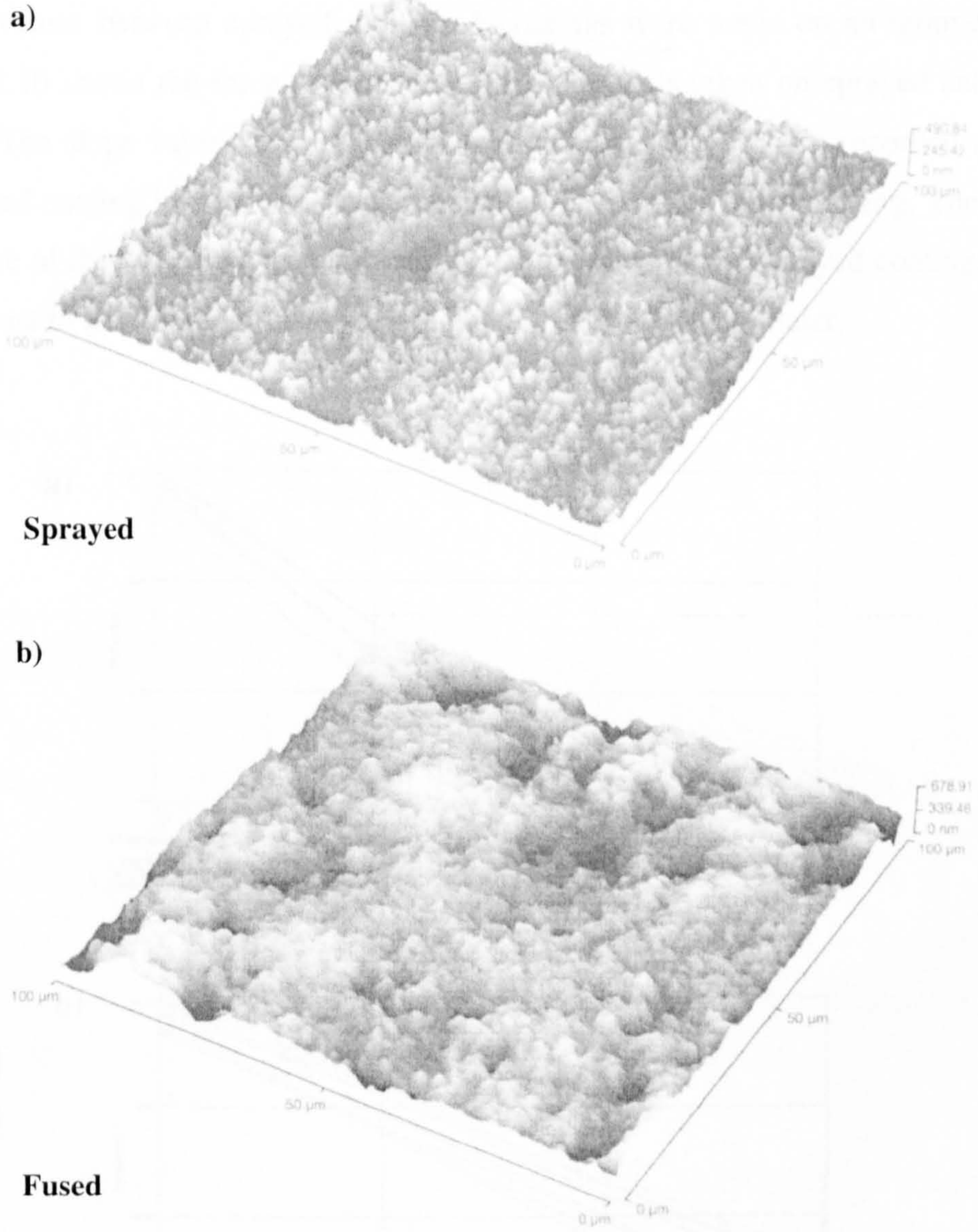


Figure 8.2.9 AFM image of polished a) sprayed coating showing tiny hardphase particles protruding out of matrix; and b) vacuum-fused coating showing hardphase particles densified and smoothened surface.

Attempts were made to quantify the microhardness of matrix and hard phase particles separately using the AFM technique but did not give consistent results due to very discrete sizes of the latter. On a more micro level, with the diamond indenter, the microhardness of areas where hard particles were lacking (pure matrix) was lower than the average microhardness by almost 18-23% in the fused coating. However, such difference was not found in case of sprayed/sealed coating. Some variances of nano hardness values between sprayed and fused coatings were made on an atomic scale. Figure 8.2.10 shows the force spectroscopy measurements taken on sprayed and fused coatings. The slope values, i.e. deflection per unit distance (nA/nm) recorded showed that sprayed coating had 0.147 nA/nm versus 0.08 nA/nm of fused coating. The higher slope value of the former signals a higher hardness value of the sprayed coating, which is in contrast to the microhardness measurements and is discussed later.

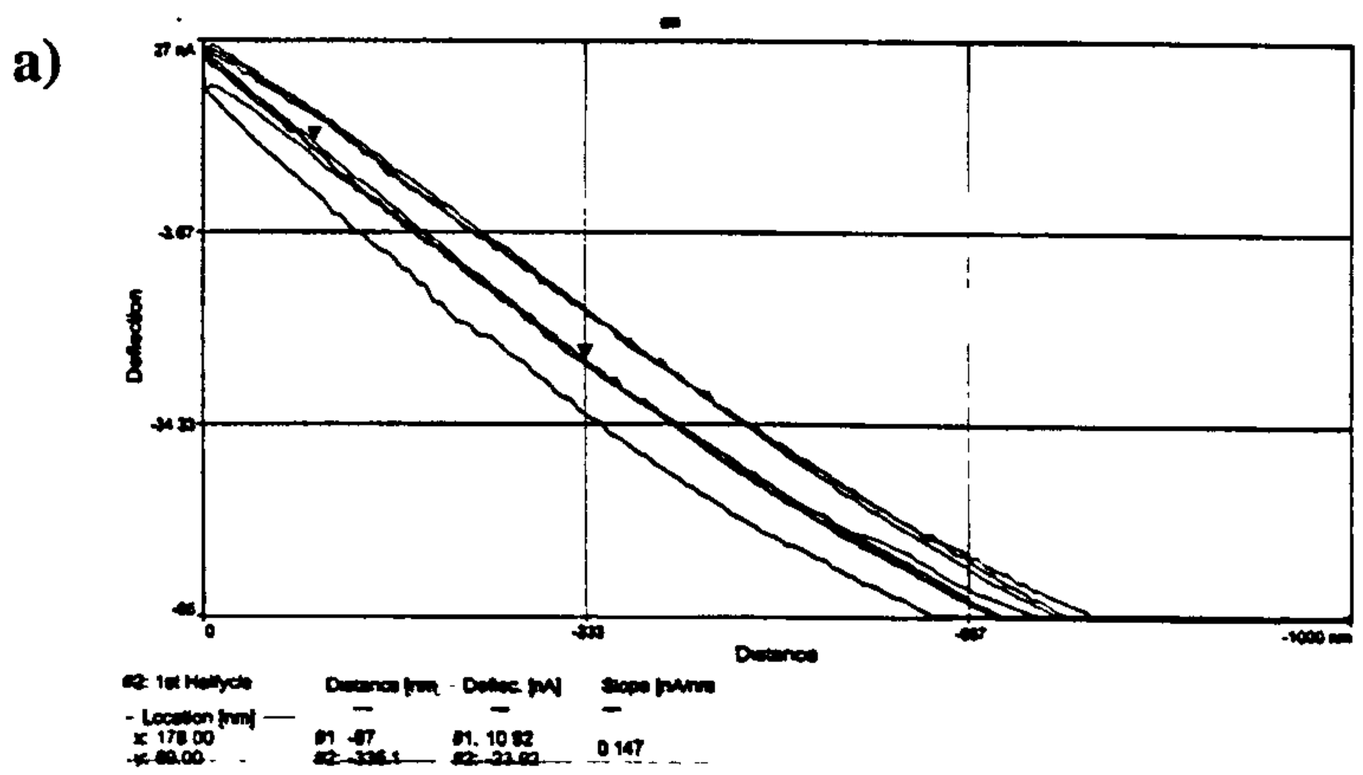


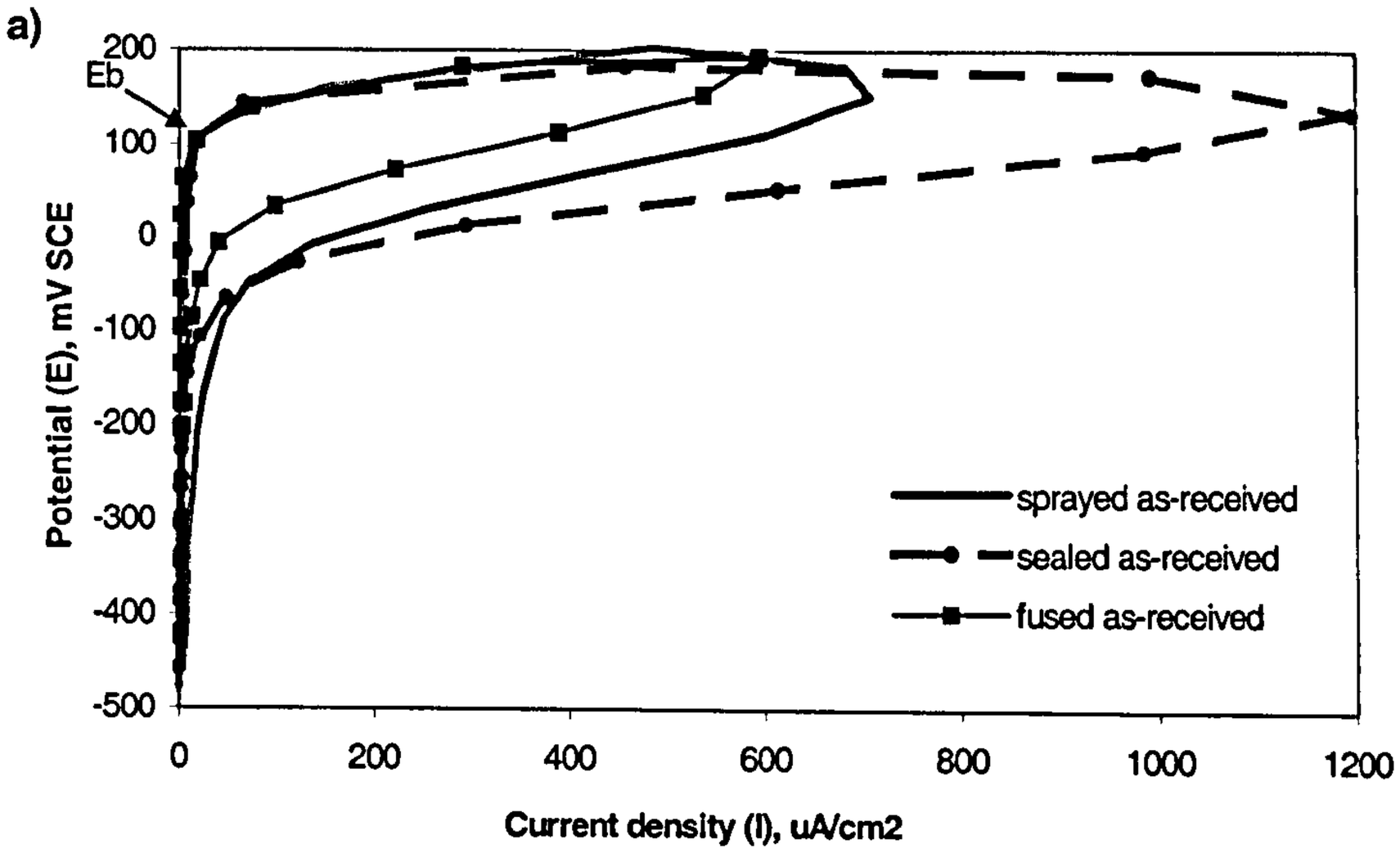
Figure 8.2.10 Force spectroscopy results: a) sprayed and b) fused coating (nA - nano ampere; nm - nano metre).

8.3 Corrosion of coating BI

This section comprises mainly the results of static corrosion tests on coating BI in as-sprayed vacuum-sealed and vacuum fused conditions. Anodic polarisation tests on coatings were carried out at 18 and 50°C in seawater. Experiments were performed on polished surfaces of the coating samples unless otherwise stated 'as-received'. The working electrolyte was made from a proprietary product 'Instant Ocean', which contains all the major ionic constituents of seawater, dissolved in distilled water to yield a salinity of 35,000ppm. The specimens were subjected also to free corrosion tests (immersed in static electrolyte for a maximum of 1-month exposure period). Moreover, anodic polarisation tests were carried out after the specimens without pre-corrosion and also on specimens, which had been pre-corroded for 2, 5 and 10 consecutive days to see the effect of pre-corrosion and how the anodic polarisation characteristics change as a function of time. Cathodic polarisation tests were also performed on all specimens under the investigation. Stainless steel (UNS S31603) and carbon steel (BS970 En8) are once again considered in this section for comparative purpose and the two materials were tested at 50°C.

Electrochemical corrosion tests at ambient temperature

Accelerated anodic polarisation tests were conducted on each of the samples in the as-received condition and then after polishing to a diamond finish. Figure 8.3.1a shows the anodic polarisation plot on the three coatings (as-sprayed, vacuum-sealed, vacuum-fused) in the as-received condition at 18°C and Fig. 8.3.1b shows the response after polishing at the same temperature. It is clear that there is no difference between the response of either coating in a saline solution at 18°C. All coatings exhibited very low currents on shifting the potential from the free corrosion potential for a potential range up to around +100mV (SCE). At this point (denoted the breakdown potential, E_b) a rapid rise in current is observed and this indicates that corrosion has initiated. The scan reversed (i.e. the potential was shifted to more negative values) when a current density of 500μA/cm^2 was attained and the potential moved towards the free corrosion potential. The maximum current density 'i_{max}' reached on reversal of the potential scan is indicative of the extent to which corrosion can propagate once corrosion had initiated.



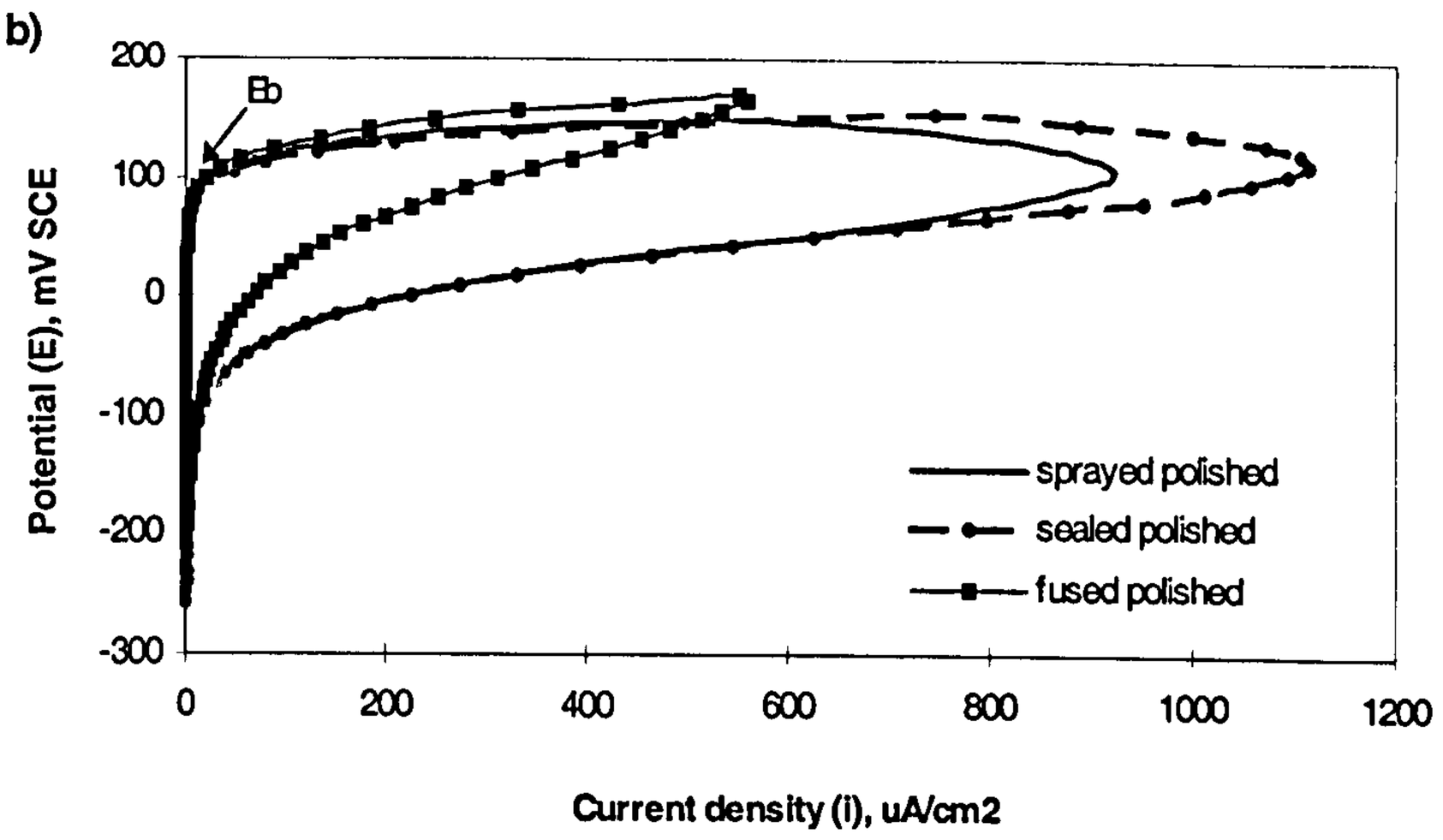


Figure 8.3.1 Anodic polarisation of a) as-received; and b) polished surfaces of the coatings in static saline solution at 18°C.

Table 8.3.1 gives details of the parameters from the anodic polarisation curves. A range of values is given to reflect the degree of replication carried out in the study. It is apparent from Table 8.3.1 that although there is no difference in 'E_b' and hence the ability for corrosion to initiate, it would appear that the vacuum-fused coating is less susceptible to corrosion propagation as shown by the lower current density (i_{max}) attained during anodic polarisation. Also, free corrosion potentials 'E_{corr}' measured after 1-hour exposure prior to the polarisation tests for as received vacuum-fused coatings

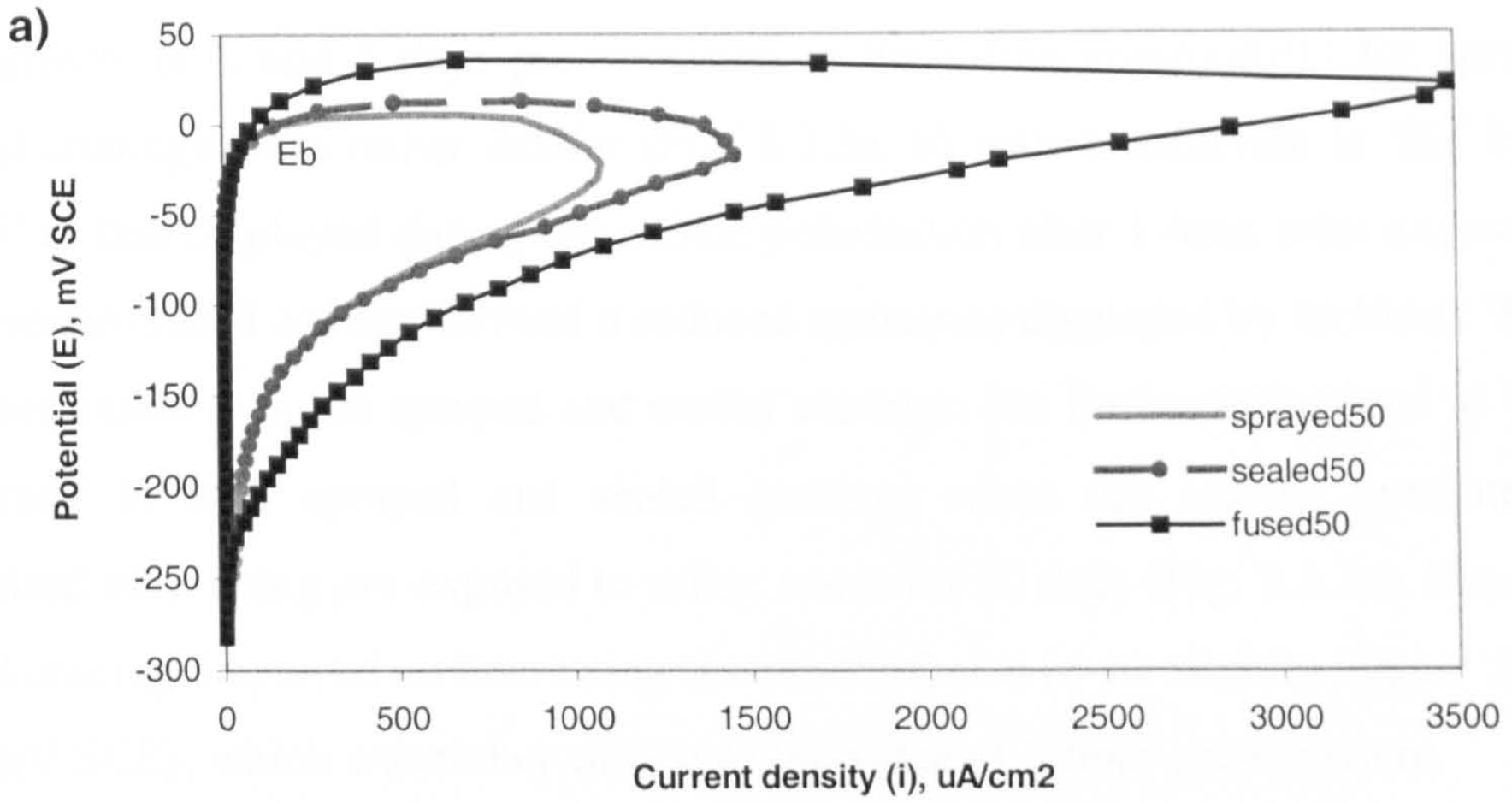
were consistently more positive than those of sprayed/sealed coatings. However, after polishing all the coatings displayed rather similar 'E_{corr}' values, which are clearly shown in Table 8.3.1.

Coating	As-received		Polished		i_{max}
	E_{corr}, mV	E_b, mV	E_{corr}, mV	E_b, mV	$\mu A/cm^2$
Sprayed	-478 -464 -452	95 100 110	-232 -398	85 105	705 - 920
Sealed	-456 -355 -280	100 105 100	-270 -255	90 80	1115 - 1195
Fused	-203 -176 -209	105 100 90	-219 -227	90 90	560 - 693

Table 8.3.1 Parameters of as received and polished coatings from anodic polarisation in static saline solution at 18°C.

Effect of temperature

It is well known that temperature plays an important role in the initiation and propagation of corrosion on passive materials such as stainless steels. In this study the temperature was increased to 50°C and the effect on the anodic polarisation curve was assessed. In a comparable manner to passive alloys it was shown that the resistance to the onset of corrosion was lessened as the temperature was increased. Figure 8.3.2a shows how 'E_b' was reduced at the higher temperature and interestingly the three coatings, as at 18°C, showed comparable characteristics. The comparative breakdown potentials 'E_b' for the coatings at 18 and 50°C are shown by column chart in Fig. 8.3.2b. Figure 8.3.2b also shows for comparative purpose 'E_b' of stainless steel (UNS S31603) under similar condition and its wide scattering of 'E_b' unlike the coatings which displayed rather a very little scattering of the values during several experimental tests. However, in contrast with the results trend at 18°C the vacuum-fused coating displayed much higher maximum current ($3500\mu A/cm^2$) at 50°C than the as-sprayed ($1080\mu A/cm^2$) and vacuum-sealed ($1460\mu A/cm^2$) coatings. The hysterisis loops of all the coatings investigated revealed no repassivation potential shown by no intersection of forward and reversed scan curves. The parameters 'E_{corr}', 'E_b' and 'i_{max}' from the anodic polarisation test performed at 50°C are shown in Table 8.3.2.



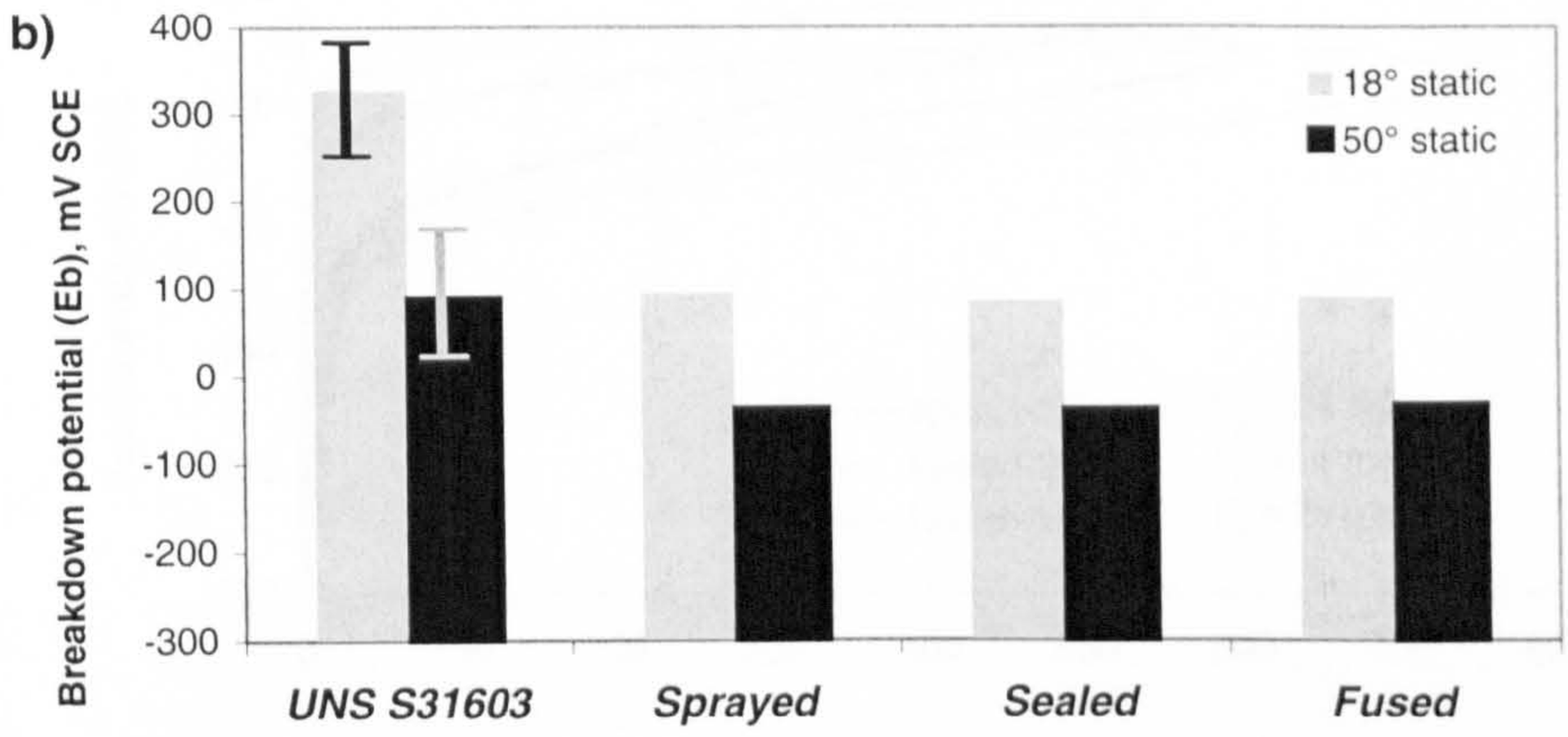


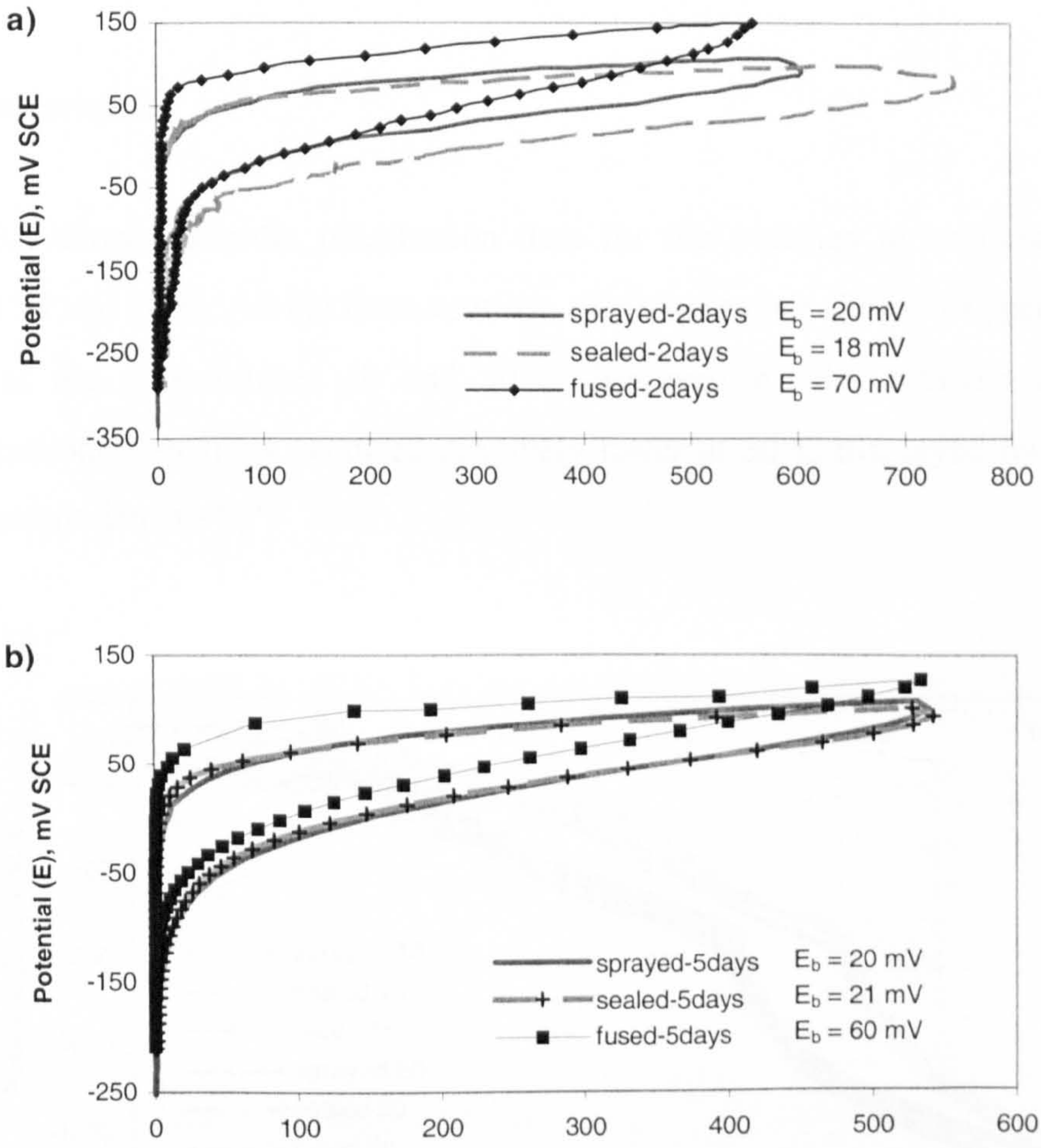
Figure 8.3.2 a) Anodic polarisation of polished surfaces of the coatings in static saline solution at 50°C; b) breakdown potentials of the coatings and stainless steel (UNS S31603) at 18 and 50°C.

Coating	E_{corr}, mV	E_b, mV	i_{max}, $\mu A/cm^2$
Sprayed	-268 -303	-29 -44	1080 1302
Sealed	-247 -222	-33 -41	1460 1935
Fused	-281 -244	-35 -28	3500 3310

Table 8.3.2. Parameters of polished coatings from anodic polarisation in static saline solution at 50°C.

Effect of pre-corrosion

The effects of 2 and 5 days pre-corrosion in the saline environment for sprayed and sealed coatings were rather similar (Fig. 8.3.3a, b) with a reduction in 'E_b' by almost 70mV of that displayed during the anodic polarisation after 1-hour prior exposure. Also the vacuum fused coating showed a reduced resistance displayed by its lower 'E_b' but to a lesser extent than the sprayed and sealed coatings. No further reductions in 'E_b' were observed in both sprayed and sealed coatings when the coating specimens were polarised after being pre-exposed to saline water for 10 days (Fig. 8.3.3c). However, the fused coating displayed an interesting feature displayed by its slightly higher 'E_b' (about +90mV SCE), which was rather similar to the value of 1-hour pre-exposure.



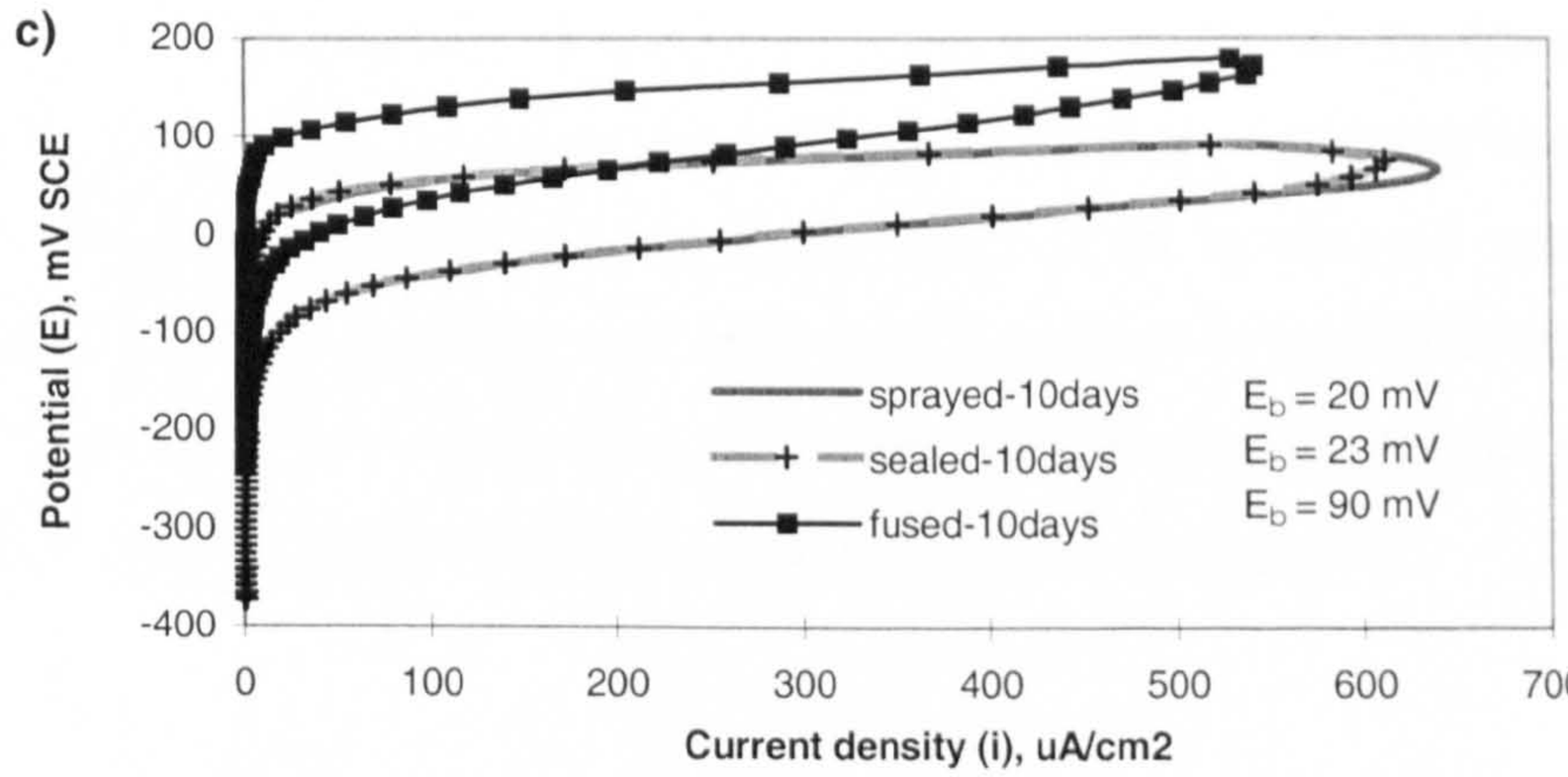


Figure 8.3.3 Anodic polarisation after pre-exposure to static saline solution at 18°C: a) of 2 days; b) 5 days; and c) 10 days.

Cathodic polarisation

Figure 8.3.4 shows cathodic polarisation data for the coatings in artificial seawater solution at 18 and 50°C. All the three coatings exhibited rather similar oxygen reduction reactions at the temperatures 18 and 50°C displayed by the cathodic curves. As expected cathodic reactions occurred relatively faster at 50°C displayed by the higher limiting current density 'i_L'.

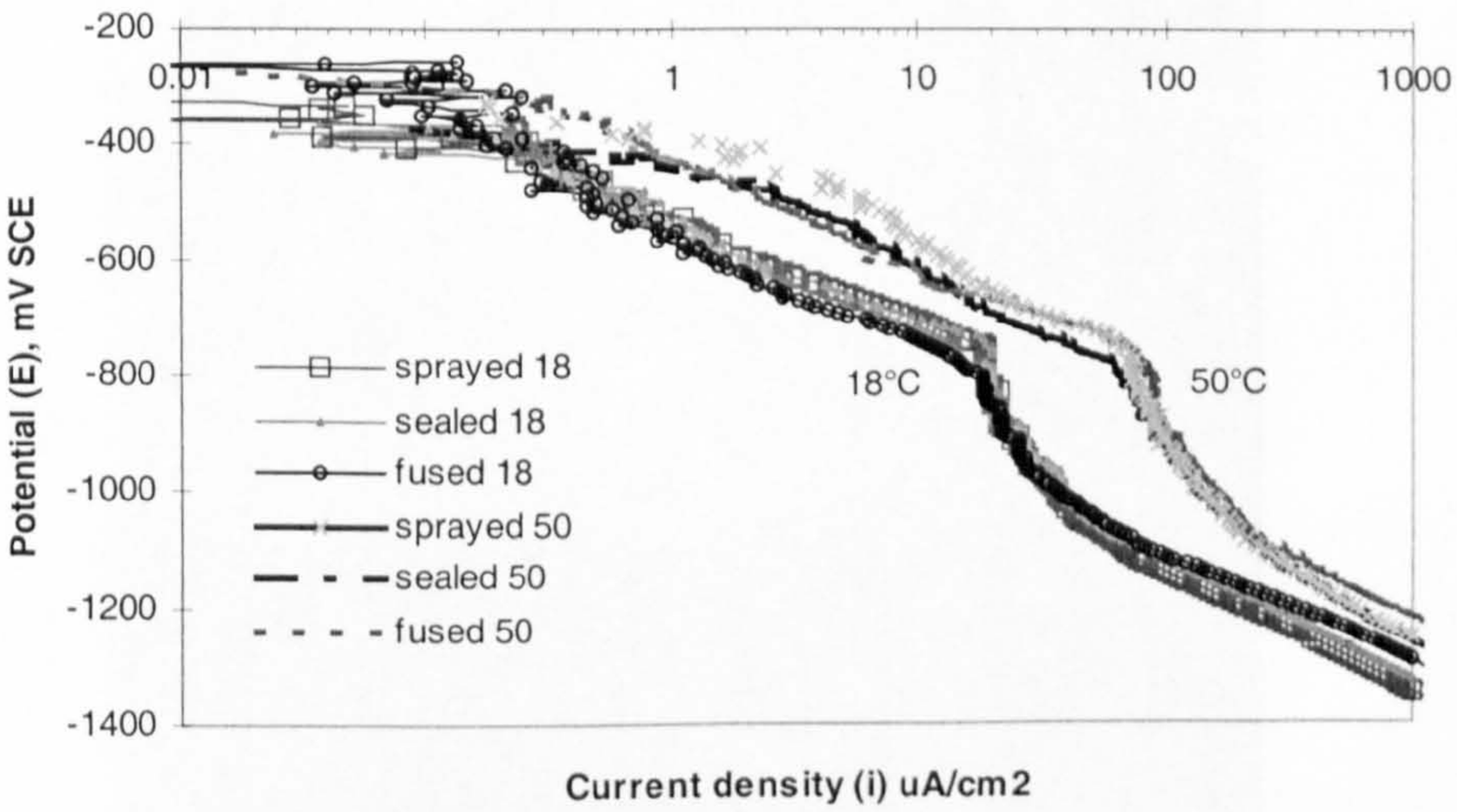
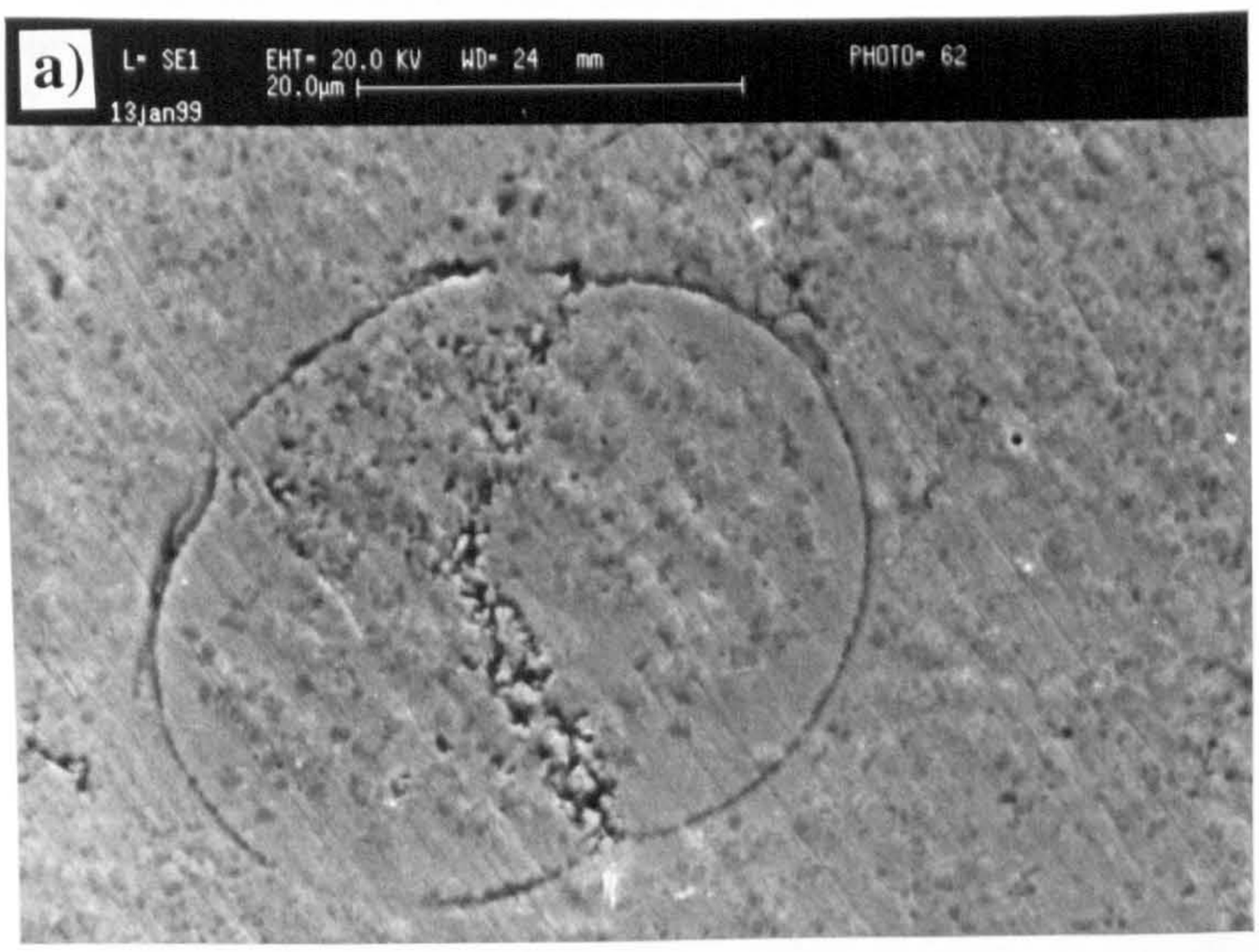
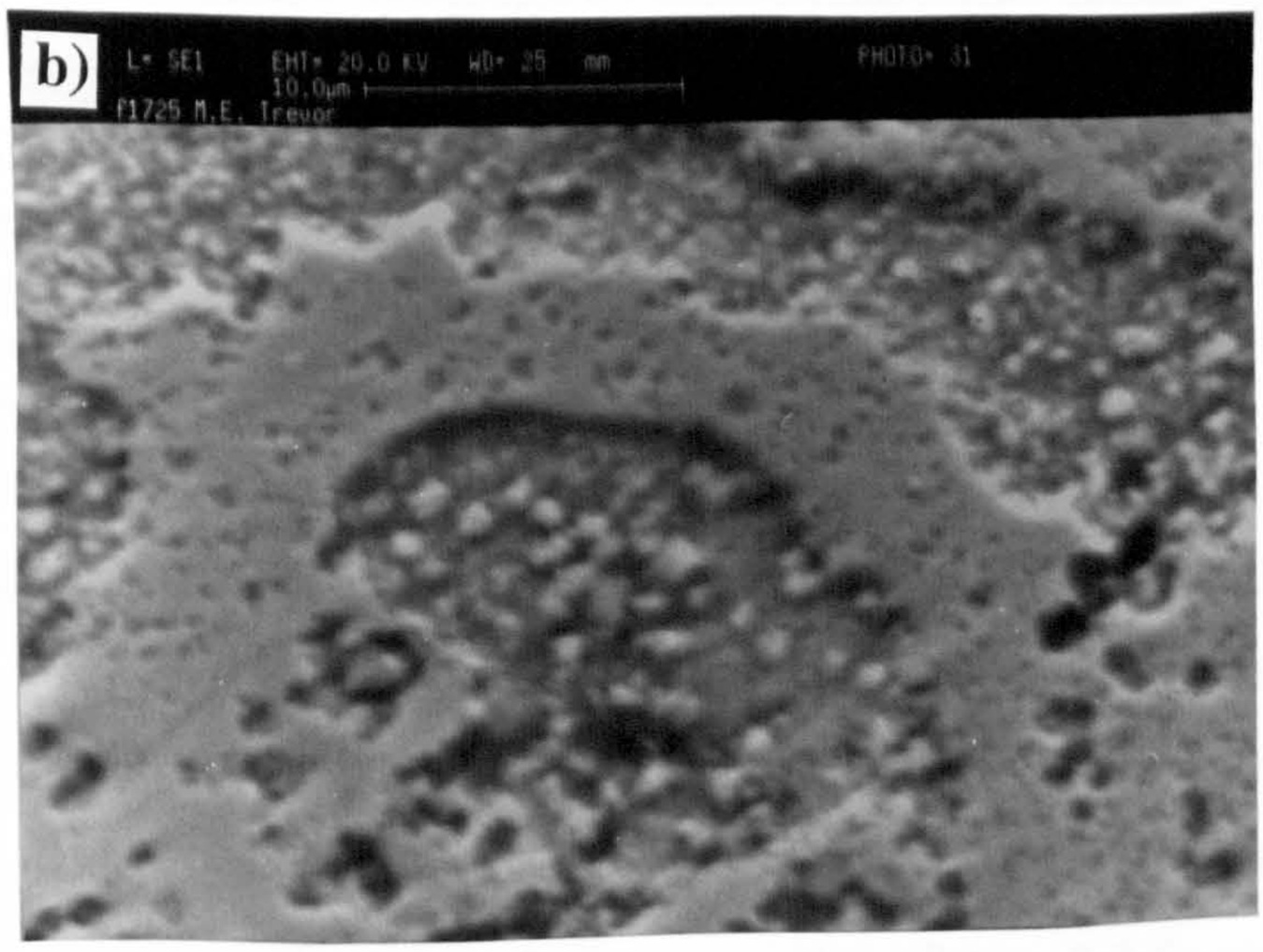


Figure 8.3.4 Cathodic polarisation of polished surfaces of coatings.

Attack Mechanisms

Analysis of the electrochemical measurements (anodic polarisation) by consideration of the parameter 'E_b', which is most commonly used to indicate corrosion resistance does not show any difference in the relative performance of the as-sprayed, vacuum-sealed and vacuum-fused coating. Close examination of the extent of corrosion attack and the attack mechanisms shows that there is a difference, which accounts for the variations in i_{max} and more specifically the smaller i_{max} on the fused coating at 18°C.





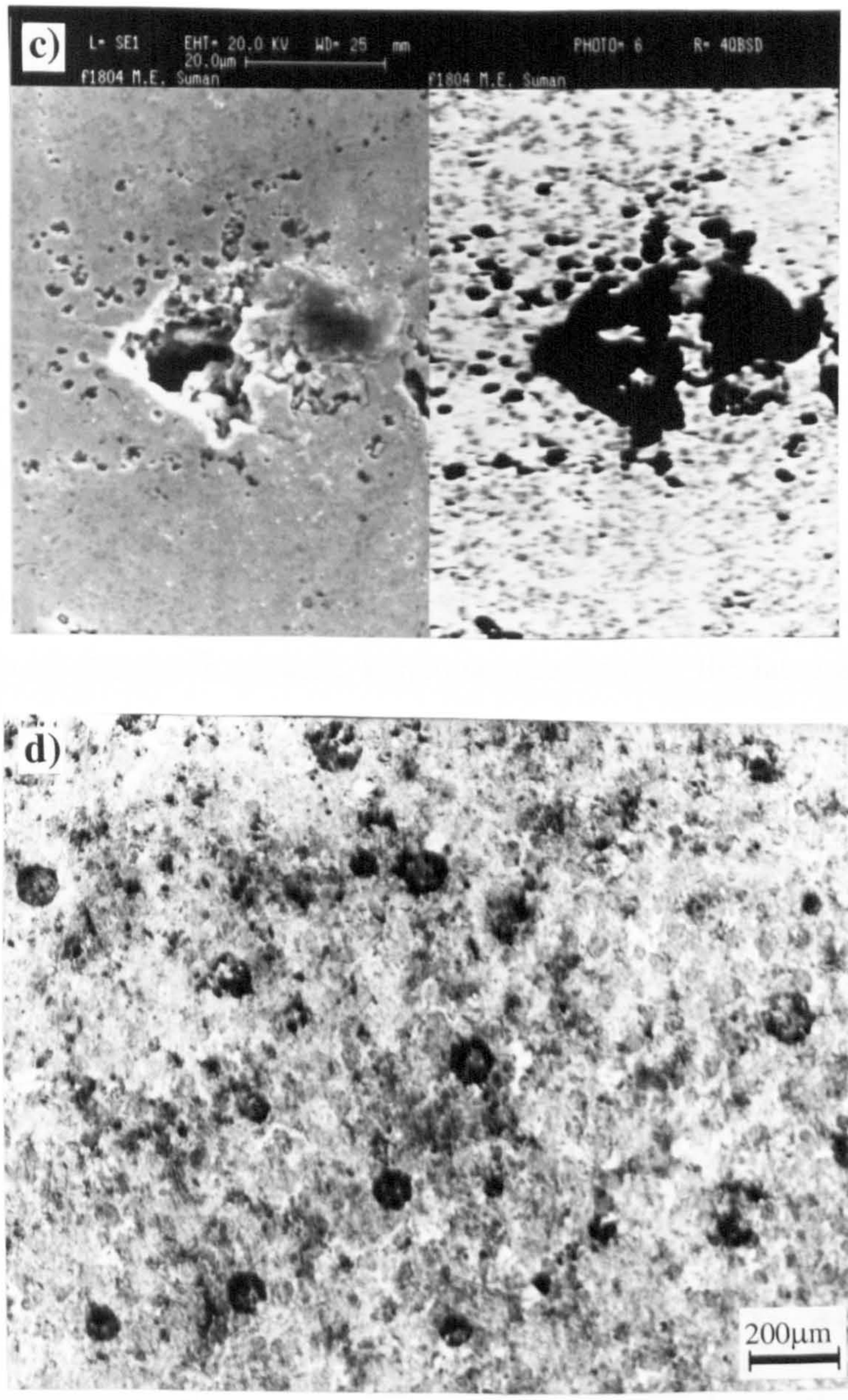
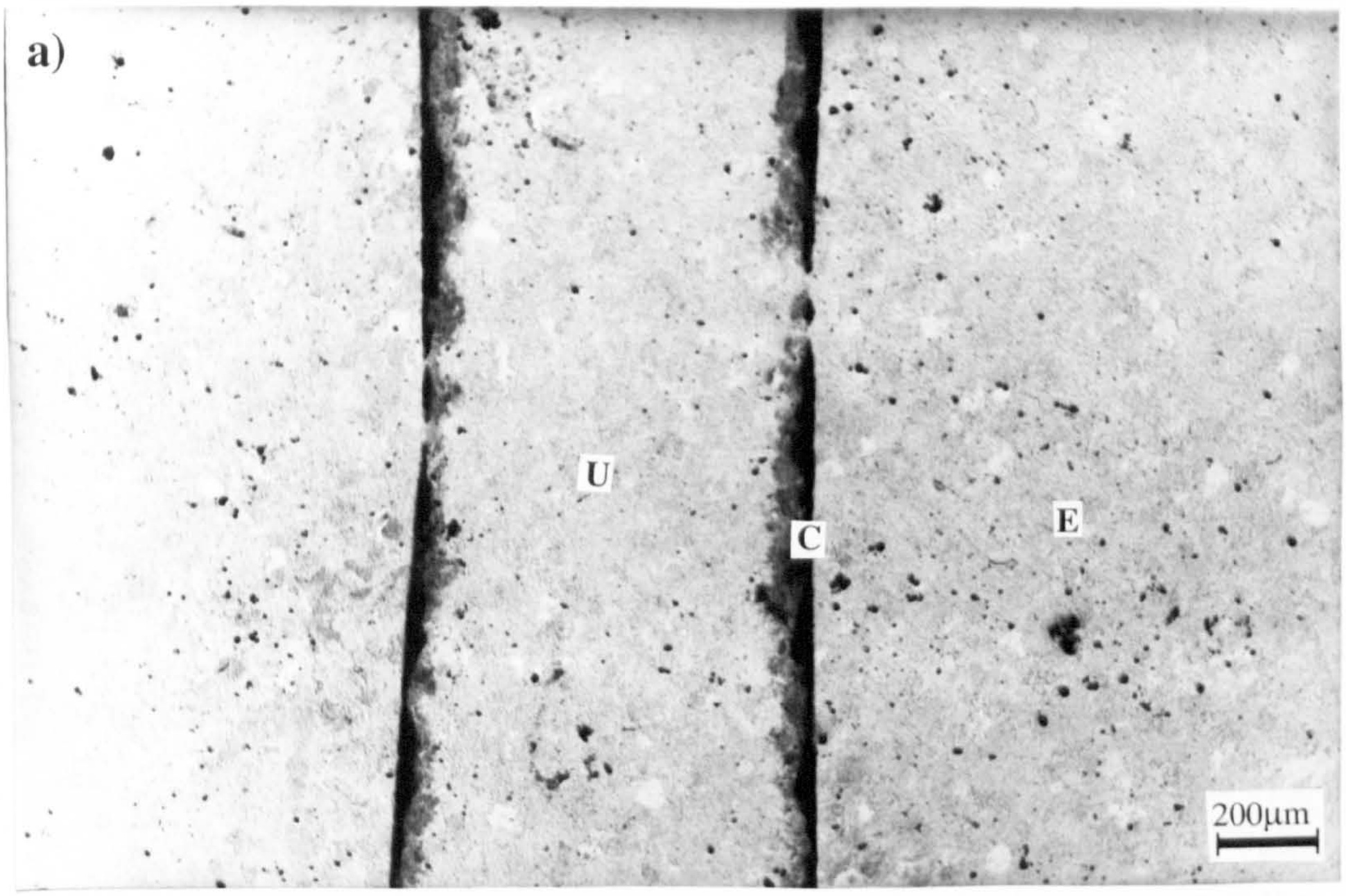


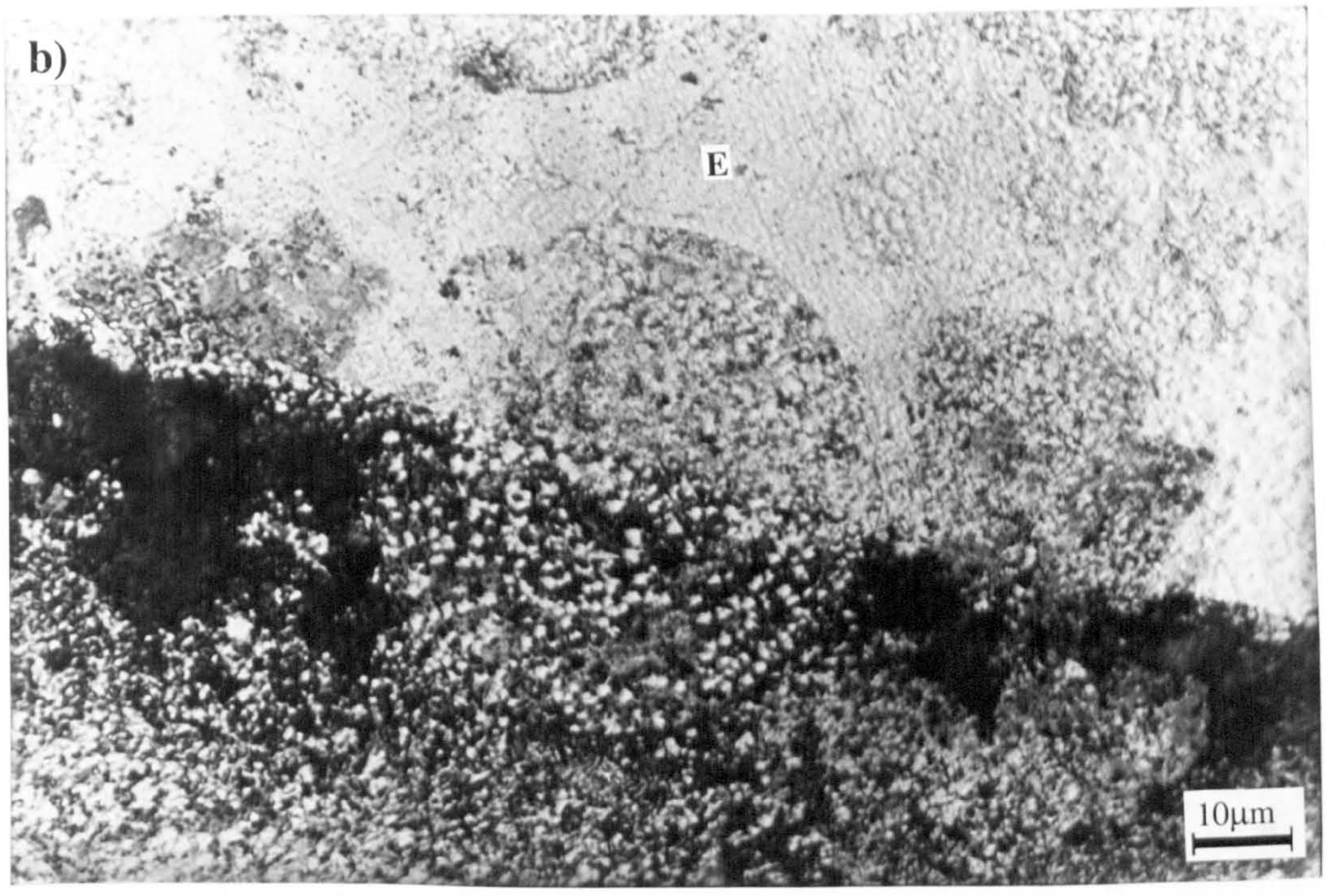
Figure 8.3.5 a) secondary SEM image of as-sprayed coating after anodic polarisation at 18°C showing splat boundary attack; b) severe matrix corrosion at 50°C leaving the hard particles unsupported; c) split SEM image of the same coating after anodic polarisation at 50°C showing macro pit at exposed region; and d) low magnification micrograph showing severe corrosion attack on sprayed coating at 50°C.

It was stated previously that after fusion of the coating, no trace of splat boundaries was detected and this has been shown in this study to have implications for the corrosion resistance of the coating. As detailed in Table 8.3.3 especially at 50°C there is severe attack at the splat boundary possibly due to a crevice corrosion mechanism and this can lead to removal of entire splats to form macropits. Figure 8.3.5a shows the initiation

stage of such attack at an exposed region in the sprayed coating at 18°C after anodic polarisation, which also shows localised removal of the hardphase particles forming micropits. Figure 8.3.5b illustrates severe corrosion of the matrix at 50°C at the exposed region resulting in the hard particles being left unsupported. The increased severity of a fact at 50°C is clear from Fig. 8.3.5c, which shows macropitting as a result of splat removal. Moreover, Fig. 8.3.5c also gives an indication of occurrence of further attack within the same pit. The increased temperature had displayed an extensive attack on the entire exposed area of the sprayed/sealed coating with loss of several splat particles as shown in Fig. 8.3.5d.

In addition to the localised attack at the splat boundaries, another localised attack mechanism observed was crevice attack, which occurred under the lacomit sealant (Fig. 8.3.6a). At the crevice regions denoted by 'C' (shown by dark lines), deep attack was visible after anodic polarisation. Higher magnification (Fig. 8.3.6b) revealed how such a crevice effect can accentuate in a half splat under the lacomit strip, while the other half on exposed area remaining less affected.





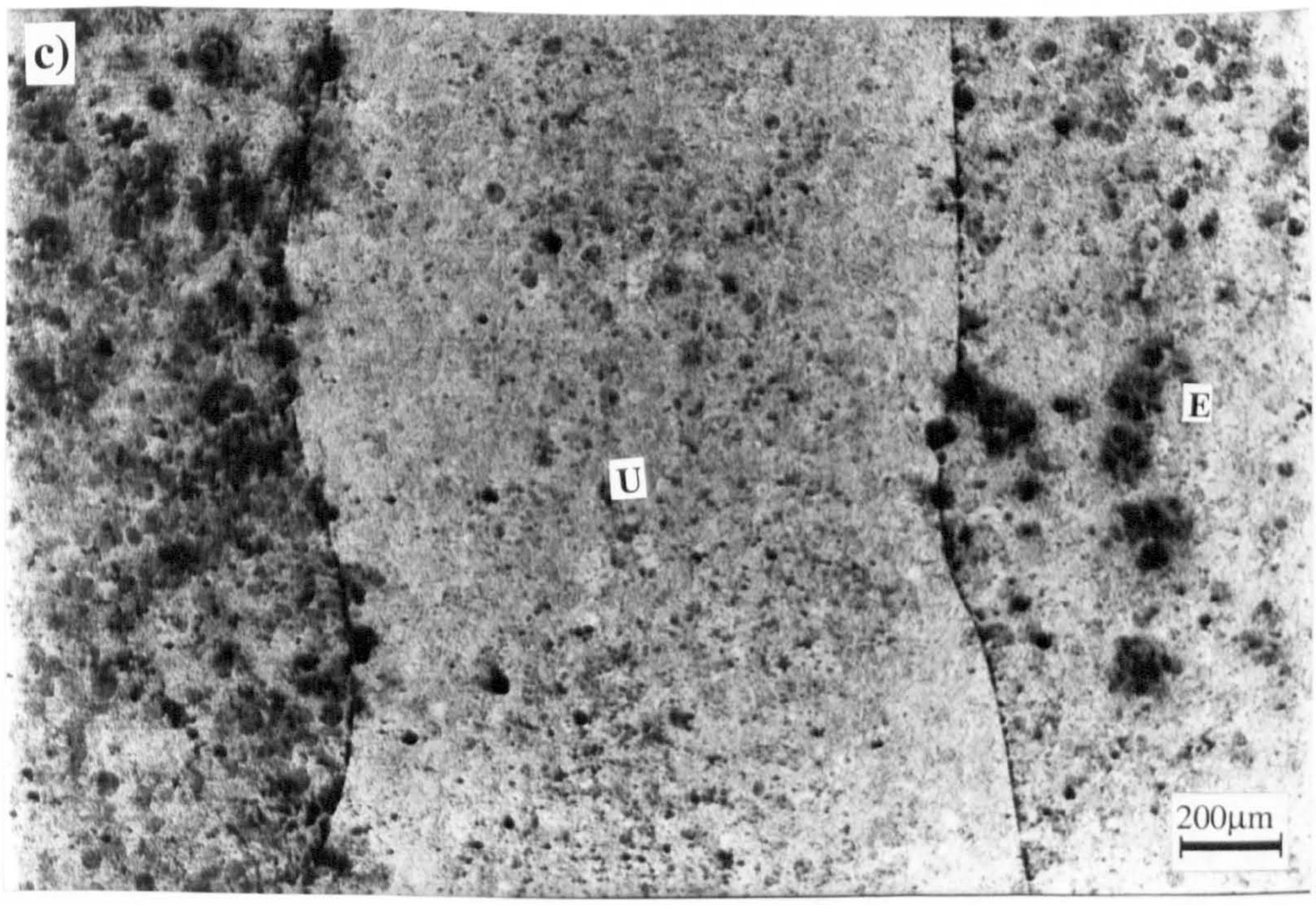


Figure 8.3.6 a) Crevice corrosion on sprayed coating after anodic polarisation at 18°C; b) higher magnification of the crevice region; and c) crevice corrosion of the same coating at 50°C.

On increasing the temperature to 50°C the extent of crevice attack lessened substantially particularly in the as-sprayed coating but increased attack on the exposed regions (Fig. 8.3.6c) was observed.

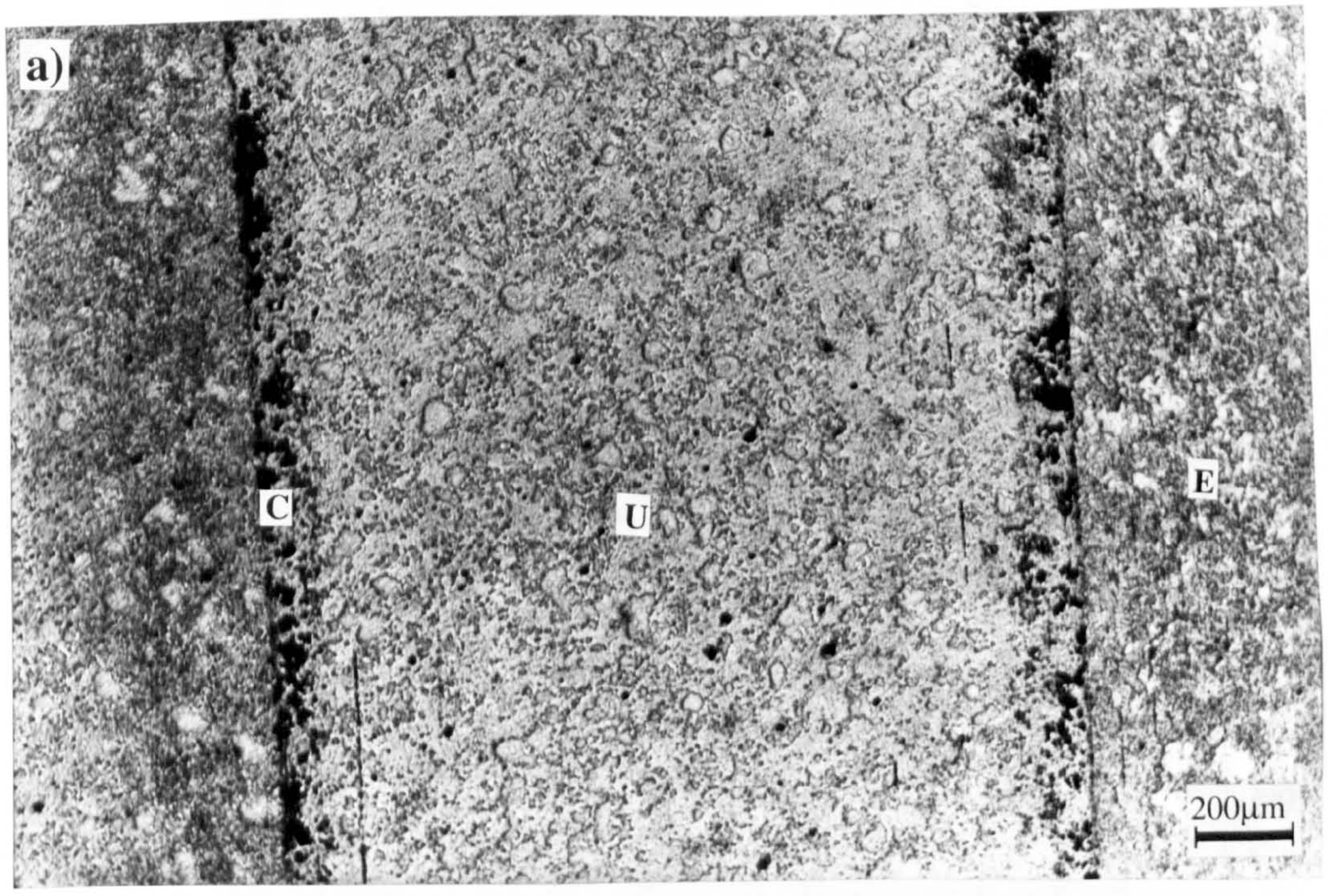
The vacuum-sealed coating displayed similarity to the as-sprayed coating in all aspects of corrosion mechanisms, however there existed one significant difference especially at 50°C, which is shown in Table 8.3.3.

Coating	Total crevice length (mm)		Maximum pit depth (μm)		Comments	
	18°C	*50°C*	*18°C*	*50°C*	*18°C*	*50°C*
As-sprayed	47-50	9-12	4	5	Corrosion initiation on exposed surface-etching effect	Exposed region severe corrosion at splat boundaries
Vacuum-sealed	50-55	35-40	5	5	Similar to above	Similar to above
Vacuum-fused	15-30	12-18	6	7	Less attack than above on exposed regions. No splat boundaries visible. Some micro-pitting	Etching on free exposed area and micropitting

Table 8.3.3. Corrosion mechanisms of the coatings after anodic polarisation at two temperatures

It has been stated that on the vacuum-fused coating there were no visible splat boundaries and hence no corrosion initiation associated with individual splat regions. In addition there was visibly less severe crevice corrosion observed on the vacuum-fused coating compared with the sprayed/sealed coating. On the vacuum-fused coating it was evident that the most dominant mechanism of corrosion was in the form of very localised micropitting, which was clearly associated with the individual hardphase particles and their removal once corrosion of the surrounding material had occurred.

This form of attack was accentuated at the crevice regions and is clearly shown in Fig. 8.3.7a and Fig. 8.3.7b. The back-scattered SEM micrograph of the crevice region in Fig. 8.3.8a clearly showed the preferential dissolution of the binder matrix around Mo rich white blocky hard particle '1' and Cr rich hard particle '2'. The scale of attack was much less on the exposed surface at 18°C, but on increasing the temperature to 50°C, most of the exposed area was attacked with micropitting as shown in Fig. 8.3.8b.



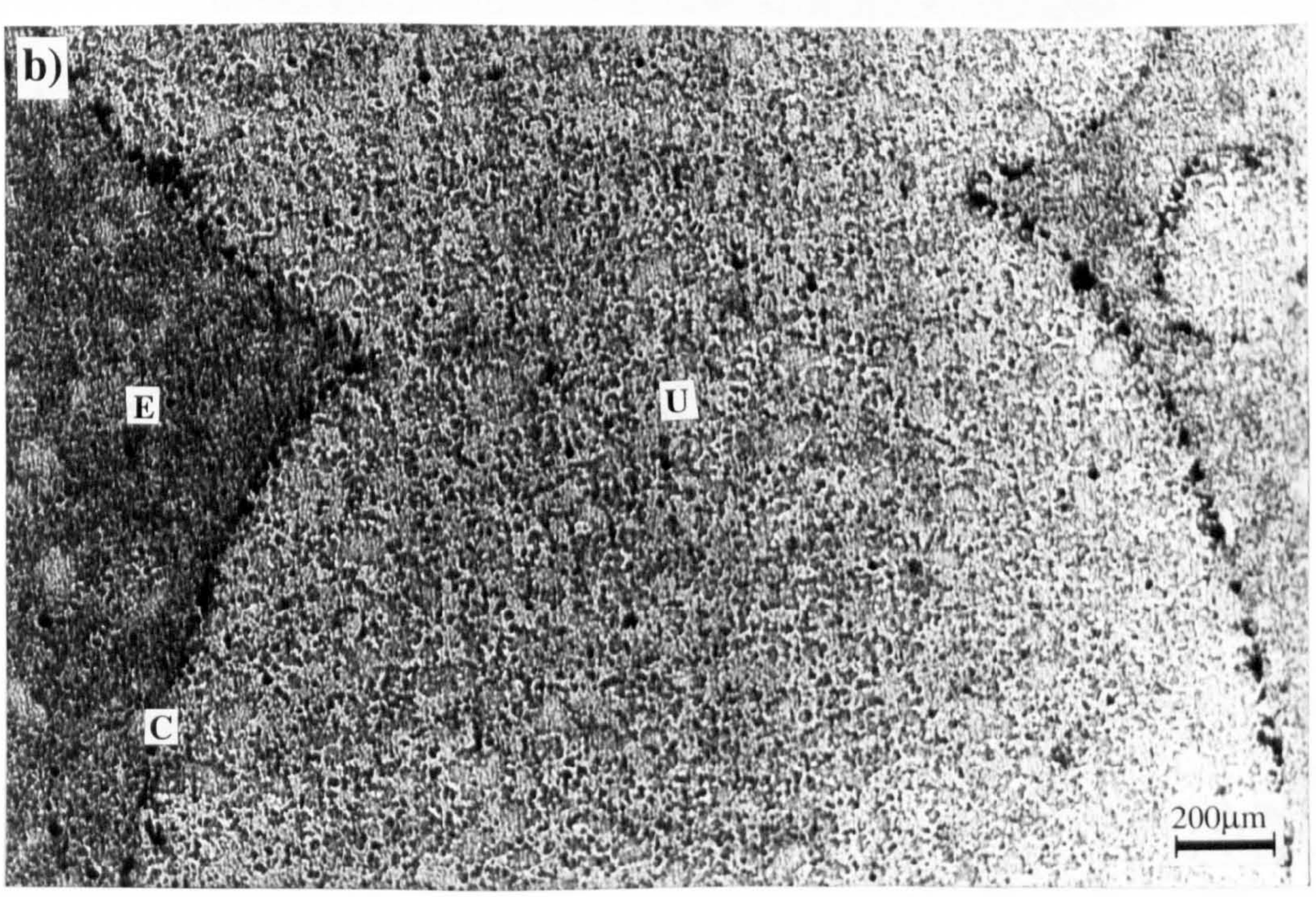


Figure 8.3.7 Crevice corrosion of the vacuum-fused coating under the central lacomit strip after anodic polarisation in static seawater at: a) 18°C; and b) 50°C.

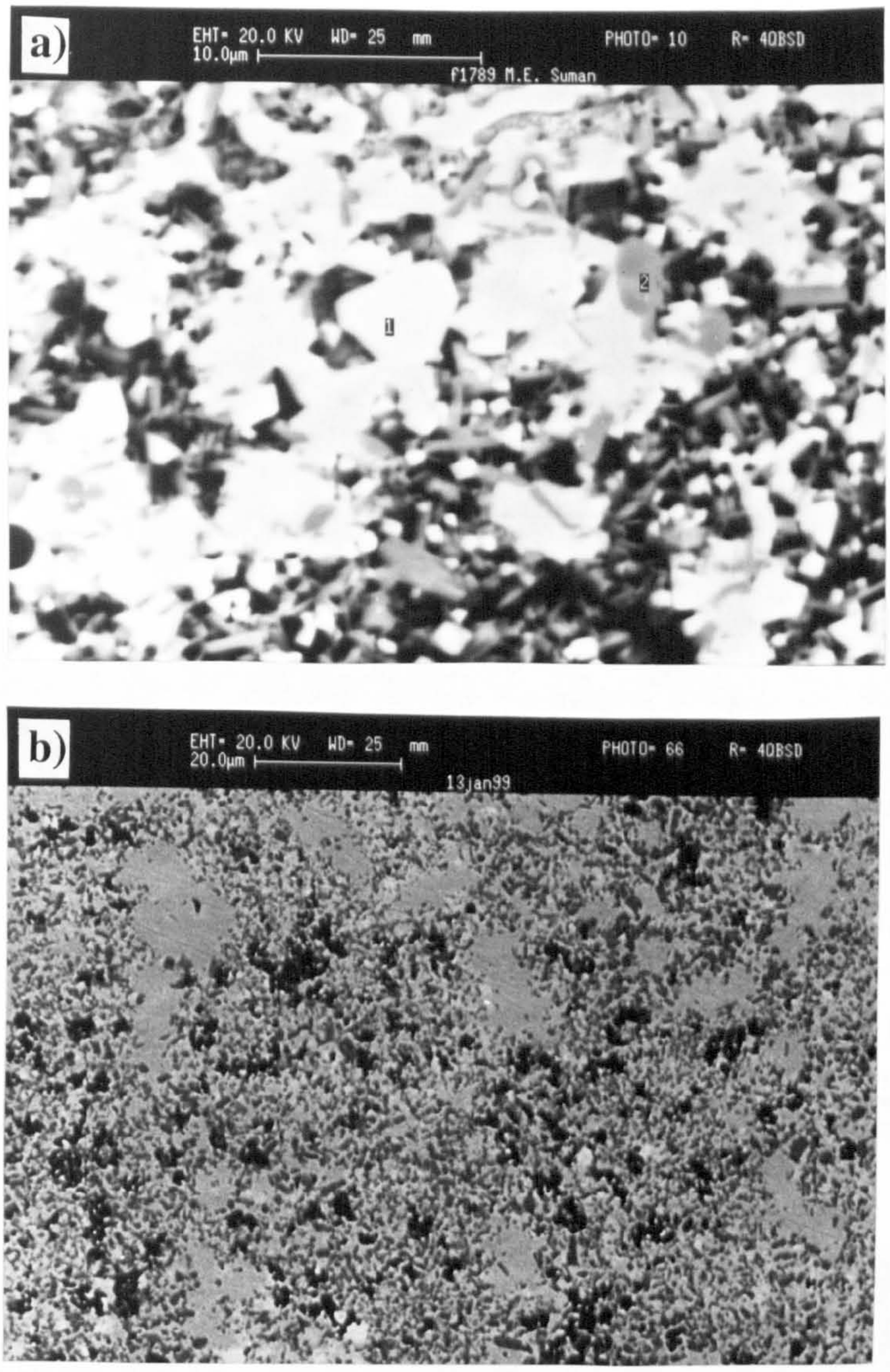


Figure 8.3.8 Back-scattered SEM micrographs of vacuum-fused coating after anodic polarisation at 50°C: a) preferential matrix dissolution under crevice; and b) micropitting at exposed region.

Microscopy after pre-corrosion tests

Anodic polarisation performed after 5 days static pre-corrosion (at E_{corr}) displayed some reduction of 'E_b' in the sprayed/sealed coating. This feature appeared to be associated with corrosion attack, which had occurred primarily at the crevice region. Figure 8.3.9 shows the severe crevice attack on the sprayed/sealed coating after 5 days exposure to static seawater, before and after anodic polarisation in the same environment at 18°C. The reduction in 'E_b' was smaller on the vacuum-fused coating compared to the sprayed/sealed coating, which was demonstrated by less crevice corrosion on the fused

coating. Figure 8.3.10 shows crevice regions of the fused coating after 5-days free pre-corrosion (at E_{corr}) in the same environment, before and after anodic polarisation.

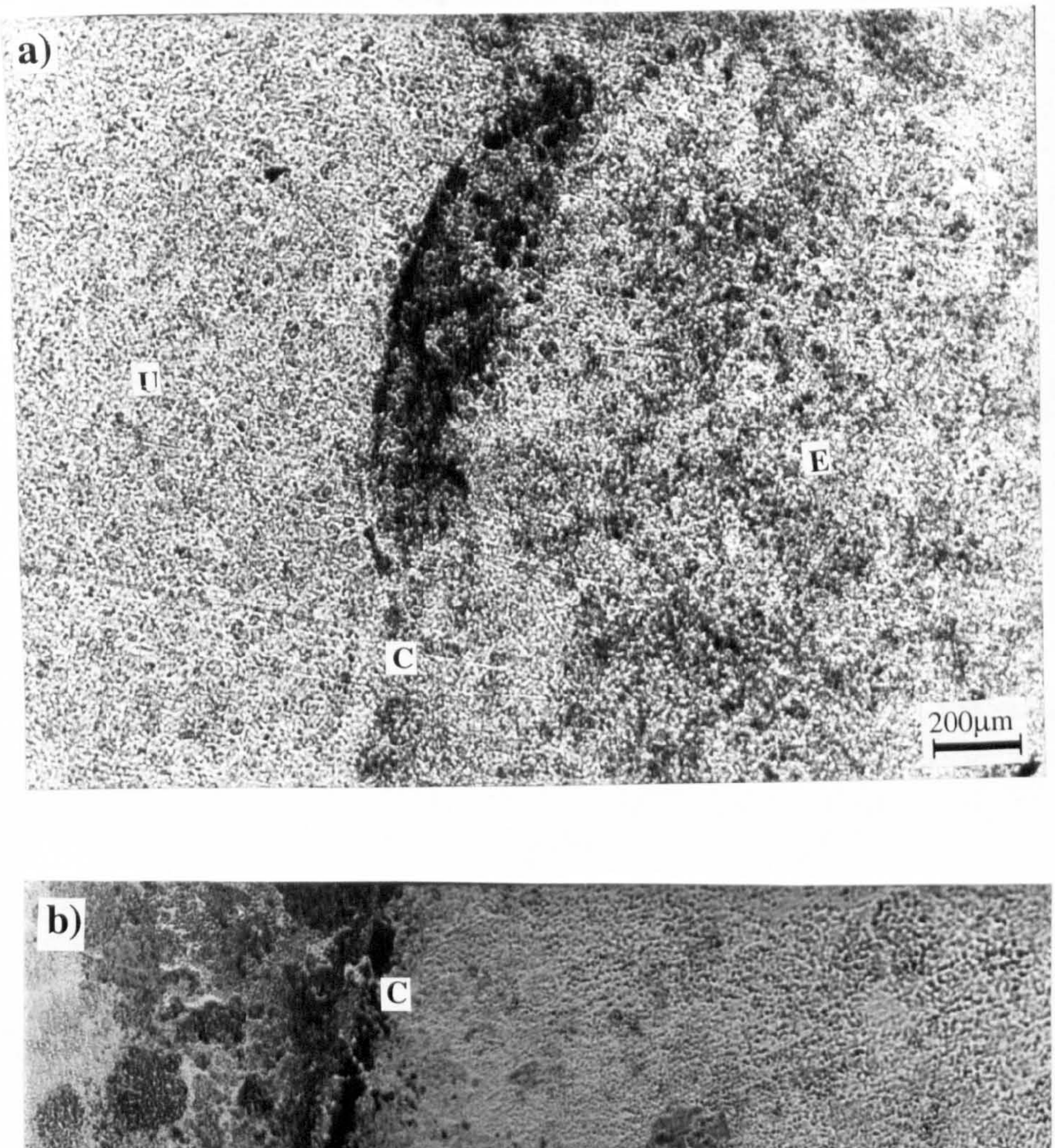
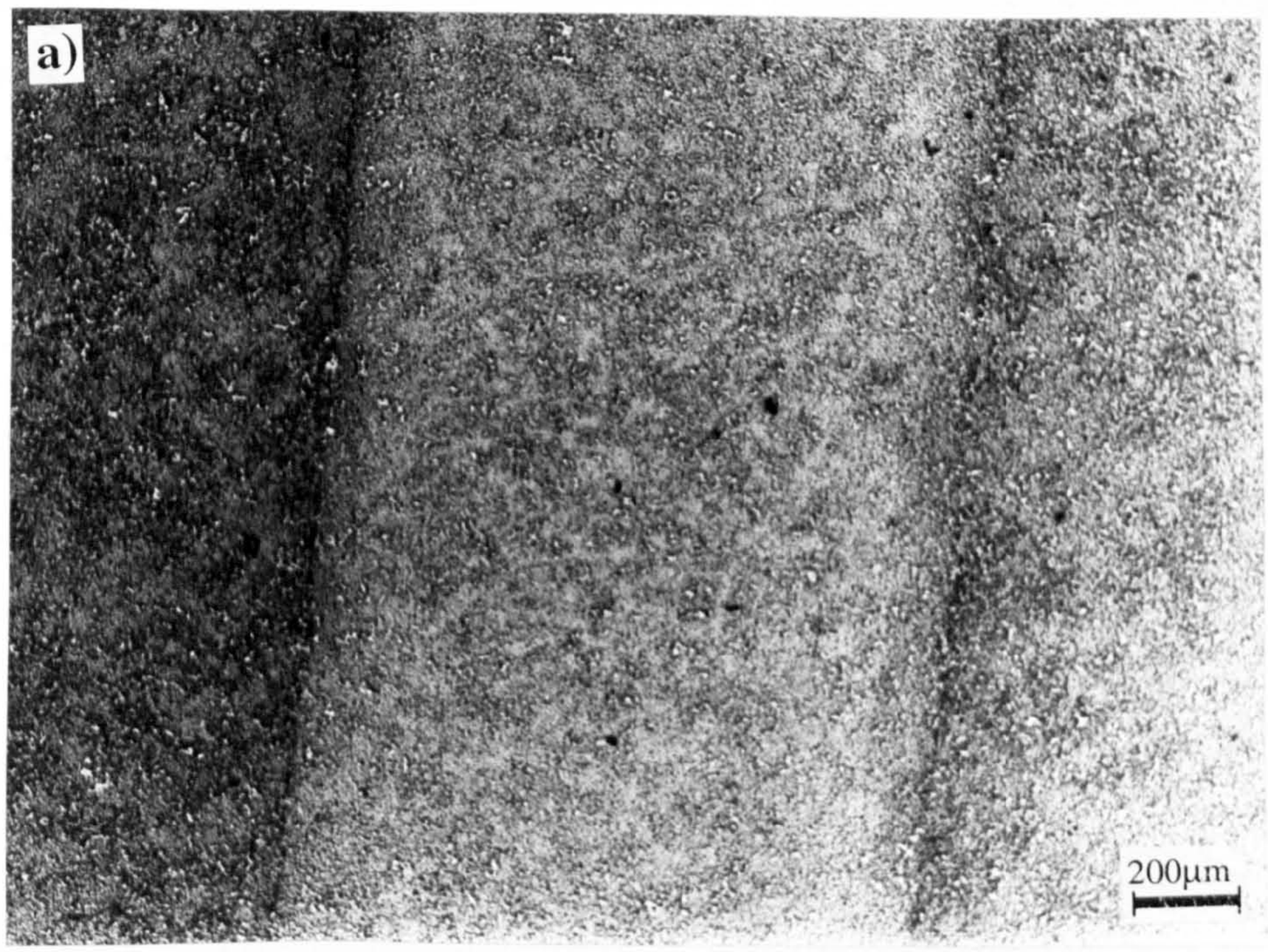


Figure. 8.3.9 Light optical micrographs of the sprayed coating after 5-days pre-corrosion: a) without anodic polarisation; and b) after anodic polarisation.



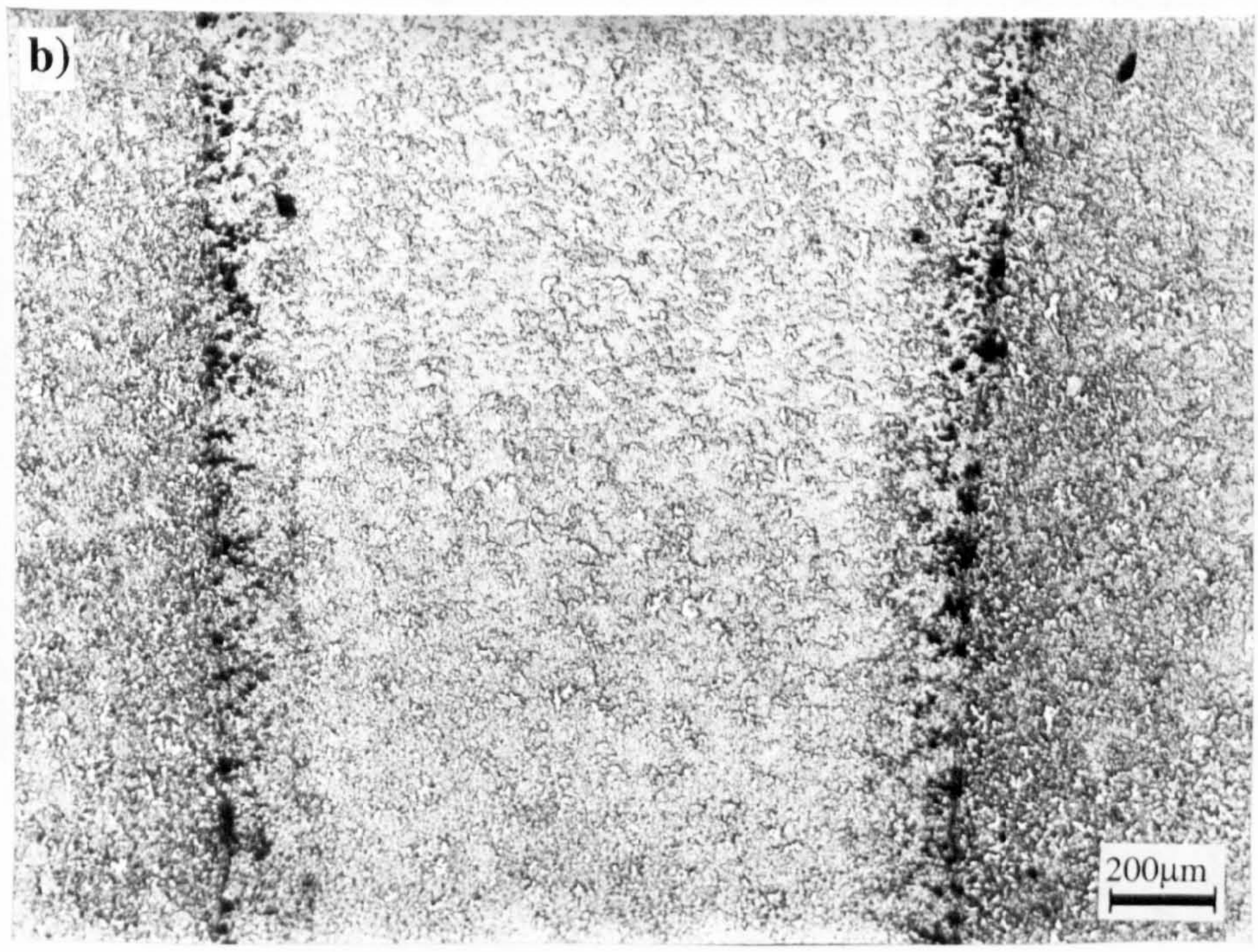
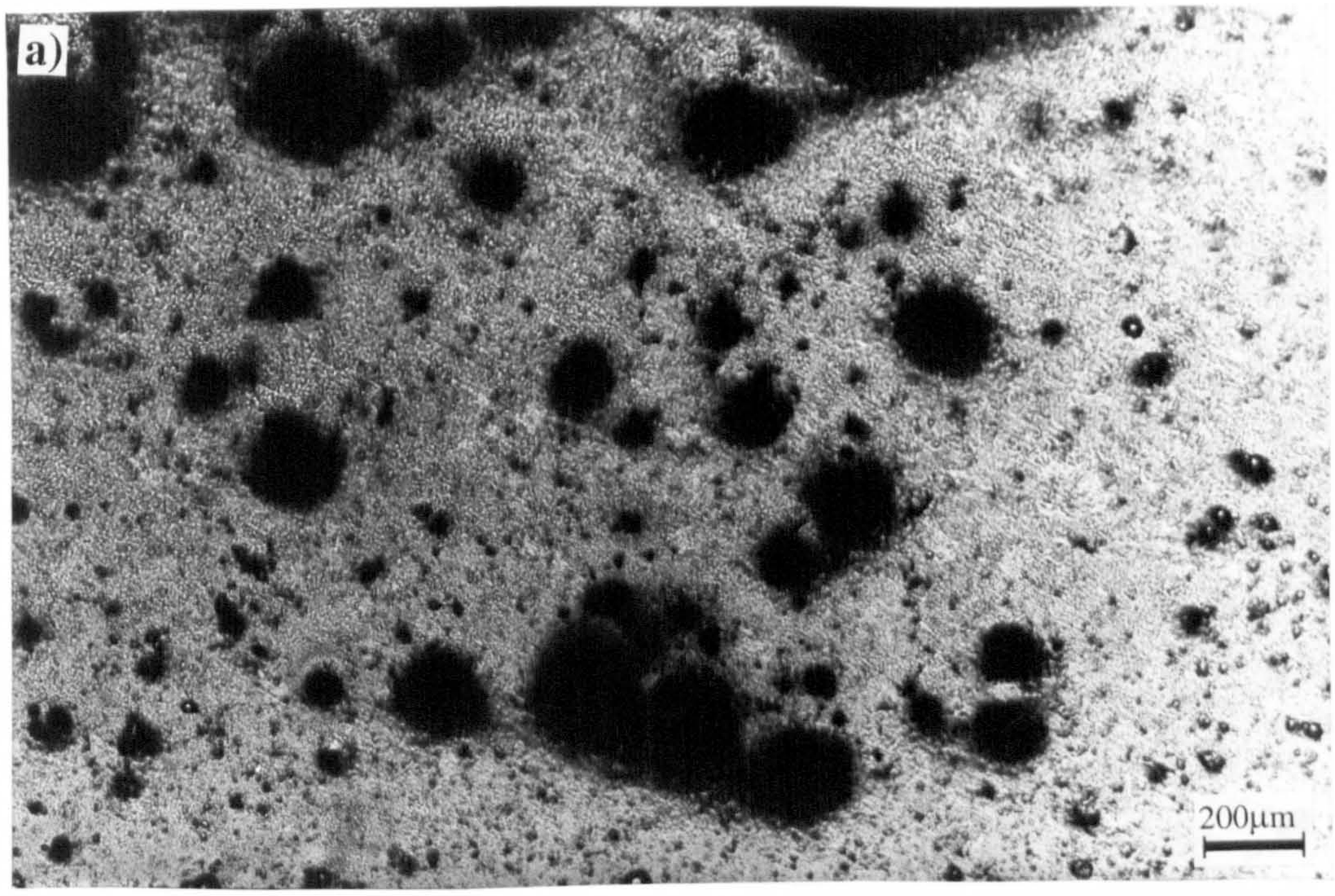


Figure. 8.3.10 Light optical micrographs of the vacuum-fused coating after 5-days pre-corrosion: a) without anodic polarisation; and b) after anodic polarisation.

Extended Exposure Tests

Extended exposure tests were carried out on the as-sprayed, vacuum-sealed and vacuum-fused coatings by keeping the samples immersed under the naturally corroding condition at 18°C. The exposed coatings surfaces were examined after successive 1,2 and 4 weeks period and the extent of corrosion attack was observed both under light optical and high-resolution scanning electron microscopes. Microscopic observation after 1-week immersion already showed visible corrosion product on the exposed surface of the as-sprayed coating. During this 1-week period, the fused coating exhibited no significant change of its exposed surface. Figure 8.3.11a shows the corrosion product on the exposed area of the sprayed coating after 2-weeks of immersion. Higher magnification observation revealed that there was attack on the fused coating as well after the 2-weeks period but in a microscale (Fig. 8.3.11b), which shows clear attack around hardphase particles.



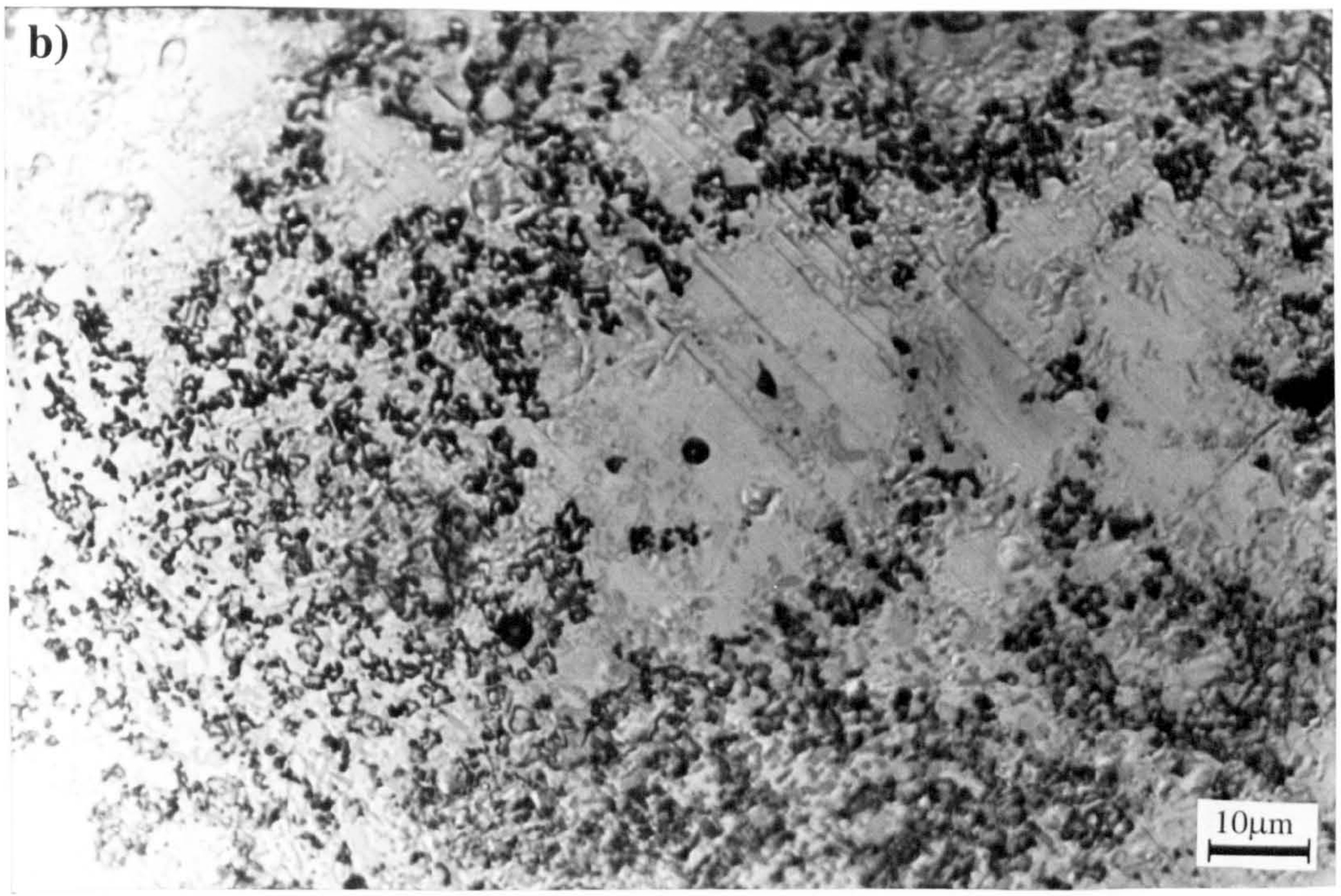


Figure 8.3.11 a) Corrosion product on sprayed coating after 2-weeks of immersion in static seawater at 18°C; and b) micropitting on vacuum fused coating after the same period of exposure.

Specimens observed after a 1-month period evidenced heavy corrosion product on both as-sprayed and vacuum-sealed coatings. The vacuum-fused coating exhibited relatively much less corrosion product. Figure 8.3.12a and b show low magnification micrographs of as-sprayed and fused coatings after 1-month immersion in static seawater. Fig. 8.3.12c shows the corrosion of the stainless steel (UNS S31603) under similar condition for comparison. Figure 8.3.12 clearly demonstrates that the attack has intensified primarily at the exposed surface/lacomit interface (crevice) denoted as 'C'. The symbols 'U' and 'E' represent the areas under the lacomit strip and the exposed surface respectively.

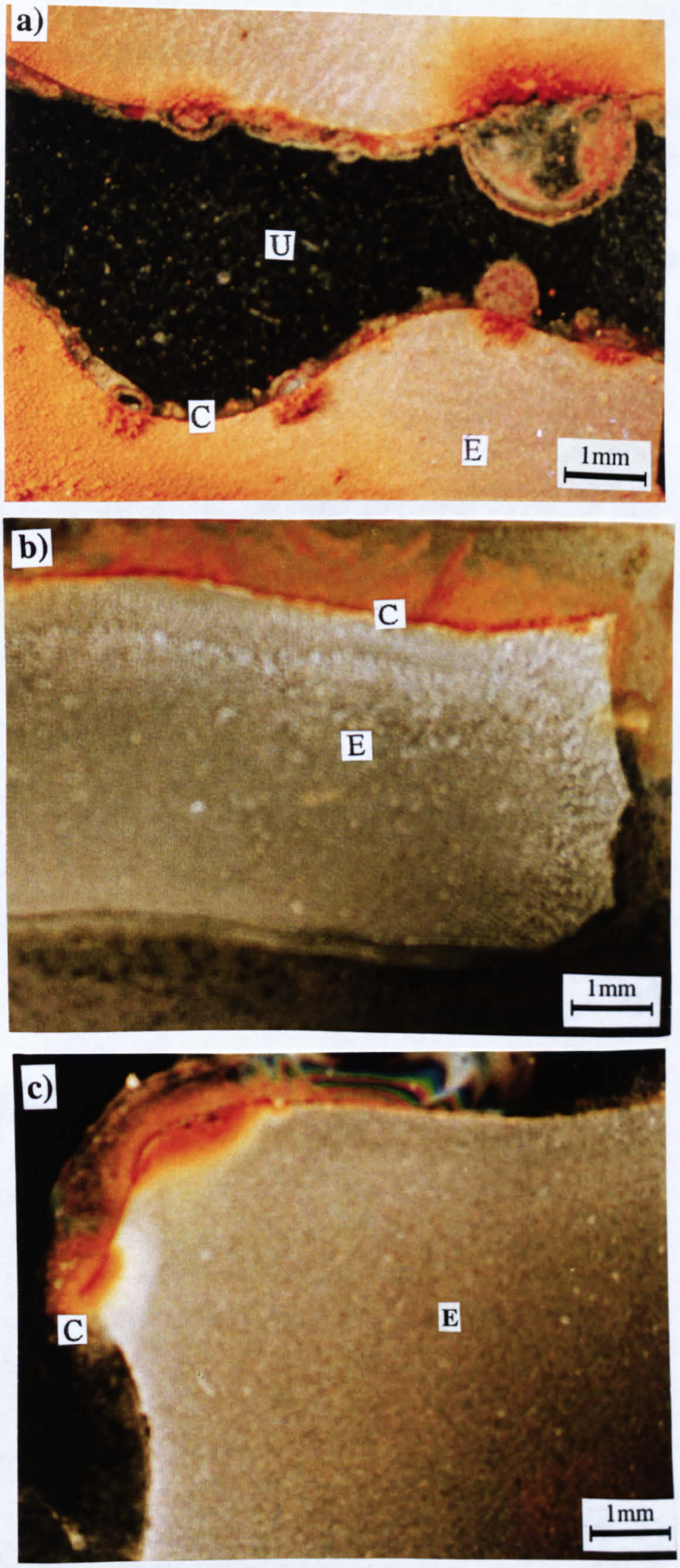
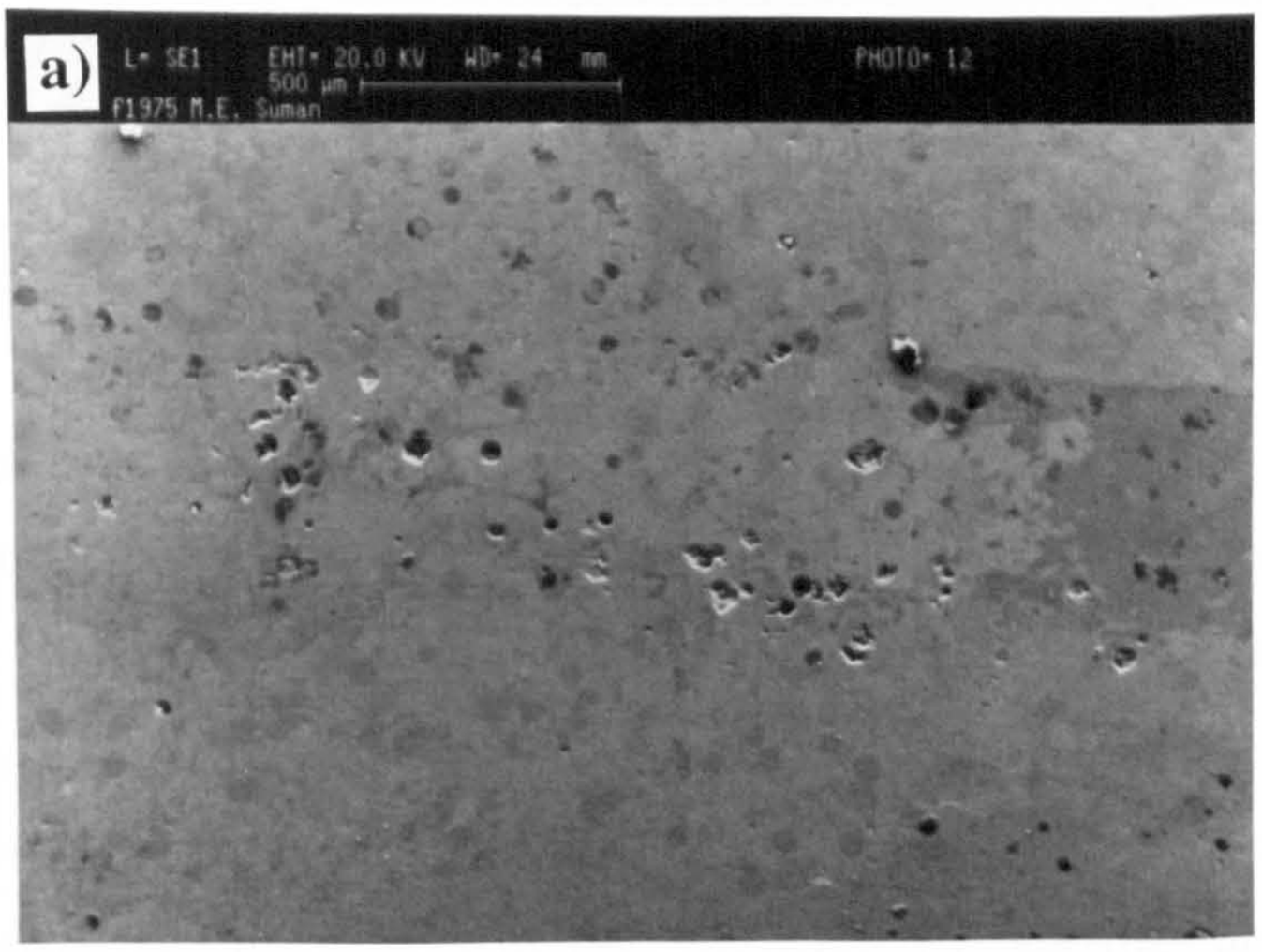
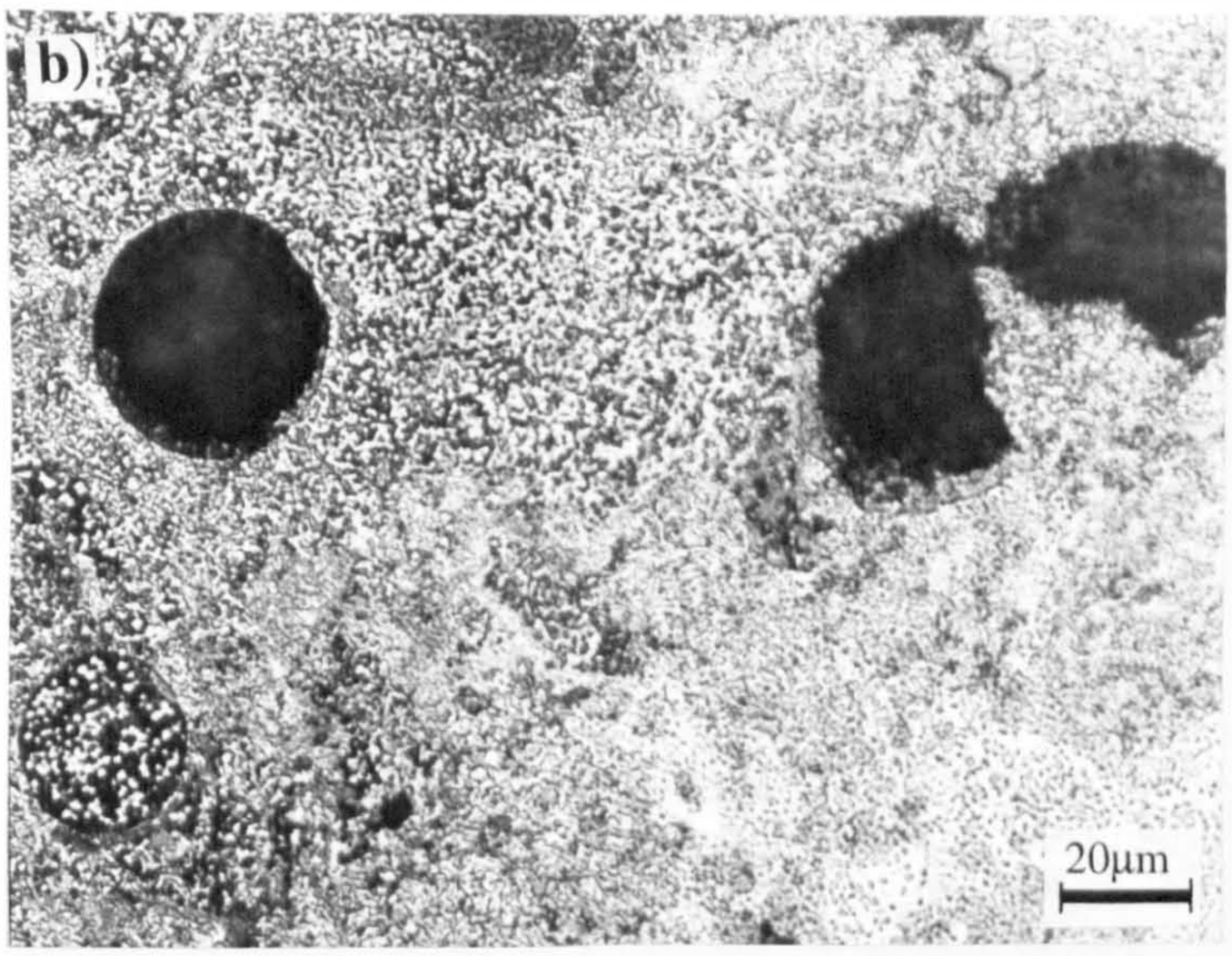


Figure 8.3.12 Light optical micrographs of a) sprayed; b) fused; and c) UNS S31603 after 1-month free immersion in static seawater at 18°C (U- under lacomit strip; C- crevice; E-exposed area).

The true mechanism of corrosion attack was revealed after removing the corrosion product from the surface using Clarke's solution. Figure 8.3.13a shows the macro scale secondary SEM micrograph of the sprayed coating under the lacomit strip showing a large number of individual splat particles dislodged from the crevice region and Fig. 8.3.13b shows one of the splat particles dislodged from the free exposed surface while the adjacent splat particle shows most of the severe corrosion attack around the hardphase particles. Localised removal of Cr rich globular particles of the sprayed coating forming micropits was also observed after the 1-month exposure (Fig. 8.3.13c).





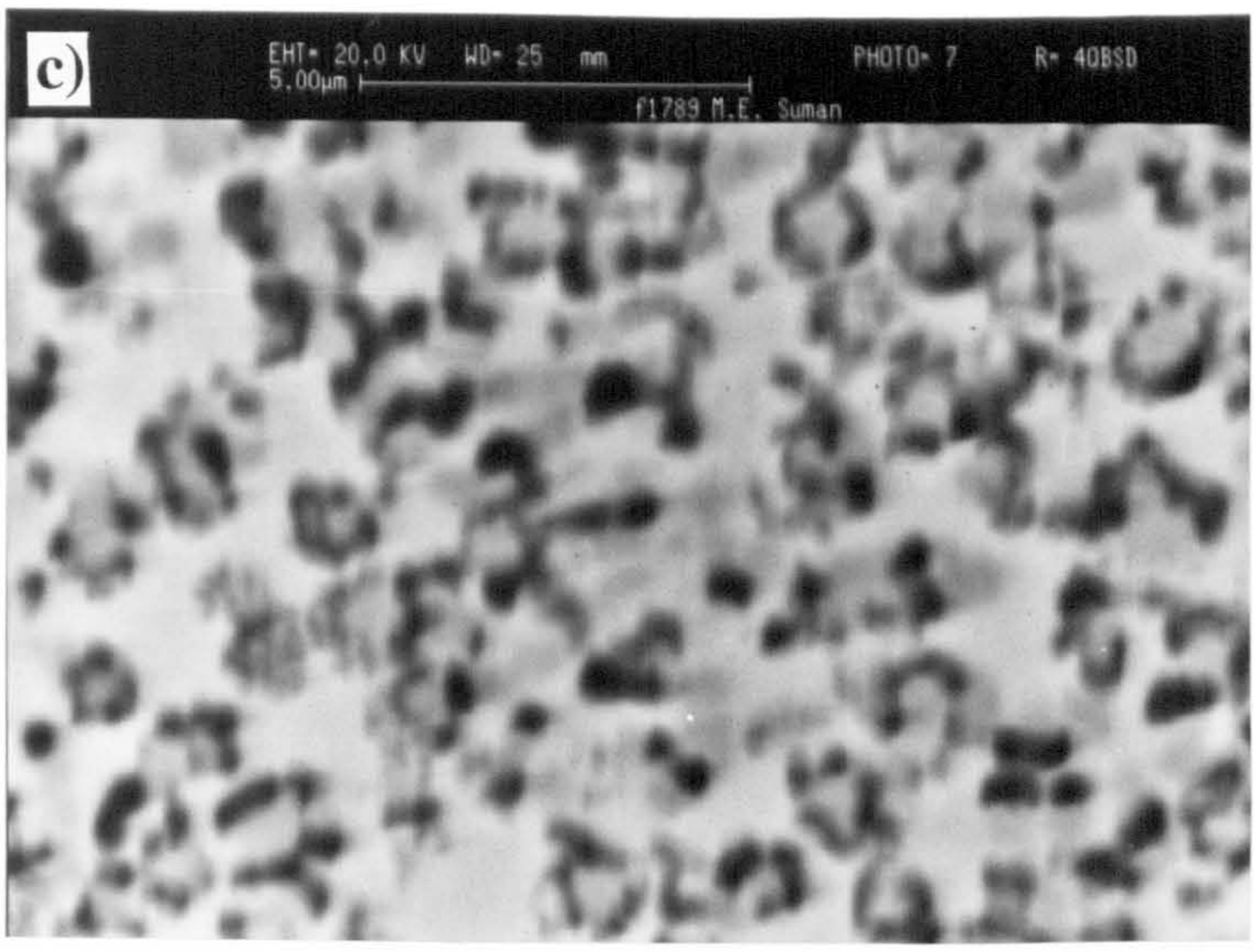
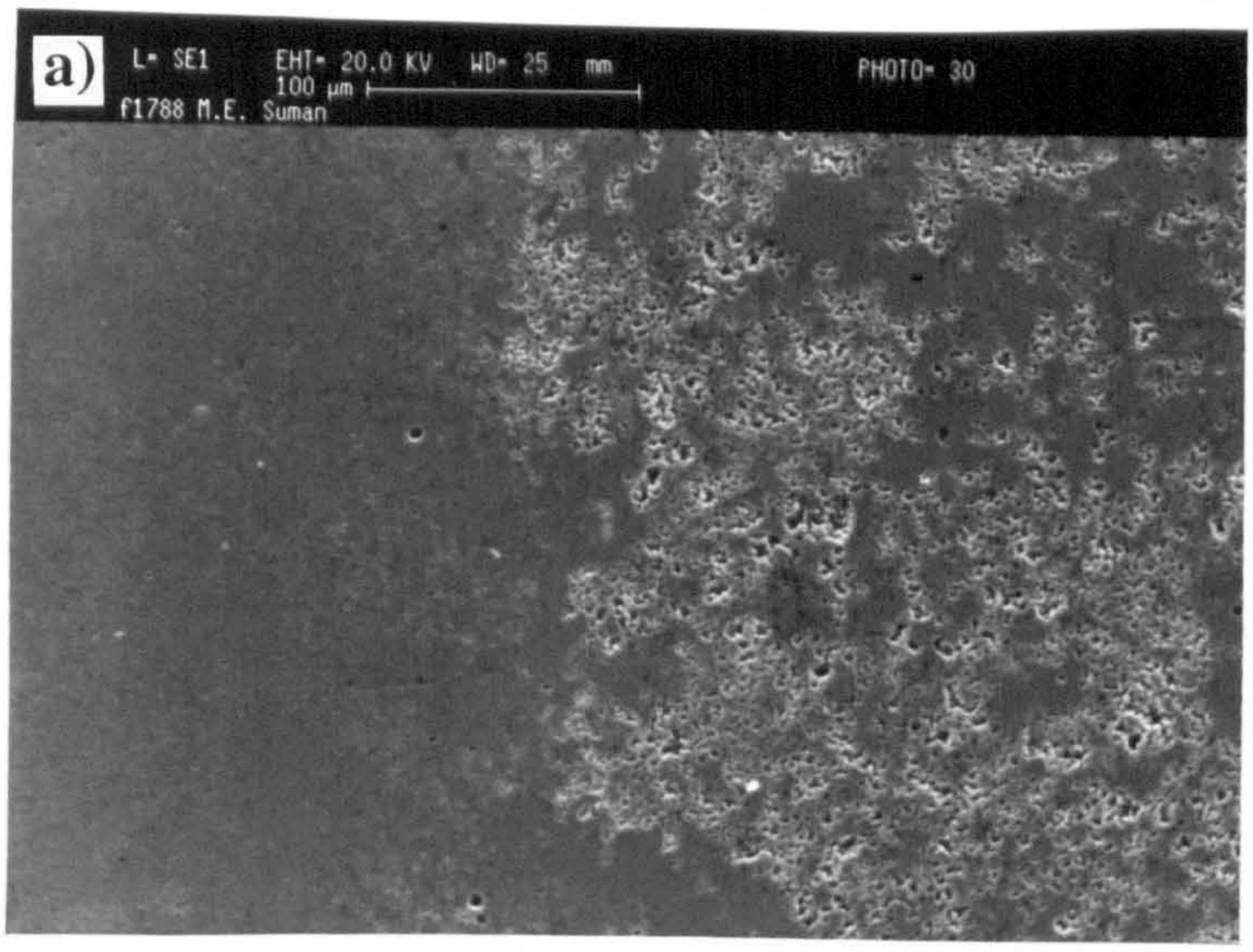


Figure 8.3.13 Secondary SEM micrographs of the as-sprayed coating showing a) severe crevice attack under the lacomit strip; b) corrosion attack at exposed surface; and c) micropitting due to fall of Cr rich hardphase particles on the exposed surface.

The vacuum-fused coating displayed mechanisms of corrosion attack similar to that, which had been displayed after anodic polarisation. There was some noticeable crevice attack on the fused coating, which is clear under the lacomit strip with severe micropitting as shown in Fig. 8.314a. Detailed observation on a more microscopic level showed corrosion of the exposed area was associated with the preferential dissolution of the binder matrix around the hardphase particles by leaving the hard particles unsupported. These loosened particles eventually fall to form micropits (Fig. 8.3.14b).



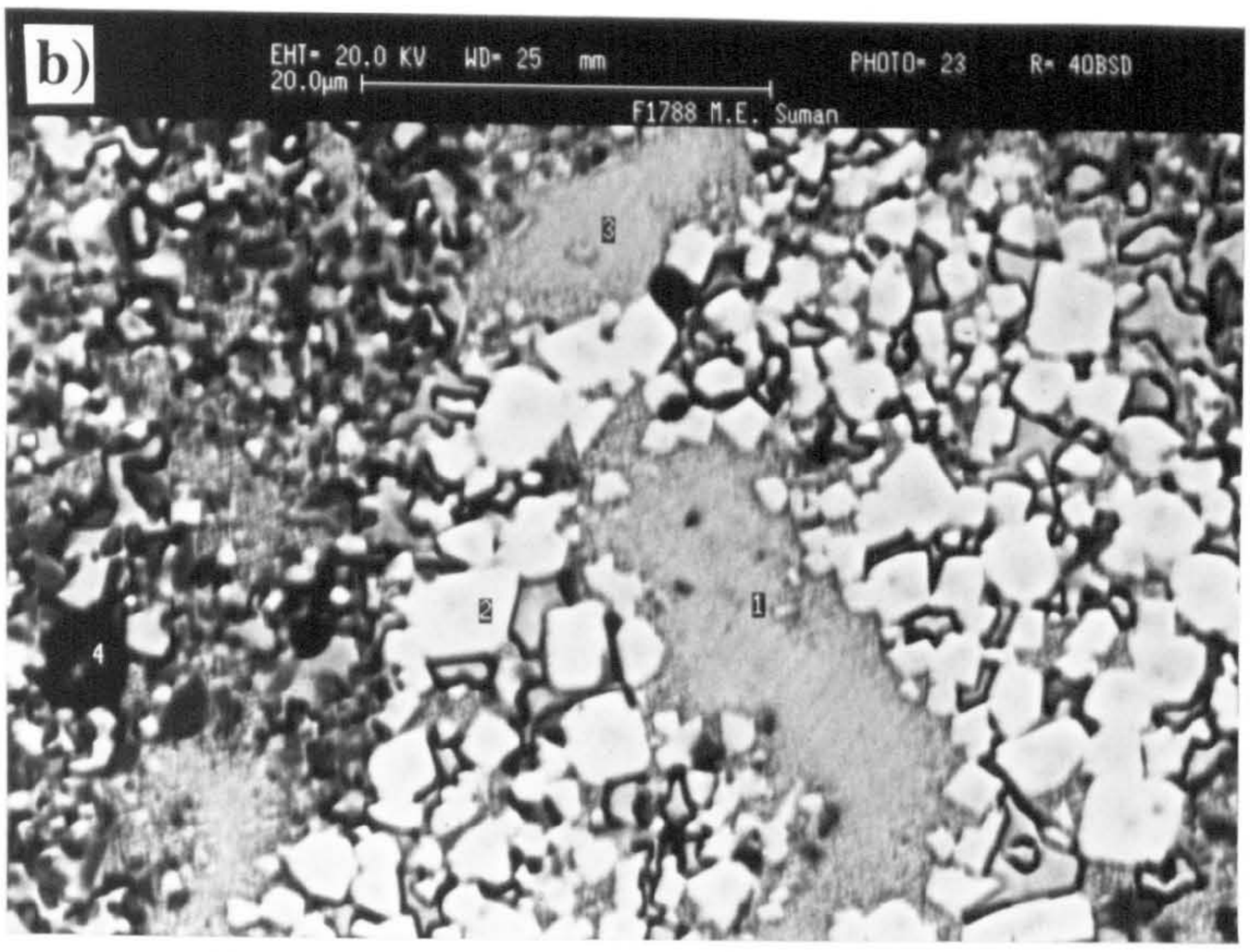
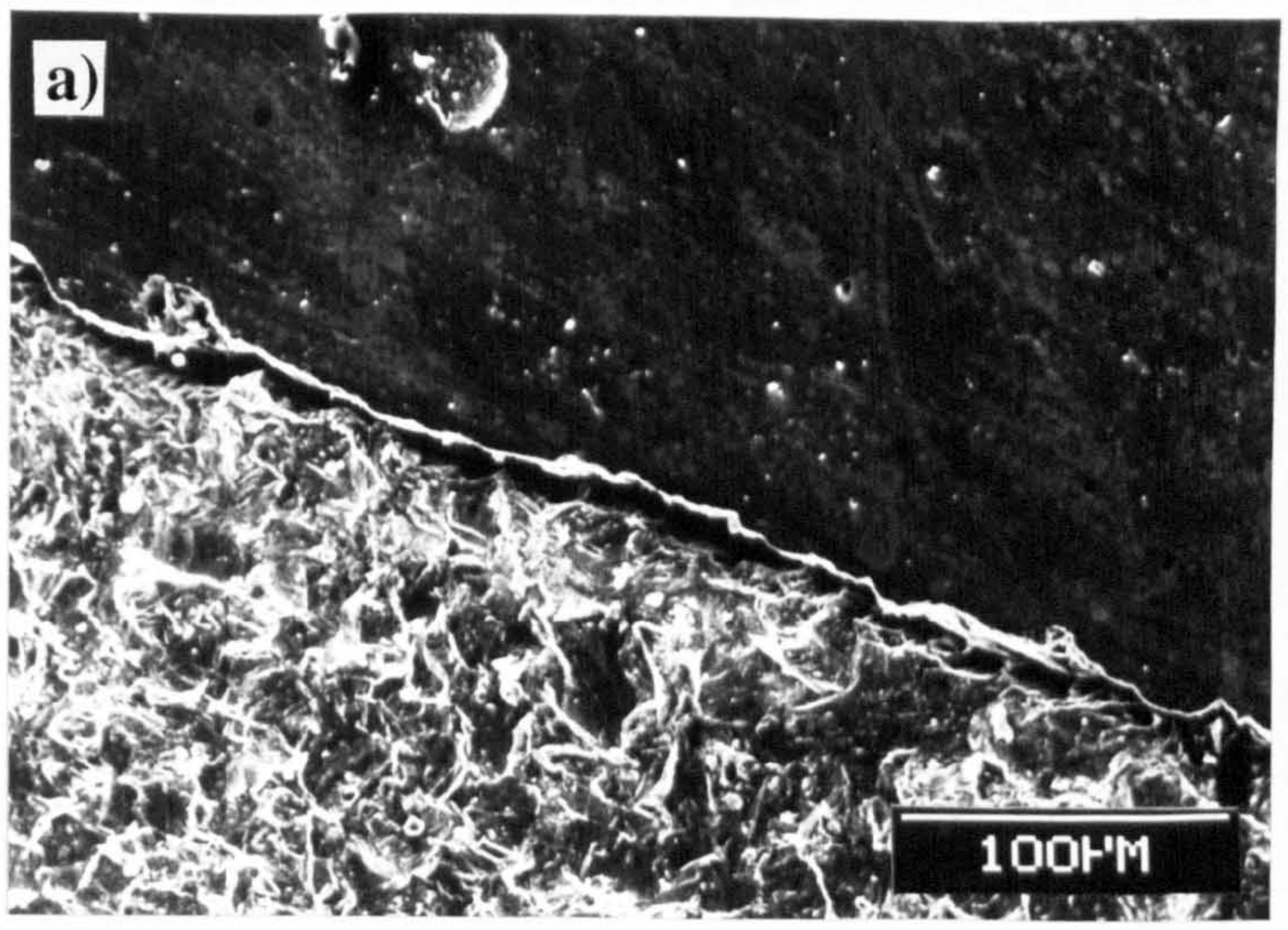


Figure 8.3.14 a) Severe crevice under the lacomit strip; and b) preferential dissolution of the matrix surrounding the hard particles of vacuum-fused coating after 1 month immersion in static seawater at 18°C.

Assessment of Galvanic Interactions between Coating and Substrate

Free immersion tests at E_{corr} were performed for an extended period of 1-month for the as-sprayed, vacuum-sealed and vacuum fused coatings on carbon steel substrate 'Coating BI'. For comparison, same coatings on stainless steel substrate 'Coating BII' were also investigated to assess the galvanic effect at the coating/substrate interface. Specimens were mounted in cross sections as described in section 7.4 of Chapter 7. The electrolyte used was artificial seawater of 35000ppm salinity, while the temperature was maintained at 18±2°C. After the test period, the coatings were removed from the electrolyte and cleaned with the Clarke's solution to remove the corrosion product from the coatings surface. Both as-sprayed and vacuum-sealed coating displayed very identical characteristics shown by their photomicrographs before and after the test and hence, only the as-sprayed coating is discussed in this report. Coatings with stainless substrate showed no evidence of any attack at the coating/substrate interface, while attack on the coatings themselves was readily visible. The attack mechanisms in the coatings with stainless steel substrate exposed in cross sections were rather similar to those displayed by corroded surfaces exposed in plan, which have already been illustrated before under subsection 'Extended Exposure Test'. This section will thus focus on the coating with carbon steel substrate.

Substrates of both sprayed and fused coatings showed extensive corrosion as expected. Close examination of the extent of corrosion attack and the attack mechanism exhibited a difference between the two coating investigated. Figure 8.3.15a shows a distinct zone of relatively excessive attack of the substrate material near to the coating/substrate interface with its 'knife line attack' on the sprayed coating. The fused coating displayed different mechanisms of corrosion attack (Fig. 8.3.15b), primarily on and around the 'basal black keys'. It is apparent that there is an excessive localised attack around the 'keys' but in a more micro level compared to a more macro level galvanic attack on the sprayed coating. This presumably shows a somewhat superior bonding of the fused coating that might prevent from easier delamination of the as-sprayed coating from the substrate.



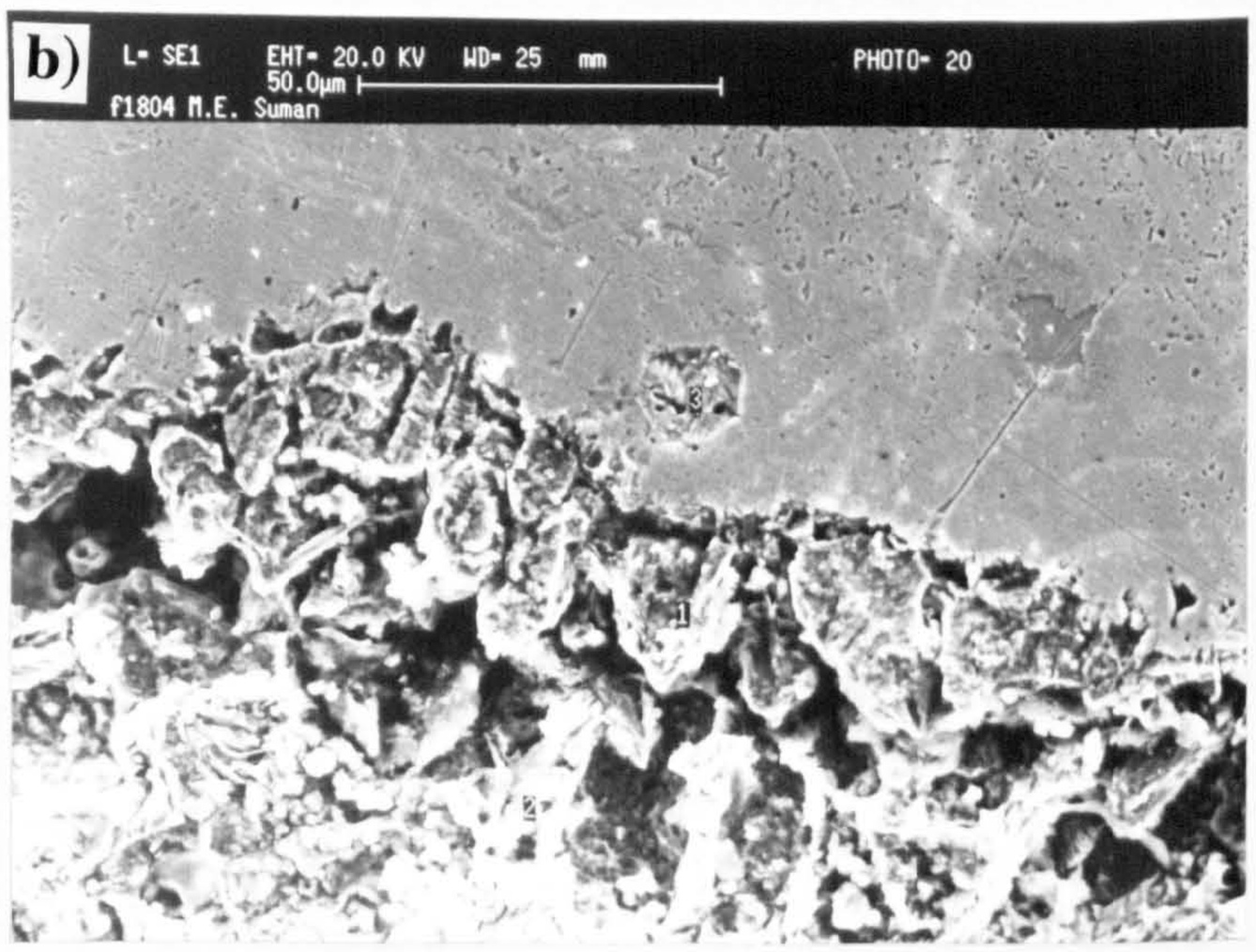


Figure 8.3.15 SEM micrographs showing severe corrosion attack at coating/substrate interface: a) as-sprayed; and b) vacuum-fused coatings after 1-month immersion in artificial seawater at 18°C.

Furthermore, the corroded specimens were once again subjected to successive grinding on 600 and 1200 grit abrasive papers approximately for 5 minutes and then finally polished to diamond finish. This revealed the clear 'knife-line attack' on the sprayed coating (Fig. 8.3.16a), separating the coating from the substrate, while Fig. 8.3.16b shows the interface of the fused coating with localised attack near the 'black basal keys'. Further microscopic observations revealed the occurrence of corrosion attack on the coating itself on both sprayed and fused coating with similar mechanisms as on plan surface with both macropitting due to splat loss and micropitting due to hardphase particle loss.

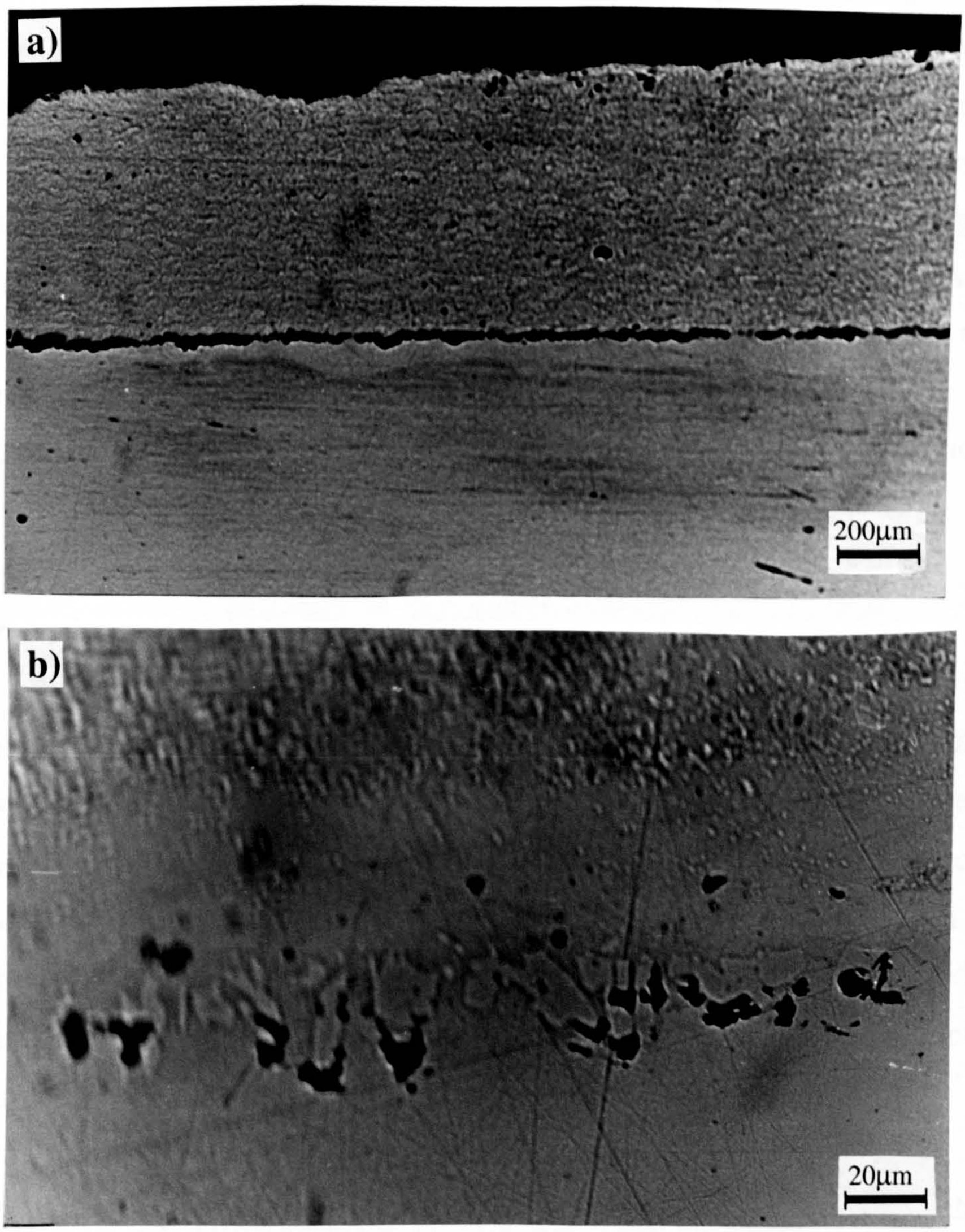


Figure 8.3.16 Light optical micrographs of a) sprayed; and b) fused coating after polishing 1-month corroded cross sections in diamond suspension.

8.4 High velocity liquid impingement of Coating BI

In the previous section of Chapter 8, the corrosion behaviour of as-sprayed, vacuum-sealed and vacuum-fused surfaces of *Coating* BI in static conditions was described. This section considers the corrosion behaviour of the same coating in tests conducted under the influence of a high velocity single-phase seawater jet impinging normally (90° angle) onto the specimen surface. The electrolyte used was artificial seawater free from added solid and the impingement velocity was $72ms^{-1}$ unless otherwise stated. The nozzle diameter of the impinging jet was 1mm. Anodic polarisation tests were performed at both 18 and 50°C to determine the effect of increased temperature. All tests were carried out in the submerged condition (i.e. both impinging liquid jet and coating surface under investigation were immersed in the seawater) unless otherwise stated. Some tests described as 'unsubmerged' involved the sample being impinged in air. The specimen was kept at a distance of 10mm from the nozzle exit. All the specimens were polished unless referred to 'as-received'. Continual reference to the electrochemical behaviour and microscopical examination of the materials in static seawater is made in order to ascertain what effects the impinging flow induces in fundamental terms.

Electrochemical corrosion behaviour at 18° C

Anodic polarisation results of the coatings (as-sprayed, vacuum-sealed, vacuum-fused), stainless steel (UNS S31603) and carbon steel (BS970 En8) under high velocity impingement of $72ms^{-1}$ at temperature of 18°C are shown in Fig. 8.4.1a, which clearly shows a potential benefit of these coatings compared to the uncoated specimen under such an extremely high-velocity impingement. Figure 8.4.1b shows the expanded plots for the maximum current density of $100\mu A/cm^2$, which enables the differences at smaller current densities to be distinguished.

The stainless steel specimen still exhibited a classic passive behaviour under the impingement conditions as was displayed previously in the static conditions. However,

the breakdown potential 'E_b' is comparatively much lower under the high-velocity impingement than in the static water, followed by the vacuum-fused coating.

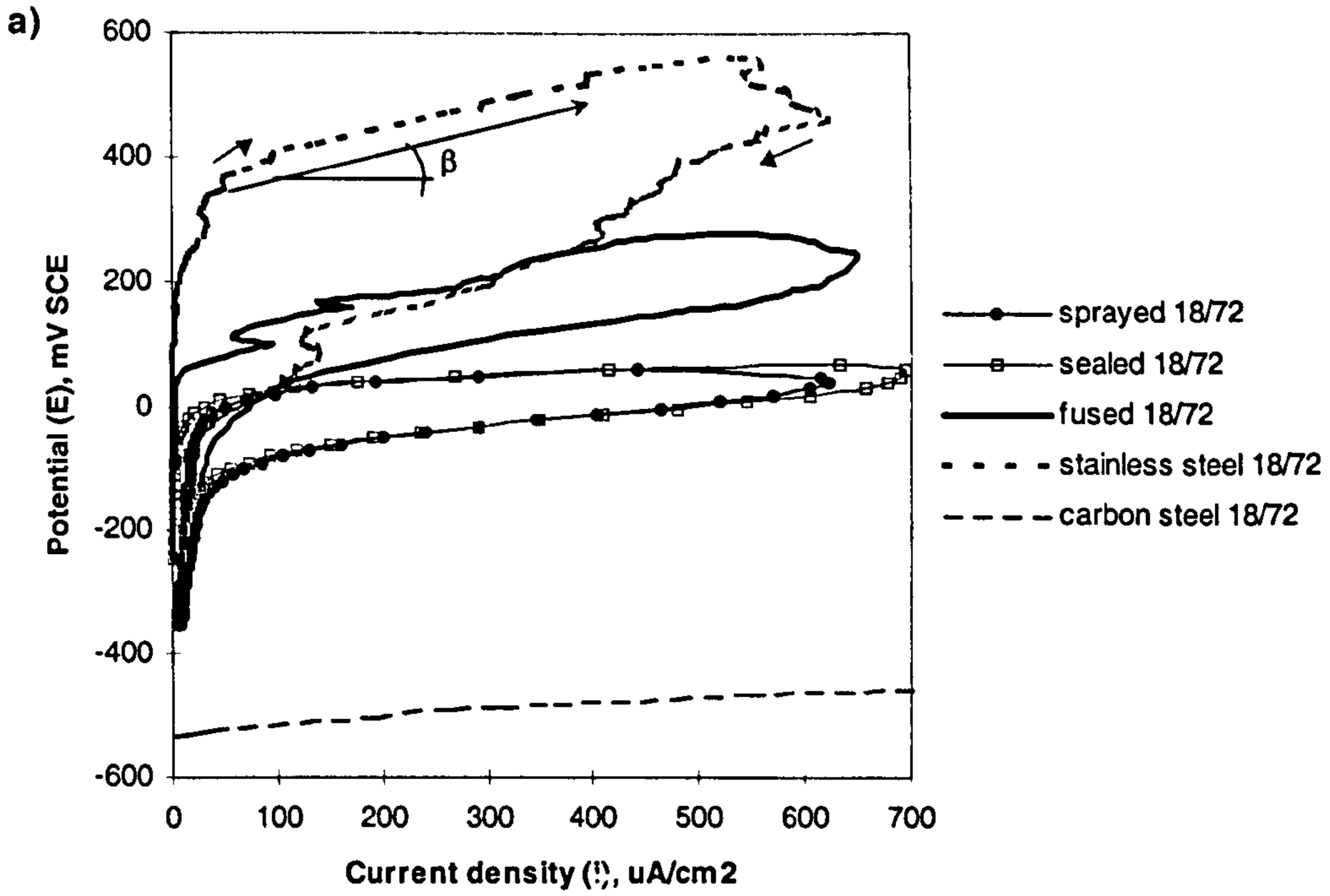


Figure 8.4.1 Anodic polarisation results of the polished surfaces under high-velocity seawater jet impingement (18/72 refers to 18° and 72ms^{-1}): a) full scan; and b) forward scan with maximum current density of 100μA/cm^2.

Another interesting feature displayed by both the stainless steel and the fused coating under high velocity impingement condition unlike the sprayed and sealed coatings was that after recording the breakdown potential 'E_b' there was a steep angle 'β' made by the forward scan with the current axis as shown in Fig. 8.4.1a, which might possibly indicate some interesting outcomes in corrosion mechanisms but they need verification and will be attempted in later sections.

Figure 8.4.1 also indicates that both the stainless steel and the fused coating attempted a breakdown-repassivation process shown by the symbol '↔' during the forward scan. Another interesting feature displayed by the stainless steel was that there was a reduction of i_{max} value compared to much higher i_{max} achieved in static condition before it actually starts the reverse scan. The vacuum-sealed coating showed what can be called as a semi-passive nature shown by the passage of a very small amount of current (about 5μA) until it reaches the potential value of about 150mV positive from the E_{corr}. After this potential it showed a clear indication of the breakdown potential 'E_b'. The significant effect of the high velocity impingement was pronounced on the sprayed coating, shown by the steady increase of the current up to 20μA until the forward scan reaches the potential value at about -50mV after which it begins to record higher current values similar to 'E_b'.

On reversing the scan back to E_{corr} all three coatings exhibited substantial decay in current within a potential drop of approximately 100mV in contrast to that of the stainless steel, which displayed a similar amount of current decay within a much larger potential drop of about 300mV and also exhibiting larger loop area.

Some distinctions between the tested materials can be made from the electrochemical parameters obtained during anodic polarisation under high velocity seawater impingement. Results from the replicate experiments are presented in Fig. 8.4.2. The E_{corr} of as-sprayed coating is comparatively more negative (about 100mV) than sealed or fused coatings. The stainless steel was found to have a more positive E_{corr} as can be seen from Fig. 8.4.2a. On starting the high-velocity jet, E_{corr} of as-sprayed coating decayed just after 15 minutes of impingement by almost 100mV. The vacuum-sealed coating displayed a potential change in either direction from the value exhibited in the

static condition by ±50mV by the end of 15 minutes free impingement of the jet before starting the anodic polarisation. Whereas E_{corr} of vacuum-fused coating remained unaltered before and after 15 minutes of high velocity impingement of liquid jet.

Another way of differentiating the materials tested was by assessing the 'E_b' value of the coatings. The 'E_b' value of the stainless steel was much more positive than rest of the coatings. Looking at the coatings performance, the vacuum-fused coating displayed a superior resistance to corrosion initiation under impingement conditions by its slightly higher 'E_b' at about +50mV as shown in Fig. 8.4.2b.

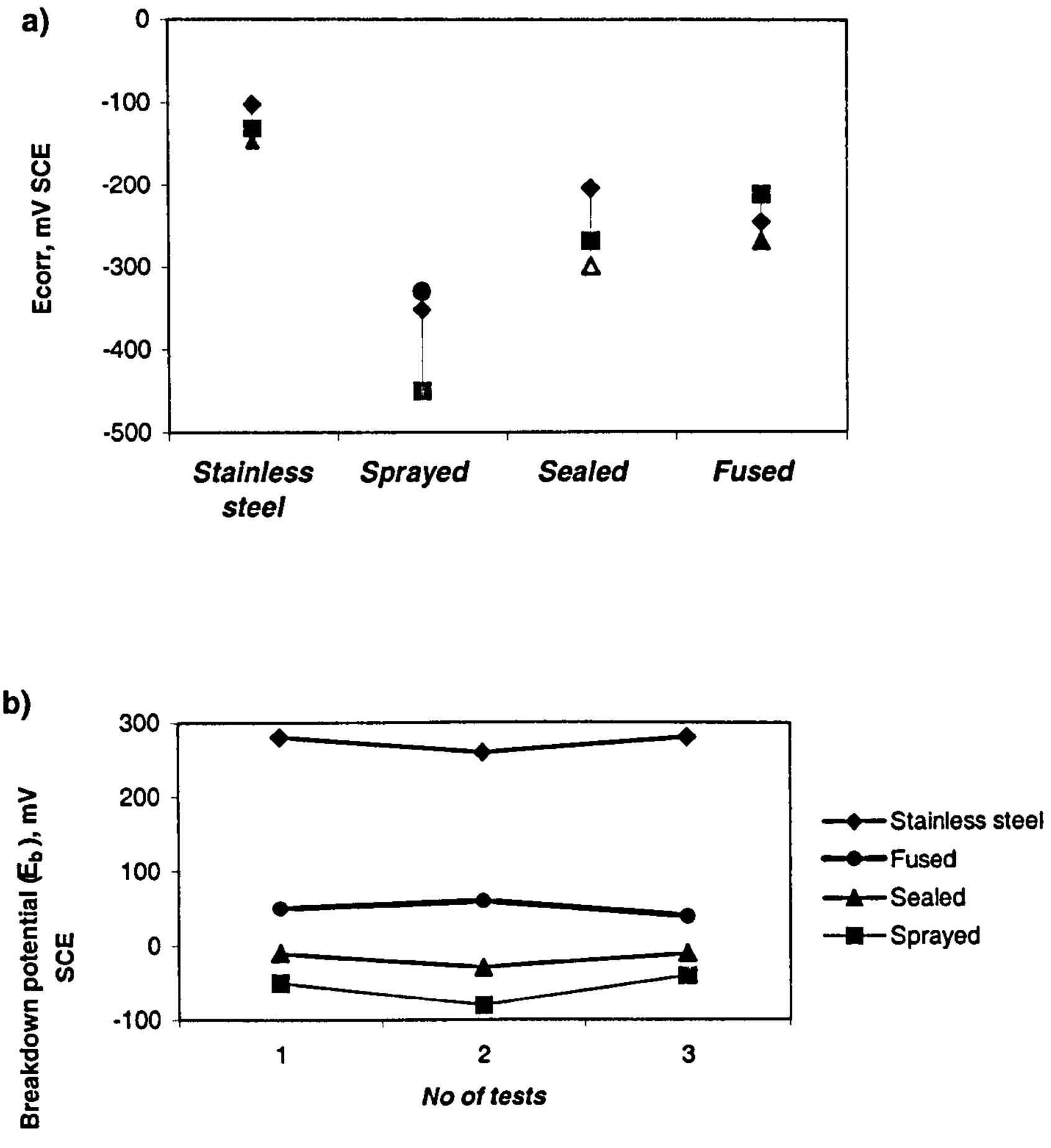
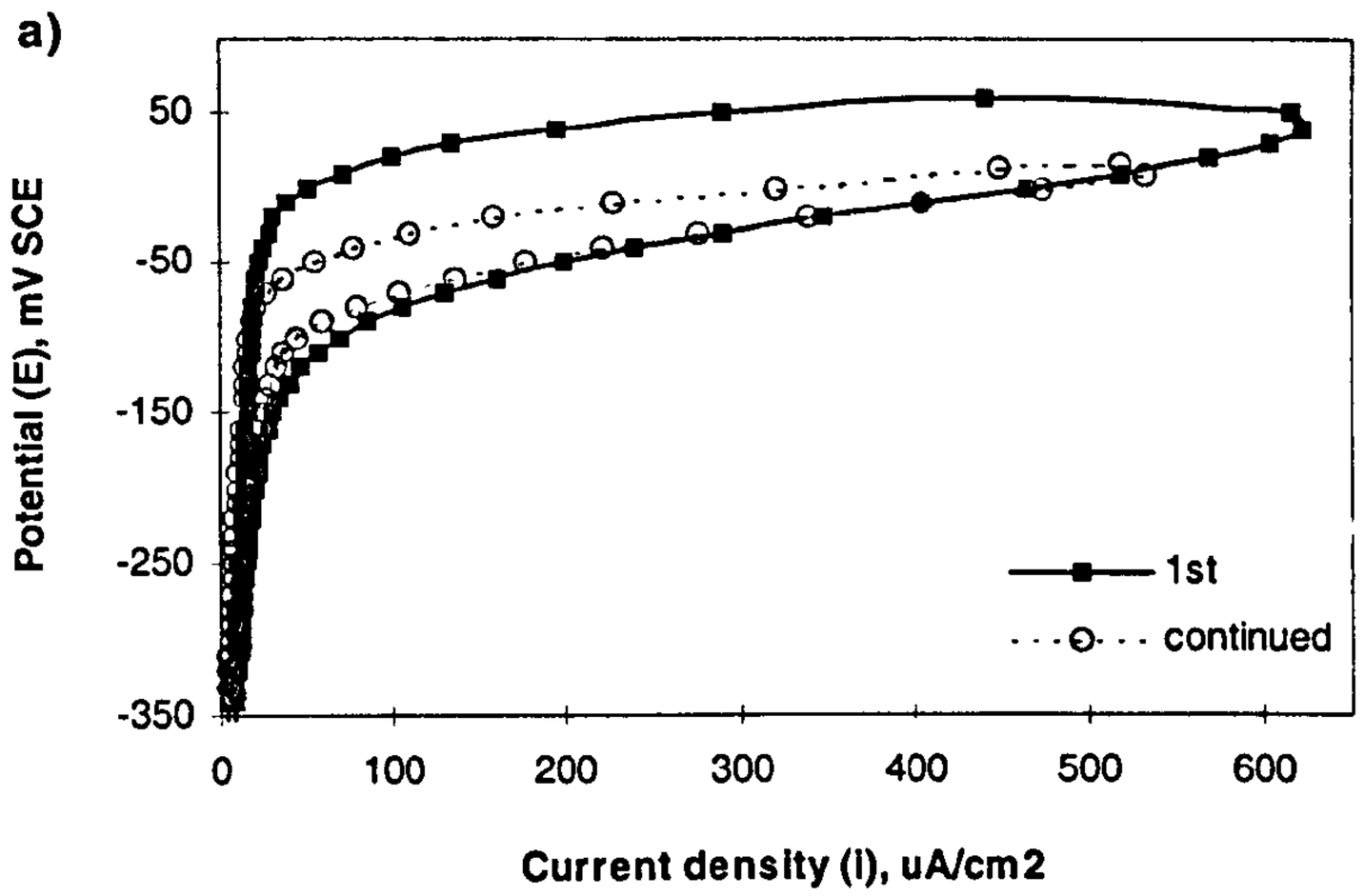
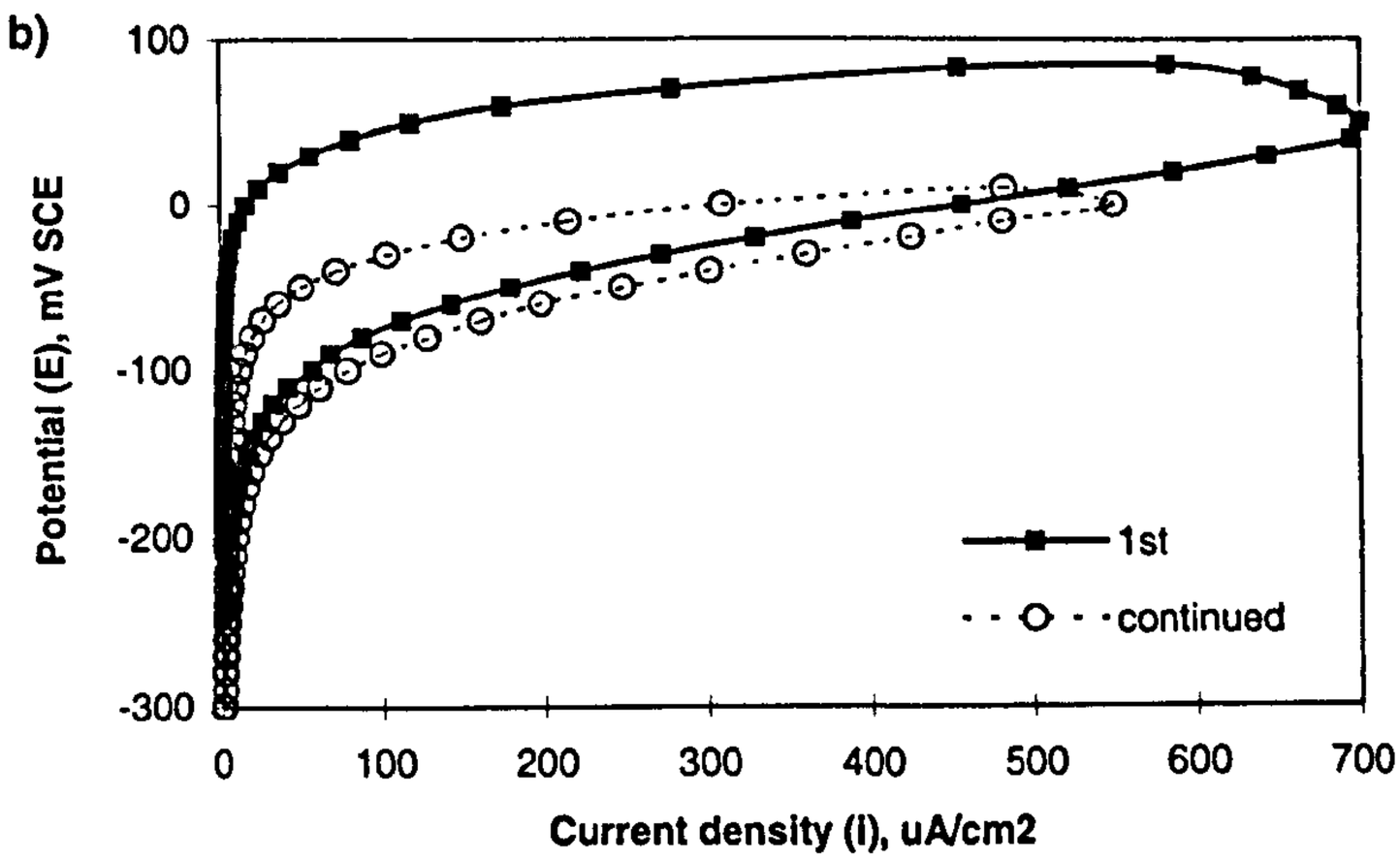


Figure 8.4.2 Scattering of a) E_{corr}; and b) E_b during anodic polarisation under high velocity impingement of seawater at 18°C.

Effect of continuation

In some experiments, the specimen was subjected to an initial anodic polarisation under the impinging jet. Further anodic polarisation tests were continued on the same specimen after stopping the impinging jet and leaving the specimen in static condition for another 1-hour followed by 15 minutes high-velocity jet impingement, while the environmental condition being undisturbed. During this period E_{corr} was set up and the second anodic polarisation was continued. Such tests were performed to see if there is any effect of prior accelerated erosion-corrosion on the electrochemical behaviour of the specimens on further impingement conditions.





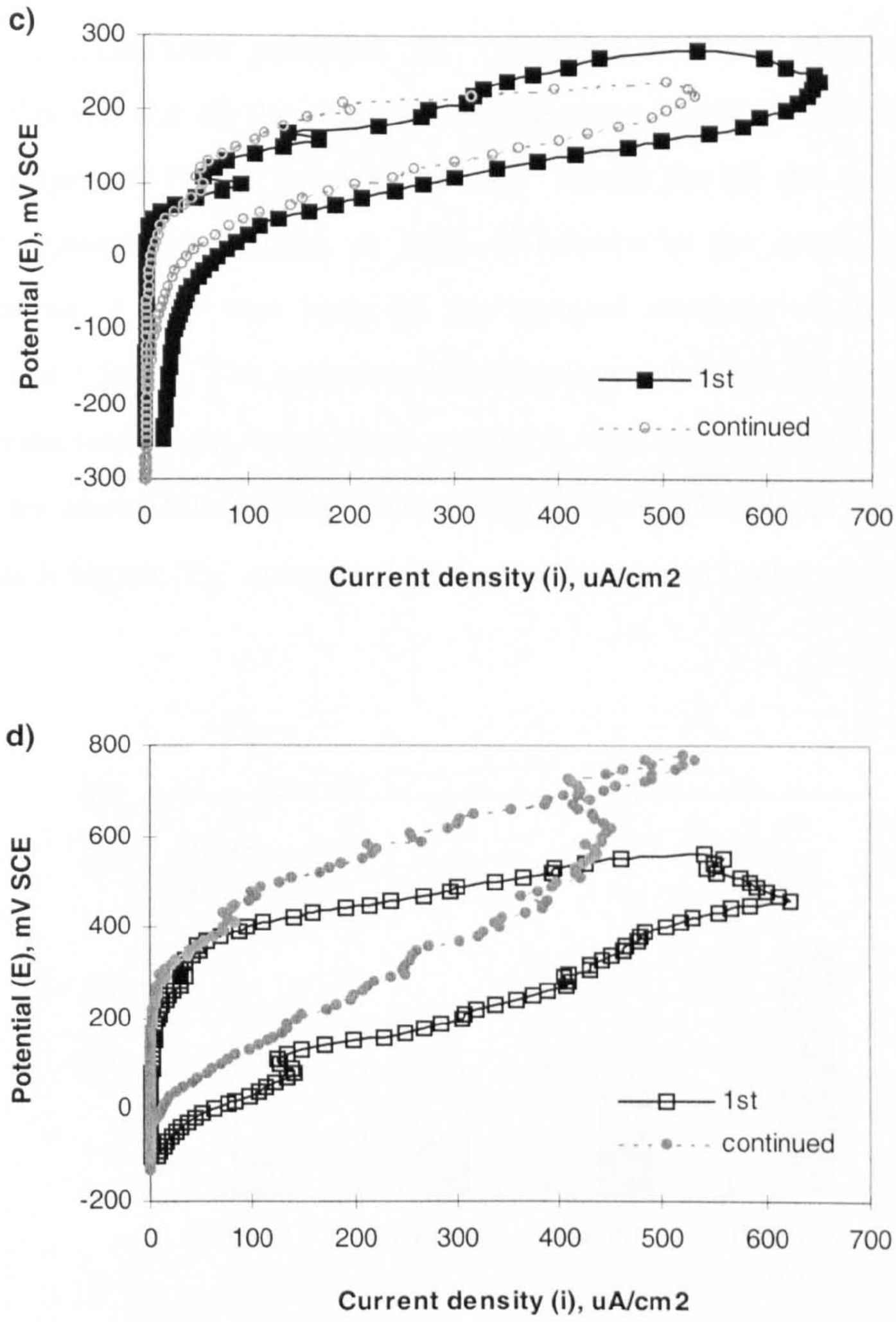


Figure 8.4.3 Anodic polarisation showing the effect of continuation: a) as-sprayed; b) vacuum-sealed; c) vacuum-fused coatings; and d) stainless steel UNS S31603.

Both as-sprayed and vacuum-sealed coatings in continued experiments displayed reductions in 'E_b' by about 40-70mV from the experiment conducted for the first time as shown in Fig. 8.4.3a, b. However, the vacuum-fused coating and the stainless steel did not show any significant change during the two tests performed (Fig. 8.4.3c, d).

Effect of high-velocity jet impingement

The reduction of breakdown potential 'E_b' compared to those obtained under static condition was distinct for all the materials tested once the high velocity single-phase liquid jet was imposed. Figure 8.4.4 shows 'E_b' values for all the materials tested in static and impingement conditions. A large difference in the corrosion performance measured in terms of 'E_b' was seen on the sprayed coating, where the 'E_b' value lowered by almost 150mV. The sealed coating displayed the 'E_b' value reduced by 100-120mV. The reduction in the breakdown potential was the smallest in the case of the fused coating by about 50mV only. The stainless steel still displayed superiority by exhibiting a much higher 'E_b' compared to the coatings even under severe impingement conditions.

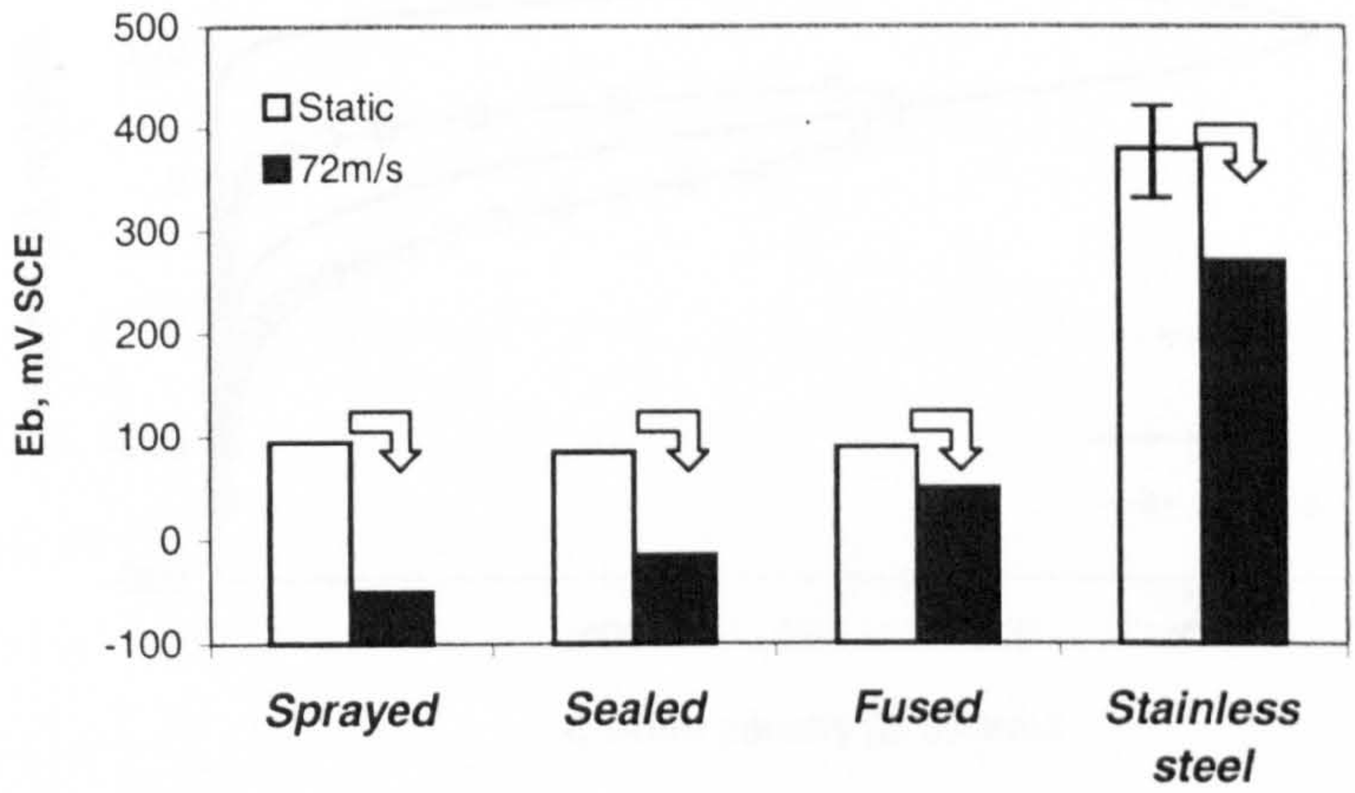
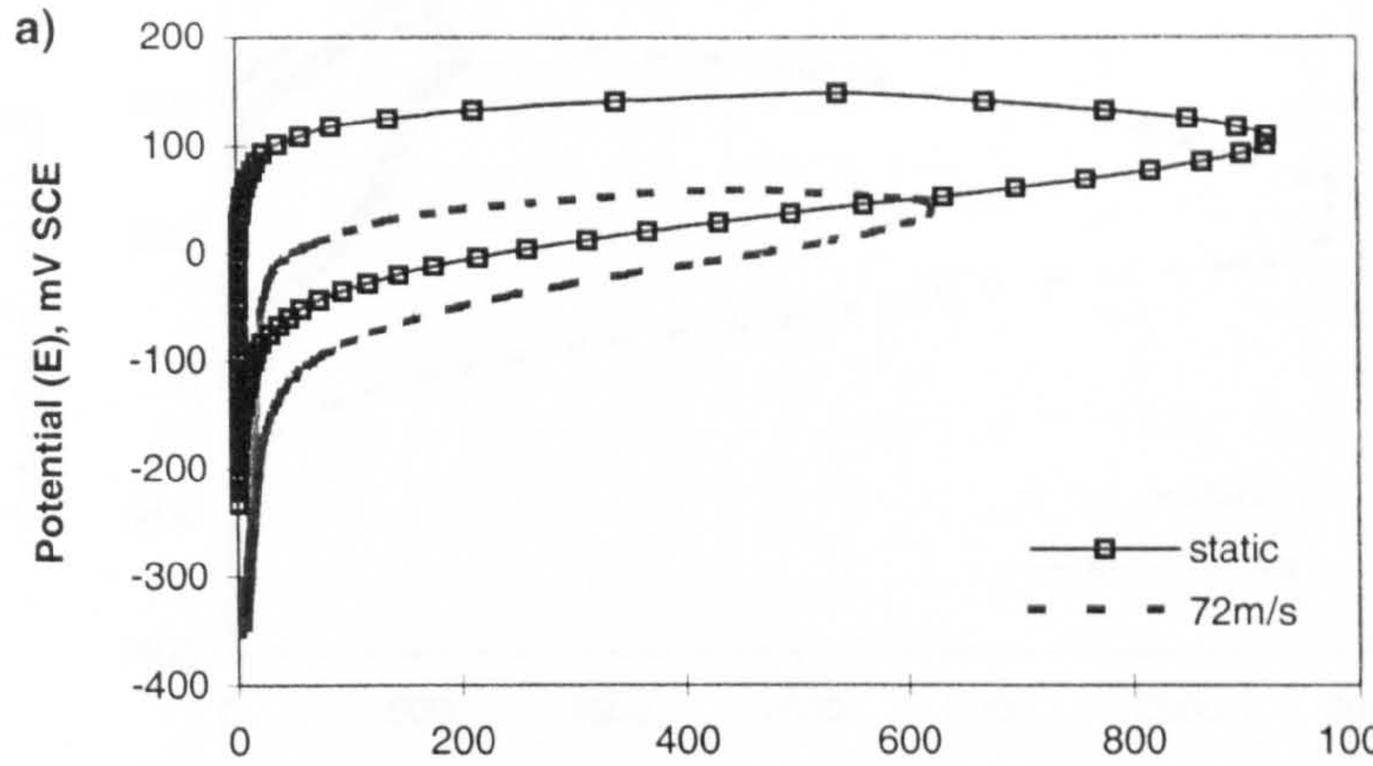


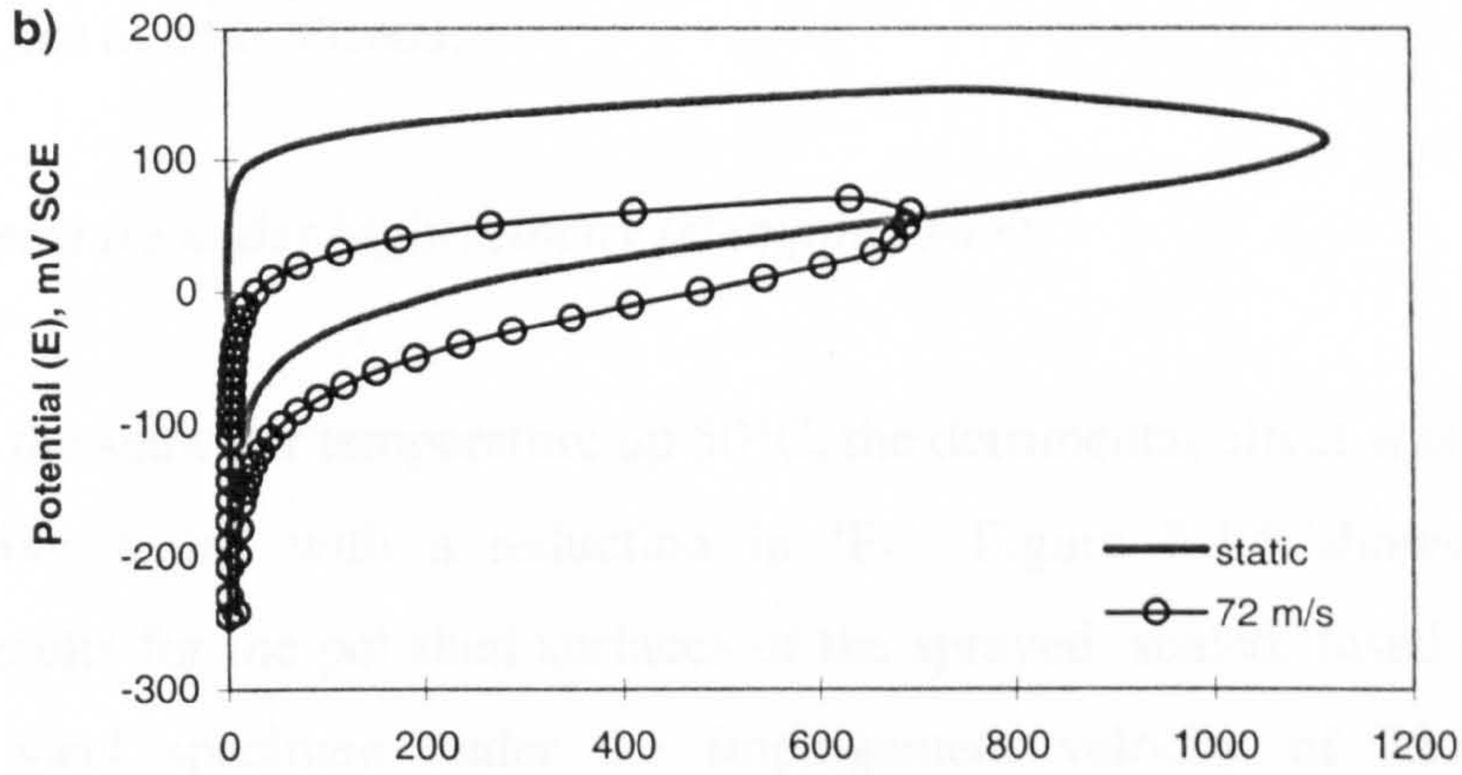
Figure 8.4.4 Reduction of breakdown potential 'E_b' of polished surfaces of the materials after being imposed a high-velocity impingement of seawater jet at18°C.

Figure 8.4.5 displays the full loops of the anodic polarisation tests for all the materials tested. Both as-sprayed and vacuum-sealed coatings exhibited reduction in the loop area under impingement condition (Fig. 8.4.5a, b) and such was significantly pronounced on the stainless steel as shown in Fig. 8.4.5d. However, the vacuum-fused coating displayed a contrasting behaviour with relatively larger loop area under impingement condition to that formed in static condition (Fig. 8.4.5c). These features might indicate a difference in the corrosion mechanism of these materials and in the later sections the correlation will be investigated, supported by the microscopic observations.

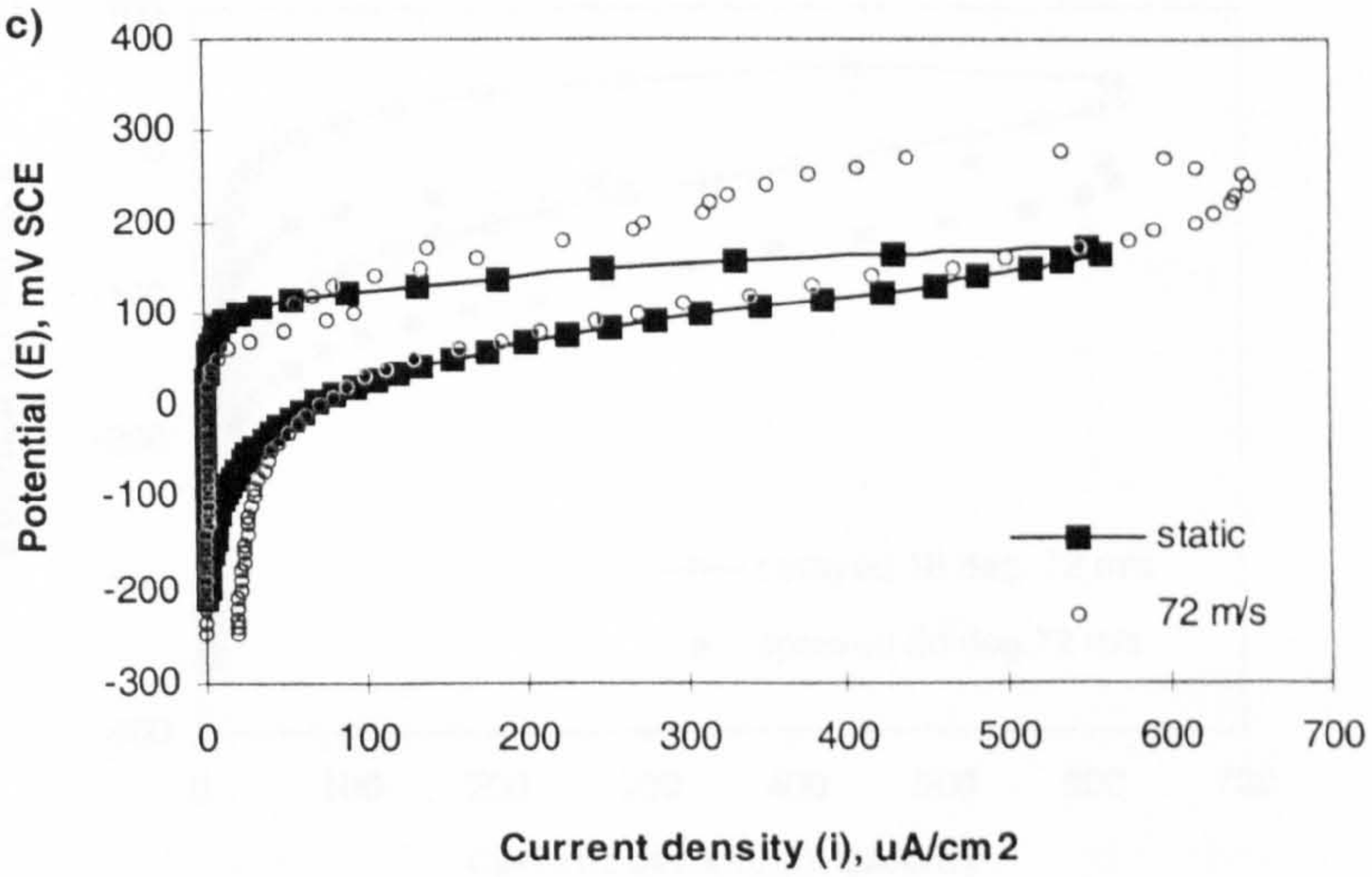
a)


Potential (E), mV SCE
200
100
0
-100
-200
-300
0
200
400
600
800
1000
static
72m/s
Current density (i), uA/cm2

b)


Potential (E), mV SCE
200
100
0
-100
-200
-300
0
200
400
600
800
1000
1200
static
72 m/s
Current density (i), uA/cm2

c)


Potential (E), mV SCE
400
300
200
100
0
-100
-200
-300
0
100
200
300
400
500
600
700
static
72 m/s
Current density (i), uA/cm2

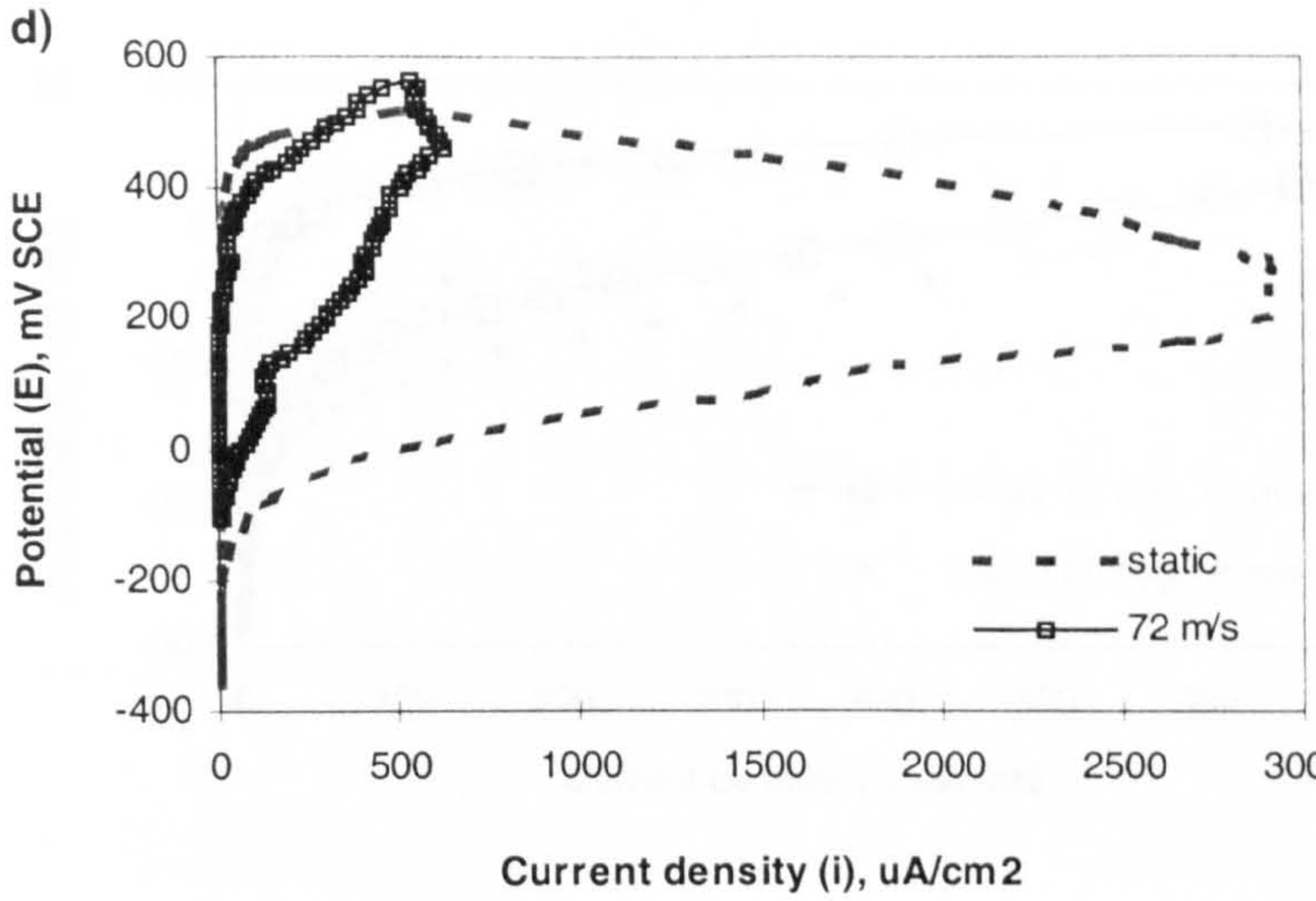
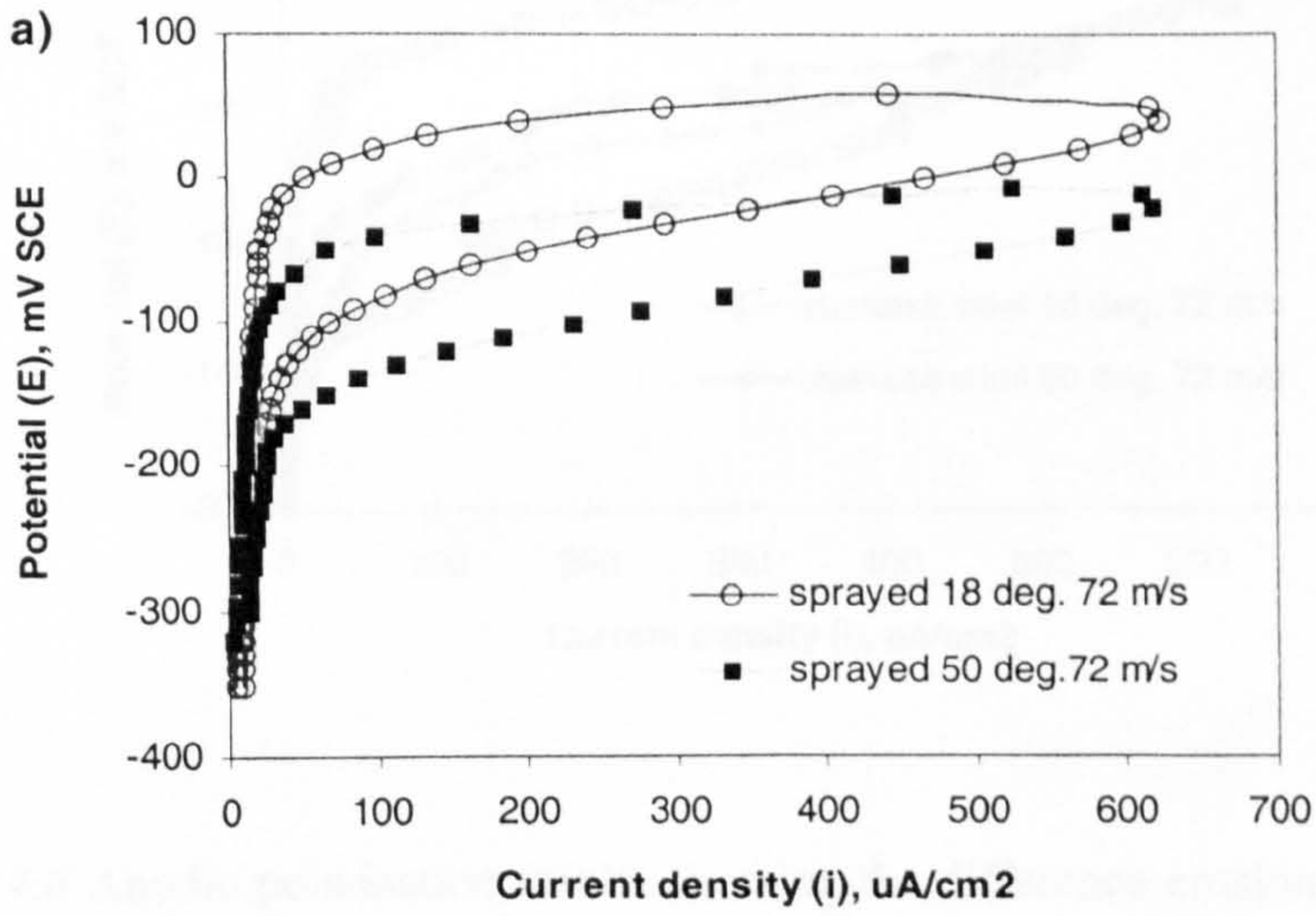


Figure 8.4.5 Anodic polarisation of polished surfaces under static and high velocity liquid impingement in seawater at 18°C: a) sprayed; b) sealed; c) fused coatings; and d) UNS S31603.

Effect of temperature under high-velocity jet impingement

On increasing the seawater temperature up 50°C, the detrimental effect was observed on all the materials tested with a reduction in 'E_b'. Figure 8.4.6 shows the anodic polarisation results for the polished surfaces of the sprayed, sealed, fused coatings and the stainless steel specimen under the impingement velocity of 72ms^{-1}. Anodic polarisation results of 18°C were once again shown to compare the two results obtained.



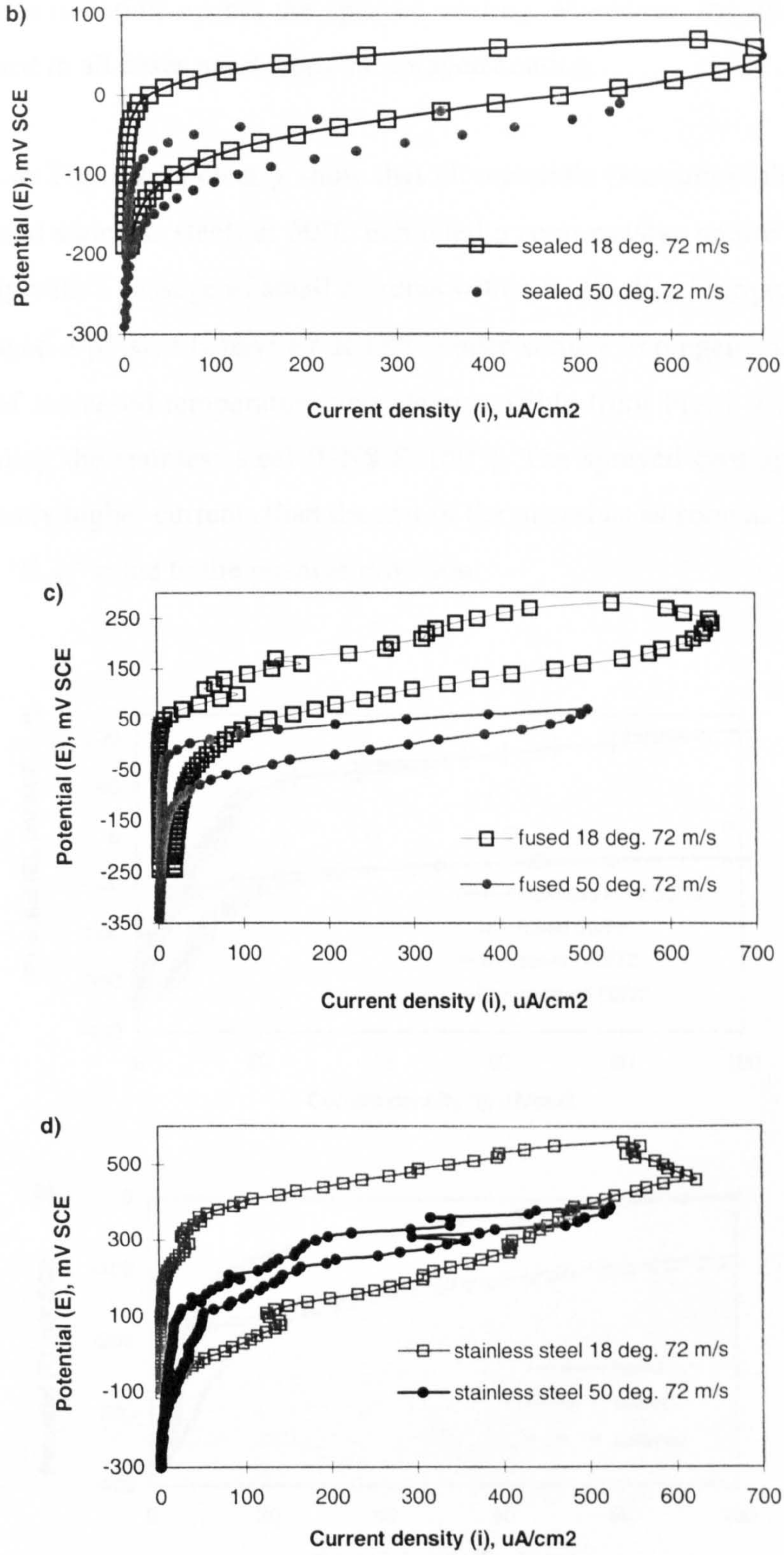


Figure 8.4.6 Anodic polarisation results showing the difference erosion-corrosion behaviour at 18 and 50°C, 72ms^{-1}: a) sprayed; b) sealed; c) fused coatings; and d) UNS S31603 all in polished condition.

Another interesting aspect is that free corrosion potential 'E_{corr}' was lowered by almost 100mV for all the materials except the sprayed coating. Moreover, the hysterisis loop size had decreased in all cases apart from the sprayed coating.

Expanded plots in Fig. 8.4.7a clearly show that all materials (vacuum-sealed, vacuum-fused coatings and stainless steel) at 50°C exhibited a semi-passive nature as had been stated previously with a passage of small currents within its 'E_b-E_{corr}' range, while these materials displayed a passive behaviour at 18°C under similar impingement conditions. The influence of increased temperature was clearly visible from Fig. 8.4.7a on all the materials including the stainless steel (UNS S31603). The sprayed coating once again displayed relatively higher currents than the rest of the materials as soon as the scan was moved from its 'E_{corr}' value to the positive direction.

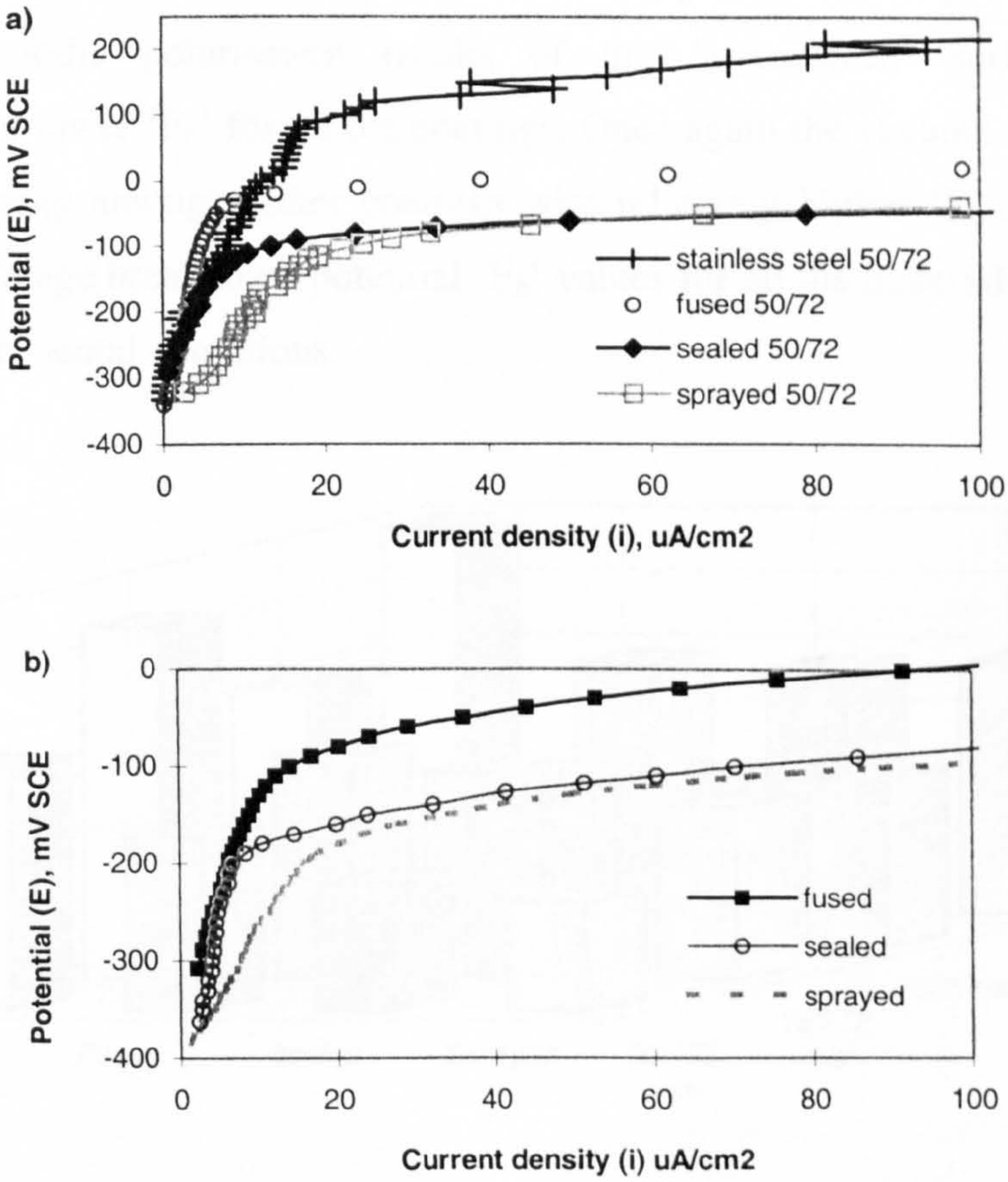


Figure 8.4.7 Forward scans from anodic polarisation results under high-velocity 72ms^{-1} impingement at 50°C a) polished; and b) as-received surfaces of the coatings.

All materials under high velocity impingement at 50°C exhibited some initial currents but the amount was less than 20μA until the anodic polarisation scan reaches the potentials value at which there were clear indications of breakdown potential. Table 8.4.1 shows the different electrochemical parameters obtained under 72ms^{-1} of impingement at 18 and 50°C.

Material	*18°C impingement*			*50 °C impingement*		
	E_{corr}	E_b	i_{max}	E_{corr}	E_b	i_{max}
Sprayed	-380	-30	621	-332	-130	735
Sealed	-216	-20	700	-290	-100	709
Fused	-230	50	649	-315	-30	564
UNS S31603	-116	250	623	-300	80	524

Table 8.4.1 Electrochemical parameters under 72ms^{-1} impingement.

Anodic polarisation tests were performed under impingement conditions at 50°C also on the 'as-received' surfaces of the coatings without being subjected to polishing. Figure 8.4.7b shows anodic polarisation results of the 'as-received' surfaces, which consistently had a lower 'E_b' for all the coatings. Once again the vacuum-fused coating exhibited superiority amongst other coatings with relatively higher 'E_b'. Figure 8.4.8 represents the average breakdown potential 'E_b' values for all the materials investigated in different experimental conditions.

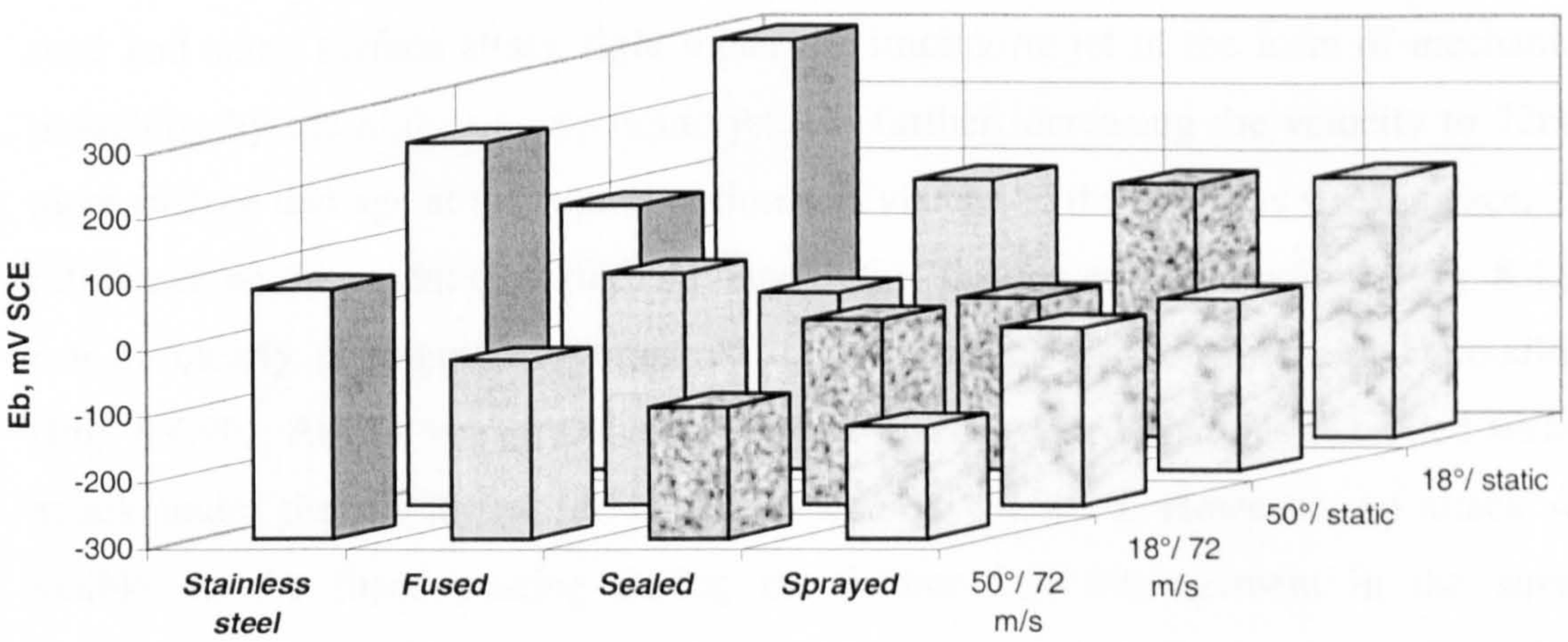


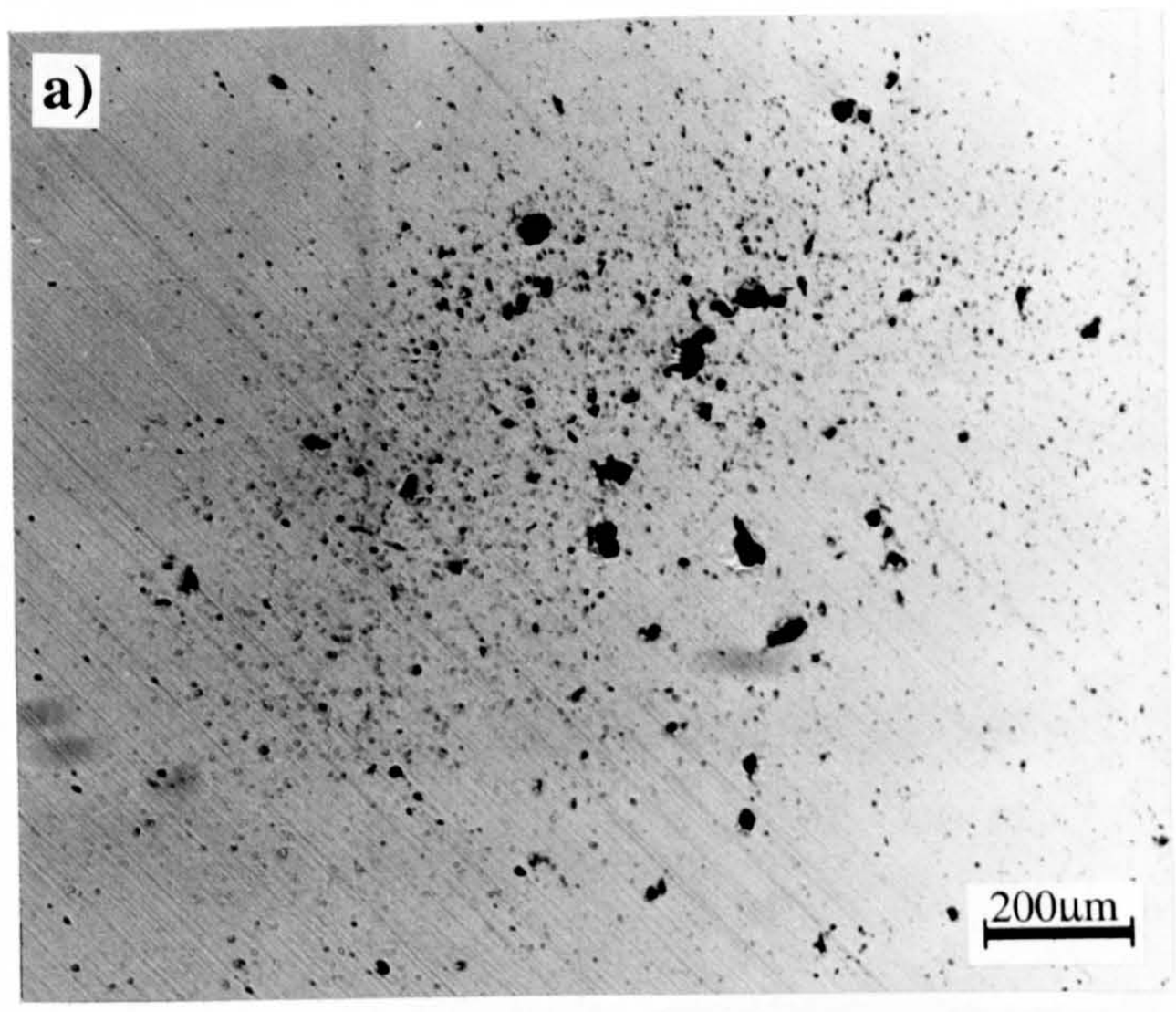
Figure 8.4.8 Comparison of average breakdown potentials 'E_b' of the polished surfaces.

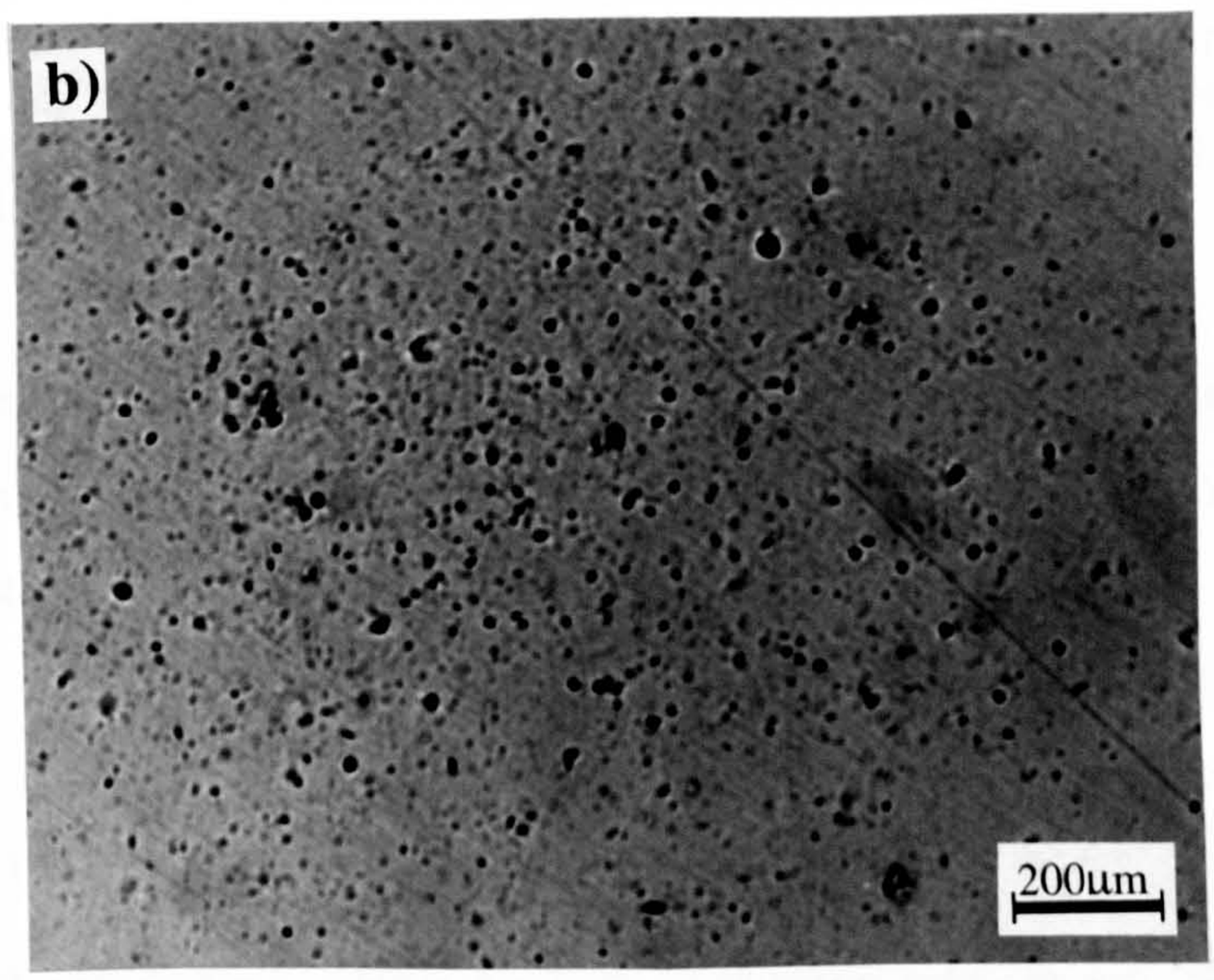
Microscopic observations after high-velocity impingement

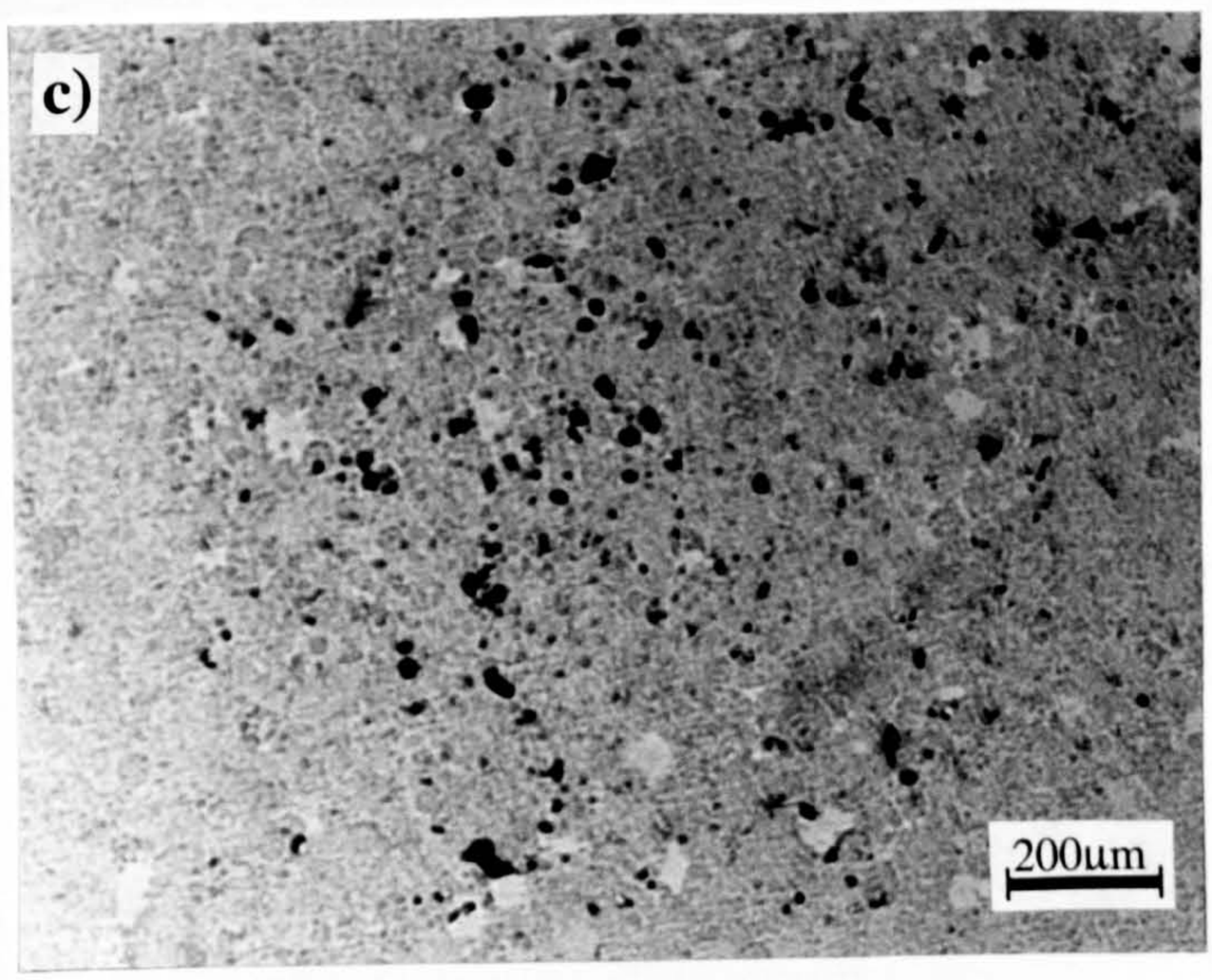
Observations after 1-hour free impingement at 18°C

All the tests of this project are performed in the 'submerged' condition except for a few experiments described below being performed in an 'unsubmerged' condition. This condition however, does not allow electrochemical tests to be performed but can give some indication about the damage compared with the submerged condition, where the stagnant mass of fluid can reduce the surface damage. Some distinctions of surface attack can be seen in 'unsubmerged' and 'submerged' conditions, which can have some practical implications after draining of the pipe systems and/or passing of a high velocity corrosive fluid into the system with dry surface (e.g. newly installed pump components). The results reported in this section comprise tests performed mainly at $72ms^{-1}$ impingement velocity, however few tests were performed also at lower velocities to see at what velocity surface damage begins to occur.

Initial impingement tests in the 'unsubmerged' condition, performed at $25ms^{-1}$ for 1 hour did not show any sign of surface deterioration on the polished surfaces of the sprayed, sealed or fused coatings and the stainless steel. The velocity was increased up to $50ms^{-1}$ and the tests were repeated for all the materials for 1 hour. The coatings still displayed a clear polished surface after the 1-hour impingement, however the stainless steel had some surface attack right under the impinging jet in the form of mechanical ploughing by the high-velocity liquid jet. On further increasing the velocity to $72ms^{-1}$ more surface damage at the central region was visible on the stainless steel surface. The difference on the extent of surface damage in the 'unsubmerged' condition (Fig. 8.4.9a) can be clearly distinguished compared to lesser attack in the 'submerged' condition (Fig. 8.4.9b). At this velocity, the sprayed as well as sealed coatings exhibited surface attack under the impinging jet as shown in Fig. 8.4.9c, d. However, no attack was visible on the fused coating during the 1-hour free impingement in the similar 'unsubmerged' condition, when observed under the light optical microscope. Only SEM observation revealed a very little surface damage occurring on the fused surface under the impinging jet.


a)
200um


b)
200um


c)
200um

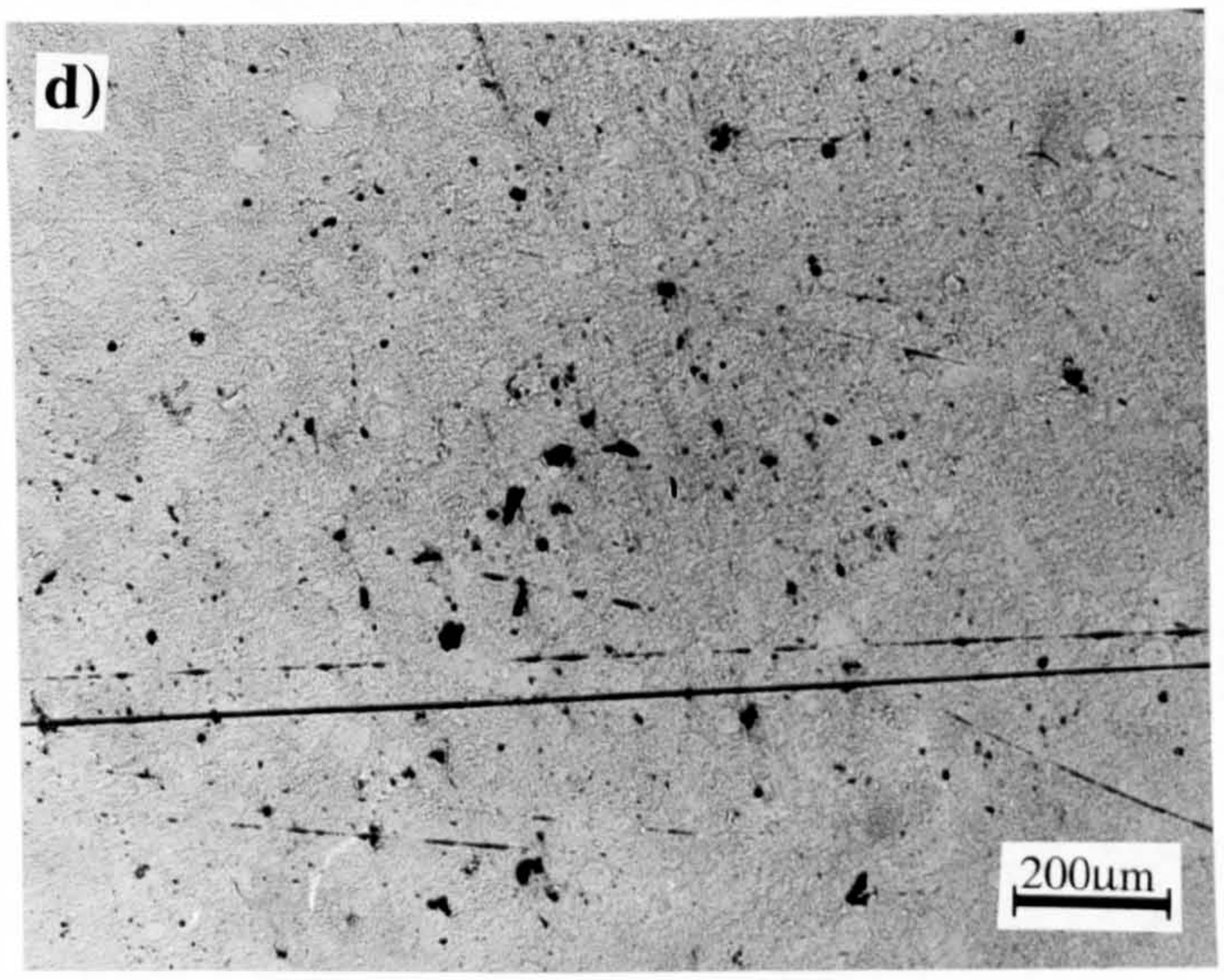


Figure 8.4.9 Light optical micrographs of central wear regions under the jet on polished surfaces of: a) UNS S31603 (unsubmerged); b) UNS S31603 (submerged); c) sprayed; and d) sealed coatings (unsubmerged) after 1-hour high-velocity 72ms^{-1} seawater jet impingement at 18°C.

Higher magnification revealed the surface damage occurring on the stainless steel surface was associated with the material removal in the form of ploughing by the high-velocity water jet as said earlier and more details will be illustrated in section 8.5. The as-sprayed and the vacuum-sealed coatings displayed rather similar complex mechanisms of material removal associated with particles' splat boundary attack, cracking due to high-pressure jet, crack propagation and flaking of material chunks as shown in Fig. 8.4.10a and b. The mechanism of material loss on the sprayed and sealed coatings was similar to that displayable by a brittle material. It is to be noted that, however the attack mechanisms were rather similar in the sprayed and sealed coatings, but some distinction were revealed during the microscopic observations that the attack on the surface of the sealed coating was a little less than that occurring on the sprayed coating. On the other hand, material loss on the fused coating displayed ductile behaviour in the form of mechanical ploughing by the high-pressure liquid jet (Fig. 8.4.10c) forming craters with raised lips. The attack described above had occurred only under impinging jet and was spread within the 1mm diameter of the jet.

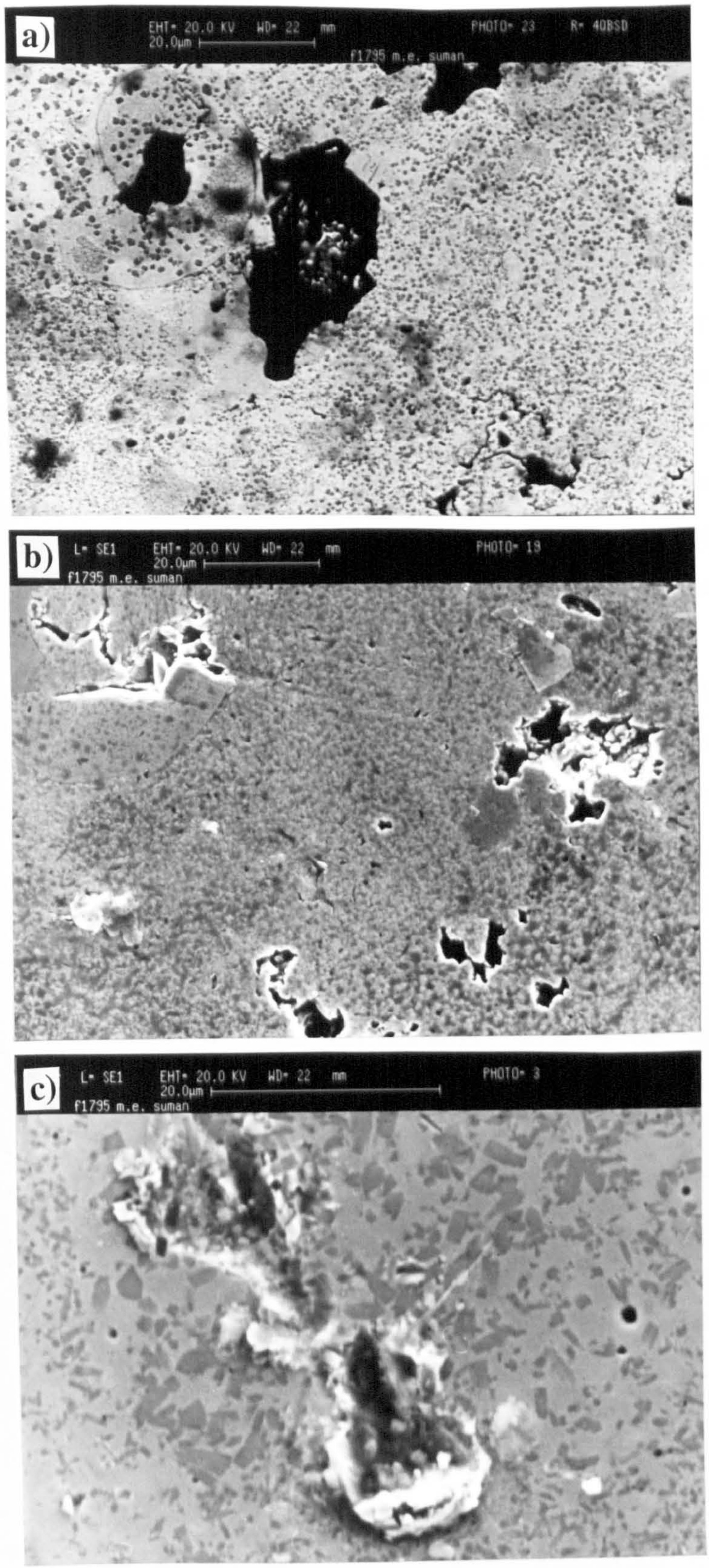


Figure 8.4.10 SEM micrographs of the central wear region after 1-hour impingement in unsubmerged condition: a) back scattered image showing splat boundary attack, flaking of chunks and crack propagation; and b) secondary image showing material removal on the sprayed coating; c) ductile ploughing of the matrix on the fused coating with raised lips from the crater at $72ms^{-1}$.

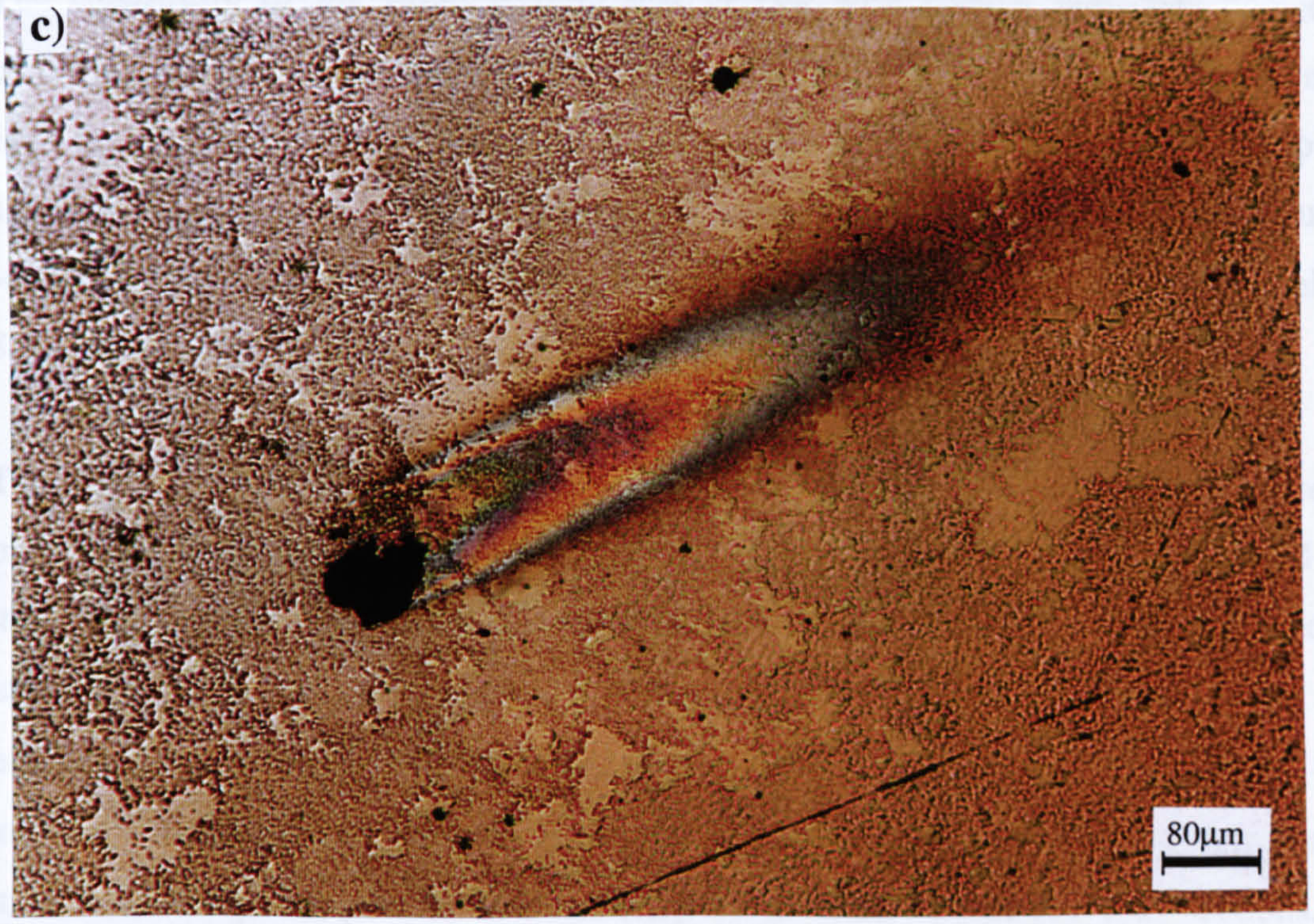
Observation after anodic polarisation

The higher initial current displayed by the sprayed coating during anodic polarisation in the previous section during high-velocity impingement is a matter of interest. As said in the experimental section of Chapter 6, the anodic polarisation was started after 15 minutes of impingement during which E_{corr} settled. Microscopic observations were carried out just after the 15 minutes of free impingement in the submerged condition at $72ms^{-1}$, which revealed some attack at the central region already occurring on the as-sprayed coating due to the mechanical effect of the liquid jet. However, no visible damage was observed on the sealed and the fused coatings after the same condition. The initial higher currents displayed by the sprayed coating appear to be associated with the existing defects that had occurred during the initial 15 minutes impingement.

Figure 8.4.11a and b shows the corrosion attack in the form of comet shaped streams on the sprayed and sealed coatings after 1-hour impingement and anodic polarisation. It appears that the attack was a little less on the sealed coatings than that on the sprayed coating.




b)
80μm


c)
80μm

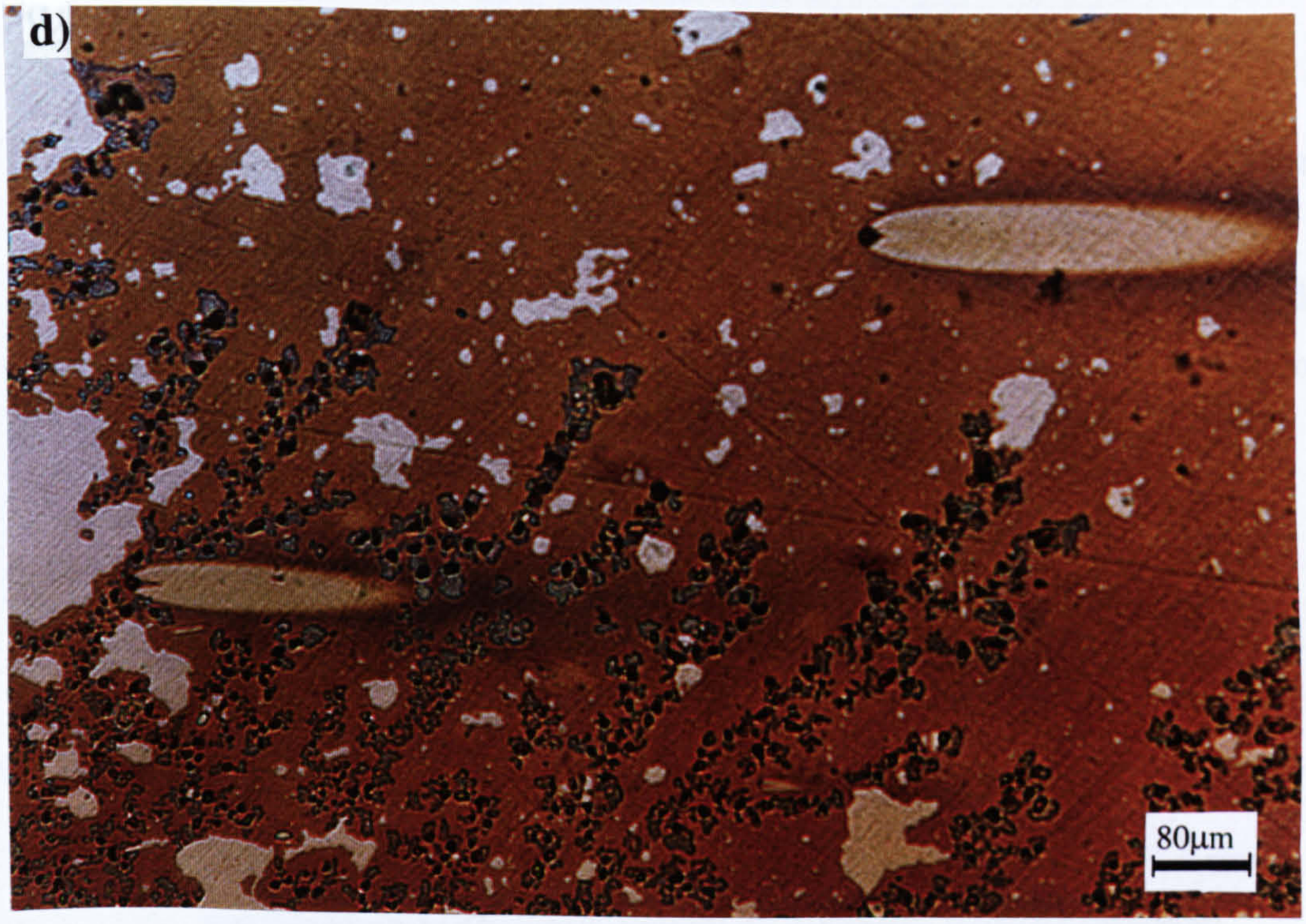


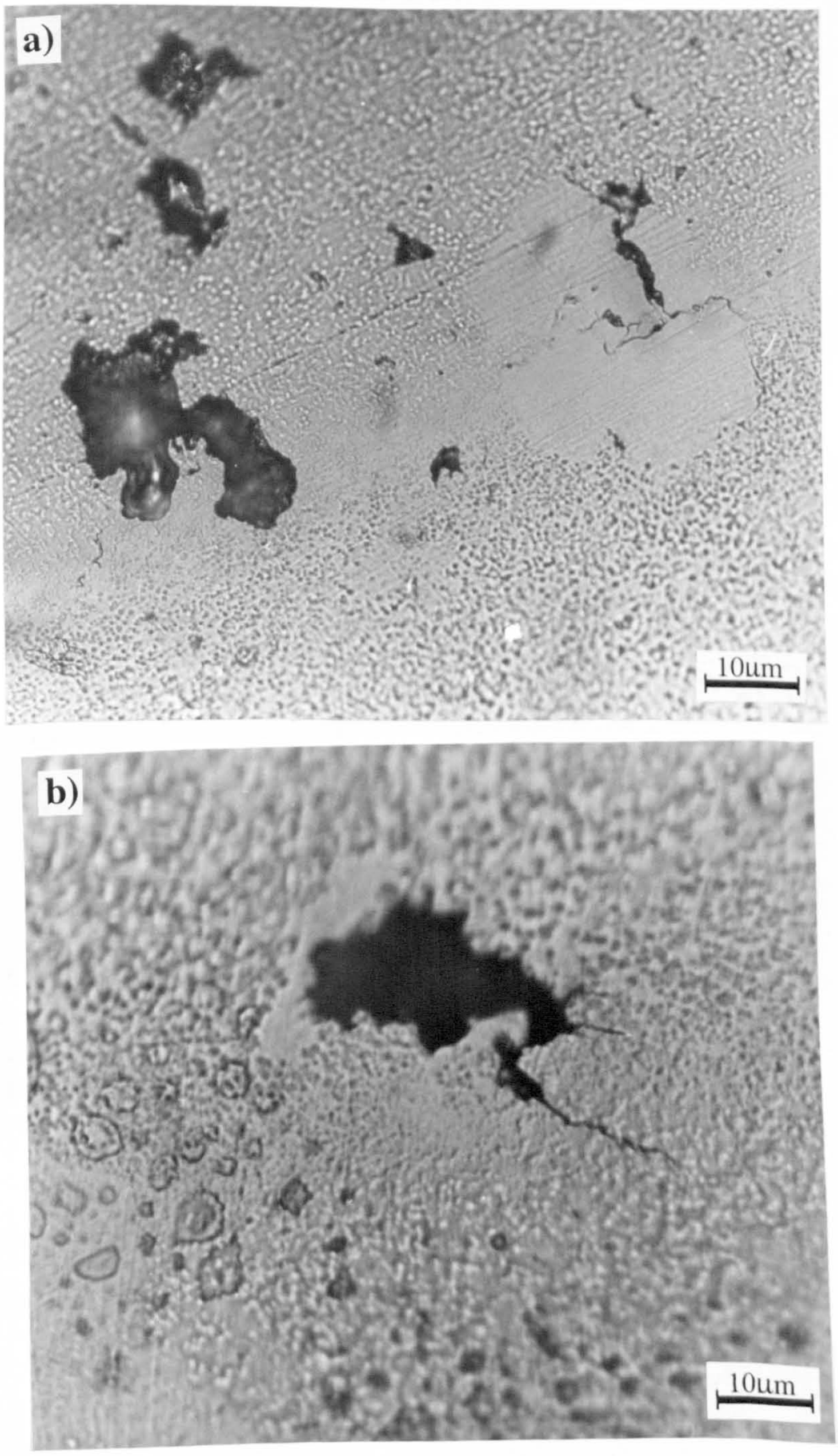
Figure 8.4.11 Corrosion attack at outer region of the specimen a) sprayed; b) sealed; c) fused coatings; and d) UNS S31603 after 1-hour high-velocity seawater jet impingement and anodic polarisation at 18°C.

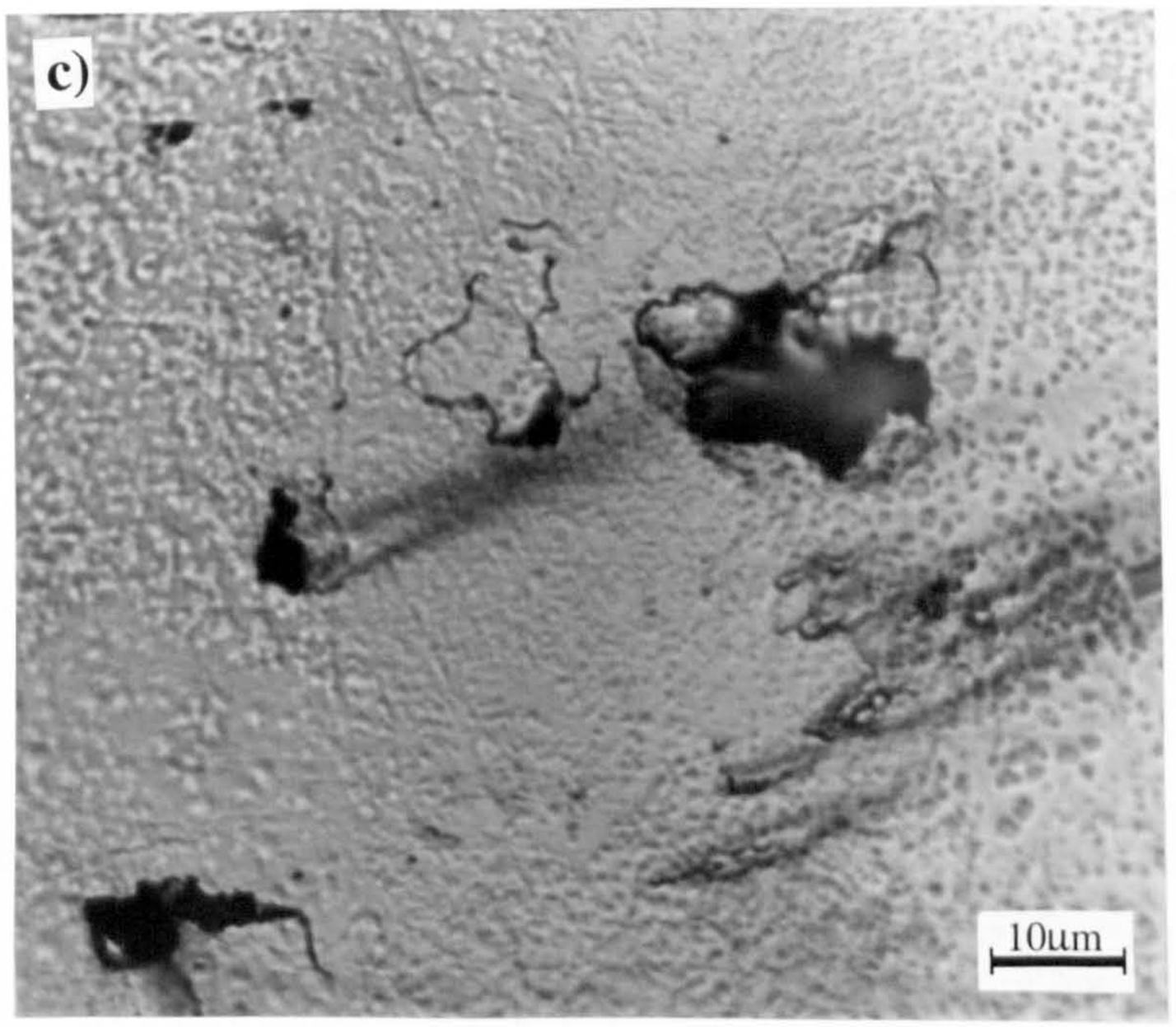
The superiority of the fused coating was shown with only a very few comet pits observed on the surface. One of the comet pits on the fused coating was shown in Fig. 8.4.11c. The stainless steel also exhibited corrosion attack in the form of comet pits as shown in Fig. 8.4.11d. Another form of corrosion attack on the stainless steel surface was associated with the formation of a thick brown coloured film, which covered almost 80% of the exposed surface.

The attack mechanism was mainly divided into two different regions. The central region of the polished surface of the sprayed and sealed coatings had attack associated with many surface cracks and crack propagation, which eventually led to dislodgement of the large chunks of materials resulting in macropits as shown in Fig. 8.4.12a and b. A maximum macropit depth of about 14μm was detected on the sprayed coating. On a microscale, corrosion attack on the sprayed and sealed coatings had also occurred at the individual hardphase particle/matrix interfaces as illustrated in previous sections. The outer region displayed attack primarily in the form of comet-shaped streams, in which

the corrosion products were emanating either from macropits or micropits as described earlier.

Figure 8.4.12c shows an example of corrosion product emanating from the hardphase/matrix interface forming smaller comets, which also shows a macropit at the comet head of a bigger comet. A small amount of crevice corrosion was also evidenced under the araldite strip, which was not more than 6-8mm of the total length covered (Fig. 8.4.12d).





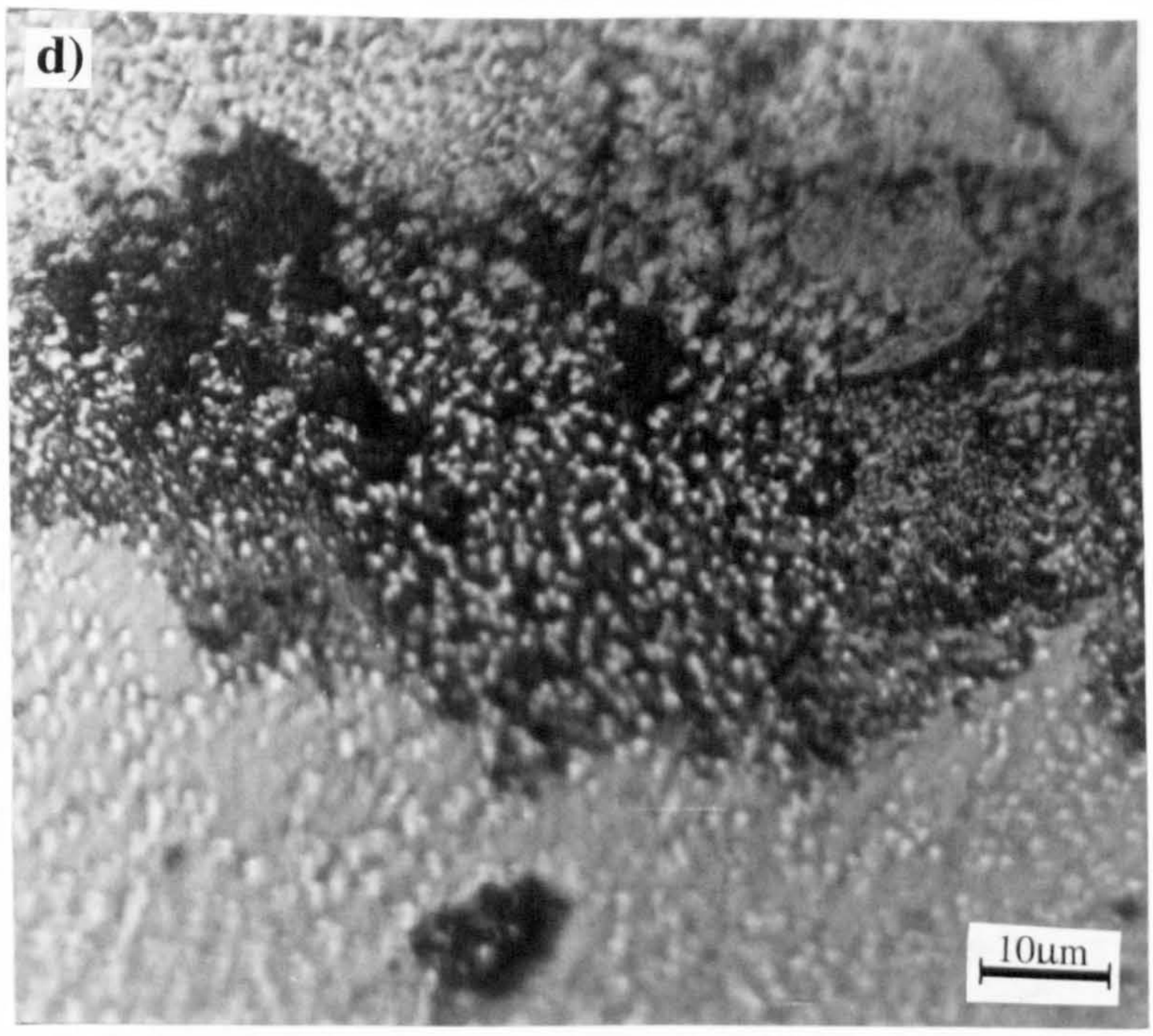


Figure 8.4.12 Corrosion attack on sprayed/sealed coating after anodic polarisation under 72ms^{-1} impingement at 18°C: a) Cracking and macropits due to dislodgement of chunk materials (central region); b) crack propagation from the existing pit (central region); c) attack at the hardphase/matrix interface; and d) crevice corrosion.

Corrosion attack on the fused coating had occurred only at the outer region in the form of comets. These comet pits were significantly deeper than those on the sprayed or sealed coatings. The largest pit depth was measured to be about 24μm. No attack was observed at the central region associated with the liquid jet but initiation of the matrix

corrosion was observed all over the exposed area. Significant crevice corrosion on the fused coating was observed under the araldite strip as shown in Fig. 8.4.13a. SEM microscopy of the same region revealed that the crevice corrosion was associated with a preferential dissolution of the matrix leaving the unsupported hardphase particles resulting in their dislodgement (Fig. 8.4.13b).

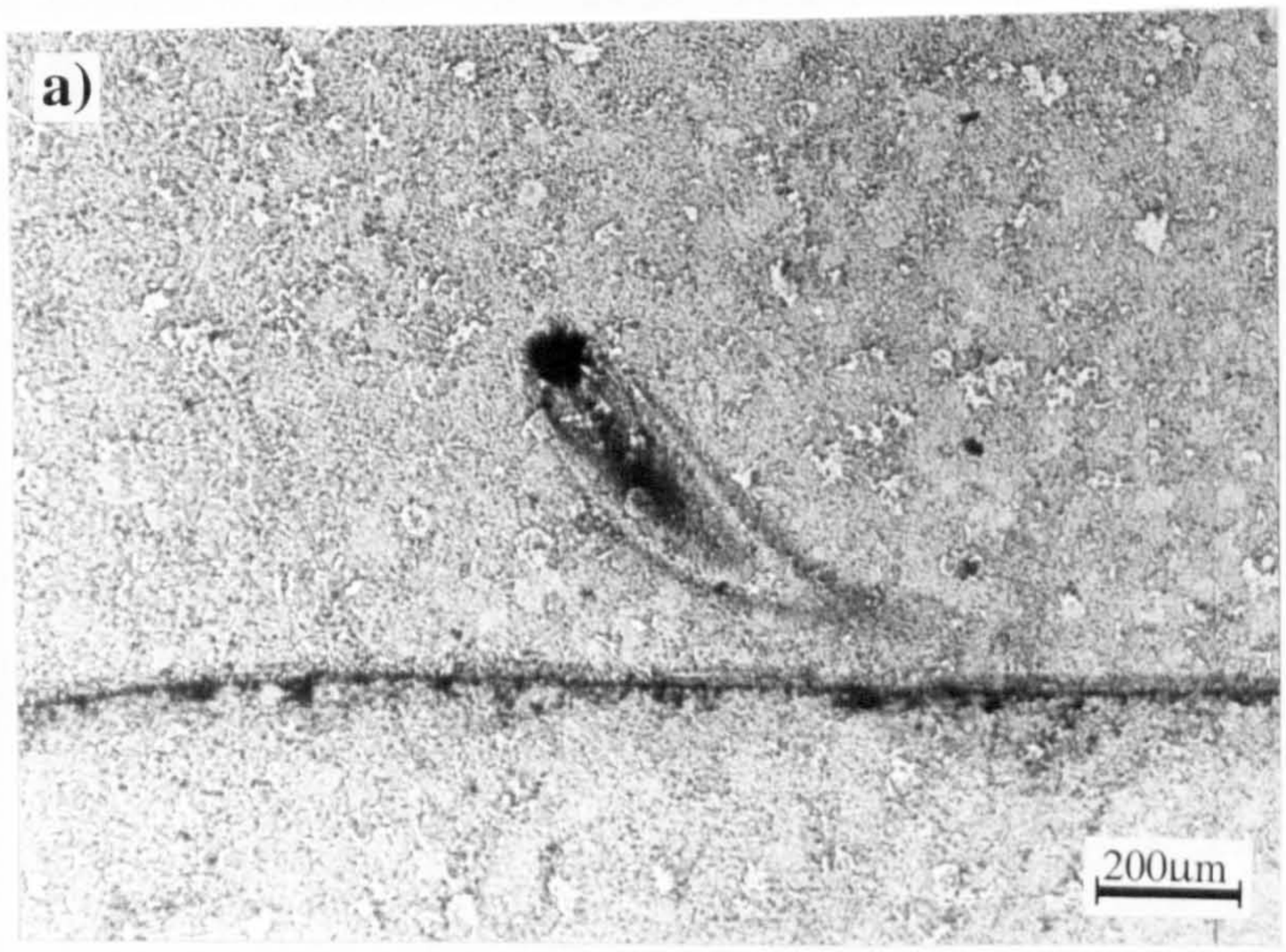
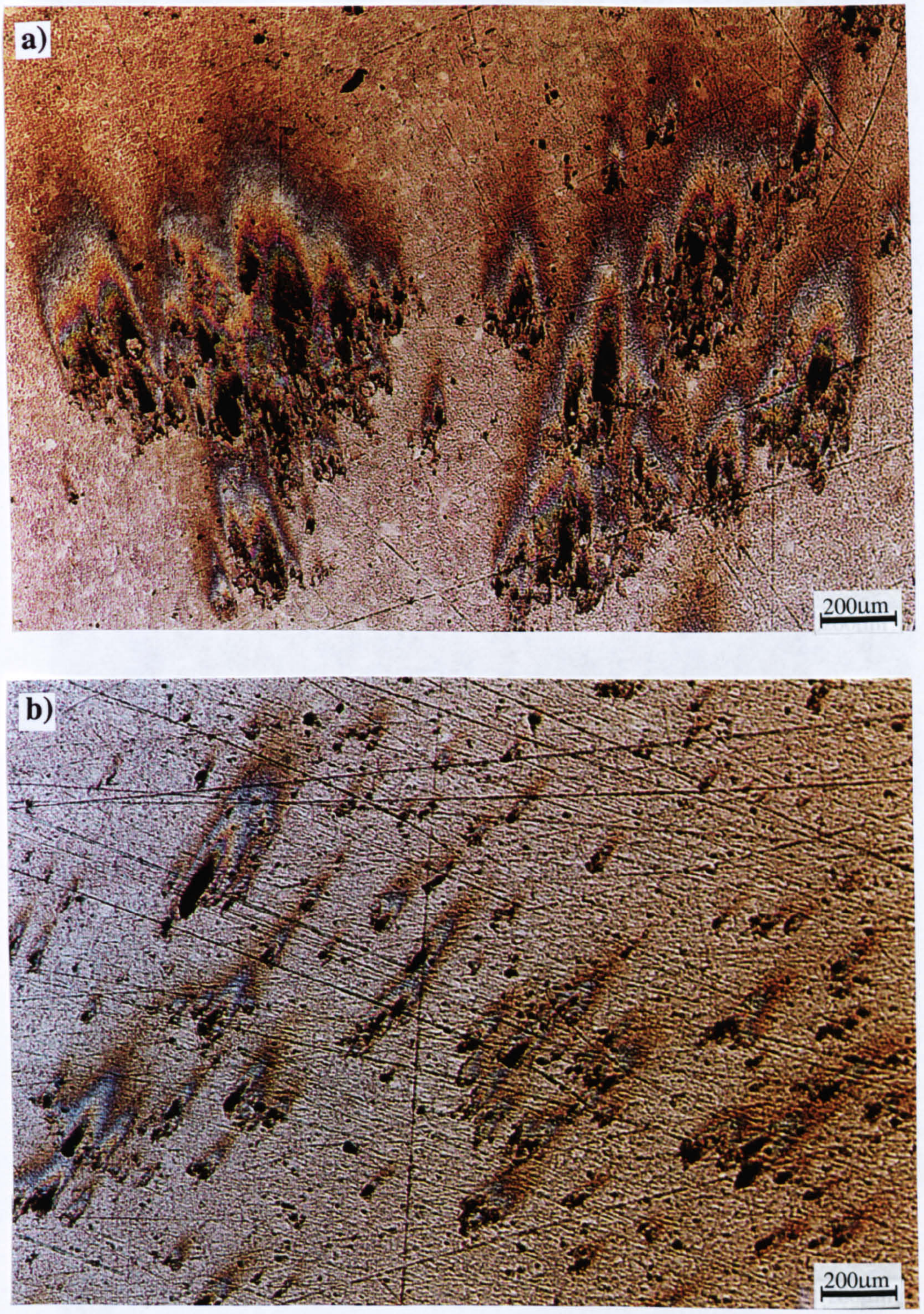
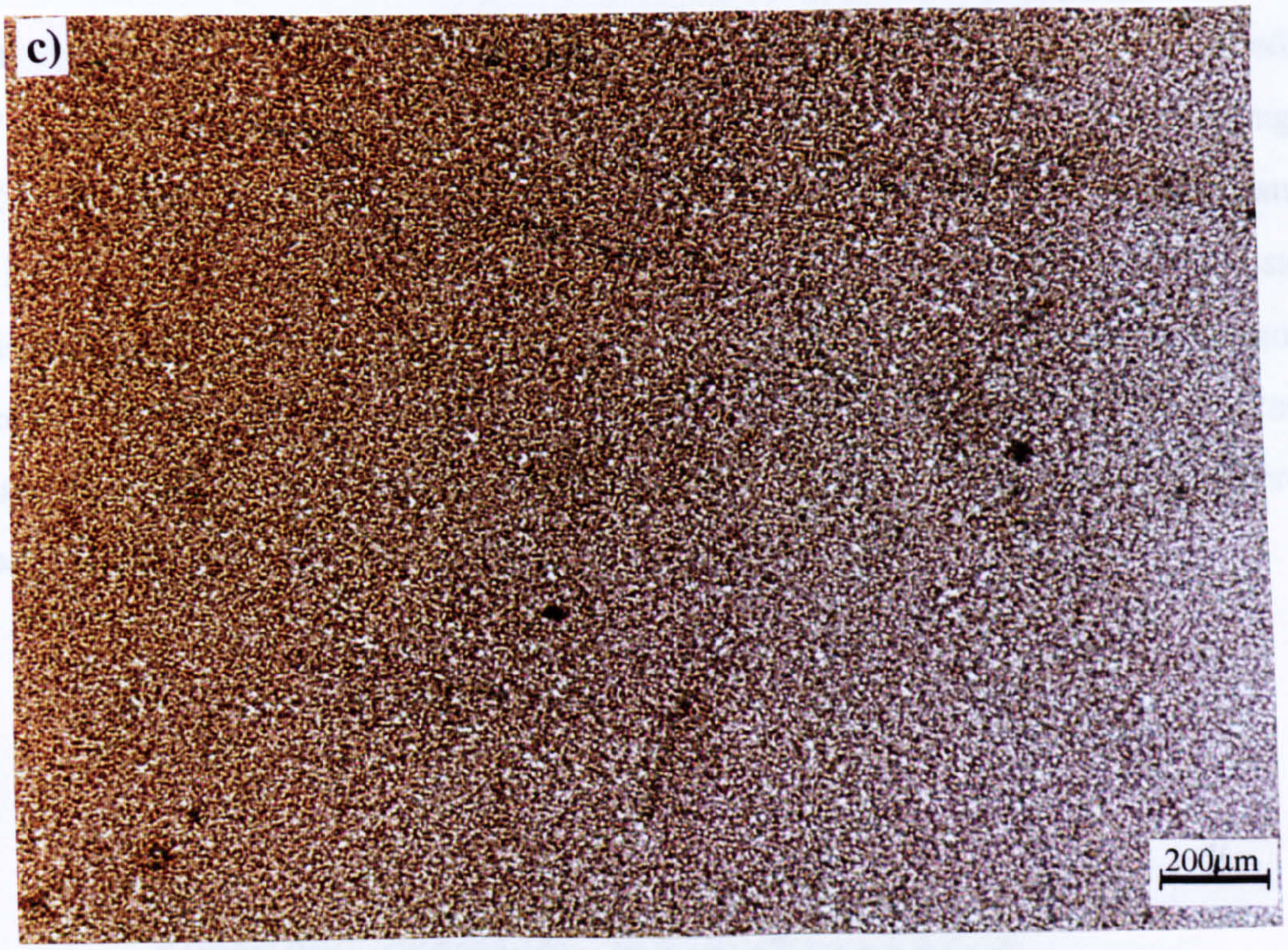


Figure 8.4.13 a) Optical micrograph showing severe crevice corrosion under the araldite strip; and b) SEM micrograph of the same region showing corrosion mechanism associated with preferential dissolution of the matrix leaving the unsupported hardphase particles resulting in their dislodgement at 18°C.

The increased temperature of 50°C resulted in much severe corrosion attack on all the materials tested. Figure 8.4.14 shows the low magnification optical micrographs of outer region of the coatings and the stainless steel after anodic polarisation under high-

velocity impingement at 50°C. More attack was obvious in Fig. 8.4.14 on the sprayed coating than on the sealed coating under similar experimental condition. Figure 8.4.14c and d clearly shows the severe corrosion of the fused coating and the stainless steel respectively with clearly visible dull matrix on the fused coating and a thick multicoloured film over the entire surface of the stainless steel specimen.





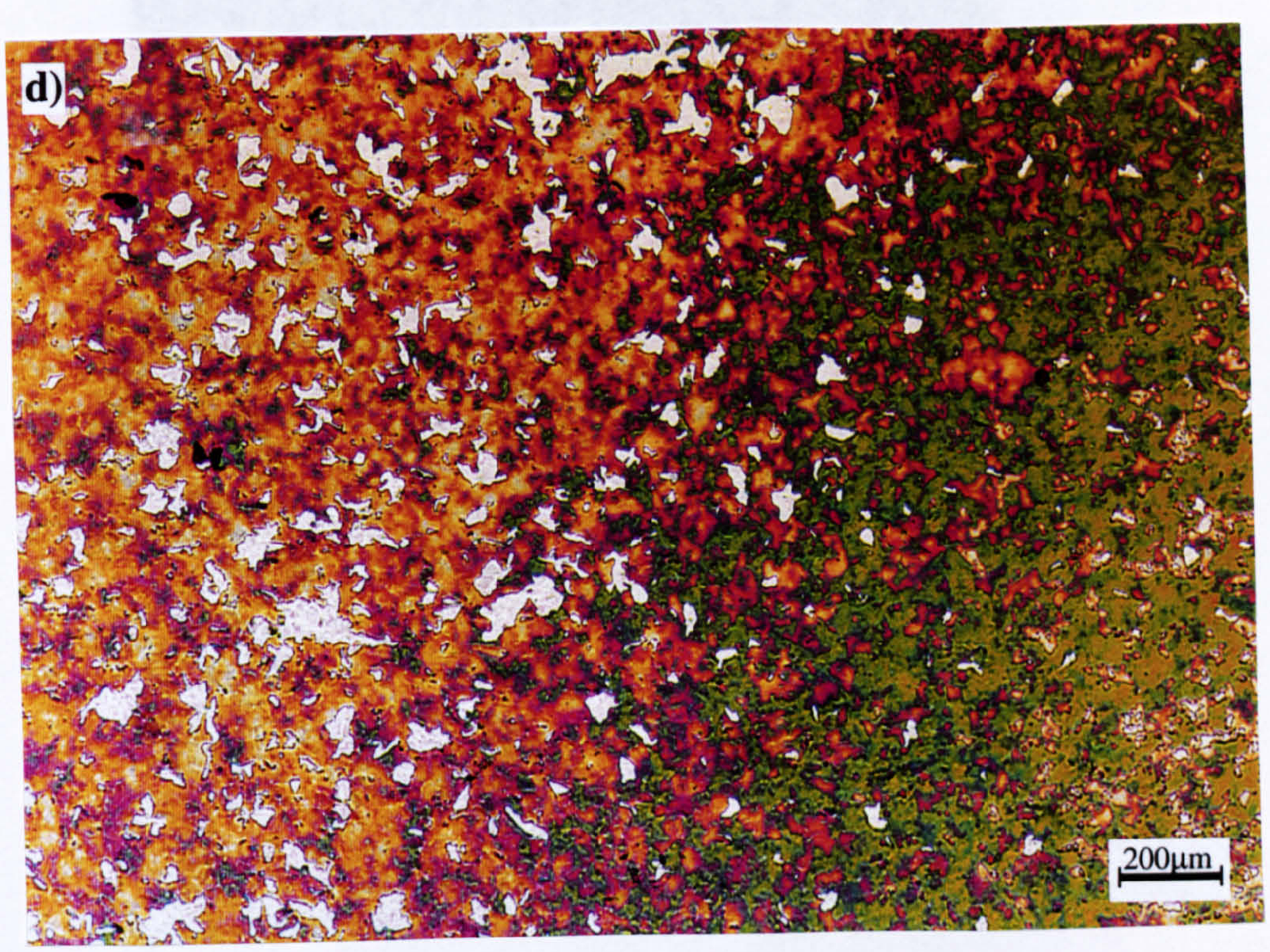
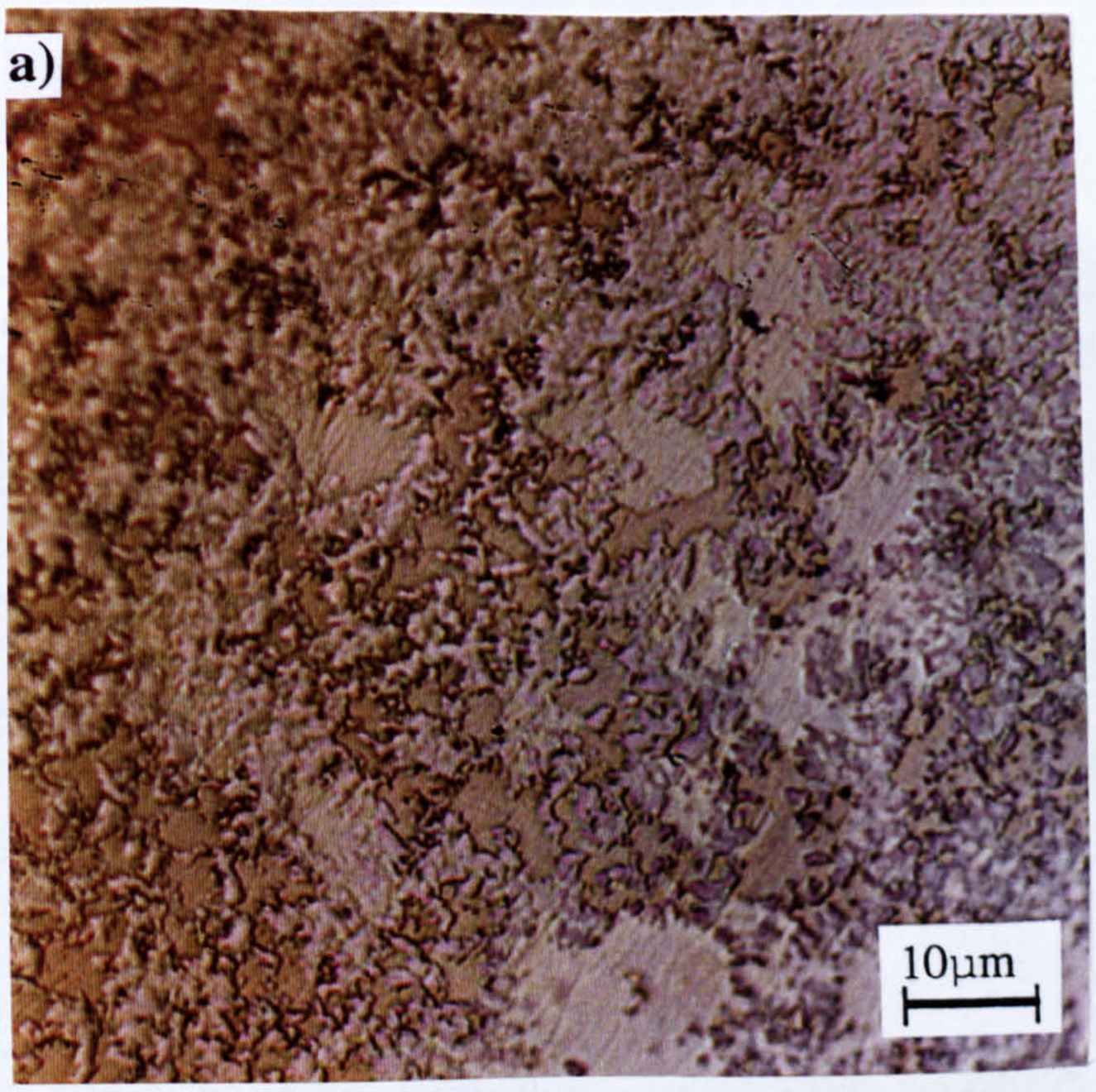
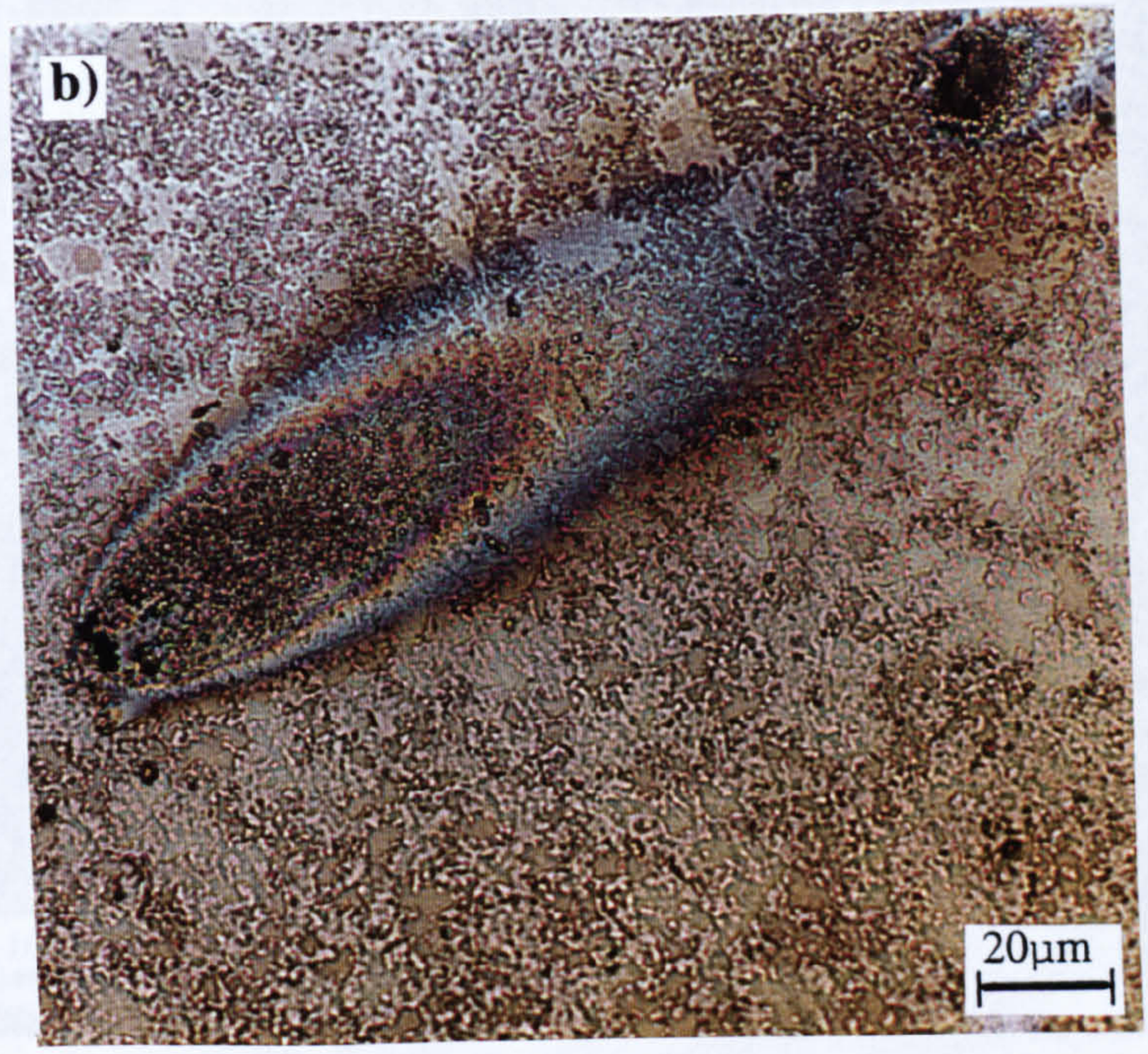


Figure 8.4.14 Corrosion attack at the outer region after anodic polarisation under 72ms^{-1} impingement at 50°C: a) sprayed; b) sealed; c) fused coatings; and d) UNS S31603.

Higher magnification in Fig. 8.4.15a clearly shows the matrix corrosion over the entire exposed surface of the fused coating. An interesting observation was that the comet pits on the fused coating were significantly smaller at 50°C compared to that observed at 18°C. Figure 8.4.15b shows one of the biggest comet attack seen on the fused coating at 50°C. More crevice corrosion was evidenced on the fused coating once the temperature was increased up to 50°C (Fig. 8.4.15c). Comet pits formed on the stainless steel surface at 50°C were much larger than those observed at 18°C. Figure 8.4.15d shows the comets formed on the stainless steel surface after anodic polarisation under 72ms^{-1} jet impingement at 50°C. Some differences of corrosion mechanisms at different temperatures are detailed in Table 8.4.2.




b)
20μm

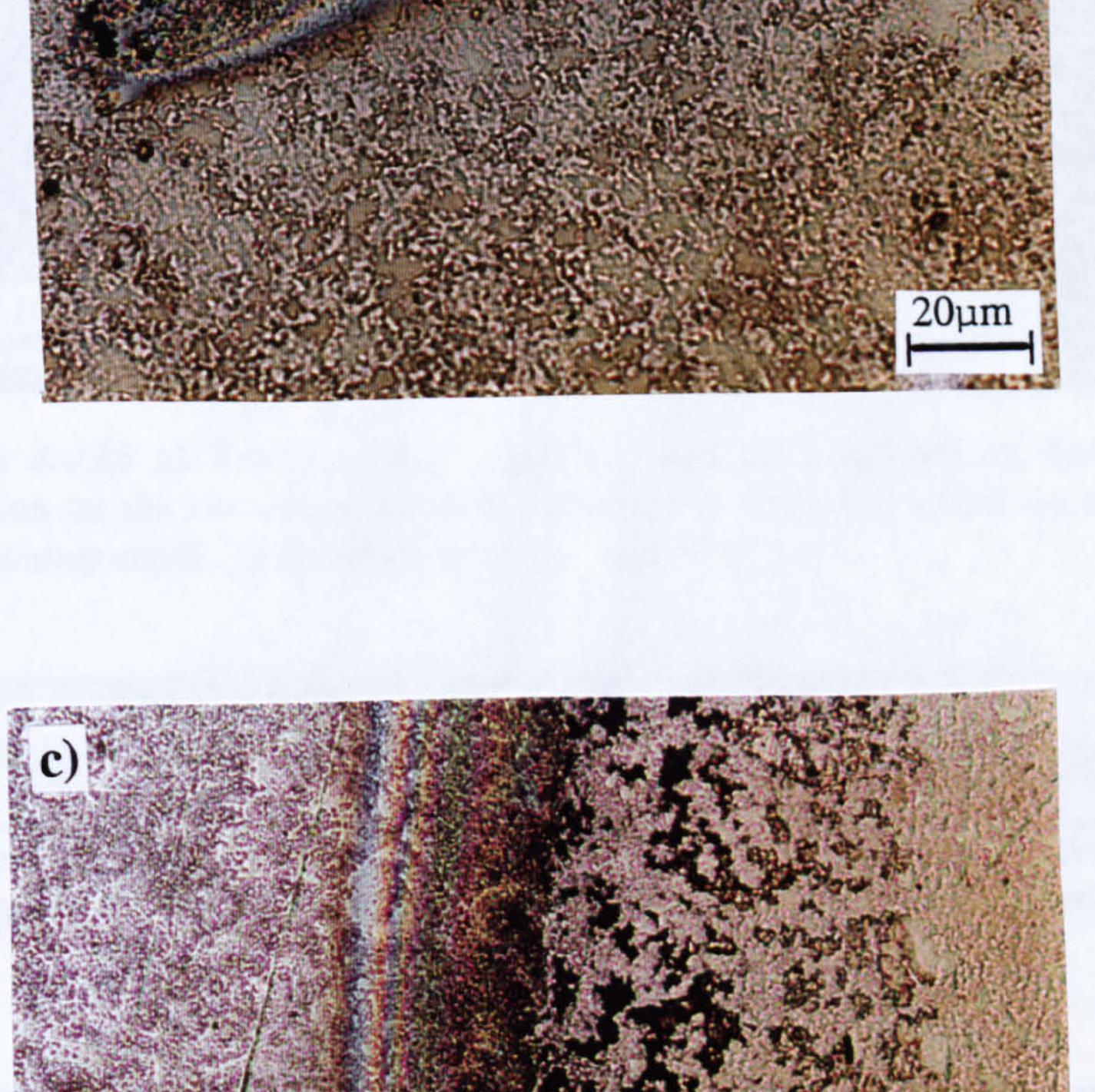

c)
80μm



Figure 8.4.15 a) Severe matrix corrosion; and b) comet pit; c) severe crevice corrosion on the surface of a fused coating; and d) comet attack on the stainless surface after anodic polarisation at 72ms^{-1} and 50°C.

Coating	Total crevice length (mm)		Maximum pit depth (μm)		Comments	
	18°C	*50°C*	*18°C*	*50°C*	*18°C*	*50°C*
As-sprayed	4-6	9-14	14	20	Severe corrosion attack at both central and outer wear regions associated with cracking, crack propagation, flaking	Corrosion attack increased than at 18°C
Vacuum-sealed	5-8	10-12	12	16	Similar to above	Similar to above
Vacuum-fused	25-30	64-66	24	8	Much less attack at outer region, etching of matrix corrosion	Enhanced corrosion of matrix over the entire exposed surface.
UNS S31603	30-32	43-47	4	7	Matrix corrosion shown by a thick coloured film formation over the entire surface.	Increased corrosion attack shown by coloured film over the entire surface.

Table 8.4.2. Corrosion mechanisms on coatings after anodic polarisation at two temperatures under 72ms^{-1} impingement.

8.5 High velocity liquid erosion-corrosion of Coating BII

Section 8.4 showed the electrochemical corrosion behaviour of *Coating* BI and stainless steel under high-velocity impingement condition at 18°C and how the increased temperature affects the resistance to corrosion degradation of all materials. This section will include erosion-corrosion behaviour of *Coating* BII, conducted under similar condition as in previous experiment except the temperature being kept at 18°C.

Weight loss measurement

Under solid-free liquid impingement at $72ms^{-1}$, all coatings (as-sprayed, vacuum-sealed, vacuum-fused coatings) displayed a zero weight loss after a 1-hour test, except for the stainless steel, which showed a small weight loss of about 0.1mg. Further experiments were conducted for a total of 6 days with the sample coupons being weighed after 1, 2, 4, 6 days and observed under the microscope to visualise the weight loss mechanism. Weight loss results obtained are given in Table 8.5.1 and reveal higher material losses for the as-sprayed and vacuum-sealed coatings after the 4-days test by almost 2 times. The vacuum-fused coating, in contrast, displayed significant resistance over the 4-days period and showed almost no weight loss. A small amount of weight loss on the vacuum-fused coating was observed only after 6-days exposure. Application of cathodic protection (CP), conducted for 2 days, significantly reduced the weight loss. Figure 8.5.1 shows the least weight loss displayed by vacuum-fused coating after 6 days of solid free liquid impingement.

Material	**TWL under liquid impingement**					**Weight loss under CP**
	1 hour	***1 day***	***2 days***	***4 days***	***6 days***	***2 days***
As-sprayed	0.0 0.0	0.5 0.6	1.1 1.0	1.9 1.8	2.3 2.5	0.9 0.7
Vacuum-sealed	0.0 0.0	0.5 0.4	1.2 0.9	1.8 1.7	2.6 2.4	0.8 0.7
Vacuum-fused	0.0 0.0	0.0 0.0	0.0 0.0	0.0 0.1	0.3 0.4	0.0 0.0
UNS S31603	0.1 0.1	0.5 0.5	0.7 0.8	0.9 0.8	0.9 1.2	0.6 0.6

Table 8.5.1 Weight loss results (mg.) of polished specimens under solid-free liquid impingement at 18°C and $72ms^{-1}$.

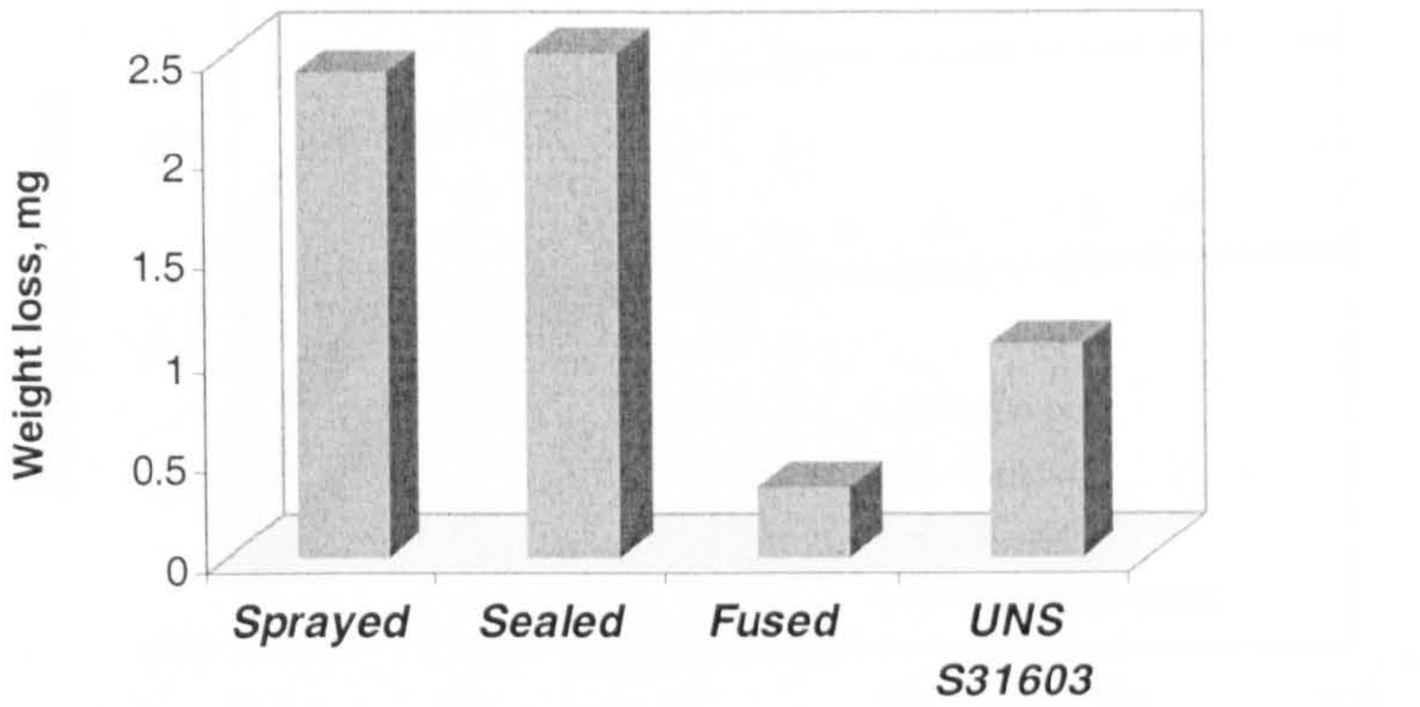
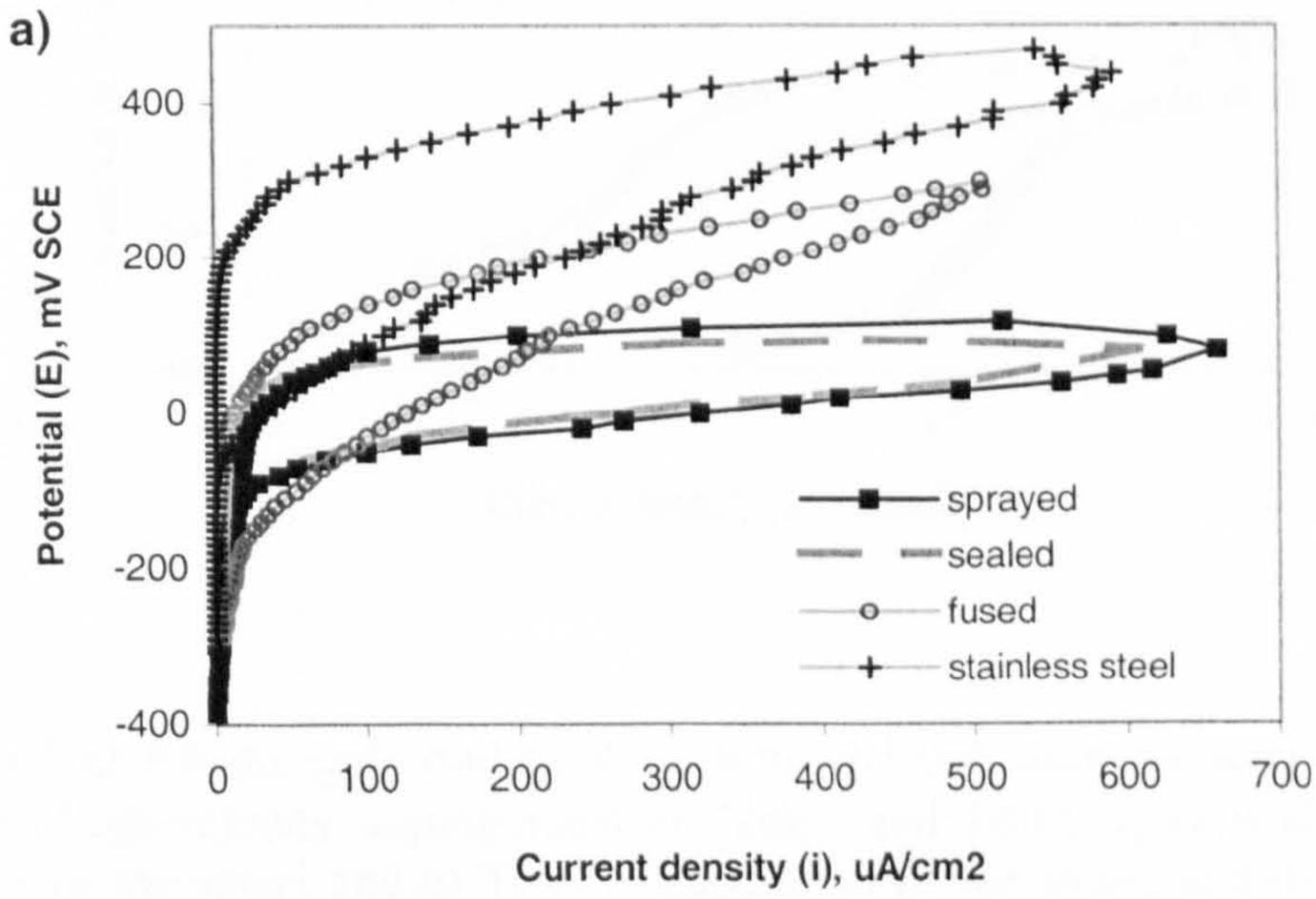


Figure 8.5.1 Average weight loss after 6 days solid-free liquid impingement under $72ms^{-1}$ jet velocity and 18°C.

Anodic polarisation

The results of the anodic polarisation tests on as-sprayed, vacuum-sealed, vacuum-fused coatings and stainless steel 'UNS S31603' performed after 2 days of $72ms^{-1}$ solid-free high velocity impingement at 18°C are shown in Fig 8.5.2a. The stainless steel displayed a classic passive behaviour-represented by the low currents over a wide range of potential even under such severe impingement condition. The breakdown potential 'E_b' shown in Fig. 8.5.2b for the stainless steel was about +200mV SCE.



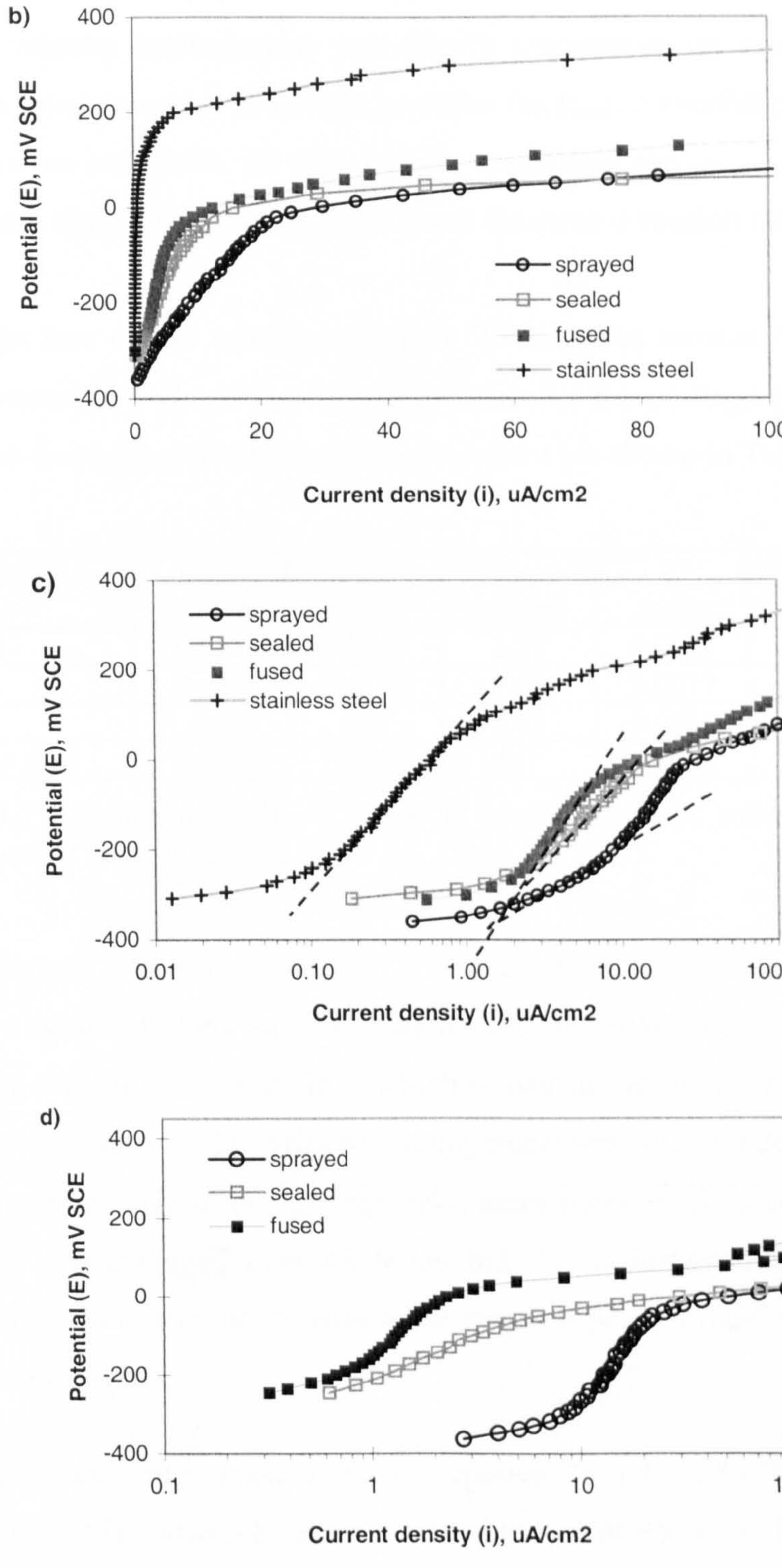


Figure 8.5.2 a) Anodic polarisation of *Coating* BII (on stainless steel substrate) after 2-days high-velocity impingement at 72ms^{-1} and 18°C; b) expanded anodic polarisation of the same; and c) Tafel extrapolation of the same; and d) reference Tafel extrapolation plots for *Coating* BI (on carbon steel substrate) from anodic polarisation results performed after 1-hour high-velocity impingement.

In contrast vacuum-sealed and vacuum-fused coatings exhibited a semi-passive behaviour displayed by a small amount of initial current in the 'E_b-E_{corr}' region. The effect of high velocity impingement was clearly pronounced on as-sprayed coating displayed by its steady increase of current just after the E_{corr}. Nevertheless Tafel plots in Fig. 8.5.2c give an indication of difficulty in specifying the 'i_{corr}' for the sprayed coating, it appears that all the coatings have about the same corrosion rate.

The total weight loss due to erosion-corrosion 'TWL'; pure erosion 'E' with applied CP; pure corrosion 'C' and synergy 'S' components for the coatings and the stainless steel under solid-free high-velocity liquid impingement are shown in Tables 8.5.2.

Material	**TWL** mg/hr	**E** mg/hr	**i_{corr}** $\mu A/cm^2$	**C** mg/hr	**S** mg/hr
Sprayed	0.022	0.0166	1.57	0.0074	-0.002
Sealed	0.022	0.0156	1.65	0.0077	-0.001
Fused	0.0	0.0	1.45	0.0068	-0.006
Stainless steel	0.016	0.0125	0.1	0.0005	0.003

Table 8.5.2 Breakdown of 'E', 'C' and 'S' under 2-days of solid-free liquid impingement at $72ms^{-1}$ and 18°C.

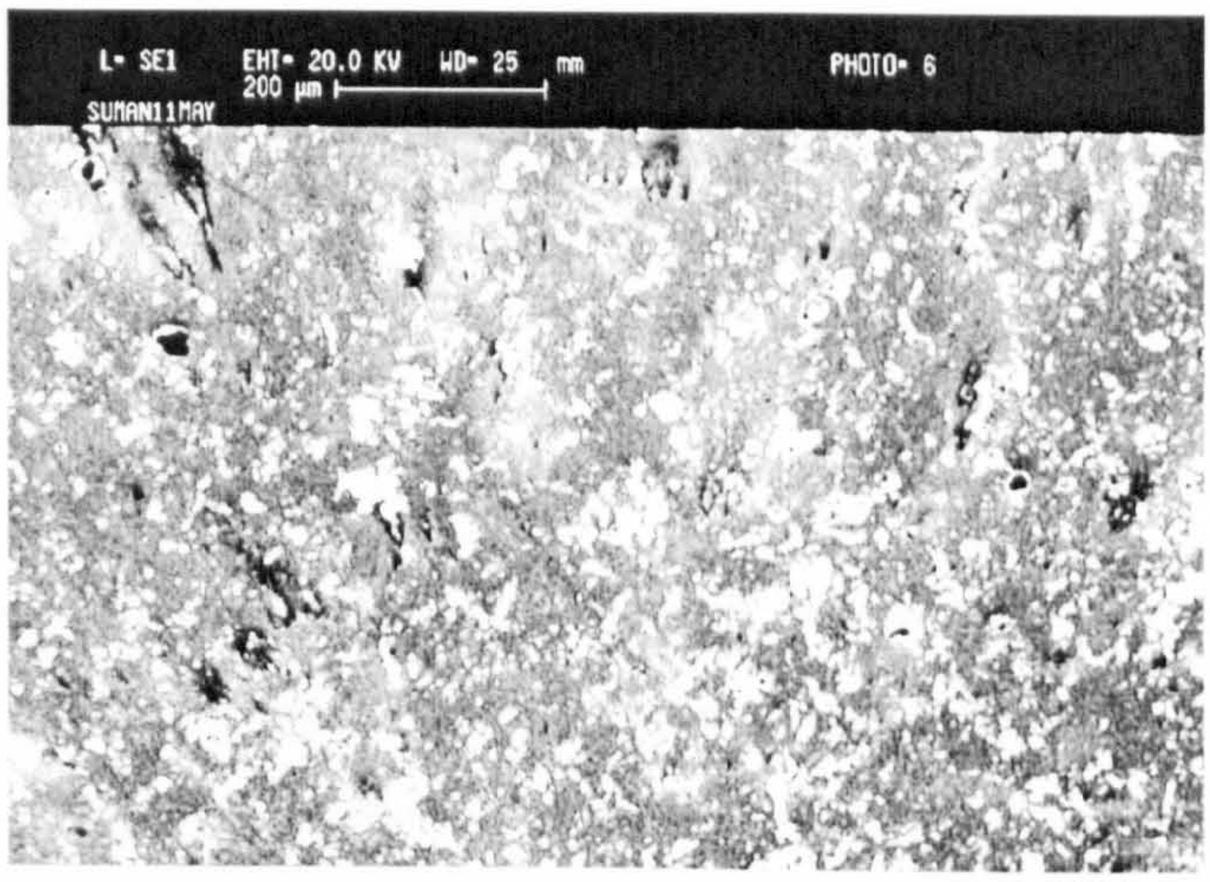
Table 8.5.2 displays negatives synergies 'S' for the coatings during the 2-days test. However, these values are very small in magnitudes. Moreover there is a complication due to corrosion rate variation with time, which is also shown by a lower corrosion rate after immediate exposure to high velocity impingement test (Fig. 8.5.2d) than displayed by the 2-days impingement tests. Consequently, assessment of 'S' is complex, because 'TWL' and 'E' are averaged over 48 hours but 'C' is instantaneous at 48 hours. Therefore, reliable estimation of 'S' over these long test periods requires more frequent corrosion rate monitoring.

Another question mark over these apparent negative 'S' relates to the fused coating, where measured 'TWL' after 48 hours is zero but 'C' at 48 hours is finite. At face value, this is impossible and obviously arises an account of experimental errors in measuring such low material losses and/or increases in corrosion rate will be the passage of time. Nevertheless, the notion of possible negative synergies will be discussed in Chapter 10.

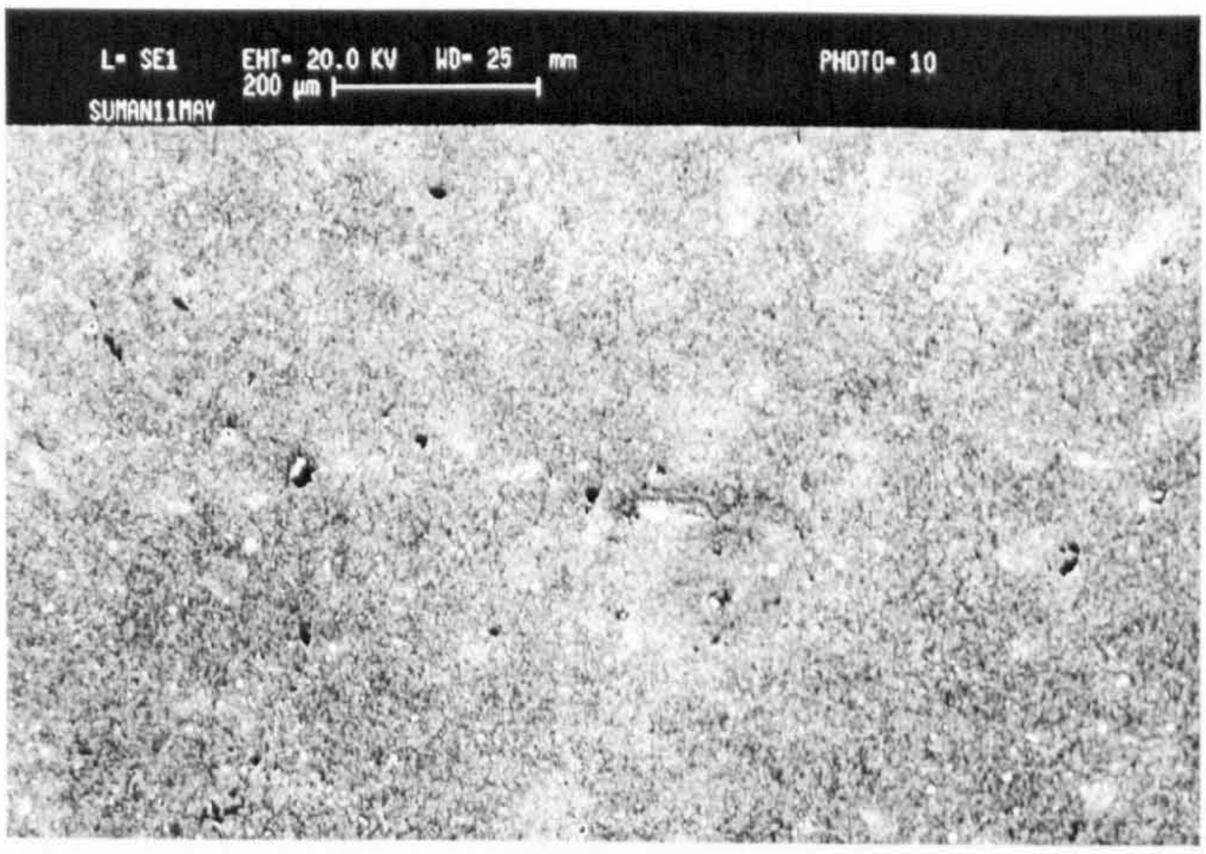
Attack mechanisms after erosion-corrosion under high velocity impingement

Microscopic observation revealed some of the interesting mechanistic approaches that showed the difference on erosion-corrosion behaviour between the materials tested. Once again both sprayed and sealed coating displayed rather similar modes of damage mechanism and hence only photomicrographs of the sprayed coating will be referred in the text. SEM images in Fig. 8.5.3 show severe damages right under the high velocity impinging jet on the polished surfaces of the specimens. Superiority of the fused coating is displayed by its least material damage under the central jet.

a)



b)



c)

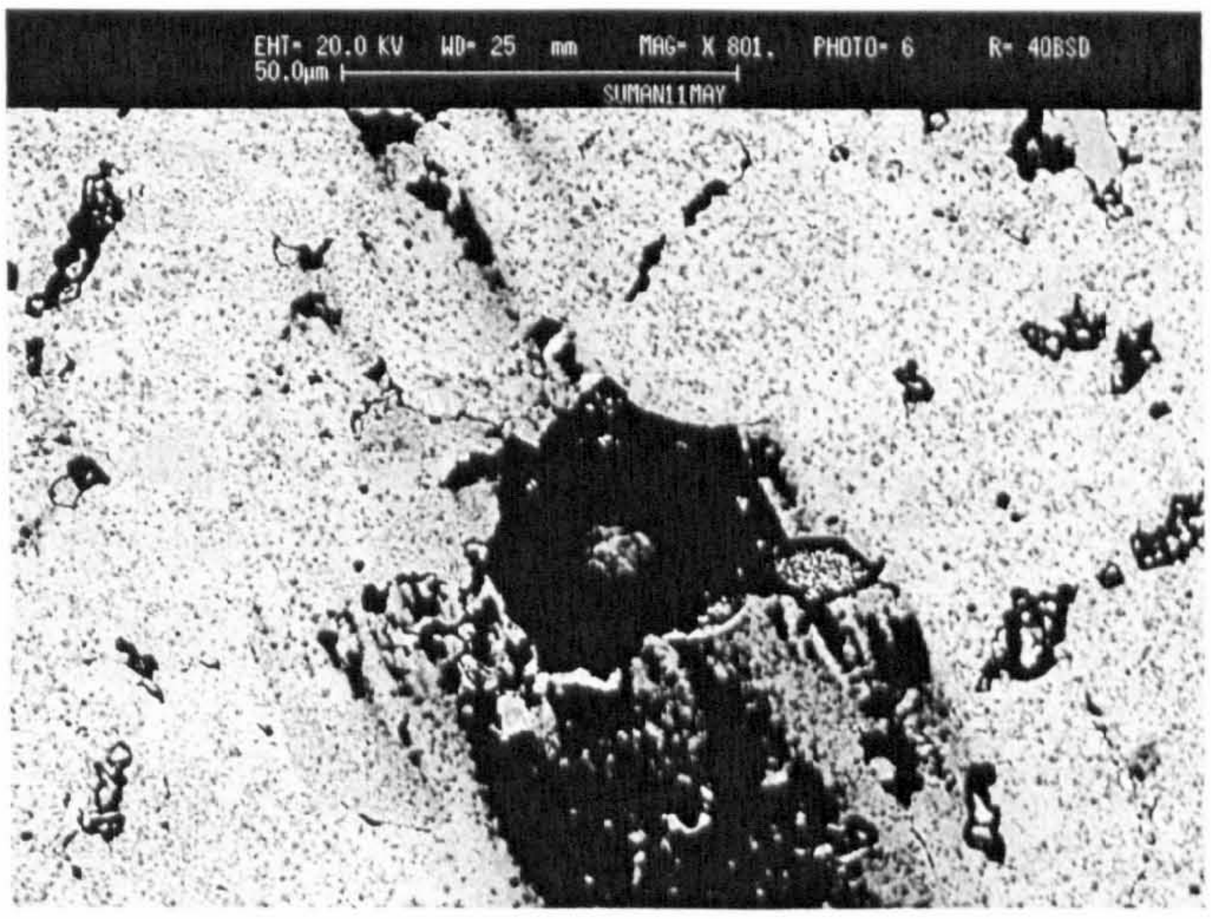


Figure 8.5.3 SEM micrographs showing damage under central jet after 6-days of solid-free 72ms^{-1} impingement without polarisation: a) sprayed coating; b) fused coating; and c) UNS S31603 in submerged condition.

Central wear region

Distinctions in material loss mechanisms were readily visible after 6-days of solid-free liquid impingement. The as-sprayed coating displayed a rather brittle failure mechanism shown by the extensive drilling under the central wear region by the high velocity water jet and further propagation of the cracks from the existing pits, which results in the removal of larger material chunks (Fig. 8.5.4a). Another mechanism is the corrosion attack around the individual splat particles that results in loss of splats on continuous impact of corrosive water jet as shown in Fig. 8.5.4b.

a)



b)

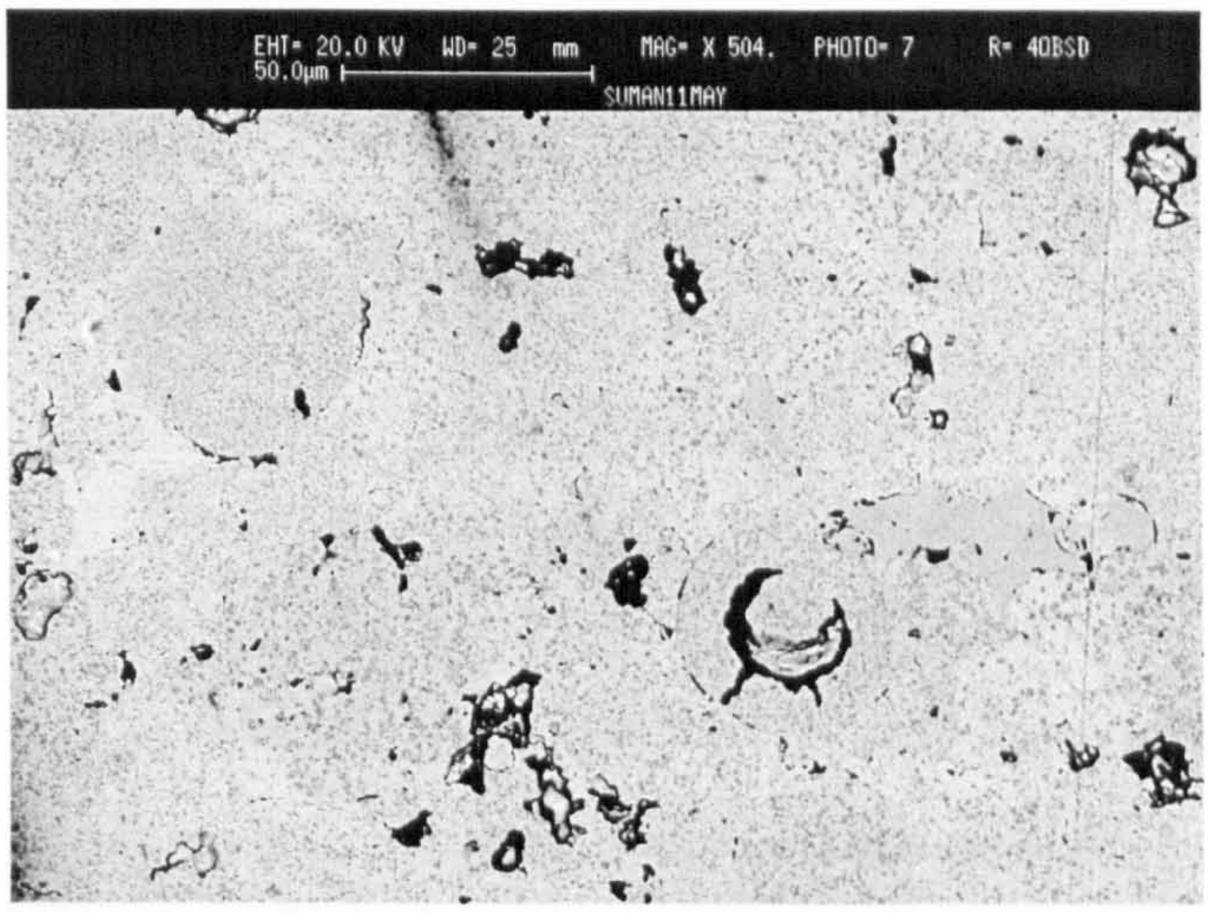


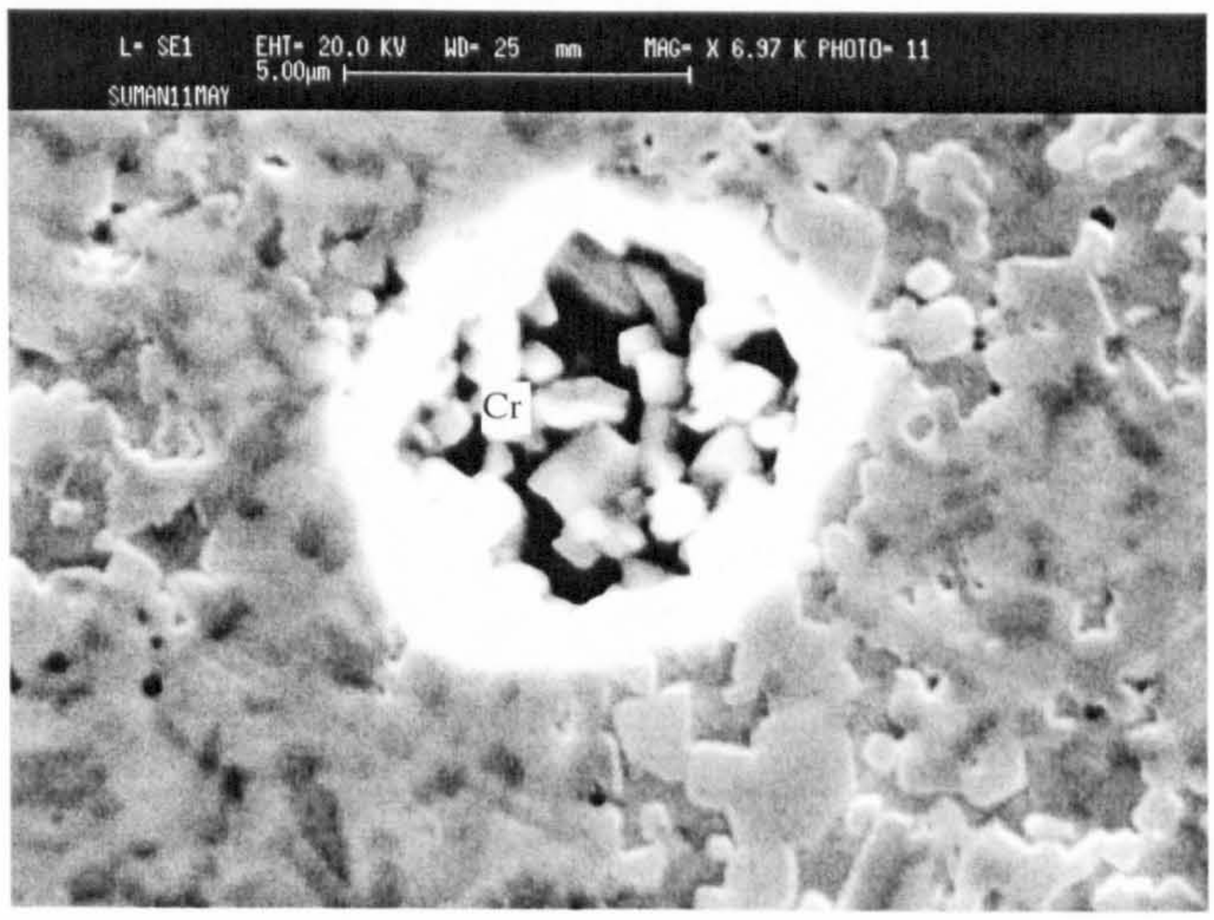
Figure 8.5.4 Higher magnification SEM images of central region of the sprayed coating after 6-days free impingement showing a) corrosion product emanating from a macropit and crack propagation; b) corrosion attack around several splat particles.

In contrast, the vacuum fused coating displayed a ductile ploughing effect (Fig 8.5.5a) shown by its material being removed under the central wear region and formation of shallow craters with raised lips during the 6-days free impingement. Figure 8.5.5a also shows corrosion of the exposed area with micropitting due to hard particles' loss as described in previous section. Another form of a possible localised corrosion was observed at the central wear region on the vacuum fused coating showing pit propagation within the existing pit. Figure 8.5.5b shows such an example, which was anodically polarised after 2-days of solid-free liquid impingement. Microanalysis on particles denoted 'Cr' within the pit revealed that they were chromium rich hard particles amounting up to 35% Cr, which are left unsupported after the surrounding matrix had corroded. Material removal on the stainless steel is shown in Fig 8.5.5c with a formation of a deep crater 'C' with raised lip 'L'. This lip breaks on subsequent impacts of the liquid-jet resulting in material loss.

a)



b)



c)

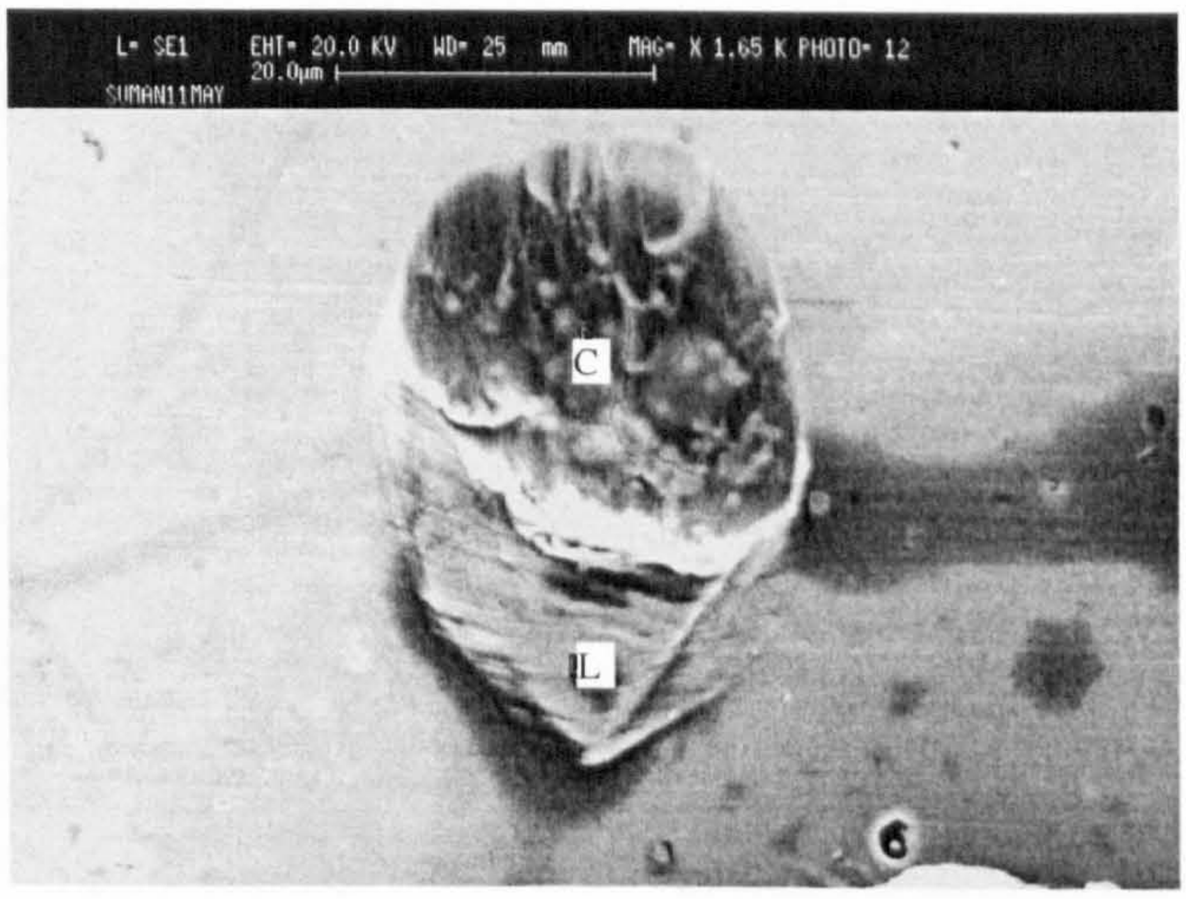
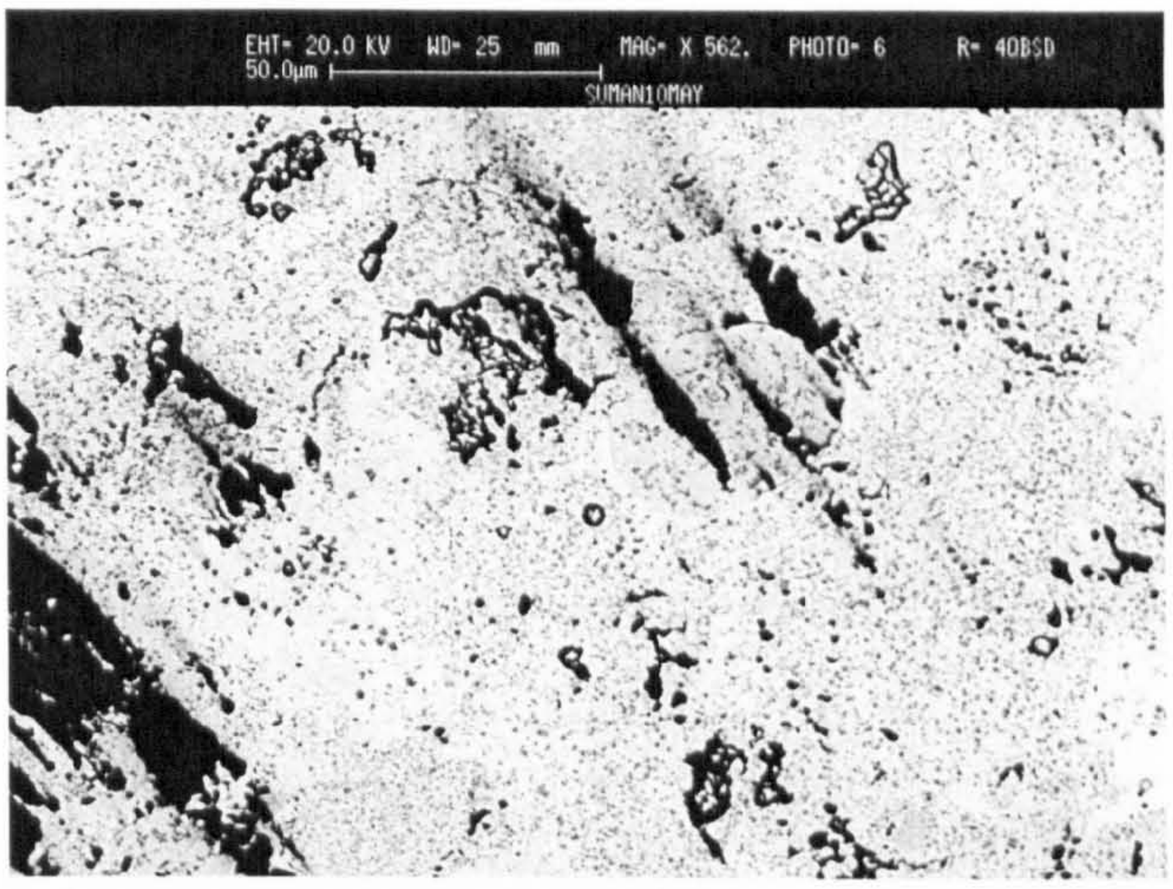


Figure 8.5.5 SEM images showing central wear region of a) vacuum fused coating after 6-days free-impingement; b) pitting corrosion within the local pit (anode) after 2-days free-impingement and anodic polarisation; and c) UNS S31603 after 6-days of solid-free liquid impingement at 72ms^{-1} jet velocity and normal impact.

Outer wear region

The wear mechanism at the region 5mm away from the centre showed corrosion attack with a large number of comet streams on the as-sprayed and vacuum-sealed coatings, which were emanating primarily from the corrosion attack at the particles splat boundaries resulting in their dislodgement due to mechanical action of the impinging jet. Figure 8.5.6a shows such corrosion mechanism after the anodic polarisation of the sprayed coating. In addition localised removal of the hardphase particles to form micropits was also observed on the sprayed and sealed coatings.

a)



b)

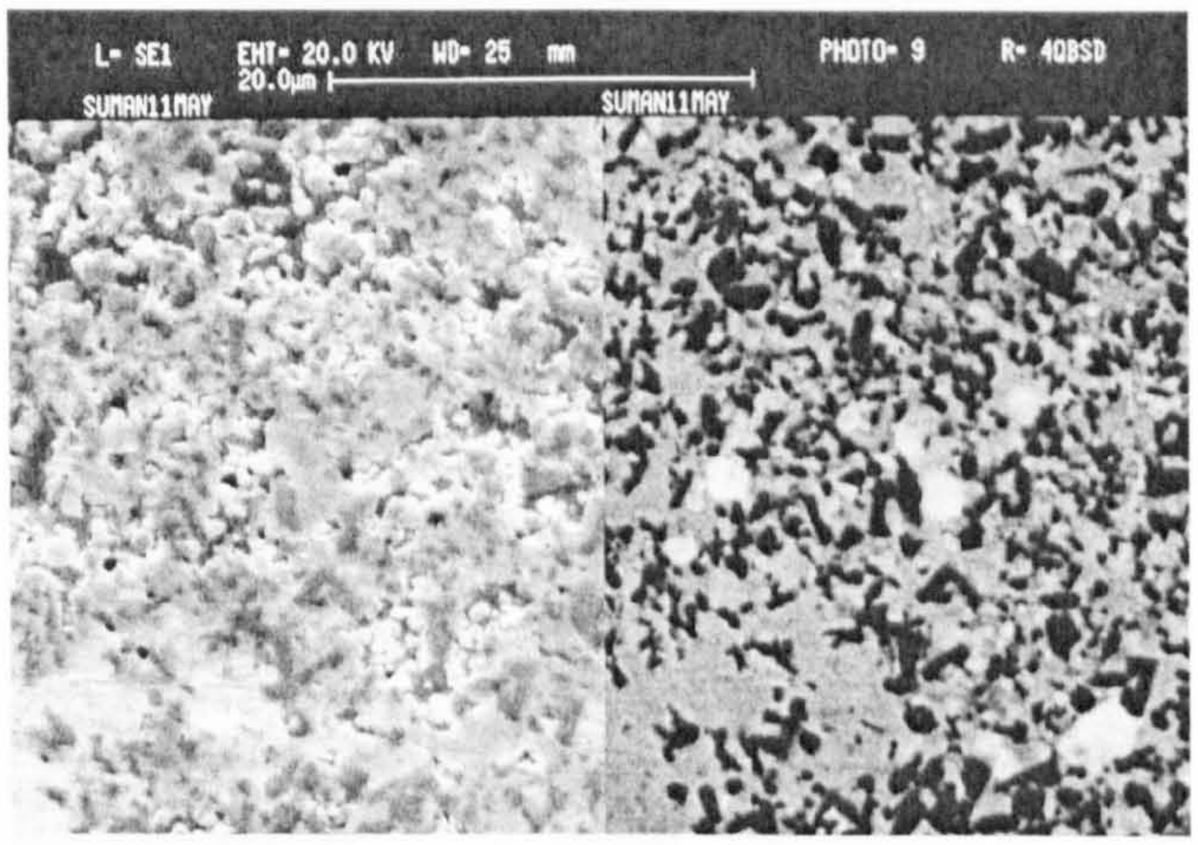
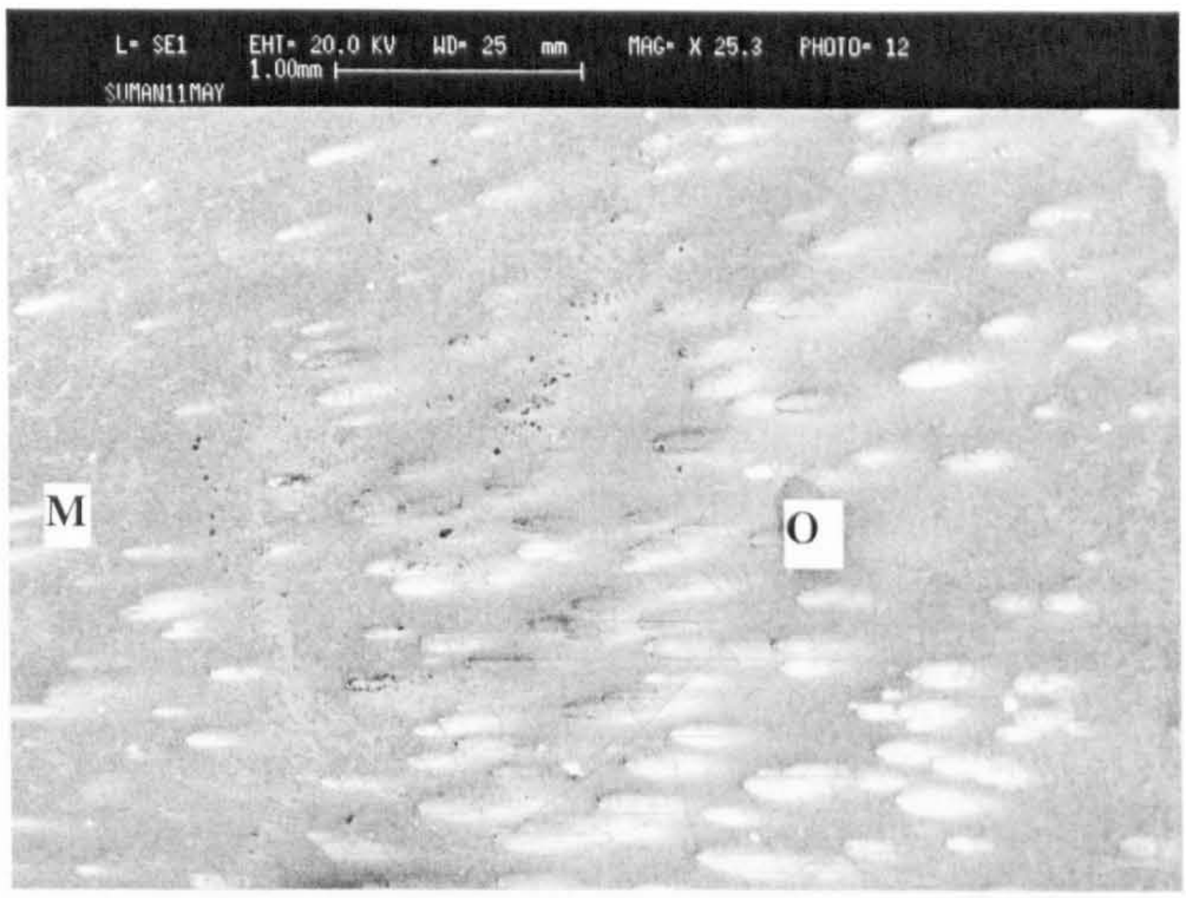


Figure 8.5.6 Corrosion attack at outer region 5mm away from the centre; a) macro loss due to comets on as-sprayed coating; and b) micro loss due to micropitting on vacuum-fused coating after 2-days of high velocity liquid impingement plus anodic polarisation.

On the fused coating, once again the most predominant mechanism of corrosion attack under impingement condition was in the form of very localised micropitting at the outer region due to loss of hard particles (Fig. 8.5.6b). No evidence of comet pitting was observed in the vacuum-fused coating.

Comet attack was easily visible on the stainless steel after 6-days of liquid impingement. Figure 8.5.7a shows a stream of corrosion product emanating from the comets into the flow directionality at the region 'O', 5mm away from the centre after 2-days impingement plus anodic polarisation. The higher magnification SEM image revealed that the pithead is quite deep as shown in Fig. 8.5.7b. The slight attack in the central region 'M' was appeared to be associated with grain boundary attack, which also shows corrosion product emanating out of the dislodged grain leaving several pits (Fig. 8.5.7c).

a)



b)



c)

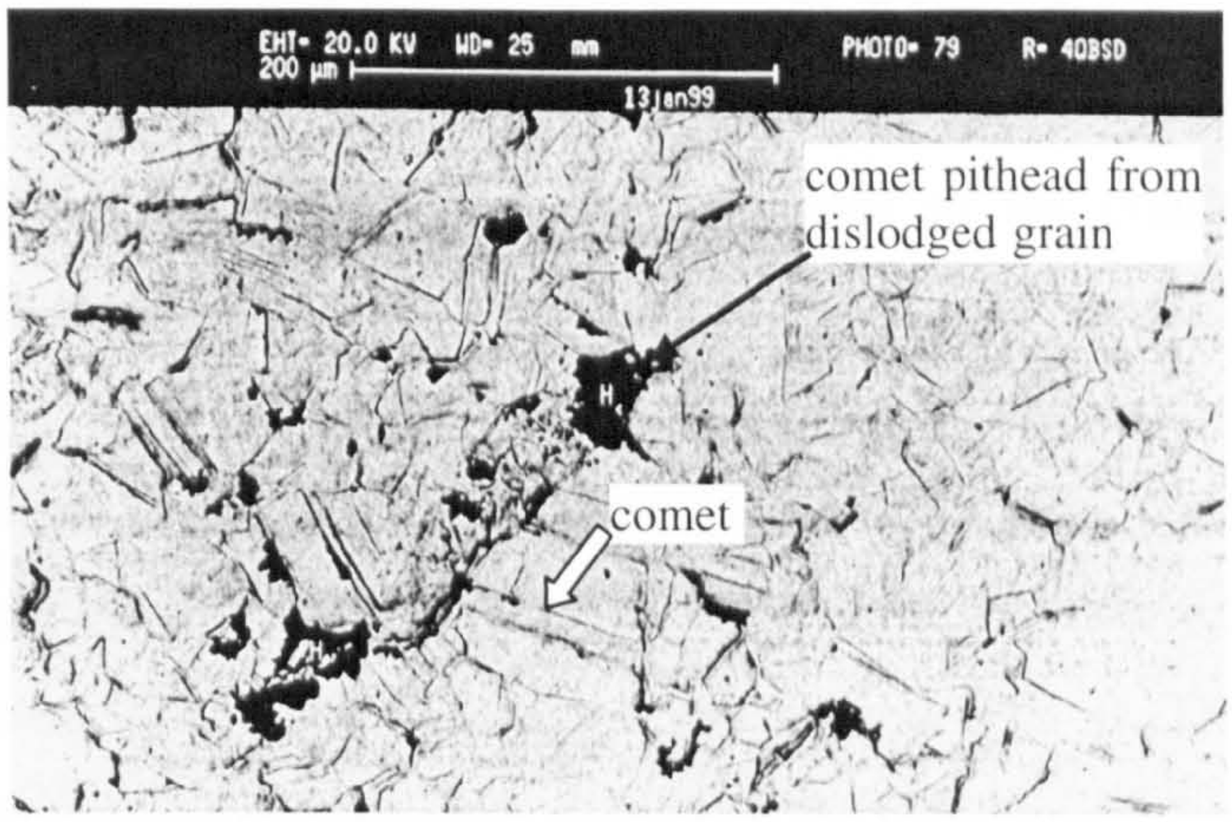


Figure 8.5.7 a) Stream of comets at region 5mm away from the centre showing middle region 'M' and outer region 'O'; b) higher magnification of one of the comet heads from region 'O' showing deep pit; and c) higher magnification of the depressed region 'M' showing intergranular attack on UNS S31603 after 2-days of impingement plus anodic polarisation.

In addition attack in the form of skidding tracks was also visible on the surface of the stainless steel as shown in Fig. 8.5.8 at the outer region of low angle impingement.

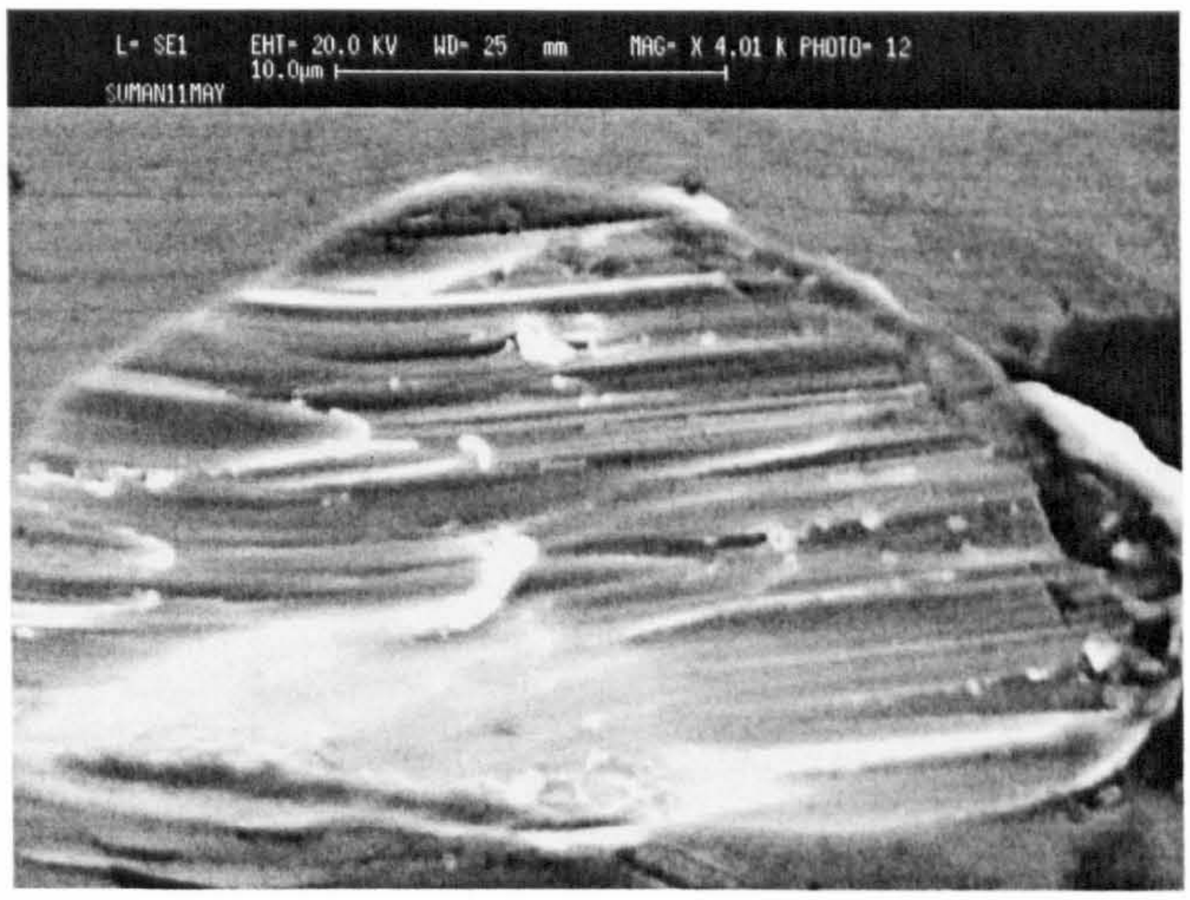


Figure 8.5.8 SEM secondary image of a skidding track (low angle attack) on UNS S31603 at outer region after 2-days of solid-free high velocity liquid impingement.

8.6 Liquid and solid-liquid erosion-corrosion of Coating BII

In the previous section the erosion-corrosion behaviour of the coatings under high-velocity liquid impingement condition free of solid and distinctions in mechanisms of coating deterioration were discussed. This section will generally comprise the comparison between the three coatings under severe erosion-corrosion conditions, when solid particles are present in saline water. The electrolyte medium was a 3.5% NaCl solution with commercially available 800ppm silica sand type B. Details of erodent particles and experimental procedure are described in Chapter 6. Parallel tests were carried out in a similar environment but without adding solid particles. This simulated the effect of solid particles in erosion-corrosion conditions that are likely to occur in real applications.

Weight loss measurement

Under solid-free liquid impingement at 17ms^{-1}, both the as-sprayed and vacuum-sealed coatings (Fig. 8.6.1) exhibited similar weight loss trends during the 6-days tests with an indication of increased material loss rates occurring at longer times. The vacuum-fused coating however showed significantly lower weight losses compared to the as-sprayed and vacuum-sealed coatings. A smaller relative increase in weight loss between 4 and 6-days exposure was measured on the vacuum-fused coating.

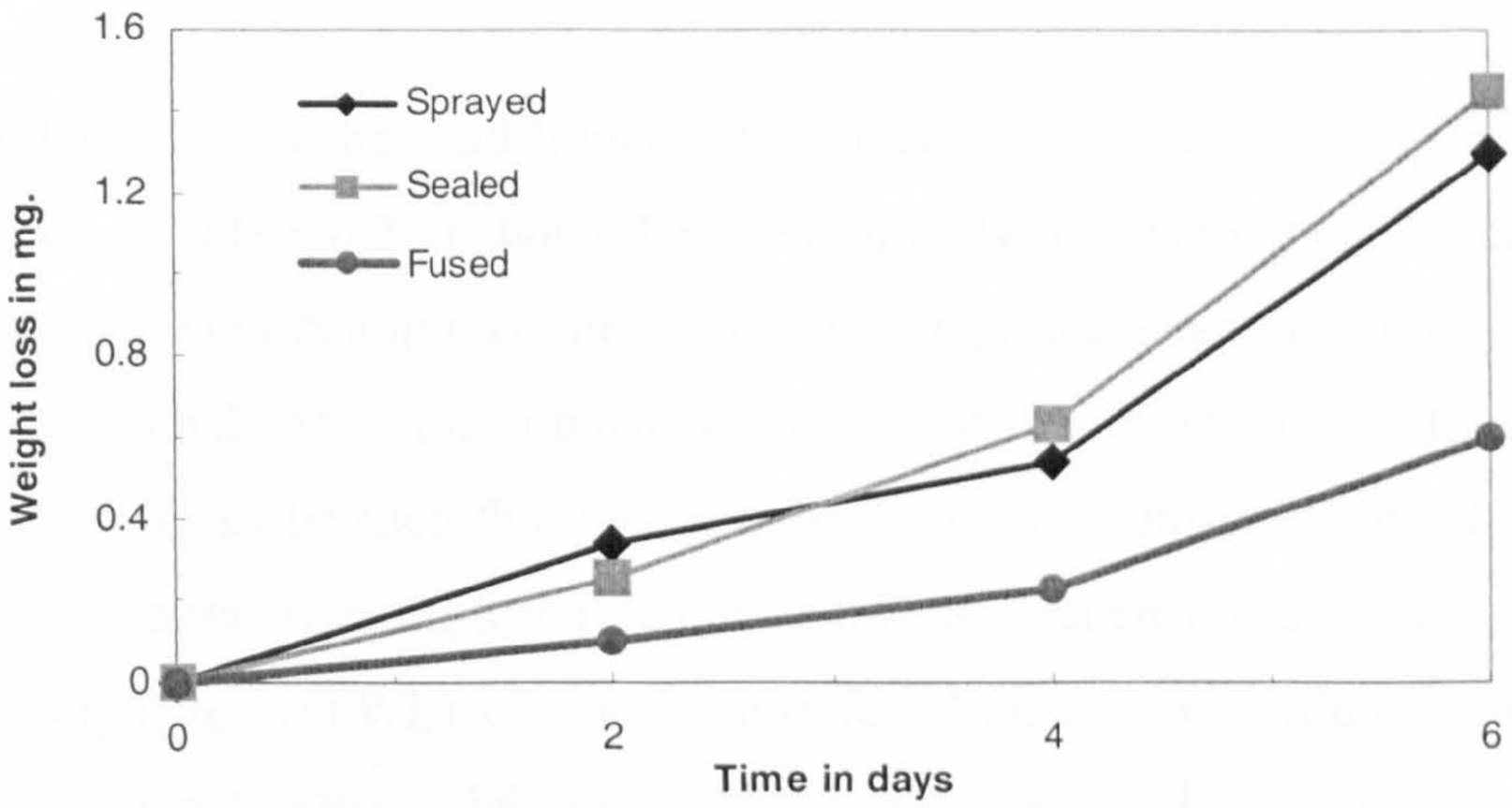


Figure 8.6.1 Total weight loss (TWL) of polished surfaces under solid-free liquid impingement (17ms^{-1}, 18°C, 90° impingement).

As shown in Table 8.6.1 the application of CP significantly reduced the total material losses in both the as-sprayed and vacuum-sealed coatings. In the case of the vacuum fused coating the application of CP for 6-days under liquid impingement resulted in no measurable weight loss.

Coating (Polished)	**TWL in mg. under solid-free liquid impingement**						**Weight loss in mg. under CP**	
	2 days	*Avg.*	*4 days*	*Avg.*	*6 days*	*Avg.*	*2 days*	*6 days*
As-sprayed	0.3 0.4 0.4	0.37	0.5 0.6 0.5	0.53	1.5 1.3 1.1	1.30	0.2 0.1	0.8 0.7
Vacuum-sealed	0.3 0.2	0.25	0.6 0.7	0.65	1.5 1.4	1.45	0.2 0.2	0.7 0.6
Vacuum-fused	0.1 0.0 0.2	0.10	0.2 0.3 0.2	0.23	0.6 0.8 0.4	0.60	0.0 0.0	0.0 0.0

Table 8.6.1 Weight loss results of polished surfaces under solid-free liquid impingement at $17ms^{-1}$.

Coating (Polished)	**TWL in mg. without application of CP**							**Weight loss in mg. under CP**	
	1 hr	*Avg.*	*2 hrs*	*Avg.*	*3 hrs*	*Avg.*	*4 hrs*	*1 hr*	*4 hrs*
As-sprayed	1.4 1.6	1.5	*3.5* *3.2*	*3.35*	*5.7* *5.9*	5.8	7.3	0.9 1.0	3.7
Vacuum-sealed	1.5 1.3	1.4	3.4 3.1	3.25	5.6 5.7	5.65	7.4	1.1 0.8	3.8
Vacuum-fused	0.6 0.8 0.5	0.64	1.5 1.2	1.35	1.9 2.1	2.0	2.4	0.2 0.3	0.6 0.6

Table 8.6.2 Weight loss results of polished surfaces under solid-liquid impingement at $17ms^{-1}$.

The weight loss data for the solid-liquid tests conducted over periods of up to four hours are presented in Table 8.6.2. It should be noted initially that even after 1-hour exposure to solid-liquid erosion conditions, the weight loss is greater than after 6-days in liquid erosion. Figure 8.6.2 shows the comparison in weight loss trends for the three coatings and once again it can be seen that the as-sprayed and vacuum-sealed coatings show a similar trend and the vacuum-fused coating exhibits a much lower material loss rate. The total weight loss (TWL) of the vacuum-fused coating was almost one third in magnitude compared to the weight losses of the as-sprayed and vacuum-sealed coatings under similar conditions after the 4-hours tests. The application of CP again resulted in a substantial reduction of weight loss for all the three coatings investigated, the effect

being much more pronounced in the vacuum fused coating where a reduction of 75% after 4-hours exposure was achieved.

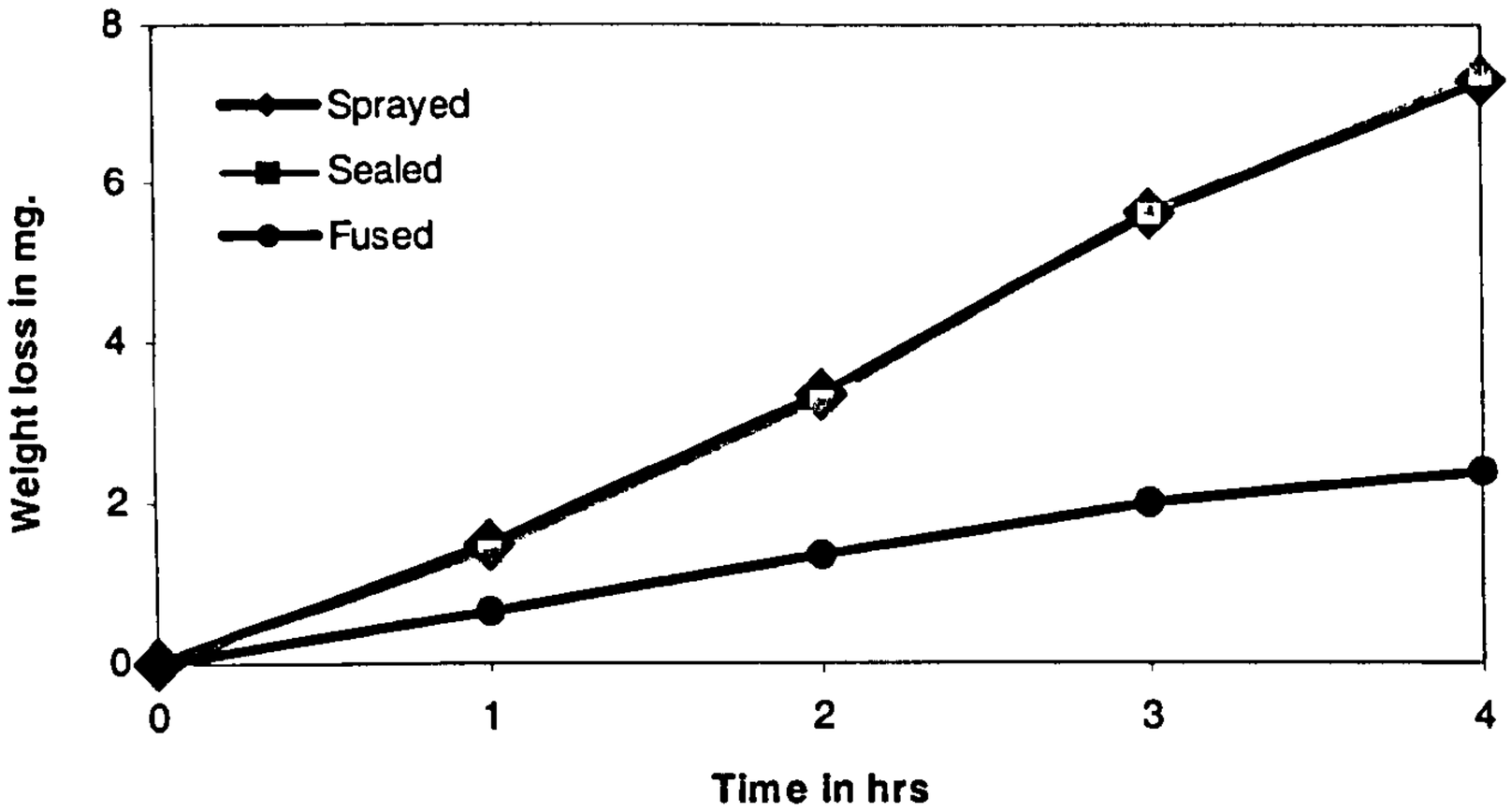


Figure 8.6.2 Weight loss trend of HVOF polished coatings under 800 ppm solid-liquid impingement in 3.5%NaCl at 18°C.

Total weight loss due to erosion-corrosion 'TWL'; pure erosion with applied CP 'E'; pure corrosion 'C' and synergy 'S' components for polished surfaces of the sprayed/sealed/fused coatings under solid-free liquid and solid/liquid impingement are shown in Tables 8.6.3 and 8.6.4.

Material	**TWL** mg/hr	**E** mg/hr	**C** mg/hr	**S** mg/hr
Sprayed	1.3	0.75	0.0007	0.55
Sealed	1.45	0.65	0.0009	0.80
Fused	0.60	0.0	0.0017	0.59

Table 8.6.3 Breakdown of 'E', 'C' and 'S' under solid-free liquid impingement

Material	**TWL** mg/hr	**E** mg/hr	**C** mg/hr	**S** mg/hr
Sprayed	1.5	0.95	0.094	0.46
Sealed	1.4	0.95	0.09	0.36
Fused	0.64	0.25	0.045	0.35

Table 8.6.4 Breakdown of 'E', 'C' and 'S' under solid/liquid impingement

It can be seen that, whilst the pure corrosion contributions to overall material loss are small, the indirect effect of corrosion processes via the synergy factor is substantial especially so under solid-free impingement.

As-received surfaces without being subjected to polishing of the coatings displayed much higher weight loss compared to that of polished surfaces. Figure 8.6.3 represents weight loss diagram of the coatings after 3-hours solid-liquid impingement. Weight loss results of as-received surfaces of the coatings after 1, 2 and 3 hours test periods are presented in Table 8.6.5.

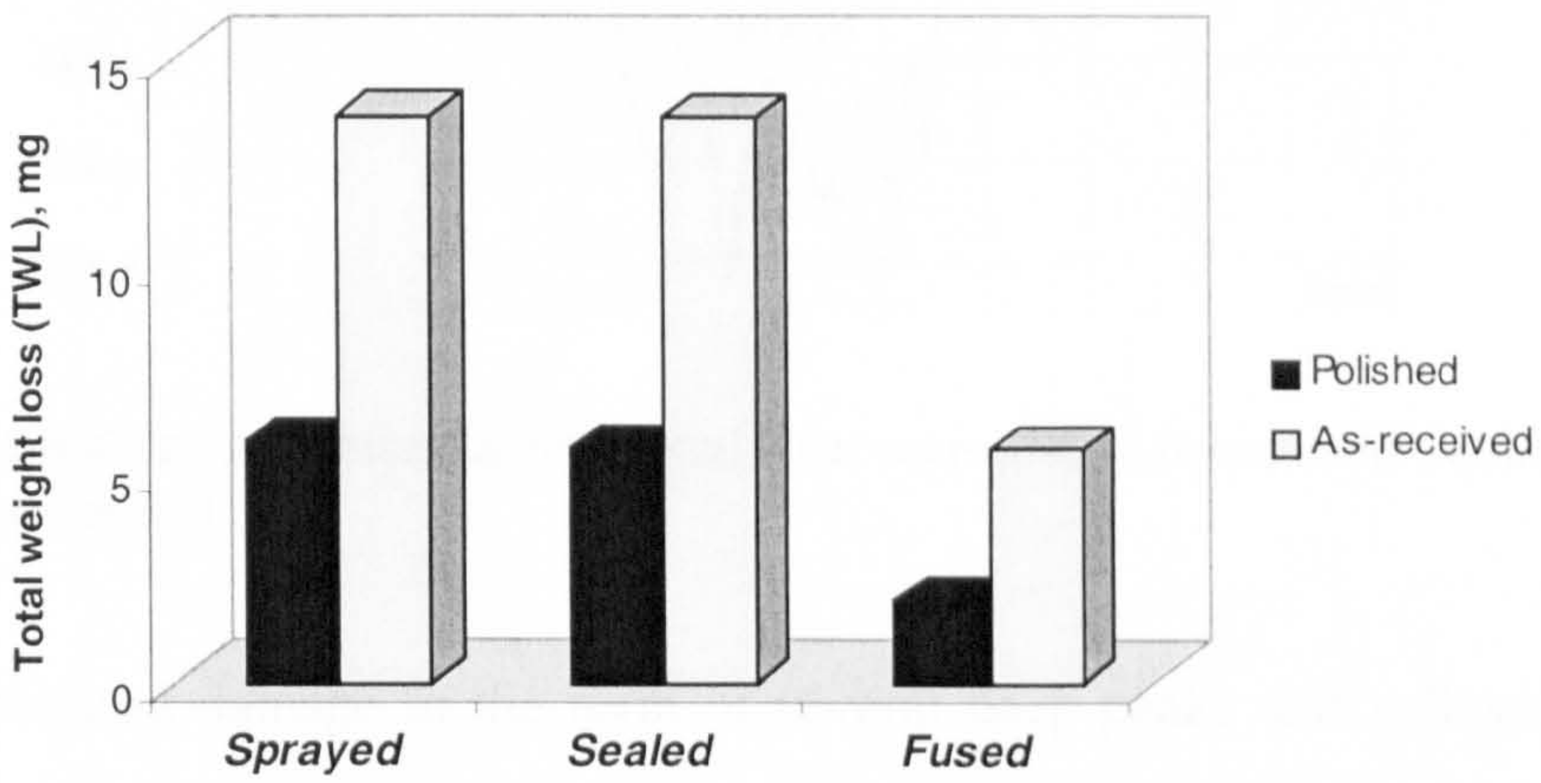


Figure 8.6.3 Weight loss of coatings in as-received and polished conditions after 3-hours solid-liquid impingement.

Coating (As-received)	**TWL in mg. without application of CP**					
	1 hr	***Avg.***	***2 hr***	***Avg.***	***3 hr***	***Avg.***
As-sprayed	*5.6* *5.3*	*5.45*	*9.3* *9.1*	9.2	13.7	13.7
Vacuum-sealed	5.5 5.2	5.35	9.4 9.1	9.25	13.4 13.9	13.65
Vacuum-fused	2.3 2.1	2.2	4.3 3.9	4.1	5.6 5.7	5.65

Table 8.6.5 Weight loss of as-received surfaces under solid-liquid impingement at $17ms^{-1}$.

Surface Topography

The Talysurf traces (Fig. 8.6.4) of the wear scars under the impinging jet in solid-liquid conditions are in agreement with the higher material loss of the sprayed and sealed coatings compared to that of the vacuum fused coating. The sprayed coating exhibited a much deeper groove after the same exposure.

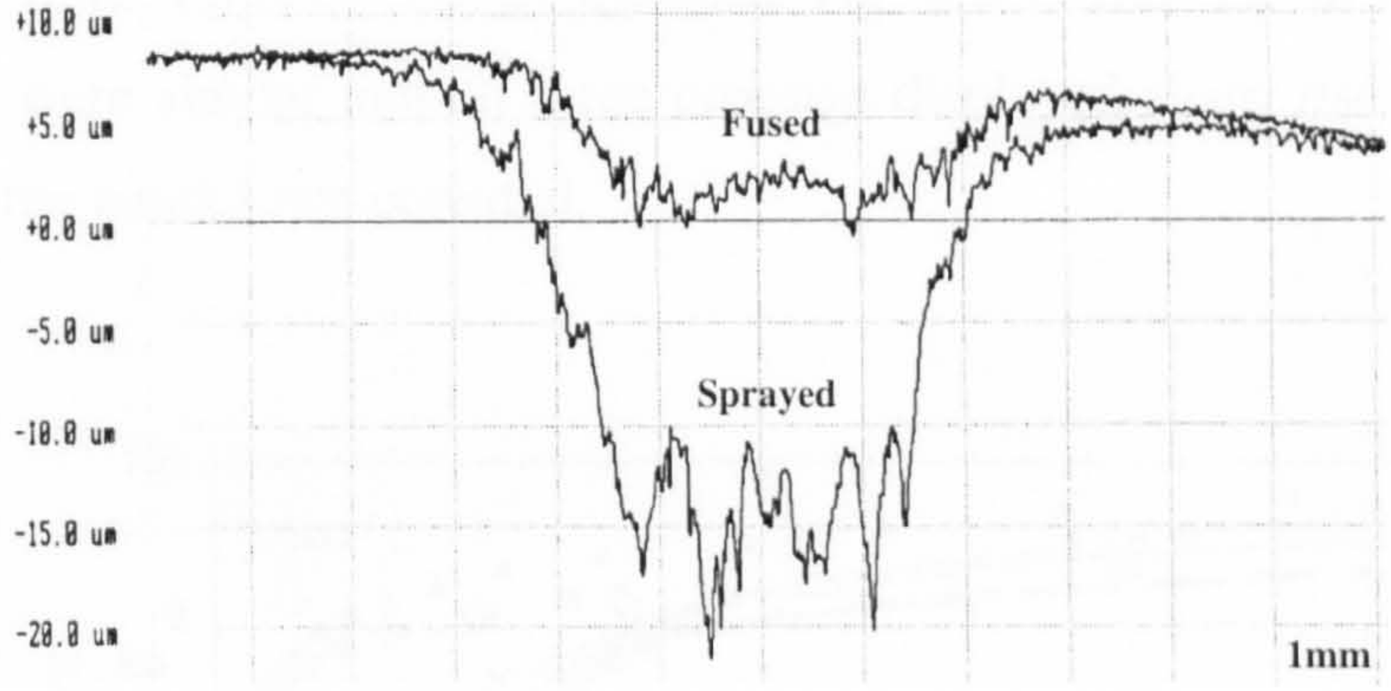


Figure 8.6.4 Talysurf traces under central wear scars after 4-hours solid-liquid impingement with CP.

Moreover, localised damage in the form of several deep peaks and valleys inside the groove were observed in the as-sprayed coating compared with a much smoother surface of the wear scar on the vacuum fused coating sample. One interesting feature of the wear scar is the apparent difference in the geometry on the two materials. The wear scar on the fused coating showed a region out from the stagnation point, where the thickness loss was greatest as typical for a ductile material as in the case of UNS S31603 described in Chapter 7 section 7.5. The sprayed coating showed the maximum thickness loss in the centre of the scar typical for a brittle material. The maximum thickness loss of the sprayed coating ranged between 30-35μm, whereas that for the vacuum fused coating ranged between 8-10μm. This is indicative of a much faster penetration of the solid-liquid jet exposing a bare metal substrate on the sprayed coating compared to that on the fused coating. The traces in Fig. 8.6.4 were scanned (using a scanner) and the resulting images were examined using *Image Analysis* software. This revealed the fractional area of the material removed in the sprayed coating was 3 times higher in magnitude than that for the fused coating.

Anodic polarisation

The results of the anodic polarisation sweeps of the coating with three different surface treatments in solid-free and solid-liquid impingement conditions are shown in Fig. 8.6.5. The polarisation curves for all the three coatings after 6-days solid-free impingement were similar and displayed what is regarded as classic passive behaviour. This is represented by the very low currents measured over a wide range of potential from 'E_{corr}' to some value of 'E_b' as shown in Fig. 8.6.5. The 'E_b' in Fig.8.6.5 for all three coatings were similar and all three coatings displayed sharp rises in the current densities after the breakdown potential.

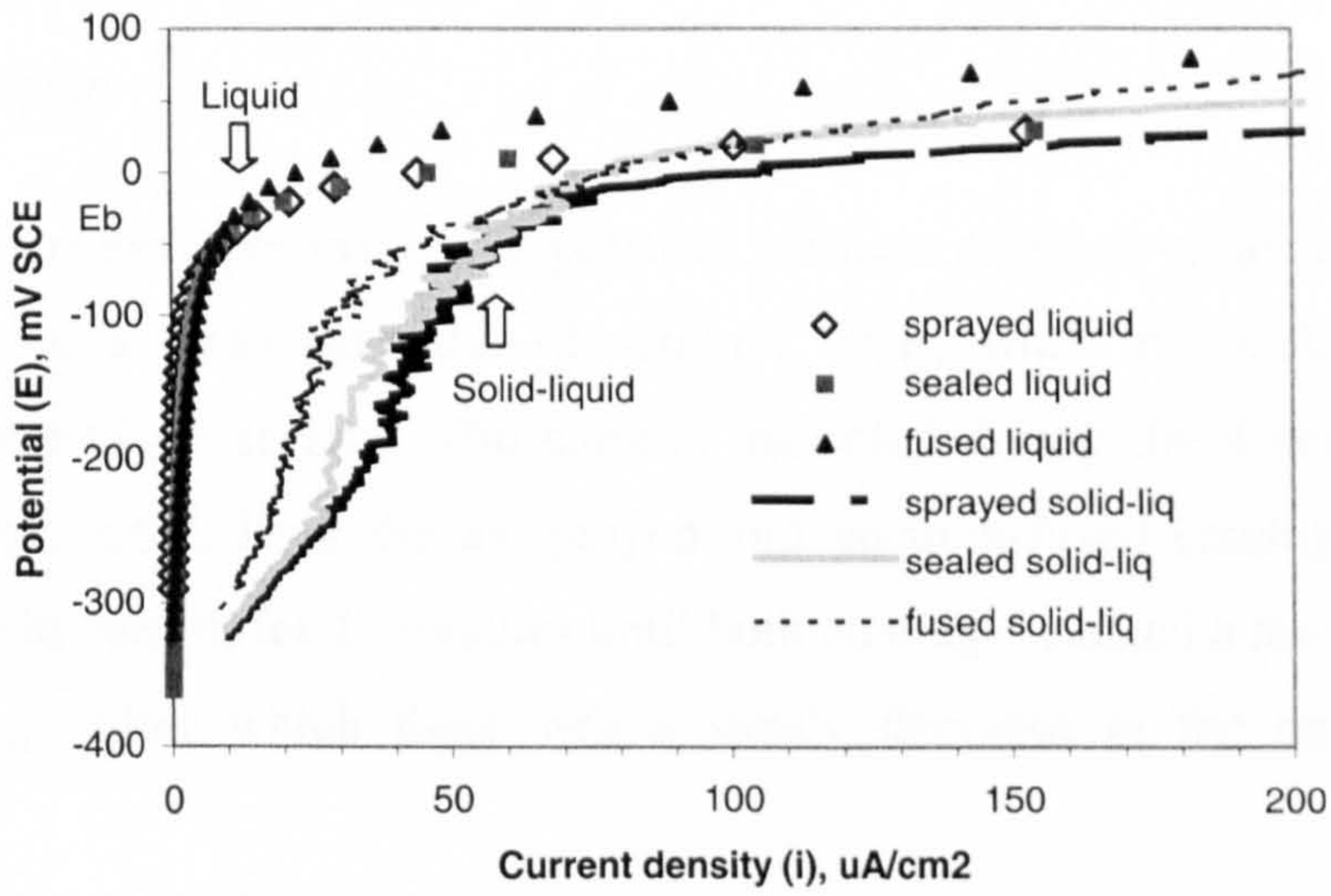


Figure 8.6.5 Anodic polarization in impingement tests ($17ms^{-1}$, 18°C, 3.5% NaCl salt-water, pH 8).

In contrast, under solid-liquid impingement, the current density steadily increased immediately once the potential was shifted in the positive potential direction from the 'E_{corr}'. This is indicative of active corrosion occurring which is an activation-controlled process and can be described by the well-known Tafel relationships. The corrosion current densities were determined by Tafel extrapolation and are shown in Fig. 8.6.6. It can be seen that the corrosion current density of the fused coating, however, under solid-liquid condition was found to be almost half of the values displayed by the as-sprayed and vacuum-sealed coatings.

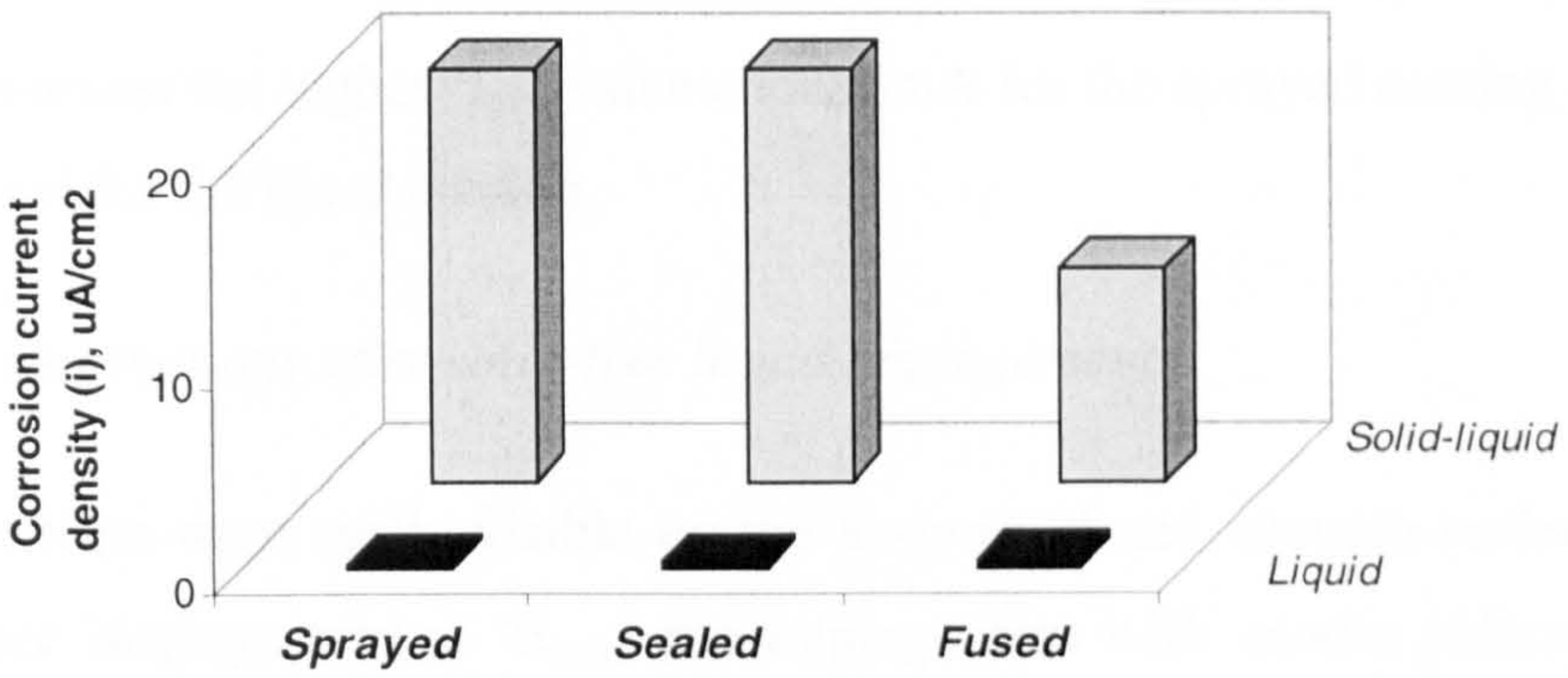


Figure 8.6.6 Corrosion current densities of the coatings under solid-free liquid and solid-liquid impingement conditions.

Cathodic protection

Potentiostatic tests were performed for polished surfaces of the as-sprayed and vacuum-fused coatings at a fixed potential of -800mV SCE, while the solid/liquid jet is impinging on the target surface. The currents recorded during the 4-hours period are presented in Fig. 8.6.7. Both the as-sprayed and vacuum-fused coatings displayed a steady increase in current for 15 minutes until both coatings reached a maximum current denoted by 'I_{pk}', after which there was a steady decrease in the currents until it stabilised.

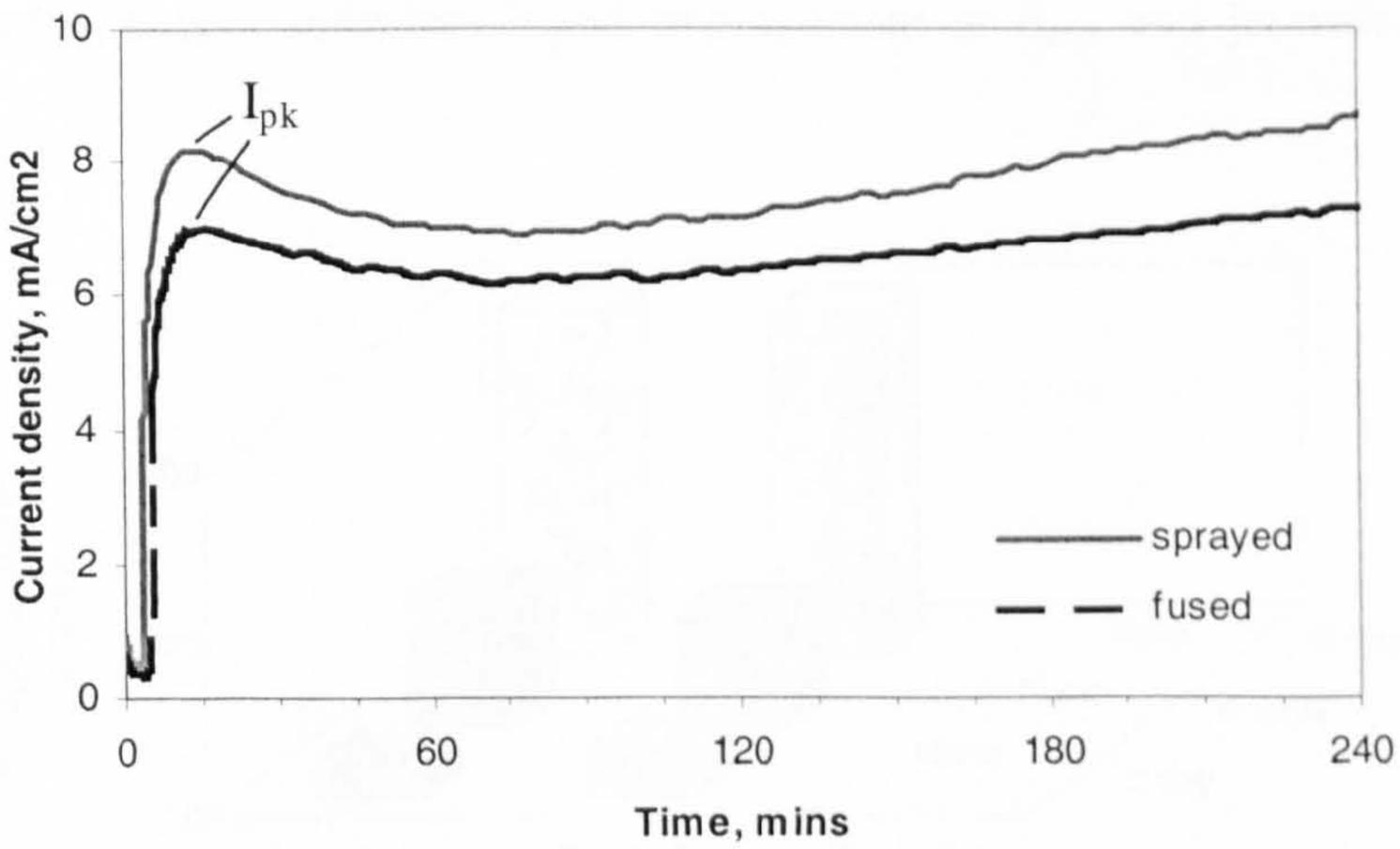


Figure 8.6.7 Cathodic currents of the as-sprayed and vacuum-fused coatings under solid-liquid impingement.

After 90 minutes there was again an increase in the cathodic current. Figure 8.6.7 shows a very similar trend of the cathodic currents for both coatings. Nevertheless, Fig. 8.6.7 clearly demonstrates the higher 'I_{pk}' value about 8mA for the sprayed coating compared to 7mA required for the fused coating.

Microscopic observations after solid-free liquid impingement

Corrosion products were easily visible on the as-sprayed and vacuum-sealed coatings under both free impingement at 'E_{corr}' and impingement with anodic polarisation. On the macroscopic level, corrosion product in the form of comet-shaped streams was easily distinct on the sprayed and sealed coatings just after 2-days impingement and was significantly increased after 6-days tests (Fig. 8.6.8a and b).

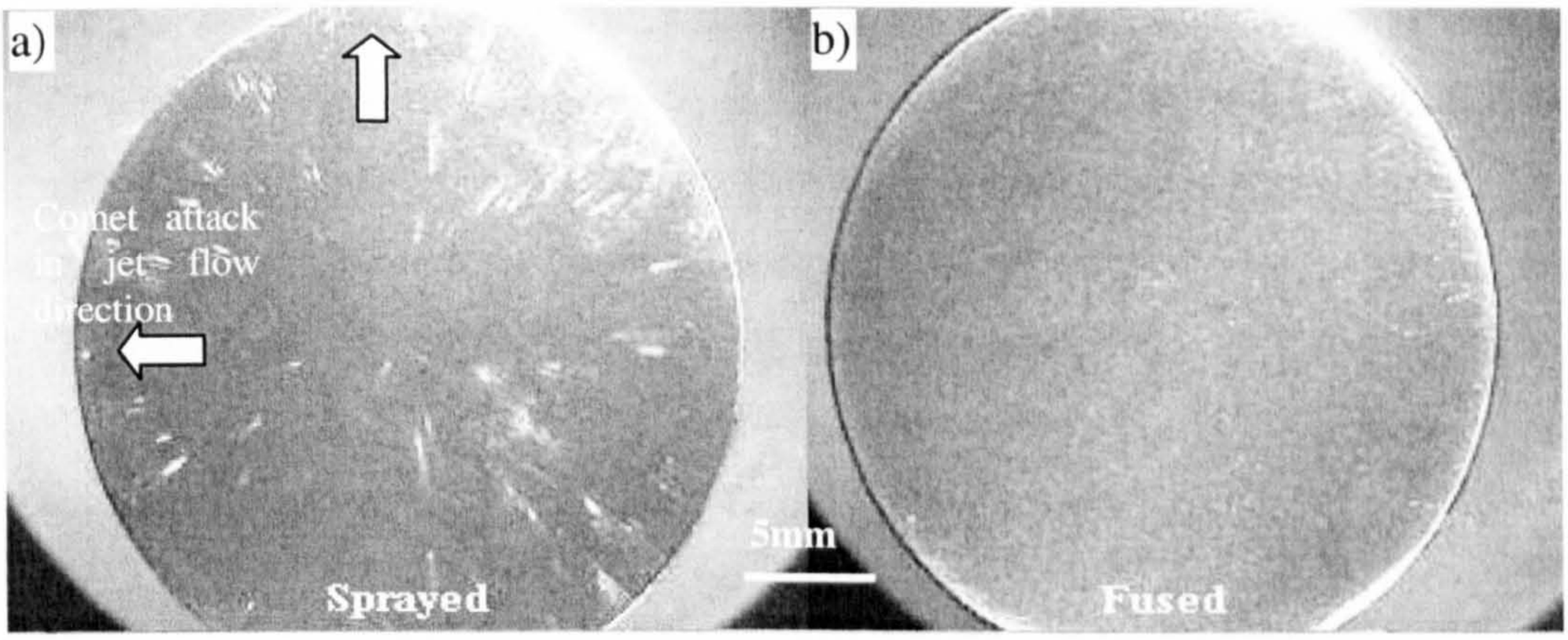


Figure 8.6.8 Light optical micrograph of a) as-sprayed; and (b) vacuum fused coatings after 6-days solid-free liquid impingement at E_{corr} and jet velocity of $17ms^{-1}$.

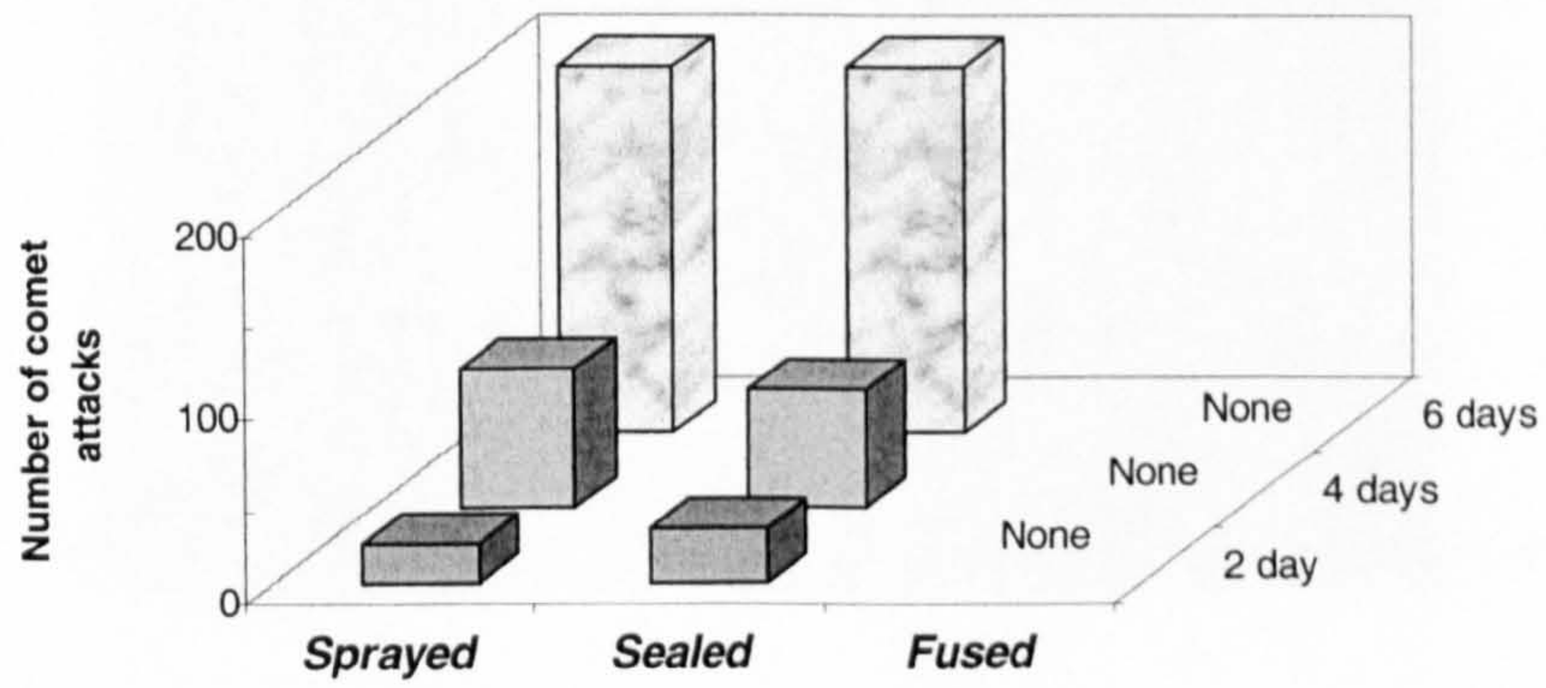
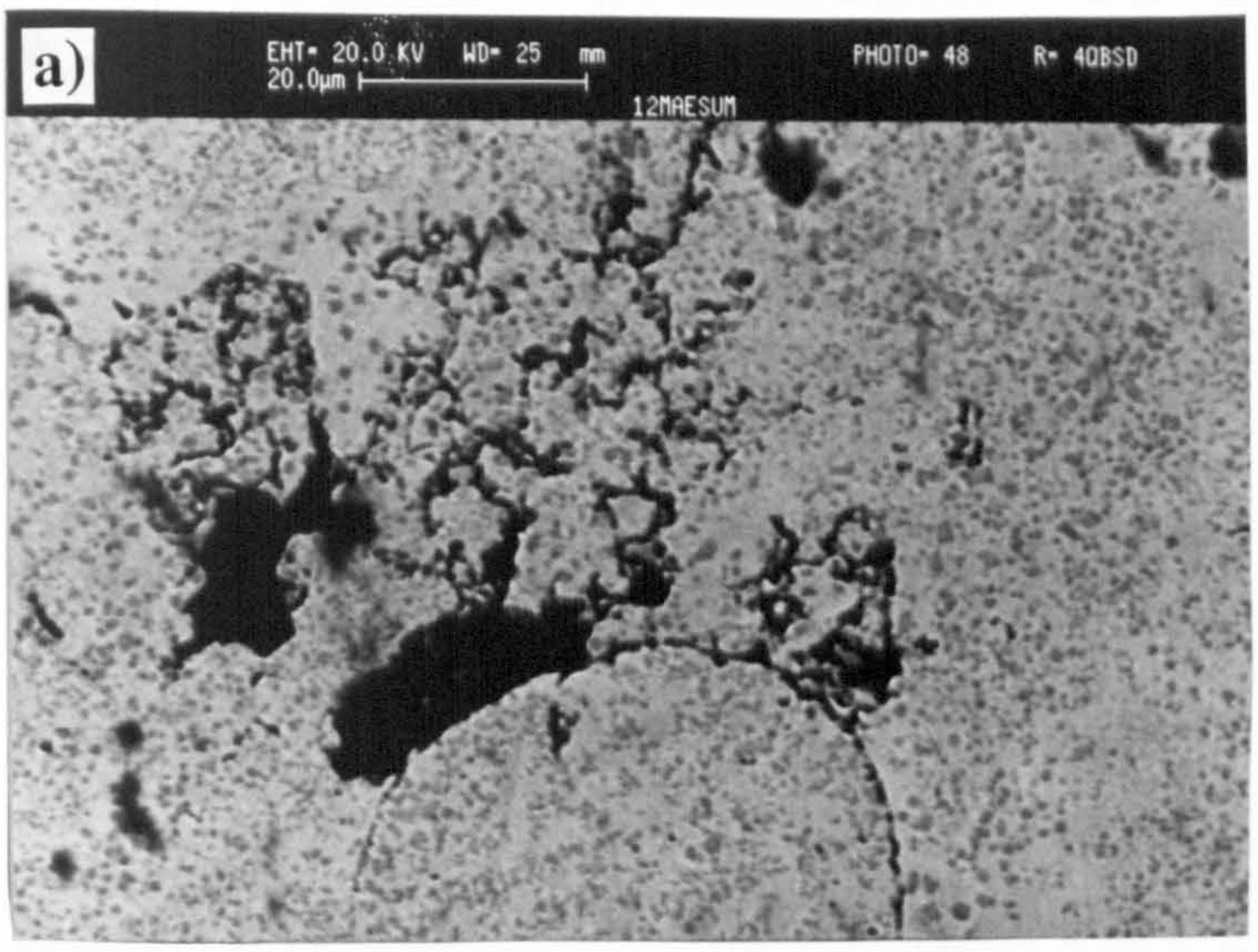
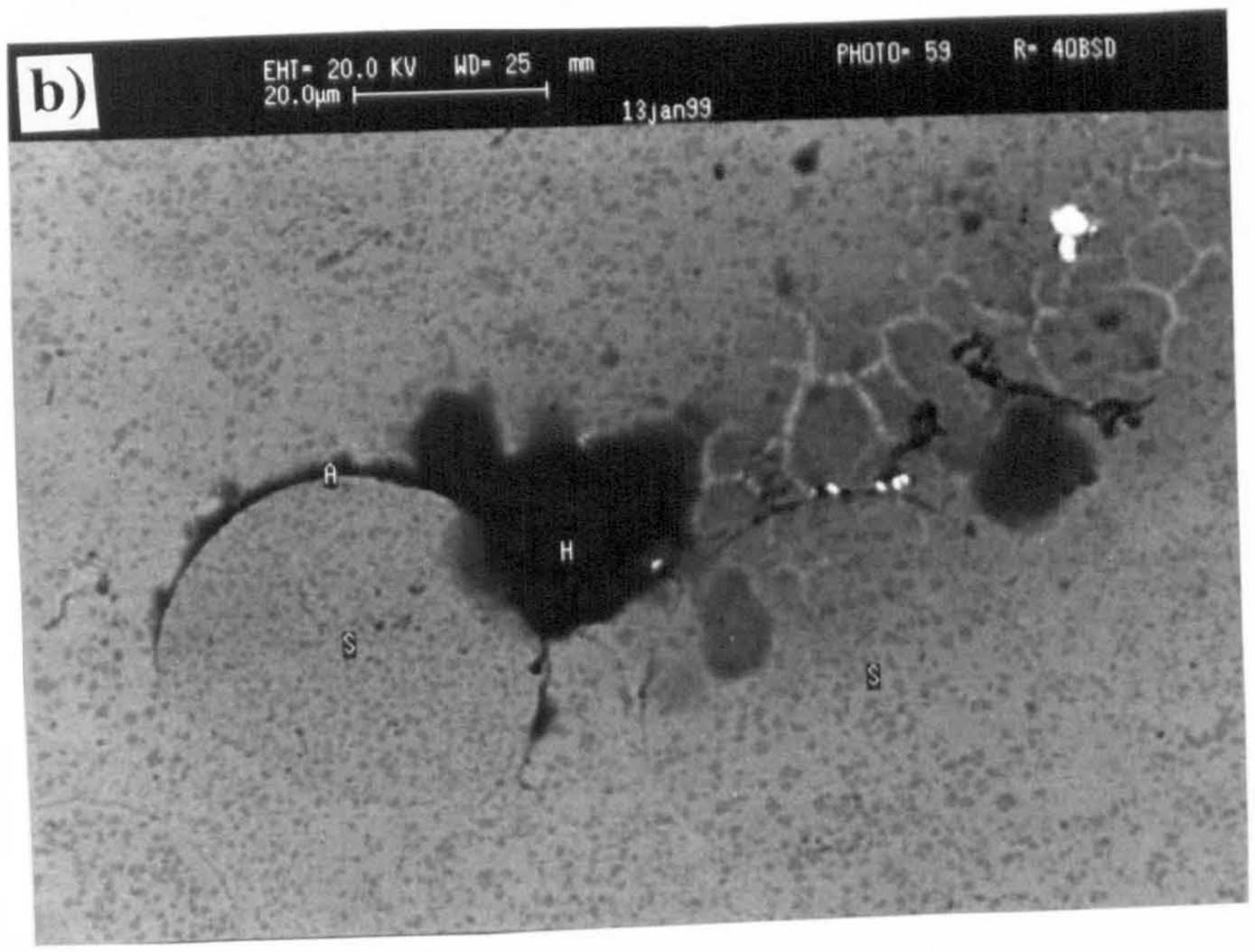


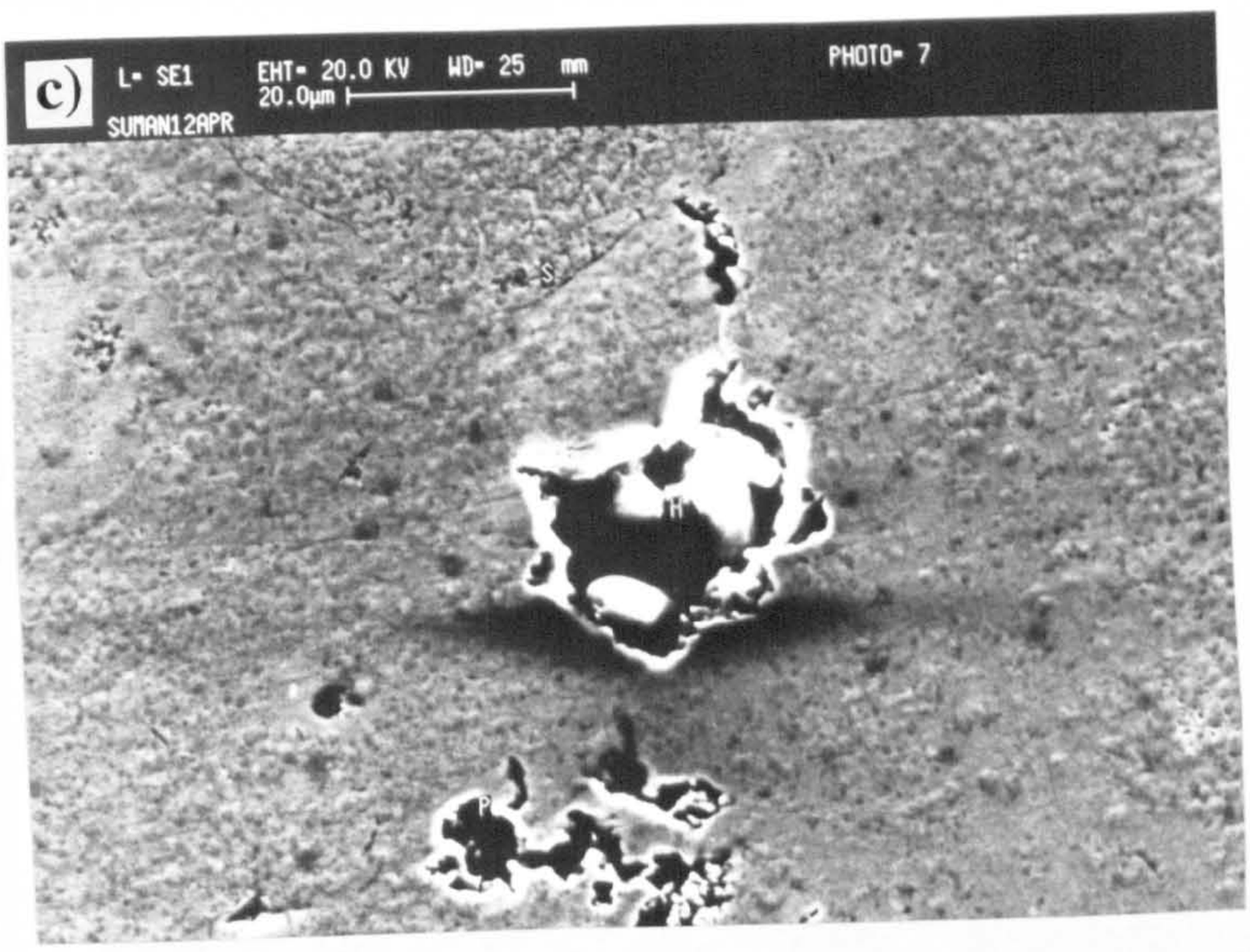
Figure 8.6.9 Comet shaped attacks on coatings after solid-free liquid impingement under jet velocity of $17ms^{-1}$ at E_{corr}.

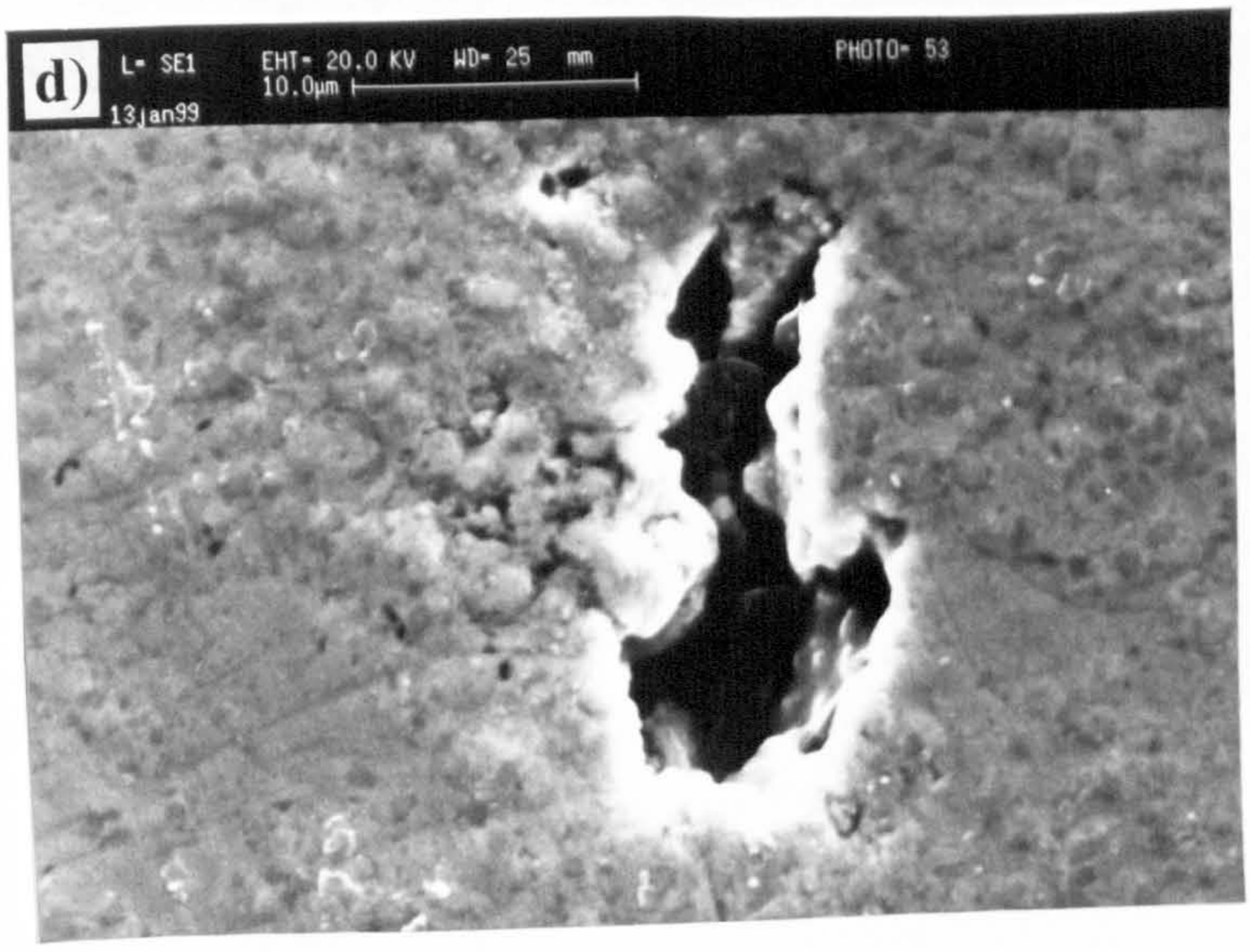
These 'comet' streams were principally seen in the area out from under the direct impingement zone (i.e. at out of the 1mm-diameter impingement zone). This feature has previously been observed on the stainless steel and the HVOF coating after anodic polarisation as reported in the previous Chapter. The number of 'comets' counted as a result of the attack is shown in Fig. 8.6.9. In contrast, no such comets were observed on the vacuum fused coating during the entire 6-days impingement tests (Fig. 8.6.8b).

Complex corrosion mechanisms were observed in the as-sprayed, vacuum-sealed and vacuum-fused coatings. Corrosion on the sprayed and sealed coatings was more at the macro level comprising of preferential attack around the individual splat boundaries (Fig. 8.6.10a), after which the corrosion mechanism enhances underneath the splat particle working as local anode cell (crevice) and thus loosening it. Fig. 8.6.10b shows corrosion product 'H' emanating from underneath the particle splat 'S' forming a comet shaped corrosion product. This leads to eventual removal of the whole particle splat being dislodged resulting in 'macropit' as shown in Fig 8.6.10c and further excavation of the existing pit (corrosion of subsequent layer at local cell) to form relatively deep holes (Fig. 8.6.10d). In addition a smaller scale mechanism of attack was evident, associated with micro-galvanic corrosion at the hard particles/matrix interfaces resulting in their dislodgement forming 'micropits' Fig. 8.6.10e.




b)
EHT= 20.0 KV WD= 25 mm
20.0µm
13jan99
PHOTO= 59 R= 40BSD
A
H
S
S


c)
L= SE1
EHT= 20.0 KV WD= 25 mm
20.0µm
SUMAN12APR
PHOTO= 7
S
H
P


d)
L= SE1
EHT= 20.0 KV WD= 25 mm
10.0µm
13jan99
PHOTO= 53

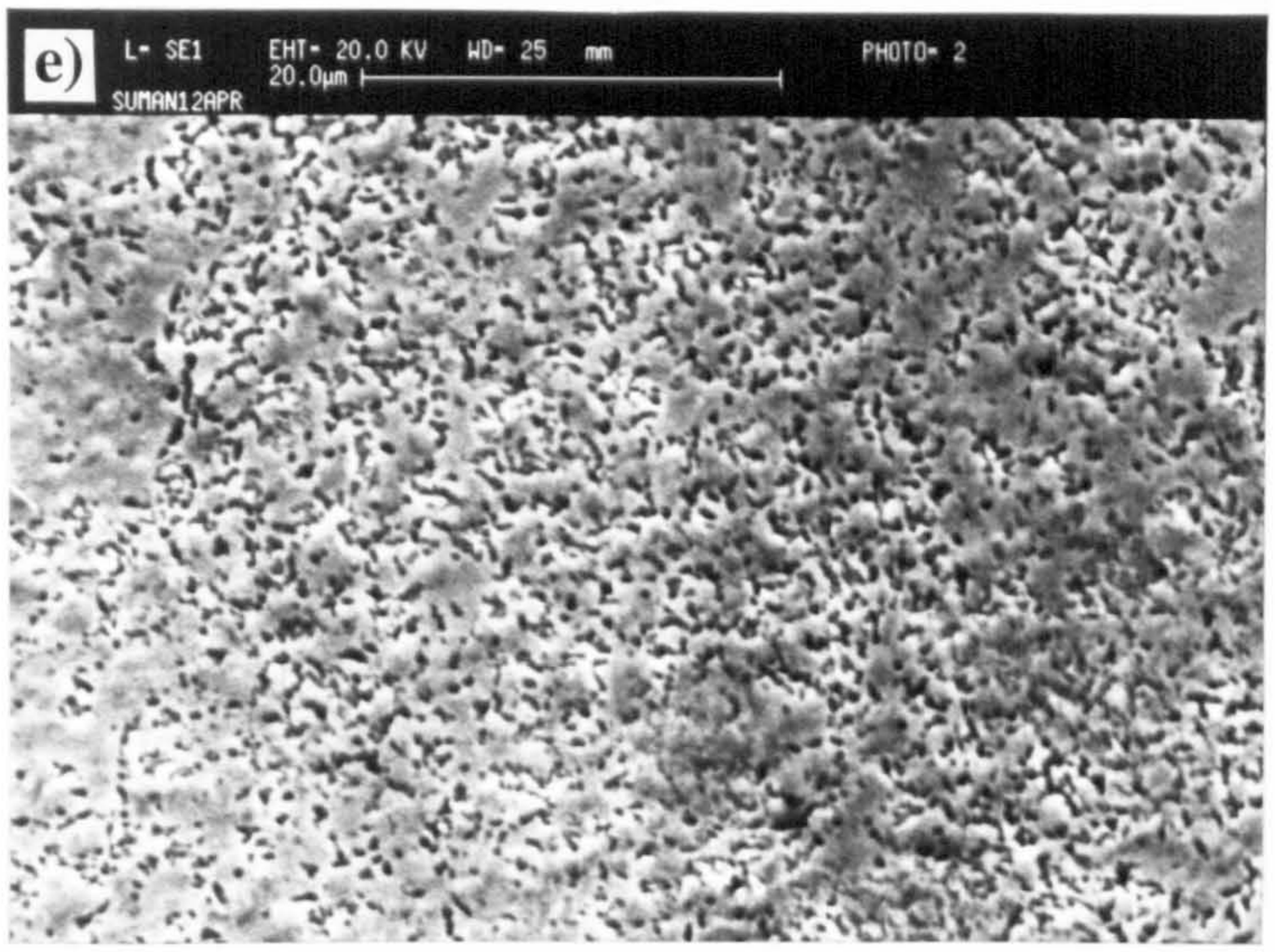
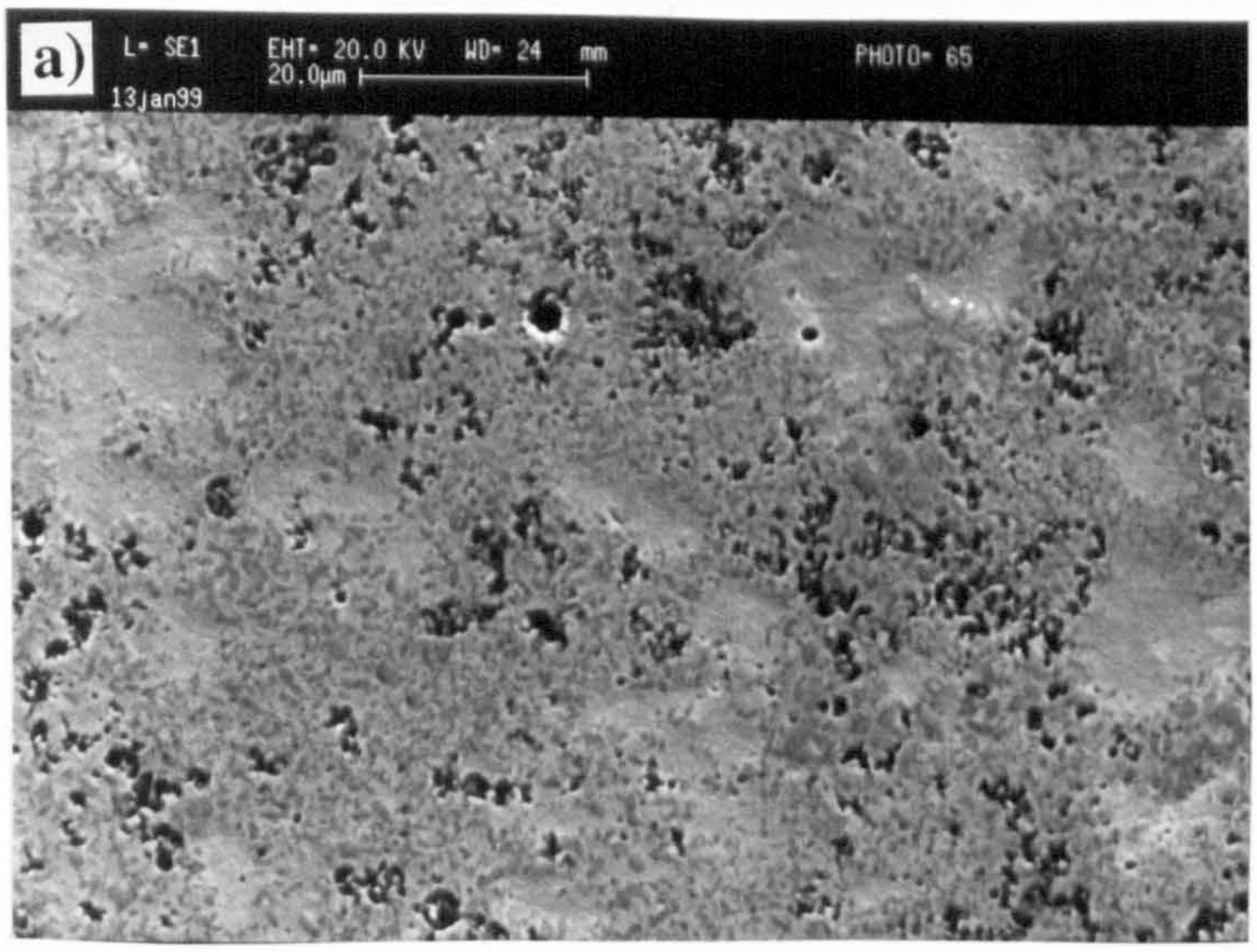


Figure 8.6.10 Corrosion attack on sprayed coating after 6-days of solid-free liquid impingement under 17ms^{-1} jet velocity at 18°C: a) attack at particle splat boundaries; b) comet-shaped corrosion product emanating from underneath the particle; c) macropit at comet head due to splat dislodgement; d) deep pit at the comet head; and e) micropitting

In the case of the vacuum fused coating the attack mechanism were essentially at the micro level with "micro-pitting", occurring uniformly over the entire surface Fig. 8.6.11a. The pits were very much smaller than the splat particles, which caused pit formation on the sprayed and sprayed/sealed coating.



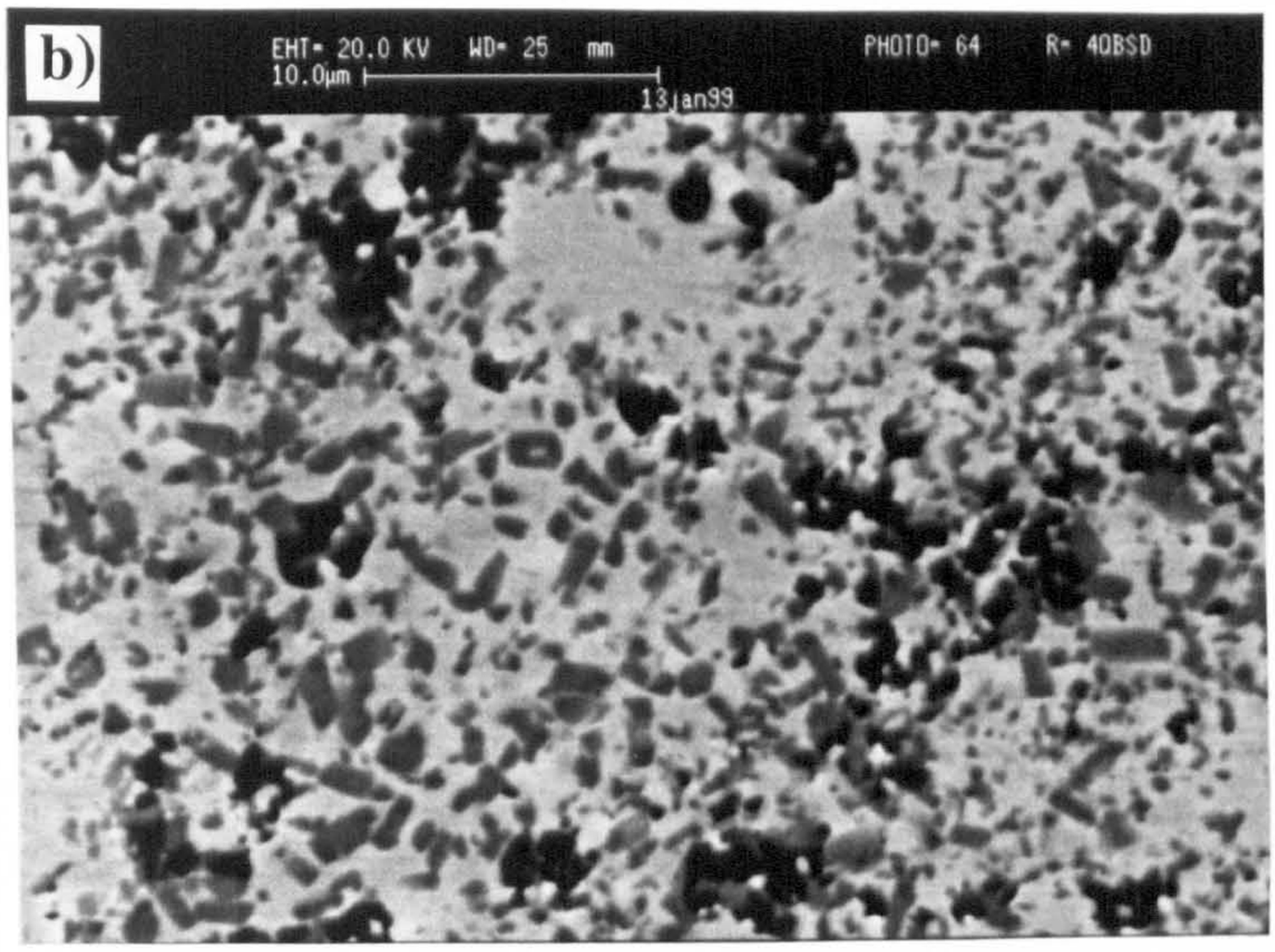
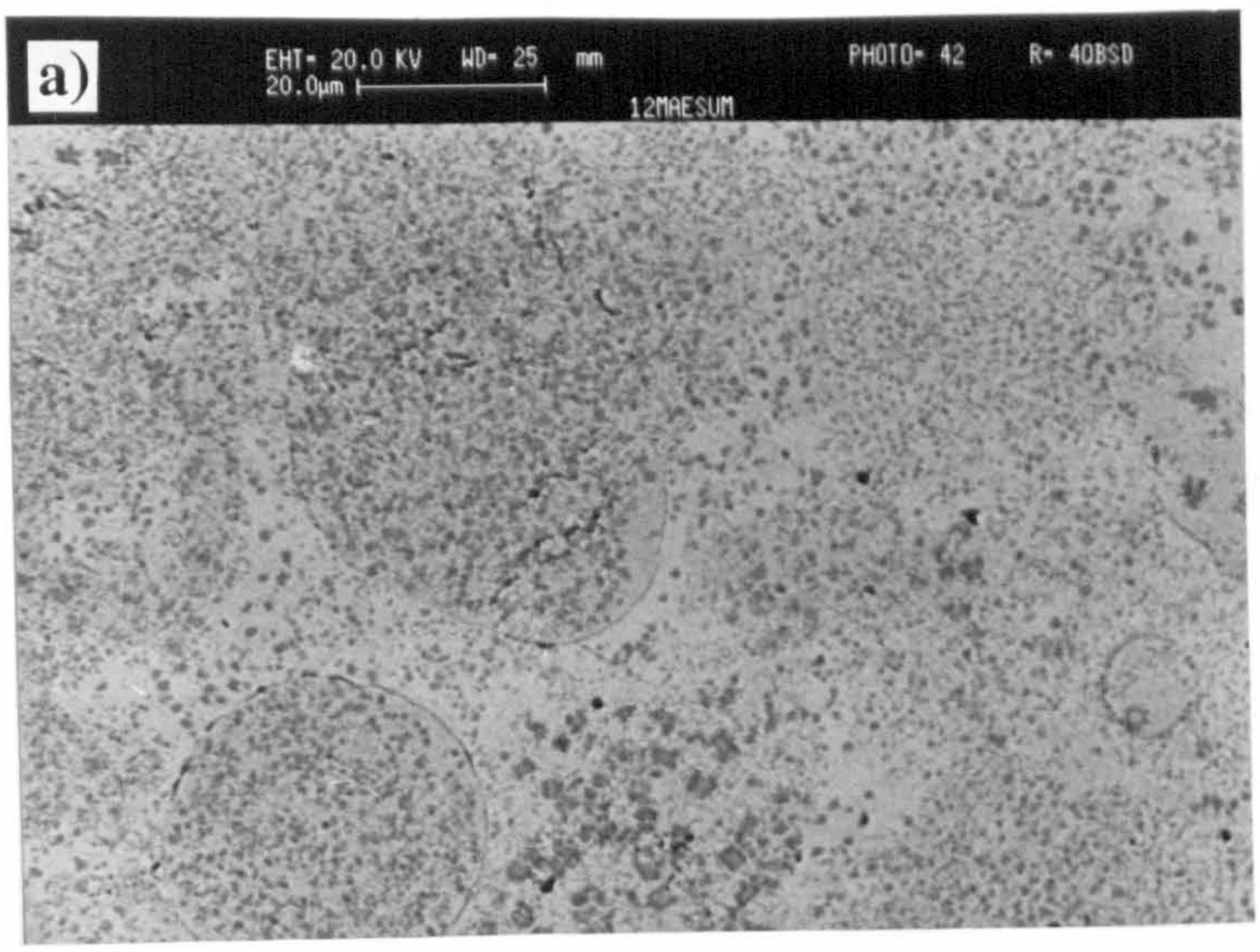


Figure 8.6.11 Back-scattered SEM micrographs of the vacuum-fused coating showing: a) micropitting on the exposed surface; and b) micropitting mechanism due to loss of hard particles after 6-days of solid-free liquid impingement ($17ms^{-1}$, 18°C).

The back-scattered SEM photograph in Fig. 8.6.11b clearly shows the formation of micropits due to dislodgement of hard phase particles. In addition, corrosion of matrix was evident at several places of the exposed surface and was true for all the three types of coatings investigated.



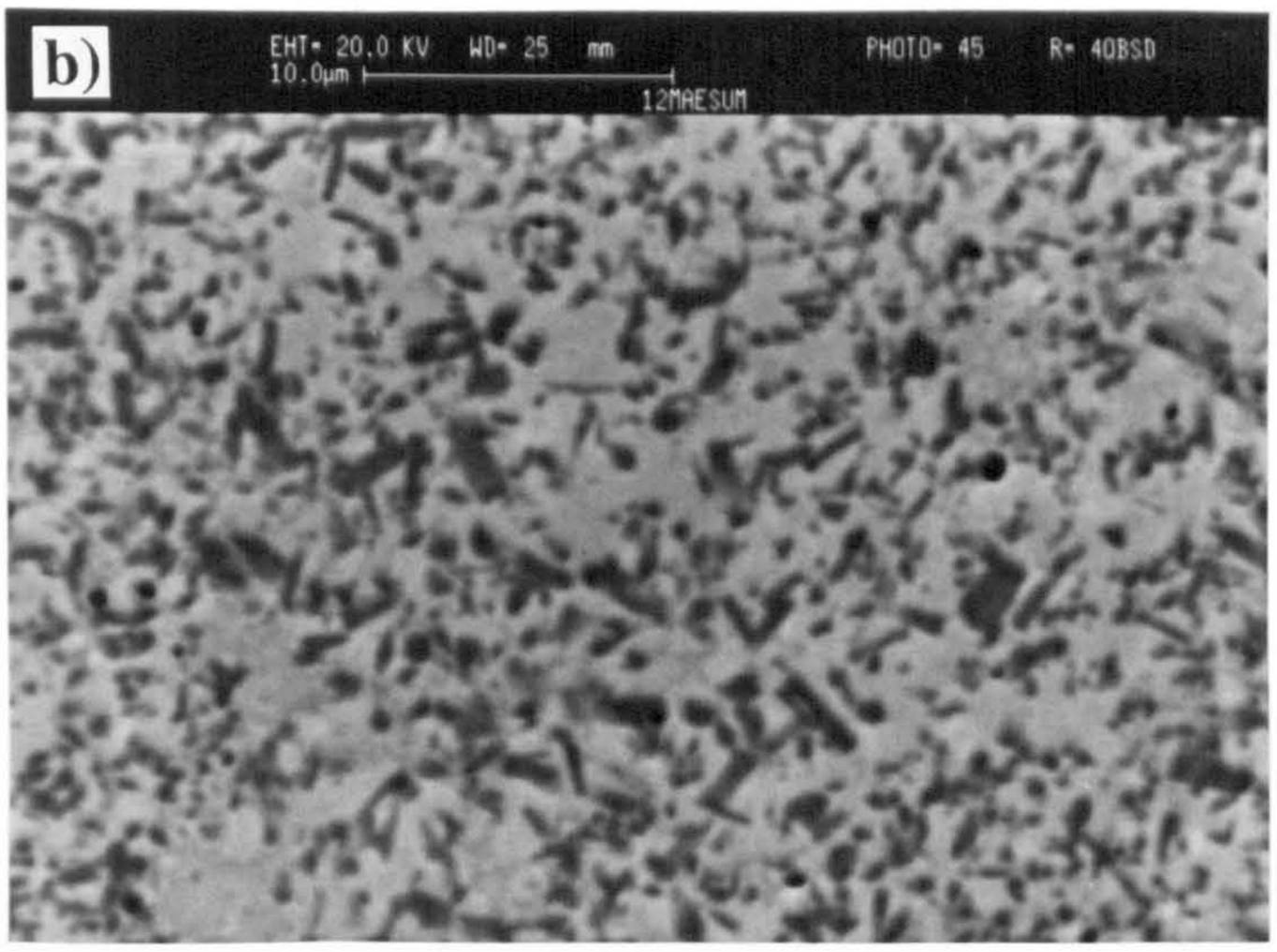
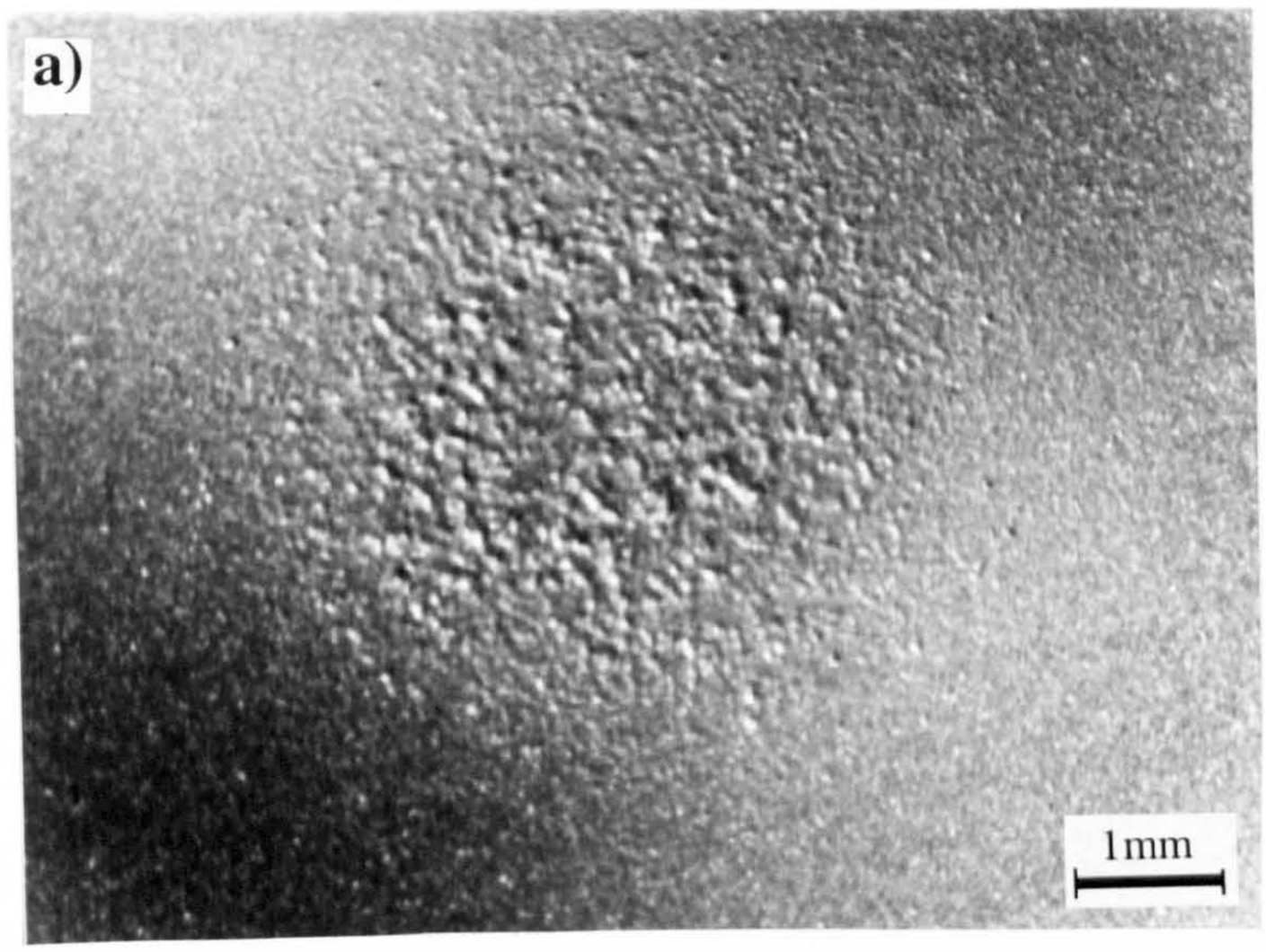


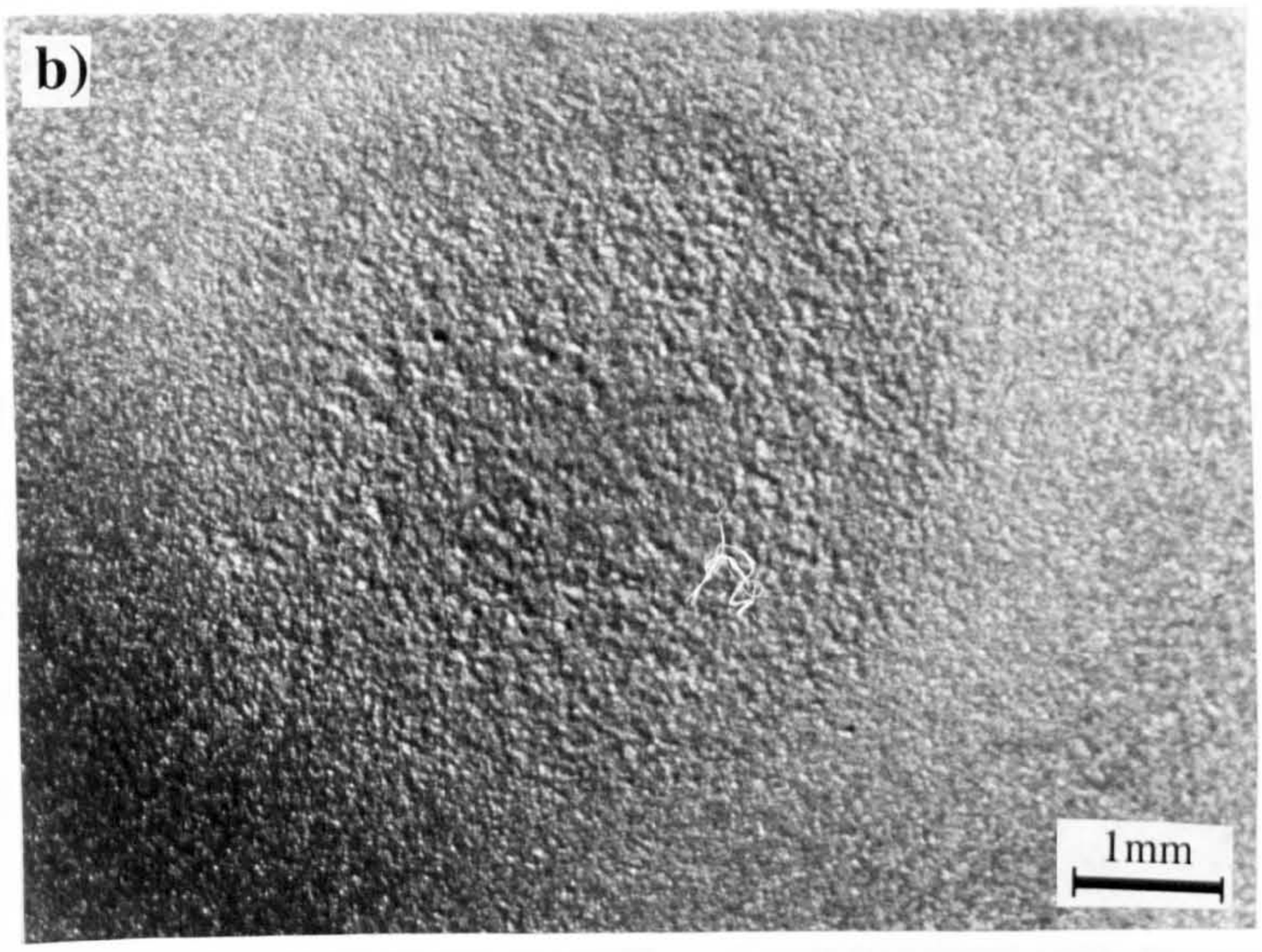
Figure 8.6.12 Back-scattered SEM micrographs of a) as-sprayed; and b) vacuum-fused coatings after 6-days of solid-free liquid impingement ($17ms^{-1}$, 18°C) under cathodic protection (CP) at -800mV SCE.

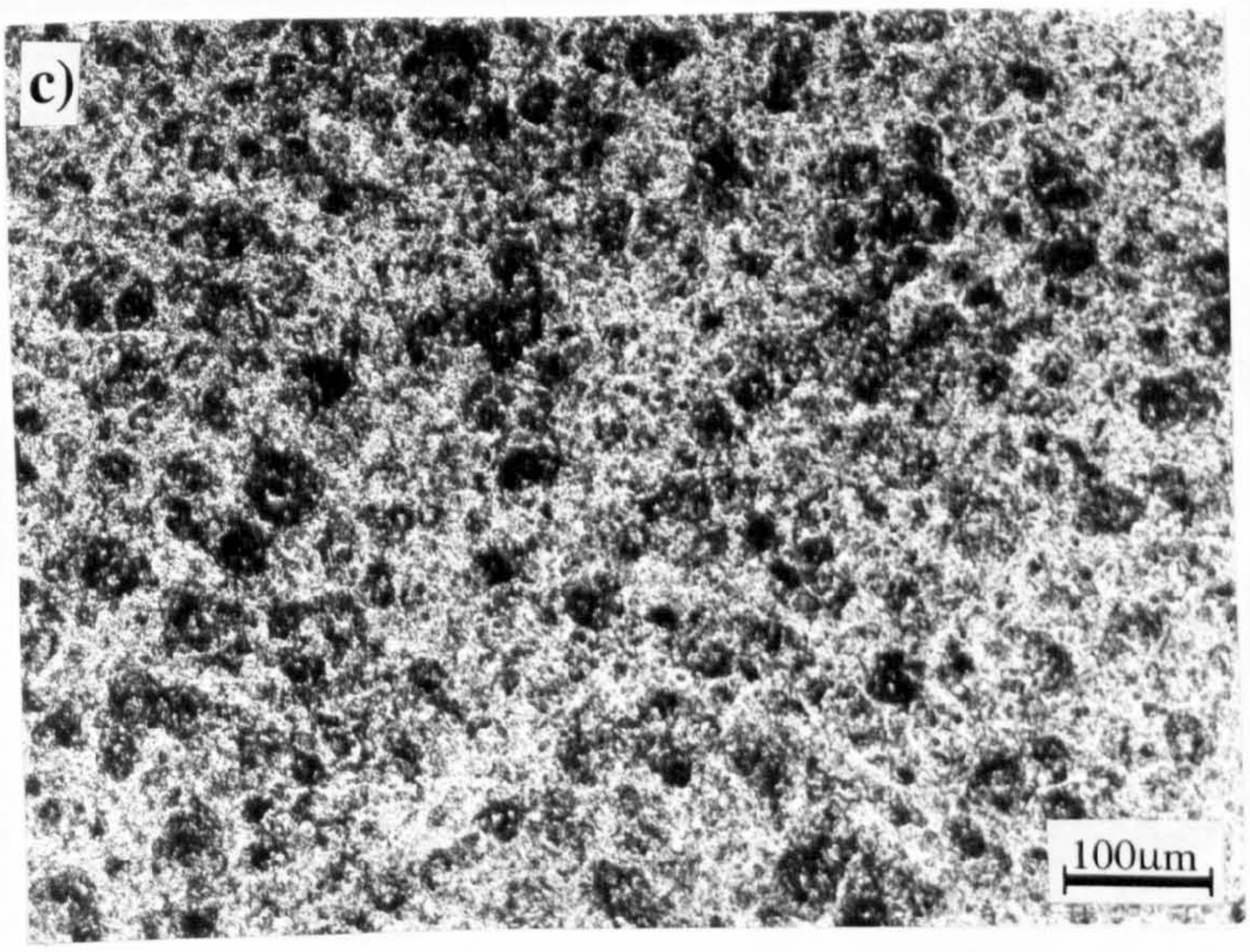
The application of CP significantly reduced the extent of the corrosion on the sprayed/sealed coatings during the 6-days exposure as shown in Fig. 8.6.12a. Moreover, under similar conditions of CP no distinguishable corrosion was observed in case of the vacuum fused coating (Fig. 8.6.12b).

Microscopic observations after solid-liquid impingement

Examination of specimens after solid-liquid impingement showed clear central wears scars after just a one-hour test, demonstrating the much higher material loss with addition of solid particles. The low magnification photographs (Fig. 8.6.13a and b) show the higher material loss on the sprayed coating under the impinging jet compared to the vacuum-fused coating and also show the much rougher wear scar surface on the sprayed coating. The roughened surface seemed to result from a drilling action of the impinging sand-liquid slurry, which formed relatively large-holes "macro-pits" (Fig. 8.6.13c), at the sites of which chunks of material were dislodged compared to much smoother surface of the fused coating (Fig. 8.6.13d). The size of the holes was much larger than the average splat and was therefore not simply as a result of splat dislodgement. A similar drilling effect has been observed during solid-liquid erosion, as has been described in previous Chapter 7 for *Coating* AI.


a)
1mm


b)
1mm


c)
100um

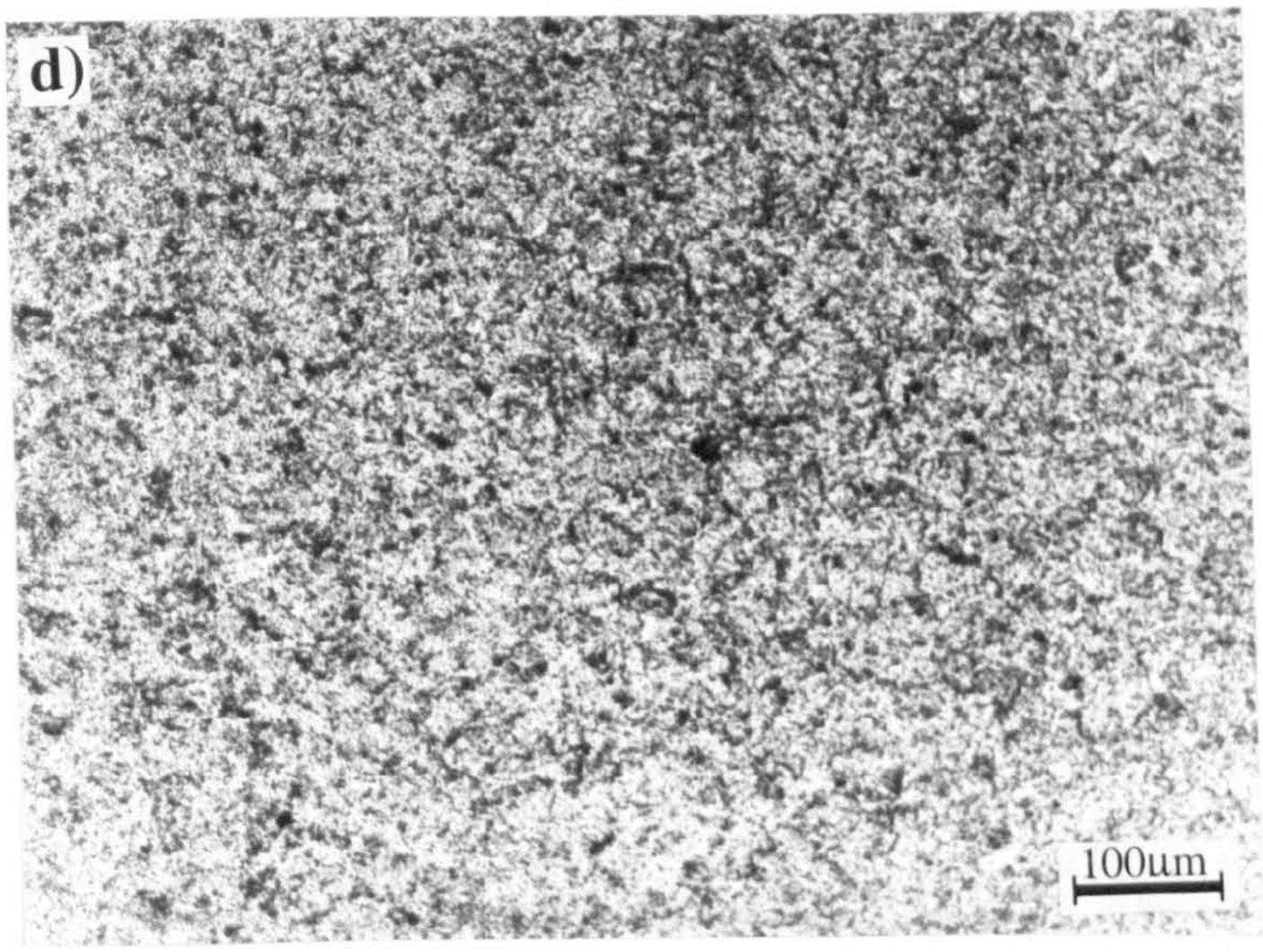
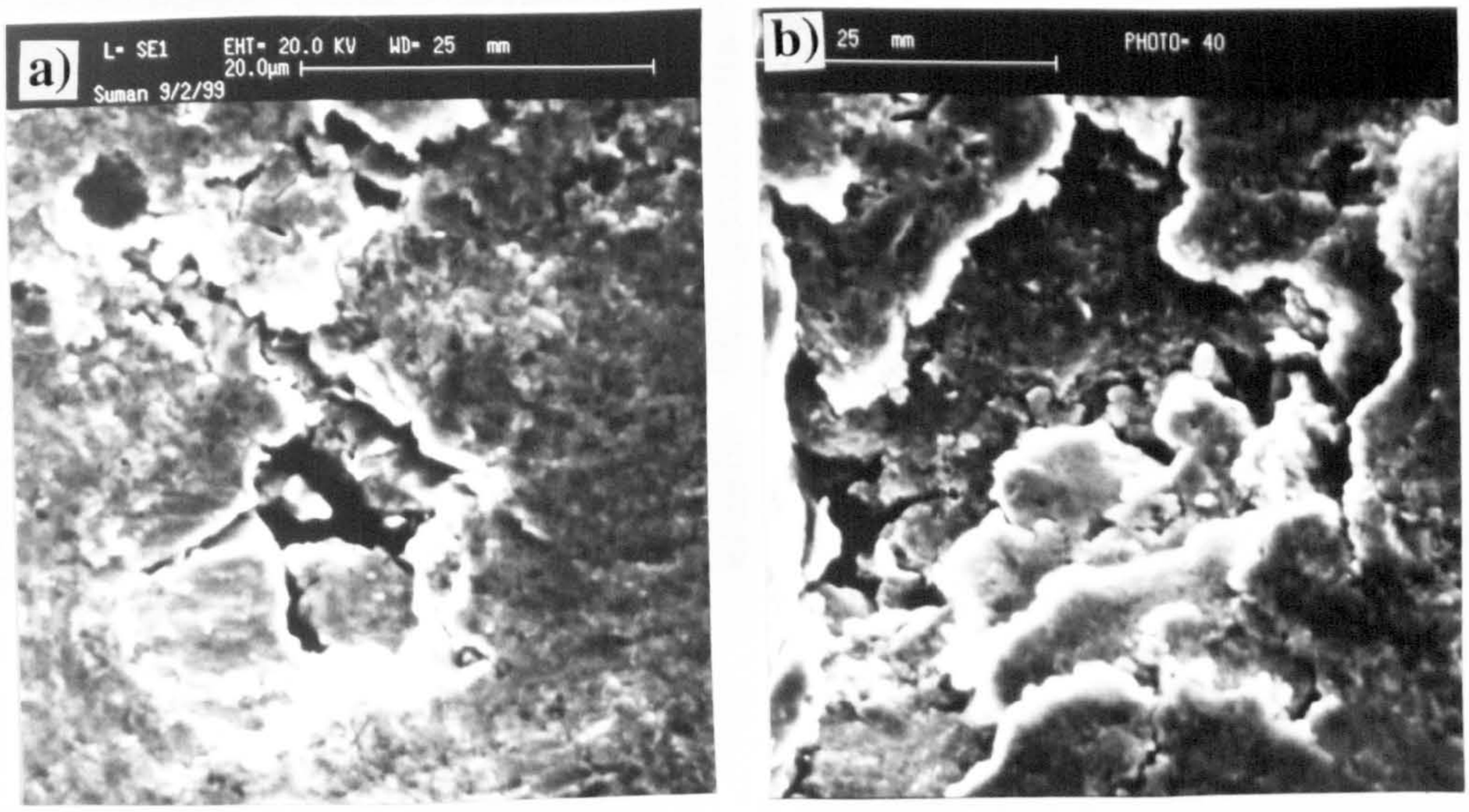


Figure 8.6.13 Central wear scars after 1-hour sand-liquid impingement: a) on the as-sprayed coating; b) vacuum-fused coating; c) higher magnification of 'a' showing large holes; and d) higher magnification of 'b' showing smoother surface.

The enlargement of the pits at the central wear region was found to be associated with lateral crack propagation within the splat boundaries of the sprayed and sealed coatings (Fig. 8.6.14a). Figure 8.6.14a also shows further drilling of the existing hole by both mechanical and electrochemical action of the impinging slurry jet and thus enlarging it. Figure 8.6.14b shows a severe material loss of the as-sprayed coating under the impinging slurry jet by a complex mechanism of corrosion of large fragments of the material and their mechanical removal on subsequent impact of the continuous jet. Material loss in the case of the vacuum-fused coating was associated merely with ductile ploughing and some loss of hardphase (Fig. 8.6.14c).



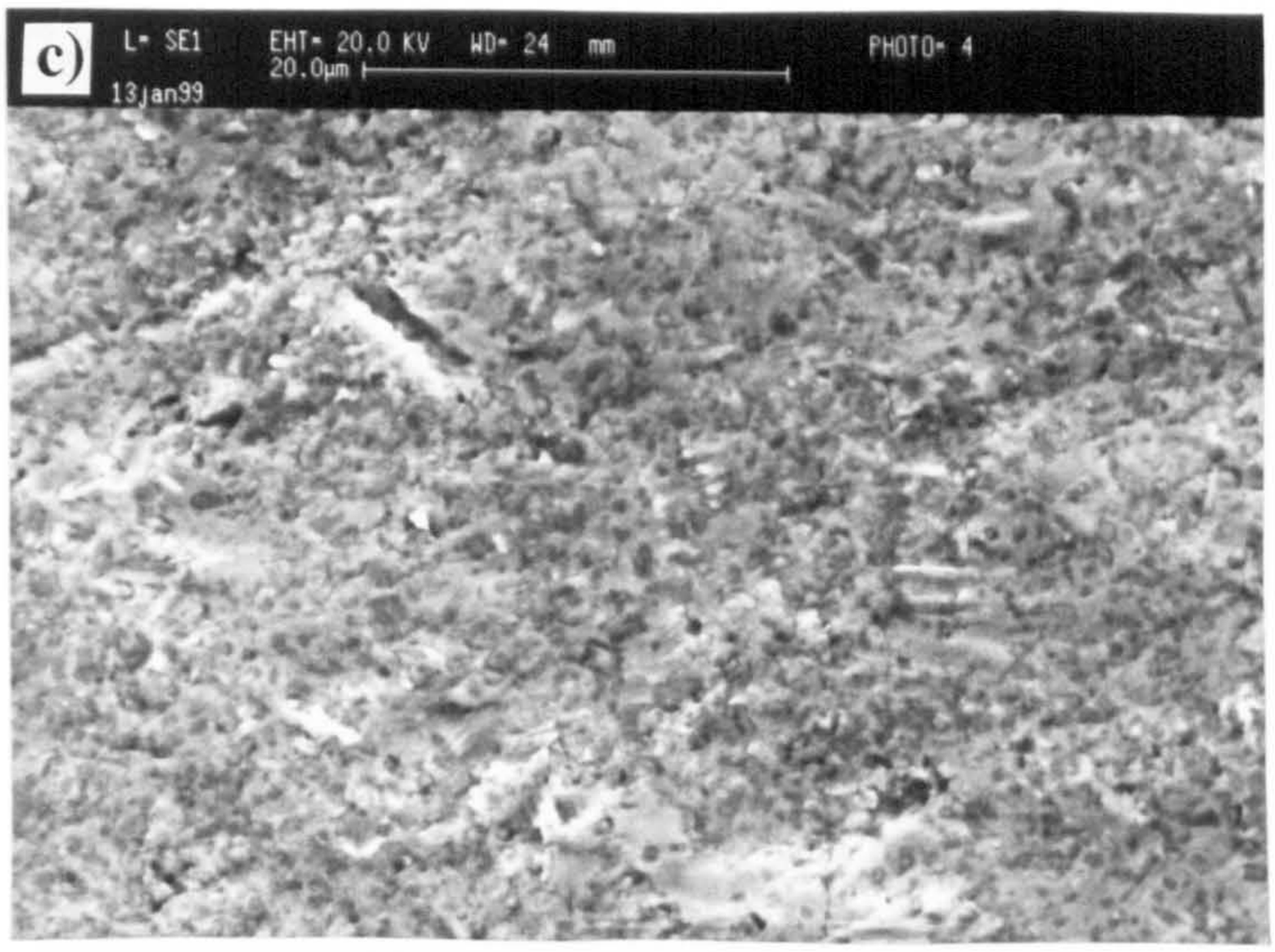


Figure 8.6.14 Secondary SEM micrographs of central wear region: a), b) as-sprayed; and c) vacuum-fused coating after 1-hour sand-liquid impingement.

Material losses in coatings also occurred outside the central zone at low impact angle and formed craters and eventual material loss by removal of the raised lips from the crater on subsequent slurry impacts. Microscopic observations also revealed the loss of hard phase particles being eroded away together with the chunk of matrices being removed. Craters formed by the low angle skidding of the erodents on the sprayed and sealed coatings (Fig. 8.6.15a, b) were relatively severe compared to those on the vacuum fused coating (Fig. 8.6.15c).

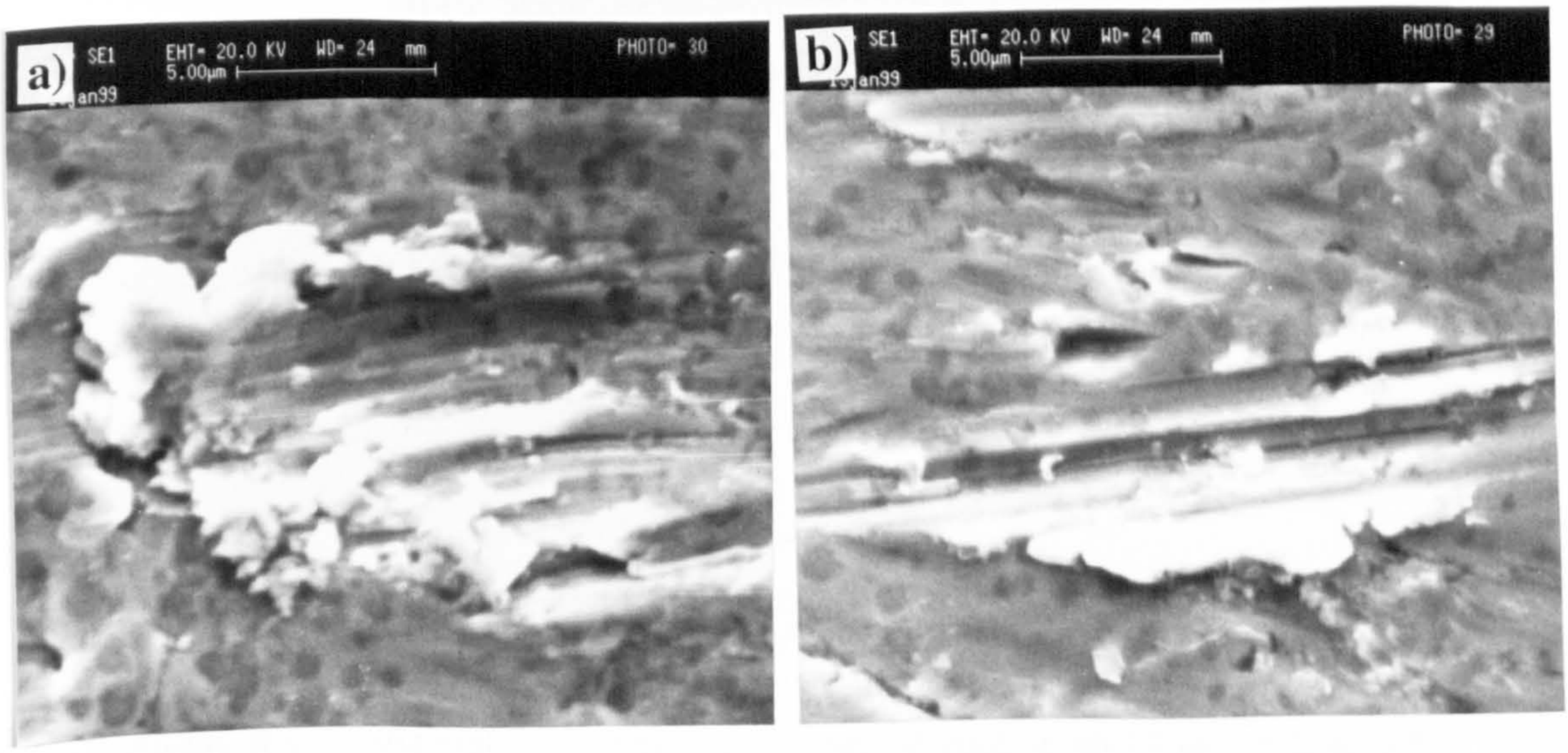




Figure 8.6.15 Secondary SEM micrographs showing material removal mechanism at low angle impingement: a), b) sprayed/sealed; and c) vacuum-fused coatings under sand-liquid impingement (17ms^{-1}, 18°C).

It should be noted that even under the solid-liquid erosion stream, corrosion at splat boundaries was still observed on both the sprayed and vacuum-sealed coatings (Fig. 8.6.16).

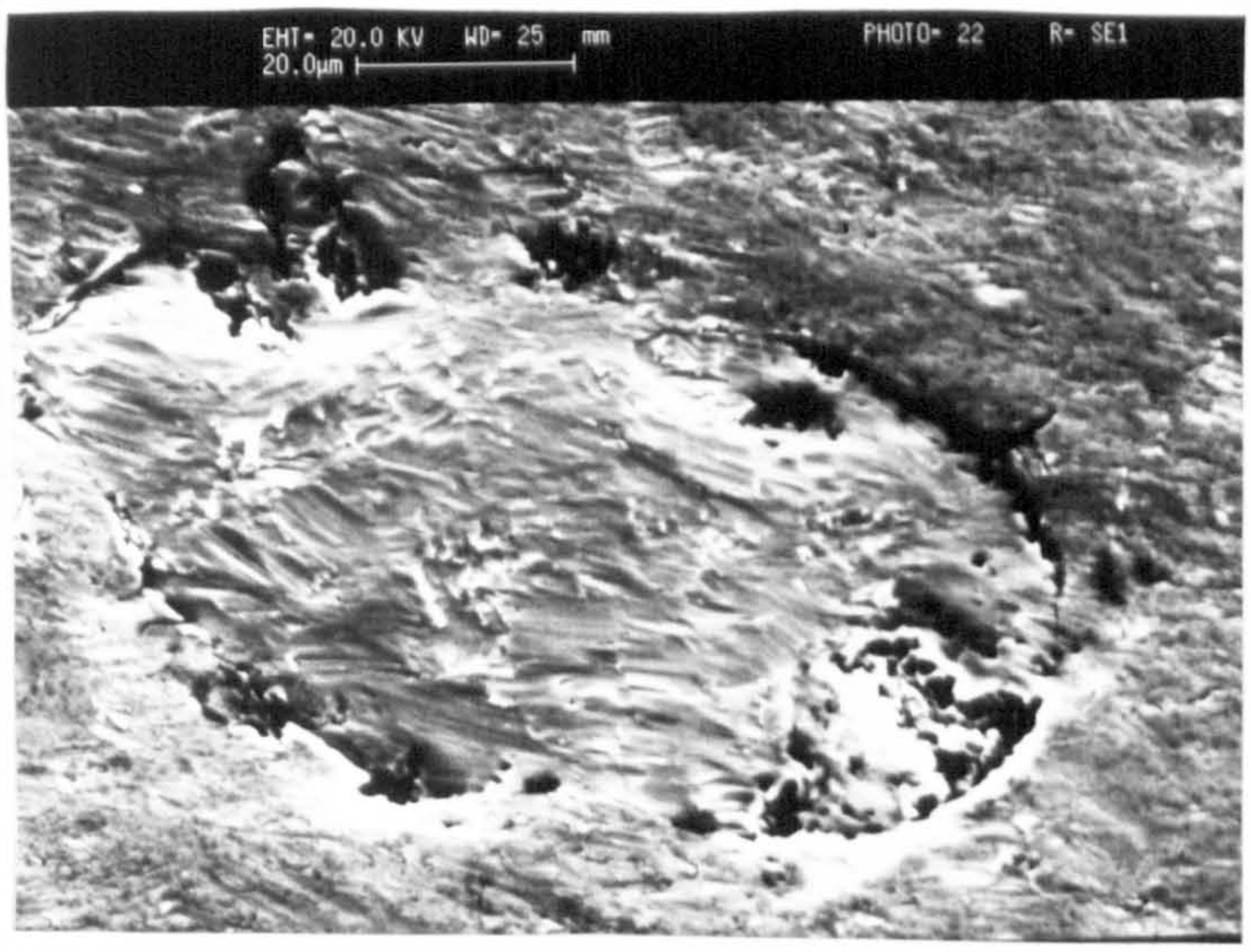


Figure 8.6.16 Material loss on the sprayed/sealed coating associated with particle splat boundary attack at outer region.

CHAPTER 9.

9.1 Liquid erosion-corrosion of stainless steel with different radii

Objective

Results described in previous Chapters have shown clearly the different erosion-corrosion behaviour in various regions of the specimen. The most obvious feature in this respect was the complex wear scar under and adjacent to the impingement under solid-liquid impingement. Even during solids-free liquid impingement there were variable deterioration features in different parts of the specimen. Corrosion attack in the form of comet shaped streams were evident at velocities $17ms^{-1}$ and $72ms^{-1}$, which occurred mainly in the region away from the central impingement region. At lower velocity about $17ms^{-1}$, no attack was observed at the region 'C' right under the central jet. However on increasing the velocity up to $72ms^{-1}$, region 'C' displayed surface attack primarily due to the mechanical effect as described previously in the form of ploughing of material. It was thus recognised that useful further insight into the complex erosion-corrosion behaviour would be obtained by the study of electrochemical behaviours of different regions of the area under the impinging jet and how the flow characteristic of hydrodynamics might influence the different regions in erosion-corrosion conditions. Due to the difficulty in obtaining HVOF coated specimens of the small diameter (4mm) needed in the later stages of the project, it was decided to undertake a preliminary study of these matters on the stainless steel material. It was noted that this would provide useful further information on these complex interactions both relevant to erosion-corrosion of stainless steel but also enabling suggestion to be made for future work of this kind of thermal sprayed coating. Initial investigations were carried out under solid-free liquid impingement on stainless steel UNS S31603 specimens.

Experimental technique

The experimental procedure comprised the study of concentric stainless steel specimens as shown in Fig. 9.1. The central cylindrical specimen 'C' of diameter 4mm was mounted concentrically with an outer ring shaped specimen 'O' with both the specimens being soldered separately at the rear side of the specimen so that there was no electrical contact between the two specimens. The specimens were mounted in a non-conductive epoxy-resin as stated in Chapter 6.

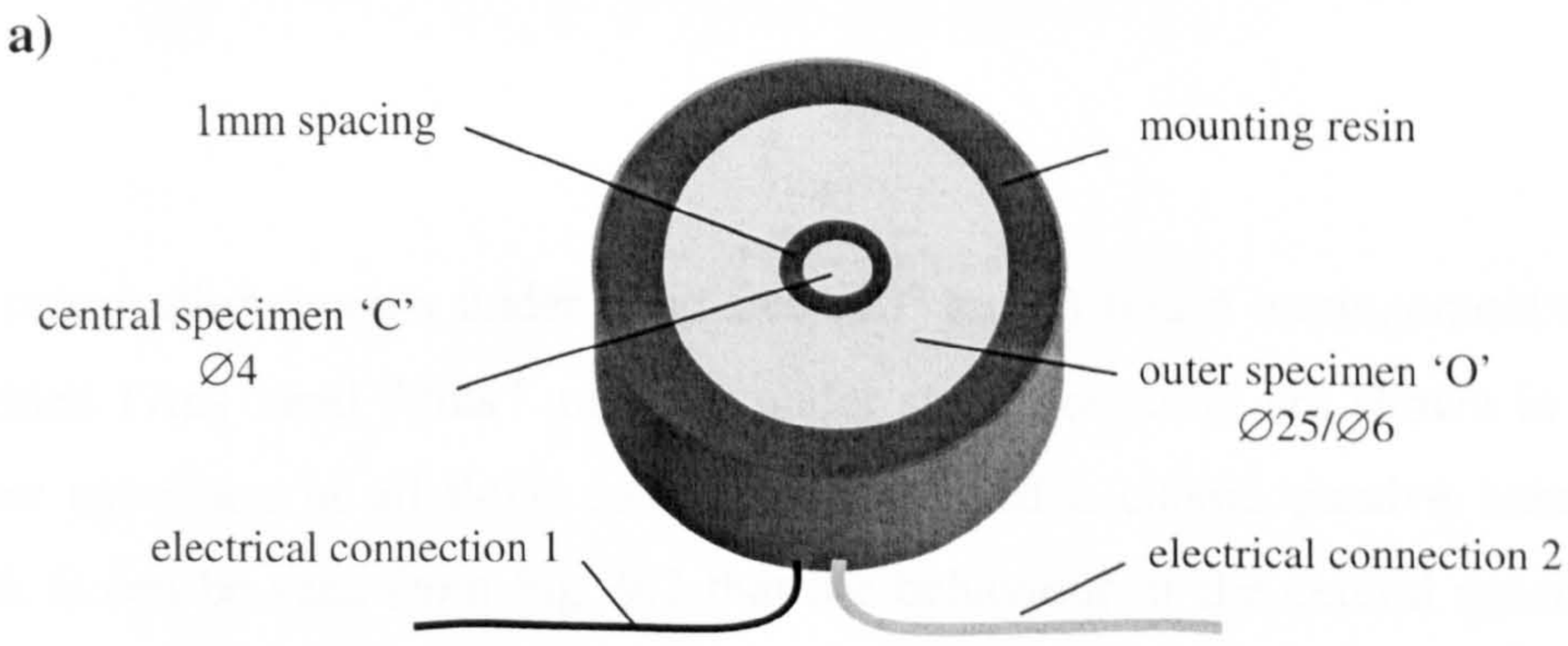
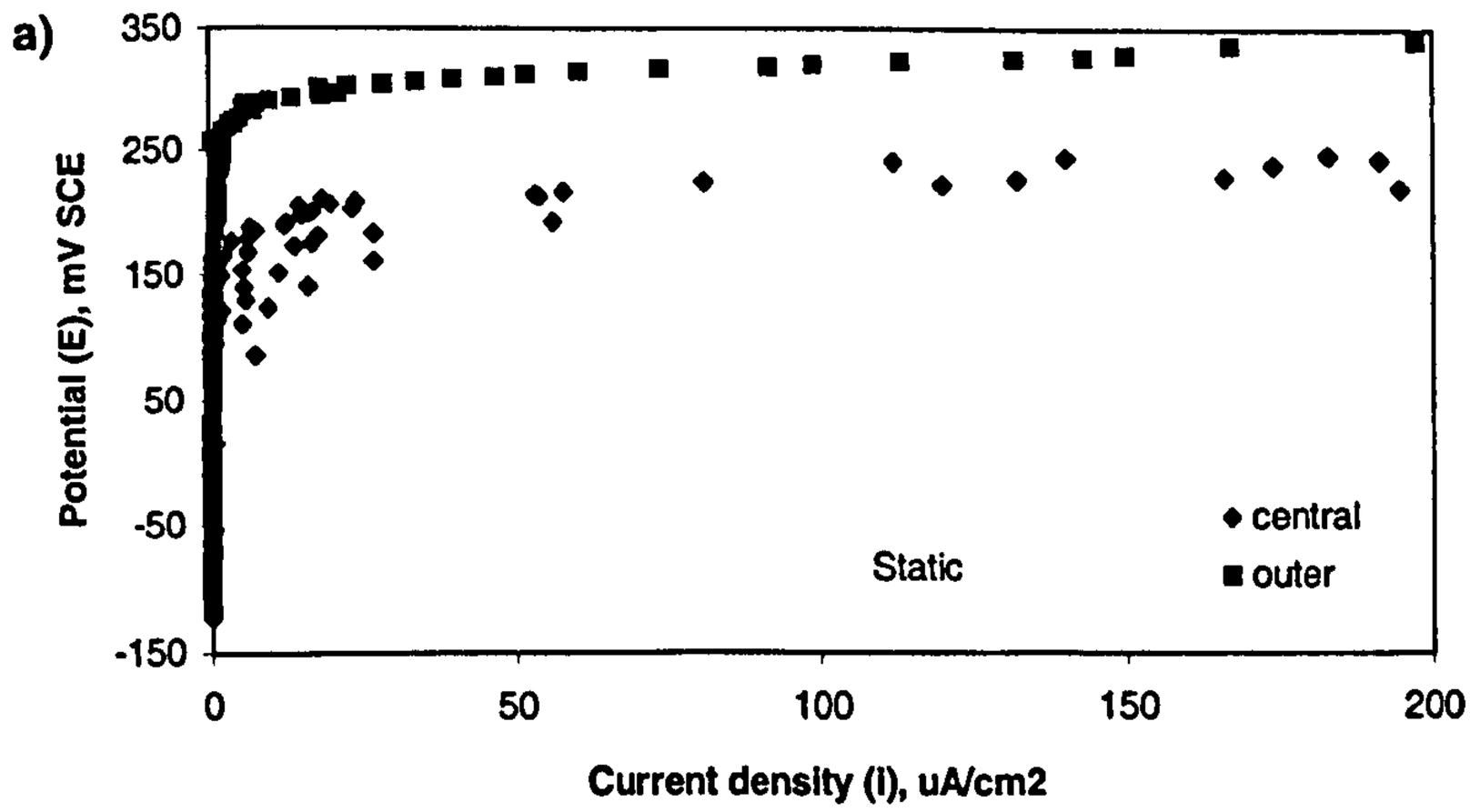


Figure 9.1 a) assembly of concentric specimens: central 'C', outer 'O' mounted in a non-conductive epoxy resin; b) schematic diagram of the liquid impingement rig, P_1 - low pressure pump, P_2 - high pressure pump.

Both specimens were connected to computer-controlled potentiostat, where the individual specimens are polarised cathodically and anodically in a computer controlled potentiostat, which allowed both the specimens to investigate at a single time, while under the impinging jet. All the experimental procedure was similar to that already explained previously. The spacing between the central 'C' and outer 'O' specimens was kept 1mm. The exposed area of 'C' was $0.13cm^2$ and that of 'O' was $4.72cm^2$. The diameter of the nozzle was 1mm. Anodic polarisation sweeps were started once again after 15 minutes of free impingement at E_{corr}. The electrolyte used was 3.5% NaCl solution made in the distilled water and the temperature was maintained at 18°C.

Results

Anodic polarisation sweeps under solid-free (90° angle) liquid impingement condition at velocities $17ms^{-1}$ and $72ms^{-1}$ and also under static condition are shown in Fig. 9.2. The outer specimen in all three conditions displayed a classic passive behaviour as expected. It can be seen from Fig. 9.2 that the behaviour of the central specimen was similar in both static condition and under direct impingement of $17ms^{-1}$ is that for a significant range of potential positive to E_{corr}, low currents (typical of a passive behaviour) were recorded. However, earlier breakdown of the passivity with lower E_b of the central specimen compared to the outer specimen (despite of the similar experimental conditions) can be presumably due to the higher crevice effect as the small central specimen is surrounded by a larger area of the mounting resin.



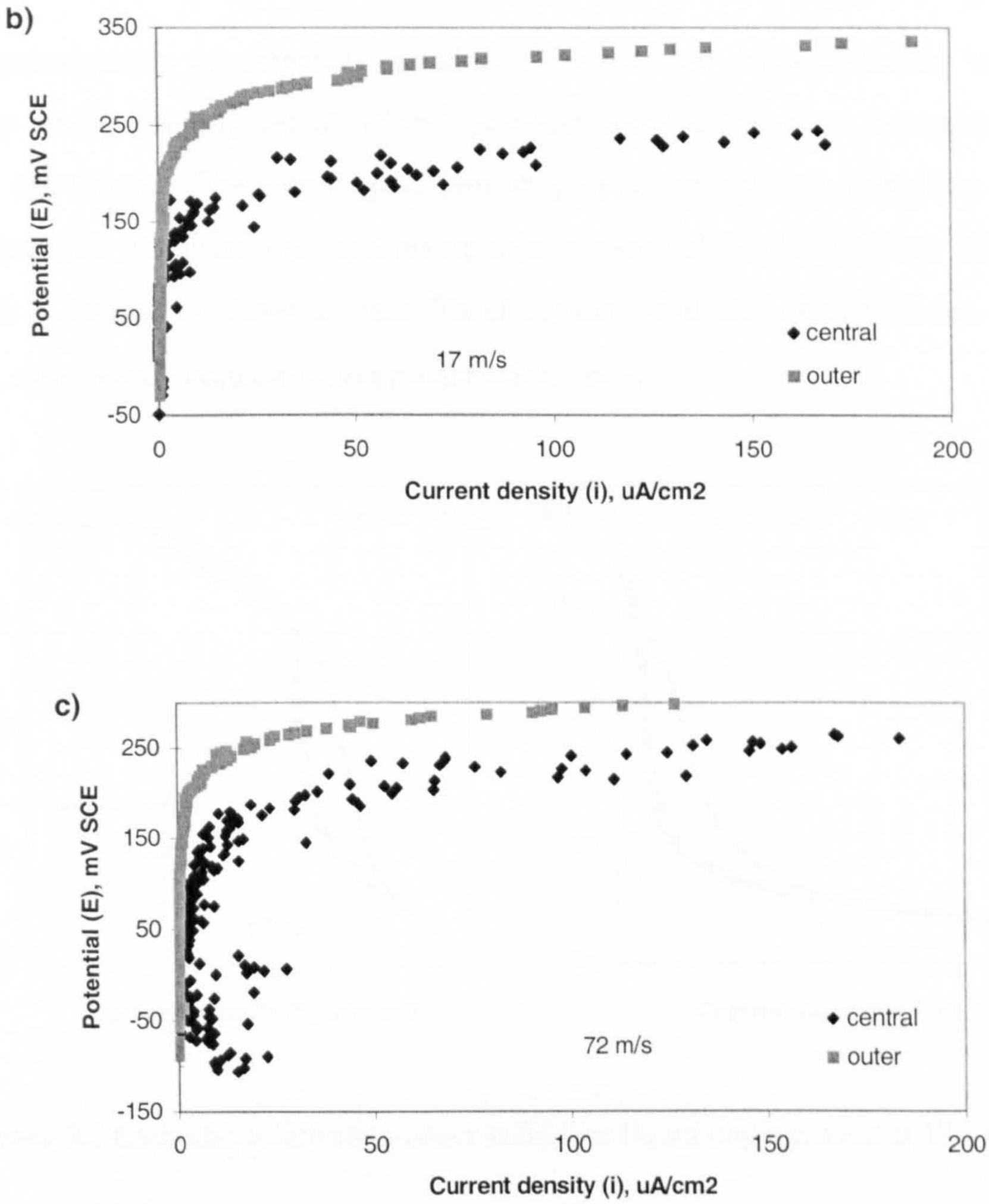


Figure 9.2 Anodic polarisation results under solid-free impingement: a) static b) 17ms^{-1}; and c) 72ms^{-1} in 3.5% NaCl solution at 18°C.

But at 72ms^{-1} (Fig. 9.2c), an interesting characteristic was demonstrated by the central specimen, which showed scattering of the current densities of several tens of μA/cm^2 immediately after the anodic scan was commenced. This provided evidence of periodic breakdown and repassivation of the protective film under free corrosion condition at this high velocity.

Cathodic polarisation

Cathodic polarisation experiments conducted under the hydrodynamic conditions imposed by the impinging jet at $17ms^{-1}$ showed some differences between the two concentric specimens. The outer specimen displayed an oxygen reduction cathodic reaction shown by its initial low currents up to a current value of 2-3$\mu A/cm^2$ (Fig. 9.3a), after which it began to show a clear Tafel region until the current value of about 30$\mu A/cm^2$, after which concentration polarisation starts.

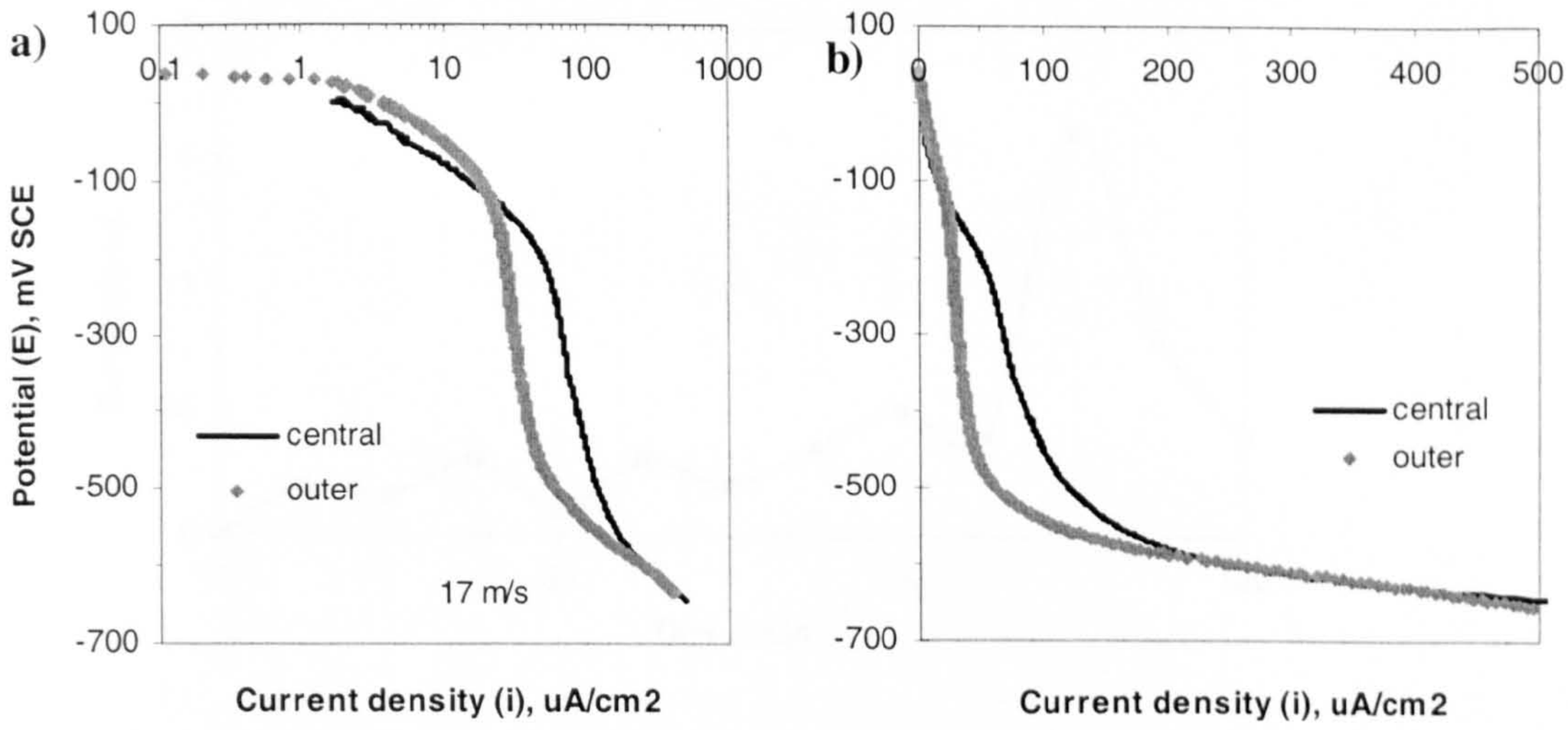


Figure 9.3 Cathodic polarisation under solid-free liquid impingement at $17ms^{-1}$.

The central specimen showed an immediate increase of current as soon as the liquid jet impingement was imposed with its depolarised cathodic reaction, until it reached the current value of about 60-70 30$\mu A/cm^2$, after which concentration polarisation begins. However, Fig. 9.3b shows that the hydrogen evolution reaction was not affected by the hydrodynamic conditions at different regions of the specimen.

Galvanic current measurement

Part of the rationale behind these experiments with the separate inner and outer specimens was to see if there is any galvanic current flow between the two regions under hydrodynamic condition. Moreover, the observation from the anodic polarisation tests of a slightly more negative 'E_{corr}' of the central sample and the fluctuating active

tests of a slightly more negative 'E_{corr}' of the central sample and the fluctuating active passive behaviour of the central specimen at $72ms^{-1}$, provided further indirect indication that galvanic interaction may be occurring. The currents flowing from the inner specimen to the outer one during a three hour period of solid-free liquid impingement at $72ms^{-1}$ velocity are shown in Fig. 9.4 from which it can be seen that the galvanic currents (whose polarity was consistent with the central specimen being the anode) were in fact quite small with a maximum recorded current of 1.6μA. This however, represents a current density on the central specimen of about 12$\mu A/cm^2$.

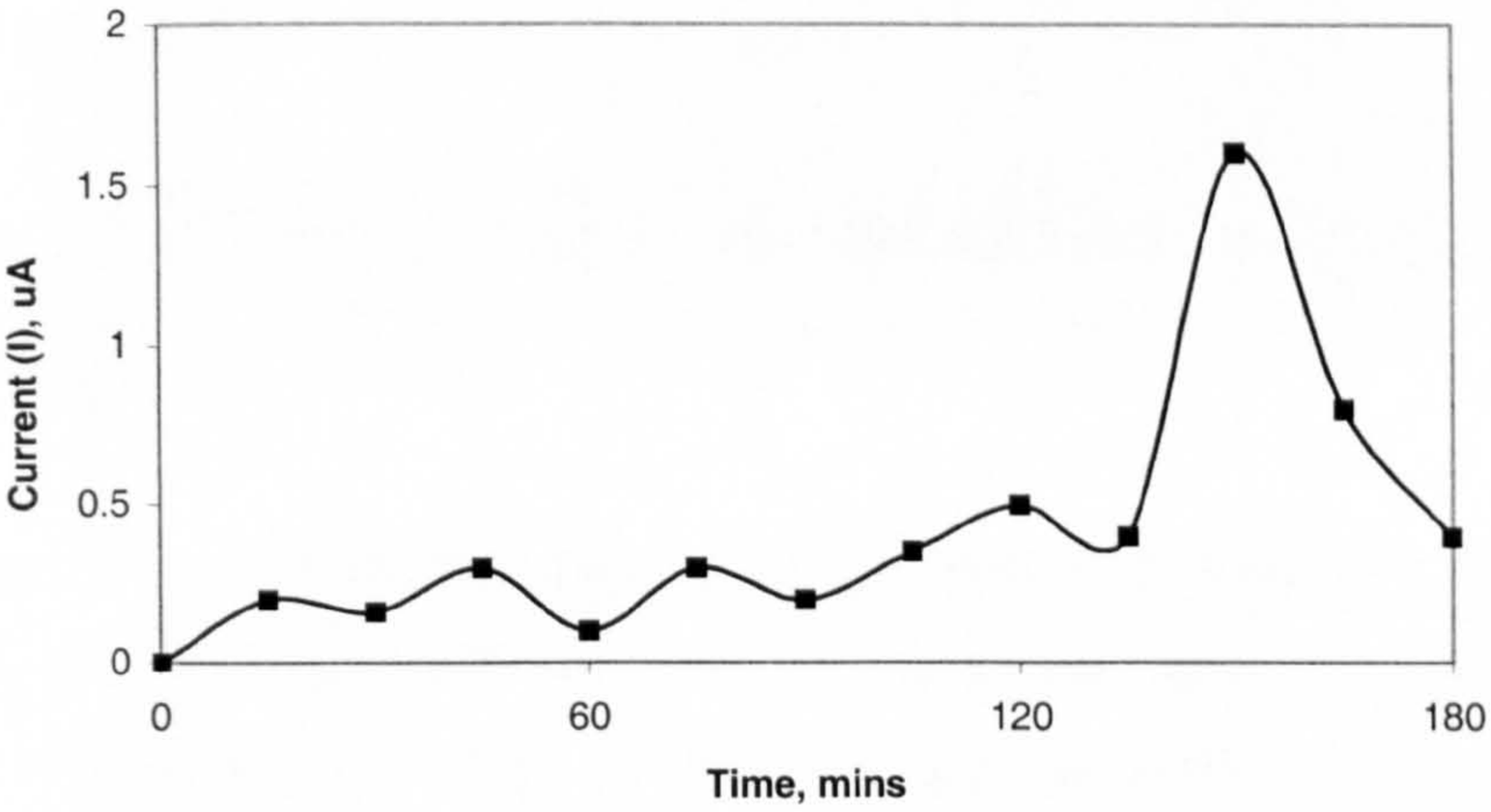


Figure 9.4 Galvanic current between inner and outer specimens recorded during 3-hours of solid-free liquid impingement ($72ms^{-1}$) at E_{corr}.

Microscopic observations after impingement tests

Microscopic observations showed corrosion product on the central specimen just after the termination of the anodic polarisation under impingement of $17ms^{-1}$. Figure 9.5 clearly shows the area directly under the impinging jet (about 1mm diametrical area) to be clear and unattacked, while the region away from the central 1mm diameter shows streams of corrosion product (in comet shape) moving towards the flow directionality. The outer specimen also displayed few tiny pits, which were visible only under very high magnification, but they did not take any comet shape. Crevice corrosion at the central specimen-spacing interface was also observed.

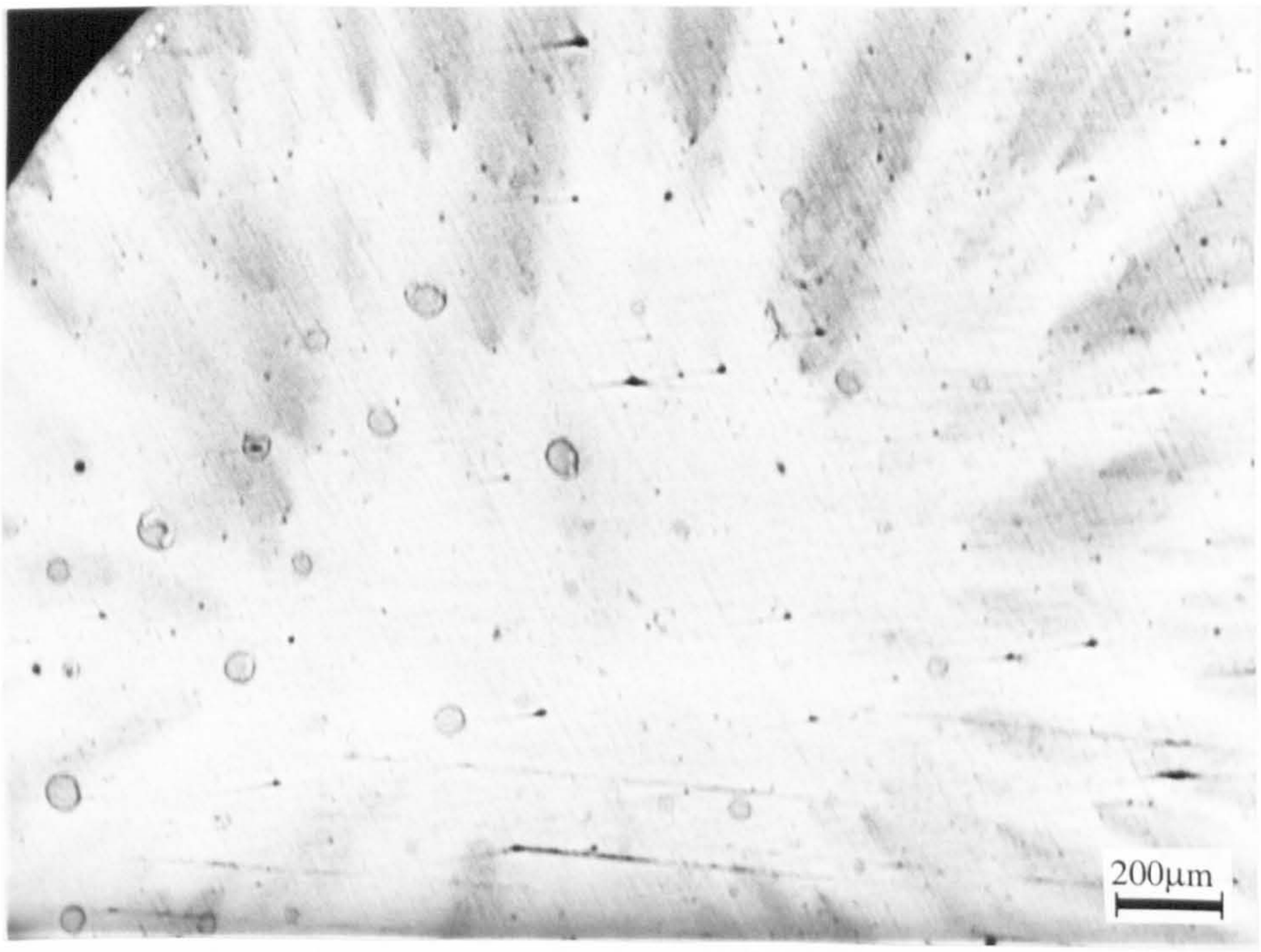


Figure 9.5 Corrosion attack on central specimen after anodic polarisation under impingement of $17ms^{-1}$.

However, after anodic polarisation under jet velocity of $72ms^{-1}$, a wear scar directly under the jet of about 1mm diameter on central specimen was distinct (Fig. 9.6a). Higher magnification revealed several tiny pits on central specimen. In addition, material removed in the form of craters ploughed by high velocity liquid jet (Fig. 9.6b) was clearly visible as has been illustrated in Chapter 8. The outer specimen showed several pits and comet configuration after the test period as shown in Fig. 9.6c.

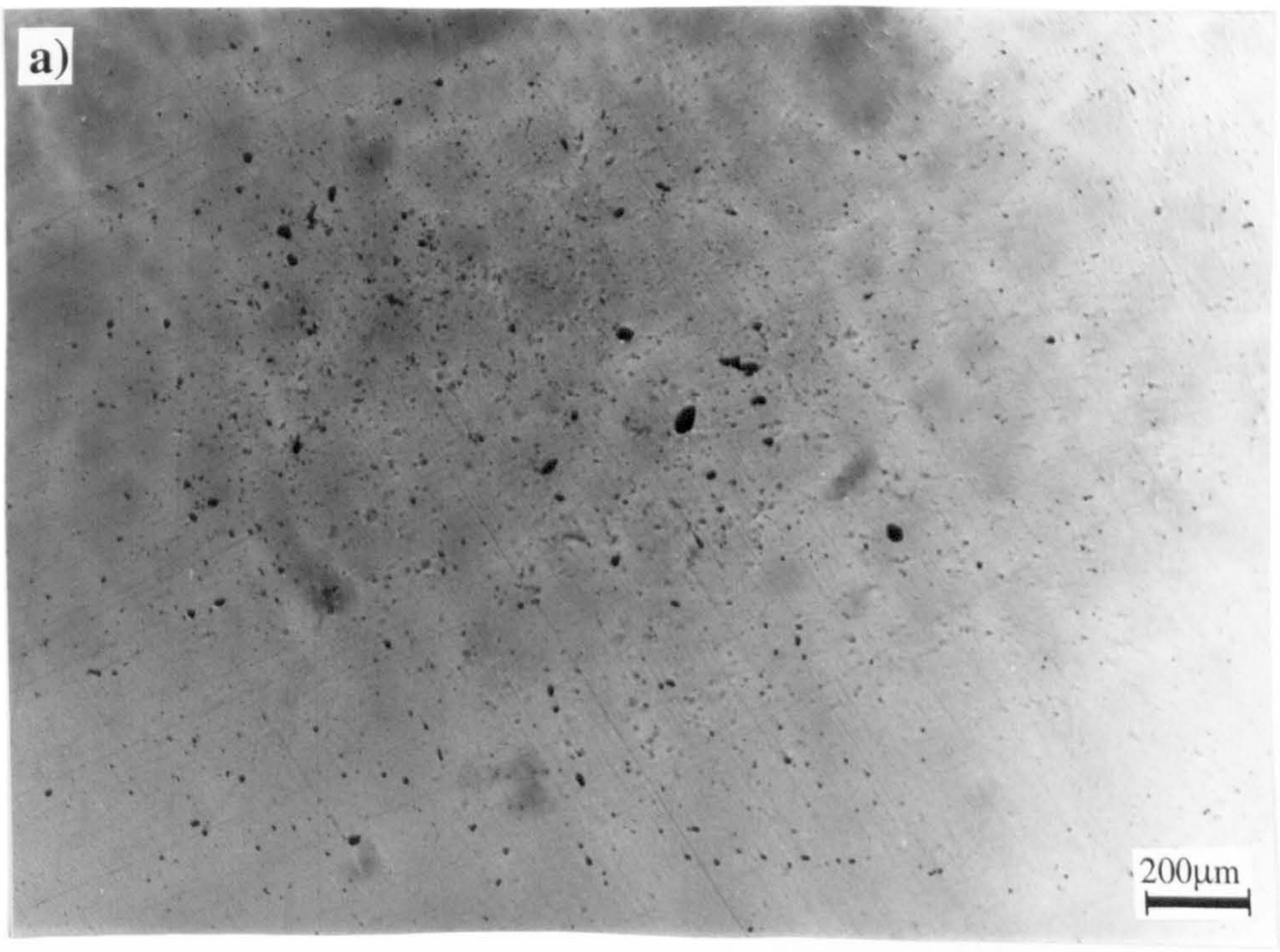






Figure 9.6 Anodic polarisation under 72ms^{-1} impinging velocity: a) optical micrograph of central wear region; b) higher magnification of the central region showing tiny pits and ductile ploughing; c) pitting of outer specimen.

Difference was clearly visible when the specimen was polarised in static condition. The central specimen exhibited a large number of pits over the entire surface as shown in Fig. 9.7. Maximum pit depth of about 10μm was found. The outer specimen also displayed similar type of pitting attack but the amount of pits was relatively very small compared to the central specimen.

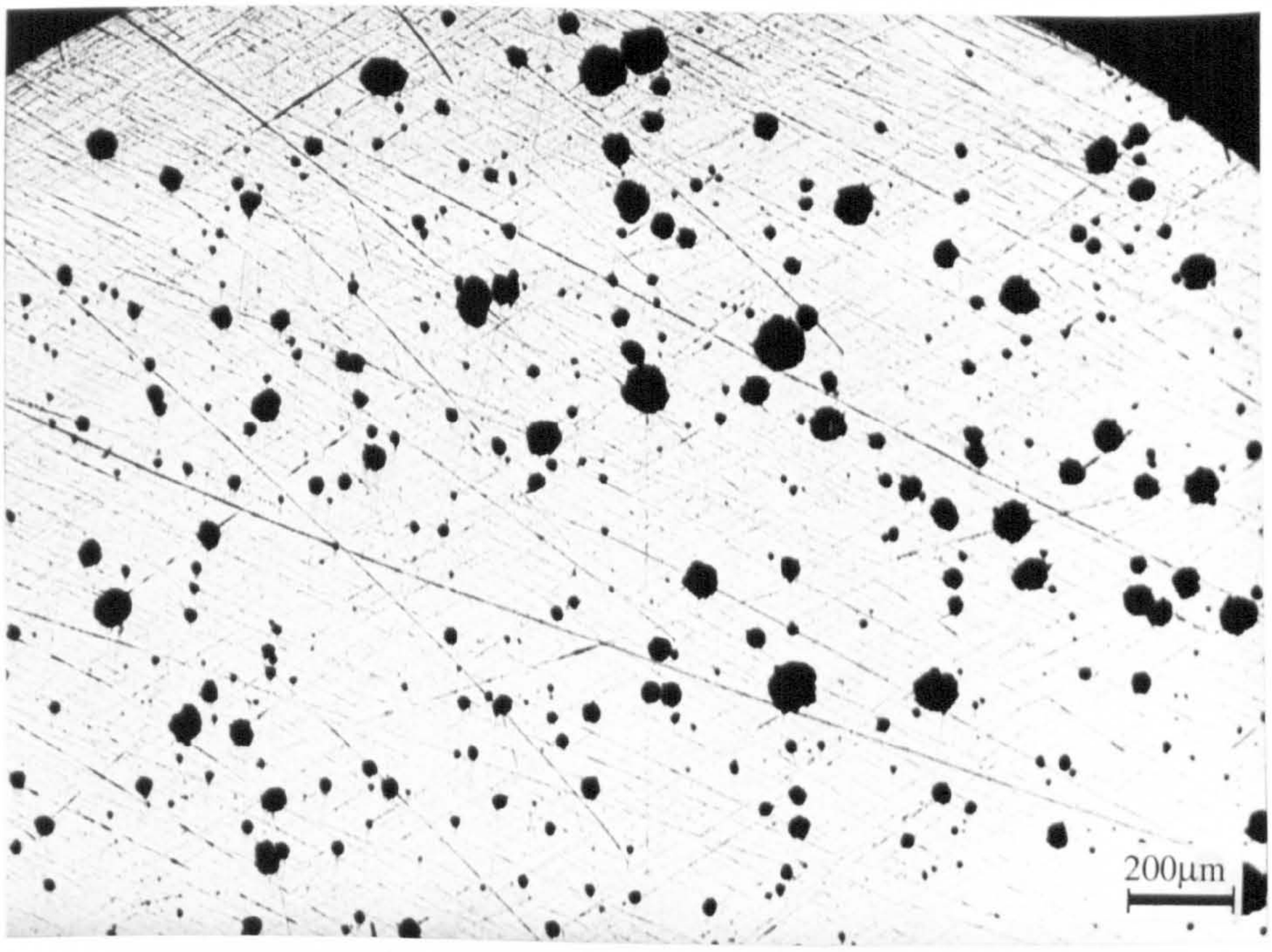


Figure 9.7 Optical micrograph showing pitting attack on central specimen after anodic polarisation in static condition.

CHAPTER 10. DISCUSSION

10.1 General

As pointed out in the 'Introduction' section of Chapter 1, surface engineering techniques are increasingly being used as potential remedies for material degradation and particularly in cases, where severe corrosion or erosion-corrosion is likely to occur. Such techniques encompass processes capable of creating and/or modifying surfaces to provide enhanced performance e.g. resistance against corrosion and erosion-corrosion.

There was a viewpoint that the major consideration in relation to the corrosion behaviour of cermet coatings is the susceptibility of the substrate material to corrosive attack by ingress of corrosive fluid via-interconnected pores in the coating (Ashary and Tucker, 1991). However, more recent studies (Neville and Hodgkiess, 1996) have shown that the cermet coating itself is susceptible to corrosive attack in aqueous environments and, in cases where interconnected porosity is low, this can be the main means of attack. Works by Berget (1998) have considered the erosion-corrosion performance of mainly WC-based coatings in seawater environments and have shown that degradation was associated with the corrosion of the metal matrix, which will eventually lead to dislodgement of WC hard particles. Material degradation mechanism of a coating system, which includes both the coating and the substrate in severe corrosive environment, is very complex and is even more complex when the corrosive environment contains solid particles.

This Chapter will attempt to discuss the matters concerned with the corrosion and the erosion-corrosion behaviour of the coatings studied as part of this work and the findings will be related to the existing literature in this field. Moreover, an attempt is made to correlate the coating performance to the coating chemical and physical characteristics.

10.2 Powder characterisation

SEM micrographs revealed that powder samples of *Coating* A and *Coating* B supplied by two different commercial coating companies had many similarities in shape and size. Gas-atomised powder A and water-atomised powder B were both spherical in shape with identical surface structure, which according to Kretschmer et al. (1997), is typical of the ease with which spherical powder particles of NiCrSiB are produced. Pawlowski (1995) has reported that water-atomised powder particles of the non self-fluxing type are usually irregular.

An interesting feature of both the powder particles was that several particles were enriched in Ni compared with the nominal coating composition. Some particles did not contain any hardphase particles and some had only a few tiny hardphase particles distributed within the metal matrix. It would appear that the regions identified in the coating free from hardphase particles, resulted from spraying of these particles. The phase determination by XRD of the powder particles of both types revealed that they comprised mainly a solid solution of complex compound NiCrFe and $Cr_{23}C_6$ hardphase particles. However, there were some differences between the two powders with their other hardphase particles content. Powder A displayed existence of $Ni_{16}Cr_6Si_7$, whereas powder B comprised Ni_5Si_2 and Cr_3NiB_6. This was also supported by the cross-sectional SEM images of the powder particles with their different types of hardphase particles (shown by their atomic number contrast) as stated previously in the Chapters 7 and 8.

As well as their different structural characteristics, another important aspect of the powder particles is their different masses as the size ranges varied between 3 to 45μm and in HVOF guns, a parameter such as particle exit velocity is only the average value. For a given flux of powder particles, smaller particles might have a relatively small kinetic energy compared to the bigger ones and this can result in a decrease in coating quality than that can be achieved. Sieving of the particles and spraying of a more uniformly distributed particle sizes can lead to optimisation of processing parameters and achieve maximum coating quality with higher density, higher hardness, less intersplat voids and even greater homogeneity. Berget et al. (1998) concluded that

powders having a narrow powder grain size distribution give coatings of higher quality than powders with wider grain size distribution, the conclusion being based upon WC based coatings. Moreover, non-spherical particles, as shown in section 7.1, can also lead to heterogeneity in the coating quality as irregular shaped particles might not adhere properly during the contact with the sprayed surface. This could be associated with the formation of irregular splats due to different moments of inertia of irregular powder particles as the they leave the HVOF gun barrel.

10.3 Coating characterisation

As already explained in the Results Chapters, both coatings A and B supplied by two different manufacturers are very much alike in their microstructural appearance with a very low coating porosity and well adhered splats overlapping on one another in a lamellar structure. There were a certain amount of powder particles clearly, which resulted in splats denuded with hardphase particles. Thus producing a coating where some regions had a very low distribution of the hardphase particles and is shown in optical and SEM micrographs on the cross section. Such evidence was even more clear on the plan-polished surface of the coatings in Fig. 10.3.1, which shows a powder particle containing hard phases overlapped onto another powder particle constituting mainly of the metal solution.

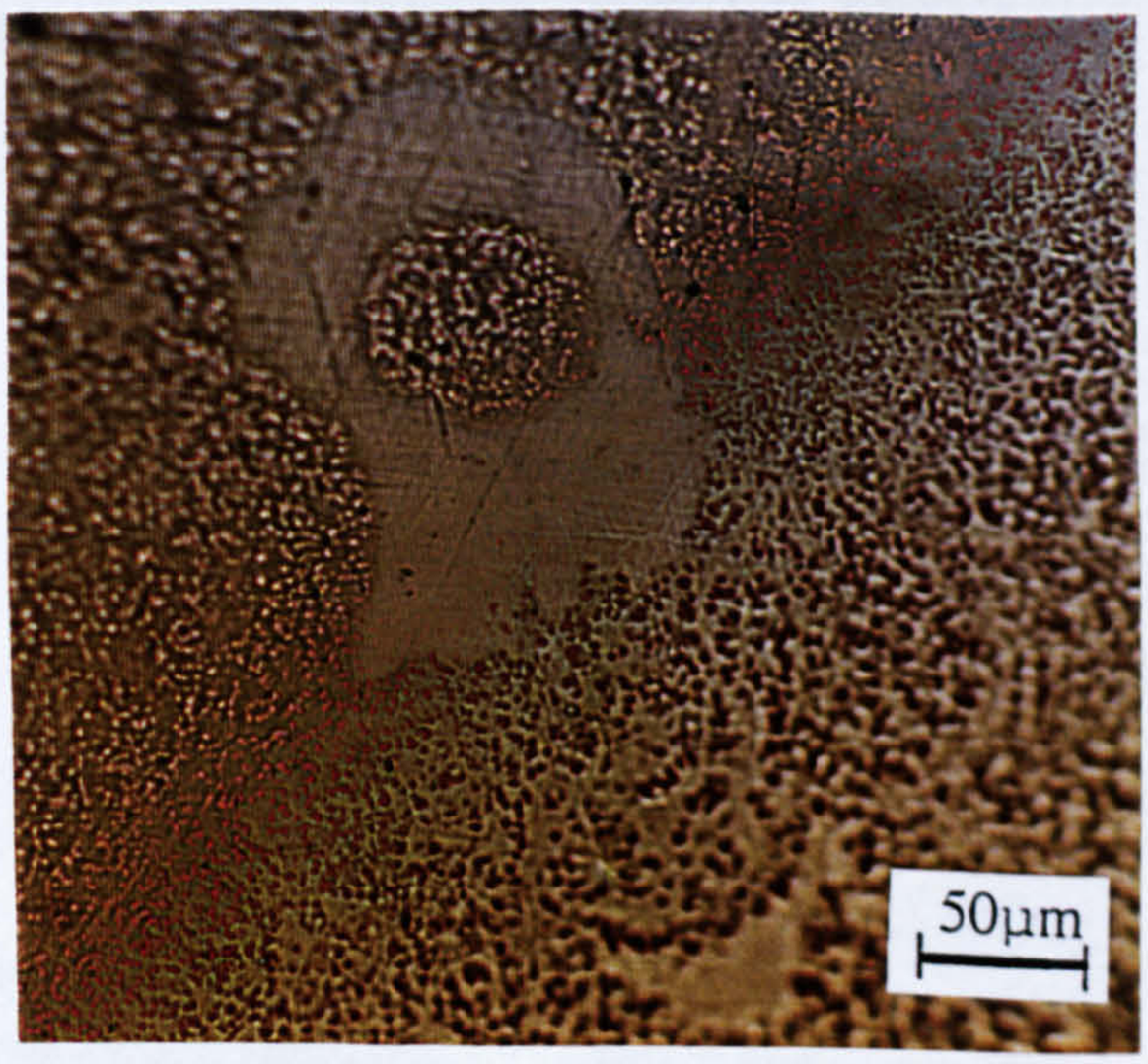


Figure 10.3.1 Overlapping of two powder particles different in hardphase content.

Such non-homogeneity of the coating however on a microscale can possibly result in varied wear performances of the different regions under severe erosion-corrosion condition, when hardness of the area under impact is of most significance. Such variations in hardness distribution were fully supported by the microhardness measurements performed on the coating surface. Microhardness value was also measured on the areas of metal matrix, where hardphase particles were denuded, which displayed the microhardness reduced by 5-7% of the value that was measured at regions where hardphase particles were uniformly distributed. This value is probably underestimated due to 3-D nature of the coating.

The few defects that were encountered on both the coatings were mainly interlamellar voids formed during impacts of powder particles onto the surface. This could have resulted due to insufficient kinetic energy achieved by semi-molten particles to fully adhere the surface. Another possibility could be a degree of flattening which determine the nature of interlamellar bonding (Kuroda, 1998). Moreover, high magnification SEM micrographs as shown in Fig. 8.2.1b revealed several splat particles having clear splat boundary separations, which were related to premature loss of individual splat particles due to preferential corrosion attack around these areas and will be discussed in more detail in the corrosion section. Microadhesion between particle splats has been shown to increase with an increasing density, viscosity and velocity of the impinging particle droplet (Sobolev et al., 1997). Figure 10.3.2 shows the schematic representation of the inter-lamellar void and splat boundary around the powder particle on the coating.

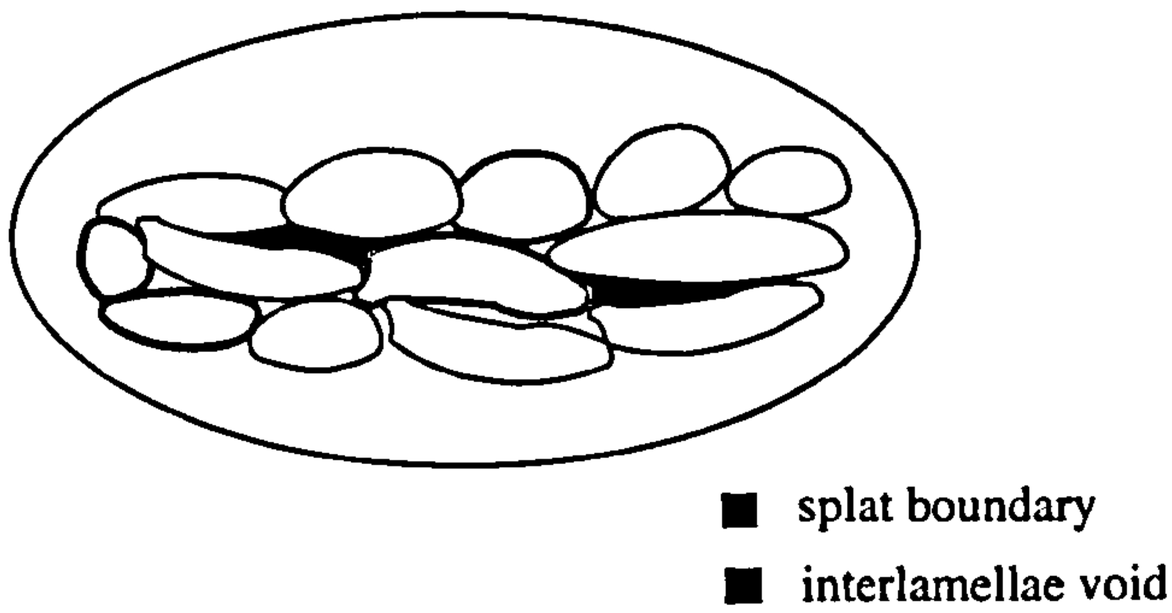


Figure 10.3.2 Cross-sectional schematic representation of splat boundary and inter-lamellae void formed during coating formation.

XRD patterns of the powder particles were compared with the patterns of the as-sprayed coating, which showed no phase transformations during the spraying process and retained their parent phases as in the powder particles. Vickers hardness measured at different regions on the cross section of the sprayed coating were slightly variable but it was not conclusive that the middle region had a higher hardness value than the top layer due to work hardening of the former due to continuous impacts of high velocity impinging droplets, which form layered structure (Kuroda, 1998).

10.4 Post surface modification

The surface modification techniques such as vacuum-sealing by polymer resin impregnation and vacuum-furnace fusion at high temperature were performed on the *Coating* B. Microscopic observation did not reveal any distinguishable differences once the coating surface was vacuum-sealed. The details of the sealant material could not be obtained from the coating supplier, however it can be presumed that polymeric sealant penetrated into the splat boundaries and the voids explained earlier through capillary action and application of the sealant in vacuum. However, it is to be noticed that the porosity levels in the HVOF coatings supplied were very small. Figure 10.4.1 shows the schematic representation of a HVOF coating sealed with polymer impregnation. The light grey area represents the sealant material.

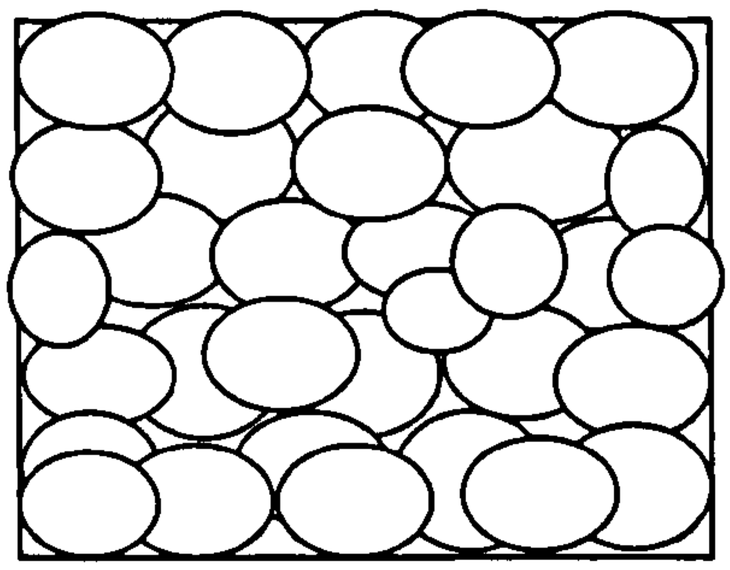


Figure 10.4.1 Schematic diagram of the HVOF sprayed coating with polymer sealant. The sealant is shown in light grey colour for highly exaggerated schematic representation.

Significant changes in both microstructure and phase transformations were visible once the sprayed coating was subjected to vacuum-furnace fusion process. Splat boundaries

of the impacted splat particles were clearly eliminated. Moreover, no such interlamellar voids were observed. The coating obtained was dense and less porous than the sprayed coating due to coalescence of individual splats. Also the hard particle sizes were significantly bigger than on the sprayed coating and this could have resulted due to coalescing of the tiny hardphase particles during diffusion. However, it is more likely that the fusion causes formation of new phases and this is supported by the XRD results. Another noticeable feature of the fused coating was the diffusion at the coating/substrate interface, which resulted in the metallurgical bonding of the coating to the substrate. This can have practical implications for the integrity of the coating/substrate interface during high-pressure jet impingement.

An increase in hardness of about 20 to 30% was measured on the fused coating, which was attributed to densification of the coating (density was increased by about 20%) and also to the formation of molybdenum rich hardphase particles. This was supported by the XRD patterns of the fused coating, which differentiated from the sprayed/sealed coating with the appearance of Cr_3NiB_6, $Fe_2Mo_2B_2$ and Fe_2MoB_4 that were not present in the sprayed/sealed coatings. The higher hardness of the fused coating was in contrast to measurements by the force spectroscopy obtained from the AFM, which showed a smaller slope of the fused coating confirming lower nanohardness. However, it is appreciated that measurements by AFM does not give bulk coating properties and that the AFM measurements were made of the outermost layer, which is probably not representative of the coating as a whole.

10.5 Specimen preparation

Both polishing technique and sealing the interface between the coating and the mounting resin could be of much importance during corrosion tests. Improper polishing with many pullouts could result in the increased surface area of the exposed surface that could give different results during corrosion experiments. This could be even of greater importance in erosion-conditions, when these pores (pullouts) can act as possible sites as micro-roughness bringing turbulence or local anode cells.

Now turning into sealing of the coating/mounting interface, which is already explained, in the experimental techniques in Chapter 6. The importance of effectively sealing the interface between the coating and the mounting resin is enormous for corrosion tests and it is even more necessary for conducting erosion-corrosion tests. The high-velocity jet impingement creates higher possibilities for the corrosive fluid to penetrate into the substrate resulting in false results such as different E_b, or E_{corr} than the actual values. The selection of a proper sealant is important to resist high breaking forces of the impinging jet. Tests performed on polished specimens displayed higher effectiveness of the glue. Similar adhesives frequently failed in as-received condition of the coatings presumably due to roughness of the surface resulting in breaking of the adhesive sealant (type F2015), making the test procedures more ineffective and troublesome. One of the tests performed of vacuum-fused coating applied onto a carbon steel substrate is shown below in Fig. 10.5.1 illustrating the possibility of obtaining false results displaying unusually for the coating a very negative E_{corr} (- 480mV) and an active forward scan. Such an effective sealing plays a crucial role when the coating is applied onto an active substrate e.g., carbon steel. Similar false results were also displayed when the polarisation tests were performed on the coating specimens in static condition. If specimen surface/mounting resin interface is not sealed properly then we would possibly be getting results for the substrate material.

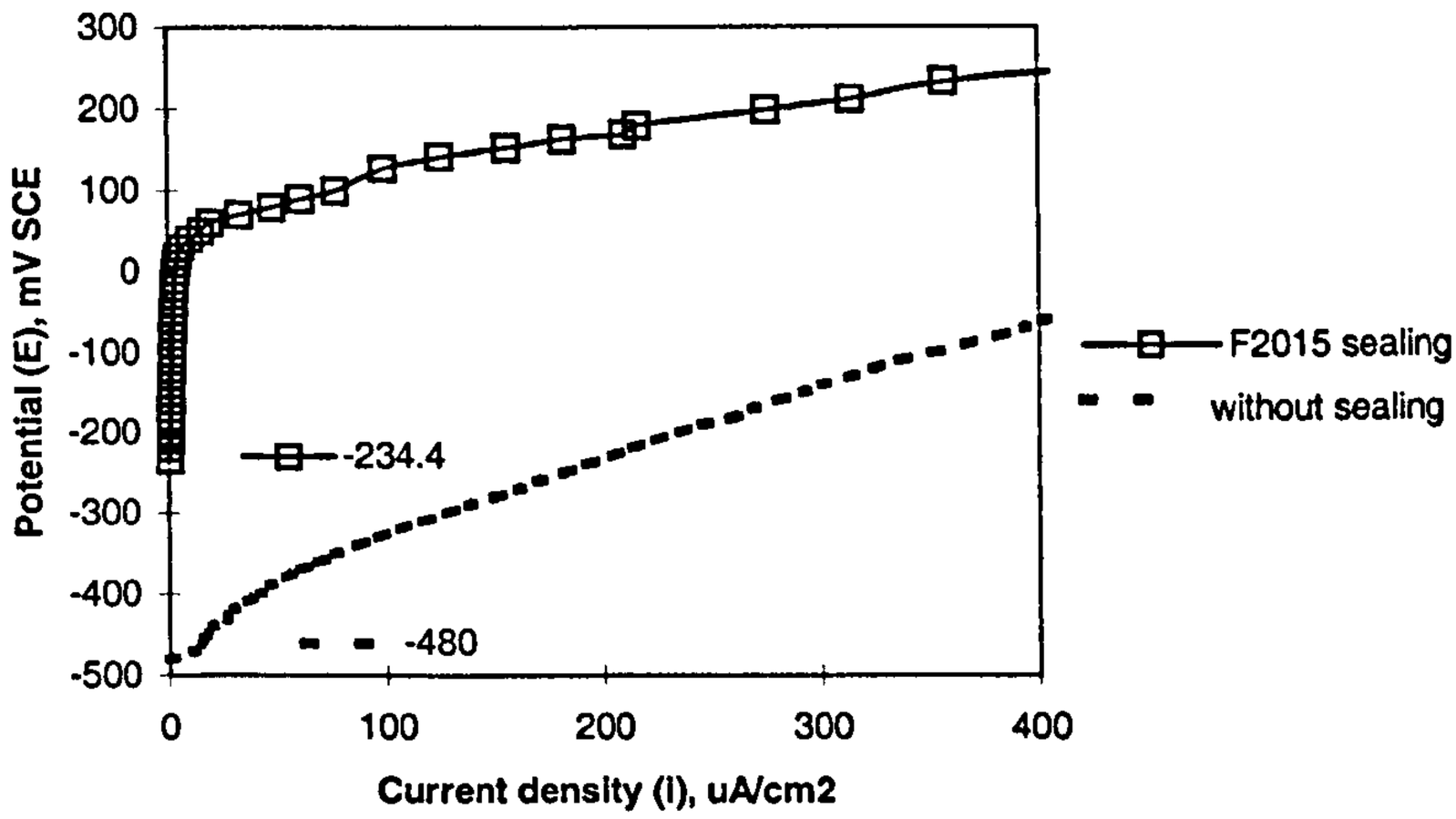


Figure.10.5.1 Vacuum fused coating showing anodic polarisation results with sealed and unsealed edges in high-velocity seawater jet impingement test at $72ms^{-1}$, 18°C (coating was applied onto a carbon steel substrate).

An example of a false result was demonstrated when one of the as-sprayed coatings applied onto the carbon steel substrate was sealed with a lacomit varnish and anodically polarised at 18°C in static seawater. Severe corrosion product in the form of brown rust was visible coming out from the lacomit-applied interface. On removal of the lacomit it was found that there was a small pinhole on the lacomit strip which could have occurred while the lacomit was applied onto the specimen. The specimen was isolated from the cold mounting and its cross sectional side was examined. The corrosion product was proved to be coming out from the carbon steel substrate leaving a deep pit at the coating/substrate interface with a substantial amount of corrosion of the substrate. Figure 10.5.2 shows an optical micrograph of the corroded area with a large pit. Such example could have practical implication, which might lead to failure of the coating due to breaking once the external force (mechanical loading or high pressure jet) is exerted on the specimen.

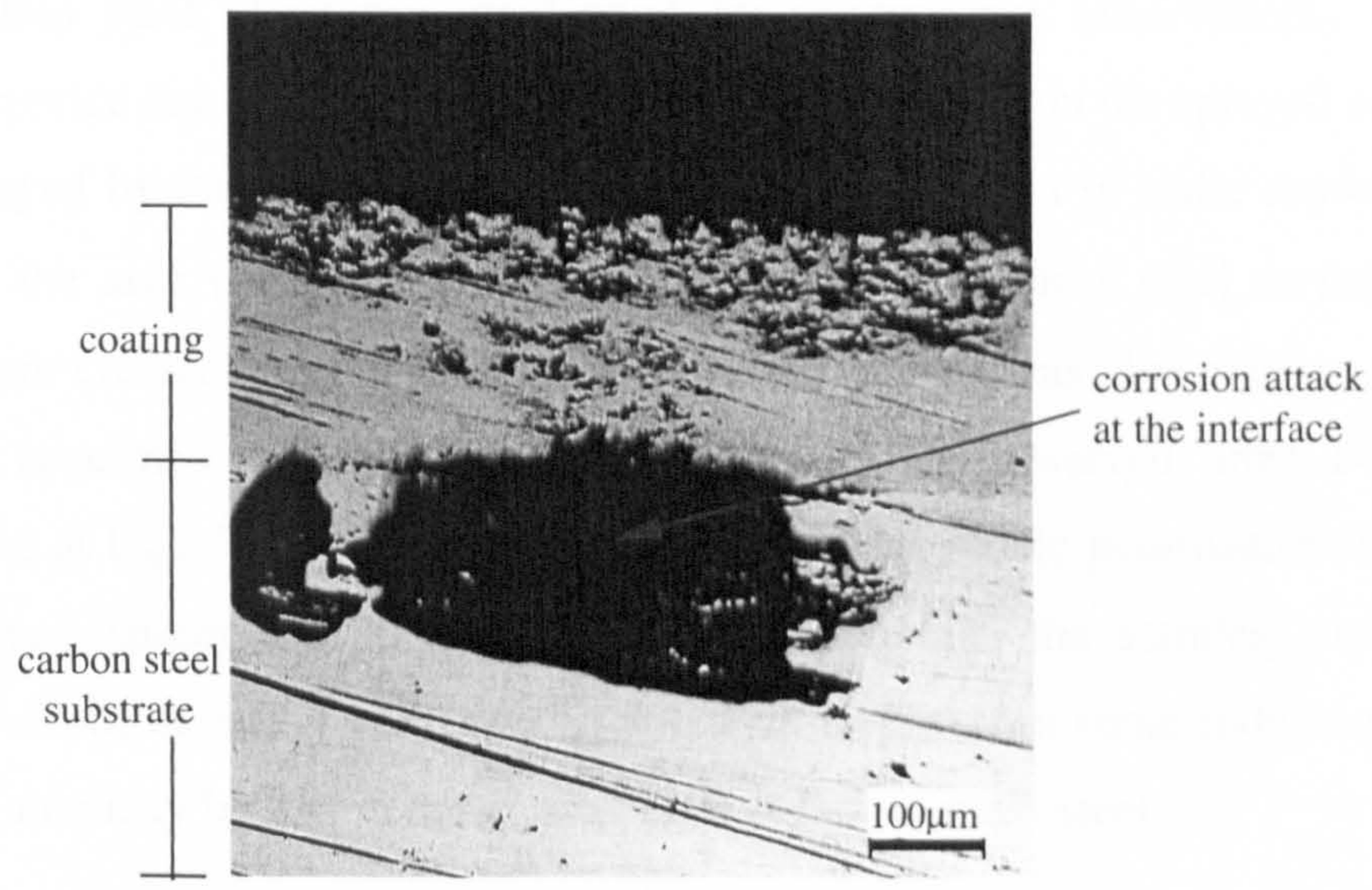


Figure.10.5.2 Cross sectional view of a HVOF as-sprayed coating showing severe corrosion attack at the coating/substrate interface after anodic polarisation in static seawater at 18°C due to leakage of corrosive fluid through a pinhole on lacomit strip.

This gave an idea for the application of a central lacomit on the specimen surface, which can be considered as a reliable method for determining actual crevice corrosion mechanism and not the corrosion of the substrate material.

10.6 Electrochemical behaviour and corrosion mechanism

Electrochemical behaviour of coating A and the stainless steel

It was shown that the HVOF as-sprayed *Coating* AI could effectively protect the carbon steel substrate (BS970 En8) in a highly corrosive static saline environment at ambient temperature. The as-received coating displayed a classic passive behaviour in a similar manner but inferior to that of austenitic stainless steel (UNS S31603) shown by the passive range 'E_b-E_{corr}' prior to the eventual breakdown of the passive film at potential denoted by 'E_b', after which higher current densities were recorded until a limiting maximum current density was achieved. After this current value, the polarisation scan was reversed. The hysterisis loop of the coating was comparable in a similar manner to that of the stainless steel, however the loop size was relatively smaller indicative of less susceptibility of the coating to localised attacks (such as crevice and pitting corrosion) than the stainless steel. This was confirmed by microscopic observations, which revealed both crevice corrosion and pitting attack to a less extent on the sprayed coating than that displayed by the stainless steel after anodic polarisation in static seawater at 18°C. 80% of the area under the lacomit applied on the stainless steel surface had undergone severe crevice corrosion. In addition severe pitting was also evident on the stainless steel specimen. Similar characteristics were also observed after 1-month natural exposure at E_{corr}. The study shows clearly from the anodic polarisation that the coatings are more susceptible to initiation of corrosion than the stainless steel but comparison of depth of attack after anodic polarisation provides some indication that the penetration rate may be less in the coating than in the stainless steel.

The reproducibility of the electrochemical measurements on the coating was much greater than the stainless steel under similar conditions. This suggests that prediction of coating behaviours is much easier. Parallel experimental tests performed on the coating on a stainless steel substrate gave identical results confirming the coating's corrosion resistance is independent of the substrate material. This is an important finding to confirm that penetration of the coating by the corrosive liquid is not the sole corrosion concern. An interesting effect observed on the coating with either substrate was the worsening of the corrosion resistance when the as-sprayed surface was polished to

diamond finish. The anodic polarisation curve displayed what was somewhat indicative of pseudo passive behaviour as explained in the Results section. This finding has implications in engineering applications in which surface finishing is the necessity to achieve a required tolerance and hence the benefits of the as-sprayed surface will be undermined. Neville and Hodgkiess (1996) have also demonstrated similar results for WC-based coatings in seawater environment at ambient temperature.

The addition of (4.5-6.4%) Mo in *Coating* AII resulted in an increased corrosion resistance displayed by its much higher 'E_b' (almost 100mV more positive) than the Coating AI without Mo. In particular, there was less crevice corrosion as measured under the lacomit strip of the Coating AII about 8-11% only compared to 11-15% of the Coating AI. It is worth noting that severe crevice corrosion was observed on *Coating* AI after just 2-weeks free corrosion test, whereas no such corrosion was observed on Coating AII until 3-weeks free corrosion in similar environmental conditions. Also visual examination revealed more general corrosion of the free surface on *Coating* AI than on *Coating* AII just after the 2-weeks free exposure in saline aqueous environment at ambient temperature. Such beneficial effects of alloying with Mo to cermet coatings similar to their well-known effects in wrought metals have also been reported by Kretschmer et al. (1997) for self-fluxing Ni-base alloys in strong mineral acids. Similar effects of increased corrosion resistance with increasing Cr and Mo was also reported by Berget et al. (1998) for WC-base cermet coatings in saline environments. Moreover, on polishing the as-sprayed surface to a diamond finish, *Coating* AII still retained its classic passive behaviour as demonstrated by the as-sprayed surface unlike pseudo-passive behaviour demonstrated by the polished *Coating* AI. However, lowering of 'E_b' by almost 70-80mV than that of the as-sprayed surface was displayed by the polished surface indicative of a decrease in coating resistance.

Attack mechanisms of Coating A and stainless steel

Corrosion attack mechanisms of such a multiphase coating are extremely complex. As explained in the Results Chapter, the sprayed *Coating* AI suffered both 'general' and 'localised' forms of corrosion attack. *Coating* AII displayed rather similar corrosion mechanisms. 'General' is the term that describes when an extensive area of the exposed free surface had undergone uniform corrosion attack. 'Localised' attack that was

considered in earlier sections refers to, for example, crevice or pitting corrosion. All of these phenomena were interrelated in terms of the mechanisms of corrosion in cermet coatings. Also in this work definition of new terms such as 'macropitting', which generally refers to pitting associated with the loss of a whole particle splat or chunk of matrix (usually whose sizes are greater than 5μm) and 'micropitting', defined as the pitting associated with the loss of tiny hardphase particles within the particle splats (whose sizes are usually less than 5μm) has been necessary.

Figure 10.6.1 shows the schematic representation of stages of the corrosion mechanism of a sprayed *Coating* AI and AII and can be described as follows:

- Stage I:

  As-polished surface of the coating prior to corrosion test.

- Stage II

  Preferential attack around splat boundary, initiation of matrix corrosion within the splat and micro-galvanic attack at the hardphase particle/matrix interface. This appeared to be random.

- Stage III

  Corrosion becomes more extensive after longer period exposure.

- Stage IV

  Macropitting due to loss of individual particle splats or matrix chunks, severe matrix corrosion that results in hardphase particles left unsupported and micropitting due to removal of tiny hardphase particles.

- Stage V

  Corrosion of next layer particle splat at regions where macropitting had occurred due to already existing local anode sites (pits).

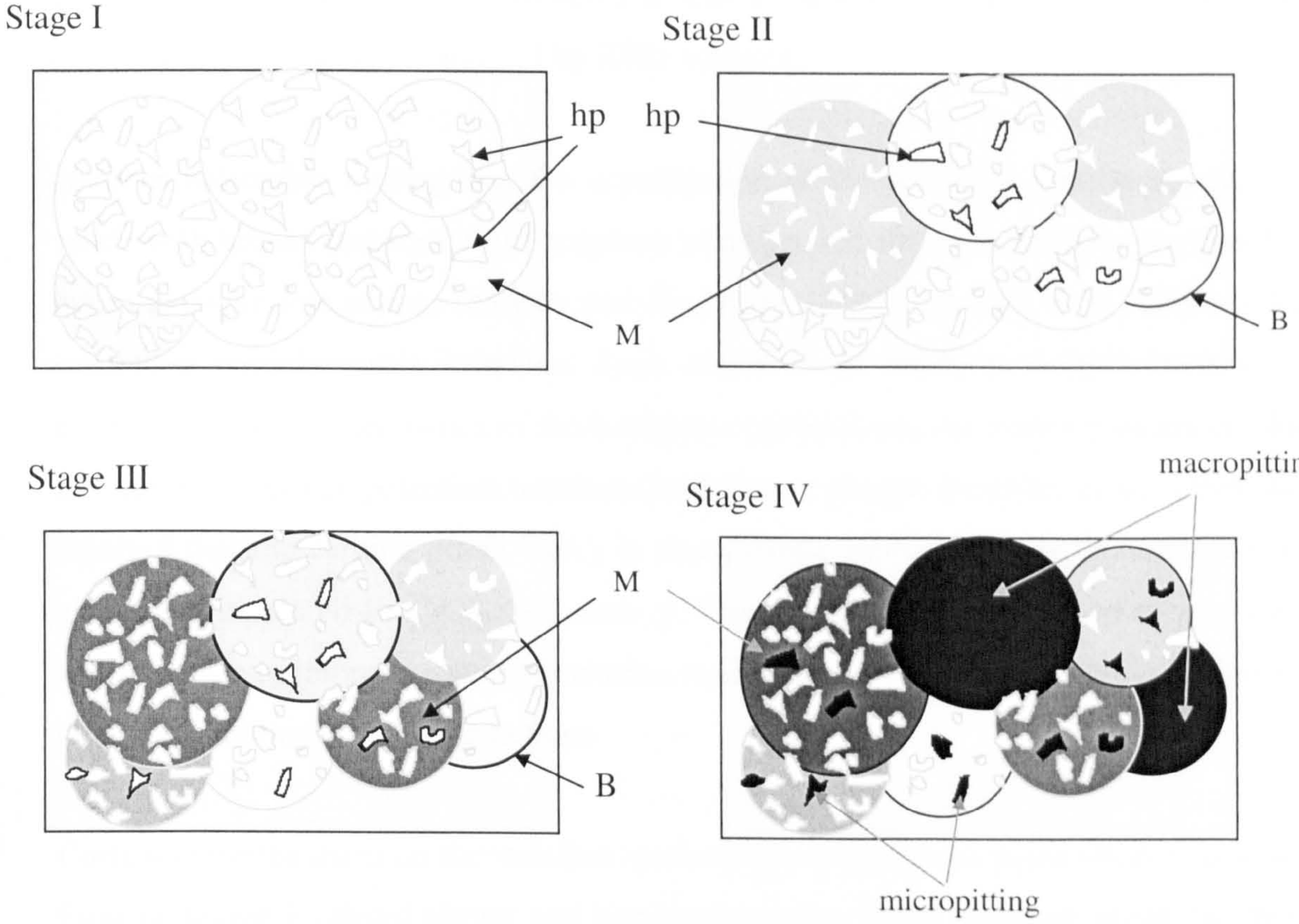


Figure 10.6.1 Stage I- Plan surface as-polished, Stage II - Attack around splat boundary 'B' of a splattered particle, corrosion attack initiation around hardphase particles 'hp' and matrix 'M' starts changing colour into light brown, Stage III - Continuation of corrosion of 'M' with conversion into dark brown and around 'hp', Stage IV – Hardphase particles 'hp' and splat particles loss resulting in both micropitting and macropitting.

A major aspect of the coating degradation mechanism is as defined in stage II, preferential corrosion attack around splat boundary, which could also be attributed to the metal oxides often concentrated at splat boundaries formed during in-flight of molten particles (Smith et al., 1997). As explained earlier, splat boundary separation (gap) could also degrade the performance of the coating. Several circumstances have been reported for the increased oxide level in HVOF sprayed coatings (Smith et al., 1997), amongst which high oxygen concentrations in HVOF spray plume with increasing stand-off distance from the nozzle exit is of importance. However, the same author has also reviewed the point introduced by other authors that the oxidation of splat particles decreased with increased standoff distance, which was explained by the fact that oxidation decreased with decreased substrate temperature at larger standoff

distances. This gives an indication that an optimum standoff distance should be selected for a proper HVOF spraying. However it should be noticed that no oxide phase was detected in the Coating AI and AII by XRD analysis.

Another noticeable finding was the accentuation of the corrosion process on particle splats with higher abundance of hardphase particles and this was partially attributed to micro-galvanic interactions (Neville and Hodgkiess, 1997; Takatani et al., 1996) at the hardphase particle/matrix interface. Such attack could likely to happen because of different corrosion chemistries of the hardphase particles and the matrix presumably due to different electrode potentials between the different phases. Dearnley et al. (1996) had reported that the carbide phase Cr_7C_3 is significantly more anodic with respect to the nickel matrix in a Ni-Fe-Cr-B-Si-C coating. This poses a challenge to coating engineers and scientists to improve coating corrosion resistance by tailoring the coating chemistry in order to minimise such interactions.

Corrosion mechanisms on the stainless steel surface after anodic polarisation was in the form of severe localised pitting and crevice corrosion. Such localised attack has been well known on the austenitic stainless steels (Neville, 1995) and believed to be occurring mainly at inclusions but no related mechanistic approach has been defined properly.

Both crevice corrosion and the pitting corrosion on the free surface of the stainless steel specimen have demonstrated rather similar corrosion mechanisms. Severe pitting on the free surface was observed to be associated with severe intergranular corrosion and loss of individual grains. The crevice corrosion had also occurred due to severe pitting rather in a large area under the crevice region. Pits and crevices are thought to propagate by similar mechanisms once they have formed (Trethewey and Chamberlain, 1995).

Galvanic Interactions between a coating and the substrate.

Galvanic couples between an exposed coating and the substrate are inevitable in many coated components and this work has demonstrated that the severity of such interactions is likely to vary substantially for different coating/substrate combinations. Free corrosion tests of exposed cross sections indicated that such effects are less substantial

for thermal sprayed coatings applied to a stainless steel than for coated carbon steel component. With respect to thermal sprayed coatings applied to carbon steel, such galvanic effects might in fact confer a partial benefit by reducing the corrosion rate of the coating, i.e. the coating component acting as the cathode. However, on the anodic segment of the couple, the carbon steel substrate, the corrosion rate will be accelerated. Such galvanic corrosion interactions of HVOF sprayed NiCrCB and WC-CoCr coatings have also been demonstrated by Hodgkiess and Neville (1997).

The more practical implication of applying a coating in particular on a cheap active material such as carbon steel should therefore be considered with caution. First of all no flaws on the coating should be allowed nor any open areas of contact points between the coating and the substrate (edge of the coated region of a component) should be exposed to the corrosive environment as this could lead to penetration of a corrosive fluid into the active substrate, which can cause severe corrosion of the substrate due to galvanic effect and will result in undermining the underlying substrate. In addition 'knife-line attack' adjacent to coating/substrate interface as has been presented in the Results section and this might lead to premature loss of bonding. Moreover coating thickness on such a substrate should be applied with enough thickness as development of a local anode cell (at existing former pits) as mentioned above can lead to penetration of a highly corrosive fluid into the underlying substrate of a thin coating.

The effect of heat treatment such as vacuum-fusion (which had resulted in a metallurgical 'keying' between the coating and the substrate) also showed excessive corrosion attack at the coating/substrate interface as would be expected with a carbon steel substrate but microscopic observation revealed that there exists a difference in particular less severity at the interface with the fused coating than the sprayed one. As explained earlier in Chapter 8, the macro level excessive 'knife-line attack' on the sprayed coating would easily result in the delamination of the coating from the substrate in contrast to the micro level localised attack around the 'black keys' of the fused coating, which would prevent the earlier loss of bonding between the coating and the substrate.

Electrochemical corrosion behaviour of Coating BI and attack mechanism

Before discussing the effect of environmental conditions; mainly saline solution, temperature and post surface treatments such as vacuum-sealing and high temperature vacuum-fusion processes, it is useful to describe the major distinctions between the as-sprayed coatings supplied by two different commercial manufacturers. As has been described in the results chapters, Coating AII supplied by manufacturer A and Coating BI supplied by manufacturer B have many similarities in their chemical composition and microstructural appearances as identified by EDX and SEM. However there were some differences in their phase compositions shown by the XRD patterns despite of similar major peaks of NiCrFe as the matrix.

The as-received sprayed Coating BI displayed similar electrochemical performance as the as-received sprayed Coating AII characterised by the breakdown potential denoted as 'E_b' and also by the hysterisis loop despite the fact that the Coating BI was experimented in artificial seawater and Coating AII was experimented in 3.5% NaCl solution. A distinctive feature displayed by the *Coating* BI from the *Coating* AII is that no such reduction in 'E_b' was observed on *Coating* BI after polishing of the as-sprayed surface to diamond finish. This may have very important practical implications in the real application where surface finishing is necessary to achieve a required tolerance.

Another noticeable aspect of the polished surface of the *Coating* BI is that it recorded higher 'i_{max}' by about 200μAcm^{-2} than the *Coating* AII. This could explain the severe crevice corrosion observed under the lacomit strip applied on the Coating BI, which resulted in 75-83% of the crevice corrosion compared to only 8-11% of the Coating AII after the anodic polarisation at ambient temperature. The severity of such high crevice corrosion attack can be clearly seen in Fig. 8.3.6a of Chapter 8.

Now coming to the mechanistic approach, the sprayed coating BI displayed similar corrosion attack mechanisms as coating AII in a static solution at ambient temperature. The attack mechanisms such as preferential splat boundary attack, macropitting due to

splat loss, matrix corrosion and micropitting all could be seen on the polished surface of the sprayed Coating BI.

Effect of post-spray surface modification in the corrosion behaviour of Coating BI

The effect of vacuum-sealing of the coating by polymer impregnation or high temperature vacuum-fusion had very little effect on the corrosion behaviour of *Coating* BI at 18°C as displayed by the breakdown potentials 'E_b' of all the coatings. The influence of a polymer sealing post treatment for HVOF sprayed coatings has been demonstrated to be less effective to corrosion resistance also by several other authors (Neville and Hodgkiess, 1996). Tobe (1998) illustrated similar findings of a polymer sealing to HVOF coatings and reasoned that such ineffectiveness could be attributed to the very low porosity in the HVOF coatings. Nevertheless, sealing can benefit after final mechanical finishing such as grinding, polishing etc. as suggested by Wielage et al. (1998) to the coatings similar to Coating AI, whose resistance to corrosion decreases after polishing the as-sprayed surface. The drawbacks of sealing the HVOF sprayed coatings for merely the corrosion resistance such as in the case of *Coating* BI could possibly be associated with greater crevice effect demonstrated by the vacuum-sealed coating after the anodic polarisation (also supported by the highest 'i_{max}'). This could presumably be interrelated with micro-crevice attack that can occur at splat boundaries and pores filled with the polymeric sealant.

On the other hand a little more positive 'E_{corr}' value of the vacuum-fused coating during the 1-hour settlement period could indicate of some benefits of the fusion process, which was also shown by the lowest 'i_{max}' value obtained during the anodic polarisation and vice-versa for the sprayed/sealed coating. Arsenault et al. (1998) concluded that coatings with more positive corrosion potential 'E_{corr}' are more resistant to corrosion attack but assessment of E_{corr} only does not give quantitative measure of the corrosion behaviour since it is dependent on the cathodic kinetics as well.

In addition, 1-month free immersion test also showed that there was less crevice corrosion on the fused coating at the region where lacomit sealant was applied

compared to excessive corrosion product at the same region on the sprayed/sealed coatings.

It has been demonstrated that both the sprayed and sealed coatings displayed rather complex corrosion mechanisms in the static solution at *18°C with both macropitting and* micropitting. On the other hand the vacuum fused coating showed a rather different mechanism of corrosion attack. The splat boundary attack as had been observed on the sprayed and sealed coatings was completely eliminated and the crevice corrosion was comparatively less on the fused coatings than that was observed on the sprayed and sealed coatings. However, corrosion attack in the form of micropitting was observed on the fused coating and such was attributed to the preferential dissolution of the binder metal matrix at hardphase particles/matrix interfaces and their eventual dislodgement.

However, it is difficult to rank the sprayed, sealed and fused coatings in terms of 'E_b', which is often considered as an important electrochemical parameter, there is an incentive to consider that the fusion process confers overall benefit in terms of corrosion resistance in static saline solution at ambient temperature.

Effect of increased temperature in static corrosion behaviour of Coating BI

The effect of increased temperature to 50°C was to reduce the corrosion resistance of all the materials investigated displayed by the decreased breakdown potential 'E_b' (still displaying a classic passive behaviour) and enhanced corrosion of the free exposed area. Figure 8.3.5b in the Results section demonstrated severe matrix corrosion at 50°C, which leaves the hardphase particles unsupported. The corrosion mechanism was rather similar at 50°C to that displayed at 18°C such as matrix corrosion, macro and micropitting as in the sprayed and sealed coatings and micropitting as in the vacuum-fused coating. However, at 50°C, significant reductions in the crevice attack were observed for all the coatings, that could have resulted due to the dominant 'general corrosion' attack on the exposed surface. A very high current density 'i_{max}' achieved by the fused coating at 50°C may be indicative of 'micropitting' of the exposed surface on a larger scale, i.e. more uniform corrosion attack over the entire surface. In addition

increased temperature had resulted in a little higher pit depths on all the coatings measured.

Effect of pre-corrosion on the electrochemical behaviour of Coating BI

The effect of up to 5-days pre-exposure to saline solution had resulted in a reduced resistance to corrosion attack displayed by lowered breakdown potentials 'E_b' for the sprayed and sealed coatings and such had resulted also for the vacuum-fused coating but to a lesser extent. Anodic polarisation tests performed on the sprayed and sealed coatings after 10-days pre-corrosion displayed no further reduction in the 'E_b'. On the fused coating the 'E_b' had even increased after the 10-days pre-corrosion. Such characteristics are not very clear, as there had been an evidence of the initiation of the corrosion attack after 10-days free exposure and there remains the question mark for this behaviour. Such characteristic of becoming more resistant to corrosion attack with the exposure time was demonstrated for the stainless steel and was attributed to the 'ageing effect of the oxide' present on the stainless steel (Bardal et al., 1993b). Similar effect could have occurred in the fused coating but such could last possibly for a very short transition period after which, the corrosion attack increases again.

10.7 Erosion-corrosion behaviour in solid-liquid and solid-free liquid impingement of 17ms^{-1} at 18 ℃.

Erosion-corrosion mechanism of Coating AI and UNS S31603

Solid-liquid impingement

This study has provided a number of indications of the complexities of erosion-corrosion mechanisms in aqueous conditions and, in particular, of the important role of corrosion processes in governing the total material loss. Reference to Table 7.5.5a and b demonstrates that the contribution of the corrosive processes measured, as a difference 'TWL - E' was indeed significant for both the sprayed *Coating* AI and the UNS S31603. Several authors (Madsen, 1988; Neville et al., 1995 and Hodgkiess et al., 1998,

Hodgkiess and Neville, 1998b) have defined this corrosion contribution to total erosion damage as the sum of 'C' and 'S' as described in section 3.6 of Chapter 3.

The various contributors to overall weight loss under solid-liquid impingement are conveniently illustrated in the pie charts shown in Fig. 10.7.1.

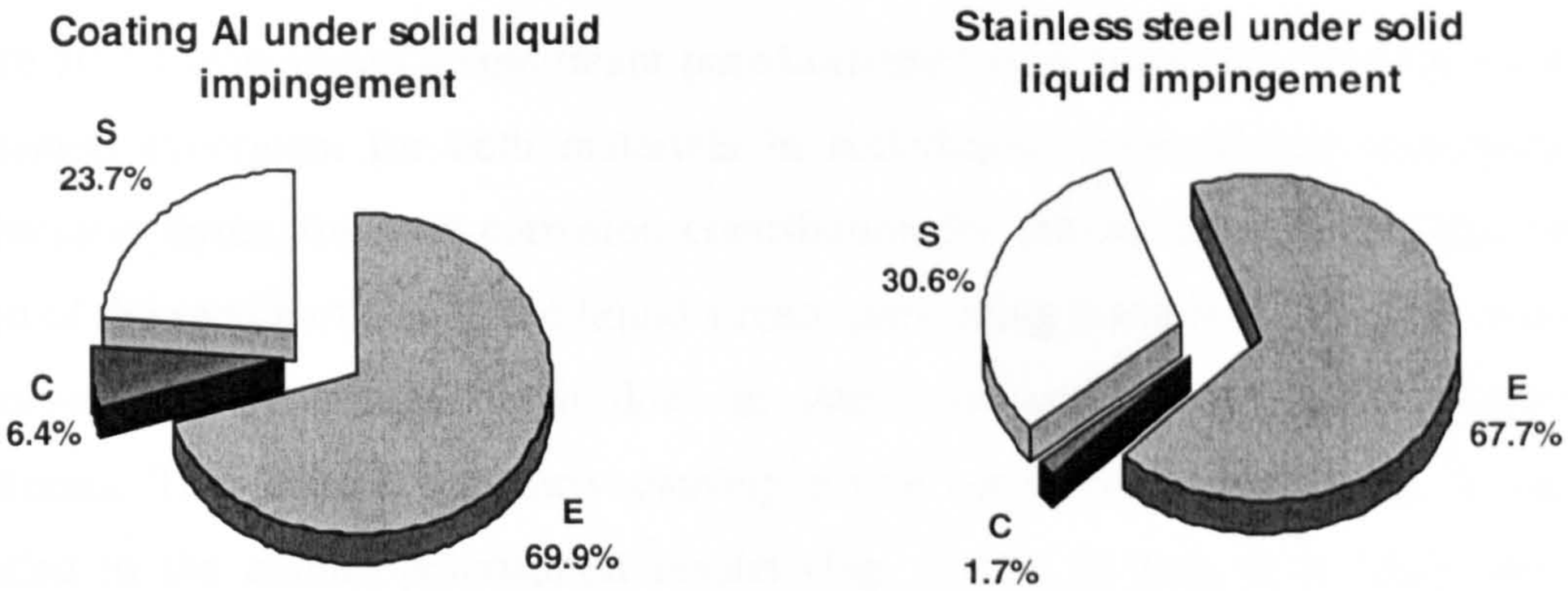


Figure 10.7.1 Breakdown of total weight loss into pure erosion (E), pure corrosion (C) and interactive synergy (S) components (Coating AI) under solid-liquid impingement (3.5%NaCl, 18°C, 90° impingement, 17ms^{-1}, 800ppm silica sand).

These show rather similar pure-erosion proportions to overall material loss for the two materials. However, the actual weight loss by erosion for the stainless steel was twice that for the *Coating* AI. This reflects the generally lower erosion resistance of metals in comparison with ceramics or ceramic-base composites. As expected, the erosion mechanisms for the two materials were observed to be different with the stainless steel exhibiting typically ductile erosion damage involving extensive plastic deformation in the central area and as deep ploughing and cutting in the outer regions. Erosive attack on *Coating* AI was contrasting and indicative of 'brittle' process with visibly less plastic deformation occurring out from the central jet region implying that the sand particles at low angle had insufficient kinetic energy to remove the hardphase particles, or were deflected by the hardphase particles protruding from the surface and were therefore less able to impact the matrix. The Talysurf traces in Fig. 7.5.7 are in good agreement with the ductile or brittle nature of the two materials investigated. The central region of the coating specimen showed interesting attack in the form of deep

holes, larger than the size of individual hardphase particles, which had been drilled away during solid/liquid impact. It is postulated that these are evident on the coating and not on the stainless steel due to the non-uniformity of the coating surface as the potential for small micropits to be formed on removal of hardphase particles is great. When this occurs, the impinging jet stream causes turbulent sites at these micropits and drilling occurs.

Figure 10.7.1 also shows a significant pure-corrosion component for *Coating* AI and a substantial synergism for both materials in solid/liquid impingement conditions. In mechanistic terms, the pure-corrosion contribution for the stainless steel is due to the action of the sand particles in the liquid stream preventing a stable passive film existing to prevent charge transfer as it does in static and solid-free liquid impingement conditions. This feature, of slurry causing active corrosion at high rates, is clearly revealed in the anodic polarisation results (Fig. 7.5.2). In fact, it is likely that the corrosion behaviour involves repetitive formation and immediate mechanically induced breakdown of a passive film as has been reported by Neville et al. (1995) in a study of stainless steel in similar erosion-corrosion conditions. Similarly, a cyclic process of depassivation and repassivation of the austenitic stainless steels (AISI 304 and 316L) caused by particles impacting on the surface has been reported by Hirooka and Robinson (1998) in flowing ($8ms^{-1}$) 3.5% NaCl solution containing sand particles. The absence of a stable passive film on the stainless steel may also contribute to the high synergism 'S' observed by facilitating enhanced metal loss on bare-metal surface than on an oxide-filmed one.

For the coating, the pure corrosion rate is obviously much greater than in the absence of solids in the liquid stream (Fig. 7.5.2). This is probably associated with the increased surface area for corrosion, consequent upon the drilling action of the solid/liquid impinging stream and this feature is also likely to contribute to the higher pure corrosion rate of the coating than for the stainless steel in the solid/liquid conditions. However, the intermittent passive film destruction/reformation process, discussed above, on stainless steel is another probable contributor to this comparative behaviour.

For the coating, the 'S' factor is likely to involve enhancement of erosion damage by roughening the surface of the coating on a microscale as a result of selective corrosive

attack on particular coating constituents followed by faster removal of 'unsupported protruding material' by sand particles. There was some evidence from microscopy that the sites for the pre-cursor selective corrosion include splat particle boundaries, which might result in dislodgement of the splat particle by erosion forming 'macropits'. On a smaller scale, preferential corrosion of the metallic matrix also leaves the intervening hardphase particles relatively unsupported and protruding slightly from the surface and hence more vulnerable to dislodgement by the action of impinging sand particles. Such micro-roughening by selective attack on the metallic binder (which might also involve the micro-galvanic mechanisms at the matrix/hardphase interface forming 'micropits') was observed during solid-free impingement in this study and similar results have also been reported for tungsten carbide-cobalt-chromium coatings by various authors (Rogne at al., 1996, 1997; Berget et al., 1998; Arsenault et al., 1998). Another contributor to the synergism is likely to be abrasive wear as the corrosion products are forced along the specimen surfaces by the liquid stream.

Solid-free liquid impingement

Turning now to solid-free impingement, comparison of the weight losses under free-corrosion and cathodic protection conditions (Table 7.5.5) reveals that the pure erosion component 'E' is minimal and that all the deterioration involves corrosion processes. The results of the anodic polarisation and microscopy indicate more severe corrosion, in solid-free impingement conditions, on the coating than on stainless steel displayed by extensive corrosion attack in the form of comet-shaped streams. The coating displayed, in a similar complex mechanism described above associated with 'macropits' formed by the splat losses, corrosion of the binder matrix and the preferential corrosion attack at the hardphase/matrix interface forming 'micropits'. The comet attack on the stainless steel surface was observed to be associated with pitting attack at sulphide inclusions. Thus the inherently poorer corrosion resistance of the coating, as opposed to the stainless steel, accounts for the interesting observation of the better erosion-corrosion resistance of the stainless steel in solid-free conditions. However, it should be emphasised that the overall erosion-corrosion material loss rates on both materials are extremely low in these circumstances of the absence of solid particles in the impinging liquid.

Erosion-corrosion mechanism of Coating BII

The previous section discussed the difference between the Coating AI and the UNS S31603 in both solid-free liquid and solid-liquid impingement conditions. This section will discuss erosion-corrosion behaviour of the coating BII in similar environmental conditions. Emphasis will be placed on the comparison between the erosion-corrosion behaviour of the as-sprayed, vacuum-sealed and vacuum-fused coatings.

Solid-free liquid impingement

Under solid-free liquid impingement, the complex mechanism of material loss in the sprayed and sealed coatings was rather similar to that displayed by the *Coating* AI associated with 'macropits' due to splat loss, corrosion of the binder matrix and the micro-galvanic attack at hardphase/matrix interface forming 'micropits'.

Material loss in the vacuum-fused coating was on a micro level associated primarily with micro-galvanic attack at the hardphase/matrix interface. Dissolution of matrix also resulted in unsupported hardphase particles protruding out from the matrix, which further dislodged on subsequent liquid jet impacts.

The application of CP had significantly reduced the material loss in the sprayed and sealed coatings almost to half of that displayed in impingement at the 'E_{corr}'. The effect of CP was remarkably pronounced in the case of the vacuum-fused coating where all the material loss was eliminated under the CP, signalling the important role of corrosion in determining the material's overall erosion-corrosion resistance.

In solid-free liquid conditions, the corrosion rates for all the coatings were very small within the range of 0.0007-0.0009mg/h for the sprayed and sealed coatings and ranged between 0.0015-0.0019 for the vacuum fused coating. The slightly higher rate of erosion-corrosion on the fused coating might possibly indicate more uniform rate of corrosion over the entire surface, which was also shown by microscopic observations. The sprayed and sealed coatings had generally undergone localised attack at splat boundaries resulting in the splat dislodgement and further propagation within the splat.

liquid impingement. For the vacuum fused coating, E = 0, that means the total weight loss is governed by the synergy 'S'. In the sprayed and sealed coatings the 'S' was between 42-52 % of the 'TWL'.

Solid-liquid impingement

Under solid-liquid impingement as illustrated in Table. 8.6.4, the corrosion proportions for both the sprayed and sealed coatings after 1-hour tests are rather similar yielding values of about 6%. The corrosion proportion of the fused coating is about 7% rather similar to sprayed and sealed coatings. The pure erosion proportions of the sprayed and sealed coatings are again rather similar yielding 60% and 68% respectively. However there is a significant fall in erosion proportion on the fused coating yielding only about 39%. This reflects the observed higher erosion-corrosion resistance of the vacuum fused coating in comparison to sprayed and sealed coatings under solid-liquid conditions. These figures of the pure erosion contribution to overall material loss also provide evidence of the beneficial effect of CP in substantially reducing erosion-corrosion damage (in a similar way to that discussed in the preceding section for solid-free condition). The lower CP currents for the vacuum-fused coating compared to the sprayed coating (Fig. 8.6.7) provide further evidence of the superior erosion-corrosion resistance obtained by the post-spray fusion process.

Central wear scars revealed the damage mechanisms in the sprayed and sealed coatings rather similar with brittle like nature. Actions of both mechanical impact as well as corrosion resulted in a loss of individual splats and chunks of material which further acted as possible sites for subsequent drilling. This resulted also in lateral crack propagation at existing pits and eventually higher rates of material loss. In contrast much less damage was observed on the vacuum-fused coating under the central jet, which displayed a ductile behaviour.

At regions away from the centre, the sprayed and sealed coatings showed large skidding tracks with lips formed at the end, which eventually break on further impacts. In contrast, the fused coating has significantly smaller skidding tracks in the same region. This is in agreement with higher hardness value of the vacuum-fused coating compared to the sprayed and sealed coatings.

Another form of defect than can be formed in the sprayed coating (possibly from interlamellar voids) as a result of compression of the coating layer during continuous impacts of solid-liquid slurry. This compressive force might result in the compaction of the splattered particles resulting in loosening the interparticle bonding. Thus the defects (cracking around interparticle) are again formed making these sites vulnerable to both electrochemical and mechanical interactions resulting in excessive material loss. This mechanism of material loss implies a possible increase in erosion-corrosion rate as a function of time but is contrary to the findings (Bjordal et al., 1995a) that the rate of material loss in WC-Co cermet coatings was stabilised after long term exposure under solid-liquid conditions.

Moreover, bombardment of the solid-particle stream might produce high internal stresses in the roughened surface of sprayed and sealed coatings with such stresses possibly leading to tearing and detachment of portions of material under impingement. This problem seems to be unlikely in the vacuum-fused coating.

10.8 Electrochemical and mechanical interactions under 72ms^{-1} high-velocity impingement of Coating BI

Impingement jet/specimen configuration, which has been used for the great mass of this work and also by others represents a quite reasonable simulation of practical erosion-corrosion situations, namely a relatively fine jet impinging on a large component. Moreover, this simple configuration clearly represents an appropriate one for the commencement of erosion-corrosion studies and indeed has yielded extremely valuable information on the erosion-corrosion behaviour in this and other research program.

However, as can be readily anticipated without study and as has been observed in this and other studies, the detailed erosion-corrosion mechanisms vary in different hydrodynamic region of such a 'composite' specimen and measurements of weight loss obtained directly gravimetrically or indirectly via electrochemical corrosion monitoring, represent 'averages' of different degrees and types of attack in the different regions of the specimen. As just one example of this, the weight loss measured after an erosion test under CP is very likely to be more concentrated on the zone directly under the jet to a

the specimen. As just one example of this, the weight loss measured after an erosion test under CP is very likely to be more concentrated on the zone directly under the jet to a probably greater extent than in the case for the TWL under erosion-corrosion conditions and the pure corrosion component.

Thus it is desirable, as a second stage in erosion-corrosion investigations, to extend the scope of the experimental study to tests on the separate regions of a 'large specimen'. This is why, towards the end of this project, such experiments were undertaken on stainless steel samples (see Chapter 9) since the procurement of suitable HVOF-sprayed samples of good coating quality was not possible in the time scale involved.

The electrochemical monitoring performed under a high-velocity seawater jet impingement of $72ms^{-1}$ at 18°C showed that the effect of imposing a solid-free liquid jet is to reduce the corrosion resistance of the sprayed, sealed and fused coating and also the stainless steel displayed by their reduced breakdown potentials 'E_b'. The superior corrosion resistance of the stainless steel was once again demonstrated by its much higher 'E_b' compared to the coatings under solid-free impingement conditions.

The reduced 'i_{max}' under high-velocity impingement compared to that of static polarisation is indicative of a decrease in localised corrosion attack, particularly the crevice corrosion for the sprayed and sealed coatings. Such can be attributed to the dominant corrosion attack on the exposed surface, which is accentuated at the central region imposed by the severe impinging jet. However, this characteristic is a bit confusing for both the fused coating and the stainless steel.

The effect of increased temperature (50°C) under high-velocity is to further reduce the corrosion resistance of all the coatings including the stainless steel shown by the much reduced 'E_b' compared to that displayed at 18°C. The ranking of the materials to corrosion resistance that can be given in terms of 'E_b', under high-velocity impingement conditions for both temperatures is shown in Fig. 10.8.1.

The vacuum-sealing appeared to have a slightly better corrosion resistance than the sprayed coating shown by the instantaneous anodic polarisation tests. The reason for

this could be the bonding of the individual splat particles due to 'cementing effect' caused by the polymer sealant that fills the inter-splat gaps. But such effect could possibly hold only for a very short period and is negligible.

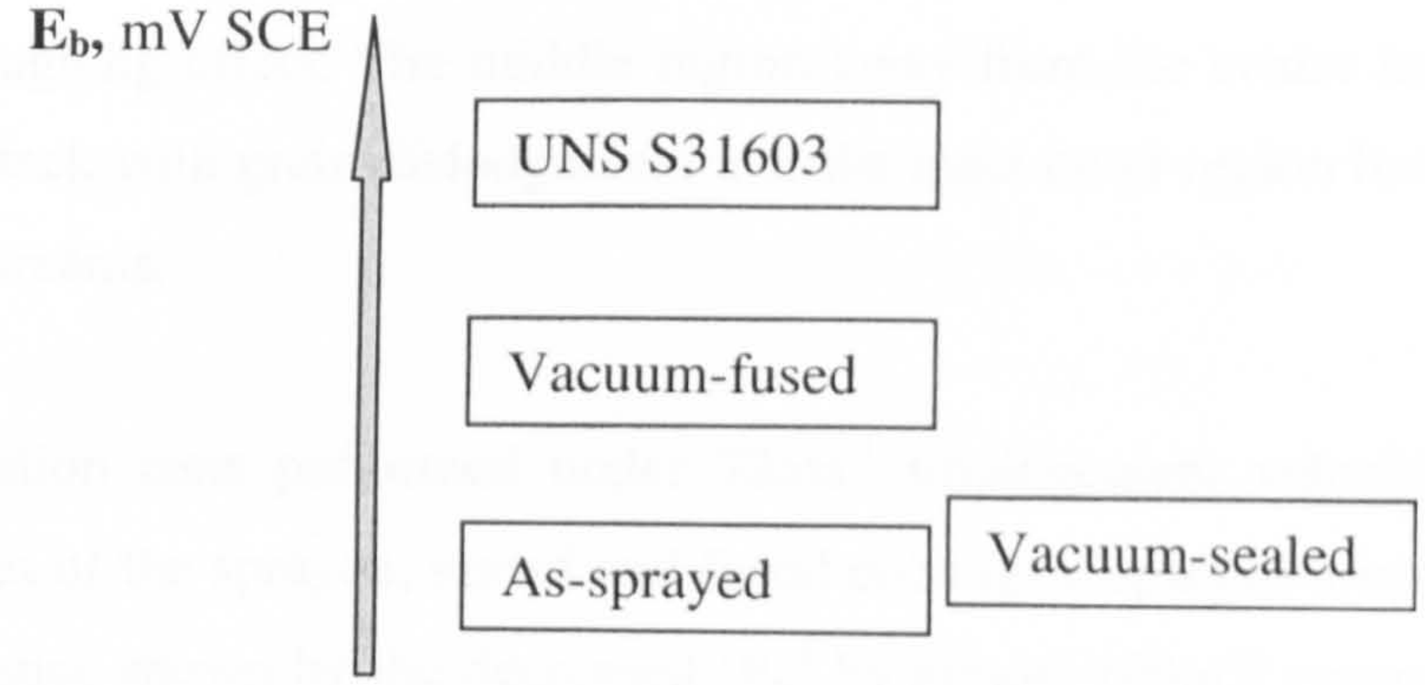


Figure 10.8.1 Ranking of materials in terms of 'E_b' under solid-free high-velocity liquid impingement.

*The vacuum-fusion had displayed distinct benefits towards the increased erosion-*corrosion resistance of the coating and that can be attributed to mainly two reasons:

1. Higher volume fraction of the strengthening carbides and borides hardphase particles (higher hardness) that resists the severe mechanical impact of the liquid jet.
2. Coalescing of splat particles resulting in a homogeneous 'ductile like' material that avoids preferential concentrated stresses at splat boundaries, which causes cracking and crack propagation forming macropits.

The material loss mechanisms in the sprayed and sealed coatings were complex and were associated with cracking and crack propagation (preferentially at splat boundaries) that results in macro loss mechanism and further drilling at the existing pits. In addition to this, micro-loss mechanisms were also observed on the sprayed and sealed coatings as discussed in the Results Chapter. Nevertheless, the attack was accentuated at the central region directly under the high-velocity impinging jet.

The erosion-corrosion mechanism of the vacuum-fused coating was associated with the corrosion of the matrix leaving the hardphase particles unsupported and also

micropitting associated with the preferential attack at the hardphase particles/matrix interface.

The stainless steel showed primarily 3 regions of attack under the high-velocity impingement (Fig. 8.5.3c and Fig. 8.5.7a, b, c). The central region under the jet had mechanical ploughing effect. The middle region away from the centre had undergone intergranular attack with grain dislodgement and the most outer region had pitting with comet-shaped streams.

Anodic polarisation tests performed under $72ms^{-1}$ impingement velocity on the as-received surfaces of the sprayed, sealed and fused coatings displayed a reduction in the corrosion resistance shown by the decreased 'E_b' by almost 100mV compared to those obtained on the polished surfaces. This can have practical implications where, the coated component is subjected to high-velocity impingement, with any mechanical finishing such as grinding, polishing etc. The reason for such decreased corrosion resistance could be the micro-roughness of the as-received surface. Such micro-roughness can act as the sites for the formation of high turbulence, subsequently increasing the severity of the jet impingement and/or material from the micro-roughness chipped by the cutting effect of the high-velocity jet could act as erodent particles as the test was performed in a circulated loop.

Total weight loss 'TWL' measurements taken during the 6-days test under $72ms^{-1}$ high-velocity impingement of a seawater jet at 18°C clearly showed a superior erosion-corrosion resistance of the fused coating compared to the sprayed and sealed coatings with the stainless steel having intermediate resistance (Table 8.5.1). Both the fused coating and the stainless steel displayed 'ductile ploughing' effect (Fig. 8.5.5). The least erosion-corrosion resistance of the sprayed and sealed coatings, which in fact was rather similar shown by the weight loss data was attributed to 'brittle behaviour' caused by cracking and crack propagation, which results in macro losses of the materials (Fig. 8.5.4). This is an important finding since it demonstrated that the fusion post-treatment converts the sprayed material into one like a stainless with ductile property but also with much greater hardness.

Another feature of the erosion-corrosion behaviour of this coating under the high-velocity, solid-free impingement condition was the apparent negative synergies as shown in Table 8.5.2. This is in complete contrast to other parts of this research (e.g., solid-liquid and solid-free liquid erosion-corrosion tests performed at 17ms^{-1}), where distinct and substantial positive synergies were displayed. In fact there is some doubt about the reliability of these negative 'S' values because, as argued in section 8.5 of Chapter 8, the actual negative 'S' values were very small, associated with very low rates of weight loss and subject to additional uncertainty on about of possible variations in the (again very small) pure corrosion rate. In summary, more work would be required to clear up this uncertainty concerning the sign and value of the synergies in these particular conditions.

Another complicating aspect of the notion of negative synergies is that, as other have also reported (Bjordal, 1995), accounting for negative 'S' values in terms of erosion-corrosion mechanisms is not a trivial matter. Nevertheless, for completeness, it is pertinent to record that negative synergies have been occasionally reported in the past. Bjordal (1995) recorded small negative synergies for one WC-base cermet coating (but not for other cermet coating) but with such relatively large scatter so as to provide substantial doubt upon their statistical significance. The same author yielded large negative synergies for a duplex stainless steel in condition of high velocity (36.7ms^{-1}) and sand loadings (2500ppm) but with positive 'S' values in less severe erosion-corrosion conditions. Bjordal (1995) also quotes other research in which negative synergies in some, but not all erosion-corrosion conditions for carbon steel and duplex stainless steels. In contrast, Neville et al. (1995) obtained a significant positive 'S' values for a duplex stainless steel in erosion-corrosion condition of comparative severity to those used by Bjordal. Bjordal suggested that the negative synergies with stainless steel might be due to more erosion damage occurring during application of CP because of the intermittent formation of a passive film of different composition, hence reduced protectiveness at the relatively negative potential during cathodic protection.

10.9 Effect of pre-erosion and pre-corrosion

As has been discussed earlier the corrosion behaviour of such multiphase coatings is very much time dependent. Such a property of a coating can be of practical importance in the static corrosion performance of the coated component after being subjected to erosive environments or in the erosion-corrosion performance after being exposed to static saline solutions during shutdown periods.

It has been demonstrated in section 7.6 of Chapter 7 that Coating AII no longer displayed passive behaviour in a static polarisation test just after the 1-hour pre-erosion of the polished surface. This could be attributed to several possible factors: 1) the extensive roughening of the central wear region under the slurry jet; 2) splat boundaries attack occurring at outer region away from the centre associated with preferential corrosion attack during the 1-hour impingement; and 3) cracking induced by the sand-liquid jet. The corrosion rate of the pre-eroded surface was almost 15 times higher to that displayed by the as-polished surface (please refer to Table 7.6.1) and this is indicative of incapability of the coating to reform its protective layer after once being disrupted. A similar effect, of a reduction in the breakdown potential 'E_b' of an initially smooth surface brought about by an erosion-corrosion period in chloride solution for 304L stainless steel has been observed by Sasaki and Burstein (1996).

Now turning into the effect of pre-corrosion behaviour of the *Coating* AII. The 5-weeks pre-exposure of the coating in static saline solution had resulted in the corrosion of the exposed surface and primarily, as has been discussed earlier, the preferential corrosion attacks at splat boundaries to loosen the interparticle bonding. The further impact of the solid-liquid slurry was to drill the already loosened splat particles causing extensive macro losses. However, the complex corrosion mechanism associated with matrix corrosion and also the micro-galvanic attack at hardphase/matrix interface is also of importance for the intensification of the erosion-corrosion processes. A severe drilling was accentuated under the impinging slurry jet. Such localised severe drilling by the slurry jet of the pre-corroded surface might signal the restriction of such a coating to use for longer period purposes.

10.10 Different regions under high-velocity liquid jet.

Initial investigation carried out on concentric specimens of the stainless steel material under a solid-free impinging jet to identify the erosion-corrosion mechanism at different regions of the specimen under the flowing jet provide some interesting insights that can be related to a hydrodynamic flow condition.

First, the anodic polarisation tests on the separate specimens confirmed that the corrosion behaviour is substantially different in severe (i.e. high velocity) hydrodynamic condition directly under the jet than in location remote from the direct impinging zone. This experimental demonstration of such variable behaviour can not be clearly obtained from the normal 'composite' specimen.

Secondly, and of probable greater significance, was the demonstration of galvanic interaction between the central (anodic) zone and the surrounding regions. This factor represents a much less obvious contribution to enhanced degradation of the directly impacted zone in a component subjected to impingement corrosion and might well be as especially significant feature in large components (small anode/large cathode).

It is interesting to note that similar, but understandably more substantial distinctions between attack on the central and outer regions of a stainless steel have been observed during solid-liquid impingement by Hirooka and Robinson (1998).

In summary, this preliminary assessment of the behaviour of different regions of a sample subjected to erosion-corrosion has yielded clear evidence of the value of such an experimental strategy in investigations of mechanisms and extent of erosion-corrosion. In relation to the main focus of this research, it would clearly be beneficial to undertake such studies on cermet coatings. Even at this juncture, it is probably not unreasonable to speculate that the behaviour of such cermet materials might be rather different than the stainless steel studied in this research. This is on account of the differences in basic corrosion and erosion-corrosion mechanisms of the cermets (e.g., less tendency to form passive film, more complex micro-scale effects in comparison to stainless steel).

CHAPTER 11

Concluding Remarks and Recommendations for Future Work

This final chapter, because of the diversity of the study is intended to summarise the important findings in each section and identify areas to which further research should be directed.

'Surface engineering' as an attractive option to provide the desired properties of the surface material for use in severe corrosive and corrosive-erosive environments should be based from a starting designing stage to final manufacturing process. On the manufacturing stage for a coated component the selection of proper powder, spraying parameters and post spray treatment could be of most importance.

The findings demonstrated that the HVOF sprayed coatings can be produced with very little gross and interfacial porosity and high hardness. The XRD results displayed no phase transformation during spraying of the coating. The hardphase particles are well distributed within the binder matrix except a few places where hardphase particles are denuded. The post spray treatment in particular high temperature vacuum-fusion had resulted in a change of the coating microstructure. This was displayed by a complete elimination of the splat boundaries. The resultant coating became denser with a reduced coating porosity and increased hardness. The diffusion at the coating/substrate interface resulted in a metallurgical bonding of the coating and the substrate.

Anodic polarisation results concluded that a carbon steel component could be protected significantly in a corrosive saline environment, using a proper HVOF process. The addition of molybdenum increased the corrosion resistance of the coating. The findings showed that the sprayed coatings possess significant corrosion resistance compared to the active behaviour of the carbon steel. The two different sprayed coatings supplied by two different companies displayed rather similar corrosion resistance thus providing strong evidence of a generic pattern of durability by the NiCrSiB cermet coatings. The type of substrate had no effect on the corrosion performance of the coating, however, careful precaution has to be taken for use of the coating on a carbon steel substrate to

avoid any galvanic interaction. It is likely that the coating on a carbon steel substrate with the application of CP would not suffer this type of galvanic attack.

So far as the sprayed coating itself is concerned the corrosion mechanism is rather complex and involves corrosion of the matrix, micro-galvanic corrosion attack at hardphase/matrix interface and most significantly preferential attack around splat boundaries with the attack being accentuated at the crevice regions. Anodic polarisation tests did not show any significant effect of the post spray treatments. However, some distinctions can be made with the microscopic observation, which indicated a slightly improved corrosion resistance of the vacuum-fused coating and was attributed to micro-loss mechanism as opposed to macro-loss mechanism of the sprayed and sealed coatings. All the coatings suffered enhanced corrosion as the temperature was increased. The long-term exposure signals that the degradation mechanism of these generic coatings is time dependent.

The effect of high-velocity impingement of a saline solution without suspended solids at ambient temperature was to reduce the corrosion resistance of the sprayed, sealed and fused coatings and the stainless steel. The material removal in the form of cracking and crack propagation was dominant in the sprayed and sealed coatings immediately under the jet, whilst the stainless steel suffered mechanical ploughing under the jet. The vacuum-fused coating displayed a superior performance displayed by its least weight loss measured.

The work has demonstrated the complexity of the mechanisms of erosion corrosion in HVOF-sprayed NiCrSiB cermet coatings that is likely to be mirrored in other sprayed cermets. The deterioration process involves substantial and complex interactions between corrosion and erosion and a significant contribution to overall material loss that is attributable, either directly or indirectly, to corrosion processes.

Although the superiority of the cermet, in comparison with a stainless steel metallic alloy in aqueous slurries has been confirmed, the rates of degradation of the cermet were still high partly on account of the contributions from corrosion processes. The influence of corrosion was reflected in the greater material losses from the cermet

(compared to stainless steel) during solid-free impingement. Nevertheless, the erosion-corrosion rates were very small for both materials in such conditions.

The findings emphasise the potential benefits for erosion-corrosion performance of cermets if improvements, via coating composition and/or thermal spray process parameters, in basic corrosion resistance can be secured.

The findings emphasise the potential benefits of surface treatment of thermally sprayed coatings by high temperature post-spray fusion process. The influence of vacuum-sealing reflected no effect on both solid-free and solid-liquid erosion-corrosion material losses from the coating. The fused coating distinctly displayed a better performance to erosion-corrosion even under solid-free impingement condition by exhibiting less weight loss measured. The weight loss measured under the solid-liquid impingement substantially increased for all the coatings, signalling the adverse effect of the presence of solid particles in the solution but was almost halved for the vacuum fused coating compared to the sprayed and sealed coatings.

The application of CP was seen to be extremely beneficial in all erosion-corrosion conditions studied and was most effective on the fused coating under the solid-free liquid impingement condition with no weight loss detected during the 6-days test with cathodic protection.

By virtue of the short study on the stainless steel, the work has also demonstrated the value of undertaking experiments on concentric specimens. Such an approach enables identification in detail of the different forms of attack in different regions of an eroded component and also reveals galvanic interactions between such distinct zones.

Future Recommendations

In terms of durability issues with the cermet types of coatings studied herein, it would be useful to further augment 'the database' of knowledge by further work on the following topics:

Static corrosion

- Static corrosion studies in a wider range of environments than the 'seawater-type' saline solution studied in this work.
- Investigations comprising longer time scales than employed thus far.
- Comparison of the corrosion resistance of thermal-sprayed coatings of Ni-Cr-Si-B (and others) against more established coatings such as chromium and nickel plating.

Erosion-corrosion

- Extensions of the studies to a range of lower angles of incidence, a wider range of impact velocities and solid loadings and wider range of aqueous environments.
- Parallel to the preliminary tests on the stainless steel undertaken herein, study of the influence of specimen size and galvanic interactions between the directly-impacted and surrounding regions in a range of erosion-corrosion conditions.

Turning to HVOF-process aspects, the sprayed coatings supplied by two different commercial manufacturers exhibited rather similar corrosion and erosion corrosion mechanisms and this proves similar generic natures of the coatings. As has been discussed the preferential corrosion attack occurred at splat boundaries led to macro loss mechanism. Thus the incentive is that further improvement via spray parameters (oxygen-fuel ratio, spray distance) and the most important is spraying of powder particles with similar grain sizes, density and chemical composition can probably give better coating properties. Smaller sized particles would minimise the possibility of macro loss. Moreover, more research needs to be done in improving via coating chemistry in a multiphase coating, more practical relevance of which could be, matching of the electrode potentials between the different phases that constitute a coating. Thus minimising the possibility of micro-galvanic interactions.

List of References

ABD-EL-KADER, H. and EL-RAGHY, S. (1986) Wear-Corrosion Mechanism of Stainless Steel in Chloride Media, *Corrosion Science,* Vol. 26, No. 8, p.647-653.

AHN, H. S. and LEE, C. H. (1998) A study of the wear characteristics of plasma sprayed NiCrSiB/WC-12Co mixed coating, In: *Proceedings of the 15th International Thermal Spray Conference* edited by Coddet C., Nice, France, May 25-29, Vol. 1, p.175-180.

AL-ABDALLAH, M. M. (1996) Impedance measurements on Inconel and Monel alloys in Dead Sea water and sulphate solution, *British Corrosion Journal*, Vol. 31, No 3, p.213-217.

ALFONSSON, E and QVARFORT, R. (1992) Investigation of the Applicability of some PRE Expressions for Austenitic Stainless Steels, *Materials Science Forum,* Vol. 111-112, p.483-492.

AL-HASHEM, A., CACERES, P. G., ABDULLAH, A. and SHALABY, H. M. (1997) Cavitation corrosion of duplex stainless steel in seawater, *Corrosion,* Vol. 52, No. 2, p.103-113.

AMOS, T. (1996) Aerospace wear and corrosion-resistant coatings-a perspective, *Journal of Aircraft Engineering and Aerospace Technology*, Vol. 68, No.3, p.23-25.

API-RP-14E (1991) Recommended Practice for Design and Installation of Offshore Production Platform Piping Systems, *American Petroleum Institute,* 5th ed., Washington DC, p23.

ARSENAULT, B., LEGOUX, J. G. and HAWTHORNE, H. (1997) Slurry Erosion of High Velocity Oxy-Fuel Thermal Sprayed Coatings, In: *Proceedings of the 1st United Thermal Spray Conference,* edited by C. C. Berndt, Indianapolis, Indiana, Sept. 15-18 p.97-106.

ARSENAULT, B., LEGOUX, J. G. and HAWTHORNE, H. (1998) Slurry and Dry Erosion of High Velocity Oxy-Fuel Thermal Sprayed Coatings, In: *Proceedings of the 15th International Thermal Spray Conference* edited by Coddet C., Nice, France, May 25-29, p.231-236.

ASHARY. A. A. and TUCKER, R. C., JR. (1991) Corrosion characteristics of several thermal spray cermet-coating/alloy systems, *Surface and Coatings Technology,* 49, p.78-82.

ASHWORTH, V. (1987) *Corrosion Protection Techniques.* In "Corrosion: Industrial Problems, Treatments and Control Techniques" edited by Ashworth V., Pergamon Press, p.1-15.

AURET, J. G., DAMM, O. F. R. A., WRIGHT, G. J. and ROBINSON, F. P. A. (1993) The pressure and velocity dependence of flow-type cavitation erosion, *Wear*, 170, p.185-190.

BAIN, E. C., ABORN, R. H. and RUTHERFORD, J. B. (1933) *Trans. Amer. Soc. Steel Treating*, Vol. 21, p.481.

BARBEZAT, G., KELLER, S. and WUEST, G. (1997) Internal Plasma Spray Process for Cylinder Bores in Automotive Industry. In: *Proceedings of the 1st United Thermal Spray Conference* edited by Berndt C. C., ASM International, 15-18 Sept. Indianapolis, p.11- 15.

BARBEZAT, G., KELLER, S. and WUEST, G. (1998) Internal Plasma Spray Process for Cylinder Bores in Automotive Industry, In: *Proceedings of the 15th International Thermal Spray Conference* edited by Coddet C., 25-29 May, Nice, France, Vol. 2, p.963-974.

BARDAL, E., BJORDAL, M., EGGEN, T. G., ROGNE, T. and SOLEM, T. (1993a) Prevention of erosion and corrosion in slurries using various inorganic coatings, *10th European Corrosion congress*, July, Barcelona, p.158-164.

BARDAL, E., DRUGLI, J. M. and GARTLAND, P. O. (1993b) The Behaviour of Corrosion Resistant Steels, A Review, *Corrosion Sci.*, Vol. 35, No. 1-4, p.257-267.

BARDAL, E., EGGEN, T. G., ROGNE, T. and SOLEM, T. (1995) The erosion and corrosion properties of thermals spray and other coatings, In: *Proceedings of the International Thermal Spray Conference*, p.645-650.

BELL, G. R. (1984) Various ways of fusing sprayed deposits, *Coatings and surface treatment for corrosion and wear resistance* edited by Strafford K. N., Datta P. K. and Googan C. G., Ellis Horwood Limited, Chichester, p.125-149.

BENCHAITA, M. T., GRIFFITH, P. and RAVINOWICZ, E. (1983) Erosion of Metallic Plate by Solid Particles Entrained in a Liquid Jet, *Journal of Engineering for Industry*, Aug., Vol. 105, p.215-222.

BERGET, J. (1998) *PhD Thesis*, University of Trondheim, Norwegian Institute of Technology, Department of Machine Design and Materials Technology, Norway.

BERGET, J., BARDAL, E and ROGNE, T. (1998) Effects of Powder Composition on the Erosion, Corrosion and Erosion-Corrosion Properties of HVOF Sprayed WC Based Coatings, In: *Proceedings of the 15th International Thermal Spray Conference* edited by Coddet C., Nice, France, May 25-29, Vol.1, p.305-312.

BERNDT, C. C. and KOWALSKY, K. A. (1996) Early Thermal Spraying – JTST Historical Patent # 2*, *Journal of Thermal Spray Technology*, Vol. 5, No. 4, Dec., p.399-400.

BHAGAT, R. B., CONWAY, J. C., AMATEAU, M. F. and BREZLER, R. A. (1996) Tribological performance evaluation of tungsten carbide-based cermets and development of a fracture mechanics wear model, *Wear,* Vol. 201, No. 1-2, p. 233-243.

BITTER, J. A. (1963 a) A study of erosion phenomena, Part I, *Wear,* Vol. 6, p.5-21.

BITTER, J. A. (1963b) A study of erosion phenomena, Part II, *Wear,* Vol. 6, p.169-190.

BJERREGAARD, L., GEELS, K. OTTESEN, B. and RUCKERT, M. (1996) *Metalog Guide,* Published by Struers A/S, Denmark.

BJORDAL, M. (1995) Erosion and Corrosion of Ceramic-Metallic Coatings and Stainless Steel, *PhD Thesis*, University of Trondheim, Norwegian Institute of technology, Department of machine Design and Materials Technology, Norway.

BJORDAL, M., BARDAL, E., ROGNE, T. and EGGEN, T. G. (1995a) Combined erosion and corrosion of thermal sprayed WC and CrC coatings, *Surface and Coatings Technology,* Vol. 70, p.215-220.

BJORDAL, M., BARDAL, E., ROGNE, T. and EGGEN, T. G. (1995b) Erosion and corrosion properties of WC coatings and duplex stainless steel in sand-containing synthetic seawater, *Wear,* Vol. 186-187, p.508-514.

BJORDAL, M., ROGNE, T., BARDAL, E (1996) Erosion and corrosion of thermal spray ceramic-metallic coatings, *Thermal Spray Conference,* Essen, Germany, p.102-106.

BLACK BOX (1996) Report on the official investigation into the 1996 TWA air disaster, *Channel 4,* 15.07.98.

BLANN, G. (1997) The Effects of Manual vs. Semi-Automatic Metallographic Specimen Preparation of Thermally Sprayed Coatings, In: *Proceedings of the 1st United Thermal Spray Conference* edited by Berndt C. C., ASM International, 15-18 Sept. Indianapolis, p.965-969.

BLANN, G. and VOORT, G. V. (1997) Tech-Notes: Using microstructural analysis to solve practical problems, Vol. 1, Issue 2, Published by Buehler Ltd.

BODGER, B. E., McGRANN, R. T. R. and SOMERVILLE, D. A. (1997) The Evaluation of Tungsten Carbide Thermal Spray Coatings as Replacements for Electrodeposited Chrome Plating on Aircraft Landing Gear, *Plating and Surface Finishing*, September, p.28-31.

BRIJESH, V. and HANSSON, I. H. (1990) The Cavitation Erosion-corrosion of Stainless Steel, *Corrosion Science,* Vol. 30, No. 8/9, p.761-770.

BRISCOE, B. J., PICKLES, M. J., JULIAN, K. S. and ADAMS, M. J. (1997) Erosion of polymer-particle composites coatings by liquid water jets, *Wear*, 203-204, p.88-97.

BRITISH CORROSION JOURNAL (1996) Published by The Institute of Materials, Vol. 31, No. 1, p.9.

BROWNING, J. B., (1992) And Now, Hypersonic Velocity Impact Fusion Spraying, In: *Proceedings of the International Thermal Spray Conference & Exposition*, Orlando, Florida, USA, 28 May-5 June, p.123.

BURLEIGH Literature (1991), *The Scanning-Probe Microscope Book*, Burleigh Instruments Ltd., Herts, UK.

CHANDLER, K. A. (1985) *Marine and Offshore Corrosion*, Butterworths Ltd.

CHANDRA, S., KLISIEWICZ, J. W. and SCHONENBERG, R. Y. (1994) The examination of pipe components degraded due to the erosion-corrosion phenomenon, ASME (PVP) Vol. 285 p. 17-24.

CHASE, D. P., RYBICKI, E.F. and SHADLEY, J. R. (1992) A Model for the Effect of Velocity on Erosion of M80 Steel Tubing due to the Normal Impingement of Solid Particles, In *Transactions of the ASME*, March Vol. 114, p.54-63.

CHEXAL, B., GOYETTE, L. F., HOROWITZ, J. S. and RUSCAK, M. (1996) Predicting the impact of chromium on flow-accelerated corrosion, *Pressure Vessels and Piping Codes and Standards*, ASME, Vol. 338, p.159-165.

CIRCLE 202 (1999) Sand and Erosion Probe, *Materials Performance*, NACE, June, Vol. 38, No. 6, p.16.

CLARK, H. McI. (1991) On the impact rate and impact energy of particles in a slurry pot erosion tester, *Wear*, Vol. 147, p.165-183.

CLARK, H. McI. (1992) The influence of the flow field in slurry erosion, *Wear*, Vol. 152, p.223-240.

CLARK, H. McI. and BURMEISTER, L. C. (1992) The influence of the squeeze film on the particle impact velocities in erosion, *Int. J. Impact Engineering*, Vol. 12, No. 3, p.415-426.

COSTA, V., DIAS, A. M., RANGEL, C. M. and CRUZ, L. F. (1996) Corrosion behaviour of mild steel beneath porous plasma sprayed coatings, *British Corrosion Journal*, Vol. 31 (3). p. 227-232.

COVINO, B. S. JR., CRAMER, S. J., BULLARD, S. J., HOLCOMB, G. R., COLLINS, W. K. and McGILL, G. E. (1999) Thermal Spray Anodes for Impressed Current cathodic Protection of Reinforced Concrete Structures, *Materials Performance*, Vol. 38, No. 1, p.27-33.

CROOK, P. (1991) Practical Guide to Wear for Corrosion Engineers, *Material Performance*, February.

DATTA, P. K. and GRAY, J. S. (1993) *Surface Engineering,* Vol. 1, The Royal Society of Chemistry, Cambridge.

DAVIES, J. T. (1972) *Turbulence Phenomena,* Academic Press, New York and London.

DEARNLEY, P. A., OESTGAARD, M., BETTS, A. J. and WRIGHT, G. A. (1996) Corrosion response of fusion coated austenitic stainless steel, *British Corrosion Journal*, Vol. 31 (3), p. 235-238.

DELAET, M. and CODDET, C. (1997) Thermal Spray Coating Developments for Piston Rings to be Used in Tomorrow's Duty Engines. In: *Proceedings of the 1st United Thermal Spray Conference* edited by Berndt C. C., ASM International, 15-18 Sept. Indianapolis, p.1-9.

DI-VERNIERI CUPPARI, M. G., WISCNOWSKI, F., TANAKA, D. K. and SINATORA, A. (1999) Correlation between microstructure and cavitation-erosion resistance of high chromium cast steel-preliminary results, *Wear,* 225-229, p.517-522.

DNV-RP-0501 (1996) Recommend Practice Erosive Wear in Piping Systems, *Det Norske Veritas.*

DORFMAN, M. R., KUSHNER, B. A., ROTOLICO, A. J. and DeBARRO, J. A. (1993) Development and Applications of Corrosion Resistant Thermal Sprayed Coatings, In: *Surface Engineering,* Vol. III, Process Technology and Surface Analysis, edited by Datta P. K. and Gray J. S., p.5-15, The Royal Society of Chemistry, Cambridge.

DUNDAS, J. J., and BOND, A. P. (1985) Corrosion resistance of stainless steels in seawater, *Material Performance*, Vol. 24 (10), p.54-59.

DURET, C. and PICHOIR, R. (1983) Protective coatings for high temperature materials: Chemical Vapour Deposition and Pack Cementation Processes, In: *Coatings for high temperature applications,* edited by Lang E., Applied Science Publishers Ltd., England, p.33-78.

DVORAK, M. (1998) Assessment of HVOF Coatings for Wet Corrosion Protection, In: *Proceedings of the 15th International Thermal Spray Conference,* Vol. 1 edited by Coddet C, 25-29 May, Nice, France, p.95-100.

EBDON, P. R. (1993) Electroplated Metal Matrix Composites, In: *Surface Engineering,* Vol. III, Process Technology and Surface Analysis, edited by Datta P. K. and Gray J. S., p.92-96, The Royal Society of Chemistry, Cambridge.
EG & G Princeton Applied Research, *Basics of Corrosion Measurements.*

ENGEL, L. and KLINEGELE, H. (1981), *An Atlas of Metal Damage,* translated by Murray S, Wolfe Publishing Ltd., London and Carl Hanser Verlag, Munich, Vienna.

ENGEL, P. A. (1978) Impact wear of materials, *Wear,* Vol. 48, p.18.

EVANS, U. R. (1981) *An Introduction to Metallic Corrosion,* 3rd edition, Edward Arnold (Publishers) Ltd., London.
FERVEL, V., NORMAND, B., CODDET, C. and DELAET, M. (1998) Tribological properties of Mo/NiCrBSi thermal spray deposits, In: *Proceedings of the 15th International Thermal Spray Conference* edited by Coddet C., 25-29 May, Nice, France, Vol. 1, p.237-241.

FINNIE, I. (1958) The mechanism of erosion of ductile metals, *Proc. 3rd U.S. Nat. Congr. Applied Mechanics,* ASME, NY, p.527-532.

FINNIE, I. (1960) Erosion of surfaces by solid particles, *Wear*, Vol. 3, p.87-103.

FONTANA, M. G. and GREENE, N. D. (1978) *Corrosion Engineering,* McGraw-Hill, New York.

FONTANA, M. G. and STAEHLE, R. W. (1970) *Advances in Corrosion Science and Technology*, Plenum Press, New York.

GARCIA-ALONSO, M. C., ESCUDERO, M. L., LOPEZ, V. and MACIAS, A. (1997) Characterisation and Corrosion Behaviour of Laser Surface Alloyed Ni-Cr-W-Mo-Cu-C-B Coatings, *ISIJ International*, Vol. 37, No. 2, p.161-168.

GARDEGA, T. W., LANZA, V. and ROEBUCK, A. H. (1986) Thermal Spray Coatings, *Journal of Protective Coatings & Linings*, January, p.44-47.

GELLINGS, P. G. (1976) *Introduction to corrosion prevention and control for engineers,* Delft University Press, The Netherlands.

GIRALT, F. and TRASS, O. (1975) Mass Transfer from Crystalline Surfaces in a Turbulent Jet, Part 1, *The Canadian Journal of Chemical Engineering*, Vol. 53, Oct., p.505-511.

GIRALT, F. and TRASS, O. (1976) Mass Transfer from Crystalline Surfaces in a Turbulent Jet, Part 2, *The Canadian Journal of Chemical Engineering*, Vol. 54, June, p.148-155.

GREATHOUSE, G. A. and WESSEL, C. J. (1954) *Deterioration of Materials, causes and preventive techniques,* Reinhold Publishing Corporation.

GREAVES, W. H. and JACKSON, W. J. (1995) Steel, In: *Kempe's Engineers Year-Book,* edited by Sharpe C., C1/557, M-G Information Services Ltd., UK.

GROC, M., PAWLOWSKI, L. and SMUROV, I. (1997) Modelling of the Laser Engraving at Plasma Sprayed Al_2O_3, TiO_2 and Al_2TiO_5 Coatings for Anilox Rolls. In: *Proceedings of the 1st United Thermal Spray Conference* edited by Berndt C. C., ASM International, 15-18 Sept. Indianapolis, p.41-48.

GROSS, K. A., BEN-NISSAN, B., WALSH, W. R. and SWARTS, E. (1998) Analysis of Retrieved Hydroxyapatite Coated Orthopaedic Implants, In: *Proceedings of the 15th*

International Thermal Spray Conference edited by Coddet C., 25-29 May, Nice, France, Vol. 2, p.1133-1138.

GUILLEMETTE, R. (1998) The Development and Implementation of Thermal Spray Coatings for Helicopter Components, In: *Proceedings of the 15th International Thermal Spray Conference* edited by Coddet C., 25-29 May, Nice, France, Vol. 2, p.1033-1038.

HACKETT, C. M., SETTLES, G. S. and MILLER, J. D. (1993) On the gas dynamics of HVOF thermal sprays, *Proceedings of the 1993 National Thermal Spray Conference*, Anaheim, CA, 7-11 June, p.167-172.

HEARLEY, J. A., LITTLE, J. A. and STURGEON, A. J. (1998) Oxidation properties of NiAl intermetallic coatings prepared by high velocity oxy-fuel thermal spraying, In: *Proceedings of the 15th International Thermal Spray Conference* edited by Coddet C., 25-29 May, Nice, France, Vol. 2, p.89-94.

HEITZ, E. (1991) Chemo-Mechanical Effects of Flow on Corrosion, C*orrosion*, Vol. 47, No. 2, p.135-145.

HELALI, M. and HASHMI, M. S. J. (1996) Production of free standing objects by high velocity oxy-fuel (HVOF) thermal spraying process, *Journal of Materials Processing Technology*, Vol. 56 p.431-438.

HIROOKA, S. and ROBINSON, M. J. (1998) Electrochemical Measurements of Erosion-corrosion on Austenitic Stainless Steels in Flowing 3.5% NaCl Solution Containing Sand Particles, Report presented for *Corrosion of Components for Industrial and Offshore Applications in Flowing Environments*, organised by Institute of Corrosion, 10 June, Heriot-Watt University, Edinburgh.

HOAR, T. P. (1971) Report of the committee on corrosion and protection, *HMSO*, London.

HODGKIESS, T. and LIM, C. W. (1993) Aspects of Galvanic Corrosion Behaviour of a Range of Materials in Sea Water, *Corrosion Science*, Vol. 35, Nos. 1-4, p. 269-283.

HODGKIESS, T. and NEVILLE, A. (1997) An Assessment of Galvanic Effects in Thermal Sprayed Coating Systems, In: *Proceedings of the 1st United Thermal Spray Conference* edited by Berndt C. C., ASM International, 15-18 Sept. Indianapolis, p.167-174.

HODGKIESS, T. and NEVILLE, A. (1998a) An Analysis of Environmental Factors Affecting Corrosion Behaviour of Thermal Spray Cermet Coatings, In: *Proceedings of the 15th International Thermal Spray Conference* edited by Coddet C., 25-29 May, Nice, France, Vol. 1, p.63-68.

HODGKIESS, T. and NEVILLE, A. (1998b) Erosion-corrosion of Metals and Cermets: Some Comparative and Contrasting Features, Report presented for *Corrosion of Components for Industrial and Offshore Applications in Flowing Environments*, organised by Institute of Corrosion, 10 June, Heriot-Watt University, Edinburgh.

HODGKIESS, T. and NEVILLE, A. (1999) The role of advanced materials to combat erosion-corrosion in aqueous environments, *Stainless Steel World,* July/August, p.39-42.

HODGKIESS, T., MACIVER, A. and CHONG, P. Y. (1987) Galvanic Studies Related to the use in Desalination Plant of Corrosion-Resistant Materials, *Desalination*, Elsevier Science, Amsterdam, 66, p.147-170.

HODGKIESS, T., NEVILLE, A. and SHRESTHA, S. (1998) Electrochemical and Mechanical Interactions During Erosion-corrosion of a High-Velocity Oxy-Fuel Coating and a Stainless steel, paper presented in ICEAW, '98, (In press to be published in *Wear,*).

HOLCOMB, G. R., CRAMER. S. D., BULLARD, S. J., COVINO, B. S., JR, COLLINS, W. K. and GOVIER, R. D. (1997) Characterization of Thermal-Sprayed Titanium Anodes for Cathodic Protection, In: *Proceedings of the 1st United Thermal Spray Conference* edited by Berndt C. C., ASM International, 15-18 Sept. Indianapolis, p.141-150.

HOLSER, R. A., PRENTICE, G., POND, R. B. Jr and GUANTI, R. (1990) Use of Rotating Cylinder Electrodes to Simulate Turbulent Flow Conditions in Corroding Systems, *Corrosion Science*, Sept. 1990, 764-769.

HONDROS, E. D. (1993) Surface Engineering-the new challenge in material technologies, In: *Surface Engineering,* Vol. I, Fundamentals of Coatings, edited by Datta P. K. and Gray J. S., p.1-9, The Royal Society of Chemistry, Cambridge.

HUCHIN, J. P. (1998) The Place of Thermal Spraying in Industry Today and the Prospects for the Future, In: *Proceedings of the 15th International Thermal Spray Conference* edited by Coddet C., 25-29 May, Nice, France, Vol. 2, p.925-931.

HUMPHREY, J. A. C. (1990) Fundamentals of fluid motion in erosion by solid particle impact, *Int. J. of Heat and Flow*, Vol. 11, No. 3, p.170-195.

HUSSAINOVA, I., KUBARSEPP, J. and SHCHEGLOV, I. (1999) Investigation of impact of Solid Particles against Hardmetal and Cermet Targets, *Presented in 12th International Conference on Wear of Materials,* Atlanta, Georgia, 25-29 April.

HUTCHINGS, I. M. (1992) *Tribology: Friction and Wear of Engineering Materials*, Edward Arnold, London.

IJSSELING, F. P. (1989) General guidelines for corrosion testing of materials for marine application, *Br. Corr. J.*, Vol. 24, No. 1, p.55-78.

INTERNET 1, http://www.tafa.com/waterjet

INTERNET 2 http://www.tafa.com/5000.htm

INTERNET 3 http://www.corrosion.com/thermal

IRONS, G., POIRIER, D. and ROY, A. (1995) Thermal Spraying-Current Status and Future Trends, In: Proc. Conf., Kobe, Japan, 22-26 May, Vol. 1, p.205-209.

IRVING, R., KNIGHT, R. and SMITH, R. W. (1993) The HVOF Process-the hottest topic in the thermal spray industry, *Welding Journal*, July, p.25-30.

ISHIKAWA, K., SUZUKI, T., KITAMURA, Y. and TOBE, S. (1997) Corrosion Resistance of Thermal Sprayed Titanium Coating with Resin Seal in Chloride Solution, In: *Proceedings of the 1st United Thermal Spray Conference* edited by Berndt C. C., ASM International, 15-18 Sept. Indianapolis, p.203-208.

JACOBSON, B. E. and McGUIRE, G. E. (1983) Techniques for Structural Analysis of Deposited Materials: Correlation of Film Structure and Properties, In: *Coatings for High Temperature Applications*, edited by Lang E., Applied Science Publishers Ltd., England, p.218.

JENKINS, R. and DeVRIES, J. L. (1993) An Introduction to X-ray powder diffractometry, catalogue by N. V. Philips Gloeilampenfabrieken, Eindhoven, Holland.

KANE, R. D. and CAYARD, M. S. (1999) Understanding Critical Factors that Influence Refinery Crude Corrosiveness, *Materials Performance*, Vol. 38, No. 6, p.48-54.

KARIMI, A. and VERDON, Ch. (1993) Hydroabrasive wear behaviour of high velocity oxyfuel thermally sprayed WC-M coatings, *Surface and Coatings Technology*, Vol. 62, p.493-498.

KARIMI, A., VERDON, C., MARTIN, J. L. and SCHMID, R. K. (1995) Slurry Erosion Behavior of Thermally Sprayed WC-M Coatings, *Wear*, Vol. 186, No. 2, p. 480-486.

KASTNER, W., NOPPER, H., RESNER, R. (1993) Pipelines protection from corrosion-erosion, *Atomnaya Energiya*, Oct., Vol. 75, No. 4, p.286-294.

KEMBAIYAN, K. T. and KESHAVAN, K. (1995) Combating severe fluid erosion and corrosion of drill bits using thermal spray coatings, *Wear*, Vol. 186, No. 2, p.487-492.

KHAN, M. S. A., CLYNE, T. W. and STURGEON, A. J. (1997) Microstructure and Abrasion Resistance of WC-Co Coatings Produced by High Velocity Oxy-Fuel Spraying, In: *Proceedings of the 1st United Thermal Spray Conference*, edited by C. C. Berndt, Indianapolis, Indiana, Sept. 15-18 p.681-690.

KIM, Y.-J, ANDRESEN, D. M., LAU, Y.-C. and OFFER, H. P. (1996) Corrosion Potential Behaviour in High-Temperature Water of Noble Metal-Doped Alloy Coatings Deposited by Underwater Thermal Spraying, *Corrosion*, Vol. 52, No. 6, p.440-446.

KNAPP, J. K. and NITTA, H. (1997) Fine-particle slurry wear resistance of selected tungsten carbide thermal spray coatings, *Tribology International*, Vol. 30, No. 3, p.225-234.

KOZYREV, S. P. (1980) The Genesis of Cavitation Wear, *Trenie Iznos*, Vol. 1, No. 5, p.793-808.

KRETSCHMER, I., HEIMGARTNER, P., POLAK, R. and KAMMER, P.A. (1997) New Fusible Alloys with Enhanced Corrosion Resistance, In: *Proceedings of the 1st United Thermal Spray Conference* edited by Berndt C. C., ASM International, 15-18 Sept. Indianapolis, p.199-202.

KREYE, H., SCHWETZKE, R., BUSCHINELLI, A. and BOCCANERA, L. (1998) cavitation Erosion Resistant Coatings Produced by Thermal Spraying and Weld Cladding, In: *Proceedings of the 15th International Thermal Spray Conference* edited by Coddet C., 25-29 May, Nice, France, Vol. 1, p.269-273.

KUMAR, A., BOY, J., ZATORSKI, R. and MARCH, P. (1997) Cavitation Resistance of Thermal Spray Coatings, In: *Proceedings of the 1st United Thermal Spray Conference,* edited by Berndt C. C., p.83-90, 15-18 Sept., Indianapolis, Indiana,

KUMAR, D. and MODI, S. C. (1995) Technological Advancement in Thermal Spraying through HVOF Process, *Transactions of the Metal Finishers' Association of India*, Vol. 4, No. 1, Jan.-Mar., p.43-48

KURODA, S. (1998) Properties and Characterisation of Thermal Sprayed Coatings-A review of Recent Research Progress, In: *Proceedings of the 15th International Thermal Spray Conference* edited by Coddet C., 25-29 May, Nice, France, Vol. 1, p.539-550.

LEE, S. W. and WANG, B. Q. (1996) Erosion Phenomena of the Low Carbon Steel and Thermal Sprayed Coatings at Elevated Temperature, *Fluid Engineering Division Conference,* Vol. 1, ASME, p.767-772

LESTER, T., HARRIS, S. J., KINGERLEY, D. and MATTHEWS, S. (1997) Thermally Sprayed Ternary Materials for Enhanced Corrosion Protection, In: *Proceedings of the 1st United Thermal Spray Conference* edited by Berndt C. C., ASM International, 15-18 Sept. Indianapolis, p.183- 189.

LEVY, A and CHIK, P. (1983) The effects of erodent compositions and shape on the rosin of steel, *Wear,* Vol. 89 (2), p.151-162.

LEVY, A. and MAN, Y. F. (1985) Corrosion-erosion rates/mechanisms of 9Cr1Mo steel, *Corrosion 85*, 338, March 25-29, Boston, Massachusetts.

LEVY, A. V. (1995) *Solid Particle Erosion and Erosion-corrosion of Materials,* ASM International, USA.

LEVY, A. V. and WANG, B. (1988) Erosion of Hard Material Coating Systems, *Wear,* Vol. 121, p.325-346.

LEVY, A., YAN, J. and PATTERSON, J. (1986) Elevated Temperature Erosion of Steels, *Wear,* Vol. 108, p.43-60.

LU, Y. C., IVES, M. B. and CLAYTON, C. R. (1993) Synergism of alloying elements and pitting corrosion resistance of stainless steels, *Corrosion Science,* Vol. 35, Nos. 1-4, p. 89-96.

LUGSCHEIDER, E. and JOKIEL, P. (1993) Characterisation of Particle Reinforced Nickel Hard Alloys produced by Thermal Spraying, In: *Proceedings of the 1993 National Thermal Spray Conference*, Anaheim, CA, 7-11 June, p.411-416.

LUGSCHEIDER, E., JOKIEL, P., MESSESCHMIDT, V. and BECKSCHULTE (1993) Subsequent sealing of thermally sprayed coatings to increase corrosion resistance, *Institute of Materials,* London, p.46-51.

LYNN, R. S., WONG, K. K. and CLARK, H. McI (1991) On the particle size effect in slurry erosion, *Wear,* Vol. 149, p.55-71.

MADSEN, B. W. (1988) Measurement of erosion corrosion synergism with a slurry wear test apparatus, *Wear,* Vol. 123, p. 127-142.

MAGOME, M., HARA, K., SANO, K. and UEDA, Y. (1998) Influences of Metal Sprayed Coating Artificial Dental Root on the Vital Tissue, In: *Proceedings of the 15th International Thermal Spray Conference* edited by Coddet C., 25-29 May, Nice, France, Vol. 2, p.1079-1082.

MANSFELD, F. (1988) Don't be afraid of electrochemical techniques-but use them with care! *Corrosion Science,* March, p.856-868.

MANSFELD, F. B and BERTOCCI, U. (1981) *Electrochemical Corrosion testing,* ASTM, Philadelphia PA.

MANUEL, R., YUNG, E. (1994) Metal Seated Ball Valves with Carbide Coatings, In: *Proceedings of the 7th National Thermal Spray Conference*, 20-24 June, Boston, Massachusetts, p.111-114.

MATTHEWS, A., LEYLAND, A., FANCEY, K. S., JAMES, A. S., ROBINSON, P. A., HOLIDAY, P., DEHBI-ALAOUI, A and STEVENSON, P. R. (1993) Developments of Plasma-assisted PVD Processing, In: *Surface Engineering,* Vol. III, Process Technology and Surface Analysis, edited by Datta P. K. and Gray J. S., p.99-110, The Royal Society of Chemistry, Cambridge.

McCARTNEY, D. G. (1998) High Velocity Oxy-fuel Thermal Sprayed Coatings: Processing, Characterisation, and Performance, *Powder Metallurgy*, Vol. 41, No.1, p.14-15.

McDONALD, D. D., MANKOWSKI, J., KARAMINEZHAAD-RANJBAR, M. and HU, Y-H. (1988) Apparatus for Controlled Hydrodynamic Electrochemical and Corrosion Studies in High-Temperature Aqueous Systems, *Corrosion,* Vol. 44. No. 3, p.186-192.

McINTYRE R. (1996) Plasma sprayed coatings versus high velocity oxy-fuel processes, *Material World*, Aug., p. 455-457.

MEYER, U., BROSNAN, C.C., BREMHORST, K., TOMLINS, R. and ATRENS, A. (1994) A new impinging jet test rig used to identify the important parameters in service erosion- corrosion in Bayer liquid and to study the damage morphology, *Wear*, Vol. 176, p.163-171.

MOHANTY, M., SMITH, R.W., De BONTE, M., CELIS, J.P. and LUGSCHEIDER, E. (1996) Sliding wear behaviour of thermally sprayed 75/25 Cr_3C_2/NiCr wear resistant coatings, *Wear*, Vol. 198, p.251-266.

MOLLICA, A., TREVIS, A., TRAVERSO, E., VENTURA, G., DE CAROLIS, G. and DELLEPIANE, R. (1988) Crevice Corrosion Resistance of Stainless Steels in Natural Seawater in the Temperature Range of 25-40 C, *Corrosion*, April, Vol. 44 (4), p.194-198.

MOMMA, T. and LICHTAROWICH, A. (1995) A study of pressures and erosion produced by collapsing cavitation, *Wear*, 186-187, p. 425-436.

MOSKOWITZ, L. (1997) The Effects of Post Heating an HVOF Sprayed Fusible Coating, In: *Proceedings of the 1st United Thermal Spray Conference* edited by Berndt C. C., ASM International, 15-18 Sept. Indianapolis, p.519-525.

MOSKOWITZ, L. N., (1992) Application of HVOF Thermal Spraying to Solve Corrosion Problems in Petroleum industry, In: *Proceedings of the International Thermal Spray Conference & Exposition*, Orlando, Florida, USA, 28 May-5 June, p. 611-618.

NAISBITT, G., ALDERTON, T. and BRUCE, C. (1997) Technology Transfer. In: *Proceedings of the 1st United Thermal Spray Conference* edited by Berndt C. C., ASM International, 15-18 Sept. Indianapolis, p.59-63.

NELSON, J and VOORT, G. V. (1997) *Tech-Notes*: Using microstructural analysis to solve practical problems, Vol. 1, Issue 1, Published by Buehler Ltd.

NESTLER, M. C., PRENZEL, G. and SEITZ, T. (1998) HVOF Spraying vs. Hard Chrome Plating Coating Characteristics and Aircraft Applications, In: *Proceedings of the 15th International Thermal Spray Conference*, edited by Coddet C, Vol. 2, 25-29 May, Nice, France, p.1073-1078.

NEVILLE, A. (1995) An Investigation of the Corrosion Behaviour of a Range of Engineering Materials in Marine Environments, *PhD Thesis*, Vol. 1, University of Glasgow, UK.

NEVILLE, A. and HODGKIESS, T. (1996) Corrosion Behaviour and Microstructure of Two Thermal Spray Coatings, *Surface Engineering*, Vol. 12, No. 4, p. 303-312.

NEVILLE, A. and HODGKIESS, T. (1997a) The Corrosion Behaviour of a Cermet Coating Applied by HVOF Spraying, In: *Proceedings of the 1st United Thermal Spray Conference* edited by Berndt C. C., ASM International, 15-18 Sept. Indianapolis, p.161-166.

NEVILLE, A. and HODGKIESS, T. (1997b) A study of the corrosion resistance and microstructure of a laser treated layer on duplex and austenitic stainless steels, *Surface Engineering II,* Royal Society of Chemistry.

NEVILLE, A. and HODGKIESS, T. (1997c) Study of effect of liquid corrosivity in liquid-solid impingement on cast iron and austenitic stainless steel, *Brit. Corr. J.,* Vol. 32, No. 3, p.197-205.

NEVILLE, A., HODGKIESS, T. and DALLAS, J. T. (1995) A study of the erosion-corrosion behaviour of engineering steels for marine pumping applications, *Wear,* 186-187, p.497-507.

NICOLL, A. R., BACHMANN, A. MOENS, J. R. and LOEWE, G. (1992) The Application of High Velocity Combustion Spraying, In: *Proceedings of the Int. Thermal Spray Conference & Exposition,* Orlando, Florida, 28 may-5 June, p. 149-152.

NIEMI, K., VUORISTO, P., MANTYLA, T., BARBEZAT, G. and NICOLL, A.R. (1992) Abrasion Wear Resistance of Carbide Coatings Deposited by Plasma and High Velocity Combustion Processes, *Proceedings of the International Thermal Spray Conference & Exposition,* Orlando, Florida, USA, p.685-689.

NORMAND, B., LIAO, H., LANDEMARRE, O., CODDET, C. and PGETTI, J. (1998) Corrosion resistance of thermal spray Inconel 690 coatings, In: *Proceedings of the 15th International Thermal Spray Conference* edited by Coddet C., 25-29 May, Nice, France, Vol. 1, p.69-73.

OHLIGER, A., SZELAGOWSKI, P. and SCHAFSTALL, H-G. (1990) Thermal Spraying-Recent Developments for Underwater application, In: *Proceedings of the National Thermal Spray Conference*, Long Beach, CA, USA, 20-25 May, p.193-200.

OKA, Y. I., OHNOGI, H., HOSOKAWA, T. and MATSUMURA, M. (1997) The impact angle dependence of erosion damage caused by solid particle impact, *Wear,* Vol. 203-204, p.573-579.

PALASAMUDRAM, S. L. and BAHADUR, S. (1997) Particle characterisation for angularity and the effects of particle size and angularity on erosion in a fluidised bed environment, *Wear,* Vol. 203-204, p.455-463.

PARKER, D. W. and KUTNER, G. L. (1991) HVOF-Spray Technology poised for growth, *Advanced Materials and Processes*, Vol. 4, p.68-74.

PAWLOWSKI, L. (1995) *The Science and Engineering of Thermal Spray Coatings,* John Wiley & Sons.

POTZL, R. (1994) Laser Remelting of HVOF Coatings, *Materials Science Forum,* Vol. 163-165, p.595-602.

POULSON, B. (1990) Mass transfer from rough surfaces, *Corrosion Science,* Vol. 30, No. 6/7, p.743-746.

PREECE, C. M., BRUNTON, J. H. (1980) A comparison of liquid impact erosion and cavitation erosion, *Wear,* Vol. 60, p.269-284.

PRICE, J. C. (1998) The Application of Thermal Spraying Technology in the Oil and Gas Industry, In: *Proceedings of the 15th International Thermal Spray Conference* edited by Coddet C., 25-29 May, Nice, France, Vol. 2, p.1103-1107.

RAJARATNAM, N. (1976) *Turbulent Jets,* Elsevier Scientific Publishing Co.

REINERS, G., KREYE, H. and SCHWETZKE, R. (1998) Properties and Characterisation of Thermal Spray Coatings, In: *Proceedings of the 15th International Thermal Spray Conference* edited by Coddet C., 25-29 May, Nice, France, Vol. 1, p.629-634.

RICHARD, C. S., BERANGER, G., LU, J, FLAVENOT, J. F. (1996) The influences of heat treatments and interdiffusion on the adhesion of plasma-sprayed NiCrAlY coatings, *Surface and Coatings Technology,* Vol. 82, p.99-109.

RIGNEY, R. W., GRUBOWSKI, A, McCAW, R. and SCANDEL, K. (1998) Component Repair and Chrome Plating Replacement with New Thermal Spray in the United States Navy: Successes and the Future, In: *Proceedings of the 15th International Thermal Spray Conference* edited by Coddet C., 25-29 May, Nice, France, Vol. 2, p.975-979.

ROBERT, E., COLSON, P. E., NORMAN, J. and MORIBER, P. E. (1997) Corrosion Control, *Civil Engineering*, p.58-59, March.

ROGERS, F. S. (1995) Thermal spray for corrosion control: A Competitive Edge for Commercial Shipbuilding, *Journal of Ship Production*, February, Vol. 11, No. 1 p.53-55.

ROGNE, T, SOLEM, T. and BERGET, J. (1997) Effect of Metallic Matrix Composition on the Erosion-Corrosion Behaviour of WC-Coatings, In: *Proceedings of the 1st United Thermal Spray Conference,* edited by Berndt C. C., 15-18 September, Indianapolis, Indiana, p.113-118.

ROGNE, T., BJORDAL, M., SOLEM, T. and BARDAL, E. (1996) The Importance of Corrosion on the Erosion-Corrosion Performance of Thermal Spray Ceramic-Metallic Coatings, In: *Proceedings of the 10th ASM National Thermal Spray Conference*, edited by Berndt C. C., Cincinnati, Ohio, 7-11 Oct., p.207-215.

ROGNE, T., SOLEM, T. and BERGET, J. (1998) Effect of Composition and Corrosion Properties of the Metallic Matrix on the Erosion-Corrosion Behaviour of HVOF Sprayed WC-Coatings, *Corrosion 98,* No. 495, p.1-13.

SAKAMOTO, A., FUNAKI, H. and MATSUMURA, M. (1995b) Influence of galvanic macro-cell corrosion on the cavitation erosion durability assessment of metallic materials, International cavitation erosion test of Gdansk, *Wear,* 186-187, p.542-547.

SAKAMOTO, A., YAMASAKI, T. and MATSUMURA, M. (1995a) Erosion-corrosion tests on copper alloys for water tap use, *Wear*, 186-187, p.548-554.

SALAMA, M. M. (1993) Erosion Velocity Limits for Water Injection Systems, *Material Performance*, July, Vol. 32, No. 7, p.44-49.

SALMAN, A. D., GORHAM, D.A. and VERBA, A. (1995) A study of solid particle under normal and oblique impact, *Wear*, Vol. 186-187, p.92-98.

SALVAGO, G. and FUMAGALLI, G. (1996) Application of Breakdown Potential Distribution in Corrosion Comparisons of Stainless Steels, *Corrosion Science*, Vol. 52 (10), p. 760-767.

SARICIMEN, H., JARRAH, N. R. and ALLAM, I. M. (1994) Corrosion of 316L austenitic stainless steel under desalination plant conditions, *British Corrosion Journal*, Vol. 29 (4), p.280-286.

SARKAR, A. D. (1977) *Wear of Metals*, Pergamon Press.

SASAKI, K. and BURSTEIN, G. T. (1996) The generation of surface roughness during slurry erosion-corrosion and its effect on the pitting potential, *Corrosion Science*, Vol. 38, No. 12, p. 2111-2120.

SAUER, J. P. (1997) The use of metallographic standards in calibration of the polishing process, In: *Proceedings of the 1st United Thermal Spray Conference* edited by Berndt C. C., ASM International, 15-18 Sept. Indianapolis, p.955-957.

SAYWELL, W. A. (1996) Thermal Spray Industry continues to develop, *MPR*, Elsevier Science Ltd., April, p.34-37.

SEDRIKS, A. J. (1986) Effect of Alloy Composition and Microstructure under Passivity of Stainless Steels, *Corrosion*, July, Vol. 42 (7), p.376-388.

SHADLEY, J. R., SHIRAZI, S. A., DAYALAN, E., ISMAIL, M. and RYBICKI, E. F. (1996) Erosion-Corrosion of a Carbon Steel Elbow in a Carbon dioxide Environment, *Corrosion*, Sept. Vol. 52, No. 9, p.714-723.

SHAH, R., WANG, K-C., SAMPATH, K., PARTHASAATHI, S., JO, J. and ONESTO, E. J. (1994) Towards Manufacturing High Quality Thermal Spray Coatings, In: *Proceedings of the 7th National Thermal Spray Conference*, 20-24 June, Boston, Massachusetts, p.675-681.

SHIMIZU, K., NOGUCHI, T., KAMADA, T. and TAKASAKI, H. (1996) Progress of erosive wear in spheroidal graphite cast iron, *Wear*, Vol. 198, p.150-155.

SHREIR, L. L. (1963 a) *Corrosion*, Vol. 2, Newnes-Butterworths, London.

SHREIR, L. L. (1963 b) *Corrosion*, Vol. 1, Newnes-Butterworths, London.

SHRESTHA, S., HODGKIESS, T. and NEVILLE, A. (1999) The effect of Post-treatment in the Erosion-corrosion Performance of HVOF Sprayed Coatings, Poster paper presented in the 12th International Conference of Wear of Materials, GA, Atlanta, USA, 25-29 April.

SIITONEN, P., CHEN, S. L., NIEMI, K. and VUORISTO, P. (1992) Electrochemical Method for Evaluating the Corrosion Resistance and Porosity of Thermal Sprayed Coatings, In: *Proceedings of the International Thermal Spray Conference & Exposition*, Orlando, Florida, 28 May-5 June, p.853-858.

SIITONEN, P., KINOS, T. and KETTUNEN, P.O. (1994) In: *Proceedings of the 7th National Thermal Spray Conference*, Boston, USA, June 1994, p. 105-110.

SILVERMAN, D. C. (1984) Rotating Cylinder Electrode for Velocity Sensitivity Testing, *Corrosion*, Vol. 40 (5), 1984, 220-226.

SILVERMAN, D. C. (1988) Rotating Cylinder Electrode – Geometry Relationships for Prediction of velocity-Sensitive Corrosion, *Corrosion*, Vol. 44 (1) 1988, 42-49.

SLIKKERVEER, P. J., BOUTEN, P. C. P., VELD, F. H., and SCHOLTEN, H. (1998) Erosion and damage by sharp particles, *Wear*, Vol. 217, p.237-250.

SMITH, M. F., DYKHUIZEN, R. C. and NEISER, R. A. (1997) Oxidation of HVOF-Sprayed Steel, In: In: *Proceedings of the 1st United Thermal Spray Conference* edited by Berndt C. C., ASM International, 15-18 Sept. Indianapolis, p.885-893.

SOBOLEV, V. V., GUILEMANY, J. M. and CALERO, J. A. (1995) Dynamic processes during in-flight motion of Cr_3C_2-NiCr powder particles in High Velocity Oxy-fuel (HVOF) spraying, *Journal of Materials Processing & Manufacturing Science*, Vol. 4-July, p.25-39.

SOBOLEV, V. V., GUILEMANY, J. M. and CALERO, J. A. (1997) Formation of Structure of HVOF Sprayed WC-Co Coating on a Copper Substrate, In: *Proceedings of the 1st United Thermal Spray Conference* edited by Berndt C. C., ASM International, 15-18 Sept. Indianapolis, p.943-948.

SPARKS, A. J. and HUTCHINGS, I. M. (1991) Transitions in the erosive wear behaviour of a glass ceramic, *Wear*, Vol. 149, p.99-110.

SRIDHAR, K., KHANNA, A. S. and DESHMUKH, M. B. (1998) Formation of highly corrosion resistant alloys using laser surface alloying, In: *Proceedings of the 15th International Thermal Spray Conference* edited by Coddet C., 25-29 May, Nice, France, Vol. 1, p.43-48.

STACK, M. M. (1996) Erosion-corrosion Mapping in Dry and in Aqueous Environments, *Zairyo-to-Kankyo*, Vol. 45, p.551-559.

STACK, M. M. and BRAY, L. (1995) Interpretation of wastage mechanisms of materials exposed to elevated temperature erosion-corrosion using erosion-corrosion maps and computer graphics, *Wear*, Vol. 186-187, p.273-283.

STACK, M. M., CORLETT, N. and ZHOU, S. (1998) Some thoughts on the effect of elastic rebounds on the boundaries of the aqueous erosion-corrosion map, *Wear*, Vol. 214, p.175-185.

STACK, M. M., WANG, H. W. and MUNZ, W. D. (1999) Some thoughts on the construction of erosion-corrosion maps for PVD coated steels in aqueous environments, *Surface and Coatings Technology*, Vol. 113, p.52-62.

STACK, M. M., ZHOU, S. and NEWMAN, R. C. (1995a) Indentification of transitions in erosion-corrosion regimes in aqueous environments, *Wear*, Vol. 186-187, p.523-532.

STEFFENS, H. D. (1983) Spray and detonation Gun Technologies, Laser-assisted Techniques, In: *Coatings for High Temperature Applications*, edited by Lang E., Applied Science Publishers Ltd., England, p.121-138.

STEFFENS, H. D., GRAMLICH, M. and NASSENSTEIN, K. (1994) Thermal Spraying, *Materials Science Forum*, Vols. 163-165, p.559-572.

STEINSMO, U., ROGNE, T., DRUGLI, J. M. and GARTLAND, P. O. (1997) Critical Crevice Temperature for High-Alloyed Stainless Steels in Chlorinated Seawater Applications, *Corrosion*, Jan., Vol. 53 (1), p. 26-32.

STERN, M. and GEARY, A. L. (1957) Electrochemical Polarisation, *J. of Electrochem. Soc.*, Vol. 104, No.1, p.56-62.

STRINGER, J., STALLINGS, J. W. and WHEELDON, J. M. (1989) Wastage in bubbling fluidized-bed combustors: An update, In: *Proceedings of 10^{h} International Conference on Fluidization Bed Combustion*, San Francisco, CA, p.857-862.

STRUTT, J. E., ROBINSON, M. J. and TURNER W. H. (1981) Recent developments in Electrochemical Corrosion Monitoring Techniques, *The Chemical Engineer*, Dec., 375, p.567-572.

SUNDARRAJAN, G. (1991) The depth of plastic deformation beneath eroded surfaces the influence of impact angle and velocity, particle shape and material properties, In: *Proc. Int. Conf. On Wear of Materials*, ASME, New York, p.111-122.

SUNDARRAJAN, G. (1995) The solid particle erosion of metallic materials: The rationalization of the influence of material variables, *Wear*, Vol. 186-187, p.129-144.

SUNDARRAJAN, G. and ROY, M. (1997) Solid particle erosion of metallic materials at room and elevated temperatures, *Tribology International*, Vol. 30, No. 5, p.339-359.

TALIA, M., LANKARANI, H. and TALIA, J. E. (1999) New experimental technique for the study and analysis of solid particle erosion mechanisms, *Wear*, Vol. 225-229, p.1070-1077.

TANI, K. and NAKAHIRA, A. (1998) Applications of HVOF Sprayed WC Cermet Coatings for Paper Mills, In: *Proceedings of the 15th International Thermal Spray Conference* edited by Coddet C., 25-29 May, Nice, France, Vol. 2, p.1097-1102.

THORPE, M. L. and RICHTER, H. J. (1992) A Pragmatic Analysis and Comparison of the HVOF Process, In: *Proceedings of the International Thermal Spray Conference &Exposition,* Orlando, Florida, 28 May-5 June, p.137-147.

THORPE, R. J. and THORPE, M. L. (1993) High Pressure HVOF-An Update, In: *Proceedings of the 1993 NTSC,* Anaheim, CA, 7-11 June, p.199-204.

TOBE, S. (1998) A review of protection from corrosion, oxidation and hot corrosion by thermal spray coatings, In: *Proceedings of the 15th International Thermal Spray Conference* edited by Coddet C., 25-29 May, Nice, France, Vol. 1, p.3-11.

TODD, B. (1979) Corrosion and Materials Selection in Seawater Systems, *I Mech. E,* C76/79, p.57-68.

TRETHEWEY, K. R. and CHAMBERLAIN, J. (1995) *Corrosion for Science and Engineering,* 2nd edition, Longman Group Ltd., England.

TUCKER, R. C. (1998) An overview of alternative coatings for wear and corrosion resistance, In: *Proceedings of the 15th International Thermal Spray Conference,* Vol. 1 edited by Coddet C, 25-29 May, Nice, France, p.103-109.

TUCKER, R. C. and ASHARY, A. A. (1995) Advanced thermal spray coatings for corrosion and wear resistance, *Symposium,* Las Vegas, NV, Feb., p.89-98.

UHLIG, H. (1949) *Chemical and Engineering News,* 97:2764.

VENUGOPAL, A., ANGAL, R. D. and RAJA, V. S. (1996) Effect of Grain-Boundary Corrosion on Impedance Characteristics of an Aluminum-Zinc-Indium Alloy in 3.5% Sodium Chloride Solution, *Corrosion Engineering*, Feb.

VERNON, W. H. J. (1957) Metallic Corrosion and Conservation in the Conservation of Natural Resources, *Inst. of Civil Engineers*, London, p.105-133.

VUORISTO, P. NIEMI, K., MAKELA, A. and MANTYLA, T. (1994) Abrasion and Erosion Wear Resistance of Cr3C2-NiCr Coatings Prepared by Plasma, Detonation and High-Velocity Oxy-fuel Spraying, *Proceedings of the 7th National Thermal Spray Conference*, June, p.121-126.

WALLINDER, D., PAN, J., LEYGRAF, C. and DELBLANC-BAUER, A. (1999) EIS and XPS study of surface modification of 316LVM stainless steel after passivation, *Corrosion Science*, Feb, Vol. 41, No. 2, p.275-289.

WANG, B. Q. (1996a) Effect of alkali chlorides on erosion-corrosion of cooled mild steel and Cr_3C_2-NiCr coating, *Wear*, Vol.199, p.268-274.

WANG, B. Q. (1996b) The dependence of erosion-corrosion wastage on carbide/metal binder proportion for HVOF carbide-metal cermet coatings, *Wear*, Vol.196, p.141-146.

WANG, B. Q. (1996c) Erosion-corrosion of thermal sprayed coatings in FBC boilers, *Wear,* Vol. 199, p.24-32.

WANG, B. Q. (1998) Dependence of erosion-corrosion on carbide/metal matrix proportion for HVOF Cr_3C_2-NiCr coatings, *Surface Engineering*, Vol.14, No. 2, p.165-169.

WANG, B. Q. and GENG, G. Q. (1990) Erosion-corrosion of thermal spray coatings, *Surface and Coatings Technology,* 43/44, p.859-874.

WANG, B. Q. and LEE, S. W. (1997) Elevated temperature erosion of several thermal-sprayed coatings under the simulated erosion conditions of in-bed tubes in a fluidised bed combustor, *Wear,* Vol. 203-204, p.580-587.

WANG, B. Q., GENG, G. Q., LEVY A. V. and MACK, W. (1992) Erosivity of particles in circulating fluidised bed combustors, *Wear,* Vol. 152, p.201-222.

WANG, Y. and AKID, R. (1996) Role of Nonmetallic Inclusions in Fatigue, Pitting and Corrosion Fatigue, *Corrosion,* Feb., Vol. 52 (2), p. 92-101.

WARMAN Group Development (1991) Technical Bulletin, May.

WEBER, J. (1992) Flow induced corrosion: 25 years of industrial research, *Brit. Corr. Journal,* Vol. 27, No. 3, p.193-199.

WELTON, J. E. (1984) *SEM Petrology Atlas*, The American Association of Petroleum Geologists, Tulsa, Oklahoma, USA

WIELAGE, B., HOFMANN, U., STEINHAUSER, S. and ZIMMERMANN, G. (1998) Improving wear and corrosion resistance of thermal sprayed coatings, *Surface Engineering,* Vol. 14, No. 2, p.136-138.

WIGREN, J., PEJRYD, L. and KARLSSON, H. (1997) The Effect of Tungsten Contamination from the Spray Gun on the Performance of a Thermal Barrier Coating, In: *Proceedings of the 1st United Thermal Spray Conference* edited by Berndt C. C., ASM International, 15-18 Sept. Indianapolis, p.243-253

WILSON, W. H. (1995) Tribology: The Basics and Beyond. In *Kempes' Engineers Year-book*, edited by Sharpe, C., 189-240, M-G Information Services Ltd., UK.

WOLFSON, S. L. (1996) Corrosion control of subsea piping systems using thermal sprayed aluminium coatings, *Material Performance,* Vol. 35, No. 7, p.32-36.

WOOD, R. J. K. and FRY, S. A. (1989) The Synergistic Effect of Cavitation Erosion and Corrosion for Copper and Cupro-Nickel in Seawater, *Journal of Fluids Engineering,* September, Vol. 111, p.271-276.

GLASGOW UNIVERSITY LIBRARY